

# LANDSLIDES

*Causes, Types and Effects*

NATURAL DISASTER  
RESEARCH,  
PREDICTION AND  
MITIGATION SERIES

Ernest D. Werner  
Hugh P. Friedman  
Editors

NOVA

**NATURAL DISASTER RESEARCH, PREDICTION AND MITIGATION SERIES**

# **LANDSLIDES: CAUSES, TYPES AND EFFECTS**

No part of this digital document may be reproduced, stored in a retrieval system or transmitted in any form or by any means. The publisher has taken reasonable care in the preparation of this digital document, but makes no expressed or implied warranty of any kind and assumes no responsibility for any errors or omissions. No liability is assumed for incidental or consequential damages in connection with or arising out of information contained herein. This digital document is sold with the clear understanding that the publisher is not engaged in rendering legal, medical or any other professional services.

# **NATURAL DISASTER RESEARCH, PREDICTION AND MITIGATION SERIES**

## **The Phoenix of Natural Disasters: Community Resilience**

*Kathryn Gow and Douglas Paton  
(Editors)*

2008. ISBN: 978-1-60456-161-6

## **Natural Disasters: Public Policy Options for Changing the Federal Role**

### **in Natural Catastrophe Insurance**

U.S. Government Accountability Office

2008. ISBN: 978-1-60456-717-5

## **Solar Activity and Forest Fires**

*Milan Rodovanovic and Joao Fernando  
Pereira Gomes*

2009. ISBN: 978-1-60741-002-7

## **National Emergency Responses**

*Paul B. Mergenthal (Editor)*

2009. ISBN: 978-1-60692-355-9

## **Earthquakes: Risk, Monitoring and Research**

*Earl V. Leary (Editor)*

2009. ISBN: 978-1-60692-648-2

## **Hurricane Katrina: Impact, Recovery and Lessons Learned**

*Nessa P. Godfrey (Editor)*

2009. ISBN: 978-1-60692-478-5

## **Cyclones: Background, History and Impact**

*Terrance G. LaBeau (Editor)*

2009. ISBN: 978-1-60692-064-0

## **Cyclones: Background, History and Impact**

*Terrance G. LaBeau (Editor)*

2009. ISBN: 978-1-60876-711-3  
(Online Book)

## **Indigenous Knowledge and Disaster Risk Reduction: From Practice to Policy**

*Rajib Shaw, Anshu Sharma  
and Yukiko Takeuchi (Editors)*

2009. ISBN: 978-1-60741-574-9

## **Indigenous Knowledge and Disaster Risk Reduction: From Practice to Policy**

*Rajib Shaw, Anshu Sharma  
and Yukiko Takeuchi (Editors)*

2009. ISBN: 978-1-60876-674-1  
(Online Book)

## **Meltdown: Climate Change, Natural Disasters and other Catastrophes – Fears and Concerns of the Future**

*Kathryn Gow*

2009. ISBN: 978-1-60876-153-1

## **Forest Fires: Detection, Suppression and Prevention**

*Eduards Gomez and Kristina Alvarez  
(Editors)*

2009. ISBN: 978-1-60741-716-3

## **Landslides: Causes, Types and Effects**

*Ernest D. Werner and Hugh P.  
Friedman (Editors)*

2010. ISBN: 978-1-60741-258-8

**NATURAL DISASTER RESEARCH, PREDICTION AND MITIGATION SERIES**

# **LANDSLIDES: CAUSES, TYPES AND EFFECTS**

**ERNEST D. WERNER  
AND  
HUGH P. FRIEDMAN  
EDITORS**

**Nova Science Publishers, Inc.**  
*New York*



Copyright © 2010 by Nova Science Publishers, Inc.

**All rights reserved.** No part of this book may be reproduced, stored in a retrieval system or transmitted in any form or by any means: electronic, electrostatic, magnetic, tape, mechanical photocopying, recording or otherwise without the written permission of the Publisher.

For permission to use material from this book please contact us:

Telephone 631-231-7269; Fax 631-231-8175

Web Site: <http://www.novapublishers.com>

### **NOTICE TO THE READER**

The Publisher has taken reasonable care in the preparation of this book, but makes no expressed or implied warranty of any kind and assumes no responsibility for any errors or omissions. No liability is assumed for incidental or consequential damages in connection with or arising out of information contained in this book. The Publisher shall not be liable for any special, consequential, or exemplary damages resulting, in whole or in part, from the readers' use of, or reliance upon, this material. Any parts of this book based on government reports are so indicated and copyright is claimed for those parts to the extent applicable to compilations of such works.

Independent verification should be sought for any data, advice or recommendations contained in this book. In addition, no responsibility is assumed by the publisher for any injury and/or damage to persons or property arising from any methods, products, instructions, ideas or otherwise contained in this publication.

This publication is designed to provide accurate and authoritative information with regard to the subject matter covered herein. It is sold with the clear understanding that the Publisher is not engaged in rendering legal or any other professional services. If legal or any other expert assistance is required, the services of a competent person should be sought. FROM A DECLARATION OF PARTICIPANTS JOINTLY ADOPTED BY A COMMITTEE OF THE AMERICAN BAR ASSOCIATION AND A COMMITTEE OF PUBLISHERS.

### **LIBRARY OF CONGRESS CATALOGING-IN-PUBLICATION DATA**

Werner, Ernest D., 1956-

Landslides : causes, types, and effects / Ernest D. Werner and Hugh P. Friedman.  
p. cm.

Includes index.

ISBN 978-1-61470-186-6 (eBook)

1. Landslides. 2. Neotectonics. 3. Deformations (Mechanics) I. Friedman, Hugh P. II. Title.  
QE599.A2W47 2009  
551.3'07--dc22

2009015093

*Published by Nova Science Publishers, Inc. ✦ New York*

# CONTENTS

<b>Preface</b>		<b>vii</b>
<b>Chapter 1</b>	Mass Movements in Adriatic Central Italy: Activation and Evolutive Control Factors <i>Domenico Aringoli, Bernardino Gentili, Marco Materazzi and Gilberto Pambianchi</i>	<b>1</b>
<b>Chapter 2</b>	Causes and Effects of Landslides in the Monterrey Metropolitan Area, NE Mexico <i>Juan C. Montalvo-Arrieta, Gabriel Chávez-Cabello, Fernando Velasco-Tapia and Ignacio Navarro de León</i>	<b>73</b>
<b>Chapter 3</b>	Mitigation of Large Landslides and Debris Flows in Slovenia, Europe <i>Matjaž Mikoš and Bojan Majes</i>	<b>105</b>
<b>Chapter 4</b>	Geomatic Methods for Punctual and Areal Control of Surface Changes Due to Landslide Phenomena <i>L. Borgatti, L. Vittuari and A. Zanutta</i>	<b>133</b>
<b>Chapter 5</b>	Using Largest Seismically Induced Landslides for Estimating Earthquake Magnitudes and Topography Changes <i>A.R. Agatova and R.K. Nepop</i>	<b>177</b>
<b>Chapter 6</b>	Recognition of Likely Large-Scale Landslip Failure Surfaces through Geotechnical Core Logging Methods <i>Nick Thompson and Robert J. Watters</i>	<b>201</b>
<b>Chapter 7</b>	Multi-scale Analysis for Estimating Strong Ground Motion and Structure Responses <i>Tsuyoshi Ichimura and Muneo Hori</i>	<b>211</b>
<b>Chapter 8</b>	Prediction of the Seismic Displacement of Landslides Using a Multi-block Model <i>Constantine A. Stamatopoulos</i>	<b>225</b>

---

<b>Chapter 9</b>	Faults Activity, Landslides and Fluvial Catchments Triggered by the 28 December 1908 Messina Strait Earthquake (Italy) <i>Pierpaolo Guarnieri</i>	<b>251</b>
<b>Chapter 10</b>	Special Problems in Landslide Modelling: Mathematical and Computational Methods <i>Jiří Nedoma</i>	<b>263</b>
<b>Index</b>		<b>391</b>

## PREFACE

A landslide is a geological phenomenon which includes a wide range of ground movement, such as rock falls, deep failure of slopes and shallow debris flows, which can occur in offshore, coastal and onshore environments. Although the action of gravity is the primary driving force for a landslide to occur, there are other contributing factors affecting the original slope stability. Typically, pre-conditional factors build up specific sub-surface conditions that make the area/slope prone to failure, whereas the actual landslide often requires a trigger before being released. This book discusses such triggers, as well as their outcomes. Studies of landslides that have occurred in various geographical settings are also among the topics examined in this book, as well as an analysis of the factors that caused them.

Chapter 1 refers to an extended sector of Adriatic Central Italy. It is widely representative of a good part of the remaining peninsular territory, articulated in two fundamental systems: the mountainous system of the Umbria-Marche Apennine, made up prevalently of limestone structured in east verging folds and thrusts, and the second hilly-coastal system made up mainly of marly clays interspersed with sands and conglomerates structured in a monoclinial setting which ends in a narrow anticline along the Adriatic Coast. The structural setting is a consequence of the Pliocene compressive tectonics and its late effects, still active on the coast, and of an extensive tectonic phase which was activated starting in the early Pleistocene, to which a generalised and intense uplifting is associated. The genesis of high fault slopes and thrust fronts and the deep incision of the hydrographic network, to which high relief is connected, are associated to the latter.

Analysed and interpreted are the mass movements which characterise the fundamental physiographic units that make up the systems, whose action (past and present) assumes a fundamental role in the evolution of the physical landscape of the area since it re-modelled a great part of the valley incisions. Huge landslides and deep seated gravitational slope deformations characterise both the tectonic slopes and the transversal valleys of the chain. They affect, besides, the bedrock for a thickness of from a few decametres to a hundred metres and more and are frequent also along the coastal cliffs. Such great gravitational phenomena are less frequent in the hilly unit, but have a great importance there since they often affect villages which originated in the Medieval Ages. In this latter unit, besides, specific mass movements of the clayey bedrock and of the mainly silty-clayey eluvial-colluvial coverings are strongly diffused.



Through the analysis of typical cases, the predisposing, activating and evolutive control factors are identified or hypothesised. These are mainly identified in the lithostratigraphic-structural, tectonic, and seismic factors; in the hydrogeological setting connected to the intrinsic conditions of permeability of the lithotype and to the Pleistocene-Holocene climate oscillations; in the morphological setting induced by the tectonics-climate interaction; in the slope anthropization and in the related farming activities.

In Chapter 2 the authors present the evaluation of landslide causes and effects in the Monterrey Metropolitan Area (MMA), through the analysis of geometrical, geological, and structural data from slopes and the rock masses failure associated with anomalous periods of intense rainfall. The authors also explore other potential landslide causes (e.g., natural and induced vibrations). MMA landslide risk is related to the following factors: (1) *Geography*: this urban center is known as the “Mountain city”, located in the Sierra Madre Oriental (SMO) range border. The valley is surrounded by three intermediate topographic ranges (Cerro de la Silla, Cerro de las Mitras, and Cerro del Topo Chico) and the Monterrey salient, which is the main topographic structure in the area. The MMA border topography is highly scarped and rugged varying from ~540 masl at the valley to ~1,700 masl at the hill slopes. This condition generates high angle slopes which are dissected by a rectangular to dendritic drainage that discharges in the Santa Catarina river, which flows crossing the MMA; (2) *Geology*: the MMA is situated at the borders of two tectonic provinces: the SMO and the Gulf Coastal Plain (GCP). The SMO is a sedimentary sequence constituted mainly by Upper Jurassic to Upper Cretaceous carbonated and clastic marine rocks, complexly folded and thrustured during the Laramide Orogeny. The GCP corresponds to a thick Tertiary clastic sedimentary sequence characterized by an extensional deformation. All hills in and around the MMA are anticlines trending WNW-ESE and plunging into the valley, except for the SMO anticlines. Stratigraphic sequence is widely variable, lithology changes from limestone to shale, with minor contents of sandstone, siltstone, and gypsum. Unconsolidated material located at the foothills is represented by different alluvial deposits related to alluvial fans and detritus, derived from the range scarped walls. Strike and dip of sedimentary layers (WNW-ESE / 90 - 30°) have frequent inclinations in the slope directions. This situation along with a specific structural position and an adequate lithologic combination could increase the risk to trigger landslides; (3) *Climate*: the MMA is located in a zone with intense rainfall periods from August to October (normally tropical storm or hurricane related rainfalls). It is well documented that after a period (> 2 or 3 days) of extraordinary rainfall (> 200 mm) several landslides are triggered mainly in pronounced slopes altered by human activities. Mass movements have caused human and huge economic losses. The last dramatic case was observed during the Emily hurricane in 2005 when a landslide affected around 100 households and urban infrastructure; and (4) *Urban growth*: MMA has experienced an accelerated expansion during the last two decades, causing urban limits to move beyond the valley, reaching mountain toes and hillslopes. These new settlements have produced slope instability by changing the natural stable condition to a precarious stability state. Finally, documented landslides which have damaged the urban infrastructure are a combination of these factors, mainly by the interaction of rainfall and anthropogenic altered slopes. A reevaluation of landslide prevention and mitigation strategies ought to be considered by the MMA authorities.

In Slovenia, a small central European country, in the second half of the 20<sup>th</sup> century minor landslides of different forms (shallow landslides, slides, slumps – average volume of

1000 m<sup>3</sup>, rarely 10,000 m<sup>3</sup>) were prevailing, mainly triggered during short and intense rainfall events or after prolonged rainfall periods of moderate intensities. Unfavorable geological conditions are the main causes for a high slide density ( $\approx 0.4$  slide per 1 km<sup>2</sup>) in Slovenia, despite good vegetation conditions (more than 60% covered by forests).

As explained in Chapter 3, experiences with mitigation of large landslides were rare until the last decade, when four large landslides (Stože, Slano Blato, Strug, and Macesnik) with volumes of the order of 1 million m<sup>3</sup> were triggered and urged for fast mitigation. They can be placed in the category of rainfall-induced landslides that became active in unfavorable geological conditions.

The Stože Landslide with a volume of around 1.5 million m<sup>3</sup> was initiated in November 2000 as a debris landslide on the Stože slope in morainic material above the village of Log pod Mangartom in W Slovenia after a wet autumn period with no snow accumulation but rising runoff coefficients. It turned from a debris landslide on a hill slope into a catastrophic debris flow due to low inertial shear stress caused by high water content.

The Slano Blato Landslide also formed in fossil landslide masses on a contact of calcareous and flysch formations during wet autumn period in November 2000. It is ever since progressively enlarging behind the main scarp via retrogressive slumping of new and freshly weathered material that due to high water pore pressures turns into a viscous earth flow.

The Strug Landslide is a very good example of a complex slope movement, which started in December 2001 as a rockslide with a consequent rock fall that triggered secondary landslides and caused occasional debris flows. In 2002 over 20 debris flows were registered in the village of Koseč below the Strug Landslide, mainly on days with a daily rainfall accumulation of 20 to 30 mm. In 2003 and 2004 no further debris flows could be observed, therefore these events in the Strug landslide area were defined as material and not rainfall driven events.

The Macesnik Landslide above the village of Solčava in N Slovenia near the border with Austria was triggered in autumn 1989. Till 1994 there were no activities on the landslide. In the period between 1994 and 1998 the advancement of the landslide on the slope was utmost intense. Firstly, the landslide destroyed state road, and a new pontoon bridge had to be built instead. In 1996, the landslide advanced and destroyed a turn on the same state road. In 1999, a large rock outcrop stopped the advancement of the landslide. Further advancement would possibly destroy several farmhouses on its way down the valley towards the Savinja River. Possible damming of this alpine river would cause a catastrophic flooding.

The ongoing mitigation of these landslides is subjected to a special law adopted in 2002 (revised in 2005). The final mitigation is planned to be finished before the end of 2010, with estimated costs of 60.5 Mio € for all activities planned. These costs should be added to the estimated sum of 83.5 Mio € as the final remediation costs for all other registered active small-sized landslides in Slovenia. Practical experiences in Slovenia with large landslides up to now show that only strict and insightful co-ordination, interdisciplinary approach and adequate financial support may lead to a successful mitigation.

Landslides are one of the major causes of natural disasters worldwide. In the field of landslide studies, much effort has been put into investigating landslide causes and mechanisms. Geodetic and Remote Sensing methods, in addition to geological, geotechnical and geophysical techniques are fundamental to study and understand landslides. In fact, besides the use of geotechnical devices that are mainly devoted to on-site and punctual

monitoring, Geomatics may play a relevant role in the assessment of superficial movements, especially on large and non accessible areas. Nowadays, the integration of several techniques allows a wide range of landslide types in different environmental contexts to be surveyed and controlled. Besides alerting and alarming purposes, the acquired data set may also serve in numerical modeling, from the set-up of 2D- and 3D-descriptions of the slope, up to the validation of the results.

Differential Leveling, GNSS, Total Station, Laser Scanning (both airborne and terrestrial), high resolution space-borne imagery, Photogrammetry and Radar Interferometry can be used in each step of landslide studies, from site characterization onwards: to detect and to map landslide areas; to classify landslide type, state and style of activity; to monitor landslide activity; to evaluate the probability of occurrence within a given area in landslide hazard assessment; in structural and non-structural mitigation of landslide risk.

The monitoring of surface displacement may be based on topographic punctual observations or on non-contact methods.

Point-based measurements are carried out on the field by means of GNSS (by static, fast static, kinematic, Real Time Kinematic methods) or by Total Stations (triangulation, trilateration, intersection - resection, traverses, radial sides hot methods and more generally 3D or 2D networks). The elevations are determined by spirit or trigonometric leveling. All these techniques deliver 1D, 2D or 3D coordinates of some isolated point on the landslide body, and, therefore, an estimate of movement rates, along with the evaluation of their precision.

Non-contact methods are becoming a widespread technique to measure wide areas and to quantify landform changes, providing information on the displacement fields or on surface changes of point clouds. By the interpolation of point clouds, Digital Elevation Models (DEMs) are generated as support of geomorphological survey and mapping. Then, by multi-temporal DEMs comparisons, morphological changes can be assessed on a metrical basis.

Chapter 4 describes the classical and modern methods that may be adopted for analyzing superficial landslide movements, focusing on pros and cons of each method with respect to geological, geomorphological and environmental conditions.

As discussed in Chapter 5, earthquake triggered landslides are widespread phenomena in tectonically active mountain provinces. Their abundant occurrence and large volumes of displaced soil indicate great influence on the topography changes. Using such an informative object as the largest seismically induced paleolandslide the authors broadened the paleoseismogeological method developed in Russia since the 1960s. So far most of research has focused on coseismic fault motion. The seismogravitational dislocations have been used mainly for establishing epicentral zones and the timing of old earthquakes. Using the parameters of the largest landslides allow the authors to estimate magnitudes of prehistoric earthquakes, calculate the total volume of earthquake triggered landslides, the contribution of landslides caused by aftershocks and erosion rate due to seismically induced landslides. This approach was tested in the mountainous, seismically active southeastern part of Russian Altai – an area of numerous giant Holocene seismically induced landslides where the Chuya earthquake ( $M_S = 7.3$ ) took place in 2003.

Despite several objective difficulties including: 1) establishing the seismic origin of paleolandslides; 2) estimating the typical size of the largest landslides for particular region and time period; 3) determination of the landslide parameters where the joining of several detachments or considerable change of landslide's body has occurred, this approach

demonstrates the principle possibility of using the largest seismically induced landslides for estimating the paleoseismicity and earthquake induced topography changes.

The Hawaiian Scientific Drilling Project (HSDP) Phase 1 deep drilling project produced a continuous rock core extending 3.1 km into Mauna Kea volcano on the island of Hawaii. This core generally consisted of lithified but often unconsolidated subaerial and submarine lava flows (basalts) with minor amounts of ash, soil and sedimentary rocks. The primary intention for this project was to provide information about the origin and geochemical, magnetic and hydrologic conditions of the volcano but subsequent geotechnical analysis of the rock core has identified a significant natural hazard may also be present through recognition of a potential large-scale landslide failure surface, as discussed in Chapter 6.

Commonly used qualitative geotechnical logging methods, including RQD and limited GSI and RMR techniques, were initially performed. This effort identified a significant weak zone beginning at a depth of approximately 1.1 km below the ground surface, the location of a particularly unconsolidated region of hyaloclastite, or rapidly quenched basaltic glass. Subsequent strength testing of the core (point load) allowed a quantitative strength profile to be created for the entire depth of the core, thus representing the vertical strength of the volcanic edifice. Though this profile characterizes only a minute area of the overall edifice, this analysis has shown how geotechnical rock core logging methods may be implemented to identify otherwise unseen hazards or significant changes in rock mass quality.

While full three-dimensional (3D) numerical simulation is a solution to estimate strong ground motion and a seismic structure response for a given earthquake, it is difficult to carry out numerical computation because of its huge computational cost; the order of a target domain size is  $10^{4-5}$  m and the target resolution required is  $10^{-2-0}$  m. In Chapter 7, the authors present an efficient approach which is based upon multi-scale analysis to make a 3D simulation of wave propagation and amplification as well as seismic responses of an infrastructure. The formulation of the multi-scale analysis is presented, and it is validated by comparing a strong ground motion and a seismic structure response which is obtained by directly analyzing the whole system. The usefulness and applicability of this multiscale approach are also discussed.

Newmark's sliding-block model is usually employed to predict the seismic displacement of slopes. Yet, when displacement is large, the conventional sliding-block model predicts displacements that are larger than expected for the given input motion and soil strength. Alternatively, to simulate slope movement when the displacement is large, a multi-block sliding model has been proposed. Similarly to the Sarma (1979) stability method, a general mass sliding on a slip surface that consists of  $n$  linear segments is considered. In order for the mass to move, interfaces where resisting forces are exerted must be formed between nodes of the slip surface. Thus, the mass is divided into  $n$  blocks sliding in  $n$  different inclinations. For landslides, the masses and lengths of each block entering the calculation are updated in terms of the distance moved. In addition, constitutive equations that simulate strength degradation along the slip surface coupled with the multi-block model are proposed in order to simulate the triggering of the slides. Chapter 8 first describes the multi-block model and its extensions for the prediction of the seismic displacement of landslides outlined above. Then, it validates the above method by predicting the response of a well-documented earthquake-induced landslide.



The 28 December 1908 Messina Strait earthquake ranks among the most disastrous historical events in the Mediterranean, causing more than 100,000 fatalities and the nearly total devastation of the cities of Messina and Reggio Calabria.

In recent years, one of the most debated issues in this context has been the definition of the source of the 1908 earthquake. Numerous studies have dealt with the subject, and given the lack of evidence of surface faulting, the most plausible hypotheses propose a source model with a blind fault fitting the concepts of rupturing and with the inversion of the historical levelling data.

Chapter 9 presents a synthesis of geological field work associated with geomorphological analysis that define a tectonically active fault system, to which can be attributed fluvial catchments and landslides.

The novel aspect of this work comes from the comparison made between the present topography and 19th century topographic map. The analysis reveals that the modifications of the drainage network and the landslide activity, located in correspondence of some active faults, have occurred after the 1877, probably triggered by the 1908 earthquake.

As explained in Chapter 10, regions with great mountain landslides, regions with bigger climatic events (i.e., hurricanes and deluges) and regions with frequental seismic events (i.e., bigger earthquakes) with ensuing landslides represent one of the most detrimental natural hazards. These events have been responsible for some of most destructive natural disasters in terms of human and economical losses.

*Chapter 1*

## **MASS MOVEMENTS IN ADRIATIC CENTRAL ITALY: ACTIVATION AND EVOLUTIVE CONTROL FACTORS**

***Domenico Aringoli, Bernardino Gentili\*, Marco Materazzi  
and Gilberto Pambianchi***

Dipartimento di Scienze della Terra, Università degli Studi di Camerino (UNICAM),  
Camerino, Italy

### **Abstract**

This work refers to an extended sector of Adriatic Central Italy. It is widely representative of a good part of the remaining peninsular territory, articulated in two fundamental systems: the mountainous system of the Umbria-Marche Apennine, made up prevalently of limestone structured in east verging folds and thrusts, and the second hilly-coastal system made up mainly of marly clays interspersed with sands and conglomerates structured in a monoclinical setting which ends in a narrow anticline along the Adriatic Coast. The structural setting is a consequence of the Pliocene compressive tectonics and its late effects, still active on the coast, and of an extensive tectonic phase which was activated starting in the early Pleistocene, to which a generalised and intense uplifting is associated. The genesis of high fault slopes and thrust fronts and the deep incision of the hydrographic network, to which high relief is connected, are associated to the latter.

Analysed and interpreted are the mass movements which characterise the fundamental physiographic units that make up the systems, whose action (past and present) assumes a fundamental role in the evolution of the physical landscape of the area since it re-modelled a great part of the valley incisions. Huge landslides and deep seated gravitational slope deformations characterise both the tectonic slopes and the transversal valleys of the chain. They affect, besides, the bedrock for a thickness of from a few decametres to a hundred metres and more and are frequent also along the coastal cliffs. Such great gravitational phenomena are less frequent in the hilly unit, but have a great importance there since they often affect villages which originated in the Medieval Ages. In this latter unit, besides, specific mass movements of the clayey bedrock and of the mainly silty-clayey eluvial-colluvial coverings are strongly diffused.

---

\* E-mail address: [bernardino.gentili@unicam.it](mailto:bernardino.gentili@unicam.it). Tel: +39 0737 402604-03-05; Fax: +39 0737 402644; Via Gentile III da Varano, 62032 Camerino, Italy.

Through the analysis of typical cases, the predisposing, activating and evolutive control factors are identified or hypothesised. These are mainly identified in the lithostratigraphic-structural, tectonic, and seismic factors; in the hydrogeological setting connected to the intrinsic conditions of permeability of the lithotype and to the Pleistocene-Holocene climate oscillations; in the morphological setting induced by the tectonics-climate interaction; in the slope anthropization and in the related farming activities.

**Keywords:** Neotectonics; Geomorphological evolution; Pleistocene-Holocene; Deep-seated gravitational slope deformations; Landslides; Human impact; Hydrogeological “disorder”; Central Italy.

## 1. Introduction

It is well known that the deformation and/or the dislocation of rock masses are mainly connected to endogenic forces that exert themselves regionally or on more limited sectors over long periods of time (millions of years) and mainly in a discontinuous way, and that are, in any case, not controlled by the local morphological setting (tectonic or tectonic-gravitational phenomena). On a local scale and during shorter periods of time, analogous but less visible effects can be produced by gravity alone. In fact, it was possible to recognise with difficulty and not always surely landforms not directly attributable to tectonic deformation to which these, in the situation of uncertainty, often were generically associated. They consist of deep and wide deformation phenomena of the bedrock which strictly depend on the geological setting itself and on the geometry of the slope: such that the phenomena are called *deep-seated gravitational slope deformations* (DSGSDs). Their evolution generally occurred in steps, due to the extreme slowness of the continuous deformation that is periodically interrupted by instantaneous phenomena of failure (Harrison and Falcon, 1934; Stini, 1941; Jahn, 1964; Beck, 1967; Zischinsky, 1969; Zaruba and Mencl, 1969; Nemčok, 1972; Radbruch-Hall et al., 1976; Mahr and Nemčok, 1977; Ter-Stefanian, 1977; Varnes, 1978; Guerricchio and Melidoro, 1981; Sorriso-Valvo Ed., 1984; Savage and Swolfs, 1986; Savage and Varnes, 1987; Dramis and Sorriso-Valvo, 1994; Hutchinson, 1995; Agliardi et al., 2001).

These phenomena, which constitute the preparatory phase of the activation of huge landslides, rarely reach collapse. This can occur, reasonably, by means of high magnitude seismic shocks or, more rarely, due to extreme meteorological events. Similar deformation mechanisms that involve more limited portions of the slope are predisposing factors to the genesis of gravitational phenomena, which are differentiated from the previous ones for the presence of well-defined shear planes (Cotecchia, 1978; Varnes, 1978; Savage and Varnes, 1987; Hutchinson, 1988; Cruden and Varnes, 1996; McInnes and Jakeways, 2002; Rybar et al., 2002; Natau et al., 2003). From these latter, mass transport phenomena, such as debris flows and mud flows, must be distinguished (Brunsden, 1984; Costa, 1984; Pierson and Costa, 1987; Takahashi, 1991).

Important results have been achieved with relation to the recognition of activation and evolutive control factors of the phenomena and to the definition of various kinematics. To these a specific and exhaustive nomenclature has been given, which overrides localisms and has been accepted at an international level.

The studies cited, besides, have clearly demonstrated that amongst the exogenous agents that realise the remodelling of the past and present landscape, gravity has gotten a position of

primary importance in the evolution of the slopes. In particular, this happens when the slopes are characterised by sufficient relief to activate and develop specific kinematics within favourable geological and climatic contexts.

In this framework, the predominant role held by mass movements amongst the various gravitational phenomena was pointed out, even if sporadically, from the first half of the 20th century. Afterwards, the topic was carried out and developed in a particularly significant way, also as a result of the increasing applicative interest associated to it. In fact the high level of risk for human activities represented by the gravitational phenomena favoured ever more specific and in-depth analyses. The latter are fundamental not only for the correct and complete understanding of the phenomena themselves, but also for the mitigation of the risk connected to them. These are essential operations for a correct and modern territorial planning and management.

Analogous strong impulse of the research developed in Italy as well. This was favoured by the notable diffusion of gravitational phenomena on the territory with relation to its complex geological setting, by the intense recent and present tectonic and seismic activities, by the favourable morphostructural setting and, subordinately, to the favourable morpho-climatic conditions (Agnesi et al., 1978; Coppola et al., 1978; Genovois and Prestininzi, 1979; Dramis, 1984; Sorriso-Valvo, 1984, 1987 and 1989; Carrara et al., 1985; Mortara and Sorzana, 1987; Semenza, 1966-67 and 2001; Buccolini et al., 1992; Antonini et al., 1993; Dramis et al., 1995; Guida et al., 1995; Govi and Turitto, 1996; Panizza et al., 1996; Pasuto and Soldati, 1996; Canuti et al., 1998; Aleotti et al., 2000; Guadagno and Perriello Zampelli, 2000).

Slopes characterised by sufficient energy to activate the phenomena in question are common throughout much of Italian territory as they are in other zones on the earth characterised by tectonic activity. They are fully represented in the geomorphological context of central Italy (Fig. 1). In particular, in the Adriatic side where the present study has been carried out (Fig.2), the fundamental “structural” elements of the landscape are made up, in general, of two systems of regional extension, almost homogeneous from a geological and geomorphological point of view: the mountainous chain of the central Apennine (maximum height of 2,476m a.s.l. at Mt. Vettore and of 2,912m a.s.l. at Gran Sasso d’Italia) and the peri-Adriatic high-hilly and hilly landscape (from 500–700 to 1,100m a.s.l. in the southern sector). The neotectonic activity and the intense Quaternary exogenous dynamics have articulated the two systems into minor physiographic units: tectonic basins on the western side of the chain; thrust fronts characterised by sub-vertical slopes on the eastern side; transversal valleys cutting into the whole area; coastal cliffs.

The present study constitutes a synthesis of the most important results obtained in about thirty years of research done to define the importance of gravitational morphogenesis in the geomorphological evolution of Central Italy, particularly of the Adriatic side. Starting from a critical analysis of previous studies, it discusses the predisposing and evolutive control factors of the mass movement which cause the dislocation of bedrock and/or of eluvial-colluvial deposits, specific of the different physiographic units mentioned. The relative kinematics are illustrated by geological models built for a number of type-phenomena recently recognised and analysed, or with reference to previous works of the authors. As far as the kinematics and nomenclature used in the study cases are concerned, given that they make implicit reference to the authors cited above and since they constitute solid scientific acquisitions, the authors of the reference will not be repeatedly cited.



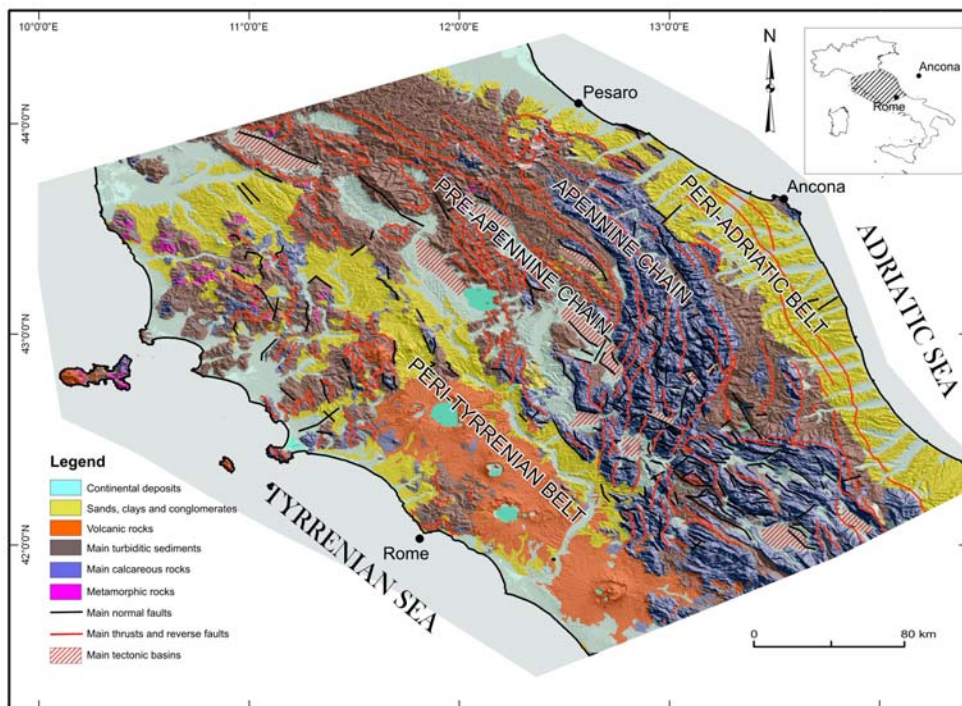


Figure 1. Litho-structural sketch of central Italy.

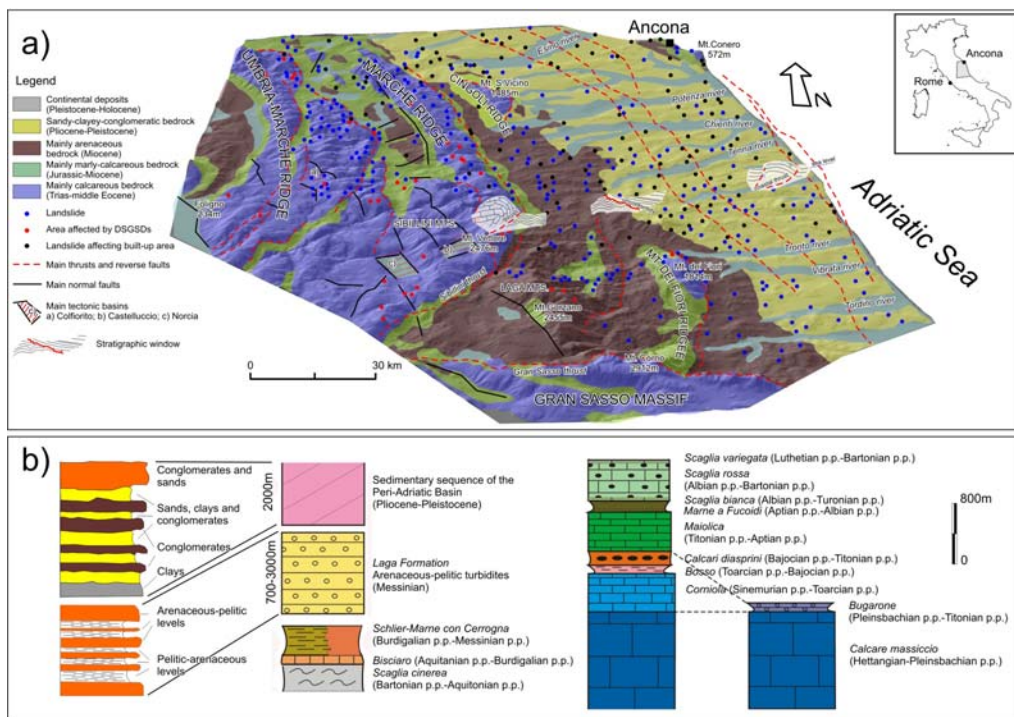


Figure 2. a) Geological sketch of the Adriatic central Italy and main mass movements; b) schematic stratigraphic column of the Umbria-Marche Succession (modified after Pierantoni et al., 2005).

## 2. Regional Setting

### 2.1. Geology, Neotectonic and Seismicity

The geological substratum of Central Italy is made by: terrigenous, volcanic and metamorphic lithotypes in the peri-Tyrrhenian belt; marly-calcareous and silicoclastic, in the pre-Apennine and Apennine sector; terrigenous, in the peri-Adriatic belt (Fig. 1). The outcropping rocks in the Apennine Chain and in the peri-Adriatic belt (the study area), belong to a marine succession originated between the late Trias and the early Pleistocene (Figs. 2a and b) (Centamore and Deiana, 1986; Deiana and Marchegiani, 2002; Cantalamessa and Di Celma, 2004). The most ancient group (Late Trias–Messinian p.p.) outcrops in the Apennine chain and is made by a sedimentary *multilayer* more than 2,000 m thick (“Umbria-Marche Sequence”); from bottom to top, only the essential lithostratigraphic elements fundamental to the correct and complete understanding of the gravitational phenomena being studied are described.

- (a.) *Calcare massiccio* (Hettangian–Pleinsbachian p.p.): stratified limestone in tough blocks without noticeable vertical heterogeneities, about 700m thick.
- (b.) *Formazione del Bugarone* (Pliensbachian p.p.–Titanian p.p.): it is made of limestones and marly limestones with frankly greenish intercalations of marls in the marly-calcareous facies; it outcrops only locally in substitution of the three previous formations with an overall thickness of 30–40 meters.
- (c.) *Corniola* (Sinemurian p.p.–Toarcian p.p.): micritic limestones finely stratified, with brown or light grey chert and with grey-green pelitic intercalations, rather abundant both in the upper part and at the base; the thickness varies from 150 to 400 meters
- (d.) *Formazione del Bosso* (Toarcian p.p.–Bajocian p.p.): it is made of a marly and marly-calcareous unit with medium-thick strata (Rosso Ammonitico); a second unit is made of limestones and marly limestones (Calcari a Posidonia). The overall thickness varies from 40 to 120 meters.
- (e.) *Calcari diasprini umbro-marchigiani* (Bajocian p.p.–Titanian p.p.): limestones and cherty limestones with thick stratification; thickness can reach 100 meters.
- (f.) *Maiolica* (Titanian p.p.–Aptian p.p.): whitish micritic limestones, in medium strata, with thin pelitic intercalations that increase towards the top of the formation. The thickness is comprised between 150 and 400 meters.
- (g.) *Marne a Fucoidi* (Aptian p.p.–Albian p.p.): the lower portion is made up of multicolored, closely layered marls and, subordinately, limestones that towards the top becomes cherty, with frequent marly levels; 80–100 metres thick.
- (h.) *Scaglia Group* (Albian p.p.–Aquitano p.p.). At the base, thin and medium layers of whitish marly limestones with black chert, (*Scaglia bianca*, 50–40 metres thick). They are followed by 200–400 metres of limestones and marly limestones that varies in color from pink to red, with chert of the same colour and analogous stratification (*Scaglia rossa*); upward, 20–40 m of polychrome of limestones, marly limestones and marls, which alternate in medium and thin layers (*Scaglia variegata*); the group ends with 100–250 metres of marly limestones, calcareous marls and clayey marls in thin layers (*Scaglia cinerea*). The transition between the Scaglia Bianca and the Scaglia

rossa formations is marked by the “*livello Bonarelli*”, 1-2 metres thick, made up of blackish bituminous clays.

- (i.) *Bisciaro* (Aquitanian p.p.-Burdigalian p.p.): limestones, cherty limestones, marly limestones and calcareous and clayey marls, in medium and sometimes thick layers; thickness comprised between 20 and 60 metres.
- (j.) *Schlier*, *Marne con Cerroghna* and *Marne a Pteropodi* (Burdigaliano p.p.-Messiniano p.p.): they consist of litho-stratigraphic units mainly constituted by marls, clayey and calcareous marls, sometimes associated with banks of calcareous turbidites (Cerroghna). The first formation (up to 200 m thick) outcrops in the northern pedemountain sector: the other two (up to 300m and 20-50 m thick respectively) outcrop in the southern one.

Arenaceous, arenaceous-pelitic and pelitic-arenaceous turbiditic sediments, whose thickness varies between the 700 metres of the northern sector to the 3,000 metres of the southern one, follow in succession along the eastern pedemountain margin and, above all, in the southern sector of the chain (*Laga* formation, Messinian). They are stratified in banks, whose thickness can reach a few decametres in the chain sector (Laga Mountains), while they have a centimetric and decimetric thickness in the pedemountain belt.

On the basement constituted by these final formations lay, in transgression, lithotypes of a Pliocene-Pleistocene sedimentary marine cycle (middle Pliocene-early Pleistocene); the contact between pre-transgressive and post-transgressive lithotypes is clearly evidenced by an erosive surface (roughly parallel to the strata plains and with directions that coincide to their immersion) that interrupts the Messinian sediments and which, therefore, must have been sub-horizontal originally; bland waves can be recognised in a roughly N-S direction (Gentili et al., 1995).

The post-transgressive succession begins, in the northern sector, with a thick and rigid rocky body, resulting from alternation of sandstones, calcarenites and thin and discontinuous conglomeratic levels, separated by rare pelitic ones; these are followed, eastward, by huge pelitic and pelitic-arenaceous units. Sandy-conglomeratic clastic levels are intercalated between these, at various stratigraphic heights. The sandy-conglomeratic levels increase their thickness and extension in the coastal belt, where they close the sedimentary cycle. In the southern sector, the base of the succession is made up of clayey levels; the pelites, classified on the basis of their grain size in clayey silts or silty clays, due to their generally high content of carbonates, are also called marly clays (Esu and Martinetti, 1965).

The structuring of the Messinian and pre-Messinian bedrock (Fig. 2) mainly occurred in the early Pliocene; the fundamental elements are represented by the association of folds and thrusts (outcropping or buried), specific of the compressive tectonics migrated from west to east and manifested, with different intensity, in the N-S direction. In fact, to the latter is closely connected the morphological setting of the chain, due to the fusion of the southern endings of the Umbria-Marche and Marche ridges into the “massif” of the Sibillini Mountains and to the tectonic overlapping of the latter onto the Terziary formations, mainly constituted by the Laga formation, along the Sibillini thrust. This element, southward, joins itself with other two important thrusts: the Olevano-Antrudoco thrust, with which it forms a regional structure, arched, with eastern convexity; the Gran Sasso thrusts, with marked northern convexity, which overlaps a mainly calcareous tectonic unit onto the terziary turbidites of the Laga formation. To the main surfaces of the above structures, secondary thrusts are

associated. Eastward from the chain, minor ridges are present, still composed of the “Umbria-Marche Sequence” lithotypes: the Montagna dei Fiori ridge, overthrust onto the Messinian terrigenous sediments; Mount Conero, along the Adriatic coast, structured by tectonic dislocations of uncertain kinematics and, subordinately, by thrusts. The Laga formation is instead characterised by sinclinalic folds with a very wide radius, interrupted by anticlinals of limited extension and thrust planes that had occurred within the lithotypes of the same formation (Calamita and Deiana, 1988; Centamore et al., 1992).

The sediments of the Pliocene-Pleistocene cycle have a regular monoclinial setting, whose inclination gradually diminishes starting from the western sector ( $15^{\circ}$ - $20^{\circ}$ ) to the Adriatic coast ( $5^{\circ}$ - $6^{\circ}$ ); the immersion goes, respectively from ENE to NE. Therefore, on the surface, the structure assumes all in all the configuration of a double flexure, with up-looking concavity and with the main axis oriented in the Apennine direction and the secondary one in an E-W direction. The structure is more complex in depth; in fact the basal sediment of the cycle (middle Pliocene) disappear immediately east of the extreme western sector of outcropping and re-appear about 30 km to the east, near the Adriatic coast (Fig. 2a). This setting, on one hand, is the result of the activation, from the end of the early Pleistocene, of an extensional tectonic phase associated with an overall and intense uplifting, developed with different entities both in the W-E and in the N-S direction; on the other hand it is consequent to the delayed effects of the compressive tectonic phase mentioned, by now not very intense and migrated towards the Adriatic coast (Deiana and Piali, 1994; D’Agostino et al., 2001). Rare normal faults (Apenninic and anti-Apenninic) with weak vertical displacement, dislocate the structure.

The effects of the extensional tectonics are little evident in the Laga formation, while they assume great importance on the western flank of the calcareous-marly chain. There, in fact, normal faults that run mainly in a N-S and NNW-SSE direction with westward dip, dislocate the previous compressive structures with displacement even of 100 metres, producing step-like blocks. Their combination with anti-Apennine faults generated the intra-mountain depressions of Colfiorito, Castelluccio and Norcia. Some of these faults are still active and able to generate strong earthquakes (Cello et al., 1998).

The study area is to be found completely within such a neotectonic context, responsible for an important seismic history characterised by intense and prolonged sequences (lasting weeks or months) and followed by periods of relative calm (Fig. 3). The oldest historic testimony refers to strong earthquakes in the period between the IXth and IIInd centuries B.C., whose epicentres were mostly on the western side of the Apennine chain; they caused the destruction of the first human settlements (801 and 446 B.C. in Spoleto; 217 B.C. in Val Tiberina; 102 B.C. in Valnerina). The earthquakes of highest magnitude (X MCS-Mercalli-Cancani-Sieberg) took place in central Italy in the XIVth and XVIIIth centuries; some of these, in particular, had destructive effects and caused thousands casualties.

Between the years 1000 and 1984 there have been about 60 earthquakes of an elevated degree (VIII-IX MCS-Mercalli-Cancani-Sieberg); the most intense phenomenon (IX MCS-Mercalli-Cancani-Sieberg), happened in 1703 and with epicentre located on the south-west slope of the Sibillini Mountains, it was characterised by numerous main shocks and its propagation towards the south also affected the northern sector of the Lazio-Abruzzo Apennine. Events of comparable intensity also affected the “nucleus” of the chain: the area between Serravalle di Chienti and Nocera Umbra, in 1279 (IX MCS-Mercalli-Cancani-Sieberg); the “Fabriano earthquake” in 1741 (IX MCS-Mercalli-Cancani-Sieberg); the area of

Camerino in 1799 (X MCS-Mercalli-Cancani-Sieberg). In 1781 (X MCS-Mercalli-Cancani-Sieberg) and in 1785 (IX MCS-Mercalli-Cancani-Sieberg) the earthquakes of the area showed numerous shocks of growing intensity, as was observed during the most recent destructive events: the "Norcia earthquake" in 1979 ( $M_w = 5.9$ , IX-X MCS-Mercalli-Cancani-Sieberg) and that of Colfiorito in 1997-1998 ( $M_w$  5.8-6.0, IX-X MCS-Mercalli-Cancani-Sieberg) (Baratta, 1901; Postpischl, 1985; Cello et al., 1998).

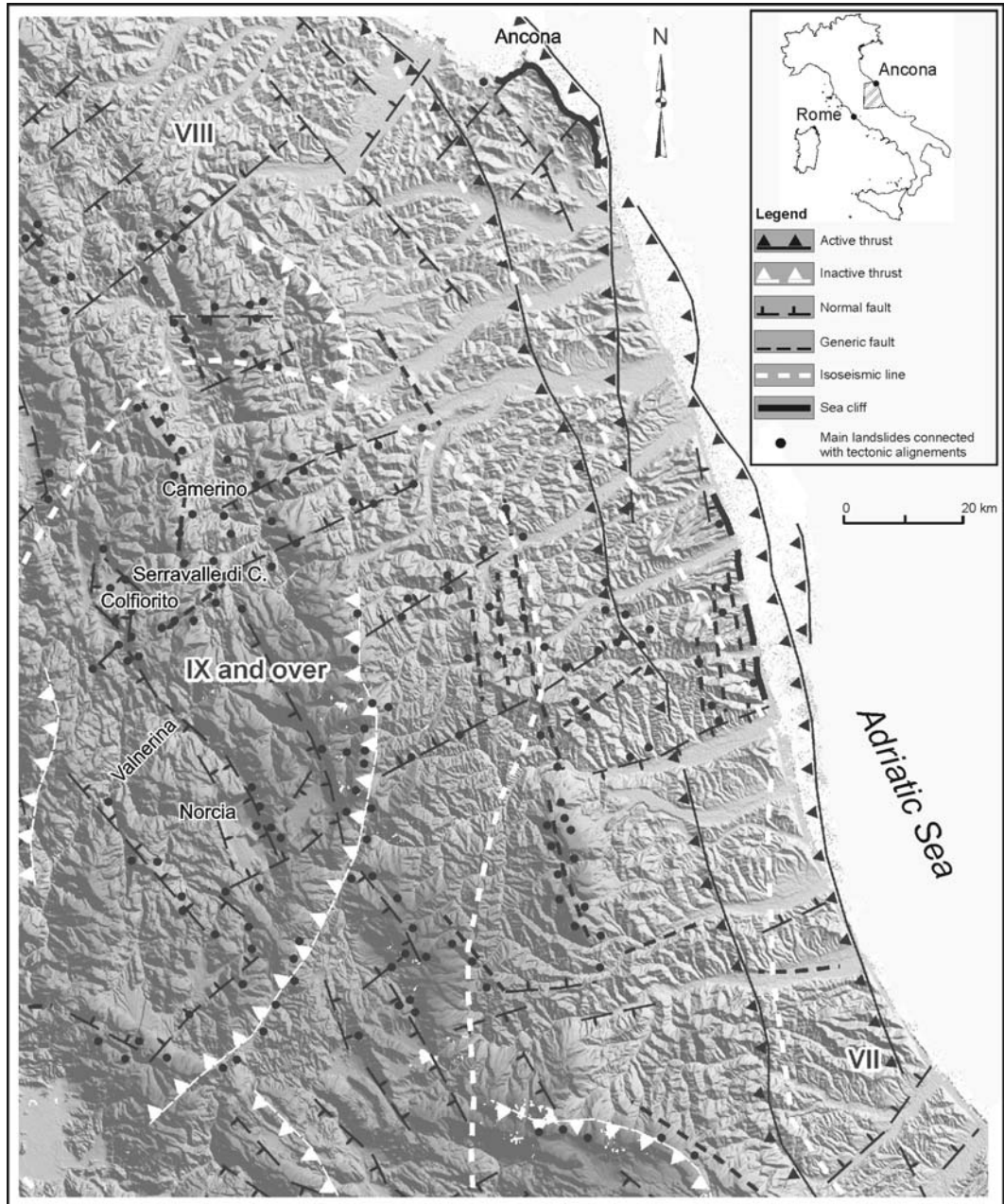


Figure 3. Main neotectonic elements and related main mass movements. Isoseismic lines from the National Institute of Geophysics and Volcanology (MCS scale).

## 2.2. Geomorphological Evolution and Climatic Conditions

The physical landscape of central Italy, like the rest of the Italian territory, in general results to be closely in conformity with its geological setting. In fact the main morphostructures, made of relieves and depressions, correspond, respectively, to areas of intense deformation and uplifting, to tectonic basins and to areas of moderate deformation and uplifting, not rarely in correspondence with monoclinical setting in the more recent terrain. In correspondence with the thrusts, due to the important shortenings produced and when there is the overlapping of rigid masses over more ductile lithotypes, are visible the clearest, most evident and the most extensive morphologic contrasts, who themselves are accentuated by selective erosion phenomena. In particular in the frontal zones, the sub-vertical calcareous slopes (relief up to and over 1,000 m) join at its foot with the much more gentle ones modelled in the marly-arenaceous lithotypes and are characterised by relief limited to a few hundreds of metres.

Till the end of the early Pleistocene the “paleo” landscape, modelled by intense areal erosion connected to arid or sub-tropical humid climatic conditions, both favourable to the peneplanation of the relief (Butzer, 1976; Haq et al., 1987), must have been characterised in general by gentle landforms characterized by weak relief (“paleosurfaces”), though not excluding the presence, on a wider scale, of sectors with even significant differences of height, considering their structural characteristics (Desplanques, 1975; Dramis et al., 1991; Gentili and Pambianchi, 1999).

Important morphotectonic elements are represented by the important undulations, N-S oriented, of the “paleosurface”, whose highest zones correspond to the most uplifted areas both in the Apennine ridge and in the peri-Adriatic belt; they constitute transversal ridges with respect the whole area and correspond to the main cliffs on the Adriatic coast.

At the end of Pleistocene, together with the beginning of the former phase of general and intense tectonic uplift that reached its maximum during the middle Pleistocene, the first elements of the landscape already outlined were consolidated. In fact the tectonic basins mentioned, whose oldest lacustrine deposits dated back to the early Pleistocene, become deeper (Blumetti and Dramis, 1993); a general and rapid deepening of the hydrographic network occurred, oriented according to the regional topographic gradient but often driven by anti Apenninic faults and by the transversal ridges mentioned, which conditioned at times, the geometry and the sedimentation processes (Coltorti et al., 1996). The evolution of the latter caused the isolation and the reduction in discontinuous limbs of the “paleosurface”, the genesis of further “surfaces” at lower elevation (remnants of wide valleys) and the incision of deep and narrow valleys, characteristics of a landscape with strong relief. A similar morphological setting favoured an intense slope dynamics, dominated by the action of gravity, that modified in a decisive way the form of the original valleys.

Such indirect tectonic effects on the morphogenesis have been emphasized or minimized by successive erosion and/or sedimentation processes associated with the different climatic conditions that occurred in the area during the middle and the late Pleistocene, which are:

- glacial and periglacial processes in mountain areas, whose respective geomorphologic evidence is given by U-shaped valleys, cirques and moraines on the highest parts of the Sibillini Mountains, of the Laga Mountains and of Gran Sasso d'Italia (Jaurand, 1998; Bisci et al., 1999) and by several generations of stratified



slope deposits that regularize the medium-low portions of the slopes. The latest belong to the end of late Pleistocene (Castiglioni et al., 1979; Coltorti and Dramis, 1995);

- accumulation at the foot of thrust fronts, of thick and wide polygenic detritic coverings;
- placing, along the main valleys, of three orders of terraced alluvial deposits, mainly made up of polygenic calcareous gravels. Their positioning began in the middle Pleistocene (first order terrace), continued in the final interval of the same period with the genesis of the second order terrace and concluded with the pleniglacial phase of the late Pleistocene (third order terrace). The whole sequence of the three orders of terracing, characteristic of the Adriatic rivers of central Italy, are generally to be observed in the mid-lower portions of the main rivers (Coltorti et al., 1991; CILLA et al., 1996).

In the Periadriatic belt, besides, the incision of the hydrographic network in the Plio-Pleistocene lithotypes disposed in a monoclinical structure produced consequent main valleys and monoclinical minor valleys. The former are almost symmetric while the latter, usually incised in the pelitic levels, are characterized by a marked asymmetry, strictly congruent with the stratigraphic and structural setting of the bedrock; channels corresponding to the N-S fractures are not rare. Therefore the relief is made by a succession of morphostructures with a characteristic triangular shape with the bases facing east and bordered westward by high structural slopes: this is a typical *cuesta* morphology whose fronts, more elevated in the central-western sector, are generally at a height of between 500 and 700m a.s.l. and converge to the south into the Mt. Ascensione “massif” (1,110m a.s.l.) (Fig. 4).

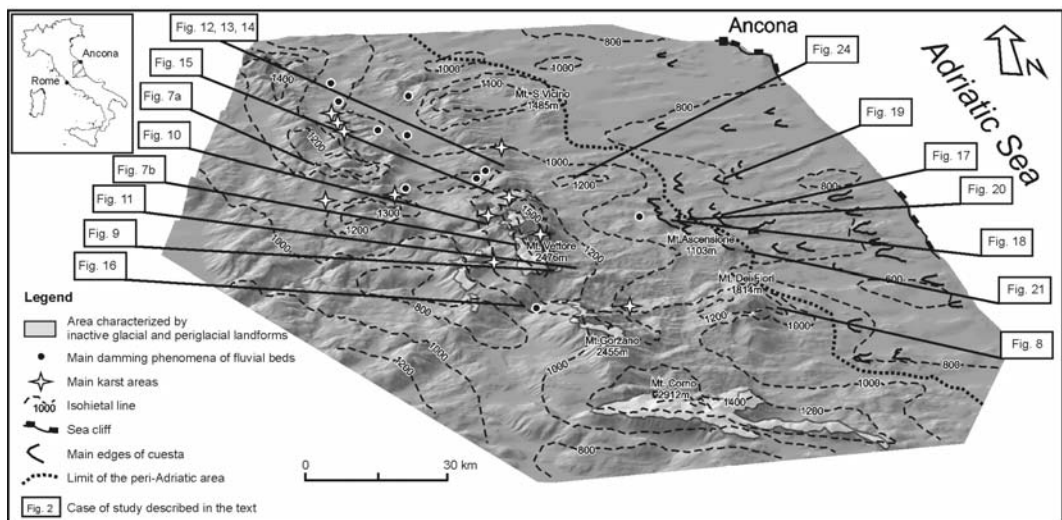


Figure 4. Main geomorphological and climatic features; location of the explanatory figures of the study cases.

Along the mid-lower portions of the slopes and at times along the water divides, bedrock is covered by wide and sometimes thick silty-clayey eluvial-colluvial and landslides deposits,



by eolian sediments and by rare stratified slope waste deposits. Among the latter, the most important deposit is to be found on Mt. Ascensione, whose two generations can be distinguished: a first one, higher, dated back to the middle or the end of the middle Pleistocene and a second one, wider, of the late Pleistocene. Originally extended for more than 10 km<sup>2</sup>, it is today reduced to limited residual limbs by means of the intense Holocene erosion (Gentili et al., 1998; Buccolini et al., in press).

The Pleistocene climatic fluctuations, also strongly influenced the Adriatic coastal area; there in fact, during the last pleniglacial phase (about 20,000 yrs B.P.), the sea reached its lowest level (100m and more with respect to the present) and stayed at that level until about 12,000 yrs B.P. After this a sea level rise, not regular but characterized by standstill or relative lowering phases, occurred, as a consequence of the following progressive climatic warming; it reached a level congruent to the present about 6,000 yrs. B.P. (Pirazzoli, 1997; Lambeck et al., 2004).

The final structuring of the landscape, and particularly of its fundamentals features, occurred at the end of the Pleistocene, while the following Holocene evolution remodelled only the minor elements. In particular, on the highest portions of the clayey slopes, the incision of the secondary hydrographic network previously outlined, ended (Buccolini et al., in press); on the contrary, along the valley floors, a fourth order of alluvial terraces, whose genesis is prevalently connected to human impact on the slopes, were forming (Gentili and Pambianchi, 1987; Coltorti, 1997).

The isohyets of Fig. 4, determined on the basis of data regarding the period 1921–2003, show average yearly values ranging between 600 mm along the coastal belt and 1500 mm on the Apennine chain. On the Adriatic side, the number of rainy days is modest, between 60 and 75, though with a strong variability throughout the year; the average daily intensities are of 10–12 mm. The dominant rainfall regime is characterised by an absolute monthly maximum in November and a second maximum in spring, more frequent in the pedemountain area; autumn results to be the rainiest season. The summer season is reasonably dry, but normally not arid. In fact, only rarely the periods without rain last more than 40 days and, besides, there is a marked difference between the pedemountain area, where there are more frequent convective-orographic storms, and the coastal area. In the last 20 years, the frequency of the exceptional meteoric events has increased sensibly, with rainfalls of 100 mm/day and of over 30 mm/hour, and return times of few years, as far as the period after 1970 is concerned. The average yearly temperatures vary between 12.5° C and 15.5 ° C; the coldest month is January (3.5°C–7°C) and the maximum temperatures are registered in July and August (22°C–25°C roughly). The yearly thermal excursion is between 17°C and 19°C while the daily one oscillates between 7°C along the coast and 10°C in the inner basins (Fazzini and Giuffrida, 2005).

The thermal-pluviometric characteristics of the period in question can be extended back in time to the second half of the 19 century; for over the previous three centuries instead, the effects of the “Little Ice Age”, characterised, at the central latitudes, by an overall increase of precipitation and by repeatedly rainy summers, were also recorded in the study area (Le Roy Ladurie, 1971; Lamb, 1982; Pinna, 1984). During the Holocene, in Italy as well as in other areas of the northern Mediterranean, cool-humid periods (8500-7500 yrs B.P., 7000-6000 yrs B.P., 5500-4500 yrs B.P.) have been recognized; such climatic conditions have been testified to by certain alpine glacial phases of advance and by flood phenomena (Provansal, 1995; Diez et al., 1996; Giraudi, 2005).

### 2.3. Geo-Mechanical and Hydrogeological Background

The numerous lithotypes of bedrock, recognised by means of biostratigraphic data in the study area, can be grouped into a limited number of fundamental litho-technical units. These, at the same time are part of two classes, based on their reological characteristics: rocks with rigid or ductile deformation. The respective geo-mechanical parameters (Tab. 1) show variations that can also be noticeable, with relation to the genetic processes, to the tectonic-deformative history and to the more or less intense weathering, as a result of the various climatic conditions that took place in succession in the area. As far as the Pliocene-Pleistocene clayey bedrock is concerned, besides, a high index of fragility is revealed, connected to the high overconsolidation degree and to the index of consistence, to the intense fracturing and to the stratigraphic discontinuities connected to the thick stratification (Dramis et al., 1987a). The geomechanical parameters of the litho-stratigraphic units formed by the association, in different proportion, of fundamental litho-technical units, show extreme values specific of the latter. Among the different types of continental deposits mentioned, considered as “soil” from the physical and mechanic point of view, on the basis of the Terzaghi-Peck classification (1967), in table 1 data concerning slope deposits alone can be found, since they are the most exposed to mass movements.

**Table 1. Main geo-mechanical parameters of the lithotechnical unit**

LITHOTYPES	Strength MPa	E Young Modulus GPa	P wave velocity km/sec	Internal friction angle $\phi$	$\gamma$ kN/m <sup>3</sup>	c MPa	
stratified limestones and marly limestones	75-100	15-90	3,0-3,8	35-50°	23-26	50.0-400.0	
marls and argillites	12.5-50	3-34	0,9-1,7	17-20°	22-26	30.0-350.0	
Sandstones and calcarenites	50-100	3-61	2,5-3,0	30-50°	23-26	80.0-350.0	
conglomerates			0,9-1,7	30-45°	22-23		
clays, marly clays	0.1-0.25		0.3-0.4	11-22°	18-22	c <sub>u</sub> 5.0-50.0	2.0-3.0
eluvial-colluvial clayey silt	0.025-0.05		0.25-0.3		17-19	1.0-5.0	1.0-2.5
slope-waste debris			0.15-0.25	25-45°	16-17.5		

The mechanical characteristics in question are significantly modified, in a negative sense, by the fracturing of rock bodies, consequent to the action of the deformative fields described above and to which the structuring of bedrock is associated. In the mainly calcareous lithotypes of the chain, it is possible to recognise numerous sets of discontinuities that result, in some cases, to be associated to specific faults (fault-related fractures). Other discontinuities, developed during the different tectonic phases of the chain structuring, have instead a regional character. Altogether, the fractures can be grouped into two main trends: one oriented roughly N-S and another roughly NNW-SSE; other sets of fractures, less frequent than the previous ones and roughly E-W and NE-SW oriented, are also present (Cello et al., 2003).

The spacing of fractures is not easy to define with characteristic values, as it depends on the lithology, frequency of stratification, possible lithological alternations and size of fault displacement to which it is related. However, in the limestones and marly limestones of the chain, it can be synthetically described in the following way: close to the main faults, the average value is around 10 cm; in the other areas the average spacing is decimetric and generally comprised between 20 and 120 cm, with a major concentration of values around 40-60 cm. This parameter, associated to the thickness of the strata, generates polyedres of different shape and with prevalent centimetric-decimetric dimension, rarely metric, exceptionally decametric. In the arenaceous Apennine (Laga Mountains), the different deformative styles, the minor frequency and intensity of the displacement with respect to the previous lithotypes and the massive stratification, produce metric or decametric prisms. Almost similar characteristics are to be found, locally, in the arenaceous-calcareous lithotypes at the base of the Pliocene-Pleistocene sequence.

Joint systems with orientation similar to that of the chain are found in the Pliocene-Pleistocene lithotypes, where, though, they are organized in bundles roughly N-S oriented. They have an extensive character and affect the more rigid and thin rock bodies. They generally dip towards west with an angle of 70°-80°, can be followed for 10 Km. and more and occasionally continue within the Messinian bedrock below (Fig. 3). Spacing, in the order of a few tens of metres, is close to constant over wide sections of the relieves, while it is reduced, at times strongly, near the edges of the highest scarps, where also vertical fractures are present. No displacements have been found at all, even though, occasionally, a close correspondence with N-S faults affecting the Messinian bedrock beneath has been found. Minor frequency and continuity, a prevalent vertical disposition and irregular areal distribution, characterise the E-W fractures. At the edges of the "banks", more recent and mainly gravitational fractures join those of the above mentioned systems (Gentili et al., 1995).

The genesis of such fracturing, as already mentioned for other areas (Wise et al., 1985; Hancock, 1991), is essentially connected to denudation processes and to phenomena of relief expansion, as a result of the rapid and intense tectonic uplifting which affected the area during the Pleistocene. An important role, besides, must have been played by the passive control exercised by the deepest structures of the pre-Pliocene basement, developed in the same direction. These would have acted as bedrock discontinuities, probably favouring the rupture of the rigid plates above. In turn, they are result of both the rapid and generalised uplifting (gravitational tectonics) and of the most intense seismic crisis (Gentili et al., 1995).

The geological setting described, gives the calcareous Apennine a high grade of conformity between the single structures it is made of and the major hydro-structures it contains. The vertical division into compartments of the latter, associated with the marly levels of the sequence, generates important aquifers: the Calcare massiccio-Corniola, the Maiolica and the Scaglia complexes. The hydraulic conductivity is, in fact, elevated, with average infiltration of about 550 mm/yr and average precipitation values from 1,000 to 1,100 mm/yr. The elevated hydraulic conductivity of the calcareous-marly chain and the permeability limit determined by the marly-clayey lithotypes beneath, as result of the thrusts, generate hydrogeological complexes on a regional scale (Sibillini Mountains, Gran Sasso d'Italia). In the Umbria-Marche Apennine the average discharges of the numerous springs fed by the above mentioned hydrostructures, rarely exceed 100 l/sec on the eastern side, while they are higher on the western one: this fact is fully congruent with the structural setting of the chain, tectonically lowered towards the west.

More in detail, the lithotypes of the study area, because of their sedimentological characteristics and tectonic-deformative history (that fractured them more or less intensively), are characterised by: i) primary permeability; ii) secondary permeability iii) mixed permeability, when the previous two types are present in similar proportions.

The first category includes Quaternary continental deposits as alluvial gravels, slope deposits, moraines and landslide accumulations); notable differences in their stratigraphic and sedimentological characteristics and, at times, differences in the cementation degree of the materials can be found.

The second category characterises the formations of the Calcare massiccio, Corniola, Calcari diasprini umbro-marchigiani, Maiolica and Scaglia (bianca, rossa and variegata); the high permeability is due to the presence of fractures of tectonic origin, in most cases enlarged by karst and secondly to the strata junction. In the Calcare massiccio formation, to this type of permeability is also connected a primary permeability (without doubt of minor importance), connected to its particular “porous” structure. As far as the Scaglia complex is concerned the hydrogeological behaviour is not uniform; where the role of the marly levels with respect to the degree of fracturing prevails, the permeability can drop drastically to very low values.

A mixed-type circulation characterises the arenaceous terrains. To the elevated primary permeability of the lithotypes is associated that of the fractures of tectonic origin. As a consequence, a rather complex groundwater circulation results. In the lithostratigraphic units like the Bisciario and in the Miocene-Pliocene arenaceous-pelitic and pelitic-arenaceous associations, the prevailing of the pelitic facies with respect to those of the calcareous or arenaceous type, makes these rocks almost impermeable, or permeable depending on the level of fracturing of the more competent levels. In general however they are considered to have medium-low permeability.

The low permeability is typical of clayey and/or marly terrains (formations of Bosso, Marne a Fucoidi, Scaglia cinerea, Schlier, Marne con Cerrognà, Marne a Pteropodi and the mainly pelitic layers of the turbiditic formations). To those units, also fine Quaternary sediments, like eluvial-colluvial and fluvial-lacustrine deposits can be associated (Nanni and Vivalda, 2005; Civita, 2008).

The permeability of terrains has been often exalted by the more or less intense weathering and by the fracturing consequent to the gravitational stress.

Karst hypogeous processes, the most important of which are found in the Calcare massiccio and Corniola, and secondarily, in the Maiolica and Scaglia rosata formations, are connected to the circulation of groundwaters. The main systems are made up of caves, channels and vertical galleries. Also minor karst systems are present, more diffused than the previous ones, and are represented by networks of centimetric and decimetric channels, that realise bands of chemical dissolution within the rocks. The spatial disposition of the systems is mainly sub horizontal and oblique, more rarely vertical.

Incisions along the flanks of deep valleys develop that do not have a casual distribution, but are organised in overlapping “planes”, conditioned by the progressive lowering of the water table. This fact is in turn connected to the above mentioned lowering of the hydrographic network. At times these correspond to belts of intense tectonic fracturing that have generated preferred ways of groundwater flow. The geometry of inclined systems, less extended than the sub-horizontal ones, is conditioned by the strata attitude, while the vertical galleries are confined to the tops of the reliefs, on calcareous pelagic formations. On the

contrary they are little developed in depth because of, among other reasons, the presence of marly units that interrupt the continuity of the permeable sequence (Fig.5). Karst systems of a certain importance also characterise the rocks at the bottoms of the tectonic basins of Colfiorito, Castelluccio and other minor ones, whose drainages are driven by karst sinks (Galdenzi and Menichetti, 1995; Aringoli et al., 2007).

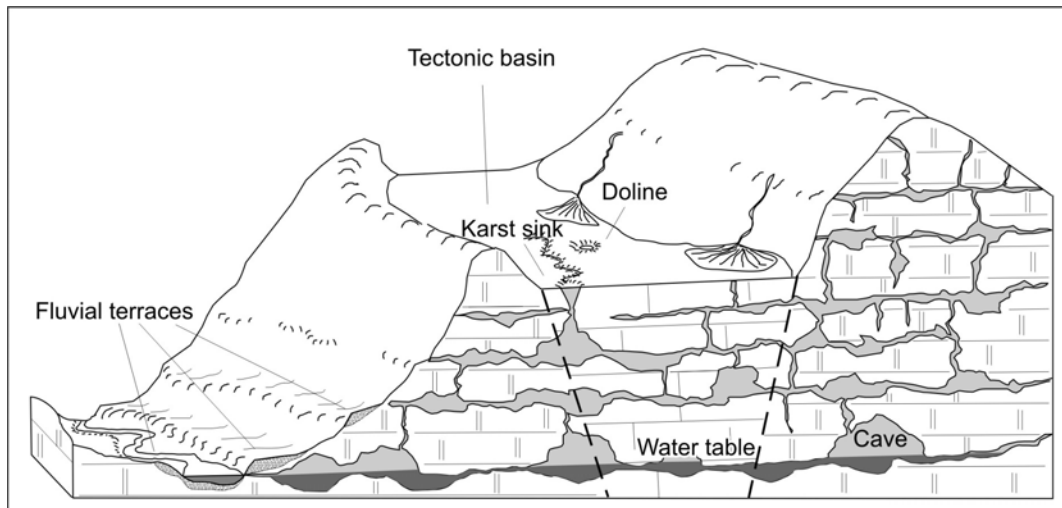


Figure 5. Sketch of the karst hypogeous landforms and their relationship with the geomorphological evolution of the river valleys.

Important for the present work is the geological setting resulting from these processes, that cause, more or less in depth within the rocky masses along the valley sides, further stratigraphic discontinuities

### 3. Landsliding Susceptibility in the Study Area, in the Italian Environmental Context

Italy, which is a “young” country from a geological point of view, possesses an elevated grade of hydrogeological risk; in fact, once earthquakes have been considered, landslide phenomena are responsible for the major number of casualties and the greatest amount of damage done to the environment and to historical–cultural and environmental heritage. Their social-economic impact is very high, so much so as to place Italy among the first in ranking in the world as far as damage caused by landslides is concerned, both in economic terms and, above all, in terms of human lives. On the basis of historical documents and oral testimonies, a significant and definite increase in the number of landslides in the last half century has been recognised, generally connected to the transformation of agricultural techniques, to the construction of infra structural networks and to the urbanisation.

An initial study of landslides in Italy, which is still valid, was done by Almagià (1910), but research received a strong impulse only after the ‘70s, with the activation of specific projects, co-ordinated by the National Council of Research, with the purpose of studying landslide phenomena. One of these (Project “Vulnerable hydrogeological areas of Italy” –

AVI), which considered the landslides from 1918 to 1990, has represented the conditions of elevated risk of landslide in Italy well. It put in evidence the following data: number of landslides recognised, 32,000; number of locations concerned, 21,000; number of victims and dispersed in the 20th century, 5,939; estimation of damages caused per year, 1-2 billion Euros. During the '90s other projects of national interest were activated with the intent of censoring, mapping and making an inventory of the phenomena. As of today, 470,000 landslides which cover a territory of about 20,000 km<sup>2</sup>, equivalent to 6.6% of the national territory have been censored (APAT, 2007).

In the Marche Region, in which the major part of the area under study is located, the systematic geomorphological surveys have revealed a territory which is strongly affected by damage due to landslides. These were in many cases integrated with investigation in the archives and by geo-technical analyses. This is clearly shown by the landslide index (Tab. 2) whose value is about triple that registered for the Italian territory as a whole.

**Table 2. Landsliding in the Marche Region (source: APAT, 2007).**

Landslides	Number of features	Total area affected by landsliding (km <sup>2</sup> )	Total area (km <sup>2</sup> )	Percentage of regional territory affected by landsliding
Representable in maps ( area > 1600m <sup>2</sup> )	39788	42.522	1881	19.41
Not representable in maps (area < 1600m <sup>2</sup> )	2735			
Land use	Area (km <sup>2</sup> )		(IF) Landsliding Index (%)	
<i>Permanent cultivations</i>	80		28	
<i>Extensive sown</i>	3.299		24	
<i>Mixed cultivations</i>	2.715		20	

On analysing the spatial distribution of the gravitational phenomena of the study area, it is shown how these recur, with various frequency, along Anti-Apennines alignments. In Fig. 2, purely as an indication, just the main gravitational phenomena are represented, divided according to the two large categories recognised by the international scientific community: landslides and deep-seated gravitational slope deformations (DSGSDs). We refer, as has already been said, to the bibliographic sources as far as the specific distinguishing elements are concerned and for the relative classification and nomenclature.

Phenomena of major dimension are extended for kilometres and show decametric-hundred metre depth. They mainly occur along the wide flanks of the chain modelled in differently dipping competent rocks. They are less frequent in the hilly region, where, though, they often affect the top area of monoclinial reliefs where historical villages, medieval or earlier, are usually located. Altogether, over 500 great mass movements have been recognised, characterised by average extensions of about 2 km<sup>2</sup> and a frequency of 0.06 phenomena per km<sup>2</sup>; slides clearly prevail with respect to the other categories. About 10% of them are DSGSDs, in which *lateral spreads* (including the *lateral spreads* s.s. and *deep-seated block slides*) prevail over *sacking* phenomena. Some minor landforms, besides these, connected to debris flow phenomena, can be recognized.

The Frequency and the Density values of landslides increase significantly in the sandy-pelitic terrains of the peri-Adriatic belt, such as to determine a diffused landsliding; damaged surfaces of an overall dimension even greater than those previous, are present. They consist, though, of different movements, coalescent or close to each other, that taken singularly follow the articulated trend of the local topography. The most diffused phenomena are the *flows* of the eluvial-colluvial coverings, recurrent usually in the mid-lower portions of the slopes. Slides, at the same time, often affect the lithotypes outcropping in the upper sectors of the same slopes. Such a complex morphodynamic context will be explained by means of the illustration and discussion of several study cases, which constitute the topic of the present work. Their location (and that of the corresponding figures) is shown in Fig. 4. It constitutes an indispensable synoptic frame.

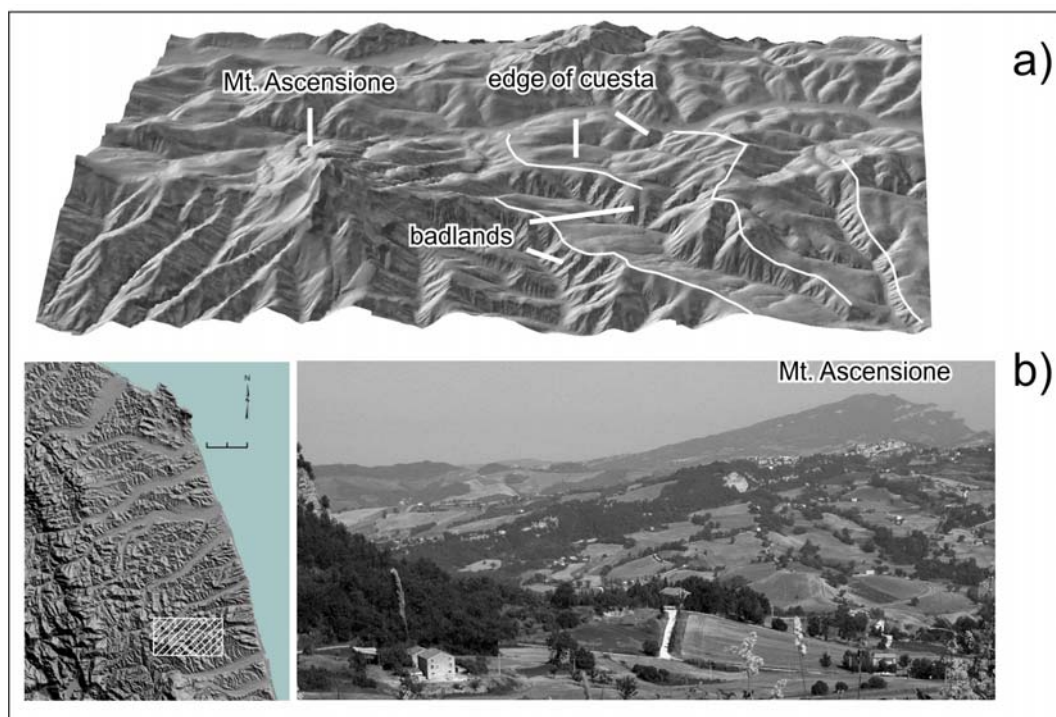


Figure 6. Monoclinical relief: a) Digital Elevation Model of the monoclinical landscape (view from south); b) panoramic view (from north).

#### 4. Gravitational Phenomena in the Central Apennine

The action of gravity in the Apennine chain area, as said before, has its main expression in the genesis of huge mass movements. For these phenomena, the studies carried out have permitted us to establish some initial correlations with the fundamental morphometrical parameters of the slopes, as well as with the geological setting: minimum relief of about 200 m, that goes up to 900 m in the most competent lithotypes; slope length between 900 and 1900 m; average slope inclination of  $22^\circ$ ; convex slope shape in more than 70% of the cases, trenches metric-decamic in length and width, while their length, in some cases, goes up to

about one kilometre. A good correspondence between tectonic alignment and the trend of crowns and trenches has been found in more than 60% of the cases. The spatial disposition of the stratified rock bodies also results important. In fact in 75% of the cases a disposition of strata which is the same as the slope and with a minor inclination with respect to the slope itself recurs (Folchi Vici D'Arcevia et al., 1996).

Marked differences are to be found in the texture of the deposits, as a result of the different types of fracturing of lithotypes. There are decimetric and metric clasts, rarely decametric, dispersed or making up coarse levels alternated with debris of a smaller grain size, widely prevalent, which derive from limestones and calcareous-marly lithotypes. Dihedres of major dimensions (metric and decametric), dispersed or piled up, with a reduced presence or absence of minor grain sizes, are produced by the massive sandstones of the arenaceous Apennines.

The analysis of the morphometric characteristics of these landforms, of the planometric relationship between the specific geomorphological elements, their "freshness" and their position with respect to continental deposits, has at times permitted their relative chronological collocation and us to recognize the different evolutionary stages: initial, medially advanced, advanced (Coppola et al., 1978; Pieruccini, 1988). As far as the overall activity of the processes is concerned, if we take into account the morphoclimatic context of the area and the position of the deposits on the slopes, we can affirm that, almost all are in an active state or dormant.

To complete the morphodynamic framework of the area we have to make brief reference to the debris flow processes, that recur in the different physiographic units of the chain, but with frequency and dimensions that are modest. They are generally located at the confluence between the canals of the secondary hydrographic network and the main valleys and in particular where the first are characterised by significant values of topographic gradient. The original fluvial-torrential or fluvial-glacial incisions are remodelled in box shaped or slightly convex little valleys. They are represented by planar slides of the detritic coverings over surfaces that are inclined roughly in the same way as the slope. They are often connected to piping phenomena or to impact with materials coming from mountainwards. The deposits show variable texture from clays to pebbles and contain rare dispersed blocks.

The geomorphological analysis or the most recent and certain debris-flows in the Sibillini Mountains (1906, 1946 and 1959 the last events, testified to orally and through data from archives) and deep historical investigation, allowed us to recognise several events. The main and most frequent ones took place during the post-medieval age, between the XVth century and the 19th century (Fabbi, 1977; Falconi, 1986). The same historical sources also testify to previous cases, at the beginning of the XIIth century. The chronology of the deposits was established, at times, by the relationship with manufactures whose the age is known.

With reference to previous and consolidated scientific knowledge already acquired for the mountain system, some gravitational phenomena, recently recognised and that refer to the main physiographic units where the same system operates, are illustrated and interpreted as follows. Due to the geological-geomorphological-hydrogeological characteristics of the sites involved and for the kinematics that characterise them, they can be considered widely representative samples of the action of gravity in the Central Apennines.



## 4.1. Mass Movements of the Tectonic Slopes

The regularity of the western side of the southern Umbria-Marche Apennine and of the bordering Lazio-Abruzzo sector is interrupted, over wide areas, by tectonic depressions, the opening of which, one next to the other, began in the early Pleistocene. On the bordering slopes, numerous cases of mass movement of large dimensions, in particular DSGSDs, have been observed and, at times, described. On the large fault slopes, gravitational phenomena have been observed along existing planes exhumed by the extensional tectonics. Within the basins, huge rock masses can be seen, placed there by gravitational collapses during the early and middle Pleistocene, when lacustrine basins were already present there. The action of gravity was manifested with maximum intensity on the eastern side of the ridges, the zone of most intense deformation and uplifting of rock bodies, due to the presence of thrusts. Their principal or secondary shear planes, outcropping or buried, intercept along their fronts the flank of the ridge. The shear planes affect both the bedrock and the thick and wide detritic coverings in the zone of tectonic contact between the lithotypes. The development of these phenomena was favoured both by the elevated relief caused by the Quaternary tectonic uplifting and by the intense seismic action, amplified on occasion by the hydrogeological conditions of the slopes (Gentili and Pambianchi, 1993; Coltorti and Farabollini, 1995; Dramis et al., 1995).

### 4.1.1. The Study Cases

#### 4.1.1.1. Mass Movements along the Bordering Slope of the Tectonic Basins

Important phenomena, which are difficult to recognize on the sole basis of geothematics surveys, have been discovered recently after the seismic crisis of Colfiorito in 1997-1998, through the interpretation, from a geomorphologic point of view, of data acquired by geological-technical investigation carried out for engineering reasons.

A particularly interesting case is that of the DSGSD of Mount Pennino, on the northern margin of the Colfiorito basin (Figs. 4 and 7a). The relief is made up mostly of the calcareous and calcareous-marly lithostratigraphic units of the “Umbria-Marche Sequence” (from the Maiolica to the Scaglia cinerea formations) affected by tectonic displacement of different types. The former geomorphological studies have evidenced the presence of great mass movements along the southern slope, which well agreed with the tectonic deformative model that shows the tendency of “attracting” rock masses towards the tectonic depression. The movements towards the north-eastern sector of the mountain top, which were registered by the trigonometric measurements of the Geographic Military Institute (Firenze, Italy) after the 1997 earthquake, were not clear. They were anomalous with respect to the tectonic stress fields, to the models of co-seismic deformation and to the displacements which were measured in other landmarks of the territory. In fact, as far as the surveys of 1995 is concerned, these latter measurements showed a horizontal displacement of the mountain top of 82 mm and a vertical displacement of -34.8 mm (Surace, 1997; Hunstad et al., 1999; Salvi et al., 2000).

These data are perfectly congruent with a deep-seated block slide kinematics that, in the case of seismic activity of high magnitude, cause a staccato displacement of the micritic limestones (with rigid behaviour) of the Maiolica formation affected by vertical

discontinuities. These latter, as a result of the zone of ductile deformation developed in the calcareous-marly and marly units (Fig. 7a of the Bugarone formation beneath, are reduced to only a few metres with respect to the original 30-40m. The frequent seismicity is the fundamental evolutive control factor of the phenomenon, but its activation can be connected to squeezing out phenomena (Zaruba and Mencl, 1969), as a result of strong weathering processes of marls induced by the constant presence of water in the important, at times, karstified aquifer of the overlying Maiolica formation. This also explains the considerable reduction of thickness of the Bugarone formation, which is difficult to attribute, as a whole, to erosion due to sliding, given the limited overall displacement, testified to by the limited opening of the summit trench. Altogether, as far as deformation is concerned, an initial stage of the phenomenon can be attested.

Another important case that has recently been taken into consideration and analysed, is that located on the eastern side of the Castelluccio basin (Fig. 4 and 7b). This phenomenon, due to the geological, geomorphological and hydrogeological characteristics of the site and to the kinematics observed, can be considered a widely representative sample of the gravitational activity in the physiographic unit in question. It involves a wide portion of a slope mainly generated by the action of a dip-slip Quarternary fault. It borders, on its eastern side, the northern portion of the basin, oriented in a roughly NNW-SSE direction, and is part of a system of “capable” faults having the same orientation. The fault in question is developed for about 30 kilometres, typical length of the capable distensive segments that characterise the area. Given the limited length of these elements, the seisms associated with them have not very high potential magnitude ( $M \leq 6$ ).

The slope analysed shows steps (straight and arched, sometimes several hundreds of metres long), counterslopes, trenches, benches, concave and convex sectors, which involve a front of about 4 km in length, 2 km in width and with a difference in level of between the 2,200 m. a.s.l. of Mt. Argentella and the 1,660 m a.s.l. of its base. The Corniola limestones, dipping according to the slope and in which cemented gravelly levels can be recognised, outcrop along the whole slope.

The tectonic contact with the micritic limestones of the Maiolica formation, mostly sub-horizontal, takes place at the base of the slope, as a result of the fault activity described. Stratimetric considerations lead us to hypothesise a vertical displacement of the fault of about 800 metres. Detailed geological and morphotectonic studies (Calamita et al., 1993) have analysed the entire development of this important dislocation, evidencing, especially in this area, planimetric anomalies which cause an evident flexure of about  $90^\circ$  in the dislocation. Along the slope, mountainward with respect to the main fault, minor tectonic elements (and associated fractures), whose linear development is much more limited (generally between 500 and 1,500m), have been recognized. Some of these have been defined active. The geological and geomorphological elements described, if interpreted on the basis of morphodynamics, can be classified as gravitational movements of two different types: translational slides and deep seated gravitational slope deformation, placed on different planes. The superficial phenomenon (to a depth of 60-70m) is characterised by translational slides of portions of the Corniola formation, driven by strata dipping the same as that of the slope and by the presence of pelitic levels. In correspondence to these levels, shear planes of neoformation, predisposed by the stratification, were formed. A deeper zone of ductile deformation, (over 100m), affects the base of the Corniola formation, characterised by an increase of the marly fraction.

Therefore, the planimetric anomaly attributed to a flexure of the main fault, not seen directly but hypothesised on a morphological basis, is to be related to the foot of the superficial movement which, moving valleyward, obliterated the fault plane. As a consequence, also the faults and the fractures considered active and located in the upper sector of the slope, given their limited extension (1,500m maximum), can be interpreted as a result of the action of gravity on discontinuities parallel to the main fault (Fig. 7b).

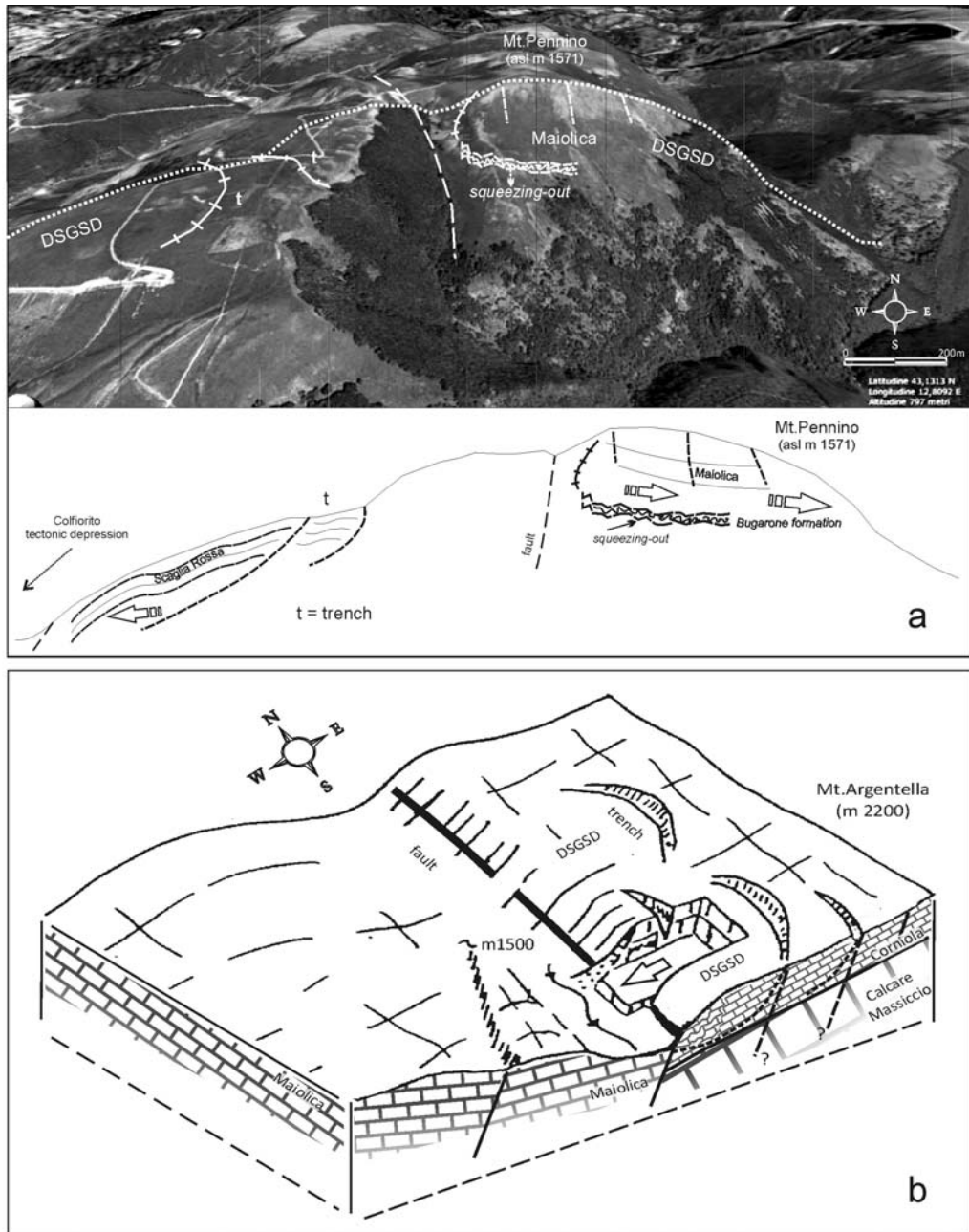


Figure 7. Sketch of the mass movement evolutionary mechanisms of: a) Mount Pennino; b) eastern side of the Castelluccio basin (Mount Argentella).

#### 4.1.1.2. Mass Movements along the Thrust Fronts

In the areas containing these dislocations, where the tectonic contact between lithotypes with marked differences in their geo-mechanical characteristics takes place (i.e. limestones on marls), two different geomorphological settings, to which normally different gravitational phenomena correspond, can be observed: i) clear slope breakage between the steep calcareous slope and the sub-horizontal marly-arenaceous one: ii) barely noticeable slope breakage, as a result of the intense erosion that cut the marly lithotype.

As far as the first setting is concerned, an evident and huge phenomenon can be seen on the eastern flank of the “Montagna dei Fiori” anticline (Figs. 4 and 8) where the calcareous-marly and marly-calcareous lithotypes of the “Umbria-Marche Sequence” are structured in a east verging asymmetric inclined fold and are overthrust onto the marly-arenaceous lithotypes of the Laga formation.

The thrust front is buried by a wide slope deposit, extended for about 15 km<sup>2</sup> on a band (roughly 15 km long and 1 km wide) parallel to the slope direction. The thickness is variable but frequently exceeds 30 metres. It consists of landslide accumulations of different types, coalescent, made of centimetric-decimetric clasts, blocks and portions of Scaglia rossa and, subordinately, Marne a Fucoidi formations, deeply fractured and sometimes made into “breccia”, with a matrix made up of centimetric debris. These materials have been buried and regularised by stratified slope waste deposits. Their original dip must have been about a few tens of degrees, taking into account their characteristic angle of internal friction (Tab. 1); the original dip was reduced by the specific mechanisms of placement (mainly rill erosion); on place measurements done on deposits show values of 15° - 20°. At the base of the deposit also a limited limb of an older generation of medially cemented material was found.

The different grain sizes of the materials are connected to the different genetic processes which have generated it: they are coarse in the upper zones, while they progressively decrease from mountain to valley, becoming prevalently pelitic towards the lowest limit. Bearing in mind the chronology of the stratified slope deposits of the area cited above, the overall placing of the deposit must have begun in the middle Pleistocene and must have been concluded with the pleniglacial phase of the late Pleistocene.

The deposit lays mostly on the mainly pelitic-arenaceous unit of the Laga formation (Centamore et al., 1992) and for a limited area, on the calcareous-marly lithotypes. Its lowest, rather articulated, limit is made evident by the numerous springs. The initial channels of the minor hydrographic network, that often dissects the deposit itself due to regressive erosive phenomena, are associated to them. The deposit can at present be collocated at a height of between 500 and 550 metres.

The flank of the structure connects to a modest valley depression parallel to the structure itself, mostly buried by thick fluvial-torrential deposits (up to 70m) made of mainly polygenic gravel of the late Pleistocene and overlayed by Holocene alluvial fans. The inner portion of the deposit is visibly cut, in part, by an hydrographic network whose minor channels show intermittent drainage. On the eastern border of the depression very rare limbs of older fluvial deposits are found (Centamore et al., 1982; Farabollini, 1999); those dated back to the end of middle Pleistocene between 450 and 520 m a.s.l.; those of the middle Pleistocene between 600 and 650 m a.s.l.

In the all over morphological setting of the slope, three topographic cross-sections with different average inclination ( $\theta$ ) and relief ( $\Delta h$ ) can be recognized. The wide calcareous and

calcareous-marly slope ( $\theta=50\%$ ;  $\Delta h=500-700$  m), was modelled by the fluvial-denudation processes cited, where mass movement played a fundamental role. The crown and the accumulations of some phenomena show clear signs of present activity. The pedemountain section which joins the valley depression shows an articulated topography essentially connected to the incision of the minor hydrographic network cited ( $\theta=25-30\%$ ;  $\Delta h$  up to about 100 m). The mass movements are rare and limited to particular local geomorphological settings. The medial section ( $\theta=25\%$  with sub-horizontal portions;  $\Delta h=100-200$  m), whose actual overall and detailed shape depends on the evolution of the accumulation cited, is of great morphodynamic interest. It locally has various benches (Fig. 8a), the major ones of  $0.5 \text{ km}^2$  and over in extension, slightly up hill laying or, more often, limited mountainward by wide and shallow trenches.

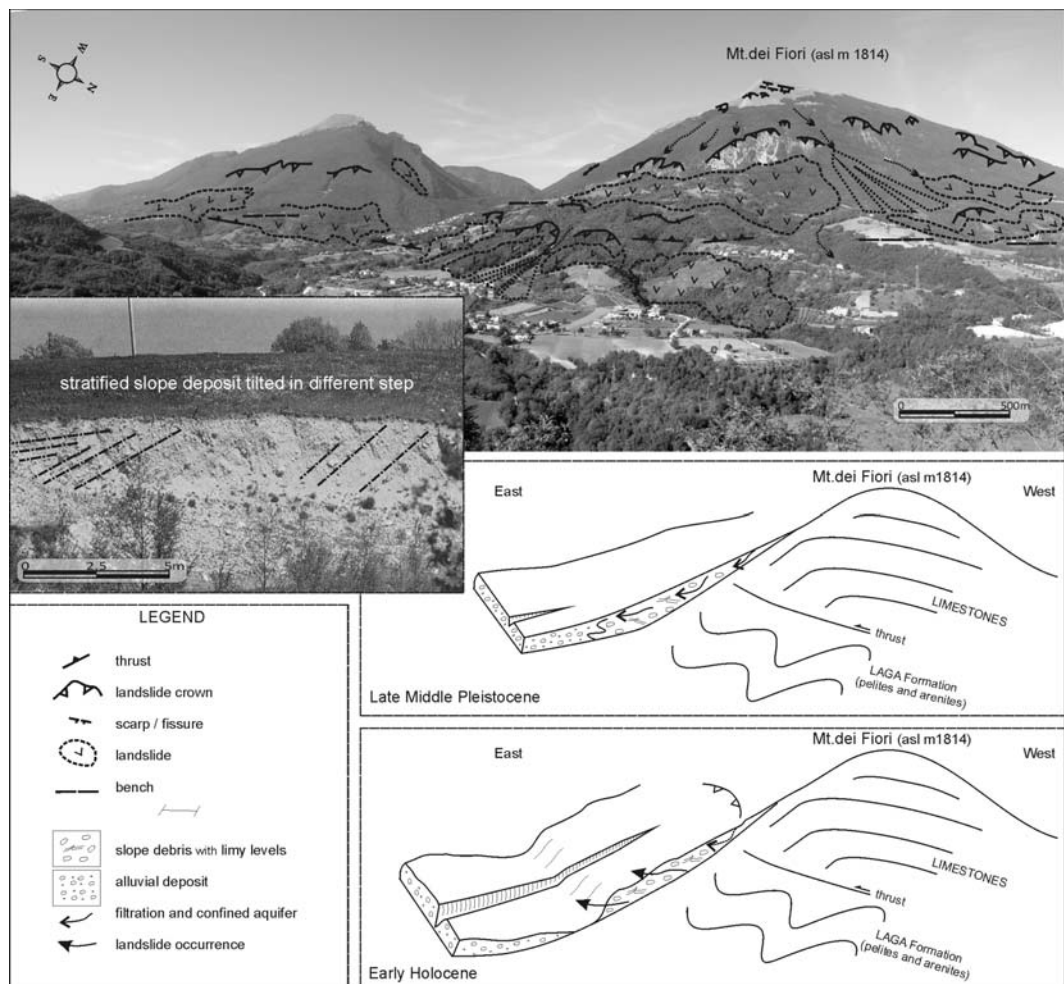


Figure 8. Geological and geomorphological features of the eastern flank of the Mount dei Fiori; morphodynamic sketches and particular of the slope deposits turned counterslope due to rotational slides.

The correct interpretation of those landforms, already attributed to fluvial processes (Mattei, 1987), was made possible by the analysis and interpretation of the geomorphological elements observed on an artificial cut placed in correspondence with one of these benches.

The stratified slope deposits covering the accumulation are of at least two generations. This is made clear by a modest angular discordance in their contact zone. They are turned counterslope by about 40°. A little way below, strongly fractured metric and decametric blocks, coming from the Scaglia and the Marne a Fucoidi formations which outcrop 500-1000 m above, appear. These elements are indisputable evidence of a sliding phenomenon which produced, with respect to the original attitude cited, an overall rotation of about 60° in the deposit (Fig. 8). The main and secondary shear planes or zones, with cycloid shape, were mainly formed in the inner part of the deposit, but could continue in the altered levels of the pelitic-arenaceous bedrock.

Both in the case in question and in analogous ones, immediately valleywards of the benches, the landslide accumulations show landforms that can be associated to successive flow phenomena, partly dismantled by fluvial-torrential erosion; these latter correspond to processes of “passive transport” of the detritic masses, as a result of shear planes or zones realised essentially in the altered portions of the pelitic bedrock. There is no evidence that the activity of the phenomena as a whole is in act or recent, except for limited reactivation controlled by local topography.

The main control factor of sliding /flows phenomena is to be seen in the hydrogeological setting of the slope. In particular the main aquifer constituted by high permeable lithotypes of the ridge, is able to supply, by way of overflow onto the impermeable surface below made of the mainly pelitic unit, the secondary aquifer, constituted by the detritic covering. This condition resulted decisive for the coming about of important piezometric increases within the deposit. Said deposit is placed over the almost impermeable pelitic units and is sealed in the front by the “diaphragm” composed of the pelitic fraction of its materials. With regard to the chronological position of the phenomenon, first rotations can be hypothesised during the final phase of the placing of the stratified slope deposits, testified to by the already mentioned angular discordance corresponding to the final glacial phase of the late Pleistocene (about 20,000 years B.P.).

The end of the mass movements must have been connected to the lowering of the piezometric surface, as a result of the important drainage in the detritic mass. This was due to the linear incision by the hydrographic network that dismantled the “diaphragm” cited and entered, more or less deeply, into the body of the deposit. This condition essentially came about in the early Holocene together with the affirmation of biostatic conditions.

As far as the second geomorphological setting is concerned, the recurrent phenomena are clearly illustrated by the landforms recognised on the eastern slope of Mount Vettore (Figs. 4 and 9). The complex geological setting is characterised by the presence of two thrust planes close together, that overthrust respectively, the oldest lithotypes of the “Sequence” (Calcare massiccio, Corniola etc.) onto the more recent ones of (Scaglia formation), and these latter onto the pelitic-arenaceous association of the Laga Formation. In the area being examined, meso-structural analyses has evidenced a considerable reduction of the inclination of the thrust planes towards the west with respect to the characteristic values of the eastern front, that normally are around 30°. The calcareous lithotypes show an attitude that goes from a subhorizontal to a roughly dipping same as the slope. Locally, the calcareous lithotypes are covered by strongly cemented stratified slope deposits.

At the top of the slope (2000 – 2200 m a.s.l.), in the zone of the narrow watershed that divides it from the Pilato valley, modelled by the Pleistocene glaciation, it is possible to find trenches parallel to the direction of the watershed and that run along its entire length (double ridge). On the steep slope modelled in limestones beneath, certain landslide crowns can be recognised above which fissures, steps, trenches, undulations and intense fracturing of the strata are present. These elements are ideally “joint” each other by a linear scarp parallel to the slope and decimetric to metric in height. The more or less straight setting of the landform, though it is connected to polygenetic processes, allow us to hypothesise a tectonic control for its genesis, exerted by an extensive dislocation, without displacement, parallel to the slope.

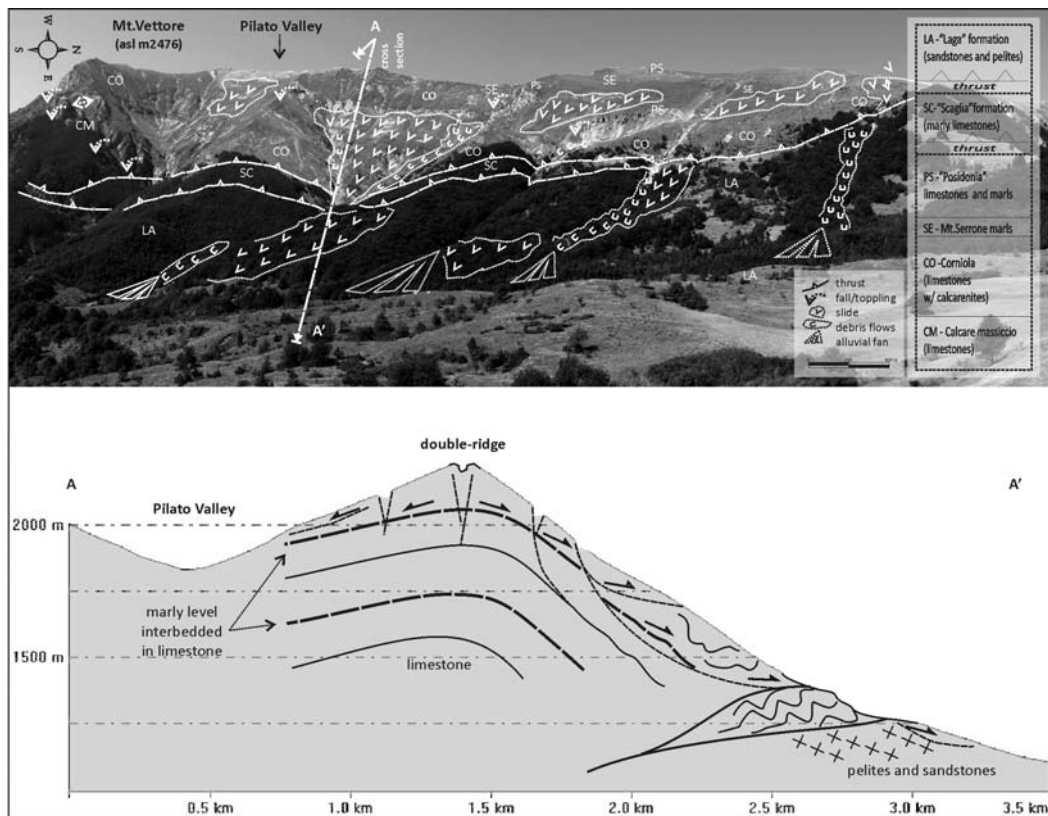


Figure 9. Geological and geomorphological features of the eastern flank of the Mount Vettore and morphodynamic sketch.

The most evident landslide accumulations, where the attitude of bedrock is clearly visible, show evident rotations counterslopes in the zone of the crown and prevalent translations in the middle portion. Less extended fall phenomena also recur; their accumulations, at the foot, often evolve into debris-flows, which in turn evolve into alluvial fans.

The “freshness” of all the elements permit us to associate the landforms along the calcareous slope to relatively “superficial” and recent gravitational phenomena. They are still in slow evolution, activated by roto-translational slides that take place, respectively, along the shear planes of neo-formation in the thickly stratified and subhorizontal rock masses, and

along shear planes predisposed by an attitude roughly dipping as the slope and by the presence of interspersed pelitic levels.

The elevated frequency and density of these phenomena, anomalous with respect to that found in other sectors of the physiographic unit, allow us to hypothesise a control of the phenomena by a zone (or more than one zone) of ductile deformation. This would be predisposed for by the probable listric geometry of the cited extensive tectonic dislocation, whose plane loses its own identity in the zone of intense tectonic fracturing between the two thrusts or in the marly levels below which are even more ductile. On the basis of morphometric-structural considerations these zones of deformation can be placed at a medium depth.

A still wider and deeper deformation, besides, should have affected both the flank of the ridge in question, as is demonstrated by the presence of double crests. As a whole, it could fall within the category of lateral spreads indicated by Jahn (1964). More in detail, a *macro-cambering* phenomenon could affect the limestones of the eastern flank due to the differential dislocation realised in the pelitic-arenaceous lithotypes below the thrust, following strong processes of *whethering*, *squeezing out* (Zaruba and Mencl, 1969) and fluvial erosion. The phenomenon, in part associated to that described by Beck (1967) and by Nemcok (1972), is testified to by a considerable reduction of inclination of the thrust plane, connected, probably, to its deformation by gravity. Almost certainly, on the western flank the effects of the glacial decompression are felt (Fig. 9).

## 4.2. Mass Movements on the Valley Slopes

In this physiographic unit, dimensions, kinematics and control factors of the gravitational phenomena can be even noticeably different, above all depending on the morphogenetic agents that have defined the slope shape in its various parts: i) the slopes of the glacial valleys in the most elevated areas; ii) the fluvial-denudational slopes of the lowest parts. The latter, in the outcoming zones of the ridges, are in most cases conditioned by the intersection of thrust planes, dipping mountainwards, that have been exhumed by fluvial incision.

The glacial decompression, following the withdrawal of the valley glaciers, is considered the most important predisposing factor of gravitational phenomena of large dimension of the first context. It acts, normally, in association with geological factors and other morphogenetic agents. Concerning this topic, there are not significant bibliographical references for the central Apennine, but only sporadic mention, if compared to the Alps where there are the most spectacular landforms and the studies are numerous (Orombelli and Sauro, 1988; Panizza et al., 1996; Soldati et al., 2004). The oldest mention regards the “Lavini di Marco” (Eastern Alps) and is made by Dante Alighieri (1265-1321), who talks about a great landslide accumulation in the *Divina Commedia* (Inferno, Canto XII, 4-9), trying also to furnish a genetic interpretation of the phenomenon.

Numerous is, instead, the quantity of research regarding the greatest mass movements of the fluvial-denudational slopes, which affect the lithotypes of bedrock. Many of these have interfered, in the past and recently, sometimes repeatedly, with fluvial dynamics, producing damming phenomena or diversions along the rivers (Fig. 4). Given the limited presence of landslide deposits, partly dismantled by fluvial erosion, the processes have been reconstructed through the analysis of the crown areas. Mostly, however, these are reconstructed by the



presence of lacustrine and/or fluvial-lacustrine deposits and landslides alternated with the gravels of the alluvial terraces of the middle-late Pleistocene and of the Holocene (Damiani and Moretti, 1968; Gentili et al., 1999). The watersheds are often affected by wide DSGSD phenomena, at their initial or medially advanced stage (Coppola et al., 1978; Pieruccini, 1988; Dramis et al., 1995).

#### **4.2.1. The Study Cases**

##### **4.2.1.1. Mass Movements of the Glacial Slopes**

In the study area, the delimitation of the huge gravitational movements which affect areas modelled by the past glacial action is, generally, made difficult by the presence of active morphogenetic processes of different types, whose materials have obliterated, completely or partly, the specific diagnostic elements. A clear example of deep seated gravitational slope deformation is present on the southern flank of Mount Bove Nord, in the Sibillini mountains massif, where traces of the Quaternary glaciations are conserved. The upper Pleistocene glaciation, the last and the most consistent of all, enlarged and deepened in several cases the cirques and the valleys of the previous glaciations.

In fact, the glacial valley that develops in a NW-SE direction, from Mount Bove Sud towards Northern Mount Bove Nord, shows a sudden deepening in its medial sector. It is probably connected to the development of a new glacial cirque or to a step of erosion in the bottom of the glacier, helped also by the presence of more erodible lithotypes outcropping along the southern slope of Mount Bove Nord (Fig. 4 and 10). The glacial excavation of the valley seems to have been the principle action, as it is hanging and isolated from fluvial incision phenomena that deeply characterised, starting from the Holocene, other surrounding valleys. Several calcareous-marly formations, characterized by the presence of marly-clayey levels of considerable thickness, outcrop widely, with attitude transversal with respect to the slope, along the medial portion of this versant. At the base, towards the valley bottom, and at the summit, towards the top of Mount Bove Nord, the mainly calcareous formations typical of the “Umbro-Marche Sequence” outcrop. This stratigraphic succession is delimited, to the north and to the east, by direct faults that separate it from the Calcare massiccio (Fig. 10). These litho-stratigraphic and tectonic conditions have prepared the slope for landsliding.

The portion of the slope affected by the DSGSD phenomenon, extended for about 1km<sup>2</sup>, has a large, roughly 500 m long, arched trench at its upper border, which progressively closes towards south-east. The direction of the trench and of its synthetic scarp coincides with the main fault systems that displace the slope mountainward, oriented in a NW-SE to about an E-W direction. Continuing towards the valley, minor trenches and huge scarps characterise the slope which shows an evident bulging (Fig. 10) in correspondence to the marly-clayey level of the Bosso formation.

This level can be interpreted as an element of ductile deformation within which the deformation involving the upper part of the Calcarei diasprini and Maiolica formations takes place. The particularity of the main trench that narrows towards SE assuming a roughly triangular shape, suggests a complex deformative kinematics which, besides developing following the maximum slope, shows a translational component towards SW, due to the lithostructural control.

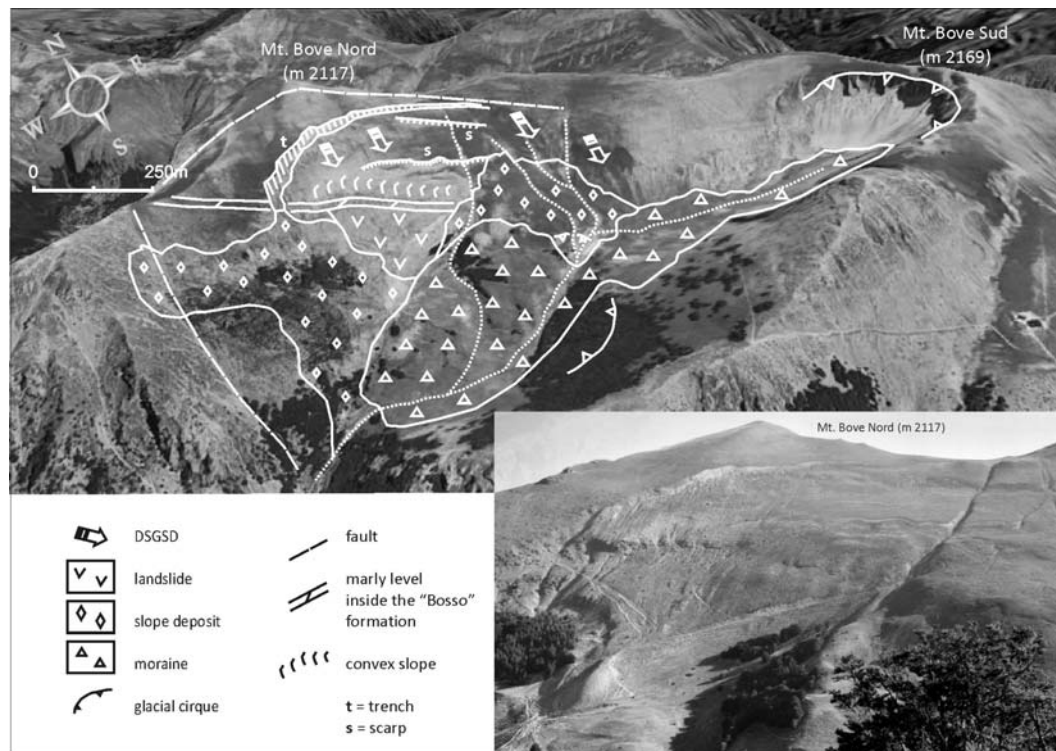


Figure 10. Glacial valley of Mount Bove: interpretative sketch of DSGSD phenomenon and panoramic view from south.

The morenic deposits, present at heights comparable with those of the base of the Bosso formation, suggest the probable presence at those heights of a glacial tongue capable, in the period of its maximum development (last pleniglacial phase, about 20,000 years B.P.), of contrasting the slopes. Its following withdrawal, which occurred probably at the end of the late Pleistocene, should have favoured the initial collapse of the slopes towards the end of the period cited or, more probably, at the beginning of the Holocene. The relative “freshness” of the landforms could confirm the youth of the deformation and of other minor gravitational phenomena present in the area.

#### 4.2.2.2. Mass Movements along the Fluvial-Denudation Slopes

Four cases are illustrated: two of which (Interprete and Borgiano) are particularly significant, respectively, for the characteristic geological setting of the arenaceous lithotypes and of those mainly calcareous; another two cases (Mount Frascare and Pescara del Tronto) clearly represent the conditioning played by the presence of main and secondary thrust planes on the morphodynamic evolution of the slopes.

##### *The Case of Interprete*

In the arenaceous-pelitic lithotypes of the Laga mountains can be observed the clearest mass movements due to the evidence of the landforms and to the relative simplicity of the kinematics. These are elements strictly connected to the regular geological setting of the

lithotypes: blocks of sandstone separated by rare pelitic levels, sub horizontal or weakly inclined that, deeply incised by the hydrographic network, have generated frequent situations of banks dipping same as the slope. Recurrent are the phenomena of *lateral spread*, often connected to translational slides. The movements usually affect huge banks dissected by direct faults, can be activated by earthquakes and are driven by topographic gradients (Dramis et al., 1987b).

A particularly significant case of translational slide, recognised and analysed recently at the foot of the accumulation where the village of Interprete is built (originally of the year 1500), is illustrated (Fig. 4 and 11).

Mountainwards with respect to the village, in a medially steep portion of the slope which corresponds to the top of an arenaceous bank, it is possible to find numerous trenches parallel to the slope with opening that increases valleywards, and numerous fractures, cracks and minor trenches, roughly orthogonal to the first, that dislocate the rocky mass in decametrically sized blocks. On the lower edge of this tract the masses result to be slightly turned valleyward with respect to their original setting, while, still lower, over the clear slope break that separates the top zone from the long and steep portion of the slope (including the inhabited centre up to the creek below), big chaotic blocks, piled up or isolated, are visible. All in all it consists of a translational slide, certainly active in the upper sector. The accumulation of the lower sector shows instead a sure state of long quiescence as the good stability of the village of Interprete, built there about five centuries ago, demonstrates.

For the correct genetic interpretation of the phenomenon it is necessary to define the particular geological context and outline its complex geomorphological evolution. A little mountainwards, in fact, the calcareous succession of the Sibillini Mountains is overthrust onto the turbidic deposits of the Laga Formation. The latter, affected in turn by the tectonic folding, are structured in narrow synclines and wide anticlines. Locally, the thrust overlaps the calcareous masses onto the pelitic arenaceous lithotypes, closely stratified and folded in a synclinal way. Further east, in the study area, the turbidites become mainly arenaceous, with massive layers (up to 10m thick) interspersed with pelitic levels. They form a wide asymmetric anticline with the eastern flank overturned. The axis of the fold, N-S oriented, close to the village of Interprete shows an evident flexure with upward concavity, probably related to the action of a transcurrent fault connected to the compressive tectonics. The flexure favoured the incision of the deep valley below (Colleluce stream), whose slopes are both characterized by attitudes dipping same as the slope.

Fluvial erosion was particularly intense on the left bank, towards which the stream was pushed by the debris flows coming from the opposite side. The fluvial erosion at the foot of the slope activated an initial translational slide, which progressed, in time, mountainwards, due to regressive erosion.

The presence of fractures, N-S and E-W oriented, in the arenaceous banks guided the setting up of the hydrographic network favouring the modelling of structural surfaces with typical triangular shape (*flatirons* (Fig. 11a and b). The evolution of the hydrographic network and the mountainward progression of the landslide phenomena has produced a widening of the spaces between the *flatirons* and the valleyward sliding of huge arenaceous blocks and/or plates. As a result, the pelitic layers below the banks in movement, became more and more vulnerable to erosion. This process was connected not only to superficial running waters but also to groundwaters stored in the arenaceous aquifer. In the steepest zones, the pelitic layers, which was eroded on its sides by the water and reduced internally by the same slides,

have been completely removed causing the contact between the arenaceous banks. This setting prevented the movement of the bank itself, whose displacement can probably be realised only in the case of earthquakes of high magnitude.

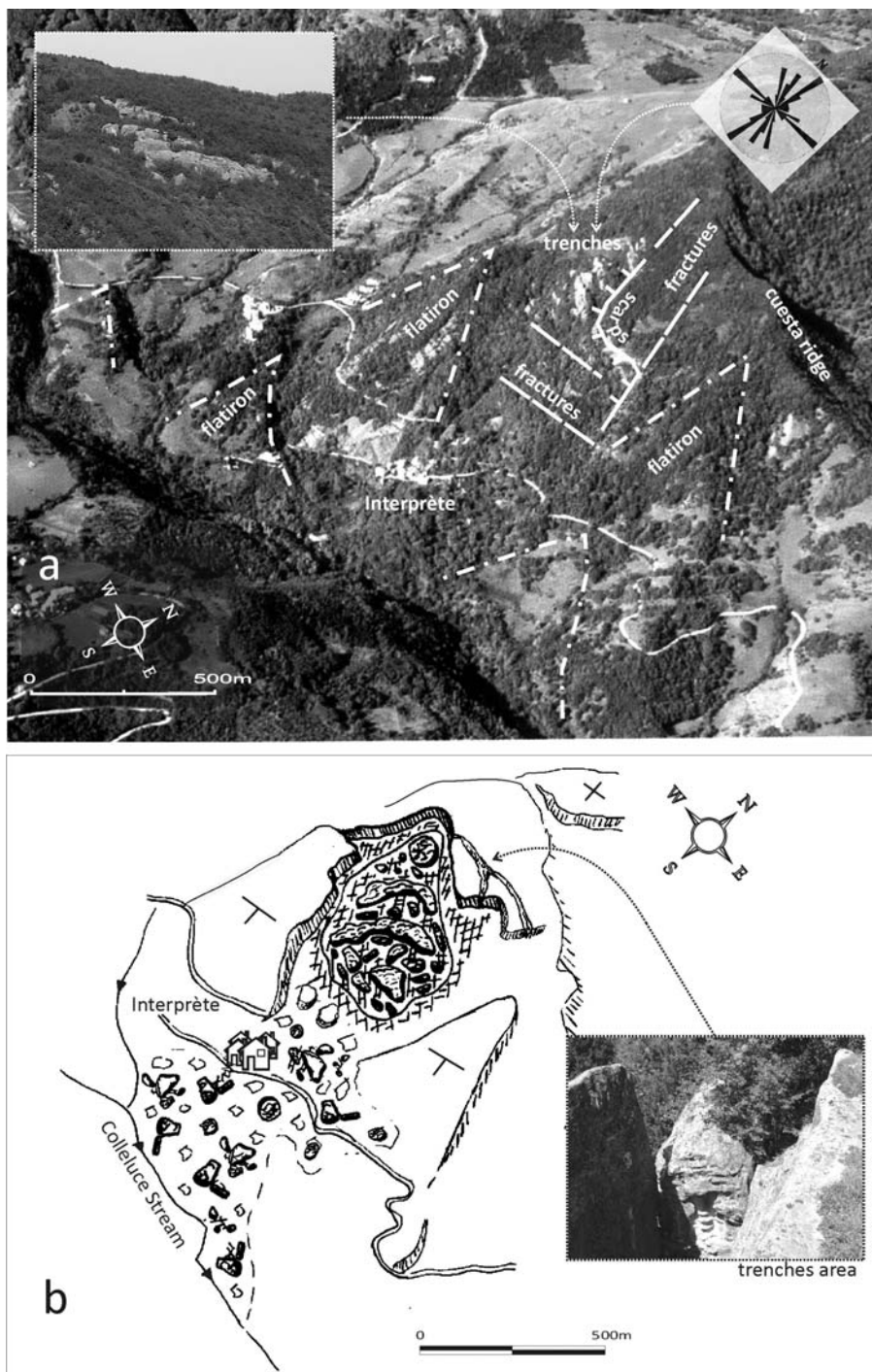


Figure 11. Interpret: a) geological and geomorphological sketch; b) interpretative sketch.

Within the valley, however, useful elements for a chronological collocation of the initial phase of the phenomenon, do have not found .

### *The Case of Borgiano*

In the folded limestones of the Marche ridge, on the hydrographic left of the Chienti River near where it exits from the ridge itself (Figs. 4 and 12a and b) and towards the foot of a slope submerged by the waters of a reservoir (Lake of Borgiano), it is possible to observe, with great difficulty, a complex mass movement. The slope is made of Maiolica, Marne a Fucoidi and Scaglia Bianca-rosata formations, dislocated in a tight anticline fold with axis roughly N-S oriented, and whose axial culmination shows an abrupt “knee bend” (a lower flexure at the valley bottom and an upper one on the mid portion of the slope). Said structure is affected by fault and fracture systems oriented roughly E-W and N-S (Fig. 13a).

The presence of a wide quarry front has allowed us to make detailed geological-structural observations that have evidenced numerous incongruities with the geological setting of the district: high up, E-W open fractures characterised by cataclasites with dip-slip striae which are in discordance with the transcurrent kinematics typical of the local faults (Fig. 13b); slightly lower, evident thinning of the bituminous schist level (“Bonarelli level”) can be observed and the limestones above are so intensely fractured as to hide its stratification (Fig. 13c). In the medial sector, fractures oriented according to the direction of the slope form a number of mini-graben. The shape of the slope is clearly convex. An evident trench interrupts the continuity of the upper part of the slope and there it is possible to observe benches and counterslopes and laterally, deviation of the hydrographic network connected to the deformation.

An opportunely located GPS monitoring system, showed, according to the maximum inclination of the slope, dislocations of the landmarks congruent with the extensional system and with the *mini-graben* observed: horizontal maximum 83cm.; vertical maximum –27.8cm. Successive geophysical surveys have shown, up to the foot of the slope, the prolonging in depth (up to 80-100m until they reach the Marne a Fucoidi formation) of the discontinuities recognized on the surface, with a sub vertical trend or with modest dip towards the valley. Under the bottom of the lake, instead, shear zones with a low angle and disposed counterslope and a significant “*bulging*” of bedrock buried by fluvial-lacustrine deposits have been found (Fig. 14).

The interpretation of the data acquired, on the basis of a morphoevolutionary point of view, has allowed us to define a geological model of the slope. It can be associated to a phenomenon of deep seated gravitational slope deformation, in particular of *deep seated block slide*, whose zone of ductile deformation is represented by the mainly marly-clayey basal unit of the Marne a Fucoidi formation (Fig. 12b). The crown zone, still affected by extension, corresponds to the tectonic E-W discontinuities that have undergone local reactivation in a gravitational and not tectonic sense. At the top, the deformation involves the calcareous unit of the Marne a Fucoidi and the Scaglia rossa, to which superficial phenomena that evolve in a discontinuous way are also connected.

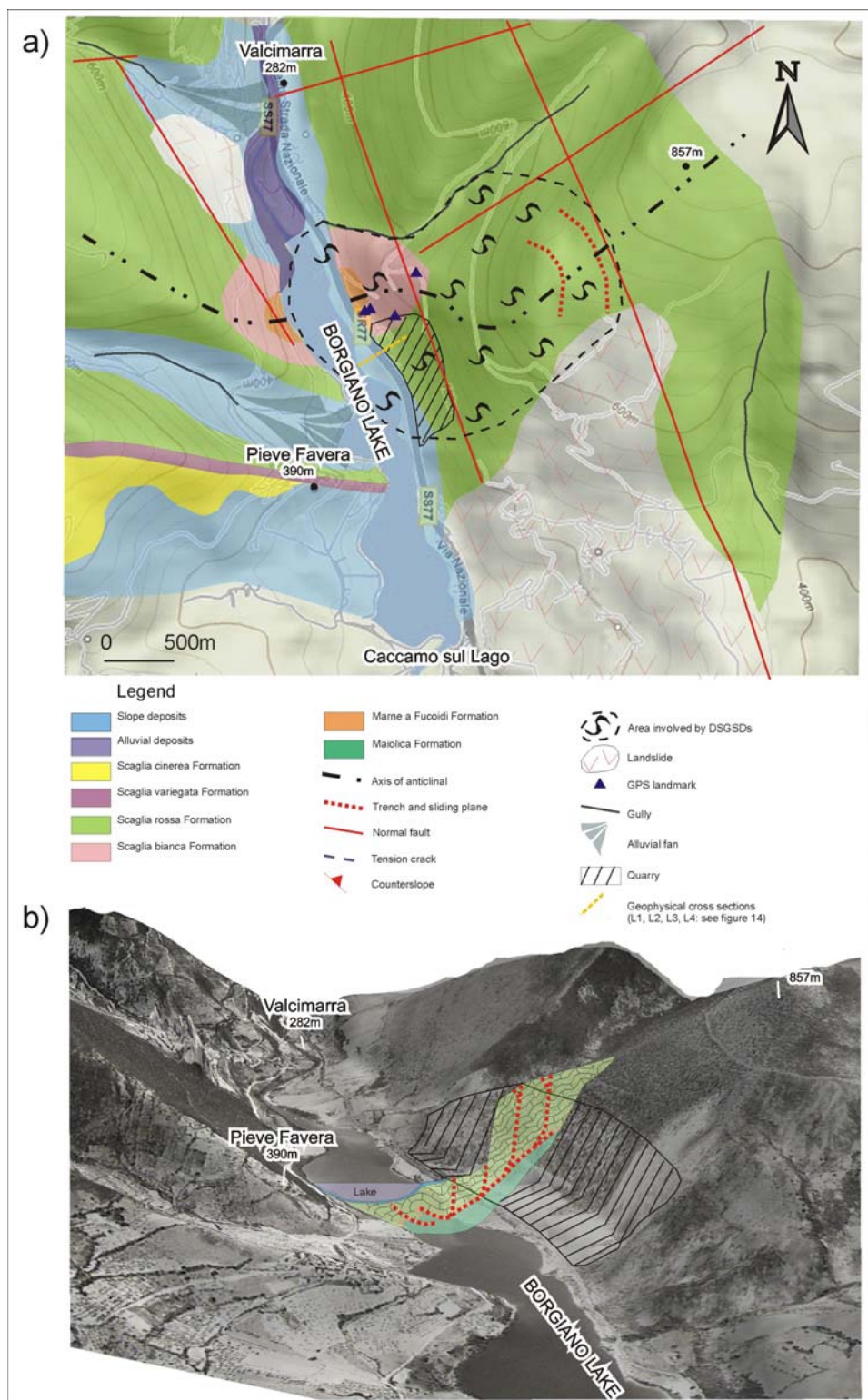


Figure 12. Borgiano: a) geological and geomorphological sketch; b) interpretative sketch.





Figure 13. Borgiano: a) main structural elements; b) fractures in the Scaglia rossa formation; c) detail of the “Bonarelli level”.

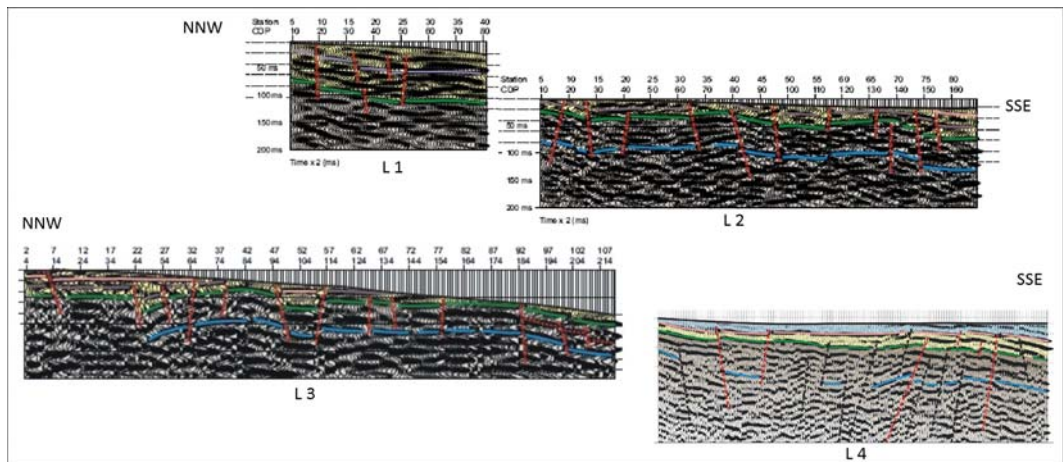


Figure 14. Borgiano: geophysical profiles (for the location see figure 12a).

### *The Case of Mount Frascare*

The study case refers to a portion of the long slope that goes from Pintura del Ragnolo (1,306 m. a.s.l.) towards north to the valley floor of the Fiastrone stream, where the reservoir with the same name is located. The stream (an affluent of the river Chienti) transversally cuts

the Marche ridge from west to east (Figs. 4 and 15a). On the slope, between the heights of about 1,200 and 1,270 m. a.s.l., at the site called Mount Frascare, the slope is noticeably deformed by mass movements, already mentioned in published scientific articles (Coppola et al., 1978; Dramis et al., 1995).

In this area outcrop the lithotypes of Maiolica, Marne a Fucoidi and Scaglia bianca and rosata formations, belonging the roof unit of the Mount Sibillini thrust with axial depression towards north. These formations gently dip towards north, in the top area of the fold, while greater angle of inclination is to be found further to the east, on the overturned flank of the fold. They are affected also by faults with different trends that can be grouped into three sets of orientation (Fig. 15b): Apeninic ( $A=N150^{\circ}-170^{\circ}E$ ), antiApeninic ( $B=N30^{\circ}-50^{\circ}E$ ) and, subordinately, roughly N-S ( $C=N10^{\circ}E$ ). The first lead to considerable displacement in a westward direction. The second have more complex kinematics: the prevalent movement is transpressive left, reactivated by a more recent transtensive right one. The last N-S faults, characterised by a transtensive right kinematics, have an “en-echelon” disposition, interrupt the previous ones and have produced important fractures ( $D=N40^{\circ}-60^{\circ}E$ ).

The Quaternary tectonics generated new discontinuities sometimes using those already cited. Further joints sets are also present (Fig. 15b): shear joints, connected to the compressive stress field and extensive joints associated to direct faults of type A. Tectonized bundles, besides, with a high clayey-marly content within the limestones overlaying the Marne a Fucoidi formation, are present; they are due, probably, to the Neogene compressive tectonics. The Pleistocene evolution of the chain produced, within the study area, a deep incision along the main valley (gorge of the Fiastrone stream), in correspondence with an important anti-Apennine tectonic element. This fact generated a particular disposition of the strata which dip same as the slope on the hydrographic right, where the study case is located.

At the edge of the large surface of Mount Frascare we find two main systems of trenches, distributed in along a belt about 1 km. long and about 400m wide. Steps, counterslopes and evident convexity characterise the lower portion of the slope. The trenches of the first system, oriented roughly NNE – SSW and found between 1,210 and 1,250 m. a.s.l. display depressions 6-7 m. deep and with a maximum width of 20 m. The second system, which develops closely mountainwards with respect to the first shows trenches that are even more than 10 m. deep, 20 – 30 m. wide and up to 800 m. long and slanting minor landforms (Figs. 15a, and b). The overall trend of these landforms is congruent with that of fractures of Type D. The major trenches are mostly vegetated and filled by debris while the minor ones are more recent and are less open and without, or almost, debris or vegetation. Between these, in the more recent years, a number of new fractures have been produced (Fig. 15b) parallel to them; they are up to 50 m. long, up to 50 cm. wide and with a depth impossible to determine. In correspondence to these fractures, besides, when the seismic events of the area of Colfiorito took place (autumn 1997) further openings of about 6 cm. were observed, valleywards and aligned with respect to the existing fractures.

Towards north-west, between Mount Frascare and Podalla, large scarps, counterslopes and undulations mainly guided by the tectonic elements present are visible. A little valleyward, the slope becomes steeper, up to over  $40^{\circ}$  and it is possible to observe, down to the valley floor of the Fiastrone stream, dormant slide crowns. Near the village of Podalla is visible a huge dormant landslide constituted by the translational slide of mainly calcareous lithotypes on the Marne a Fucoidi formation below; the crown is at present affected by numerous falls. A little further south-west a large trench is disposed according to the direction



of the slope in its upper tract and continues towards the valley with a sharp deviation, forming a curved valley completely anomalous for the overall geomorphologic setting. The bottom is flat and very wide. The hydrographic network is not very long, shows no hierarchization and adequate catchment mountainwards. At the foot of the slope, besides, you can observe an asymmetric alluvial fan deposit that allows us to hypothesise an eastward migration of the water course. (Fig. 15a).

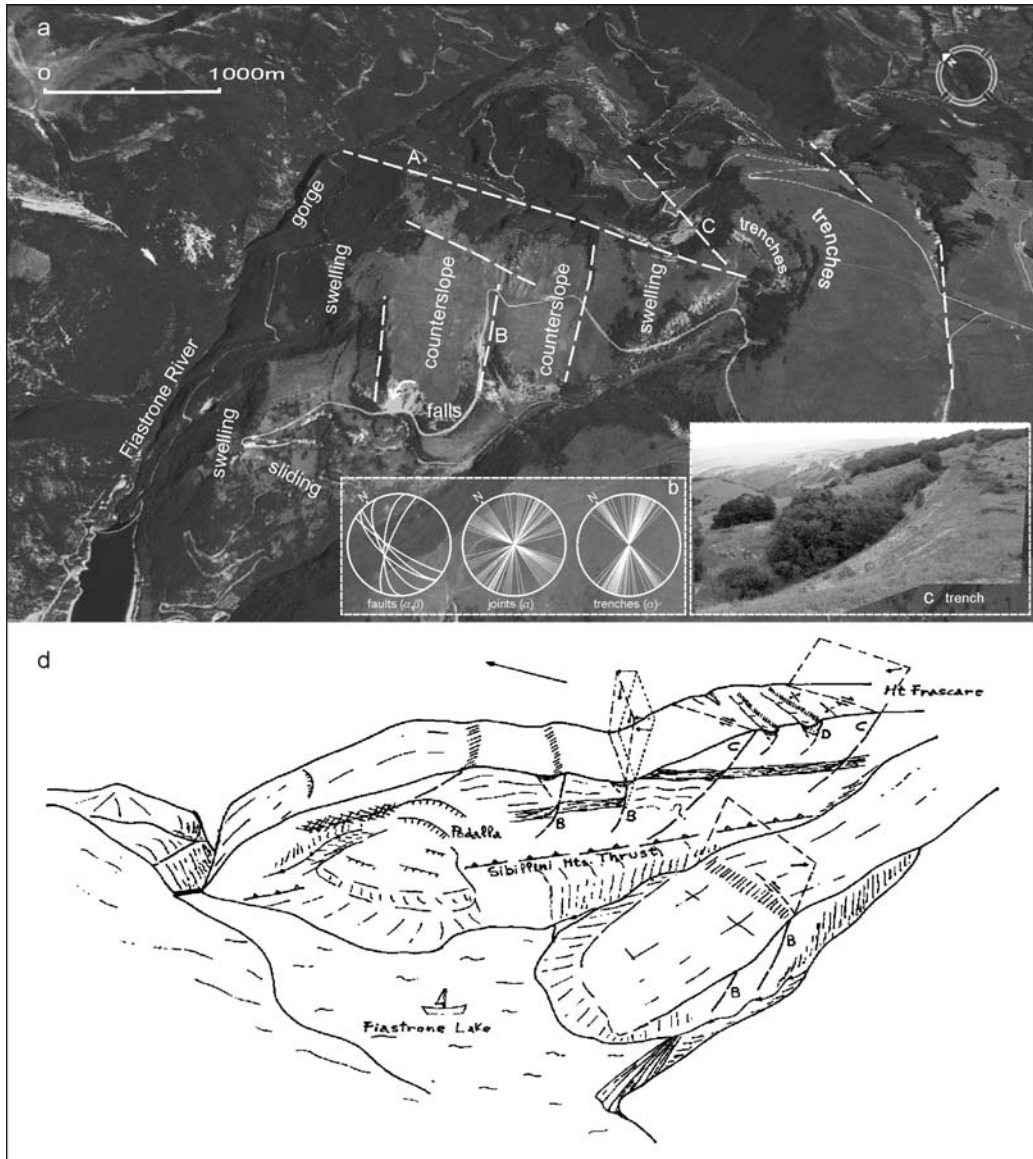


Figure 15. Mount Frascare: a) aerial photograph of the site with indication of the main geological and geomorphological features; b) stereo-plots indicating trench, joint and fault orientation; c) particular of a trench; d) interpretative sketch of the phenomenon.

The geomorphological setting described can be associated to various mass movements. The most important, from a scientific point of view and from the hazard conditions associated

is, without doubt, the DSGSD phenomenon in the upper sector of the slope to which previous studies essentially refer. The latter attributed the phenomenon to stratigraphic discontinuities (overlaying of thick rigid calcareous masses onto more ductile marly layers) to topographic (high values of relief) and seismic factors and to tectonic dislocation, both compressive and extensive. For the latter a Quaternary trascurrent right activity was hypothesised. The present study, though confirming the importance of these genetic factors, identifies an further element of control, deeper and extended; the thrust plane of the Sibillini Mountains. In particular it demonstrates the neotectonic activity and the rightward transurrence of the roughly N-S oriented fault (faults of group C); they probably are listricated on the thrust plane, responsible for the genesis of different joints set, in correspondence with which trenches were opened as a result of gravity.

Therefore, the geological model proposed (Fig. 15d), that summarises all the data acquired up till now, individuates two possible zones of deformations located at different depths: the marly level of the Marne a Fucoidi formation and the level of intense fracturing in the thrust zone. The first is associated to lateral spread phenomena in the marly limestones of the roof which are evident towards the top. The second level should favoured a deep-seated block slide kinematics, probably extended as far as the foot of the slope.

The study, besides, shows that the phenomenon is active and constitutes therefore a condition of very high geological hazard due to mass movements; to which a high level of risk for the valley bottom area, given the presence, at the foot of the deformed slope, of the reservoir mentioned.

### *The Case of Pescara Del Tronto*

Among the mass movements of the valley slopes, that of Pescara del Tronto (Fig. 4 and 16a), that involves in a different way both of the sides of the Tronto river valley, is certainly one of the most complex and extraordinary events and one of major scientific interest. In this sector the valley is narrow and deeply incised due to the convergence of the two mountain ridges: the calcareous one of the Sibillini Mountains and the turbiditic one of the Laga Mountains, oriented respectively NNE-SSW and NW-SE. The welding of these two structures is realised through the great Sibillini thrust that overlaps the calcareous lithotypes onto the turbiditic ones. In this zone, though, which is placed at the southern edge of the thrust and not on its front, a lateral contact must have also occurred between the two lithotypes along a roughly SW – NE alignment, as a result of a limited backthrusting of the turbidites onto the limestones. The backthrust, besides, drove the Tronto river path in this portion of the valley; its incision, mainly connected to lower-middle Pliocene tectonic uplifting, occurred into the arenaceous-pellitic lithotypes of the Laga formation. This is testified to both by the strong asymmetry of the valley (sub-vertical slope in the limestones and gentle dipping one in the turbidites) and by the lithological composition of the different generations of alluvial deposits, made up of, mainly, arenaceous pebbles and sandy-silty matrix.

Along the high slope on the hydrographic left ( $\Delta h=1,100$  m roughly), at a height of about 1,000 m. a.s.l., the mentioned thrust plane outcrops. In this tract it shows south-east verging and generally sub horizontal setting, that is interrupted by a modest upward concavity close to the built-up area of Pescara del Tronto. The geometric setting of the thrust plane and the contrasting hydrogeological characteristics of the lithotypes involved, have caused a particular concentration of the water drained from the huge calcareous aquifer overlapped

onto the turbiditic one. To this aquifer is connected the genesis of the spring (or group of springs) of Pescara del Tronto, whose overall capacity is of about  $1\text{ m}^3/\text{s}$ .

As declared previously (cfr. § 2.3), such an elevated capacity is a hydrogeological anomaly for the eastern sector of the Apennine chain. It is to be connected, above all, to the presence, in the surroundings of the extended hydrogeological basin, of the tectonic–karst basin of Castelluccio (about 1,350 m. a.s.l.). Along its main axis, about 4 km southwards, the above mentioned springs are located. The direction of the deep groundwater circulation is favoured and driven by karst conducts whose genesis and development are to be associated to the tectonic dislocations in the Apennine direction which are responsible for the modelling of the basin (Fig. 16b).

Mountainwards with respect to the town (and to the springs), on the calcareous lithotypes of the slope, it is possible to observe a large landslide crown between the heights of 900 and 1,150m a.s.l. It seems to be generated, given its articulated configuration, by the union of several gravitational phenomena, complex and probably rotational-translational, whose evidences (benches, counterslopes and high scarps) are still present along its slope. In correspondence to the medium high portion of the crown, the lithotypes of the bedrock are buried by deposits of recent genesis. In the lower portion, instead, corresponding to anthropic digs, stratified slope deposits (late Pleistocene) that regularized older accumulations of chaotic and heterometric debris are visible.

On the hydrographic right, the recent detailed geotematic surveys developed on the valley bottom and at the foot of the slope, have evidenced, starting from the river bed (660 m. a.s.l.) up to a height of about 850 m. a.s.l., the presence of a large calcareous “plate” made up mostly of Scaglia rossa. It lays, at the base and on the southern side, on the arenaceous pelitic turbidites of the Laga Formation and in numerous outcroppings has a still well preserved stratification. The base is an exception to this because shows an intense fracturing (levels of “breccia”). The summit portion is partially covered by a landslide accumulation made up of turbidic lithotypes of the Laga formation. The collocation in height of the upper portion of the “plate” is a bit above that of the end of middle Pleistocene (2<sup>nd</sup> order) alluvial deposit limbs, which outcrop on both sides of the river. The top of the “plate” is characterised by two benches divided by a scarp of a maximum height of about 50 m. The lower bench is even lowered due to a second scarp which reaches a maximum height of about 20 m. From the edge of the latter down to the valley bottom the difference in height is about 70m.

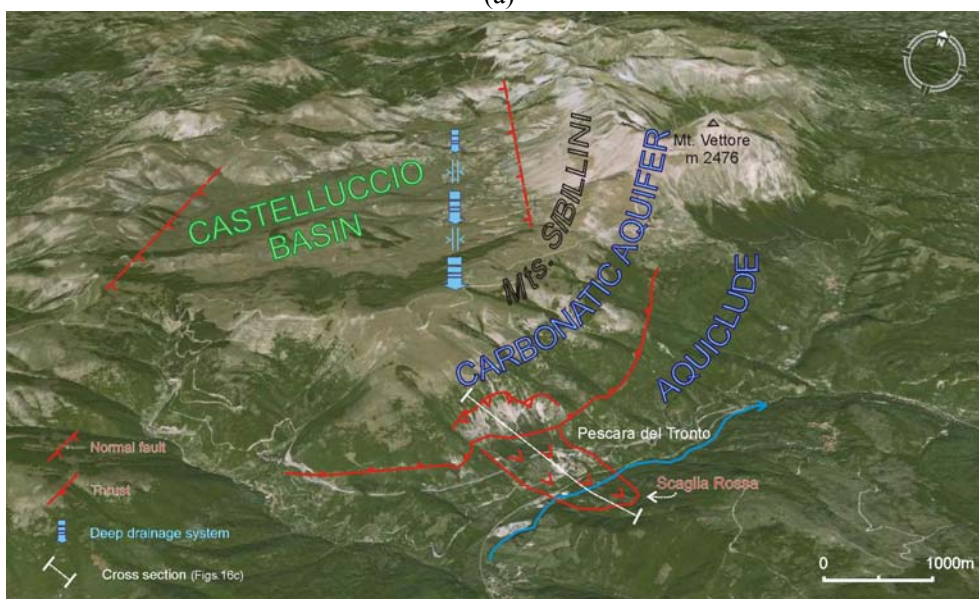
This presence, unique for the slope on the hydrographic right, is completely anomalous from a stratigraphic and structural point of view. In fact, on the hydrographic left, the same turbiditic layers overthrust, due to the thrust plane, onto the limestones of the Maiolica formation (1,000 m. a.s.l.), while the Scaglia rossa outcrops about 200m mountainwards (at 1,100 m. a.s.l.).

The data shown so far have a possible complete interpretation only through the hypothesis of a large mass movement which involved a much larger volume of material and whose the calcareous plate represents a residual limb. The probably extremely complex kinematics of the phenomena is simplified and schematically represented in Fig. 16c: 1) initial rotational-translational slide that overlapped the calcareous plate onto an eluvial-colluvial “bed” made of mainly pebbly-sandy-silty material; 2) activation of slides–flows with shear planes occurring within the eluvial-colluvial coverings and/or in the top levels of the turbidic bedrock; 3) passive transport of the plate by the above mentioned slide–flow phenomena along a gently dipping slope which was jointing the valley bottom of the end of

the middle Pleistocene; there, the deposition of the second order alluvial terraces was completed or was being completed; 4) the successive phases of valley incision, during the late Pleistocene and the Holocene, produced erosion processes at the foot of the “plate” and triggered gravitational settlings of the plate itself generating, as a consequence, numerous benches and scarps. To this phenomenon temporary fluvial dammings could be associated, which, though, specific research done has not given evidence of. In fact, from field surveys and from data obtained through boreholes, lacustrine sediments inside the alluvial deposits are not found at all.



(a)



(b)

Figure 16. Continued on next page.

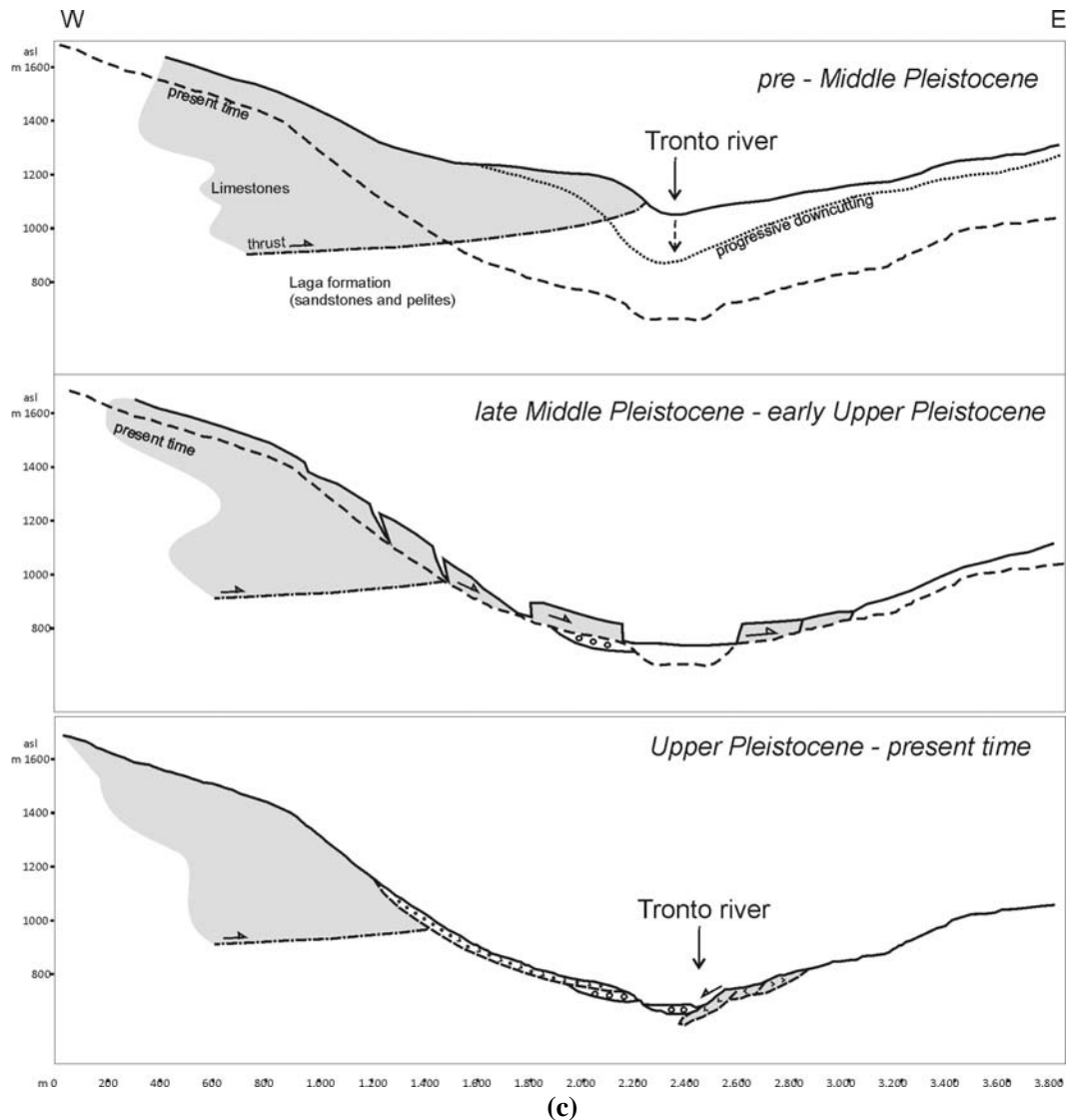


Figure 16. Pescara del Tronto: a) geological and geomorphological sketch; b) hydrogeological setting of the area; c) interpretative sketch of the mass movement.

That the phenomena is to be collocated chronologically at the end of the mid Pleistocene is demonstrated by the stratified slope deposit of the late Pleistocene that regularize the lower portion of the crown and, partially, the third order alluvial deposits.

The main predisposing factors of the mass movement can definitely be recognized: in the intense tectonic fracturing of the rocks, realised both during the placing of the compressive structures and during the uplifting and the Pleistocene extensive tectonics; in the gravitational fracturing, which was a result both of the tension release which took place within the calcareous mass following the fluvial erosion of the turbidites below and to the genesis of differential sinking in the ductile turbidites themselves; in the high relief; in the decay of geomechanical parameters of the calcareous lithotypes as a result of the genesis of karst levels developed in parallel with the fluvial deepening phases.

With regard to activation factors the following hypothesis is formed. Phase (1) favoured by: the significant increase of gravity connected to the intense seismicity of the area; the high water pressure present in the base of the acquifer, since it is fed by the endorheic basin of Castelluccio (over 300 m of difference in height) and probably still closed at the foot by a turbiditic “diaphragm”. Phases (2) and (3) favoured by the great quantity of water present on the slope and supplied by the group of springs whose capacity must have been much greater than present. In fact, in that period, the cataglacial period of the beginning of the early Pleistocene was in course, with consequent dismantling of the glacial systems of the Sibillini Mountains and the great water increase in the aquifers.

## **5. The Gravitational Phenomena of the Peri-Adriatic Belt**

The relative simplicity of the geological setting and the clear geomorphological evidence, make this system an important sample for in depth morphodynamic studies and research and for a setting up of related evolutionary models. In the physiographic unit constituted by the hilly reliefs, the morphodynamic characteristics (past, recent and current) strictly depend on the geomorphological context. The latter is characterized by repeating “cuesta” morphologies (from west to east, Fig. 6), whose sharp and evident morphological contrasts are visible on the western border of the monoclinial relief. Here, in fact, the overlapping of the rigid post-transgressive basal unit onto the more ductile pre-transgressive lithotype favoured intense processes of selective erosion. As a consequence, the bases of the high structural scarps join to the main valley floors by means of gentle pediments (acclivity ranging between 4° and 10°).

The exogenous dynamics, still intense, is dominated by mass movements, to which most of the modelling of the relatively wide valleys and of their narrow watersheds is connected. For the latter processes different kinematics, intensity and control factors can be distinguished depending on whether they occur: i) in the tough lithoid levels of the summit areas, overlapped onto mainly pelitic sediments; ii) along the clayey slopes, covered or not by significant thicknesses of continental deposits or by thin arenaceous levels. Different morphodynamic aspects characterize, instead, the mostly old-inactive sea cliffs.

### **5.1. Mass Movements in the Top Sectors of the Reliefs**

The phenomena which characterise the first section regard the arenaceous-calcarenitic-conglomeratic bodies superimposed onto marly clays or weathered levels of the pelitic-arenaceous turbidites. The kinematics of a large part of the cases analysed, defined on the basis of analyses and geomorphological interpretation, turn out to be specific for translational slides or, more rarely, deep side gravitational deformation phenomena. They are the most interesting cases from a scientific-technical and social-economic point of view, since they are tied to conditions of high geological risk for inhabited, originally medieval or earlier centres, where frequent damage, sometimes catastrophic are generated.

Such phenomena can be described by referring to one of the best known mass movements (the Montelparo landslide, discussed in several publications and the subject of numerous national and international scientific field-trips) and by illustrating and interpreting in detail another two complex cases (Mount Falcone and Montegiorgio).

### *The Case of Montelparo*

The phenomenon, already documented in the XVIII century (Pastori, 1781), regards the eastern flank of a relief modelled on alternating arenaceous, arenaceous-pelitic and pelitic-arenaceous lithotypes with a monoclinial setting, affected by a translational slide, about 1,100 m long and 500-700 m wide, on the eastern side. At the top of the relief, an evident active trench, whose maximum width is about 40 m, divides the portion subject to landsliding from that stable. (Fig. 4 and 17). The main shear (or zone) plane is collocated at a depth of between 65 and 100m, in a pelitic-arenaceous level, exposed by intense processes of fluvial incision which affect the foot of the slope (Angeli et al., 1996; Angeli and Pontoni, 2004; Dramis et al., 1993). Further studies have recognised, basing on geomorphological evidences, a probable Holocene activation of the process; attributed an important role to the fracturing of the rock bodies, above all to the N-S fractures; they have evidenced, besides, using numerical analysis, a movement not completely congruent with the maximum inclination of the slope. The model shows that both the actual evolutionary state and the activation of the phenomenon can be associated to static conditions of the slope. Seismic and/or hydrogeological effects have acted in the past (and can act in the future) much more “heavily” than for that being investigated (Aringoli et al., 2007).



Figure 17. Montelparo: main geomorphological features of the huge mass movement.

#### **5.1.1. The Study Cases**

##### **The Case of Monte Falcone**

The case of study being illustrated refers to one of the most elevated reliefs (Mt Falcone, 924 m a.s.l.) of the monoclinial landscape whose morphodynamic aspects have been defined on the basis of geomorphological analyses and interpretation.

The relief is located at the extreme western edge of the periadriatic belt (Fig. 4 and 18) and is formed of a rocky “plate” of about 150m thick, made of alternating sandstones (with varying degree of cementation), calcarenites and, secondarily, conglomerates and rare pelitic levels (Middle Pliocene). It sits on a pelitic-arenaceous unit of the Laga formation (



Messinian p.p.); the contact is clearly marked by a pre-transgressive erosive surface. The relief is bordered on the western sector by a high scarp at the base of which it is possible to find accumulation of blocks and pebbles, generated by the withdrawal of the slopes by means of falls and/or topples. These deposits become discontinuous towards the valley and are often reduced to isolated blocks (of even a few decametres square) which can be observed up to the inside of the Tenna and Aso fluvial beds. Modest bulgings of the topographic surface that lessen in pediments modelled in the Messinian turbidites are present, besides, and join the above mentioned scarp to the valley bottom (Fig. 18b).

Towards the southern edge, where the ancient village of Montefalcone Appennino (X century) arises, the “plate” is weakly lowered and less inclined. It is affected by the cited bundles of fractures Fig. 18a), by roughly vertical fissures, by limited trenches and by steps which run E-W, more or less parallel to the slope. Moreover, it is interrupted towards the east by the Trocchio stream, that cuts through its entire thickness in a 150°N direction.

Less clear are the geomorphological elements visible on the northern side, where the urban centre of Smerillo (X century) rises. Its “plate” is dissected by incisions, such as trenches and steps mostly located near the crest, oriented at about 20° N. These latter cease valleyward in the tight (10-30m) and deep (up to about 150 m) incision of the Anguilla stream that, pushed close to the transgressive contact, cuts out the upper portion. On the bottom of this stream, above all in correspondence with the incisions cited, numerous springs are found; near them the travertine crusts are still forming. Analogous deposits are also present near the numerous little waterfalls that interrupt the river bed and along it. The phenomenon of karst dissolution affecting the still active calcarenitic levels, exalt the pre-existent fracturing and contribute to the subdivision in blocks of the arenaceous-calcarenitic “plate”.

The morphodynamic interpretation of the data shown, has permitted us to formulate the synthetic evolutionary model of figure 18b, according to which the relief results to be dissected by various and complex mass movements. A minor phenomenon can be observed towards north, where the Anguilla stream path results deviated eastward by an old rock block slide. This is favoured by the presence of pelitic levels intercalated in arenaceous-calcarenitic banks and delimited mountainwards by a trench congruent with the trend of main fractures. At the foot of the elevated western scarp it is possible to observe the accumulations of important phenomena of topple and/or fall, delimited mountainwards by evident trenches (locally called “le Conche”), also oriented roughly N-S, in the direction of the main fractures.

The gravitational phenomena of greatest scientific-technical interest, given the elevated level of risk connected to the presence of the historical centres cited, is to be found along the roughly N-S direction and affects, with different intensity, the whole “plate” at the top of the relief. These are classified as DSGSDs and, in particular, as lateral spreads and deep seated block slides, taking into account the limited relative displacement (vertical and horizontal) between the blocks. The reliability of the hypothesised kinematics and their congruence with the geomorphological setting of the slopes, have been verified by numerical modelling (Crescenti et al., 2002), always carried out in static conditions on the three sections represented Fig. 18c).



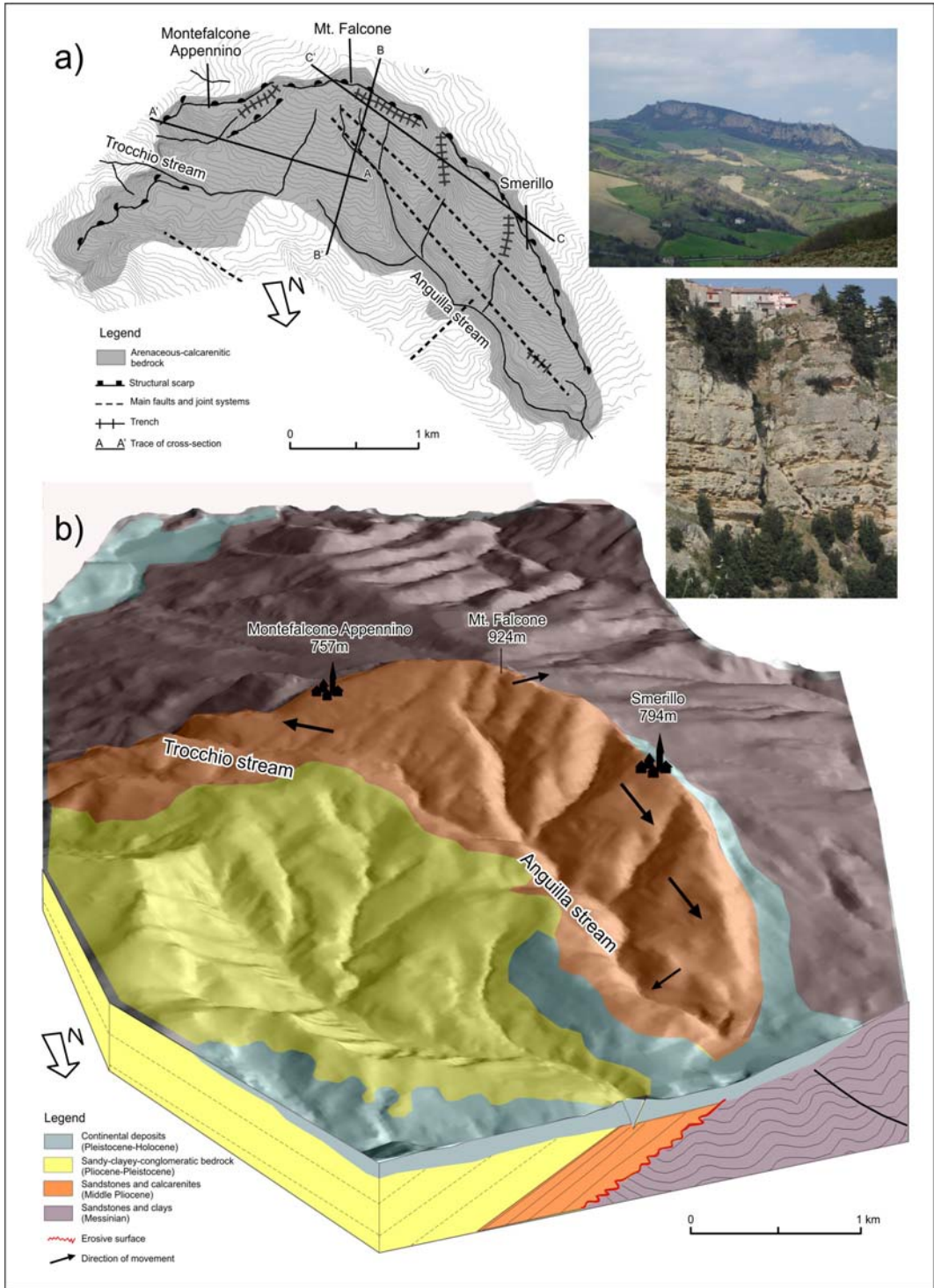


Figure 18. Continued on next page.

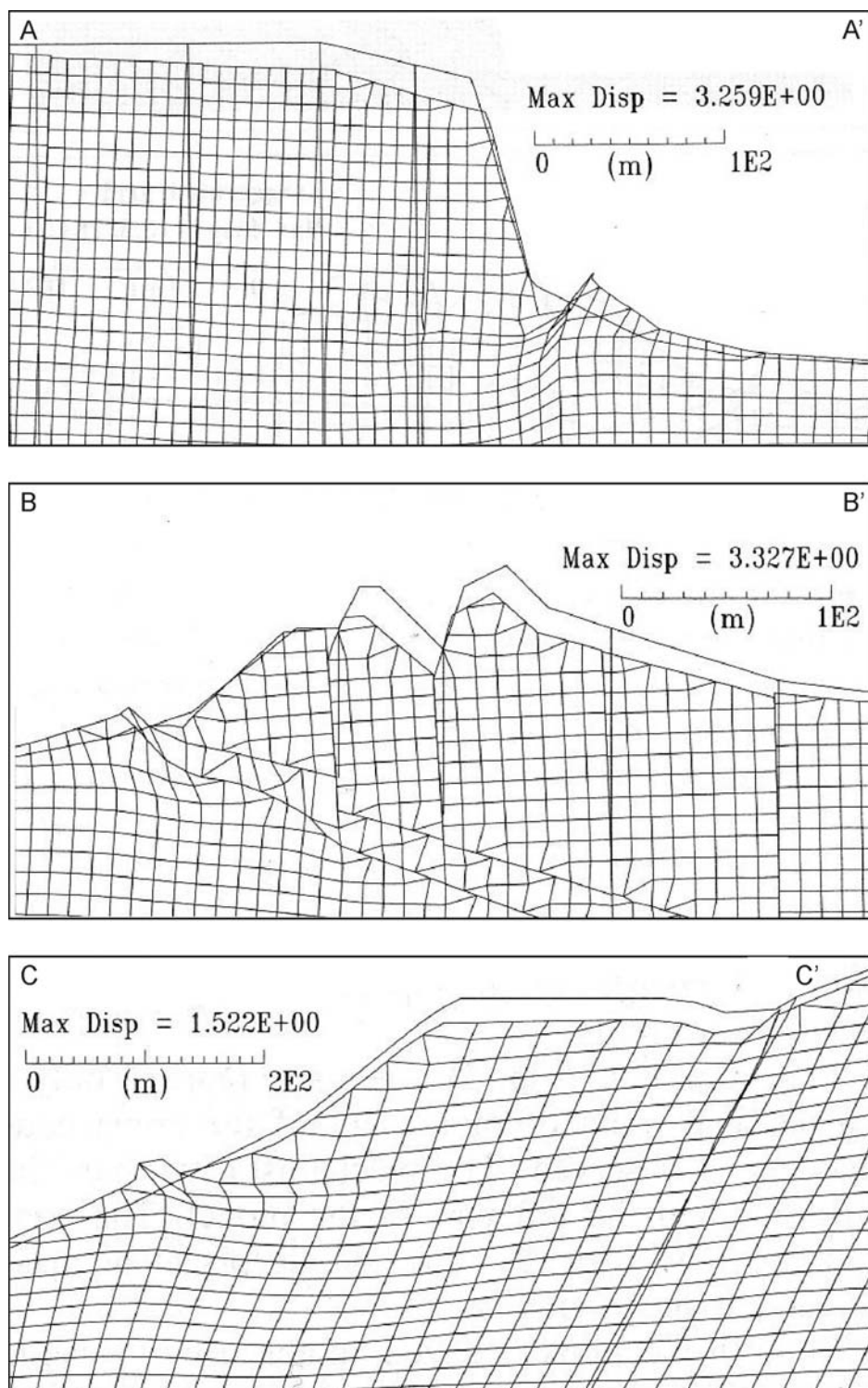


Figure 18. Mount Falcone: a) geological and geomorphological sketch and panoramic view of the southern scarp with particular of joint system; b) interpretation of deformation phenomena; c) displacements simulated by numerical modelling.

As far as control factors of the phenomena are concerned we can therefore affirm that the fundamental shear zones and/or of ductile deformation are found in the weathered level of the pre transgressive basement, composed of clays. Such strong weathering is probably due to the long period of emersion of the messinian sediments as well as to the lithostatic charges and to the constant presence of water in the arenaceous-calcareous aquifer. These clays are in part eroded and in part make up the zone of bulging present at the foot of the plate (*squeezing out* phenomena, Zaruba and Mencl, 1969). Other control factors are: elevated relief of the southern and northern slopes, related to the deep incision of the main fluvial valleys to which it is connected as well and the exposure of the pre-transgressive erosive surface; tectonic fracturing of the rocks; overlapping of rigid masses on masses with plastic behaviour. The latter condition, generating differential collapses, can increase the evolution of the whole phenomenon by exalting the pre-existent fractures of the "plate" and/or generating new ones (Mahr and Nemcock, (1977; Cancelli et al., 1987).

For the gravitational phenomena shown we can hypothesise a state of quiescence; in fact, during the most intense and recent earthquakes (1943, 1972; VIII-VI MCS Mercalli-Cancani-Sieberg, Postpischl, 1985), that produced notable damage to manufacts, reactivation of the morphologic and tectonic elements was not observed. Besides, the oldest manufacts (X century) of the villages mentioned, constituted by watch-towers built near the borders of the "plate", seem still to be well preserved. Therefore the maximum intensity of scarp withdrawal should be dated back to older periods. The phenomenon of deformation and in particular the expansion processes of the relief, are probably pre-Holocene in time when, due to the effect of rapid tectonic uplifting and the associated valley incision towards north and south with respect the relief itself (Hancock, 1991).

### **The Case of Montegiorgi**

The historical centre of Montegiorgio (Fig. 4 and 19), many centuries old as well, is located on a hill modelled in the marine sediments of the early Pleistocene, in the medial belt of the monoclinial relief. The bedrock is composed of the following lithostratigraphic succession, from bottom to top: grey-light blue silty-sandy clays; medially diagenised yellowish sands intercalated, with very variable frequency, closely stratified clays; grey massive silty clays; thick alternations of silty clays and fine sands; massive clays with fine sands; medium-coarse yellowish sands, intercalated with thin layers of grey-havana clays. The succession is closed by layers of polygenic conglomerates intercalated with frequent clayey levels and more rarely sandy layers. Eluvial-colluvial deposits and landslide accumulations bury the bedrock over wide areas. From a physical-mechanical point of view these lithotypes can be grouped into four litho-technical units: clays, sands, conglomerates and superficial deposits. The all over attitude of the strata layers is characterised by prevalent immersion to North-East, with an inclination of between 5° and 12°. Frequent fractures (and subordinately faults), whose orientation is congruent with that of the systems observed in the whole monoclinial sector, dislocate the bedrock (Fig. 19a).

On an extended area along the eastern flank of the relief, the rather deep incision of the hydrographic network, originating from it, exposes the strata junctions therefore generating a condition of downhill lay and with lean considerably minor with respect to that of the slope itself. Huge mass movements, to which the formation of scarps, counterslopes and trenches, of even considerable dimensions (up to about 100m in width, 40m in depth and 1 km in

length) is connected, have been recognized. In the south-eastern sector, in correspondence to the outcroppings of the bedrock, marked variations in the attitude of the strata can be noted.

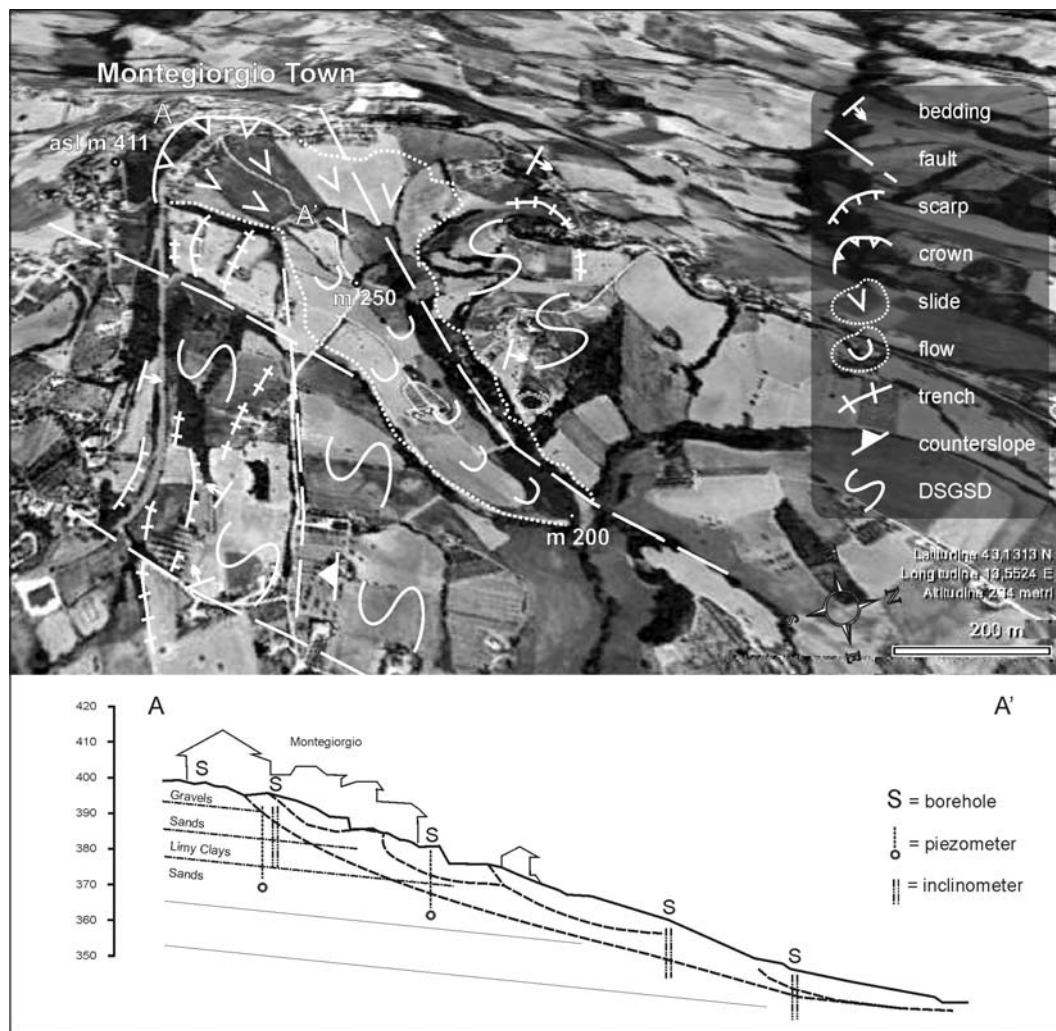


Figure 19. Montegiorgio: a) geological and geomorphological sketch; b) interpretative geological cross-section.

Geophysical surveys (seismic tomography) done inside two service tunnels (one of medieval age located 15m below the inhabited area and one, that cut through the hill, for the realization of the urban aqueduct, 25m below the former) evidenced, inside the historical centre, several shear zones, successively reached for and verified by means of geo-mechanical drilling. Within the boreholes a monitoring network composed of seven inclinometers and ten piezometers was positioned. The inclinometric data, regarding the months of April and August 2000, evidenced sensible dislocations (with a maximum value of 5mm) down to a depth of 36m; the piezometers revealed elevated values of the water table and the presence of confined aquifers in depth.

Altogether the data acquired allow us to associate the damage in the area to a complex phenomenon, which developed probably on two fundamental planes found at different depths and with different kinematics (Fig. 19b). The former, a zone of ductile deep deformation, realised very probably in the basal grey-blue clays, favoured the activation of a deep seated block-slide, the sole evidence of which we find in the south-eastern sector (Fig. 19a). The latter is a “superficial” mixed phenomenon of translational slide/flow, generated by the evolution into slide of the previous phenomenon, where several movements take place, driven by the topographic gradient.

As for other historical centres of the area, the gravitational phenomenon of the second type has shown significant re-activation in the last ten years, after a first aqueduct was brought to the inhabited centre at the beginning of the forties and a second, of greater capacity, about ten years later, fed by the springs of the limestone Apennine ridge. This hydrologic network allowed a direct and continuous flow of water in all the houses. The local concentration of water on the surface and, above all, the strong increase of water consumption and the subsequent infiltration of water in the soil substrata, initially due to the poor sewage system as well as the dispersion found for the aqueduct itself, were helped by the intense fracturing of rocky bodies, that also allowed exchanges of water between strata and/or levels characterised by different permeability. This has greatly increased the piezometrical levels and increased the level of pore pressure, activating and/or reactivating the mass movements.

The main factors of control of the great slide phenomena have therefore been individuated: in the deepening of the hydrographic network connected to the intense tectonic uplifting of the middle-upper Pleistocene, to which is associated values of relief energy that when referred to the lithotypes that make up the slope are to be considered high; in the intense tectonic fracturing of the lithotypes, also connected to the uplifting that, besides favouring the deep circulation of water, has weakened the lithoid body, predisposing it for the genesis of gravitational shear planes, and has oriented the geometry of the main embankment; in the increase of groundwater circulation, connected to the increase in water consumption, and to the orientation of the groundwater towards the medial sector of the slope as a result of the drainage preferential induced by the construction of the tunnels cited.

## 5.2. Mass Movements of the Clayey Slopes

The morphodynamic features of the periadriatic belt have been faced in numerous studies concerning the widespread and intense landslide phenomena characteristic of the clayey-marly bedrock and the extensive silty-clayey eluvial-colluvial coverings. The correlations established by means of specific geotechnical studies, identify the main control factors of the processes in the decay of the physical-mechanical parameters, essentially connected to the presence of water within the lithotypes (Tonnetti and Angeli, 1984; Bertini, 1987; Sciarra, 1988).

The present work, instead, wants to evidence the fundamental control exerted on the phenomena in question by natural factors, different than the geotechnical ones, and by anthropic factors, attempting to define, with good approximation, the evolutionary trends as well. Among the former, the conditioning exerted by the geological, geomorphological and hydrogeological setting is carefully considered. Among the latter, the role played by the evolution of the rural landscape and the associated different land use is analysed.

The geological-geomorphological setting of the monocline relief (Fig 6), characterised by extensive outcropping of marly clays intercalated with rare arenaceous-conglomeratic levels, and by asymmetric valleys (cfr. § 2.1 and 2.2), favours the genesis of typical landslides: translational slides along the slopes with downhill lay; falls-topples and, secondarily, rotational slides, onto the slope with uphill lay.

The numerous studies carried out have, though, put clearly in evidence that the phenomena of major extension and depth, even if less frequent than those cited, are made up of translational slides whose direction of movement does not coincide with the strata attitude, but is oblique with respect to them (Dramis et al., 1992).

They occur mostly in the western high-hilly zone, their thickness is normally between 10-15 m., the overall volume, even if very variable, often has values between 200,000 and 400,000 m<sup>3</sup>; often damming phenomena and/or diversions of river beds of short duration (4-6 days), are associated to them. The landslide phenomenon usually takes place through the translation of blocks of considerable dimension (up to 4,000-5,000 m<sup>3</sup>, in the cases observed), that conserve their stratification and the vegetation cover above. Only towards the foot do they lose their individuality in a chaotic accumulation that evolves in flow. The velocity of the movements is extremely variable (from cm/yr. to tens of m/h). In some cases, characterized by very rapid evolution, the piling up of the accumulation along the opposite slope has occurred, even for a few tens of metres.

For the numerous cases analysed, previous morphologies characterised by slight depressions that are not drained in the upper sector have been recognised, while the base of the slope, characterised by great steepness and decametric incisions, shows no evidence of movement. In other cases the phenomena, active for many years at varying intensities, show trenches, scarps and traction fractures that allowed us to identify the blocks (Fig. 20a).

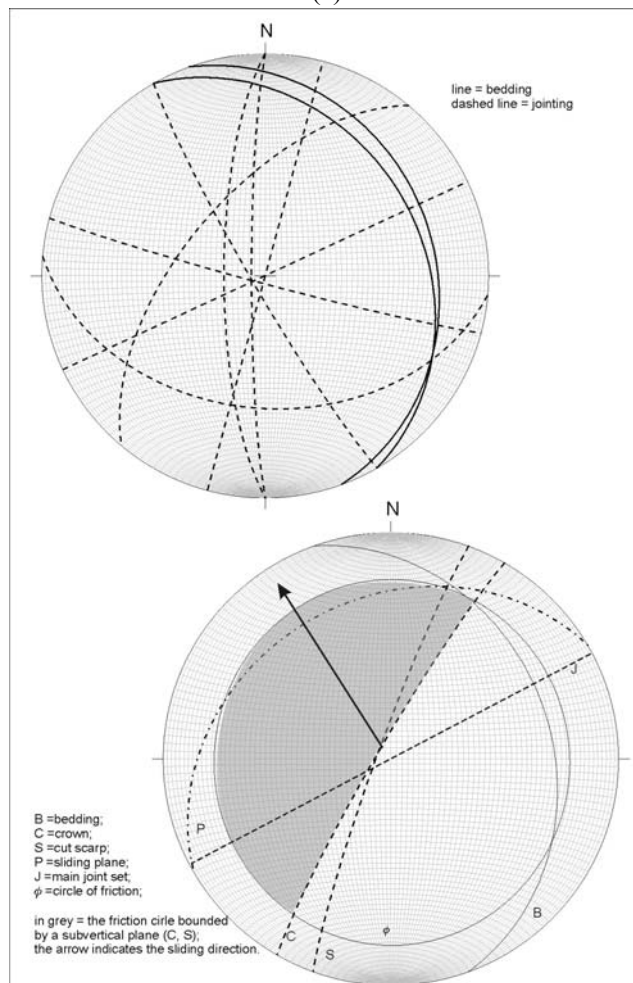
The surfaces of failure, gently sloping and sometimes disposed on a number of levels, develop usually in the medially plastic pelitic levels, generally limited by thin sandy-conglomeratic levels (10-20 cm. thick). The fracturing is elevated also in the overconsolidated clays, characterised by quite fragile behaviour. At the top of the clayey lithotype it is possible to recognise an intense secondary fracturing, which reaches a depth of a few meters.

Based on the analysis and the representation of the traces of the main planes of discontinuity, of the orientation of the scarp edges (Fig. 20b) and applying preliminary stability tests, a possible correlation between the irregular direction of movement, the strata attitude, and a number of sets of vertical or sub vertical joints has been attempted.

The genesis of these phenomena is directly connected to the recent incision of the hydrographic network whose tracts, which run parallel or obliquely with respect to the strata dip, have generated slopes with cross-hill lay, much more numerous than those with downhill lay, continually subject to remodelling due to translational slides. Such values of relief, high for the lithotypes in question, and the exposure of certain particular levels with poor mechanical characteristics, represent the predisposing factors for the activation of the phenomena. This is probably connected to the presence of aquifers within the permeable sandy intercalation.



(a)



(b)

Figure 20. Translational slide in the marly clays: a) example of damaged slope and interpretation of the gravitational movement; b) stereographic projection of structural data and of the kinematics for planar sliding (from Dramis et al., 1992, modified).



With respect to the more general aspects of the landsliding of the physiographic unit in question, one of the territories which is more representative is that of Mount Ascensione (1,110m. a.s.l.), made up of a huge conglomeratic body intercalated with the marly clays of the middle Pliocene (Figs. 2 and 6). It is considered to be a key point for the understanding of the tectonic-sedimentary and morphostructural Pliocene-Quaternary evolution of the whole peri-Adriatic belt of central Italy, but it also represents a sure reference point for the comprehension of the recent landscape modelling. In fact, the evolution of a stratified slope deposit, made up prevalently of gravels and sands of an age between 40,000 and 20,000 yrs. B.P. (Gentili et al., 1998), allows us to establish important bonds concerning Holocene morphodynamics and, particularly, the action of gravity.

This deposit, mostly overlapping the clayey bedrock on the southern and eastern sectors, was originally continuous and extended for about 10 Km<sup>2</sup>. The climatic improvement which occurred at the beginning of the Holocene, favoured its initial linear incision by means of a primordial hydrographic network developed at the end of Pleistocene. Successively, the incision continued in depth exposing the debris-clay contact (aquifer/aquiclude) and generating almost perennial springs; the latter have intensified the fluvial deepening producing, as a consequence, a significant increase in the relief. At the head and on the flanks of the little fluvial catchments widespread landslide phenomena was activated, which lead to the dismantling of a great part of the debris deposit.

For the definition of a trustworthy framework concerning the landsliding of the last 1000 years, geomorphologic analyses have found a valid support from historical research (Carlini-De Carolis, 1792; Galiè and Vecchioni, 1999; Santoni *et al.*, 2005). The latter supplied interesting data regarding the main gravitational movements, which damaged, also more than once, or destroyed, many built-up areas of the territory in question. The same sources also mentioned phenomena which happened outside the area, for as far as the Adriatic coast. A brief illustration of these cases can furnish, in the Author's opinion, a valid contribution to the understanding of the characteristic kinematics and to the definition of the control factors.

The southern side of the historical village of Castignano, built in Medieval times on a arenaceous bank overlying clays, is located on the eastern flank of Mount Ascensione (Fig. 6), and has been affected more than once by slide phenomena throughout the centuries. This has forced the population to move the village towards the northern sectors. The oldest mass movement attested to by the historical sources goes back to 1204 and was repeated for about another 10 times at least. The most frequent episodes occurred between the mid 15th century (almost continuous activity between 1450 and 1500 roughly) and the 18th century. The last event happened in 1927 and has been followed by important remedial works along the slope which are still in function (Fig. 21a).

Systematic historical references also regard the landslide phenomena of the historical centre of Appignano, placed at the confluence between two water courses which originate on the eastern flank of Mount Ascensione. It is built over alluvial deposits made up of gravels, sands and silty levels (overall thickness of about 25 m), lying on closely stratified clays which contain thin sandy levels. The southern and eastern sectors are bordered by a fluvial scarp more than 30 m height. The first news regarding fall-topple phenomena of the southern scarp go back to the mid 16th century and continue, repeatedly, in the following centuries, particularly up to the mid 18<sup>th</sup> century roughly. Testimony of the gravitational



phenomena start again at the beginning of the 19th century and they last into the 20th century. Frequency and intensity of the phenomena are, however, considerably lower with respect to that of the previous periods. Numerous works, having the purpose of ending the erosion processes at the foot of the scarp and with the intent of containing the scarp itself, have assured only brief periods of stability. The successive events have always damaged or destroyed these works.

At Ripaberarda, a village of the IV-V century located over a distal limb (mainly sandy) of the Mount Ascensione slope deposit and with a fortified castle built in 1298, at the beginning of 1500 a landslide destroyed part of the castle and the church. The period previous to the event was characterised by an intense deepening of the erosion in the creek below, cut into the clayey bedrock. In 1518 a bell tower was built, now clearly leaning westward (Fig. 21b) as a result of deformation phenomena connected to the withdrawal of the slope. In the 16th century, mass movement destroyed the village of Capradosso, built on continental deposits. Rebuilt in 1753, it is still inhabited and free of significant landslide phenomena. The castle of Porchiano, previous to 1237, located on a plate about 30 m thick made up of stratified slope deposits of the Mount Ascensione overlying clay, felt down to the valley, carrying with it various houses. The rests of the old village stands on a narrowed debris plate affected by fractures and fissures with direction roughly parallel to the slope and of clear gravitational origin that continue within the clay levels below (Fig. 21c). At Rotella, a historical centre located on a third order alluvial terrace, the church of Santa Maria (of 1430) partially collapsed together with part of the village.

The recurrent geological-geomorphological settings and the historical sources allow us to associate a large part of the mass movements cited to translational slides and to falls/topples which have affected more or less large portions of the overlying clayey units (arenaceous levels of bedrock, slope deposits, alluvial conglomerates). The initial accumulations evolved successively into flows that filled the valley of the minor hydrographic network. Of some of these only the crowns and/or the scarps remain. The accumulations, instead, were rapidly dismantled by the fluvial-torrential erosion.

The fundamental predisposing factors of the cited phenomena are found in the recurrent hydrogeological setting, characterised by the aquifer/aquiclude overlapping and in the tectonic fracturing of the lithotypes. The main activation and control factors of the repeated landslide phenomena, particularly frequent and diffused between the 14th and the 19th centuries, is revealed by the presence of large quantities of water, certainly in agreement with the climatic fluctuations of the period ("Little Ice Age"). It is responsible for: strong processes of *softening* in the clays underlying the aquifer; intense and rapid deepening of the fluvial-torrential erosion into the clayey bedrock, at the foot of the slope. Testimonies of this are found in the historical sources of the period previous to the events. The action of water could also have been exalted by the significant deforestation carried out agricultural purposes, done without creating works aiming to their stabilization (Gentili and Pambianchi, 2002; Buccolini et al., 2007). This is also true for other parts of the Mediterranean area (Garcia-Ruiz and Valero-Garcès, 1988; Ruiz-Flano et al., 1992). An important role could have been played, besides, by the frequent seismicity of the area, for which, however, we do not have secure data.

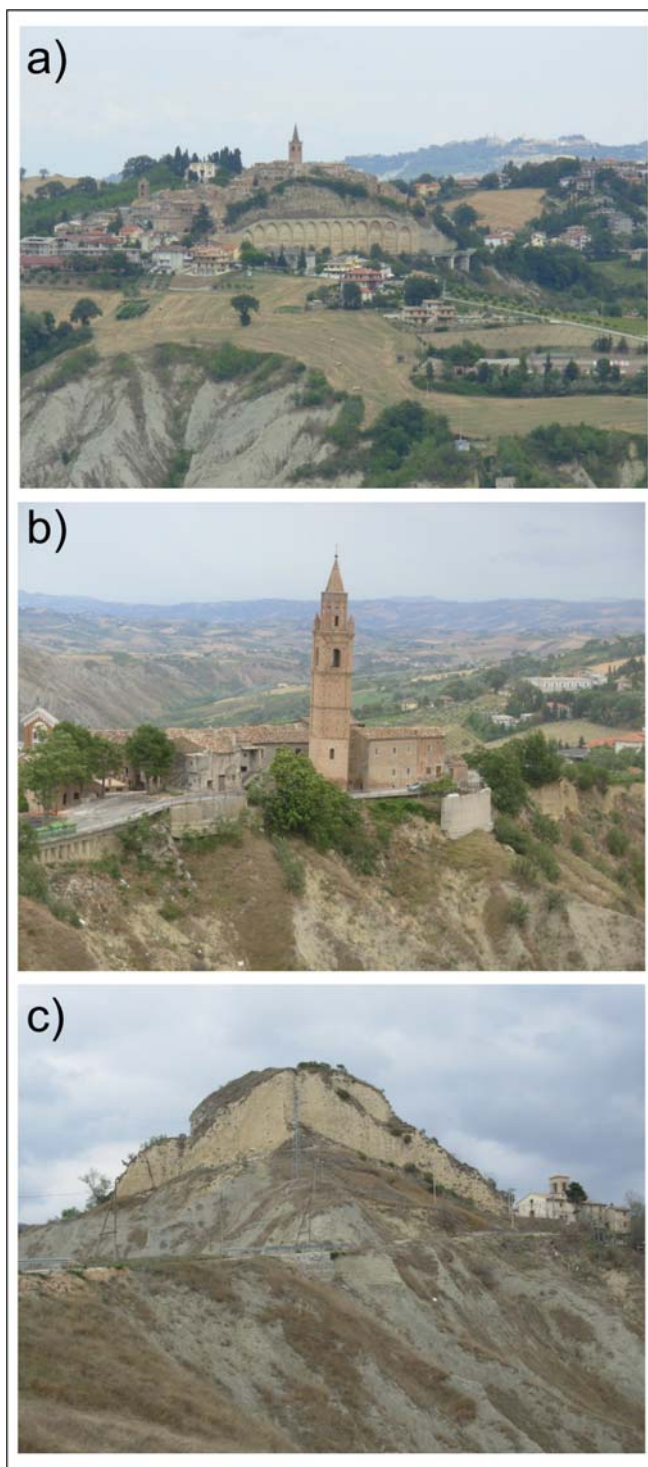


Figure 21. a) Remedial works in the southern slope of Castignano; b) tilting of the bell-tower of Ripaberarda, connected to the gravitational evolution of the scarp below, modelled in the marly clays; c) Porchiano, gravitational fissures and fractures in the continental deposit and in the underlying marly clays of the middle Pliocene.

### 5.3. Mass Movements of the Coast

The Adriatic coast of central Italy is characterised by rather wide gravelly-sandy low beaches. In a backward position, along the watersheds, medially inclined slopes and inactive cliffs alternate. The are modelled in the marine sediments of the early Pleistocene (Sicilian-Crotonian) made up of marly clays at the base and conglomerates on the top, often placed in a bland monoclinial setting. The active cliffs of Mount Conero, SE of Ancona, and of San Bartolo, SE of Pesaro (Fig. 1), are instead made up, respectively, of limestones and marly limestones and of arenaceous turbidites. Their genesis is connected to the compressive tectonic phase, still active as the frequent earthquakes prove (Console et al., 1973; Gasparini et al., 1985). Tectonic alignments with Apennine and anti Apennine direction work as extensive elements placed at different depth and interfere, in certain cases, with the compressive structures below. This is demonstrated by the seismic profiles of the coast carried out for oil exploration (Calamita et al., 1991), and also by the lower Pleistocene sediments that dip down to the sea with scarps and benches aligned according to the Apennine direction.

Different mass movements have been recognised in the active and inactive cliffs of the sector in question. The studies analysed single phenomena whose still active movement, recent or historical was certain. Exclusively referring to the present morphological setting of the emerged and submerged coast they identified the control factors: extreme climatic conditions, seismic activity, stratigraphic-structural and tectonic setting of bedrock (Cancelli et al., 1984; Coltorti et al., 1985; Crescenti ed., 1986; Guerricchio, 1988; Dramis and Sorriso-Valvo, 1994). A more recent study (Aringoli et al., 2002), allowed us to hypothesise on the basis of geomorphological elements and numerical models, deep mass movements, probably correlated to the Pleistocene-Holocene sea level oscillation.

In depth and systematic geomorphological analyses extended to the entire coastal sector evidenced the almost systematic recurrence, in correspondence to the major inactive cliffs of the medial tract Fig. 22a), of valleys roughly parallel to the coast line, whose dimensions can be even a few kilometres in length, 500 m in width and 100 m in depth. Another significant geomorphological element is the presence, east of the first, of suspended valleys on the coast that dissect the erosive summit surface modelled in the Quaternary deposits. These belong to an ancient and primordial hydrographic network that flowed out roughly perpendicular to the shoreline. They are even a few hundred metres wide and they open and deepen rapidly towards the interior.

The geomorphological elements described seem to be in net contrast with a normal evolution of the hydrographic network, but they can be associated to deep-seated gravitational slope deformation (Fig. 22b), activated in a context of rapid tectonic uplifting, to which a great increase of relief, the genesis of the faults and fractures mentioned and frequent earthquakes are associated. As far as the faults are concerned, the evolution in the listric sense of those with an Apennine direction is particularly important. This is favoured by the morphostructural setting of the coast and by the presence in depth of a huge clayey body deformed by the compressive tectonics. These faults have constituted a sure predisposing factor for the action of gravity (Dramis *et al.*, 1995).

It is believed, though, that in this context an important decisive role could have played by the late- Pleistocene sea level oscillations (cfr. § 2.2), according to the following mechanism: 1) in agreement with other authors (Pirazzoli, 1997; Lambeck et al., 2004), the sea level rising

up to the present height, in a coast with ongoing uplifting, modified the slope geometry previously regularised by the long emersion, generating a cliff; 2) the rising of the sea level also produced a general decay of the mechanical characteristics of bedrock, due to the reduction of the pore pressures (Aringoli et al., 2002); 3) this setting favoured the activation or the reactivation of great mass movements (as well as superficial phenomena whose accumulations have been eroded by the sea), of which only traces in the high sectors of the cliffs remain (Fig. 22a and b); 4) the alignments connected to the gravitational dislocations guided the setting up and the development of the hydrographic network, that has, in particular, underlined the alignments themselves; it activated, as a result of the genesis of the cliff, in agreement with what has been seen in other areas (Mizutani 1996; Trenhaile, 2002).

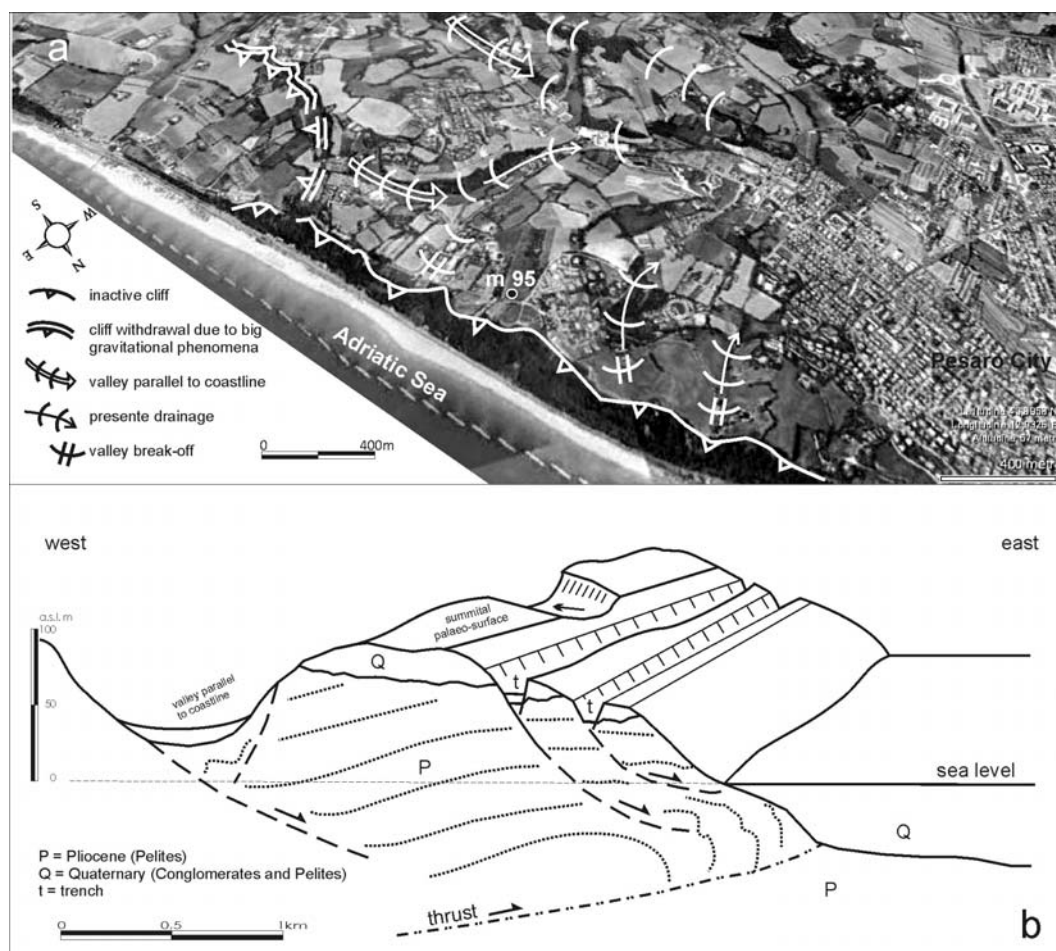


Figure 22. a) geological and geomorphological sketch of a tract of the Adriatic coast; b) evolutionary model connected to gravitational phenomena.

## 6. Evolution of Rural Landscape and Landsliding

In this chapter, upon the illustration of the evolutionary framework regarding the transformation from natural to rural landscape, reference is made to landslide phenomena

directly or indirectly connected to the agricultural occupation of the slopes and the related practices. These are widespread in the different geomorphological contexts of the study area, but are particularly important in the pedemountain zone and in the periadriatic belt, where, historically, the most intense agricultural activity is found.

A first differentiation of the Italian rural landscape from the natural one started with the Greek and Etruscan colonisation, even though definite traces of agricultural activity in previous periods have been seen. However, in these first phases, the anthropization has been carried out with the cultivation of small areas surrounded by woods, which go back to the natural vegetation after a few productive cycles once the soil has exhausted its natural productivity. The same characteristics are found in the rural landscape of the Roman age, where deforestation is much vaster (Fig. 23a). Also in this case it was followed, during the late Middle ages, by the re-occupation of the woods almost everywhere (Desplanques, 1975; Sereni, 1979). A similar situation is found in the several areas of the Mediterranean basin (Vita-Finzi, 1969; Delano-Smith, 1979).

In the study area, the anthropization of the slopes began to be significant starting from the 11th-13th centuries. In fact, the building of the first urban settlements, mainly located at the tops of the relieves (in the hilly belt) and in the pedemount or in the valley bottoms (in the mountainous sector) leads, in the surrounding areas, to the development of agroforestry-pastoral activities. These were widely extended, and gave a first decisive imprint to the rural landscape in the following centuries, both in relation to the progressive demographic increase and, above all, to the absence of stable ties between the site of cultivation and the farmer (between the 16th -17th centuries and the mid 19th century). In fact the latter extended its fields and grazing land by deforesting the areas he has been allotted and exploited the soil without taking measures to preserve it. This favoured the activation of fast and intense erosive processes which reached the rhegolithic level, making impossible further agricultural or pastoral activities. The farmer was therefore forced to move to other areas where the same procedures were repeated ("nomadism"). The repetition of the phenomenon in time and space, conferred to it indirect morphogenetic value due through the creation of general conditions of anthropic rhesistasy in a temperate climate (Gentili and Pambianchi, 2002).

The intense slope dynamics (hydric erosion and prevalent flows) and the contextual alluvial phenomena of the valley bottoms, associated to this new setting of the landscape and exalted by the pluviometric increase of the "Little Ice Age", contributed to a new definition of certain morphological features. The most significant effects were "recorded" in the fluvial-coastal Adriatic system, at least until the mid 19<sup>th</sup> century. Among these, the depositing of a fourth order of alluvial deposits, rich in clayey-sandy matrix, the generalised transformation of the river mouths from estuaries to deltas and the development of wide sandy-pebbly beaches (Aringoli et al., 2007; Materazzi et al., in press).

Successively, and above all in the first decades of the 20th century, the rural landscape of central Italy underwent noticeable modifications as a result of the affirmation of the small estates. The "nomadism" ceased, deforestation and tilling of uncultivated land were extended, but the cultivation took place upon the precautionary and contextual agricultural practises on the slopes (terraces, embankments, hedges, ditches, canals) and the continuous and careful maintenance of these. Soil conservation is, therefore, favoured. Farming activity, normally limited to a slope lower than 30%, is extended to well beyond that limit.

In this context, the "*alberata*", a cultivation made up of a vine (*Vitis vinifera*, whose first traces in the area go back to the first millennium B.C.), coupled with a maple tree (*Acer*

*campestre*), is fully affirmed and reached a frequency of one tree every 20 m<sup>2</sup>. This latter, included in “closed fields” by hedges, scarps and drainage ditches, which flow into a deepened and well outlined hydrographic network, has been a distinctive element of the rural landscape of central Italy up to the first decade of the second half of the 20th century.

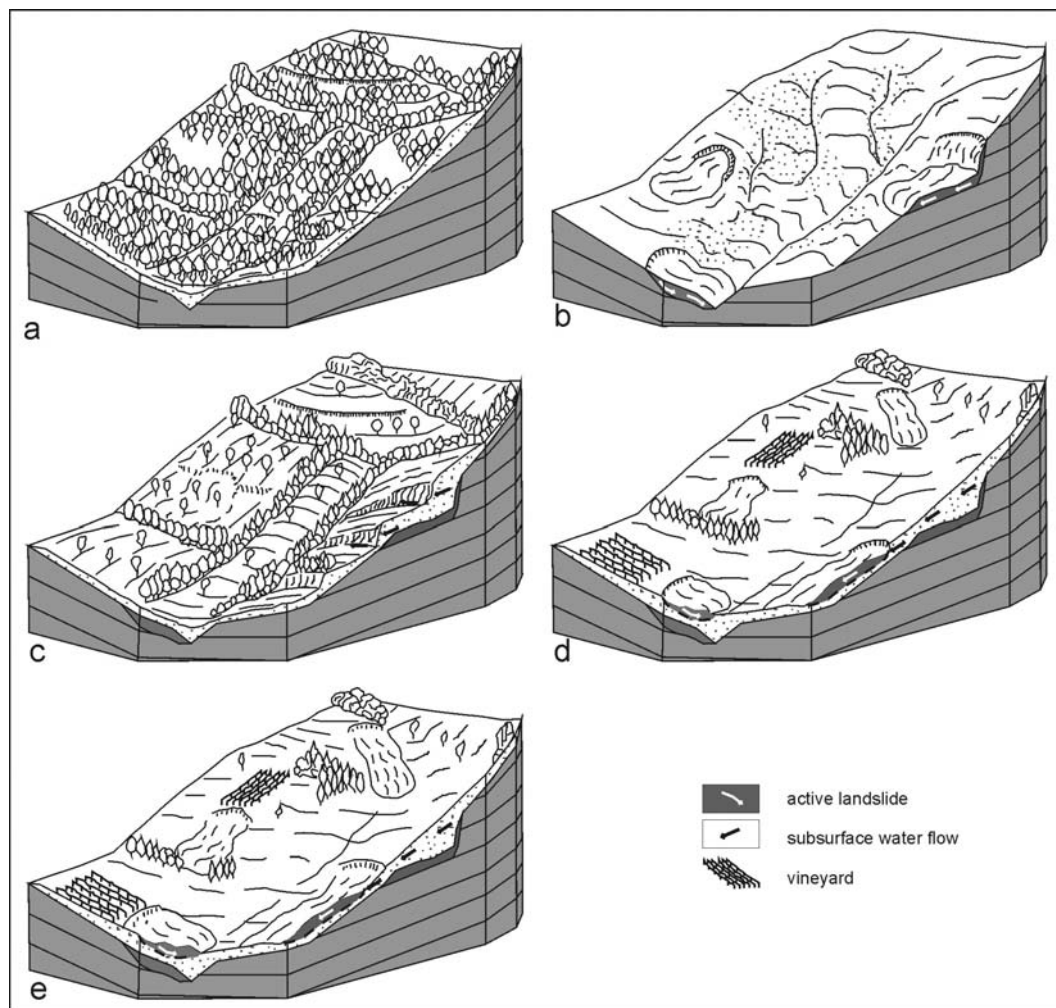


Figure 23. Rural landscape setting, corresponding to: a) the Greek-Roman colonization; b) post Middle ages period up to half of 19th century; c) the “alberata” landscape; d) post-“alberata”; e) present.

Starting from about 1960, in the study area, new techniques and crops already experimented in other parts of Italy were adopted with great rapidity. This required the passage from “closed fields” to “open fields”, realised through a previous regularization and extension of the cultivatable slope tracts; this fact required the dismantling of almost all the work done to stabilise the slope during almost a century (Calzecchi Onesti, 1957; Desplanques, 1975; Sereni, 1979; Buccolini et al., 2007).

Such a new setting represented the necessary consequence of the changed social-economic conditions that induced a practically massive exodus from the countryside. It was practically total in the mountain area, where the woods are slowly re-occupying their natural

area also because of the effect of extensive reforestation being done by man; it was diffused, instead, in the pedemountain and high hilly area. The low-hilly and coastal zones registered, as a result, a demographic increase with the realisation of massive infra structural interventions and with the development of inhabited settlements, both scattered and centralised.

It is with the affirmation of the “*alberata*”, that the most rapid and significant geomorphological modification of the slopes occurred. It happened through the following phases.

### **Phase 1**

The profile of the natural, post-deforestation, slope is relatively regularised by colluvial material of different size (pebbles, sands and silts); these are produced by intense weathering processes and areal erosion, connected to the condition of anthropic resistance caused by the deforestation itself. Only mass movements which affected the bedrock and at times are obliterated by colluvial deposits, or the more superficial ones (solifluctions, debris-flows) that mobilised the eluvial-colluvial deposits being formed (Fig. 23b) are present.

### **Phase 2. The “Alberata” Landscape**

With the realisation of works aiming to soil conservation, the slope profile was continually modified until a stable profile in “terraces” was realised. The body of the terrace, cone shaped and with its summit towards the mountain, results to be formed of sandy-silty deposits, containing dispersed centimetric-decimetric pebbles (sometimes blocks) and clayey levels. These latter often correspond to older soils, covered by the prevailing depositional processes. As a result of this setting, also the hydraulic and hydrogeologic regime of the slope is modified. Hydric erosion processes are reduced or annulled while water infiltration is, on the other hand, favoured. The permeability threshold, constituted by the underlying pelitic-sandy levels (widely prevalent in the study area), generated a neoformed aquifer into the deposit. This latter is at times organised on different levels due to the presence of clayey horizons (paleosoils). To the aquifer are also connected to diffused springs, located at the base of the “terrace” scarps, whose waters are drained by the anthropic superficial channels (Fig. 23c).

Even if there are gravitational phenomena affecting the bedrock, this geomorphological setting of the slope is such as to guarantee the best conditions of stability with regard to superficial fluvial-denudational processes (water erosion, solifluctions, flows). It is systematically diffused in the pede-mountain and high-hilly areas, where, otherwise, farming activity would be almost completely impossible due to the morphology of the slopes. In the low-hilly area, this is less extended, because not strictly necessary, given the minor steepness of the slopes.

### **Phase 3**

The mechanical regularisation of the slope, done during the last half century, rounded the edges of the scarps and accumulated the materials at the foot of the scarps themselves. The

result is a slope length similar to the original one where, at times, convex landforms corresponding to the original scarps can be recognised. Interventions on the hydrogeological setting which had developed and evolved in the previous phase of evolution have been only sporadic. The result is a hydro-geomorphological setting favourable to the activation of slope processes, in particular of flows. In fact, the groundwater circulation into the eluvial-colluvial deposit, often interrupted in the previous hydro-geomorphological setting, has been able to develop over greater length, leading therefore to a significant increase of the pore pressures that reached their highest values in the medial tract of the slope. This has favoured the activation of filtration and piping phenomena to which, normally, are associated recurrent flows whose shear planes (or zones) are found entirely within deposit itself or in the underlying levels of alteration of bedrock (Fig. 23d and e).

An attempt has been made at defining the evolutionary trends of the cited flow phenomena through the detailed analysis and the comparison of the morphodynamic setting of four sample areas, for an overall surface of 150 km<sup>2</sup> (Tab. 3). These, though they are extensions of different sizes, are widely representative of the current rural landscape of the Adriatic side. It shows substantial territorial differences between pedemountain-high hilly sector and low hilly-coastal ones, both with regard to the human settlement and to the morphological setting, mentioned above. The flow phenomena analysed regards the eluvial-colluvial coverings of the slopes modelled in different lithostratigraphic units, that show relatively high thickness (up to 10 m. and beyond) in the pede-mountain and high-hilly area, while minor thickness characterise the less steep clayey slopes, affected by an intense hydric erosion.

**Table 3. Landsliding evolution in some sample areas.**

	Tot. Ar. (km <sup>2</sup> )	Last survey (yrs. elaps.)	Observed parameters during past surveys					Observed parameters during survey of 2008					land. Incr. (km <sup>2</sup> /yr)	land. Incr. (perc./yr)
			N. phen.	Tot. Ar. Land. km <sup>2</sup>	Aver. Ext. km <sup>2</sup>	Freq. (1/km <sup>2</sup> )	Dens.	N. phen.	Tot. Ar. Land. km <sup>2</sup>	Aver. Ext. km <sup>2</sup>	Freq. (1/km <sup>2</sup> )	Dens.		
Entogge stream basin	22,3	23	177	6,55	0,04	7,92	0,29	144	9,42	0,07	6,44	0,42	0,125	1,91
Fiastrone stream basin	8,89	23	59	2,79	0,05	6,63	0,31	40	3,75	0,09	4,49	0,42	0,042	1,5
Mid Tenna river basin	100	33	52	3,63	0,05	2,8	0,13	52	5,98	0,09	3,7	0,32	0,071	1,96
Mid Tesino river basin	18,4	53	61	3,2	0,05	3,32	0,17	116	3,8	0,03	6,3	0,2	0,011	0,35

The comparison between past landsliding, represented in maps of different periods, and that present has been made. The geomorphological surveys and the interpretation of aerial photographs of different periods were carried out mostly by the Authors themselves. The data showed, clearly evidence the trend of areal increasing of the phenomena, necessarily approximated due map scale used that did not allow us to evidence the minor planimetric variations. These correspond both to the amplification of slide phenomena already active at the time of the previous survey and to the genesis of new landslides. The geomorphological



analysis (testified to also by oral testimonies) aimed to the individualisation of the position of the original sliding phenomena in the area of the slopes, has shown their recurrent location in the middle and middle low sectors of the latter. The most recent activity shows a prevalent expansion towards the medium-high sectors, or at times top ones (Fig. 24). The low map scale made it possible to represent only the main cases.

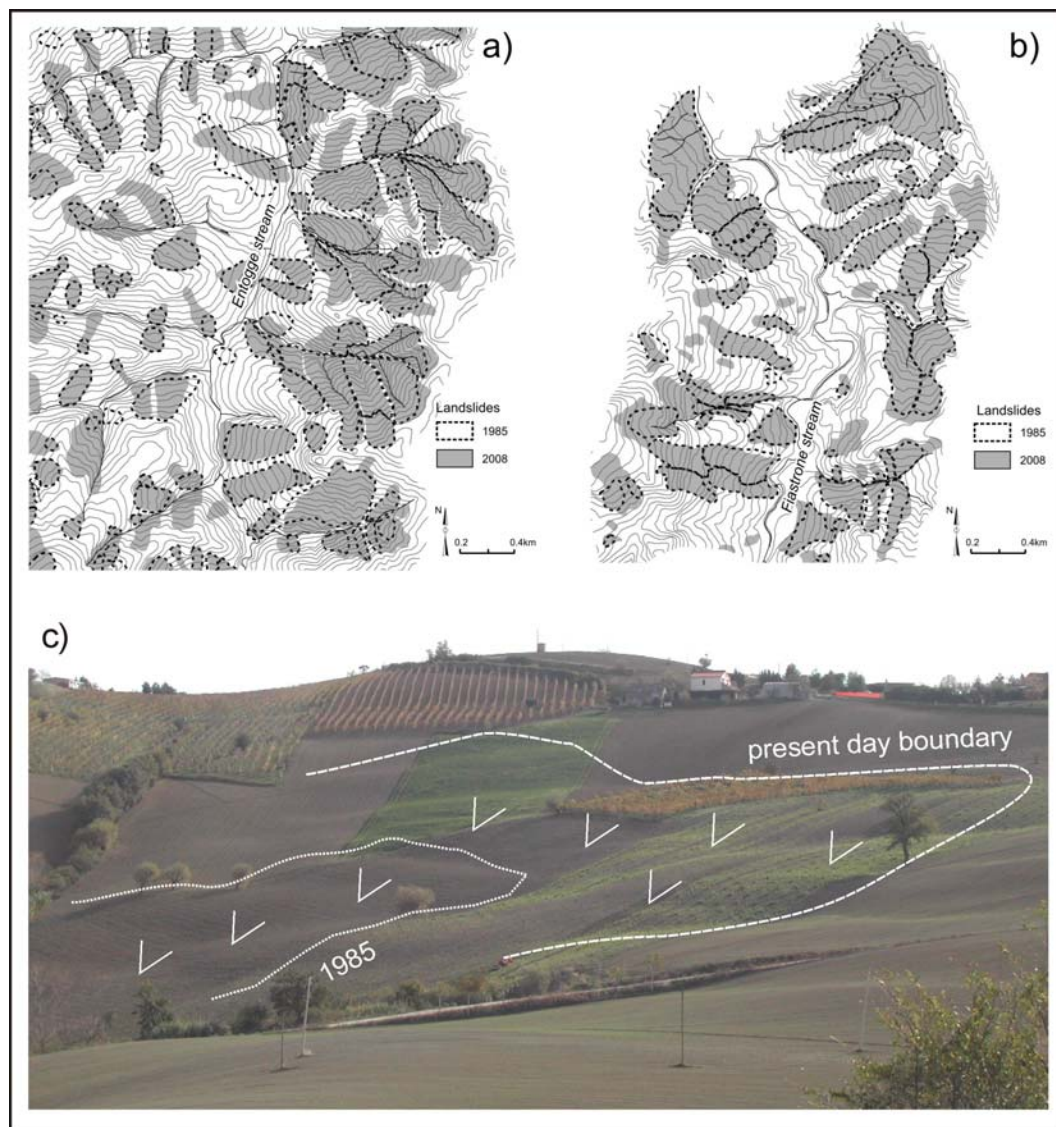


Figure 24. Evolution of flows into two sample areas: Entogge stream catchment (a) and Fiastrone stream catchment (b), from 1985 to 2008; c) landslide moved.

The congruency of the values of the increases (between roughly 1.5 and 2%), registered for the first three or four areas, all within the pede-mountain, high-hilly sector, seem particularly significant with respect to an average annual increase of the landsliding registered (1.42%). These trends have as their common denominator the hydrogeomorphical conditions connected to the cited evolutionary *phases* of the rural landscape. The considerably lower

value calculated for the fourth area, finds its full justification in the massive anthropic interventions which are connected to the repeated and extensive works of stabilisation in the medium-high sectors of the slopes, where villages, inhabited settlements and important infrastructural works are present. These are connected, in particular, to the recent increase in the presence of man.

In this framework, and with the aim of establishing the more probable correlations between different land use and slope dynamics, the behaviour of gravitational phenomena in areas occupied by vineyards has been analyzed. It has assumed, in fact, in the last 30-40 years, a role of primary importance in the agricultural economy of the study area. In the past, the production of wine, that had a significant development in the Roman age, then to disappear and reappear towards the end of the 16th century, has always been connected to the "*alberata*". Nowadays, it has developed into businesses of small and medium dimension that all in all cover an area of about 25,000 hectares of the pedemountain and, mostly, high-hilly physiographic units. The marked fragmentation of the system represents, at times, in part, an example of conservative farming on ancient rural landscape.

The data obtained from aerial photograph analysis of 1995 and of 2000 images, concerning nine sites of the Marche Region occupied respectively, by the "*alberata*" and by the vineyards are described below. Besides the aerial photo analysis, specific geomorphological surveys integrated with historical investigation and oral testimonies have been carried out.

Altogether, the surface of the sites analysed is equivalent to about 5,320 hectares (ha). Of these, in 1955, 854 ha were affected by mass movements, equivalent to 16% of the whole territory, while in 2000 the landslide phenomena involved 823 ha, equivalent to 15% (Fig. 25a). Apparently, the overall landsliding, that affects the different types of cultivation, can seem stationary. In this specific case, the land cultivated in "*alberata*" was about 2,627 ha, and of this 500 ha affected by landslides (19%); in 2000, on the other hand, the land cultivated in vineyards was 779 ha, of which 220 ha involved in landslides (28%). This data should not be interpreted as a logical equivalence which sees vineyards as being always part of landsliding increase in an area, but in particular situations the implanting of a vineyard can surely favour instability phenomena.

In fact, for vineyards of great dimensions and mainly located in mid-high sectors of the slope, in more than one case the activation, a few years after their planting, of even important mass movements at their base has been observed. These latter are the consequence of large and deep incisions that, oriented downhill, form drainage trenches and discharge water slightly valleywards of the cultivation, causing damages that often back up towards the top and involve the vineyard itself. In some cases, instead, landsliding does not increase, or is absent, both because the vines are of limited extension or placed on slopes entirely without or almost without colluvial covering, or because they end at the base of the slope and the waters, directly drained by the hydrographic network below, are not able to activate landslide phenomena and therefore regression of the heads towards the plantation itself.

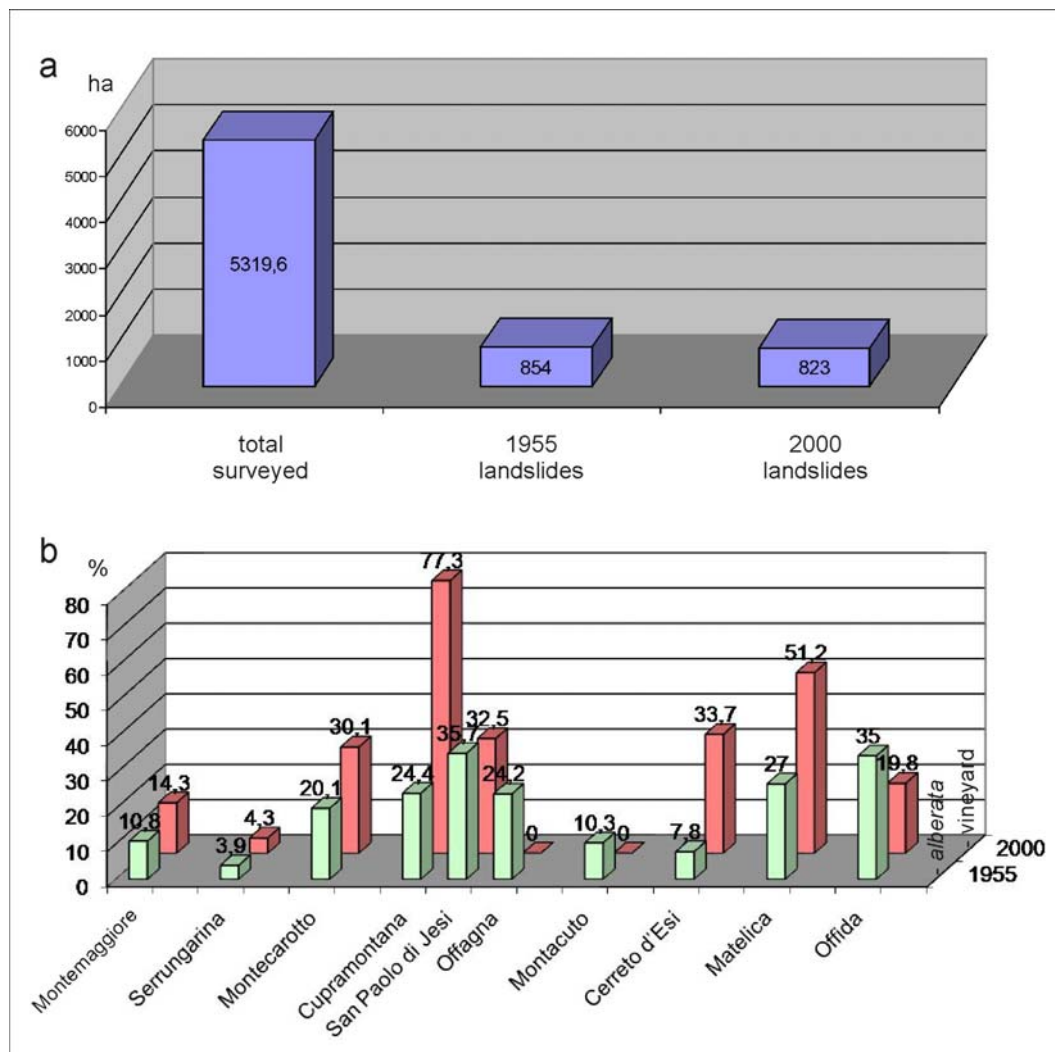


Figure 25. (a) Total area of the sites analysed and landslides surveyed in 1955 and 2000; b) landsliding related to single sites at the same frequency relative to the single sites at the same date.

More in detail, observing the graphs of figure 25b, for certain sites located in the hilly sector of the central-southern Marche, it is possible to find a notable increase of the landsliding, passing from the “alberata” to the vineyard. For others, the landsliding diminishes and in others it doesn’t change. Where the landsliding increases, the average increase was of 56%, with a maximum of 137% in the area of Cerreto d’Esi. Where it diminished, instead, the average decrease was of 42%, with a maximum of 66% at Offagna. In the area of Cerreto d’Esi and Matelica the vineyards are concentrated in a few hectares and the geomorphological damage was amplified by the intense and deep transformations of the landscape, by the presence of thick colluvial covering and by the hydrogeological setting, downhill laying, made up of alternating clays and sands. Another area where an increase in the landsliding (passing from “alberata” to vineyards - from 20% to 30%) is registered, is that of Montecarotto. The increase of the landsliding is shown above all on the slope with downhill lay, both through the enlargement of ancient slides (already present in 1955) and

through landslides of neoformation. The slopes with downhill lay are very developed (also for various kilometres), they have thick colluvial covering and the bedrock is mainly clayey with sandy intercalation.

The decrease of landsliding, as has already been mentioned, can depend on different factors: the anthropic factor is at times preponderant. In fact, in certain areas the deep agricultural transformation has mobilised great quantities of colluvial deposits and often in the medium-high tracts of the slopes, above all of the steep ones, the bedrock, which has an optimum stability, outcrops. In other areas, hydraulic remedial works along the streams and on the slopes have created favourable conditions for stability. In the area of Offida, representative of the southern Marche, the landslides affecting the slopes with downhill lay, immediately east of the inhabited area, though consistent, have undergone a sensible decrease (from 35% to 19.8%). This is probably connected to the extensive remedial works done in the 1960s and '70s for the urbanisation of different zones. On the uphill laying slopes, affected by badlands, the activity of the processes is considerably reduced as well, as a result of the massive remedial works diffused throughout wide tracts of the minor hydrographic network.

## 7. Conclusion

The present work, through the analysis of sometimes complex mass movements, puts in evidence how, in the articulated morphostructural setting of the study area, one of the main morphogenetic agents is represented by the action of gravity, whose main control factors, even if they differentiated, in part, on the basis of the different geo-environmental contexts, are represented by:

- the neotectonic activity to which high values of relief are associated; it is a result of the deep incision of the hydrographic network, of the intense fracturing of bedrock exalted by the purely gravitational stress or, at times, by tectonic gravitational phenomena, and frequent earthquakes
- the lithostratigraphic setting of bedrock, to which usually is connected the characteristic overlapping of rigid rock bodies over ductile ones
- the stratigraphic discontinuities constituted by strata planes, thrust planes or low angle faults, intense tectonized zones inside single lithostratigraphic units and surfaces of pre-transgressive erosion
- the tensional release following the withdrawal of the upper Pleistocene; this fact is, though, limited to the highest area of the chain
- the karst erosion, organised on more than one level along the valley sides, which constitutes a further "stratigraphic discontinuity"
- the hydrogeological setting, to which high values of hydrostatic pressure, of pore pressure and intense weathering processes of the clayey and marly lithotypes correspond
- the genesis of active cliffs connected to the sea level oscillation; in particular the Pleistocene-Holocene sea level rise, to which is also associated the decay of the geomechanical parameters of the lithotypes
- the intense precipitations and their regime

The superficial landslide phenomena are, besides, for the most part, a consequence of the hydrogeological “disorder” of the slopes and are caused: by the development of extensive and huge colluvial cover connected to the diffused agricultural occupation of the slopes, not re-balanced, successively, by the mechanic re-profiling of the slopes; by the implanting of cultivations (crops) that are, intrinsically, more favourable to the activation of mass movements.

## References

- Agliardi F., Crosta G., Zanchi A. (2001) - Structural constraints on deep-seated slope deformation kinematics. *Eng. Geol.* **59**, 83–102.
- Agnesi V., Macaluso T., Monteleone S. A Pipitone G. (1978) - Espansioni laterali (Lateral Spreads) nella Sicilia occidentale. *Geol. Appl. Idrogeol.* **13**, 319-326.
- Aleotti P., Baldelli P., Govi M., Polloni G. & Villani B. (2000) – *Landslide hazard assesment in the Po River Basin (Italy)*. In: *Proc. of the VIII International Symposium on Landslides, Cardiff*, 26-30 June 2000, 1, 13-18.
- Almagià R. (1910) - Studi geografici sulle frane in Italia. *Mem. Soc. Geogr. It.*, **14**, 345-435.
- Angeli M.G., Bisci C., Burattini F., Dramis F., Leoperdi S., Pontoni F. & Pontoni F. (1996) - Evolution and triggering factors of large-scale landslides affecting built-up areas in the Marche Region (Central Italy). *Quaderni di Geologia Applicata*, **3**(1), 131-140.
- Angeli M.G. & Pontoni F. (2004) – Analysis of a large-scale landslide affecting an ancient village in Central Italy. *Proc. IX Int. Symp. on Landslides (ISL)*, 28 June-2July 2004, Rio De Janeiro Brasil.
- Antonini G., Cardinali M., Guzzetti F., Reichenbach P. & Sorrentino A. (1993) - Carta inventario dei movimenti franosi della regione Marche ed aree limitrofe. *Consiglio Nazionale delle Ricerche-IRPI, Perugia*.
- APAT-Agenzia per la Protezione dell’Ambiente e per i Servizi Tecnici- AA.VV. (2007) – *Rapporto sulle frane in Italia. Il Progetto IFFI: metodologia, risultati e rapporti regionali*. Roma, 78, 681 pp.
- Aringoli D., Calista M., Crescenti U., Gentili B., Pambianchi G. & Sciarra N. (2002) - Modelling of two complex gravitational phenomena in Marche coastal areas (Central Italy). In: McInnes R. G. & Jakeways J. Eds., *Instability - Planning and Management*. Thomas Telford, London, 195-202.
- Aringoli D., Calista M., Gentili B., Pambianchi G. & Sciarra N. (2008) - Geomorphological features and numerical modelling of Montelparo mass movement (Central Italy). *Engineering Geology*, **99**, 70-84.
- Aringoli D., Gentili B., Materazzi M., Pambianchi G. & Farabollini P. (2007) - Climatic influence on slope dynamics and shoreline variations: examples from Marche Region (central Italy). *Physio-Géo*, vol. I, 1-20.
- Aringoli D., Gentili B., Materazzi M. & Pambianchi G. - Deep-seated gravitational slope deformation in active tectonic areas of the Umbro-Marchean Apennines (Central Italy). *Boll. Soc. Geol. It.*, in press.
- Aringoli D., Gentili B. & Pambianchi G. (1996) - The role of recent tectonics in controlling the deep-seated gravitational deformation of Mount Frascare (central Apennines). *Geogr. Fis. Dinam. Quat.*, **19**, 281-286.

- Aringoli D., Gentili B., Pambianchi G. & Piscitelli A.M. (2007) - The contribution of "Sibilla Appenninica" legend to karst knowledge in the Sibillini Mountains (Central Apennines, Italy). In: Piccardi L. & Masse W.B. (eds) *Myth and Geology*. Geological Society, London, Special Publications, **273**, 329-340.
- Armanini A., Fraccarollo L. & Larcher M. (2005) - Debris Flow. 142, In: Anderson M. Ed., *Encyclopedia of Hydrological Sciences*, Wiley, 2173-2185.
- Baratta M. (1901) - *I terremoti in Italia. Saggio di storia, geografia e bibliografia sismica italiana con 136 sismocartogrammi*. 950 pp.
- Beck A. C. (1967) - Gravity Faulting as a Mechanism of Topographic Adjustment. *New Zealand Journal of Geology and Geophysics*, **11**(1), 191-199.
- Bertini T. (1987) - Ambiente geologico e condizioni di rischio nell'Abruzzo adriatico: i lenti movimenti di versante. *Mem. Soc. Geol. It.* **37**, 333-340.
- Bigi S., Centamore E., Dramis F. & Salvucci R. (1995) - Sistemi distensivi in due aree dell'Appennino centrale. *Il Quaternario*, **8**(1), 71-81.
- Bisci C., Dramis F., Burattini F., Leoperdi S., Pontoni F. & Pontoni F. (1996) - The Sant'Agata Feltria Landslide (Marche Region, Central Italy): A Case of Recurrent Earthflow Evolving from a Deep-Seated Gravitational Slope Deformation. *Geomorphology*, **15**, 351-361.
- Bisci C., Ciccacci S., Dramis F., Gentili B. & Kotarba A. (1999) - The extent of Pleistocene glaciations in the western part of the Campo Imperatore (Gran Sasso Massif, Central Italy). *Landform Analysis*, **2**, 37-43.
- Blumetti A.M. & Dramis F. (1992) - Il Pleistocene inferiore nell'area nursina. *Studi Geologici Camerti*, vol. spec. 1992/1, 45-54.
- Blumetti A.M., Dramis F., Gentili B. & Pambianchi G. (1990) - La struttura di Monte Alvignano-Castel Santa Maria nell'area nursina: aspetti geomorfologici e paleosismici. *Rend. Soc. Geol. It.*, **13**, 71-76.
- Brunsden D. (1984) - Mudslides. In: Brunsden D. & Prior D.B. Eds. "*Slope instability*". Wiley, Chichester 363-418.
- Buccolini M., Gentili B., Marchetti P. & Pambianchi G. (1989) - Il sovralluvionamento olocenico nell'alto bacino del fiume Nera (Marche). *Mem. Soc. Geol. It.*, **42**, 343-349.
- Buccolini M., Crescenti U. & Sciarra N.** (1992). La frana di **Caramanico** dell'ottobre 1989: nota preliminare. *Boll. Soc. Geol. It.*, **111**, 181-191.
- Buccolini M., Gentili B., Materazzi M., Aringoli D., Pambianchi G. & Piacentini T. (2007) - Human impact and slope dynamics evolutionary trends in the monoclinial relief of Adriatic area of central Italy. *Catena*, **71**, 96-109.
- Buccolini M., Gentili B., Materazzi M. & Piacentini T. - The evolution of minor valleys in the clayey landscape of a monoclinial relief since the Last Glacial Maximum (peri-Adriatic belt, central Italy). *Geomorphology*, in press.
- Butzer K. W. (1976) - *Geomorphology from the earth*. Harper & Row, 463 pp.
- Calamita F., Cello G., Centamore E., Deiana G., Minarelli A., Paltrinieri W. & Ridolfi M. (1991) - Stili deformativi e cronologia della deformazione lungo tre sezioni bilanciate dall'Appennino Umbro-Marchigiano alla costa adriatica. *Studi Geologici Camerti*, Vol. Spec. (1991/1), 295-314.
- Calamita F. & Deiana G. (1988). The arcuate shape of the Umbria-Marche Apennines (central Italy). *Tectonophysics*, **146**, 139-147.

- Calamita F., Pizzi A. & Roscioni M. (1993) – I “fasci” di faglie recenti ed attivi di M. Vettore-M. Bove e M. Castello-M. Cardosa. *Studi Geologici Camerti*, Vol. spec 1992/1, 81-102.
- Calzecchi Onesti A. (1957) – Sistemazioni in collina. Ramo Editoriale degli Agricoltori, Roma, 348 pp.
- Cancelli A., Pellegrini M. & Tonnetti G. (1984) - Geological features of landslides along the adriatic coast. *Proc. IV ISL, Toronto*, **2**, 7-12.
- Cancelli A., Pellegrini M. & Tosatti G. (1987) - Alcuni esempi di deformazioni gravitative profonde di versante nell'Appennino settentrionale. *Mem.Soc.Geol.It.*, **39**, 447-466.
- Cantalamesa & Di Celma (2004) - Sequence response to syndepositional regional uplift: insights from high-resolution sequence stratigraphy of late Early Pleistocene strata, Periadriatic Basin, Central Italy. *Sedimentary geology* **164**, 283-309.
- Canuti P., Casagli N. & Ermini L. (1998) - Inventory of landslide dams in the Northern Apennines as a model for induced flood hazard forecasting. In: K. Andah, Editor, CNR-GNDCI-UNESCO (IHP): *Managing Hydro-Geological Disasters in a Vulnerable Environment for Sustainable Development*, Gilo Publishers, Perugia (1998), pp. 189–202 Publ. No. 1900 CNR-GNDCI.
- Carlini-De Carolis P.C. (1792) - *Memorie storiche di Castignano*. Colucci G. (ed), Fermo (Italy).
- Carrara A., D'Elia B. & Semenza E. (1985) - Classificazione e nomenclatura dei fenomeni franosi. *Geol. Appl. e Idrogeol.*, **20** (2), 223-243.
- Carraro F., Dramis F. & Pieruccini U. (1979) - Large-scale landslides connected with Neotectonic activity in the Alpine and Apennine ranges. Proceedings of the 15th Meeting “*Geomorphological Survey & Mapping*”, Modena, 213-230.
- Casadio M. & Elmi C. (2006) – *Il manuale del geologo*. Pitagora Ed., Bologna, 808 pp.
- Castiglioni G.B., Girardi A., Sauro U. & Tessari F. (1979) - Grèzes litées e falde detritiche stratificate di origine crionivale. *Geogr. Fis. Dinam. Quat.*, **2**, 64-82.
- Cello G., Deiana G., Mangano P., Mazzoli S., Tondi E., Ferrelli L., Maschio L., Michetti A., Serva L. & Vittori E. (1998) - Evidence for surface faulting during the September 26, 1997, Colfiorito (Central Italy) earthquakes. *Journal of Earthquake Engineering*, **2**, 1-22.
- Cello G., Invernizzi C., Mazzoli S. & Tondi E. (2001) – Fault properties and fluid flow patterns from Quaternary faults in the Apennines, Italy. *Tectonophysics*, **336**, 63-78.
- Centamore E., Cantalamesa G., Micarelli A., Potetti M., Berti D., Bigi S., Morelli C. & Ridolfi M. (1992) – Stratigrafia e analisi di facies dei depositi del Miocene e del Pliocene inferiore dell'avanfossa marchigiano-abruzzese e delle zone limitrofe. *Studi Geologici Camerti*, Vol spec. 1991/2, 125-131.
- Centamore E., Coltorti M., Dramis F., Cantalamesa G., D'Angelo S., Di Lorito L., Sacchi L. & Sposato A. (1982) – Aspetti neotettonici e geomorfologici del foglio 133-134, Ascoli Piceno-Giulianova. *Progetto Finalizzato Geodinamica*, C.N.R., Roma, Pubbl. n. 513, 371-387.
- Centamore & Deiana (1986) – *La Geologia delle Marche*. *Studi Geologici Camerti*, vol. spec., 145 pp.
- Ciancetti G. F. & Sciarra N. (1987) - Contributo alla conoscenza dei materiali lapidei estratti nella Regione Marche. *Quarry and Construction*, Ed. Pei, Parma, 89-96.
- Cilla G., Coltorti M., Farabollini P., Dramis F., Gentili B. & Pambianchi (1996) - Fluvial sedimentation during the early Holocene in the Marche valleys (central Italy). *Il Quaternario, Italian Journal of Quaternary Sciences*, **9** (2), 459-464.

- Civita, M.V., 2008. L'assetto idrogeologico del territorio italiano: risorse e problematiche. *Quad. Soc. Geol. It.*, **3**, 34 pp.
- Colosimo P. & Crescenti U. (1973) - Carta geolitologica ad orientamento geotecnico e della franosità della zona del Monte Conero (comuni di Ancona, Numana e Sirolo). *Mem Soc. Geol. It.*, **12**, 317-334.
- Coltorti M., Consoli M., Dramis F., Gentili B. & Pambianchi G. (1991) - Evoluzione geomorfologica delle piane alluvionali delle Marche centro-meridionali. *Geogr. Fis. Dinam. Quat.*, **14**, 87-100.
- Coltorti M., Dramis F., Gentili B., Pambianchi G., Crescenti U. & Sorriso-Valvo M. (1985) - The December 1982 Ancona landslide: a case of deep-seated gravitational slope deformation evolving at unsteady rate. *Zeitschrift für Geomorphologie, N.F.*, **29**(3), 335-345.
- Coltorti M. & Farabollini P. (1995) - Quaternary evolution of the "Castelluccio di Norcia" basin (Umbro-Marchean Apennines, Italy). *Il Quaternario*, **8**(1), 149-166.
- Coltorti M., Farabollini P., Gentili B. & Pambianchi G. (1996) - Geomorphological evidences for anti-Apennines faults in the Umbro-Marchean Apennines and in the peri-Adriatic basin, Italy. *Geomorphology*, **15**, 33-45.
- Coltorti M. & Dramis F. (1995) - The chronology of Upper Pleistocene stratified slope-waste deposits in Central Italy. *Permafrost and Periglacial Processes*, **6**, 235-242.
- Console R., Peronaci F. & Sonaglia A. (1973) - Relazione sui fenomeni sismici dell'Anconetano (1972). *Annali di Geofisica*, **26**, 148 pp.
- Coppola L., Dramis F., Gentili B. & Pieruccini U. (1978) - Paleofrane nelle formazioni mesozoiche dell'Appennino umbro - marchigiano. *Memorie della Società Geologica Italiana*, **19**, 99-109.
- Costa J.E. (1984) - Physical geomorphology on debris-flows. In: Costa J.E. & Fleisher P.J. Eds., "Developments and applications of geomorphology" 268-317.
- Cotecchia V. (1978) - Systematic reconnaissance, mapping and registration of slope movements. *Bull. I.A.E.G.*, **17**, 5-37.
- Crescenti U. (Ed.) (1986) - La grande frana di Ancona del 13 dicembre 1982. *Studi Geologici Camerti*, vol. spec., 146 pp.
- Crescenti U., Gentili B., Pambianchi G. & Sciarra N. (2002) - *Modeling of complex deep-seated mass movements in the central-southern Marches* (Central Italy). In: Rybar J., Stemberk J. & Wagner P. (eds) "Landslides". Swets & Zeitlinger, Lisse, The Netherlands. A.A. Balkema Publishers (ISBN 90 5809 393 X), 149-155.
- D'Agostino N., Dramis F., Funicello R. & Jackson J.A. (2001) - Interactions between mantle upwelling, drainage evolution and active normal faulting: an example from the central Apennines (Italy). *Geophysical Journal International*, **147**, 475-497.
- Damiani A.V. & Moretti A. (1968) - Segnalazione di un episodio wurmiano nell'alta valle del Chienti (Marche). *Boll. Soc. Geol. It.*, **87**, 171-181.
- Deiana G. & Piali P. (1994) - The structural provinces of the Umbro-Marchean Apennines. *Mem. Soc. Geol.*, **48**, 473-484.
- Delano-Smith C. (1979) - *Western Mediterranean Europe*. Academic Press, London, 453 pp.
- Desplanches H. (1975) - *Campagne ombre: contributo allo studio dei paesaggi rurali dell'Italia centrale*. Quaderni Regionali dell'Umbria, Perugia, 1, 135 pp.



- Diez A.G., Salas L., Diaz de Teràn J.R. & Cendrero A. (1996) - Late Quaternary climatic changes and mass movement frequency and magnitude in the Cantabrian region, Spain. *Geomorphology* **15**, 291-309.
- Dramis F. (1984) – Aspetti geomorfologici e fattori genetici delle deformazioni gravitative profonde. *Boll. Soc. Geol. It.*, **103**, 1-7.
- Dramis F., Farabollini P., Gentili B. & Pambianchi G. (1995) - Neotectonics and large-scale gravitational phenomena in the Umbria-Marche Apennines, Italy. In: O. Slaymaker (Ed.) - *Steepland Geomorphology*, J. Wiley & Sons, Chichester, 199-217.
- Dramis F., Garzonio C.A. & Gentili B. (1992) - Deepening of hydrographic pattern and slope stability; some sliding phenomena in the Mio-pliocene terrain of central southern Marche (central Italy). *Geoökodynamik*, Band XIII, 63-78.
- Dramis F., Garzonio C.A., Leoperdi S., Nanni T., Pontoni F. & Rainone M. (1988) – Damage due to landslides in the ancient village of Sirolo (Marche, Italy): preliminary analysis of risk mitigation on the historical site. In: Marinos P. G. & Koukis G.C. (eds.) - *Engineering Geology of Ancient Works, Monuments and Historical Sites*. Balkema Ed., Rotterdam, 217- 224.
- Dramis F., Garzonio C.A., Nanni T. & Principi L. (1987a) - Franosità e dissesti dei centri abitati delle Marche: primi risultati del censimento e dello studio delle situazioni a rischio. *Mem. Soc. Geol. It.*, **37**(1), 105-116.
- Dramis F., Gentili B. & Pambianchi G. (1987b) - Deformazioni gravitative profonde nell'area di Monte Gorzano (Monti della Laga, Appennino centrale). *Boll. Soc. Geol. It.*, **106**, 265-271.
- Dramis F., Gentili B., Pambianchi G. & Aringoli D. (2002) - La morfogenesi gravitativa nel versante adriatico marchigiano. *Studi Geologici Camerti*, Nuova Serie 1/2002, EDIMOND, 103-125.
- Dramis F., Gentili B., Rodolfi G., Bisci C., Di Eusebio F. & Pambianchi G. (1993) - *Ancient and historic landsliding in villages of Marche Region and of Tosco-Romagnolo Apennine*. In: Temporal Occurrence and Forecasting of Landslides in the European Community, Final Report of The European Community Programme Epoch, Contract 90, vol. 2, 871-888.
- Dramis F., Pambianchi G., Nesci O. & Consoli M. (1991) - Il ruolo di elementi strutturali trasversali nell'evoluzione tettonico-sedimentaria e geomorfologica della regione marchigiana. *Studi Geologici Camerti*, vol. spec. 1991/2, CROP 11, 283-286.
- Dramis F. & Sorriso-Valvo M. (1994) - Deep-seated gravitational slope deformations, related landslides, and tectonics. In: Oyagy N., Sorriso-Valvo M. & Voight B. (Eds.) - “Deep-seated landslides and large-scale rock avalanches”. *Engineering Geology*, **38** (3-4), 231-243.
- Esu F. & Martinetti S. (1965) – Considerazioni sulle caratteristiche tecniche delle argille plio-plioceniche della fascia adriatica tra Rimini e Vasto. *Geotecnica*, **4** (12), 165-185.
- Fabbi A. (1965) -Visso e le sue valli. Panetto, Perilli (eds), Spoleto, 138 pp.
- Falconi R. (1986) - *Amico Castello: origini, storia, turismo e immagini di Castelsantangelo sul Nera*. IGER, Roma, 94 pp.
- Farabollini P. (1999) – Il ruolo delle acque correnti superficiali: alcuni esempi dall'area della Montagna dei Fiori (Abruzzo nord- orientale). *Studi Geologici Camerti*, vol. spec., 93-102.

- Fazzini, M. & Giuffrida A. (2005) - Une nouvelle proposition quantitative des regimes pluviometriques dans le territoire de Italie: premiers resultats. *Climat Urbain, Ville et Architecture, Acts XVIII Colloque Internationale del Climatologie*, 361-365.
- Folchi Vici D'Arcevia C., Gentili B., Luzi L., Pambianchi G. & Viglione F. (1996) - Deep-seated gravitational slope deformation in the central-southern Umbro-Marchean Apennines: morphometric and macrostructural analyses. *Geogr. Fis. Dinam. Quat.*, **19**, 335-341.
- Galdenzi S. & Menichetti M. (1995) - Occurrence of hypogenic caves in a karst region: *Examples from central Italy. Environmental Geology*, **26**, 39-47.
- Galiè N. & Vecchioni G. (1999) - *Il Monte dell'Ascensione. Società Editrice Ricerche, Folignano (AP)*, 151 pp.
- García-Ruiz J.M. & Valero-Garcès B.L. (1988). Historical geomorphic processes and human activities in the Central Spanish Pyrenees. *Mountains Research and Development* **18**(4), 309-320.
- Gasparini C., Jannaccone G. & Scarpa R. (1985) - Fault-plane solutions and seismicity of the Italian peninsula. *Tectonophysics*, **117**, 59-78.
- Genevois R. & Prestininzi A. (1979) - Time dependent behaviour of granitic rocks related to their alteration grade. *Proc. int. congr. rock mech.* (1979), pp. 153-159.
- Gentili B., Materazzi M., Pambianchi G. & Scalella G. (con la collaborazione di Aringoli D., Cilla G. & Farabollini P.) (1998) - I depositi di versante del Monte dell'Ascensione (Marche meridionali, Italia). *Geogr. Fis. Dinam. Quat.*, **21**, 205-214.
- Gentili B. & Pambianchi G. (1993) - *Carta delle deformazioni gravitative profonde di versante e grandi frane nell'Appennino centrale* (Foglio 124 Macerata). Interlinea, Teramo.
- Gentili B. & Pambianchi G. (1994) - Gravitational morphogenesis of the Apennine chain in Central Italy. *Proc. 7th Int. IAEG Congr.*, Sept. 1994, Lisboa (Portugal), vol.II, 1177-1186.
- Gentili B. & Pambianchi G. (1987) - Morfogenesi fluviale ed attività antropica nelle Marche centro-meridionali. *Geogr. Fis. Dinam. Quat.*, **10**, 204-217.
- Gentili B. & Pambianchi G. (2002) - La dégradation géomorphologique dans quelques régions viticoles et vinicoles des Marches (Italie centrale). *Géologues*, **135**, 107-113.
- Gentili B., Pambianchi G., Aringoli D., Cilla G., Farabollini P. & Materazzi M. (1995) - Rapporti tra deformazioni fragili plio-quadernarie e morfogenesi gravitativa nella fascia alto-collinare delle Marche centro-meridionali. *Studi Geologici Camerti*, Vol. Spec. (1), 421-435.
- Giraudi C. (2005) - Middle to Late Holocene glacial variations, periglacial processes and alluvial sedimentation on the higher Apennine massifs (Italy). *Quaternary Research*, **64**, 176-184.
- Gonzalez De Vallejo L.I. (2005) - *Geoingegneria*. Pearson Education Italia Srl, 716 pp.
- Govi M. & Turitto O. (1996) - Distribuzione spazio-temporale degli eventi estremi nel bacino padano: analisi storica. *Accademia Nazionale dei Lincei, Atti dei convegni Lincei n.* **129**, 55-74.
- Guadagno F.M & Perriello Zampelli S. (2000) - Triggering mechanisms of the landslides that invested Sarno, Quindici, Siano and Bracigliano (Southern Italy) on May 5-6, 1998. - *Proc. of the 8 th Int. Symp. on Landslides, Cardiff*, June 2000, T. Thelford Ed., 2, 671-676.

- Guerricchio A. (1988) - Aspetti geologici sull'erosione dei litorali e loro influenza nel campo applicativo. *Geologia Applicata e Idrogeologia*, **23**, 29-78.
- Guerricchio A. & Melidoro G. (1981). Movimenti di massa pseudotettonici nell'Appennino dell'Italia meridionale. *Geol. Appl. Idrogeol.*, **16**, 251-294.
- Guida M., Perriello Zampelli S. & Vallario A. (1995) - Modellazione al tavolo d'attrito di base di deformazioni gravitative di versante in alcune morfostrutture tipo. *Mem.Sco.Geol.It.*, **L**, 167-178.
- Haq B. Q., Hardenbol J. & Vail P. R. (1987) - Chronology of fluctuating sea levels since the Triassic. *Science*, **235**, 1156-1166.
- Hancock P.L. (1991) – Determining contemporary stress directions from neotectonic joint systems. *Phil. Trans. R. Soc. Lond.*, **A337**, 29-40.
- Harrison J. V. & Falcon N.L. (1934) - Collapse structures. *Geological Magazine*, **71**, 529-539.
- Hunstad, I., et al., 1999. Modelling coseismic displacement during the 1997 Umbria–Marche earthquakes (central Italy). *Geophys. J. Int.* **139**, 283-295.
- Hutchinson J.N. (1988) - General Report: morphological and geotechnical parameters of landslides in relation to geology and hydrogeology. *Proc. 5<sup>th</sup> Int. Symp. On Landslides*, Lausanne, CH, AA Balkema, 1, 3-35.
- Hutchinson J.N. (1995) – Deep-seated mass movements on slopes. *Mem. Soc. Geol. It.*, **50**, 147-164.
- Jahn A. (1964) - Slope morphological features resulting from gravitation. *Zeit. Geomorph.*, suppl. Bd., 5, 59-72.
- Jaurand E. (1998) - Les glaciers disparus de l'Apennin. Publications de la Sorbonne, *Geographie*, **10**, 382 pp.
- Johnson R.B. & De Graff J.V. (1988) - *Principles of Engineering Geology*. Hamilton Printing Co., J. Wiley & Sons, Inc., 497 pp.
- Lamb H. H. (1982) - *Climate, History and the Modern World*. Routledge, London, 433 pp.
- Lambeck K., Antonioli F., Purcell A. & Silenzi S. (2004) - Sea-level change along the Italian coast for the past 10,000 yr. *Quaternary Science Review* **23**, 1567-1598.
- Le Roy Ladurie E. (1971) - *Times of feast, times of famine: a history of climate since the year 1000*. Trams. B. Bray, New York, Doubleday, 426 pp.
- Mahr T. & Nemčok A. (1977) - Deep-seated creep deformation in the crystalline cores of the Tatry Mts. . *Bull.IAEG*, **16**, 104-106.
- Materazzi M., Gentili B., Aringoli D., Farabollini P. & Pambianchi G. – *Geomorphological evidences of Late Holocene climatic variations in the central Adriatic sector*, Italy. Climatic Change (in press.).
- Mattei M. (1987) – Analisi geologico-strutturale della Montagna dei Fiori (Ascoli Piceno, Italia centrale). *Geologica Romana*, **26**, 327-347.
- McInnes R. G. & Jakeways J. Eds. (2002) - *Instability - Planning and Management*". Thomas Telford, London, 762 pp.
- Mizutani T. (1996) - Longitudinal profile evolution of valley on coastal terraces under the compound influence of eustasy, tectonism and marine erosion. *Geomorphology* **17**, 317-322.
- Mortara G. & Sorzana P.F. (1987) - Fenomeni di deformazione gravitativa profonda nell'arco alpino occidentale italiano. Considerazioni litostrutturali e morfologiche. *Boll. Soc. Geol. It.*, **106**, 303-314.

- Nanni T. & Vivalda P. (2005) . The aquifers of the Umbria-Marche Adriatic region: relationships between structural setting and groundwater chemistry. *Boll. Soc. Geol. It.*, **124**, 523-542.
- Natau O., Fecker E. & Pimentel E. Eds. (2003) – *GeoTechnical Measurements and Modelling*. Swets & Zeitlinger, Lisse, The Netherlands. A.A. Balkema Publishers, 500 pp.
- Nemčok A. (1972) - Gravitational slope deformation in high mountains. *Internat. Geol. Cong.* 24<sup>th</sup>, Montreal, Canada, Sec. **13**, Proc., 132-141.
- Orombelli G. & Sauro U. (1988) - I lavini di Marco: un gruppo di frane oloceniche nel contesto morfotettonico dell'alta Val Lagarina (Trentino). *Suppl. Geogr. Fis. Dinam. Quat.*, **1**, 107-116.
- Panizza M., Pasuto A., Silvano S. & Soldati M. (1996). Temporal occurrence and activity of landslides in the area of Cortina d'Ampezzo (Dolomites, Italy). *Geomorphology*, **15** (3-4), 311-326.
- Pastori L. (1781) - *Memorie storiche della nobil terra di Montelparo*. Stamperia Paccaroni, Fermo.
- Pasuto A. & Soldati M. (1996) – Rock spreading. In: Dikau R., Brunsden D., Schrott L. & M.L. Ibsen (Eds.) - *Landslide recognition*, J.Wiley & Sons, Chichester, 122-136.
- Pierantoni P.P., Deiana G., Romano A., Paltrinieri W., Borraccini F. & Mazzoli S. (2005) – Structural geometry along the thrust zone of the Umbria-Marche-Sabina mountain front. *Boll. Soc. Geol. It.*, **124**, 395-411.
- Pierson T.C. & Costa J.E. (1987) – A rheologic classification of subaerial sediment-water flows. In: Costa J.E. & Wieczorek G.F. Eds., “Debris flows / avalanches: processes, recognition and mitigation. *Geol. Soc. Am., Rev. Eng. Geol.*, VII, 1-12.
- Pieruccini U. (1988) - *Le deformazioni gravitative profonde*. In: Canuti P. & Pranzini E. (a cura di) "La gestione delle aree franose". Edizioni delle Autonomie, Roma, 61-83.
- Pinna M. (1984) - La storia del clima: variazioni climatiche e rapporto clima-uomo in età post-glaciale. *Mem. Soc. Geogr. It.*, **36**, 264 pp.
- Pirazzoli P.A. (1997) - *Sea -Level Changes: the Last 20,000 years* . John Wiley & Sons, Chichester. 211 pp.
- Postpischl D. Ed. (1985) - Catalogo dei terremoti italiani dall'anno 1000 al 1980. C.N.R., *Quaderni della Ricerca Scientifica*, **144**(2B), 239 pp.
- Provansal M. (1995) - The role of climate in landscape morphogenesis since the Bronze Age in Provence, southeastern France. *Holocene* **5**, 348-353.
- Radbruch-Hall D.H., Varnes D.J. & Savage W.Z. (1976) - Gravitational spreading of steep-sided ridges (“sackung”) in Western United States. *Bull. I.A.E.G.*, **14**, 23-35.
- Ruiz-Flaño P., Garcia-Ruiz J.M. & Ortigosa L. (1992). Geomorphological evolution of abandoned fields. A case studying the central Pyrenees. *Catena*, **19**, 301-308.
- Rybar J., Stemberk J. & Wagner P. (Eds) (2002) - *Landslides*. Swets & Zeitlinger, Lisse, The Netherlands. A.A. Balkema Publishers, 734 pp.
- Salvi S., Stramondo S., Cocco M., Tesaro M., Hunstad I., Anzidei M., Briole P., Baldi P., Sansosti E., Lanari R., Doumaz F., Pesci A. & Galvani A. (2000) - Modeling coseismic displacements resulting from SAR interferometry and GPS measurements during the Umbria–Marche seismic sequence. *J. of Seism.* **4**, 479–499.
- Savage W.Z. & Swolfs H.S. (1986) – Tectonic and gravitational stresses in longsymmetric ridges and valleys. *J. Geophys. Res.*, **91**, 3677-3685.

- Savage W. Z. & Varnes D. J. (1987) - Mechanics of gravitational spreading of steep-sided ridges ("sackung"). *Bull. I.A.E.G.*, **35**, 31-36.
- Sciarra N. (1988) – Geologia e geotecnica di argille consistenti del Pliocene abruzzese. *Boll. Soc. Geol. It.*, **107**, 3-15.
- Semenza E. (1966-67) - Sintesi degli studi geologici sulla frana del Vajont dal 1959 al 1964. *Mem. Museo Tridentino Scienze Natuarali*, A. XXIX-XXX, Vol. XVI (1), 3-51.
- Semenza E. (2001) – *La storia del Vaiont raccontata dal geologo che ha scoperto la frana*. Ed. Tecom Project, 280 pp.
- Sereni E. (1979) - *Storia del paesaggio agrario italiano*. Ed. Laterza, Bari, 500 pp.
- Soldati M., Corsini A. & Pasuto A. (2004) - *Landslides and climate change in the Italian Dolomites since the Lateglacial*. Catena, **55**(2), 141-161.
- Sorriso-Valvo M. Ed. (1984) - Atti del I Seminario del Gruppo Informale del C.N.R. "Deformazioni Gravitative Profonde di Versante". *Boll. Soc. Geol. It.*, **103**, 667-729.
- Sorriso-Valvo M. Ed. (1987) - Atti del II Seminario del Gruppo Informale del C.N.R. "Deformazioni Gravitative Profonde di Versante". *Boll. Soc. Geol. It.*, **106**, 223-316.
- Sorriso-Valvo M. Ed. (1989) - Atti del III Seminario del Gruppo Informale del C.N.R. "Deformazioni Gravitative Profonde di Versante". *Boll. Soc. Geol. It.*, **108**, 369-451.
- Stini J. (1941) - *Unsere Taler wachsen zu. Geologie und Bauwesen, Jahrg.*, 13 H.3, 71-79.
- Surace L. (1997) – La nuova rete geodetica nazionale IGM-95: risultati e prospettive di utilizzazione. *Bollettino di Geodesia e Scienze Affini*, n.3/97, 357-378.
- Takahashi T. (1991) - *Debris flow, IAHR Monograph Series*, Ed. Balkema, 165 pp.
- Ter-Stefanian G. (1977) – Deep-reaching gravitational deformation of mountain slopes. *Bull. I.A.E.G.*, **16**, 87-94.
- Terzaghi K. & Peck R. B. (1967) – *Soil Mechanics in Engineering Practice*. J. Wiley, New York, 729 pp.
- Tonnetti G. & Angeli M.G. (1984) - Geological, kinematical and developing features of some landslides in plio-pleistocene clayey sediments of the adriatic hilly region in Italy. *Proc. IV ISL, Toronto*, **2**, 221-226.
- Trenhaile A.S. (2002) - Rocky Coasts, with particular emphasis on shore platforms. *Geomorphology* **48**, 7-22.
- Varnes D.J. (1978) - Slope movement: types and processes. In: Schuster R.L. & Krizek R.S.(1978), *Landslides analyses and control. Transp.Res.Board.Spec.Rep.*, **176**, Nat.Acad.of Sc., 11-33.
- Vita-Finzi C. (1969) – The mediterranean valleys. *Geological changes in historical times*. Cambridge Univ. Press, Cambridge, 140 pp.
- Wise D.U., Funicello R., Parotto M. & Salvini F. (1985) - Topographic lineament swarms clues to their origin from domain analysis of Italy. *Geol.Soc.Am.Bull.*, **96**, 952-967.
- Zaruba Q. & Mencl V. (1969) – *Landslides and their control*. Elsevier, New York, an Acad. Praha, 194-202.
- Zischinski U. (1969) - Über Sackungen. *Rock Mechanics*, **1**, 30-52.



*Chapter 2*

## **CAUSES AND EFFECTS OF LANDSLIDES IN THE MONTERREY METROPOLITAN AREA, NE MEXICO**

***Juan C. Montalvo-Arrieta<sup>\*</sup>, Gabriel Chávez-Cabello,  
Fernando Velasco-Tapia and Ignacio Navarro de León***

Facultad de Ciencias de la Tierra, UANL; Ex – Hacienda de Guadalupe,  
Linares, N.L. Mexico

### **Abstract**

In this work we present the evaluation of landslide causes and effects in the Monterrey Metropolitan Area (MMA), through the analysis of geometrical, geological, and structural data from slopes and the rock masses failure associated with anomalous periods of intense rainfall. We also explore other potential landslide causes (*e.g.*, natural and induced vibrations). MMA landslide risk is related to the following factors: (1) *Geography*: this urban center is known as the “Mountain city”, located in the Sierra Madre Oriental (SMO) range border. The valley is surrounded by three intermediate topographic ranges (Cerro de la Silla, Cerro de las Mitras, and Cerro del Topo Chico) and the Monterrey salient, which is the main topographic structure in the area. The MMA border topography is highly scarped and rugged varying from ~540 masl at the valley to ~1,700 masl at the hill slopes. This condition generates high angle slopes which are dissected by a rectangular to dendritic drainage that discharges in the Santa Catarina river, which flows crossing the MMA; (2) *Geology*: the MMA is situated at the borders of two tectonic provinces: the SMO and the Gulf Coastal Plain (GCP). The SMO is a sedimentary sequence constituted mainly by Upper Jurassic to Upper Cretaceous carbonated and clastic marine rocks, complexly folded and thrustured during the Laramide Orogeny. The GCP corresponds to a thick Tertiary clastic sedimentary sequence characterized by an extensional deformation. All hills in and around the MMA are anticlines trending WNW-ESE and plunging into the valley, except for the SMO anticlines. Stratigraphic sequence is widely variable, lithology changes from limestone to shale, with minor contents of sandstone, siltstone, and gypsum. Unconsolidated material located at the foothills is represented by different alluvial deposits related to alluvial fans and detritus, derived from the range scarped walls. Strike and dip of sedimentary layers (WNW-ESE / 90 -

---

<sup>\*</sup>E-mail address: montalvo@fct.uanl.mx (Corresponding author)

30°) have frequent inclinations in the slope directions. This situation along with a specific structural position and an adequate lithologic combination could increase the risk to trigger landslides; (3) *Climate*: the MMA is located in a zone with intense rainfall periods from August to October (normally tropical storm or hurricane related rainfalls). It is well documented that after a period (> 2 or 3 days) of extraordinary rainfall (> 200 mm) several landslides are triggered mainly in pronounced slopes altered by human activities. Mass movements have caused human and huge economic losses. The last dramatic case was observed during the Emily hurricane in 2005 when a landslide affected around 100 households and urban infrastructure; and (4) *Urban growth*: MMA has experienced an accelerated expansion during the last two decades, causing urban limits to move beyond the valley, reaching mountain toes and hillslopes. These new settlements have produced slope instability by changing the natural stable condition to a precarious stability state. Finally, documented landslides which have damaged the urban infrastructure are a combination of these factors, mainly by the interaction of rainfall and anthropogenic altered slopes. A reevaluation of landslide prevention and mitigation strategies ought to be considered by the MMA authorities.

## 1. Introduction

Most of the mass movement processes that have occurred in Mexico over the last several decades have been induced by rainfall. Several cities located in different range provinces in Mexico have been susceptible to landslides. The majority of the mass movements have been triggered by extraordinary rainfall events related to hurricanes. In 1991, in Mezquitlan city (central Mexico), a rotational landslide moved ~900 000 m<sup>3</sup> causing human losses and considerable damage to a 16th century monastery. Pauline hurricane in 1997 induced several landslides and floods in Acapulco bay on the Pacific Coast. Chiapas State (Southern Mexico) was severely damaged by an extreme rainfall period in 1988. This event caused the worst consequences associated to flood and mass movement processes (Alcantara-Ayala, 2004). In 1999 during an intense rainfall period, the interaction of a tropical depression and a cold front caused massive flooding and several landslides in central Mexico. Hidalgo, Veracruz, and Puebla states registered severe damage, being the later the most harmed (Alcantara-Ayala, 2004; Alcantara-Ayala et al., 2006).

The Monterrey Metropolitan Area (here after MMA; Figure 1), the third biggest urban center in Mexico (INEGI, 2008), is settled in the Sierra Madre Oriental (SMO) range border and the Gulf Coastal Plain (GCP). Site characteristics including geological, geomorphological, and climatic features, are responsible for the generation of several MMA mass movements. Additionally, Northeastern Mexico is exposed to recurrent Atlantic tropical hurricanes that sometimes bring about extraordinary rainfall peaks. The sum of these factors, combined with an accelerated urban growth, has generated a high landslide risk for the area.

However, the available information related to landslides or debris flows for MMA is scarce. Chapa Guerrero (1993) carried out a morphologic, geologic, and tectonic analysis in adjacent flanks of the SMO in Monterrey and San Pedro Garza García municipalities. Detailed mapping of the Los Muertos anticline north region (Chipinque area) was selected to determine the landslide event causes. A geological hazard map with six risk categories was reported, including general safety recommendations to minimize the mass movement risk effects. A similar methodology was applied by Sánchez Carlín (2001), in the Cerro de la Silla northeast sector, and Chapa Guerrero and Ibarra Martínez (2008), in the northeast flank of the



Los Muertos anticline (Mederos area). A rock and soil homogeneous zone map was prepared for each site and a stability analysis was performed to determine slip wedges in artificial banks to evaluate geotechnical problems.

In spite of the mentioned contributions there is a lack of security factor analysis involving static (slope analysis, landslide runout) and dynamic (vegetation, rainfall intensity and occurrence, pore pressure increase, seismicity) parameters. In this chapter we briefly review causes and effects of MMA historical landslides, valuable information for decision making process related to future urban development and civil protection plans.

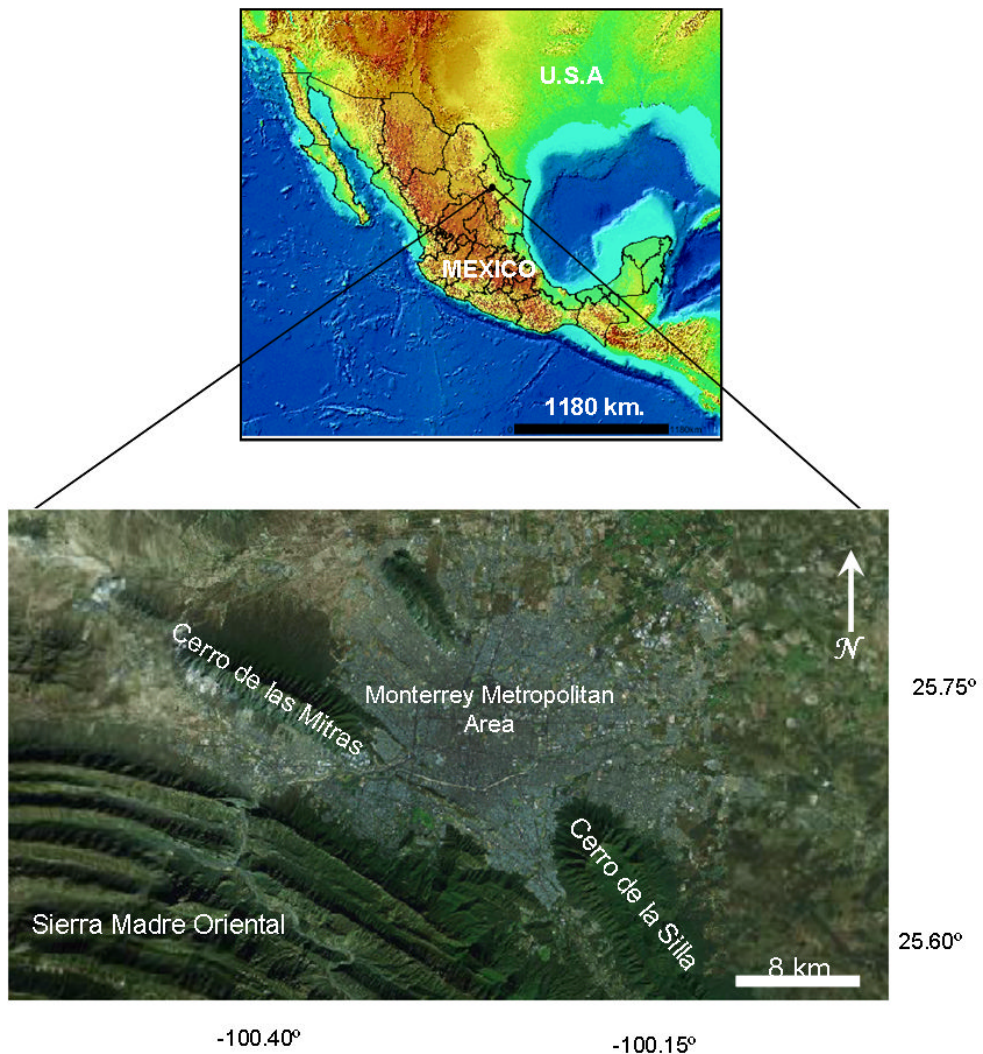


Figure 1. Location of Monterrey Metropolitan Area in northeastern Mexico.

## 2. Ubication and Demographic Growth

Monterrey city (Figure 1) was founded on September 20, 1596 in the Valle de la Extramadura, Nuevo Reyno de León. Today, MMA (25°40' North latitude; 100°19' West longitude; altitude ~537 masl) includes Monterrey city and other six municipalities: Apodaca, General Escobedo, Guadalupe, San Nicolas de los Garza, San Pedro Garza García, and Santa Catarina, covering an area of ~2200 km<sup>2</sup>. The urban zone has developed as to interconnect valley systems within Sierra de la Silla, Las Mitras, and Cerro del Topo Chico.

Monterrey reached a population of ~62,000 inhabitants in 1900, increasing to  $\sim 2 \times 10^5$  in 1940 (Alba, 1981; INEGI, 2008). The city achieved metropolitan status in the 1950s, when its growth reached the Guadalupe and San Nicolas de los Garza municipalities (Garza, 1994). At this time, the MMA population was  $\sim 3.9 \times 10^5$  inhabitants (Chart 1 and Figure 2). A 93.6% of the total metropolitan population lived in the Monterrey municipality. Between 1950 and 1960 MMA grew at an annual rate of 6.7% and the population reached  $\sim 7.2 \times 10^5$  inhabitants. In the 1960s three other urban centers were added to the metropolitan area for a total of seven and the share of the population living in the Monterrey municipality dropped to 68.3%. From 1970 to 1980, MMA annual growth rate declined to 4.6%, and only one urban center (Benito Juárez) was added. The Monterrey municipality had a growth rate of 2.2%, while the surrounding urban centers had rates several times higher. The process of metropolitanization decelerated considerably between 1980 and 1990, with an annual growth rate of 2.5% for the metropolitan region, the lowest since 1910-21. MMA had a negative growth of -0.2% in the 1980s.

**Chart 1. General population MMA data during 1950-2005 (Alba, 1981; INEGI, 2008)**

Year	Population (inhabitants)	Period growth (%)	Proportion of Mexico population (%)	Proportion of Nuevo Leon population (%)
1940	206,010	-	0.9	50.1
1950	389,629	89.1	1.5	52.6
1960	723,739	85.8	2.1	67.1
1970	1,254,691	73.4	2.6	74.0
1980	2,011,936	60.4	3.0	80.1
1990	2,573,527	27.9	3.2	83.1
1995	2,988,081	16.1	3.3	84.2
2000	3,243,466	8.6	3.3	84.6
2005	3,598,597	11.0	3.5	85.7

Industrialization was the main determinant for the metropolitan growth in Monterrey. Industrial growth was most rapid between 1950 and 1970, when 10.4% of the national industry was located in Monterrey. Industrial activities included iron and steel metalurgy, cement, glass factories, beer and chemistry. Monterrey was seriously affected by the economic crisis of the 1980s, suffering a decline of 1.1% annually and a reduction of its share of national industry down to 8.8% by 1988. Economic recuperation after 1994, in part associated to the North American Free Trade Agreement (NAFTA), led to a MMA population increase up to  $\sim 3 \times 10^6$  inhabitants in 1995.

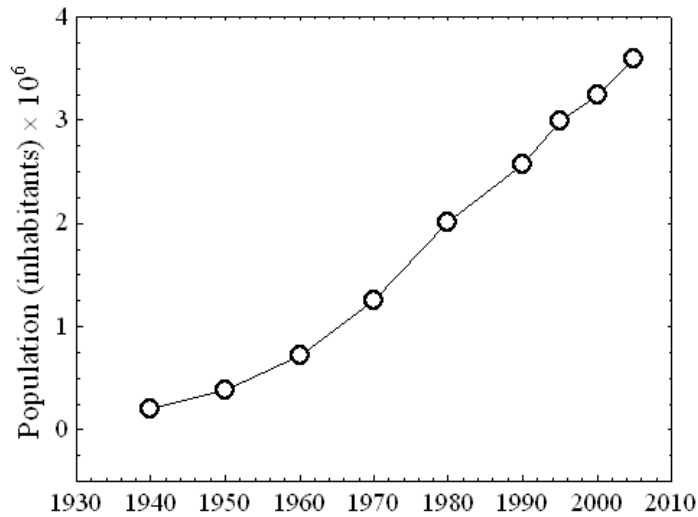


Figure 2. Population growth in Monterrey Metropolitan Area for 1930 to 2008 periods (INEGI, 2008).

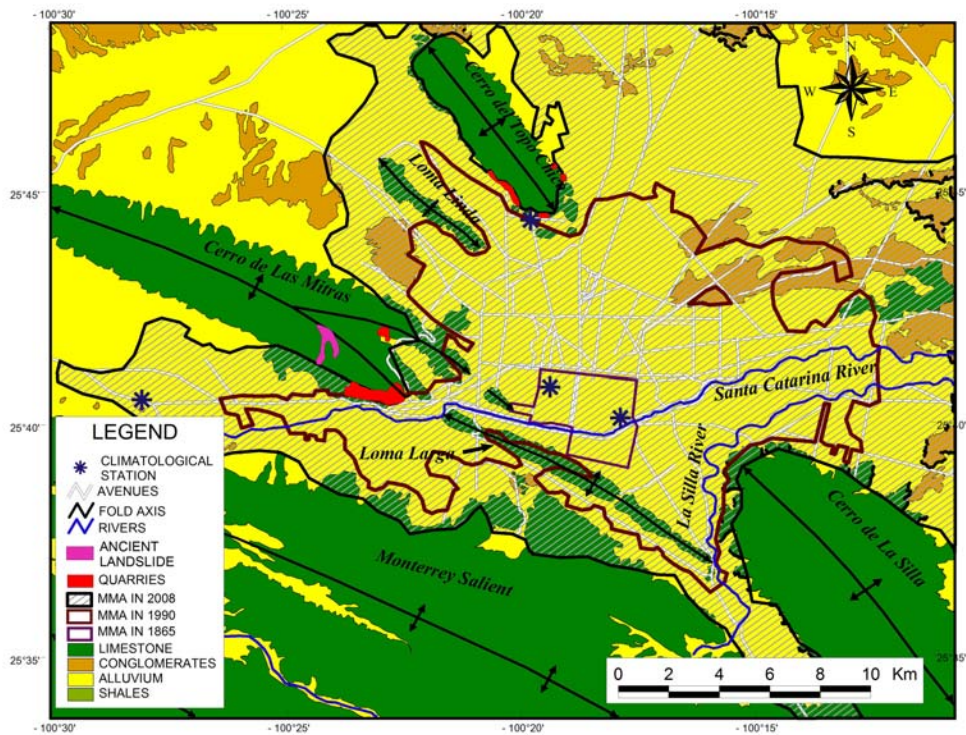


Figure 3. Generalized surficial geology map of the Monterrey Metropolitan Area. Urban area growth for 1856, 1990, and 2008 periods. Location of ancient landslides and quarries areas and climatological stations.

In the last two decades, MMA has received a strong immigration, reflecting in an increase in the population that reached  $\sim 3.6 \times 10^6$  inhabitants in 2005. Figure 3 shows the MMA urban growth for 1865, 1990 and 2008. Today, MMA population is mainly

concentrated in the valley, where government offices, service facilities, as well as commercial and residential areas are located. An important population rise is also expected for the next 20 years, implying the need for tremendous infrastructural construction.

MMA has experienced an accelerated growth over the last 20 years, causing urban limits to move beyond the valley, reaching mountain toes and pronounced and unstable hill slopes prone to landslides during extreme rainfall season.

### **3. Geological Setting**

#### **3.1. Morphological Features and Geological Setting**

The Monterrey valley is located in a wide transition zone between the SMO fold thrust belt and the GCP in Northeast Mexico (Figure 3). The MMA is conformed by a complex valley delimited in the south by the leading edge of SMO front with at least 2300 masl, which represents the highest and biggest morphological feature in the area. On the other hand, separated from the SMO, three mountains partially enclose the MMA: Las Mitras, La Silla and El Topo Chico ranges. The valley geometry is altered by isolated linear hills represented by Loma Linda in the northwest, El Obispado in the center, and the Loma Larga in the south-central part, which has a more elongated topography parallel to the SMO front and Las Mitras range (Figure 3).

#### **3.2. Lithology**

MMA ranges and hills are composed by a thick Cretaceous sequence of marine sedimentary rocks. The highest areas surrounding the MMA are represented by limestone of the Cupido and Aurora Formations which were deposited on slope and platform marine environments (Figure 4; Padilla y Sánchez, 1986; Goldhammer, 1999). The range foothills and minor hills (Loma Larga, Cerro del Obispado, and Loma Linda structures) contain marl, chert, shale, siltstone, and interbedded fine grain sandstones of Agua Nueva, San Felipe, and Mendez Formation. The valley bedrock is composed of Mendez Formation massive foliated shale (Figure 3). This clastic wedge (Figure 4) was deposited during a regional marine regression triggered by the onset of the Laramide orogeny in Western Mexico.

Tertiary and Quaternary alluvial and fluvial sediments are overlying discordantly to bedrock. The valley is filled by soft sediments deposited as terraces during accumulation-erosion cyclic changes (Ruiz-Martínez and Werner, 1997). The most recent sediments were deposited as riverbeds in Santa Catarina and La Silla rivers, both flowing eastward (Figure 3). Fluvial deposit thickness in the valley ranges from 12 - 24 meters and it is due to the presence of paleochannels caused by meandering river courses (braided-streams). Alluvial deposits are constituted by uncemented and unweathered cobble to small pebble gravel, gravelly sand, sand, and silts, cemented by calcite.

A geotechnical characterization through borehole drillings was performed during the construction of the first MMA subway transect (1987-1991). Several caves were identified in the valley center just beneath government offices, schools, and hospitals (Alva-Niño, 1995). These chemical dissolution structures are several meters in diameter and are related to

karstification processes. Montalvo-Arrieta et al. (2008) obtained the first microzonation map of seismic site class distribution in MMA based on borehole information, seismic refraction profiling, and surface geology. According to geotechnical site categories by Rodriguez-Marek et al. (2001) and BSSC soil classification ( $V_{S30}$ ), these authors proposed that C and C1-C2 sites classes are located to the south and central valley. These classes are also correlated to soft sediment maximum thickness. In foot hills, A and B site classes are dominant.

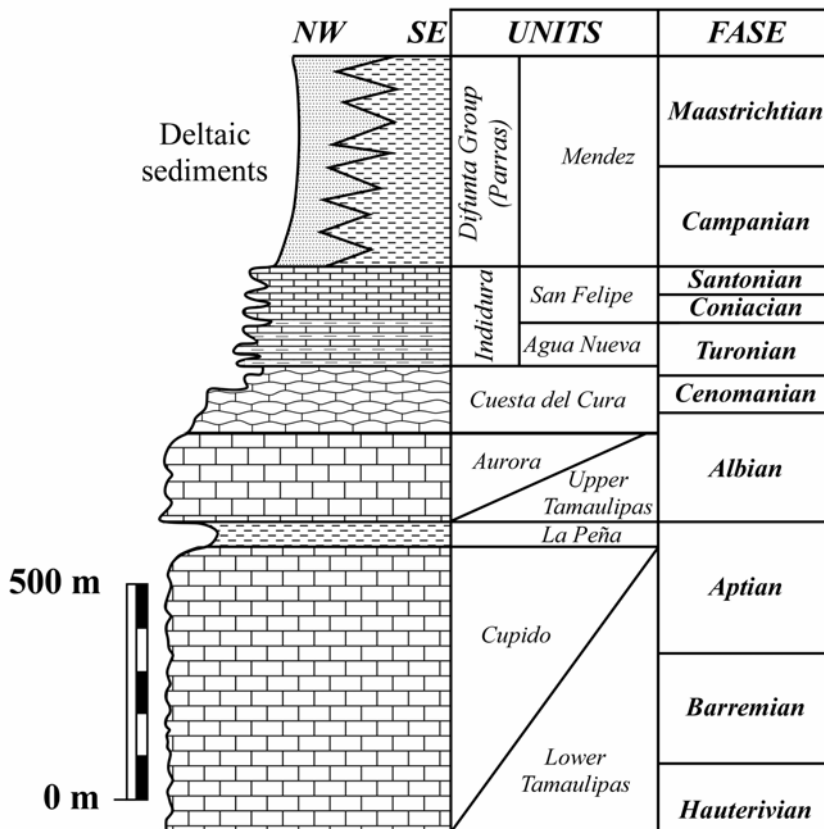


Figure 4. Stratigraphic column from the Monterrey Metropolitan Area (after Michalzik, 1988).

### 3.3. Structural Geology

In Northeast Mexico, the SMO trend curves sharply on what is known as the Monterrey Salient. This segment corresponds to a fold belt that is locally thrust (Figure 3). The fold axes, fault planes, and thrusts change their trend and produce a north-northeastward convex structure between Linares, Nuevo Leon and Saltillo, Coahuila (Padilla y Sanchez, 1982; Eguiluz et al., 2000).

All folds in the area are doubly plunging detachment folds with curvilinear hinges that extend along strike for 40–60 km, oriented WNW-ESE to NNW-SSE. Folds generally symmetric, upright to slightly north vergent, kink-style box folds with steeply dipping (70–90°) limbs are present in the Monterrey salient (Padilla y Sánchez, 1985; Marrett and Aranda-

García, 1999; Chávez-Cabello et al., 2004; Higuera-Díaz and Fischer, 2005). Symmetric, upright and moderately dipping (40-70°) limbs characterize Las Mitras, La Silla, Topo Chico, Obispado, and Loma Larga anticlines. In a general view, the positive MMA topographic features are represented by anticline crests and limbs, except for the Loma Linda hill where a syncline was documented between Las Mitras and Topo Chico anticlines (Figure 3).

## 4. Hydrometeorological Conditions

### 4.1. Climatic Conditions

As mentioned, MMA is located in the SMO and GCP borders (SPP, 1981), a physiographic region inside the Northern subtropics latitudinal zone (Strangeways, 2007). According to the Köppen classification (McKnight and Hess, 2000), MMA has a humid subtropical climate (Cfa), characterized by hot and humid summers, due to unstable tropical air masses, or onshore trade winds, and chilly to mild winters. Temperatures can be quite extreme. Meteorological records for 1886-2008 (Figure 5a; CNA, 2008) reveal that the high average temperature (28.3°C) has been observed in August. Winters are cool but not cold. The minimum average temperature (14.4°C) has been recorded in January. Temperatures below freezing are rare.

Rainfall in MMA is scarce, reaching a mean annual of 660 mm (Figure 5b). This value is comparable to  $652 \pm 19$  mm reported for the Northern subtropic zones during the twentieth century (1901-1998; New et al., 2001). Most average rainfall (472 mm) is registered between June and October (Figure 5b), mainly as a consequence of a convective system related to trade wind easterlies. September shows the greatest rainfall accumulation (175 mm, normally distributed in 7-10 days). However, the reduced average rainfall observed in July (61 mm) reflects the occurrence of the “canícula” or “dog days”, the hottest, most sultry days of summer. In this month, highly reflective cloud (HRC) parameter features a single peak. Cavazos and Hastenrath (1990) considered that the discrepancy of HRC with precipitation in September may be due to the fact that rains in this month fall in large part from stratiform cloud decks associated to tropical storms. During boreal winter (November to April), the upper tropospheric circulation is dominated by the subtropical westerly jet stream. This phenomenon breaks the convective system, establishing a dry season over much of the Caribbean Basin and Mexico. The average rainfall during November to April period reaches 131 mm. However, Cavazos (1999) reported that Northeastern Mexico exhibit significant wintertime precipitation variability associated to: (a) El Niño Southern Oscillation (ENSO) warm events (timescale: up to 18 months), a consequence of accelerated subtropical westerly jet and (b) mid-latitude cold invasions, labeled as “Nortes” (timescale: 3-7 days), that can penetrate far southward over the Mexican land bridge (Grogan, 1919; Klaus, 1973; O'Hara and Metcalfe, 1985; Schultz et al., 1998). Cold invasions may bring extensive stratiform cloudiness and rainfall on the windward side of the large mountain chains, as the Sierra Madre Oriental (Cavazos and Hastenrath, 1990). Humidity in winter can be high, although without showers. Snowfall is a very rare event.

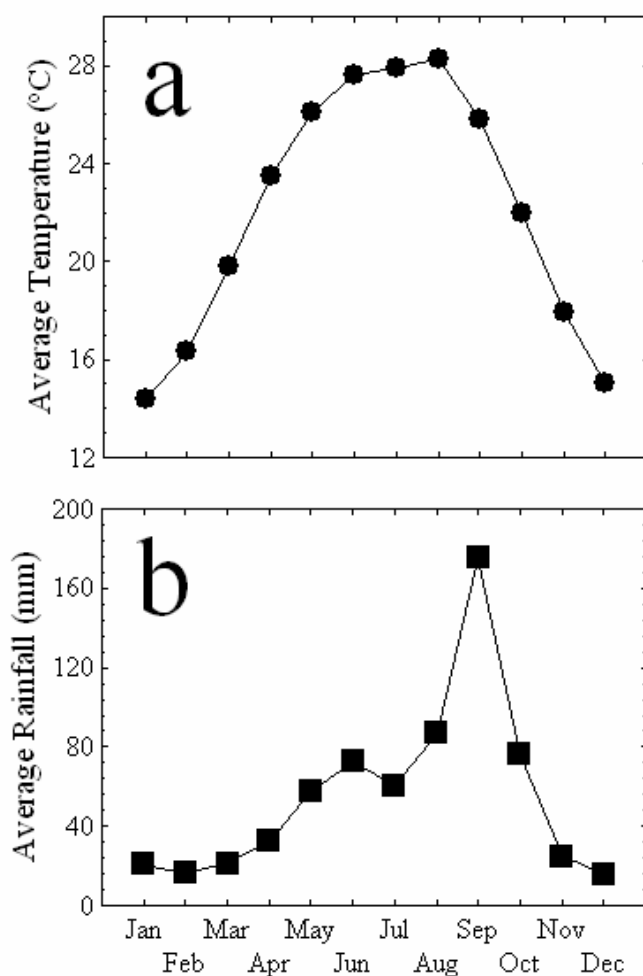


Figure 5. Monthly average data of (a) temperature (°C) and (b) rainfall (mm) for MMA recorded in Monterrey station in the period 1895-2007 (CNA, 2008).

## 4.2. Extraordinary Rainfall Events

It has been well established over several decades that rainfall is the main triggering agent for the occurrence of landslides in the MMA hilly zones. Fourteen severe flooding events, associated with Santa Catarina, La Silla, San Juan, and Pesquería rivers overflows, have been documented in 1612, 1632, 1636, 1642, 1644, 1648, 1716, 1752, 1775, 1782, 1802, 1810, 1825, and 1881 (Roel, 1938; Buentello Chapa, 1970; Nuncio et al., 1989). These extreme flood events caused social and economic disasters in MMA, as deduced of the following examples (Roel, 1938): (a) The 1612 inundation covered wide areas of the city, destroying majority of the riverside settlements, and forcing hundreds of residents to evacuate the area towards the valley south zone; (b) Forty days of uninterrupted heavy rains in August-September 1716 caused the Santa Catarina river to spill over its bank flooding La Purísima neighborhood and leaving several people missing; (c) Torrential rain fell across MMA during

October, 1881. The floods destroyed more than 200 homes, public buildings, and factories; and (d) As a result of intense rainfall periods combined with limited medical assistance programs, sanitary emergencies by epidemic malaria were declared in 1802, 1826, 1835, and 1844.

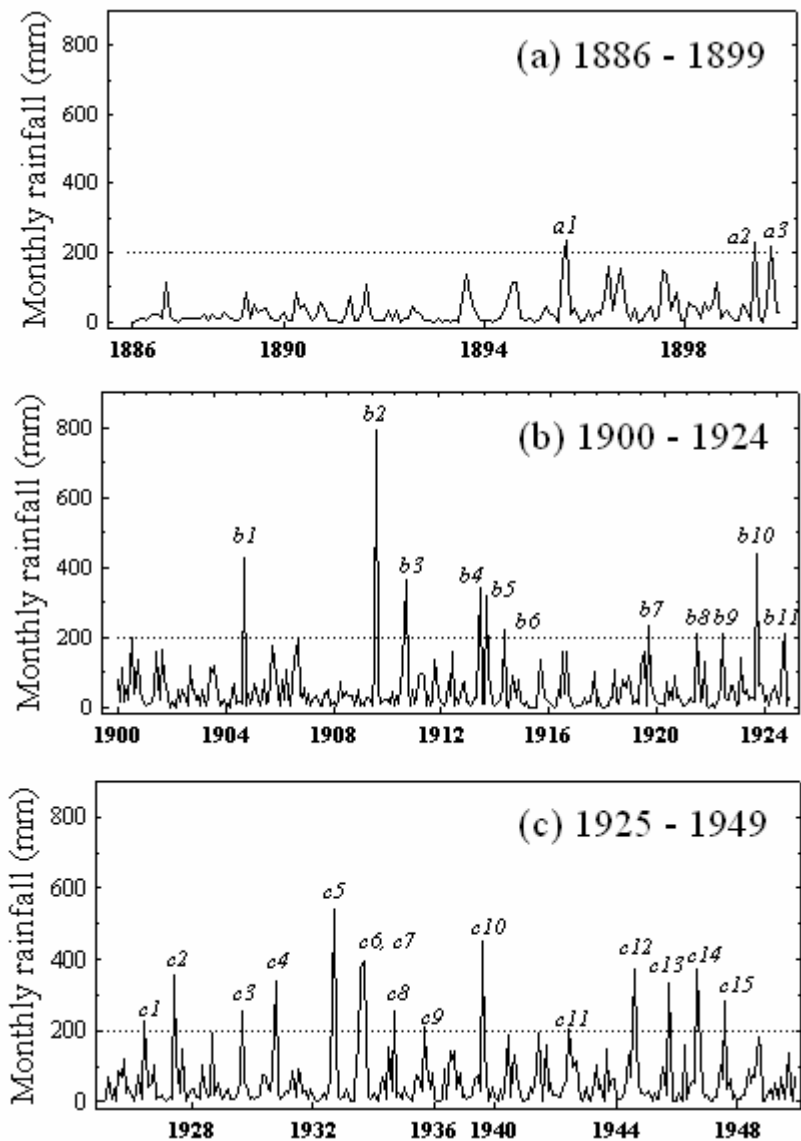


Figure 6. Historic monthly rainfall data for Monterrey station: (a) 1886-1899, (b) 1900-1924, and (c) 1925-1949. In each diagram are marked the rainfall peaks > 200 mm.

On the other hand, Figures 6 and 7 show the monthly rainfall data from 1886 to 1949, and 1950 to 2008. Chart 2 includes the historic monthly rainfall data >200 mm for Monterrey station in the 1895-2008 period (CNA, 2008). A revision reveals eight records >400 mm, all of them observed in August and September. Sometimes, as occurred in some events previous to 1895, most of the monthly rainfall has been accumulated in a very short period, as



demonstrated by the following examples (CNA, 2008): (a) MMA was affected by intense rainfall during September 6-9, 1986 (accumulated precipitation ~250 mm), that caused the overflow of the Santa Catarina river and Topo Chico, Seco, Del Obispo, and Conductores streams; (b) for October 2000 rainfall was 138 mm, with a ~75% (104 mm) accumulated on October 6; (c) the total rainfall during June 2002 was 192 mm. In an unusual event, 140 mm fell on June 28, with ~93% of this quantity being accumulated in 70 minutes; and (d) a rainfall during September 2004 was 438 mm, but 139 mm (~32 %) fell on September 2.

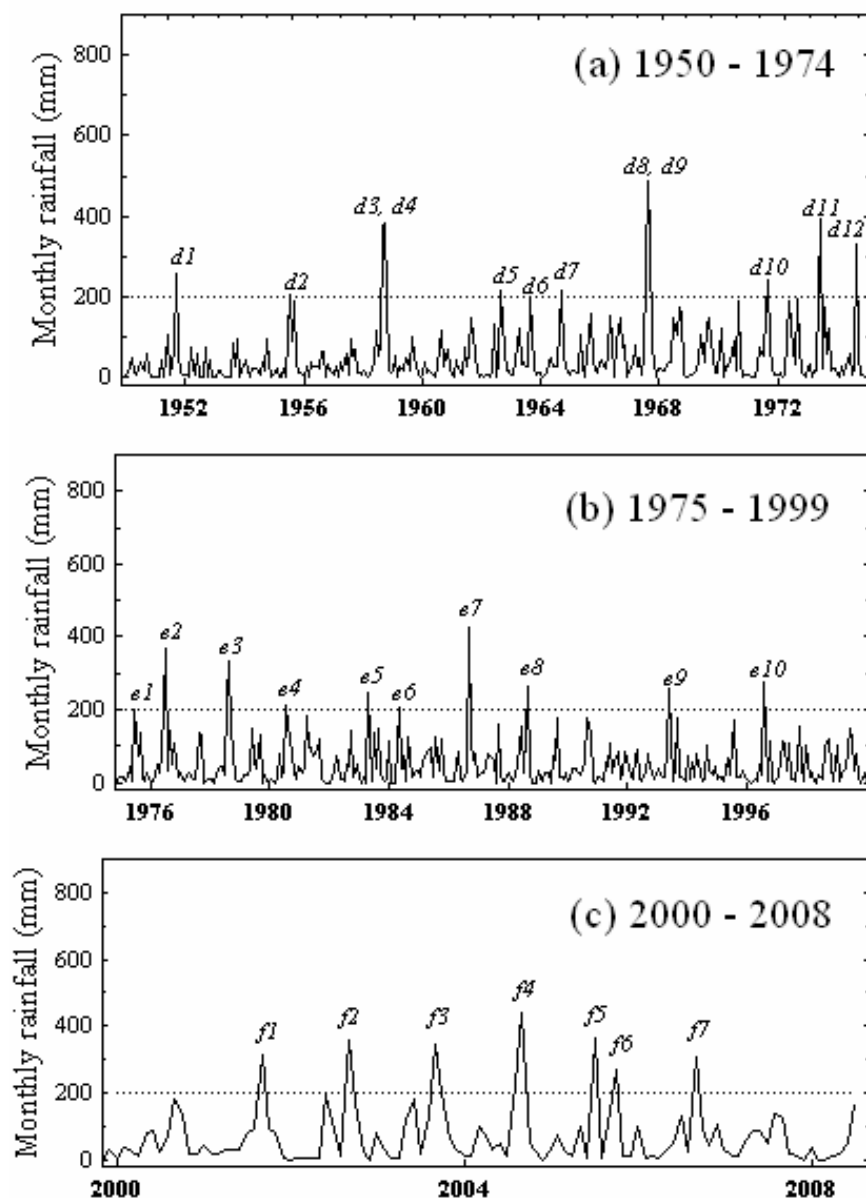


Figure 7. Historic monthly rainfall data for Monterrey station: (a) 1950-1974, (b) 1975-1999, and (c) 2000-2007. In each diagram are marked the rainfall peaks > 200 mm.

**Chart 2. Historic monthly rainfall data >200 mm<sup>\*1</sup> for Monterrey, Mexico and Atlantic Ocean hurricane or tropical storms<sup>\*2</sup> that reached the Northeast Mexico (1886-2007)**

Year	Month	Event	Rainfall (mm)	Hurricane or tropical storm					
				Name / Maximum SSS	Date Month/Day	Position Lat/Long	Wind (knots)	Pressure (mbar)	SSS
1895	Aug	<i>a1</i>	235.7	Hurricane # 2 / 2	Aug / 30	25.2/-99.5	30	-	TS
1899	Jun	<i>a2</i>	228.3	Tropical storm # 1	Jun / 27	28.8/-94.8	35	-	TS
	Oct	<i>a3</i>	216.3						
1904	Sep	<i>b1</i>	425.4						
1909	Aug	<i>b2</i>	790.8	Tropical storm # 5	Aug / 10	23.7/-99.8	30	-	TS
				Hurricane # 6 / 3	Aug / 27	23.8/-97.3	105	-	3
1910	Sep	<i>b3</i>	362.3	Hurricane # 3 / 2	Sep / 15	27.0/-99.0	35	-	TS
1913	Jun	<i>b4</i>	338.3						
	Sep	<i>b5</i>	319.3						
1914	May	<i>b6</i>	219.4						
1919	Sep	<i>b7</i>	231.3						
1921	Jul	<i>b8</i>	208.2						
1922	Jun	<i>b9</i>	211.5	Tropical storm # 1	Jun / 16	24.9/-98.2	35	-	TS
1923	Sep	<i>b10</i>	438.1						
1924	Oct	<i>b11</i>	209.6						
1926	Jun	<i>c1</i>	226.8						
1927	Jun	<i>c2</i>	358.6						
1929	Sep	<i>c3</i>	256.8						
1930	Oct	<i>c4</i>	337.3						
1932	Sep	<i>c5</i>	538.4						
1933	Aug	<i>c6</i>	376.3	Hurricane # 5 / 1	Aug / 05	25.2/-98.3	50	-	TS
	Sep	<i>c7</i>	394.4	Hurricane # 15 / 2	Sep / 25	22.8/- 100.5	35		TS
1934	Sep	<i>c8</i>	252.6						
1935	Sep	<i>c9</i>	208.4						
1938	Aug	<i>c10</i>	454.0	Hurricane # 3 / 2	Aug / 28	23.0/-98.7	55		TS
1942	Jun	<i>c11</i>	201.8						
1944	Aug	<i>c12</i>	374.7	Tropical storm # 5	Aug / 23	25.6/-99.8	25	-	TD
1945	Oct	<i>c13</i>	335.6						
1946	Sep	<i>c14</i>	371.5						
1947	Aug	<i>c15</i>	284.5	Tropical storm # 1	Aug / 02	26.3/-99.0	35	-	TS
				Hurricane # 2 / 2	Aug / 16	22.0/-99.5	45	-	TS
1951	Sep	<i>d1</i>	259.1						
1955	Jul	<i>d2</i>	204.7						
1958	Sep	<i>d3</i>	373.9						
	Oct	<i>d4</i>	384.6						
1962	Sep	<i>d5</i>	215.5						
1963	Sep	<i>d6</i>	200.8						
1964	Sep	<i>d7</i>	214.6						
1967	Aug	<i>d8</i>	488.5						
	Sep	<i>d9</i>	347.0	Hurricane Beulah / 4	Sep/22	26.7/-99.5	35	-	TS
1971	Sep	<i>d10</i>	241.5						
1973	Jun	<i>d11</i>	390.8						
1974	Sep	<i>d12</i>	330.3						
1975	Jul	<i>e1</i>	202.7						
1976	Jul	<i>e2</i>	365.8						
1978	Sep	<i>e3</i>	332.8						
1980	Aug	<i>e4</i>	213.4						
1983	May	<i>e5</i>	246.8						
1984	May	<i>e6</i>	205.9						
1986	Sep	<i>e7</i>	426.7						

Chart 2. Continued

Year	Month	Event	Rainfall (mm)	Hurricane or tropical storm					SSS
				Name / Maximum SSS	Date Month/Day	Position Lat/Long	Wind (knots)	Pressure (mbar)	
1988	Sep	<i>e8</i>	265.6	Hurricane Gilbert / 5	Sep / 17	25.0/- 100.5	35	996	TS
1993	Jun	<i>e9</i>	256.7						
1996	Aug	<i>e10</i>	275.9						
2001	Sep	<i>f1</i>	311.0						
2002	Sep	<i>f2</i>	359.4						
2003	Sep	<i>f3</i>	342.6						
2004	Sep	<i>f4</i>	437.9						
2005	Jul	<i>f5</i>	366.4	Hurricane Emily / 4	Jul / 20	25.0/-99.7	70	975	1
		<i>f6</i>		Tropical storm Gert	Jul / 25	22.5/- 100.0	25	1006	TD
2006	Sep	<i>f7</i>	308.8						

\*<sup>1</sup>Rainfall information from Comisión Nacional del Agua, Dirección Técnica Cuenca Río Bravo. Data of event column corresponds with the peaks > 200 mm showed in Figures 6 and 7. \*<sup>2</sup> Hurricane or tropical storm data from Unisys Weather web page ([www.weather.unisys.com/hurricane](http://www.weather.unisys.com/hurricane)). Name column includes the maximum category reached by each meteor according to Saffir-Simpson scale (SSS; H = hurricane; TS = tropical storm; TD = tropical depression). Additional data correspond to information for nearest position of each meteor respect to Monterrey, Mexico (Latitude: 25°40'17''N; Longitude: -100°18'31''W). Sustained wind units: 1 knot = 1.15 mph = 1.85 km/h.

MMA is located in a context where diverse meteorological events take place due to its closeness to the Gulf of Mexico. During the 1892-2008 period, 43 meteors that include all categories according to Saffir-Simpson (SS) scale (Jáuregui, 2003) made landfall on Northeastern Mexico coasts. Most of them (20) have hit as tropical storms. The list also includes one hurricane category 4 (Gilbert in September, 1988) and two hurricanes category 5 (Beulah in September, 1967; Anita in September, 1977). The trajectories of most of these meteors continued in an east-west direction. Several monthly rainfall high values observed in MMA have been associated to Atlantic hurricanes and tropical storms (Figure 8). Chart 2 also contains general information related to these events. During these extreme precipitation events, a dramatically high percentage of the average annual rainfall has been received over relatively short period of time. In particular, the influence of hurricanes in MMA has been well demonstrated by the impact of the following meteors: (a) Tropical storm # 5 - Hurricane # 6 (1909), (b) Hurricane # 3 (1938), (c) Beulah (1967), (d) Gilbert (1988), and (e) Emily-Gert (2005).

The 1909 Atlantic hurricane season (June 15 – November 30; Ellis, 1988) was average in activity, but destructive. Four meteors became major hurricanes with winds stronger than 179 km/h. Tropical storm # 5 of the this season formed on August 6 and hit Mexico twice, first on the Yucatan Peninsula and then near the border between Veracruz and Tamaulipas (Garriot, 1909). On August 9 the meteor arrived to MMA overflowing the Santa Catarina River. Buentello Chapa (1970) reported that most of the precipitation (237 mm, ~30% of the total monthly rainfall; event *b2* in Chart 2 and Figure 6b; CNA, 2008) was recorded in a period of 3 days. San Luisito (now Independencia) district was severely affected by the intense rainfall (Nuncio et al., 1989).

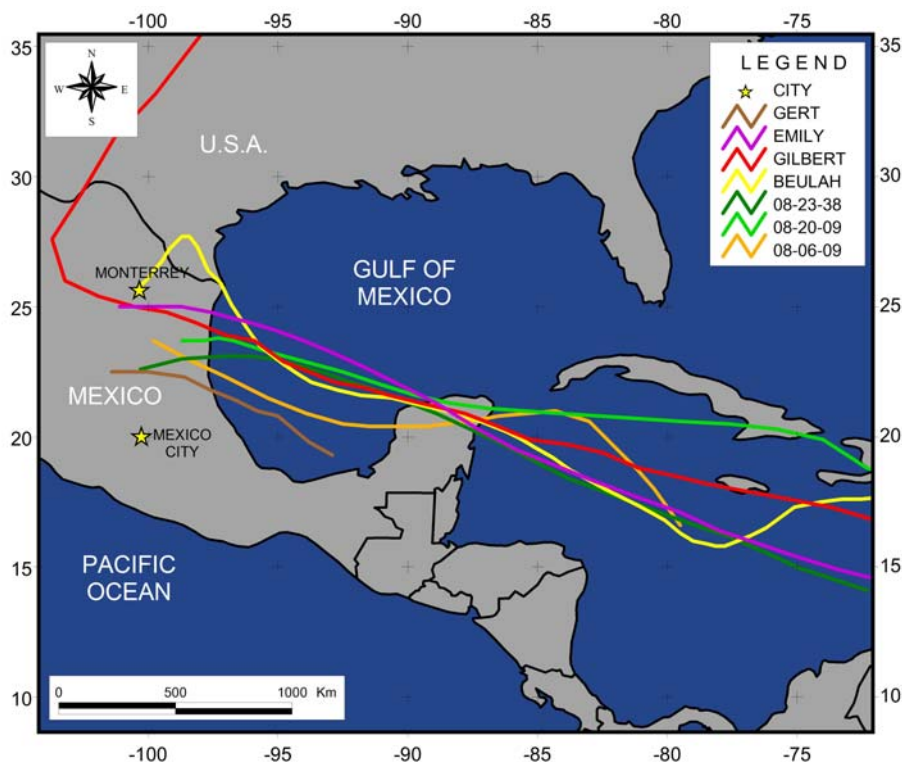


Figure 8. Tracks of major Hurricanes that strike Northern Mexico, and Monterrey Metropolitan Area.

Tropical storm # 6 of 1909 (Ellis, 1988) formed east of the Lesser Antilles on August 20. The storm strengthened to a SS category 3 hurricane (according to Safir-Simpson scale) and hit the northeastern corner of the Yucatán Peninsula. After weakening, it regained strength and hit Tamaulipas as a major hurricane on August 27. It went to MMA causing enormous loss of life and property (Garriot, 1909; Nuncio et al., 1989). After one day of intense precipitation, Santa Catarina River once more dramatically overflowed. On August 27, river flow rate reached  $\sim 7700 \text{ m}^3/\text{s}$ , with a flow velocity of 24 km/h (Nuncio et al., 1989). Rainfall accumulation for MMA in August 25-29 period was 549 mm ( $\sim 57\%$  of the total monthly precipitation; event *b2* in Chart 2 and Figure 6b; CNA, 2008). About  $1200 \text{ m}^2$  of the urban area were inundated in this disaster (Buentello Chapa, 1970). Many public and private buildings were completely destroyed during the event, especially downtown and low income suburbs. Unofficial estimates placed the death toll at 3500 and 1500 people were missing as a result of floods and mud slides.

The third storm of 1938 Atlantic hurricane season (June 1 – November 30) was discovered as a strengthening tropical storm in the central Caribbean Sea on August 23 (Tannehill, 1938). On August 28, storm # 3 made landfall as a tropical storm, with sustained winds of 129 km/h, near Ciudad Madero and dissipated inland provoking floods and landslides in the Mirador residential sector, behind the Cerro del Obispaado (Nuncio et al., 1989). Approximately 80% of monthly rainfall was accumulated in three days (event *c10* in Chart 2 and Figure 6c; CNA, 2008). After this disaster, Nuevo Leon government authorities

established a canalization project for the Santa Catarina river, although it was carried out years later during the governor Ignacio Morones Prieto administration (1949-1952).

Hurricane Beulah (Flitters, 1970) was the strongest hurricane during the 1967 Atlantic hurricane season (June 1 – November 30). It made landfall just north of the mouth of the Rio Grande as a SS category 3 hurricane. Beulah drifted over Texas, moving southwestward into Mexico where it was disrupted by the mountains at 48 km of MMA on September 22. The accumulated rainfall in September 1967 was 347 mm (event *d9* in Chart 2 and Figure 7a; CNA, 2008), more than 70% being precipitated on September 22-23. Hurricane force winds and rainfall caused much destruction: homes, buildings, and municipal structures in and around MMA were severely damaged by the flooding, debris-flow and landslides (Nuncio et al., 1989).

Gilbert, the third hurricane of the 1988 Atlantic hurricane season (August 5 – November 24), has been one of the most powerful Atlantic hurricanes in history, as it recorded a very low sea level pressure at 888 mbar (Lawrence and Gross, 1989). Gilbert's landfall as a SS category 3 hurricane hits the Northeastern Mexican coast on September 15 (sea level pressure ~1010 mbar; sustained winds ~200 km/h; Lawrence and Gross, 1989; Nuncio et al., 1989; Rosengaus Moshinsky and Sánchez-Sesma, 1990). The weakening storm passed south of MMA, bringing massive flooding to the region (accumulated rainfall ~200 mm, ~75% of the total monthly rainfall; event *e8* in Chart 2 and Figure 7b; CNA, 2008). The Santa Catarina River flow rate reaches  $1.43 \text{ m}^3/\text{s}/\text{km}^2$ , eleven times the average historic value ( $0.13 \text{ m}^3/\text{s}/\text{km}^2$ ; Rosengaus Moshinsky and Sánchez-Sesma, 1990). Approximately 200 people were killed and more than 60,000 homes were destroyed by river overflow, debris-flow and landslides. In a dramatic episode, on September 16 four buses overturned in flood waters, trapping most of the passengers inside. Therefore, a lot of a telephone and power lines were destroyed, and small villages around MMA became isolated one after the other. Damages in the MMA were estimated ~1 billion dollars (Lawrence and Gross, 1989).

Hurricane Emily (Beven II et al., 2008) was the fifth named storm, third hurricane, second major hurricane, and first Category 5 of the record-breaking 2005 Atlantic hurricane season (June 1 – November 30). Emily made a destructive landfall in San Fernando, Tamaulipas on July 20. After moving inland, Emily turned west and weakened rapidly, dissipating on July 21 over the SMO range. An intense rainfall (248 mm, 67% of the total monthly precipitation; event *f5* in Chart 2 and Figure 7c; CNA, 2008) affected the MMA during July 19-21 causing inland flooding, landslide and debris flow. One hundred communities around Monterrey were isolated after the storm. Insured damages were estimated in 4 million dollars. There were no deaths directly attributable to landfalls occasioned by Emily, although a helicopter crashed before the storm claimed two lives.

It is important to note that, Goldenberg et al. (2001) reported that an increase in the Atlantic hurricane activity has been observed starting from 1995, affecting Caribbean islands and the Gulf of Mexico coast. Goldenberg et al. (2001) suggested that the greater activity is associated to a natural climate cycle termed the Atlantic Multidecadal Oscillation (AMO), reflected in simultaneous increases in North Atlantic sea-surface temperatures and decreases in vertical wind shear. They also considered that the present high level of hurricane activity is likely to persist for ~40 years. In contrast, Mann and Emanuel (2006) have proposed that climate change is playing a dominant role in the increase of Atlantic hurricane activity. However, whatever the reasons for this phenomenon, the shift in climate calls for a

reevaluation of prevention and mitigation strategies to be implemented in the MMA, as intense rainfall in short time is the main factor to induce landslide and debris-flow.

## 5. Landslides Types in the MMA

In the MMA we separated two general types of landslides based on their historical and genetic mechanisms of movement: a) ancient landslides related to geological causes, and b) recent landslides related to anthropogenic causes. In this chapter we follow the Varnes' classification of slope movements (Varnes, 1978).

### 5.1. Ancient Landslides Related to Geological Causes

There are two types of ancient landslides related to geological causes that could be reactivated due to surface erosion during extraordinary periods of rainfall, vibration by blasting in quarries areas or by excavation during human activities such as urbanization.

#### 5.1.1. Landslide in Las Mitras Anticline

There is a major complex landslide in the southern limb of Las Mitras anticline that shows two tracks and two depositional areas (Figures 3 and 9). The landslide contains different types of materials, these are represented by fine clastic materials like clay and silt derived from argillaceous units and pebbles to huge blocks from a thick calcareous formation. The huge blocks were detached from an adversely oriented discontinuity located in the contact area between the Upper Tamaulipas and La Peña Formations. From a structural view, the block detachment area is a doubly adversely geological discontinuity, first because bedding in this area dips parallel to the slope near the top of the anticline and, second, there is a high lithological contrast between two geological units: massive limestone of Aurora underlayed by shale, chert, and marl of the La Peña Formation (Figure 4).

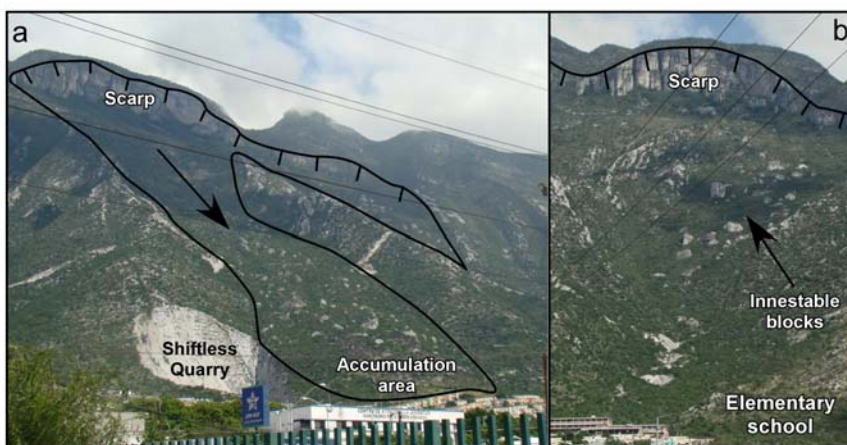


Figure 9. Ancient landslide in the south limb of Las Mitras anticline that show huge blocks that were detached from an adversely oriented discontinuity (contact between Aurora and La Peña Formation).

The main types of mass movement in this area are represented by rock fall, topple and block slide in the Upper Tamaulipas formation, and by rock and debris fall of the La Peña Formation.

### 5.1.2. Block Fall in the Chipinque Area

There are many huge blocks in the foothills of the Los Muertos anticline in the leading edge of the Monterrey salient. The Chipinque area in San Pedro Garza García shows the best exposures of huge blocks of limestone (Figure 10). In some accumulation areas, the blocks are embedded in an argillaceous matrix derived by weathering of clastic, calcareous to argillaceous beds of the Agua Nueva, San Felipe and Méndez Formation (Figure 4) which are outcropping along the north limb of Los Muertos anticline toward the MMA valley. On the other hand, major blocks are still located inside the main track of landslides (Figure 10). The types of mass movement in this area are represented by toppling and rock fall from the Upper Tamaulipas formation due to steeply dipping bedding in the north vertical limb of Los Muertos anticline.

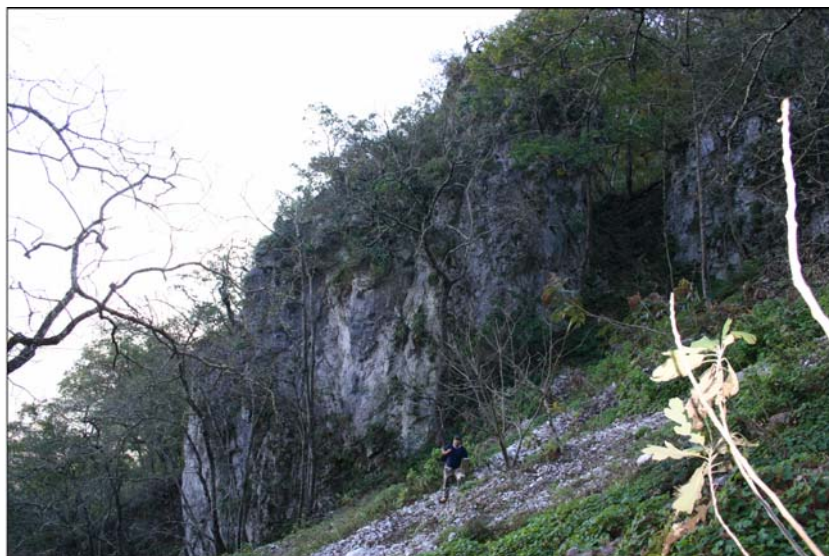


Figure 10. Important blocks in the foothills of the Sierra Madre Oriental in the Chipinque area. This kind of blocks have been displaced from the north vertical wall of the Los Muertos anticline.

## 5.2. Recent Landslides Related to Human Causes

There are a wide variety of slope failures associated to several human causes: a) mining (shiftless quarries areas), b) excavation of slopes, and c) loading of slopes. The first one is a special case for several shiftless and active quarry areas located in the southeastern part of El Topo Chico hill and Las Mitras range. The last two cases are related to urban development in the eastern foothills of Las Mitras range (Vista Hermosa, Dinastía, San Jeronimo and Cumbres districts), Chipinque, El Mirador hill, Mederos, Satelite and El Huajuco at the foothill of the SMO, and the Contry area at the La Silla range foothill.



### 5.2.1. Landslides in Quarries Areas

MMA has multiple limestone quarry areas because one of the most important Portland cement company in the world was established here. There are two major shiftless quarry areas inside the urban zone: a) The eastern area of Las Mitras range, and b) the southeastern area of El Topo Chico hill (Figure 3). The Topo Chico quarry areas are special cases due to irregular human settlements developed inside the quarries after these were shiftless by the cement industry approximately fifteen years ago.

#### Salvador Allende Landslide

Recently, a landslide occurred along a vertical rock wall that separates two quarries in the Topo Chico area in the Salvador Allende district (Figures 11 and 12). This district, among others, was settled, unbelievably, inside a shiftless quarry area and today the settlement comprises the flat area inside the quarry. Houses are built near vertical walls and their yards have different size blocks, weighting perhaps up to three tons (Figures 12 and 13). The Salvador Allende landslide occurred after a period of rainfall and fortunately no injuries were reported. However, the population is at risk due to active fractures along vertical walls that delimit the quarries (Figure 11). In almost all El Topo Chico hill the topographic relieve is strongly influenced by the structural position of bedding. Unfortunately, during industrial activities its slopes were altered by excavation in its foot, configuring instable walls inside the quarries where irregular settlement were developed and which are under high risk of translational landslides, block slides and rockfall (Figure 11).

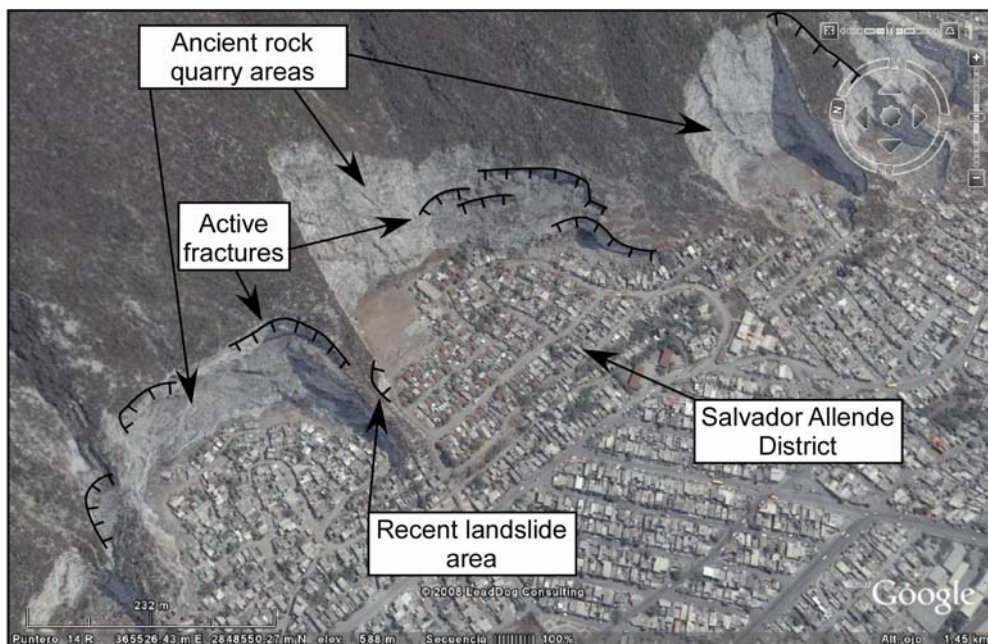


Figure 11. Oblique aerial view using Google of Salvador Allende district which is located inside of shiftless quarries areas in the municipality of Escobedo, N.L.





Figure 12. a) Frontal view of the Salvador Allende landslide, b) Close up of the accumulation zone of the Salvador Allende landslide, and c) general view of the northwestern vertical limit of the quarry in the Salvador Allende district.

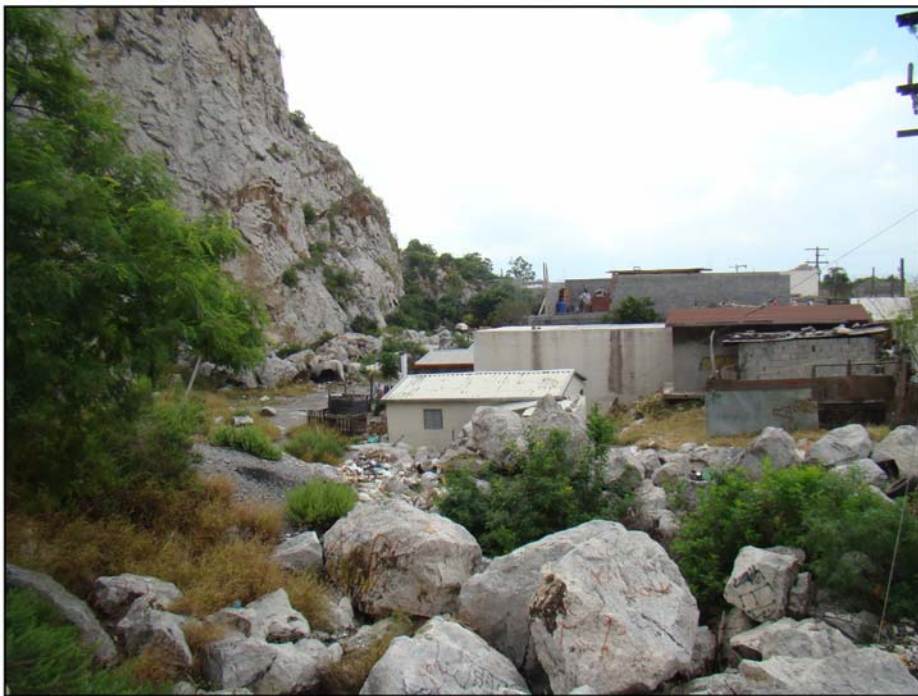


Figure 13. View of rockfalls inside of the shiftless quarry of the Salvador Allende district.

## Mitras Landslide

Six years ago an important translational landslide occurred in an active quarry known as Las Mitras (Figure 14a), in the eastern tip of Las Mitras range. This landslide caused injuries and the death of one person. The landslide had a ruptured surface parallel to the bedding that was triggered by a combination of factors: excavation at the foot of limestone beds in the slope, by water infiltration along bedding contacts and fractures. One more time during a period of rainfall, and by vibrations resulting from blasting during mining. Today, the quarry area of Las Mitras is shiftless, however, many areas inside the quarry are under slide risk (Figure 14b).

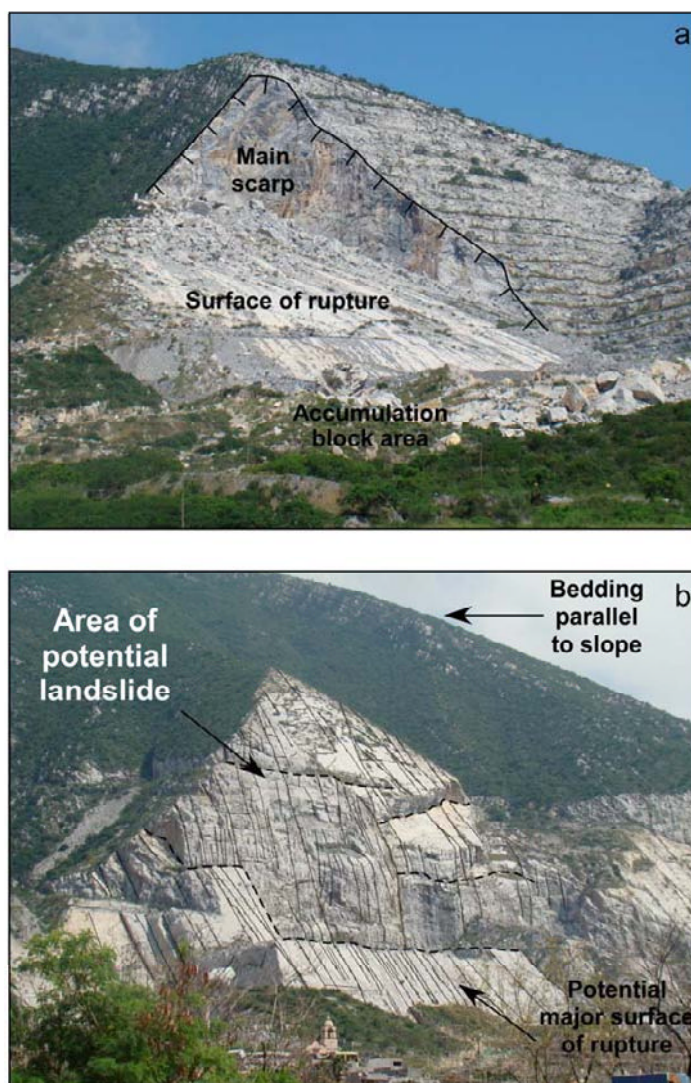


Figure 14. (a) Recent translational landslide in the Mitras quarry where a person died during the mass movement, (b) Area potentially to slide due to similar geological-structural condition as above (a).



### 5.2.2. Landslides in Slope Areas

Many landslides have occurred in slope areas due to excavation of slope or at its foot and by loading of slope or its crest during urbanization at the foothills of all ranges and hills surrounding the MMA. Many landslides have been reported recently, among the most important are: Las Lajas, El Mirador (Ibarra-Martínez, 2007), Mederos, Contry Sol district in La Silla range, block fall in Chipinque, and many debris flow during intense surface-water flow due to heavy precipitation at all foothills surrounding the MMA. In this chapter only Las Lajas landslide will be described in detail because of the similarity in behaviour to the other landslides in MMA.

#### Las Lajas Landslide

The most important landslide that occurred recently in the MMA was Las Lajas landslide (July-25<sup>th</sup>-2005). The landslide affected an important building constructed on top of weathered and densely fractured shale and marl of the Agua Nueva formation. It is located in the eastern foothill of Las Mitras range and occurred along the contact between Cuesta del Cura and Agua Nueva formations. The landslide was triggered by a short but intense rainfall period (Emily hurricane) due to heavy load on an instable slope (Figure 15). The geological conditions, where the construction was being carried out, were inadequate due to: a) bedding dips parallel to slope, b) lithology showing high density fractures, and c) the rocks are predominantly argillaceous with high contents of expanding clay minerals (montmorillonite-type). More detailed data about the MMA landslide history is reviewed in Discussion section.



Figure 15. Recent vertical aerial views of Dinastía and Torres de San Jeronimo districts that show the demolition area where a twenty story building was destroyed to mitigate the Las Lajas landslide. The close up in the right lower side shows the geometry of the Las Lajas landslide for July 25<sup>th</sup> 2005.

The demolition of the major building inside of Las Lajas landslide was performed to mitigate the mass movement; this action suddenly reduced the load and displacement in the active surface rupture. As in Las Lajas area, many actions have been carried out in MMA to mitigate mass movements such as: construction of retaining structures, minimizing surface irrigation above landslides, and directing surface water away from the landslide, among others.

## **6. Discussion**

### **6.1. Rainfall Intensity – Duration Landslide Control**

Landslide and debris flow causal factors include (Popescu, 1994): (a) ground conditions, (b) geomorphological processes, (c) environmental processes, and (d) man-made processes. Ground conditions encompass material and mass ground characteristics (engineering soil and rock properties). Geomorphological processes are morphological changes in the ground (erosion and deposition). Environmental processes include natural events such as rainfall, earthquakes, etc. Man-made processes include all kind of human activities that influence slope stability (e.g., excavation, loading, vegetation removal, etc.).

Rainfall is recognized as one of the most important trigger factor of landslides. Landslides are caused by the building up of high pore water pressure into the ground (Campbell 1975, Wilson 1989). Groundwater conditions responsible for slope failures are related to rainfall through infiltration, soil characteristics, antecedent moisture content, and rainfall history. These environmental variables are poorly known over large areas and exhibit considerable spatial and temporal variability. The first study to relate rainfall thresholds to landslide initiation was published by Caine (1980). This author investigated a total of 73 shallow (< 3 m deep) landslides on slopes that were unaffected by artificial disturbance or undercutting by streams. Using local precipitation records, he defined an upper threshold for landslide initiation (Chart 3), establishing a reasonable fit for precipitation data between 10 min and 10 days in duration, and a poor fit for longer or shorter durations. He suggested that the lack of fit for very short durations resulted from insufficient depths of water to change pore water pressure. The data were compiled from a variety of climatic and geologic conditions. As a result, the rainfall intensity-duration (ID) estimates are non-homogeneous.

Despite the inhomogeneous ID behavior, the empirical relationship between rainfall intensity, rainfall duration, and slope instability has been thoroughly documented. Scientists have put a great deal of work estimating rainfall thresholds, also as a part of landslide warning systems. These empirical thresholds have been obtained studying rainfall conditions which resulted in slope failures using the available data from different regions world-wide. The meaning of these thresholds consists of the possibility of having a general threshold which is independent from local conditions and typical rainfall patterns. Different types of global rainfall thresholds (Chart 3) for the possible generation of landslides have been proposed in literature (Innes, 1983; Clarizia et al., 1996; Crosta and Frattini, 2001; Cannon and Gartner, 2005). Recently, from an extensive and worldwide rainfall and landslide event database, Guzzetti et al. (2008) have proposed a global ID threshold (Chart 3), using a strict Bayesian statistical approach to infer the minimum precipitation values for the possible initiation of landslides and debris flows. Authors have suggested that ID thresholds can be

used in landslide warning systems where local and regional thresholds are not available. A comparison of this model to previous ID thresholds is presented by Guzzetti et al. (2008).

**Chart 3. Global rainfall intensity – duration (ID, mm/h - h) thresholds related to landslide and debris flow**

ID Number	Authors	Landslide type	Equation	Range (h)
1	Caine (1980)	Landslides and debris flows	$I = 14.82 \times D^{-0.39}$	$0.167 < D < 500$
2	Innes (1983)	<b>Debris flows</b>	$I = 4.93 \times D^{-0.50}$	$0.1 < D < 100$
3	Clarizia <i>et al.</i> (1996)	Soil slips	$I = 10 \times D^{-0.77}$	$0.1 < D < 1000$
4	Crosta and Frantini (2001)	Shallow landslide	$I = 0.48 + 7.2 \times D^{-1.0}$	$0.1 < D < 1000$
5	Cannon and Gartner (2005)	Wildfire related debris flows	$I = 7.0 \times D^{-0.60}$	$0.1 < D < 3$
6	Guzzetti <i>et al.</i> (2008)	Landslides and debris flows	$I = 2.28 \times D^{-0.20}$	$0.1 < D < 48$

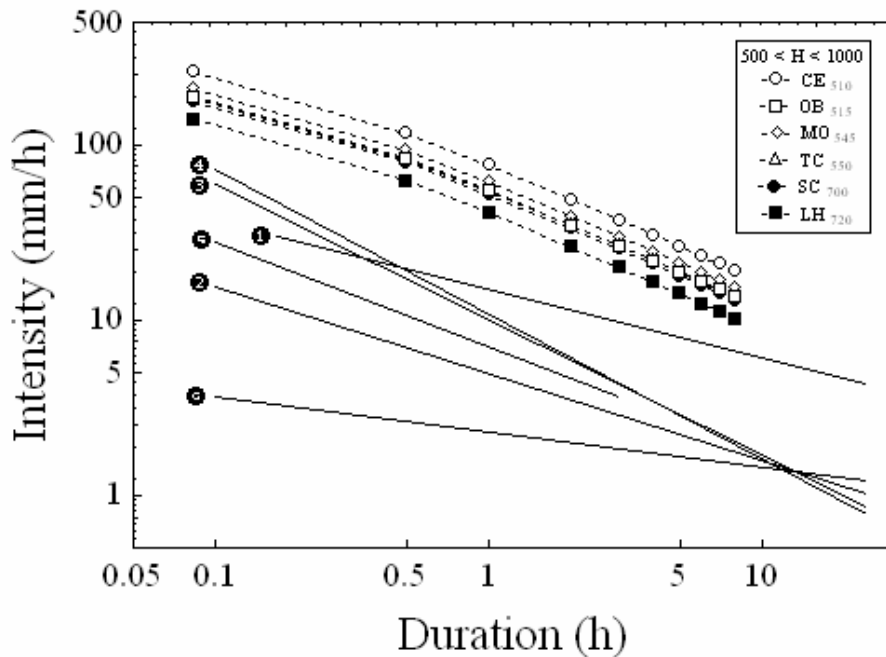


Figure 16. Rainfall intensity – duration (ID) diagrams for MMA meteorological stations (UTM position x,y): Ce = Cerrito (380075.27, 2821798.87), OB = Observatorio (366832.75, 2840672.75), MO = Monterrey (369275.06, 2839458.50), TC = Topo Chico (366219.03, 2847129.00), SC = Santa Catarina (352581.75, 2840329.00), and LH = La Huasteca (353931.86, 2836305.00). ID data have been compiled from Murillo Sánchez (2002). The diagram include global ID thresholds related to landslide and debris flow proposed by: (1) Caine (1980), (2) Innes (1983), (3) Clarizia et al. (1996), (4) Crosta and Frantini (2001), (5) Cannon and Gartner (2005), and Guzzetti et al. (2008).

Murillo Sánchez (2002) calculated rainfall intensity – duration – return period (IDRP) curves from meteorological data of 22 stations located in and around MMA, including the Monterrey station. Intensity rainfall ( $I$ ) data for various durations ( $D$ ), including 0.0833, 0.5, 1, 2, ... 8 h, were estimated applying the generalized model proposed by Chen (1983), considering a 24 h - high intensity rainfall event with a return period of 20 years. It is important to note that this return period is consistent with the extraordinary rainfall events registered in the MMA, as consequence of hurricane and tropical storm impacts, from 1909 to 2005. Figure 16 shows intensity-duration curves generated by Murillo Sánchez (2002) for MMA meteorological station data and compares it with the six published global ID thresholds included in Chart 3. Inspection of this figure reveals that the intensity expected for whole MMA region, during an extraordinary rainfall event, exceeds the global thresholds for the occurrence of shallow landslides and debris flows. The validity and significance of this interpretation has been strongly demonstrated by the tragic consequences observed by hurricane and tropical storm impacts in MMA.

## 6.2. Landslides and Intense Rainfall Events Correlation

A recopilation of MMA landslides triggered by extraordinary rainfalls periods, tropical storms and hurricanes (called rainfall events) has been made in Monterrey base on newspaper reports (El Norte and El Porvenir). Chart 4 shows the correlation between rainfall events and the mass movement descriptions registered in the local press. This review highlights that important mass movements have occurred in the Cerro Las Mitras range, Chipinque area, and Loma Larga hill. The most dramatic cases occurred after the impact of Gilbert hurricane (September 1988), when several landslides, rockfalls and debris flows were triggered by the intense rainfall. Six days after the hurricane impact, a six story building collapsed in the Mirador Hill and two people died. In October 2000, during the colision of Keith hurricane remnants with a cold front, several sectors of the Chipinque area (San Pedro Garza García) were affected by landslides, rockfalls, and debris flows, causing damage to houses. In July 2005, after an intense rainfall period related to Emily hurricane, several landslides, debris flows and rockfalls were triggered in various MMA sites, characterized by critical geomechanical conditions. The most dramatic case occurred in Torres de San Jerónimo (Las Mitras area), when a translational landslide caused severe damage that affected houses, streets, and a residential building. Government authorities evacuated 101 families and a 20-story residential building was demolished. Approximately  $3 \times 10^5$  rocks tons were removed from this site.

After 1988, landslide event frequency induced by extraordinary rainfall periods, has increased dramatically in MMA. This behavior could be explained by the accelerated urban area growth that has gone beyond the valley, reaching foot of mountains and hillslopes with pronounced slopes (Figure 3). It is important to note that 2002-2020 Monterrey urban development plan established a change in land use and building codes, allowing construction in zones with pronounced slopes, as Chipinque, El Mirador, Mederos, Satelite, Huajuco, La Silla, and the Cerro de las Mitras eastern region (Vista Hermosa, San Jeronimo, Dinastia, and Cumbres districts). Clearly, these areas are exposed to natural hazards, such as floods, landslides, and rockfalls, where building should be forbidden.

**Chart 4. Correlation between high rainfall events and landslides and debris flows in MMA (1988-2006)**

Landslides and debris flows					
Event <sup>1*</sup>	Year	Month	Rainfall (mm)	MMA Sector <sup>2*</sup>	Comments
E8	1988	Sep	265.6	CH	Landslides, rock falls and debris flows in Cerro del Mirador that damage several houses. On September 26, a six story building was collapsed with two dead persons.
	1998	Oct	120.4	CH	On October 20-26, mass movements and debris flows were documented in Olinala, Valle de San Ángel, and Chipinque Ecological Park.
	2000	Oct	138.6	CH	On October 5-7, several sectors (Colorines, Colonial de la Sierra, Olinala, Valle de San Angel, Villa Montana, Valle de Chipinque, Hacienda San Agustín, and Barrancas de Tampiquito) of San Pedro Garza García were affected by landslide and debris flows triggered due to intense rainfall associated to Keith hurricane remnants - cold front collision.
F2	2002	Sep	359.4		On September 12, the Monterrey-Salttillo highway was closed as a consequence of landslide and rock fall events.
F3	2003	Sep	342.6	MI, CH, LL	On September 21-22, mass movements affected two houses situated in Las Lajas residential sector. In Lomas del Campestre and Olinala sectors, behind Chipinque, and Colonia Independencia, behind Loma Larga, landslides injures several house buildings.
	2003	Oct	197.9	MI	On October 12, mass movement event another time occurred in Las Lajas sector
	2004	Mar	101.7	SS	On March 21-22, landslide events were observed in Cerro del Caído, Ciudad Satellite city district.
	2004	Apr	77.0		On April 27, landslides and rock falls provoked the Monterrey-Salttillo highway closing for one day.
F5	2005	Jul	366.4	MI, CH	On July 21, three deep fissures were detected in the Torres de San Jerónimo residential sector. These cracks showed 30 m in lenght, one meter in wide, and 5 m of depth. On July 25 occurred a first traslational landslide event, with a displacement ~20 cm, causing severe injuries on homes and municipal structures. As consequence, government authorities decided the evacuation of 101 families, the 20-story residential building demolition, and the removal of $3 \times 10^5$ rocks tons. A debris flow was observed on Gómez Morin avenue, San Pedro Garza García. Other mass movements were reported in Santiago-Laguna de Sánchez road.
F7	2006	Sep	308.8	LL	On October 3, a landslide event was observed in a site slope on Morones Prieto avenue.

<sup>\*1</sup> This column correponds with the extraordinary rainfall events reported in Chart 2. <sup>\*2</sup> MMA sector abbreviations: CH = Chipinque, CM = Cerro del Mirador, LL = Loma Larga, and MI = Sierra de Las Mitras.

The MMA slope instability is strongly influenced by structural-lithological factors. Many landslides are related to translational slides with ruptured surfaces parallel to bedding and along major contacts between geological formations which dips toward the valley and parallel to the slopes in almost all MMA. Under these conditions, any foothills altered by industrial or urbanization activities can be instabilized and potentially boost slides during important rainfall periods.

## 7. Additional Landslide Causes

Landslides are a major cause of damage in most large earthquakes. In the 1964 Alaska earthquake, for example, landslides caused more than half of the economic losses and a third of the fatalities (Keefer, 1984; Harp and Jibson, 1991). Several cases of landslides triggered by earthquakes are document around the world. Keefer (1999) mentioned that the lowest magnitude reported to induce a landslide is  $M = 4.0$ . These landslides can have significant geomorphic effects that vary depending on the landslide characteristics and materials, and on the settings in which the landslides occur.

Northeast Mexico is generally regarded to as a tectonically stable region, characterized by low seismicity (Figure 17) and a lack of strong ground motion records (Galván-Ramírez and Montalvo-Arrieta, 2008). García Acosta y Suárez Reynoso (1996) identify 20 historic earthquakes felt in some cities (Saltillo, Linares, Monterrey, Victoria, Villagran, La Concepción, Mier y Noriega, Dr. Arroyo and Villa de Santiago) located in the SMO. Of these historic events, the April 28, 1841 earthquake caused several injuries and fatalities near the Saltillo area (Sal; Figure 17) and was felt across a radius of approximately ~400 km. For MMA there is no evidence of any damage reported. From recent seismic catalog (*i.e.* National Seismological Service, UNAM and National Earthquake Information Center, USGS), some earthquakes are located with  $M \leq 4.5$  for the Monterrey Salient area (Figure 17). The most recent events (17/04/2006 with  $M = 4.3$  and  $M = 4.1$ ; the main event labeled as Santiago earthquake) were located at a distance of  $< 50$  km from MMA, where no damage was reported.

Although there is no historic evidence of any mass movements induced by earthquakes, recently some authors have studied the seismic risk potential in northeast Mexico and U.S.-Mexican border. Doser (1987) mentions that the seismic deformation observed in west Texas is capable of producing earthquakes as big as 6.4–7.5 magnitude, and Frankel et al. (2002) consider the maximum magnitudes for Texas 7.0–7.5. Galván-Ramírez and Montalvo-Arrieta (2008) mentioned that a possible critical scenario would represent the rupture ( $M_w = 6.5$ ) of the San Marcos fault south segment in Central Coahuila. The importance of this scenario is the settlement of three of the most populated centers in northeast Mexico (Monterrey, Saltillo and Monclova with a total population of more than seven million) located in a radius less than 150 km from the fault source. The damage associated to this hypothetical earthquake could be severe due to the fact that most of the buildings were constructed without seismic criteria. These authors using prediction equation by Toro et al. (1997) mentioned that, the expected Peak Ground Acceleration (PGA) values only for rock site obtained for Monterrey, Saltillo and Monclova are between 30 to 70  $\text{cm/s}^2$  and it would be capable of producing, or triggering, significant landslides and rock falls in the SMO where parts of these cities are located.



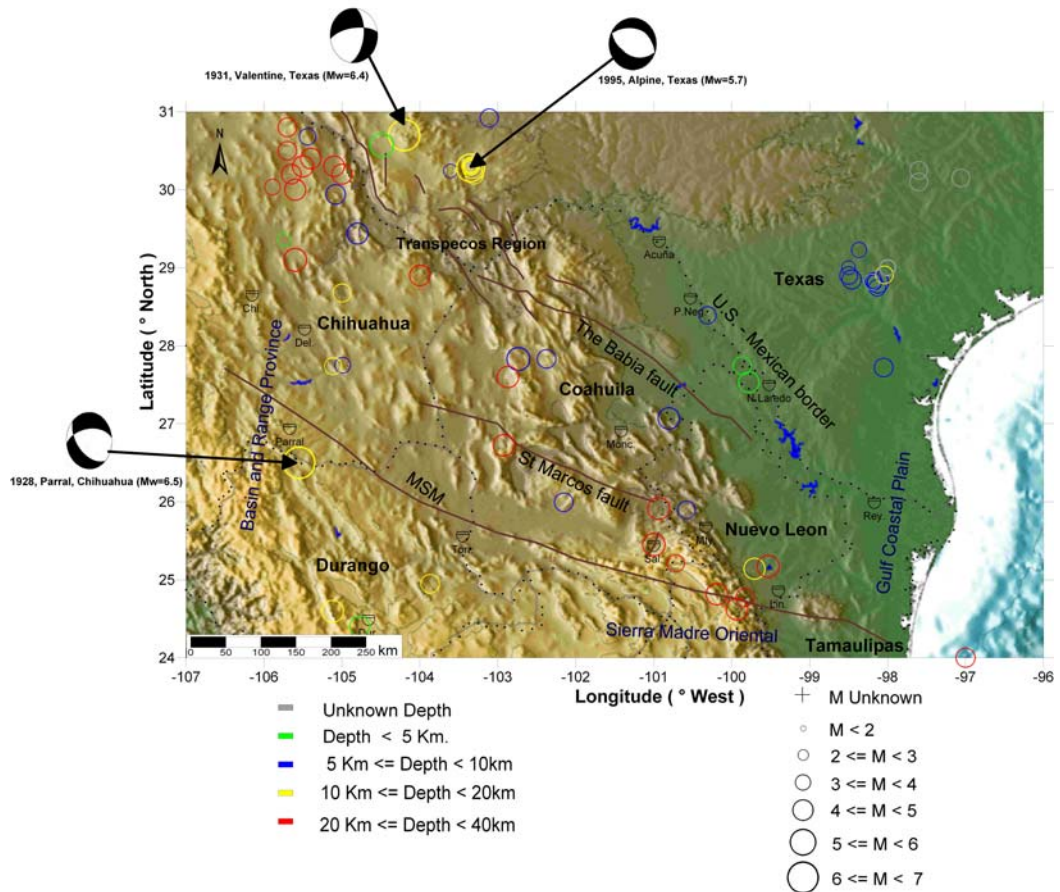


Figure 17. Northeastern Mexico and southern Texas Historic seismicity (1847-2005, Galván-Ramírez, and Montalvo-Arrieta, 2008). Open circles represents the epicentral location of the earthquakes for this period. Solid lines depict the three general north-northwest trending lineaments and faults that have been identified or postulated in northeast Mexico: the La Babia fault, the San Marcos fault, and the Mojave-Sonora megashear (MSM). Triangles indicate some of the larger cities (Acuña; Chi: Chihuahua; Del: Delicias; Parral; Tor: Torreón; Mon: Monclova; Sal: Saltillo; Mty: Monterrey; Lin: Linares; N. Laredo: Nuevo Laredo; P. Neg: Piedras Negras; Rey: Reynosa). Focal mechanisms were obtained from Doser (1987), and Doser and Rodriguez (1993).

Quintanilla López (2008), obtained PGA and Mercalli Modified Intensities (MMI) that included seismic site effects, for a hypothetical event ( $M = 6.5$ ) generated in the epicentral area of the Santiago earthquake of April 17, 2006. The PGA values obtained in MMA varied between  $40\text{--}70\text{ cm/s}^2$  and the MMI values corresponded to IV-VI. According to Keefer (1999) the Santiago earthquake could have induced some landslides in the Santiago region. Due to slopes angles characteristics ( $> 20^\circ$ ) in the Monterrey salient, La Silla and Mitras range, the values obtained for PGA and MMI for the hypothetical event proposed by Quintanilla López (2008) could be strong enough to trigger several landslides, debris flows and rock fall. Montalvo Arrieta (1996) postulated that the rupture of the La Nacion fault ( $M_w = 6.5$ ) in southern California, could cause important damage in densely populated zones of the central Tijuana region, and mentioned that the ground shaking could have an intensity of VI, which is the minimum threshold to trigger landslides in the Tijuana region.

These cities, as many other urban centers in northern Mexico, have been constructed ignoring the effects of natural risks (extraordinary rainfalls, landslides, seismicity). Therefore, it is necessary to design policies to enforce the development of effective risk-reduction programs that include: (a) the level of expected ground shaking estimation, (b) identification of susceptible sites to ground failures, and (c) the production of geographic databases, including the previous information and population distribution, type of materials and constructions techniques.

## 8. Conclusions

Landslides constitute a violent gravitational adaptation of a natural environment subjected to various factors (e.g., geology, morphology, tectonic setting, climatology, vegetation). Numerous rock mass movements and debris flows have marked the past of the MMA, the main urban center in Northeastern Mexico. The zones with a major potential landslide risk include the foothills of: (a) eastern portion of the Las Mitras range, (b) the Sierra Madre Oriental, (c) the Sierra de la Silla, and (d) the Topo Chico hill. The majority of mass movements are represented by translational and rotational landslides, rockfalls, block slides, and debris flows. The causes and the mechanism are recurrent. Landslides are triggered by intense rainfall periods. Some of them associated to Atlantic hurricane impacts in NE Mexico. An intensive urbanization, especially at the range foothills distributed in the area, and the construction in zones characterized by instable slopes have provoked the increase of landslide problems. As a result of these processes, many engineering structures in MMA have been destroyed and considerable damages have been caused to municipal infrastructure, as well as to houses and residential buildings. It is particularly important to identify rainfall thresholds that enable the definition of three alert levels (attention, warning, and alarm). In order to establish these thresholds it is necessary to collect rainfall data alone with landslide data events and to properly model future occurrence. It is also very important that specific legislation regarding the elaboration of natural hazard/risk maps, including those for landslides, be issued in such a way that it binds land use plans to hazard or risk level. The hazard from landslides in MMA could be reduced by avoiding construction on steep slopes and existing landslides, or by stabilizing the slopes. Stability could be increased if groundwater is prevented from rising in the landslide mass by: (a) covering the landslide with an impermeable membrane, (b) directing surface water away from the landslides, (3) draining groundwater away from the landslide, and (4) minimizing surface irrigation. Finally, main prevention measures to be considered in MMA urban development plans include: (a) increasing the research work on the evaluation of dynamic parameters such as hourly intensity rainfall, infiltration rate, and pressure pore, as well as the instrumentation of sites with potential movements due to natural and induced vibration; (b) to develop a strategy for landslide forecasting; and (c) to improve the laws enforcement and regulations concerning all anti-landslide initiatives.

## Acknowledgements

Thanks to M. M. González-Ramos for the critical reading of the manuscript and various useful remarks. Ing. Doroteo Treviño for providing the rainfall database and M.C. Alberto de León Gutierrez for providing aerial photo of Las Lajas landslides. This research has been partially supported by PAICYT CT1378-06 and CONACYT 25637.

## References

- Alba, F. *The population of Mexico: trends, issues, and policies*. Transaction Publishers, London, UK, 1981, pp 1-127.
- Alcantara Ayala, I. Hazard assessment of rainfall-induced landsliding in Mexico. *Geomorphology*, 2004, 61, 19-40.
- Alcantara-Ayala, I.; Esteban-Chávez, O.; Parrot, J. F. Landsliding related to land-cover change: A diachronic analysis of hillslope instability distribution in the Sierra Norte, Puebla, Mexico. *Catena*, 2006, 65, 152-165.
- Alva Niño, E. *Estudio geológico-hidrogeológico de la región noroeste (Sierra La Mitras – Cerro El Topo – Cerro El Durazno) de Monterrey, Nuevo León/México*. M.Sc. thesis. Facultad de Ciencias de la Tierra, UANL, 1997, Linares, N. L., pp 1-94.
- Alva-Niño, E. *Datos base y metodología para la elaboración de una carta ingeniero-geológica de la zona metropolitana de Monterrey, N. L., México*. B.Sc. thesis, Facultad de Ciencias de la Tierra, UANL, Linares, N. L., 1995, pp 1-82.
- Beven II, J.L., Avila, L.A., Blake, E.S., Brown, D.P., Franklin, J.L., Knabb, R.D., Pasch, R.J., Rhome, J.R., Stewart, S.R. Atlantic Hurricane Season 2005. *Mon. Wea. Rev.*, 2008, 136, 1109-1173.
- Buentello Chapa, H. La inundación de 1909: *Sus aspectos trágicos y políticos*. Publicaciones Universidad Regiomontana, Monterrey, NL, 1970, pp. 75.
- Building Seismic Safety Council (BSSC). *NEHRP Recommended Provisions for Seismic Regulations for New Buildings*, Part 1- Provisions, (FEMA 302), Federal Emergency Management Agency, Washington, DC, 1997, pp 1-290.
- Cain, N. The rainfall intensity-duration control of shallow landslides and debris flows. *Geogr. Ann. A*, 1980, 62, 23-27.
- Campbell, R. H. Soil slips, debris flows, and rainstorms in the Santa Monica Mountains and Vicinity, Southern California, *US Geol. Surv. Prof. Pap.*, 1975, 851: 1-51.
- Cannon, S. H.; Gartner, J. E. *Wildfire-related debris flow from a hazards perspective*. In: Jakob, M. and Hungr, O. (eds.). Springer, Berlin, pp 363-385.
- Cavazos, T. Large-scale circulation anomalies conducive to extreme precipitation events and derivation of daily rainfall in Northeastern Mexico and Southeastern Texas. *J. Climate*, 1999, 12, 1506-1523.
- Cavazos, T.; Hastenrath, S. Convection and rainfall over Mexico and their modulation by the Southern Oscillation. *Int. J. Climatol.*, 1990, 10, 377-386.
- Cavazos Tovar, N. P. *Microzonación de la ciudad de Monterrey, N. L., basada en geología y velocidades de propagación de ondas sísmicas*. B. Sc. thesis, Facultad de Ciencias de la Tierra, UANL, Linares, N. L., 2007, pp 1-86.

- Chapa Guerrero, J. R. *Massenbewegungen kartierung (1:1000) des Gebietes Hoya de Bocacalle-La Palmita (Ober-Jura/Kreide), Sierra Madre Oriental, México*. Dial.-Kartierung TU Clausthal, Clausthal, Germany, 1993, 54 pp.
- Chapa-Guerrero, J. R.; Ibarra-Martínez, S. E. Geological risks in urban areas in the south of the metropolitan area of Monterrey, Nuevo León, México. *Geophys. Res. Abstr. (EGU General Assembly)*, 2008, 10, A-11009.
- Chávez-Cabello, G.; Cossio-Torres, T.; Peterson-Rodríguez, R. H. Change of the Maximum Principal Stress during the Laramide Orogeny in the Monterrey Salient, Northeast Mexico, in Sussman, A.J., and Weil, A.B., eds., *Orogenic Curvature: Integrating Paleomagnetic and Structural Analyses. GSA Special Paper*, 2004, 383, 145-159.
- Chen, C. L. Rainfall intensity – duration – frequency formulas. *J. Hydraul. Eng., ASCE*, 1983, 109, 1603-1621.
- Clarizia, M., Gullà, G., Sorbino, G. Sui meccanismi di innesco dei soil slip. *Proceed. Int. Conf. Prevention of hydrogeological hazards: the role of scientific research*, 1996, 1, 585-597.
- CNA (Comisión Nacional del Agua). *Base de datos de precipitación en el periodo 1886-2008 para la estación Monterrey, N.L.*; Dirección Técnica Cuenca Río Bravo, Comisión Nacional del Agua, Monterrey, NL, 2008.
- Crosta, G. B.; Frattini P. Rainfall thresholds for triggering soil slips and debris flow, *Proceed. 2nd EGS Plinius Conf. Mediterranean Storms (Siena, Italy)*, 2001, 463-487.
- Doser, D. I., 1987. The 16 August 1931 Valentine, Texas, earthquake: evidence for normal faulting in west Texas, *Bull. Seismol. Soc. Am.* 77, 2005-2017.
- Doser, D. I., and Rodriguez, J., 1993. The seismicity of Chihuahua, Mexico, and the 1928 Parral earthquake, *Phys. Earth Planet. Int.* 78, 97-104.
- Eguiluz de A. S.; Aranda, G. M.; Marrett, R. Tectónica de la Sierra Madre Oriental, México. *Bol. Soc. Geol. Mex.*, 2000, LIII, 1-26.
- Ellis, M.J. The Hurricane Almanac. Hurricane Publications, Corpus Christi, TX, 1988, pp. 85.
- Flitters, N.E. Hurricane Beulah. A report in retrospect on the hurricane and its effects on biological processes in the Rio Grande Valley, Texas. *Int. J. Biometeor.*, 1970, 14, 219-226.
- Frankel, A. D.; Petersen, M. D.; Mueller, C. S.; Haller, K. M.; Wheeler, R. L.; Leyendecker, E. V.; Wesson, R. L.; Harmsen, S. C.; Cramer, C. H.; Perkins, D. M.; Rukstales, K. S. Documentation for the 2002 update of the national seismic hazard maps. *USGS Open-File Report* 2002, 02-420.
- Galván-Ramírez, I. N.; Montalvo-Arrieta, J. C. The historical seismicity and prediction of ground motion in Northeast Mexico, *J. South Am. Earth Sci.*, 2008, 25, 37-48.
- Garza, G. The process of metropolizing Monterrey: there must be a long-term plan. *Demos*, 1994, 7, 17-8.
- Garriot, E.B. Weather, forecast, and warnings for the month. *Mon. Wea. Rev.*, 1909, 37, 538-540.
- Goldenberg, S.B.; Landsea, C.W.; Mestas-Núñez, A.M.; Gray, W.M. The recent increase in Atlantic hurricane activity: causes and implications. *Science*, 2001, 293, 474-479.
- Goldhammer, R. K. Mesozoic sequence stratigraphy and paleogeographic evolution of northeast of Mexico, in Bartolini, C., Wilson, J.L., and Lawton, T.F., eds., *Mesozoic Sedimentary and Tectonic History of North-Central Mexico*. Boulder, Colorado, *GSA Special Paper*, 1999, 340, 1-58.

- Grogan, S.A. Northers on the East coast of Mexico, their effects, and forecast by local observations. *Mon. Wea. Rev.*, 1919, 47, 468-469.
- Guzzetti, F.; Peruccacci, S.; Rossi, M.; Stark, C. P. The rainfall intensity-duration control of shallow landslides and debris flows: an update. *Landslides*, 2008, 5, 3-17.
- Harp, E. L.; Jibson, R. W. Seismic instrumentation of landslides: building a better model of dynamic landslide behavior. *Bull. Seism. Soc. Am.*, 1995, 85, 93-99.
- Hernández-Padilla, M. *Investigaciones geológicas e hidrogeológicas del área metropolitana de Monterrey, Nuevo León, México*. B.Sc. thesis. Facultad de Ciencias de la Tierra, UANL, Linares, N. L., 1995, pp 1-94.
- Higuera-Díaz, I. C.; Fischer, M. P. Geometry and kinematics of the Nuncios detachment fold complex: Implications for lithotectonics in northeastern Mexico. *Tectonics*, 2005, 24, 1-19.
- INEGI. *Estadísticas históricas de los municipios de Nuevo León*. Instituto Nacional de Estadística y Geografía, México, D. F., 2008, pp 1-420.
- Innes, J. L. Debris flows. *Prog. Phys. Geogr.*, 1983, 7, 469-501.
- Jáuregui, E. *Climatology of landfalling hurricanes and tropical storms in Mexico*. *Atmósfera*, 2003, 193-204.
- Keefer, D. K. Earthquake-induced landslides and their effects on alluvial fans. *J. Sed. Res.*, 1999, 69, 84-104.
- Keefer, D. K. Landslides caused by earthquakes, *Geol. Soc. Am. Bull.*, 1984, 95, 406-421.
- Klaus, D. Las invasiones de aire frío en los trópicos a sotavento de las Montañas Rocallosas. *Geofís. Int.*, 1973, 43, 99-143.
- Lawrence, M.B.; Gross, J.M. Atlantic hurricane season of 1988. *Mon. Wea. Rev.*, 1989, 117, 2248-2259.
- Mann, M.E.; Emanuel, K.A. Atlantic hurricane trends linked to climate change. *EOS Trans.* 2006, 87, 233-244.
- Marrett, R.; Aranda-García, M. Structure and Kinematic Development of the Sierra Madre Oriental Fold-Thrust Belt México, in Wilson, J.L., Ward, W.C., and Marrett, R., Stratigraphic and Structure of the Jurassic and Cretaceous platform and Basin System of the Sierra Madre Oriental. a field Book and related papers: San Antonio, South Texas Geological Society, AAPG, and SEPM Annual Meeting, 1999, 69-98.
- McKnight, T.L.; Hess, D. *Physical geography: a landscape appreciation*. Prentice Hall, Upper Saddle River, NJ, 2000, pp. 223-226.
- Michalzik, D. Sedimentación y Sucesión de Facies en un Margen Continental Pasivo del Triásico al Cretácico Temprano del Noreste de la Sierra Madre Oriental, México. *Actas*, Facultad de Ciencias de la Tierra, Universidad Autónoma de Nuevo León, Linares, 1987, 2, 27-31.
- Montalvo Arrieta, J. C. Deslizamientos de laderas inducidos por terremotos en la ciudad de Tijuana, B. C. M.Sc. thesis. CICESE, Ensenada, B. C., 1996, pp 1-128.
- Montalvo-Arrieta, J. C.; Cavazos-Tovar, P.; Navarro de León, I; Medina-Barrera, F.; Alva-Niño, E. Mapping Seismic Site Classes in Monterrey, northeast Mexico, *Bol. Soc. Geol. Mex.*, 2008, 60, 147-157.
- Murillo Sánchez, M. A. *Estudio del efecto del cambio de uso de suelo en el escurrimiento en la subcuenca 24Bf "Monterrey" aplicando un sistema de información geográfica*. M.Sc. thesis, Instituto Tecnológico y de Estudios Superiores de Monterrey, Monterrey, N.L., 2002, pp. 1-119.

- New, M.; Todd, M.; Hulme, M.; Jones, P. Precipitation measurements and trends in the twentieth century. *Int. J. Climatol.* 2001, 21, 1899-1922.
- Nuncio, A.; Vigil, A., Garza, L.L., Arenal, S., Aguilera, A., Estrada, E. *Gilberto: la huella del huracán en Nuevo León. Editorial Castillo*, Monterrey, NL, 1989, pp. 244.
- O'hara, S.L.; Metcalfe, S.E. Reconstructing the climate of Mexico from historical records. *Holocene*, 1995, 5, 485-490.
- Padilla y Sánchez, R. J. *Geologic evolution of the Sierra Madre Oriental between Linares, Concepción del Oro, Saltillo and Monterrey, México*. Ph D. Thesis, Austin, Texas, University of Texas, 1982, pp 1-217.
- Padilla y Sánchez, R. J. Las Estructuras de la curvatura de Monterrey, estados de Coahuila, Nuevo León, Zacatecas y San Luis Potosí: Universidad Nacional Autónoma de México. *Revista Inst. Geol.*, 1985, 6, 1-20.
- Padilla y Sánchez, R. J. Post Paleozoic tectonics of northeast México and its role in the evolution of the Gulf of México. *Geof. Int.*, 1986, 25, 157-206.
- Popescu, M. E. A suggested method for reporting landslide causes. *Bull. Eng. Geol. Environ.*, 1994, 50, 91-94.
- Rodríguez-Marek, A.; Bray, J. D.; Abrahamson, N. A. An empirical geotechnical seismic site response procedure, *Earthquake Spectra*, 2001, 17, 65-87.
- Roel, S. Nuevo León: apuntes históricos. *Gobierno del Estado de Nuevo León*, Monterrey, NL, 1938, pp. 177.
- Rosengaus Moshinsky, M.; Sánchez-Sesma, J. Gilbert: ejemplo de huracanes de gran intensidad. *Ing. Hidrául. Mex.*, 1990, enero-abril, 13-36.
- Ruiz-Martínez, M. A.; Werner, J. Research into the Quaternary sediments and climatic variations in NE Mexico, *Quarter. Int.*, 1997, 43-44, 145-151.
- Sánchez Carlin, E. *Riesgos geológicos en el Cerro de la Silla (Monterrey, N.L.)*. B.Sc. thesis, Facultad de Ciencias de la Tierra, UANL, Linares, N. L., 2001, pp 1-90.
- Schultz, D.M.; Edward, W.; Bracken, W.E.; Bosart, L. Planetary- and synoptic-scale signatures associated with Central American cold surges. *Mon. Wea. Rev.*, 1998, 126, 5-27.
- SPP (Secretaría de Programación y Presupuesto). *Síntesis Geográfica del Estado de Nuevo León; Coordinación General de Servicios Nacionales de Estadística*, Geografía e Informática, Secretaría de Programación y Presupuesto, México City, DF, 1981, pp. 13-16.
- Strangeways, I. *Precipitation: theory, measurement, and distribution*. Cambridge University Press, Cambridge, UK, 2007, 290 p.
- Tannehill, I.R. Tropical disturbances of August 1938. *Mon. Wea. Rev.*, 1938, 66, 240-241.
- Toro, G. R.; Abrahamson, N. A.; Schneider, J. F.; Model of strong ground motion from earthquakes in central and eastern North America: best estimates and uncertainties, *Seismol. Res. Lett.*, 1997, 68, 41-57.
- Wilson, R. C. Rainstorm, pore pressures, and debris flows: a theoretical framework. *Publ. Inland Geol. Soc.*, 1989, 2, 101-117.

*Chapter 3*

## **MITIGATION OF LARGE LANDSLIDES AND DEBRIS FLOWS IN SLOVENIA, EUROPE**

***Matjaž Mikoš and Bojan Majes***

Faculty of Civil and Geodetic Engineering,  
University of Ljubljana, Ljubljana, Slovenia

### **Abstract**

In Slovenia, a small central European country, in the second half of the 20<sup>th</sup> century minor landslides of different forms (shallow landslides, slides, slumps – average volume of 1000 m<sup>3</sup>, rarely 10,000 m<sup>3</sup>) were prevailing, mainly triggered during short and intense rainfall events or after prolonged rainfall periods of moderate intensities. Unfavorable geological conditions are the main causes for a high slide density ( $\approx 0.4$  slide per 1 km<sup>2</sup>) in Slovenia, despite good vegetation conditions (more than 60% covered by forests).

Experiences with mitigation of large landslides were rare until the last decade, when four large landslides (Stože, Slano Blato, Strug, and Macesnik) with volumes of the order of 1 million m<sup>3</sup> were triggered and urged for fast mitigation. They can be placed in the category of rainfall-induced landslides that became active in unfavorable geological conditions.

The Stože Landslide with a volume of around 1.5 million m<sup>3</sup> was initiated in November 2000 as a debris landslide on the Stože slope in morainic material above the village of Log pod Mangartom in W Slovenia after a wet autumn period with no snow accumulation but rising runoff coefficients. It turned from a debris landslide on a hill slope into a catastrophic debris flow due to low inertial shear stress caused by high water content.

The Slano Blato Landslide also formed in fossil landslide masses on a contact of calcareous and flysch formations during wet autumn period in November 2000. It is ever since progressively enlarging behind the main scarp via retrogressive slumping of new and freshly weathered material that due to high water pore pressures turns into a viscous earth flow.

The Strug Landslide is a very good example of a complex slope movement, which started in December 2001 as a rockslide with a consequent rock fall that triggered secondary landslides and caused occasional debris flows. In 2002 over 20 debris flows were registered in the village of Koseč below the Strug Landslide, mainly on days with a daily rainfall accumulation of 20 to 30 mm. In 2003 and 2004 no further debris flows could be observed, therefore these events in the Strug landslide area were defined as material and not rainfall driven events.

The Macesnik Landslide above the village of Solčava in N Slovenia near the border with Austria was triggered in autumn 1989. Till 1994 there were no activities on the landslide. In

the period between 1994 and 1998 the advancement of the landslide on the slope was utmost intense. Firstly, the landslide destroyed state road, and a new pontoon bridge had to be built instead. In 1996, the landslide advanced and destroyed a turn on the same state road. In 1999, a large rock outcrop stopped the advancement of the landslide. Further advancement would possibly destroy several farmhouses on its way down the valley towards the Savinja River. Possible damming of this alpine river would cause a catastrophic flooding.

The ongoing mitigation of these landslides is subjected to a special law adopted in 2002 (revised in 2005). The final mitigation is planned to be finished before the end of 2010, with estimated costs of 60.5 Mio € for all activities planned. These costs should be added to the estimated sum of 83.5 Mio € as the final remediation costs for all other registered active small-sized landslides in Slovenia. Practical experiences in Slovenia with large landslides up to now show that only strict and insightful co-ordination, interdisciplinary approach and adequate financial support may lead to a successful mitigation.

## I. Introduction

The Republic of Slovenia being an independent and sovereign country since 25 June 1991 is located in Central Europe between the Alps and the Adriatic Sea. It has an area of 20,273 km<sup>2</sup>, bordering Italy (232 km), Austria (318 km), Hungary (102 km), and Croatia (670 km). Its coastline on the Adriatic Sea is 46 km long. In 2005 for the first time Slovenia had more than 2 million inhabitants (in 2007, population density of close to 100 per km<sup>2</sup> compared to the world average of 43 per km<sup>2</sup>) in over 6,000 settlements (SURS, 2007), half of them with up to 100 inhabitants only. The City of Ljubljana as the capital has less than 300,000 inhabitants (12.8% of the state population). The daily migration to workplaces and schools is high and it is important for the national economy and living conditions in general. A network of 1,200 km of railways and close to 39,000 km of roads connects the country. There is also high transit traffic through the country. Tourism is one of the strategic fields of development. Recreation on water (canyoning, canoeing, white water rafting, and fishing) attracts more and more tourists, mostly foreign. Slovenia is known for its varied landscape and high biodiversity. The Slovenian territory, which represents only 0.014% of our planet's land surface, is home to 2% of all known species of plants and animals.

The estimated direct (economic) damages caused by natural disasters in Slovenia are on average above 2% of GDP (in 2007 the GDP was 34.5 billion Euro or 17,076 Euro per capita – that is more than 25,000 USD per capita – reaching 89% of the average of the EU-27) with some exceptional years, as in 1990, when the flood-related economic damage itself, caused by heavy floods, was above 20% of the annual national GDP (ADCPR, 2005). Earthquakes are the most destructive natural hazards in Slovenia. The strongest historical earthquake with the epicenter in the territory of Slovenia happened on 26 March 1511 in the vicinity of Idrija (second largest mercury mine in Europe) with the estimated magnitude of 6.9. The strongest earthquake in the 20<sup>th</sup> century was registered on 12 April 1998 with the surface magnitude  $M_S = 5.7$  and the estimated intensity after the European Macroseismic Scale (EMS-98) between VII and VIII (Gosar *et al.*, 2001). This is much less than in some places elsewhere in the world, e.g. the magnitude of the 921 Chi-Chi earthquake on 21 September, 1999 in Taiwan ( $M_L = 7.3$ ,  $M_W = 7.6$ ; Lin *et al.*, 2006), triggered nearly 26,000 landslides in central Taiwan (Cheng *et al.*, 2005), and increased the frequency of debris flows by reducing the intensity and amount of precipitation required for triggering debris flows as well as accelerated landslides during the subsequent heavy rains (Lin *et al.*, 2003).



Most hazardous natural disasters apart from earthquakes, fires in the natural environment (on average more than 1,000 in a year), and droughts/heat waves (causing the highest damages in the last decade!), are rock falls, land slides, and fluvial erosion processes in many torrents and rivers. Mass wasting and soil erosion are noticeable on 43% of Slovenian territory (around 8,800 km<sup>2</sup> of labile and potentially unstable slopes). This area is crisscrossed by some 8,000 km of torrents that drain nearly 400 torrential watersheds (Mikoš, 1995; Repe, 2002). Floods and landslides are complex natural phenomena caused by local natural conditions and, with further development, more and more influenced by human activity. In Slovenia, generally speaking, unfavorable geological conditions, steep terrain and abundance of precipitation (rainfall) are the major causes of these disasters.

## II. Natural Conditions in Slovenia

### A. Precipitation and Run-Off

Slovenia has three different climates: continental, alpine and (sub-)Mediterranean. The average annual precipitation is around 1500 mm and the average annual runoff is around 1000 mm. Slovenia is thus rich in water resources, comprising mainly of groundwater and springs. Of its territory, 16,500 km<sup>2</sup> drains into the Danube River (the Black Sea), and 3,750 km<sup>2</sup> into the Adriatic Sea.

The average annual precipitation varies within Slovenia for a factor of nearly 5 (from 750 mm per year in NE continental climate of the Prekmurje plains over around 1000 mm per year in SW sub-Mediterranean climate to 3300 mm per year in NW alpine climate of the Julian Alps – climatologically the highest long-term precipitation in the Alps). The steep terrain strongly influences all types of precipitation. In Slovenia, the worst case is the combination of frontal precipitation with the orographically forced convection precipitation. The Upper Soča River basin bordering Italy is the region with highest precipitation in Slovenia. The long-term statistical analysis of heavy rainfall events shows more than 40 such events a year. More than 400 mm a day and more than 100 mm in an hour have been registered in the past. Hourly values are comparable to the rainfall intensity during typhoons elsewhere in the world, e.g. in Taiwan, but not so the daily values: Ophelia in 1990 (106 mm/h; 370 mm/day), Herb in 1996 (113 mm/h; 1749 mm/day), Zebert in 1998, Xangsane in 2000, and Toraji in 2001 (Lin and Jeng, 2000; Cheng *et al.*, 2005; Chen, 2006; Chen *et al.*, 2006; Lin *et al.*, 2006).

The dense hydrologic network of surface waters (26,989 km stream channels with an average density of 1.33 km per km<sup>2</sup>, in some areas more than 2 km per km<sup>2</sup>, in karstic areas well below 1 km per km<sup>2</sup>) (Kolbezen and Pristov, 1998), was created due to terrain of low permeability and high annual precipitation. Slovenia is situated in the headwater areas of larger alluvial rivers, thus flash torrential floods are the most frequent ones. The exceptions are the Drava and Mura rivers, flowing to Slovenia from Austria. For Slovenia, pluvial and to a less extent nival run-off regimes are prevailing. There is also significant snowfall but at lower altitudes the snow pack disappears several times during the wintertime.

Floods in Slovenia can occur all over the year, but most of them and the heaviest ones occur in spring and autumn. The humid climate causes high flows with less obvious distinctions between flood discharges with different recurrence intervals: the ratio between

$Q_{100}$  and  $Q_5$  is around 1.4 for large alluvial rivers in Slovenia (Kolbezen and Pristov, 1998). In Slovenia, there are no large natural lakes or artificial reservoirs that would significantly affect natural flood conditions (Mikoš, 2008).

In the last decades, natural reforestation (succession) of abandoned agricultural land has been very intense. Today, wooded areas cover 66.0% of the country's surface, all agricultural areas 27.8%, and built-up areas 2.8% to mention the most important categories of land cover (SURS, 2007). On the one hand, the dense vegetation cover helps to effectively reduce soil erosion, but on the other hand it has also reduced low flows and caused hydrological droughts in streams in warm summers of the last decade.

The precipitation measurements started in the mid-19<sup>th</sup> century, much like in other parts of the Austro-Hungarian monarchy. Today, there are 290 ombrometers and 49 ombrographs in operation. For precipitation measurements a C-band meteorological radar situated in the central part of the country is also used (Kolbezen and Pristov, 1998).



Figure 1. Relief map of Slovenia – 20,273 km<sup>2</sup> (from <http://ksh.fgg.uni-lj.si/ewnsi/>).

## B. Hydrogeology and Relief

Slovenia is a mountainous and hilly country (Figure 1). Only 8.6% of its territory is areas with terrain inclination less than 4% (digital terrain model 20 x 20 m; SURS, 2007). The plain lowlands consist of very permeable alluvial gravel and sand deposits with large aquifers vulnerable to pollution. An important hydro-geological characteristic of Slovenia is that about 44% of its territory is karstic (Mikoš *et al.*, 2004a), characterized by special landforms and subsurface drainage. The karst region has low stream density, surface waters soon disappear underground, and reappear in strong karstic water sources, and the region occasionally suffers

from droughts. Exceptions are the karstic poljes. These are the only areas where living conditions are favorable for human settlements, but they are also regularly flooded during the wet period of the year (especially in spring and autumn). Flooding is often caused simply by the limited capacity of the karstic sinks.

In the calcareous formations of the alpine region, rocks are overlaid by thin soils where rock slides and rock falls are prevailing, especially during strong earthquakes. Other parts of the country consist of (semi)impervious rocks of different steepness. These rock formations are mainly overlaid by unconsolidated or partially consolidated fine-grained soils, exhibiting high spatial variability. There, land sliding is the prevailing slope instability phenomenon.

### C. Flooded Areas

Moderate flush floods, torrential floods and karstic floods are yearly events in Slovenia and therefore the population is familiar with these phenomena. The large inundated areas are in lowland areas along large alluvial rivers and on karst poljes. In these areas, agricultural land of intensive production and some vital traffic connections are under threat. The total inundated areas under extreme flood event ( $Q_{100}$ ) comprise about 700 km<sup>2</sup> or 3.5% of the total surface, among those are 25 km<sup>2</sup> of urban areas, i.e. parts of the City of Celje (3rd largest town; close to 40,000 inhabitants) and the south part of Ljubljana (Mikoš *et al.*, 2004a).

## III. Land Sliding and Erosion Processes in Slovenia

Practically two thirds of Slovenian territory are subjected to different erosion processes and slope instability phenomena, as shown e.g. on the general landslide susceptibility map and the general earthquake-induced landslide hazard map of Slovenia (Mikoš *et al.*, 2004a). Slope instabilities in rocks and soils in Slovenia are bound above all to geological and morphological conditions. In the Alps, rock slides and rock falls are frequent. For example, numerous rock falls and slides were observed in western Slovenia during large earthquakes in the years 1976, 1998 and 2004 (Mikoš and Fazarinc, 2000; Vidrih *et al.*, 2001; Mikoš *et al.*, 2006b). Rock falls are also present in those areas, where rivers have incised through hard carbonaceous rocks and made gorges into the lower lying soft clastic sediments. Landslides are present first of all on hillsides and slopes of heights of the perialpine terrain composed of carbonaceous and clastic rocks. Large landslides in such rock strata are frequent, where the thick weathered surface layer is sliding. Beneath the steep slopes made of carbonaceous rocks, alluvial fans, scree and talus are frequent and strongly subjected to sliding, especially where overlying the clastic rocks. In eastern Slovenia, hilly terrain with relatively gentle slopes and wide valleys is composed of clayey and silty soils, in some places also marl, sand and clayey gravel. These soft rocks are subjected to strong weathering and as such form the basis for frequent soil slumps in thick weathered surface layers and along the inclined clayey layers. Landslide-safe areas in Slovenia are karst plateaus and karst heights, wide lowland basins and alluvial valleys.

The annual average sediment production in headwater areas in Slovenia is estimated at around 5 million m<sup>3</sup> in an average hydrological year (Mikoš, 1995), and no new estimations have been made recently. The specific annual average sediment production is estimated at

250m<sup>3</sup>/km<sup>2</sup>/year or given as a denudation rate of 250mm in 1000 years (Mikoš and Zupanc, 2000), being much higher in active sediment sources (Mikoš, 1995). On average, nearly half of this material (around 2.3 Mio m<sup>3</sup> a year) reaches the hydrological network and could be transported towards sedimentation basins (Mediterranean & Black Sea) (Mikoš, 1995). Nearly 0.5 Mio m<sup>3</sup> a year is on average temporarily deposited within the fluvial system, mainly in artificial reservoirs, built for hydropower plants along major Slovenian rivers (Soča, Sava, and Drava) in Slovenia (Mikoš, 2000a; 2000b).

Land sliding is not only a threat for buildings of any kind and to infrastructure in general, but also changes the morphology of the terrain. Landslides often release (destabilize) large amounts of sediments, which not only stay on slopes but also reach the fluvial network. Under catastrophic conditions, land sliding may lead to a torrential outburst, debris flow or dam-brake wave, as was in November 2000 the case with the first Stože debris landslide that turned after 35 hours into deadly debris flow (Mikoš *et al.*, 2004b).

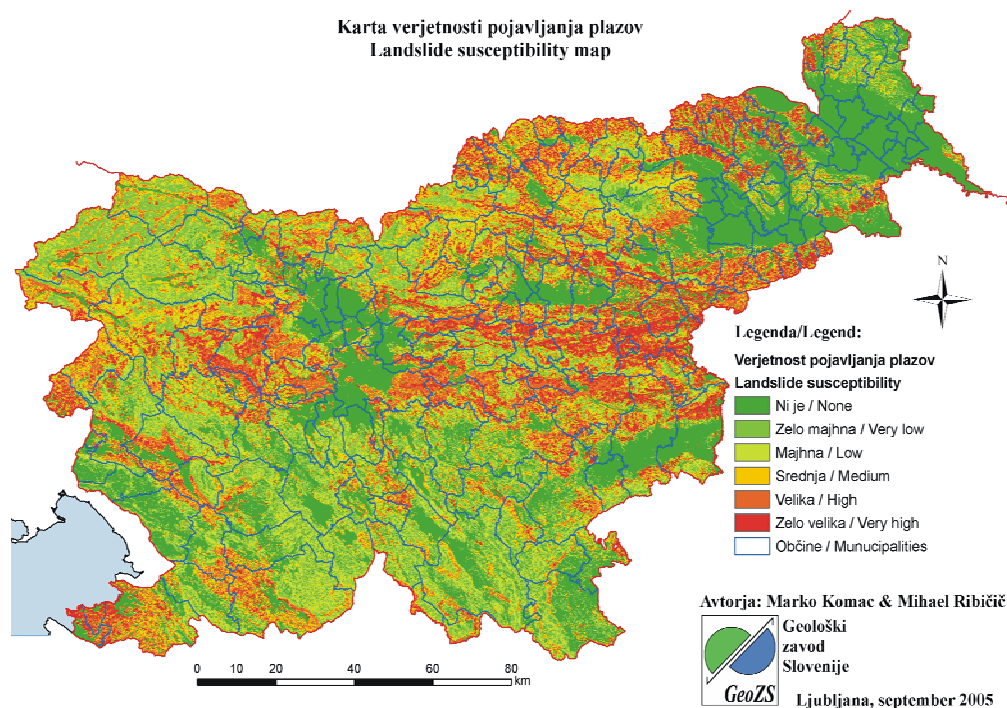


Figure 2. Landslide susceptibility map of Slovenia.

Minor landslides in Slovenia are of different forms (mainly shallow landslides, with abundance of smaller slides and slumps). They are mainly triggered during short and intense rainfall events or after prolonged rainfall periods of moderate intensities. The order of their average volume is 1000 m<sup>3</sup>, rarely 10,000 m<sup>3</sup>. Some of them have already been stabilized using technical measures, others are still active. Unfavorable geological conditions are the main causes for such a high slide density (> 1 slide per 10km<sup>2</sup>), despite good vegetation conditions in Slovenia. Such high slide density was confirmed in perialpine Slovenia using multivariate statistical methods (Komac, 2006). As a result of such an approach, a landslide susceptibility map of Slovenia was prepared (Figure 2). The next contributing factor is the

abundance of precipitation and high number of days with daily totals above 20 mm. Many slumps and slides are triggered during short and intense rainfall events or after prolonged rainfall periods of moderate intensities.

In Slovenia, over 6000 active and mainly minor landslides have been registered so far. Not all of them are part of the official landslide inventory cadastre that was incorporated into the GIS environment, i.e. software application called GIS-UJME, developed and maintained by the Ministry of Defense (ACPDR, 2005). The landslide inventory maps include more than 3500 landslides, but not rock falls and rock slides, and are one of the 85 geo-referenced databases incorporated in this system – such as databases on infrastructure, flood hazard maps, avalanche cadastre, earthquake hazard maps, fire hazard maps, etc. This electronic database is used as an internet application by the Ministry of Defense in regional Notification Centers for coordination purposes during immediate disaster relief actions led by the Civil Defense units, and as an intranet application being the information basis for their training in the Protection and Rescue Education and Training Center and for preparation of civil protection and disaster relief plans in the Administration of the Republic of Slovenia for Civil Protection and Disaster Relief (ACPDR, 2005). Unfortunately, this database is (still) not directly used for planning activities in the Ministry of the Environment and Spatial Planning in the field of hazard prevention.

#### IV. Large Landslides in Slovenia

In the last decades of the 20<sup>th</sup> century smaller rainfall-induced landslides were prevailing, especially during strong local summer thunderstorms or showers and during torrential floods, as in the case of numerous slumps and earth flows in the Kozarica and Lahomnica catchments during the 1989 flood (Fazarinc and Mikoš, 1992). Large flooding in the Savinja River basin in 1990 was associated with a large landslide near the village of Luče, and it took several

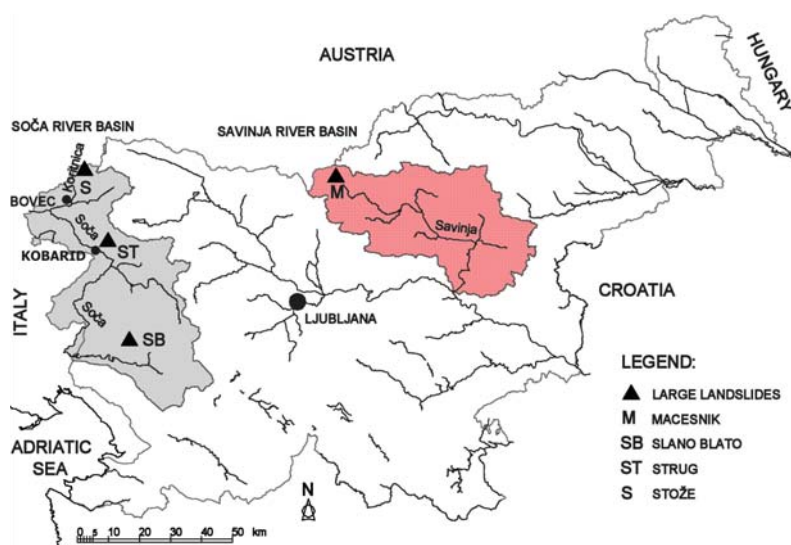


Figure 3. Locations of the four presently active large landslides in Slovenia (from Mikos et al., *Natural Hazards and Earth System Sciences*, Vol. 5, No. 6, 2005, p. 948).



years before the affected area could be successfully rehabilitated. Near the village of Solčava, in the same event in 1990, the Macesnik landslide (Figure 3) was initiated in a large old fossil landslide. This landslide grew up to a volume over 2 Mio m<sup>3</sup>, despite the technical measures executed in mid-90's, and is still active. In the last years, three more large landslides (Stože, Slano Blato, Strug; Figure 3) were triggered in Slovenia. Each of them had a volume of the order of 1 Mio m<sup>3</sup>.

The Stože landslide and Slano Blato landslide were triggered in the very wet year 2000. In December 2001, the Strug landslide was initiated as a combination of a primary rock fall, a secondary landslide and occasional debris flows from the rock fall source area during intense rainfalls (Mikoš *et al.*, 2006a). All of them can be placed in the category of rainfall-induced landslides that became active in unfavorable geological conditions. Similar experiences can be found elsewhere in the Alps and in the Carpathians.

### A. Stože Landslide

The Stože Landslide in W Slovenia with a volume of around 1.5 million m<sup>3</sup> was initiated on November 15, 2000 as a debris landslide on the Stože slope in a moraine (glacial till) above the village of Log pod Mangartom in W Slovenia after a wet autumn period (1638.4 mm in 48 days before the event, more than 60 % of the average annual precipitation) with no snow accumulation but rising runoff coefficients. It turned from a debris landslide on a hill slope (possibly caused by artesian pressures, Figure 4) into a catastrophic debris flow (Figure 5) due to low inertial shear stress caused by high water content (Mikoš *et al.*, 2004b).



Figure 4. The Stože slope after the debris landslide.

The Stože debris flow had two phases: the first (dry) one ended after less than 1 km in the channel of the Mangart Creek, and the second (wet) one initiated after 35 hours by rainfall and infiltration, when it traveled through a narrow channel of the Predelica Torrent for 4 km to Log pod Mangartom (Figure 6 and further downstream to the narrow Koritnica River valley, stopping after 7 km. This debris flow was the largest event of this kind in the last century in Slovenia.



Figure 5. Helicopter view of the debris-flow pathway from the source area on the Stože slope across the regional road Bovec-Tarvisio (Italy).



Figure 6. Helicopter view of the debris flow deposits in Log pod Mangartom after the devastating debris flow in November 2000 – the Predelica Torrent flows from above into the Koritnica River, coming from the right.

The debris flow reached the village in a few minutes, killed 7 people in their homes, destroyed 6 and severely damaged 23 residential or farm buildings as well as devastated nearly 15 ha of agricultural land, mainly pastures. The Stože debris flow was mainly depositing its masses along its flow path and only locally eroding some very narrow sections. Debris deposits were locally deep as much as 10 meters, and were so wet that large machinery was unable to work on it for nearly two weeks. Finer fractions of debris masses were immediately transported downstream in suspension together with wooden debris, and deposited along the Soča River, where some local flooding was caused (Brilly *et al.*, 2002).

The maximum flow velocity of the debris flow was estimated to be well over 10 m/s in the steep and narrow channel of the Predelica Torrent, and between 3 and 5 m/s in the more open valley of the Koritnica River. These estimated values were confirmed using one- and two-dimensional mathematical models for debris flows (Četina *et al.*, 2006). As the main triggering factor, prolonged rainfall of 1638.4 mm in 46 days prior to the event with the return period well above 100 years was recognized by a hydrologic analysis (Mikoš *et al.*, 2004b). The remaining masses on the Stože slope are the main reason for concern and possible new debris flows in the future.

One- and two-dimensional mathematical modeling of debris flows (Četina *et al.*, 2006) was also used for optimization of the two main river channel form in the area (Predelica Torrent and Koritnica River) to convey debris flows and floods (Fazarinc *et al.*, 2006), and to prepare the hazard map for the village of Log pod Mangartom (Mikoš *et al.*, 2006d). This map was used to declare safe areas for construction of buildings (houses) destroyed by the November 2000 debris flow. In 2008, the mitigation is slowly coming to its end; also the construction of a new 110-m long arch bridge across the Mangart Creek that was destroyed by the debris flow in November 2000 (Figure 5).

The total direct economic damages were estimated at more than 10 million USD. If the Stože debris flow magnitude is compared to other case studies documented in the Alps (van Steijn, 1996), it can be put into the group of “very high-magnitude” events. Even though its return period cannot be estimated from the local historical data, one can roughly estimate it to be well above 100 years.

## B. Strug Landslide

The Strug Landslide is a very good example of a complex slope movement that was triggered as a rockslide on the south-west slopes of the Planica Mountain (1376 m a. s. l.) in the Krn Mountains above the Koseč village (650 m a. s. l.) near Kobarid in the Julian Alps, W Slovenia (Figure 7). It had an estimated volume of 95,000 m<sup>3</sup> and was triggered at the contact between high permeable calcareous rocks (Cretaceous scaglia) thrust over nearly impermeable clastic rocks (Cretaceous flysch). After a sudden drop of 15 m in December 2001, the rockslide average velocity exponentially slowed down to less than 10 m/year until the end of 2002, and came to a practical still stand in 2003. A few days later in December 2001, a rock fall with an estimated volume of 45,000 m<sup>3</sup> was initiated within the rockslide. The kinetic push of the rock fall caused the immediate displacement of a translational soil landslide with a volume of 180,000 m<sup>3</sup> that partially slipped into the torrential ravine of the Brusnik Stream (Figure 8). After the rockslide suddenly dropped for 15 m in December 2001,



its velocity exponentially slowed down to less than 10 m per year until the end of 2002, and came to a practical still stand in 2003 (Mikoš *et al.*, 2006a).

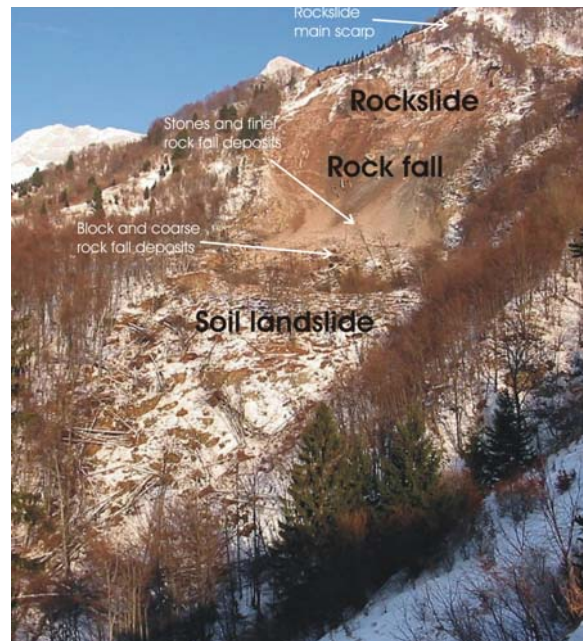


Figure 7. The Strug Landslide source area in December 2001.

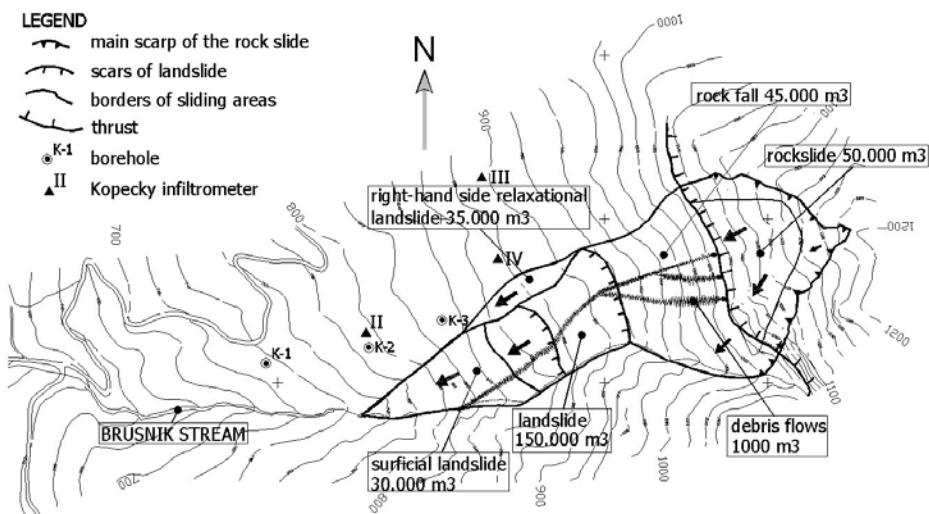


Figure 8. The Strug Landslide is a nice example of a so-called complex landslide (from Mikos *et al.*, Natural Hazards and Earth System Sciences, Vol. 6, No. 2, 2006, p. 262).

Soon after the rock fall in December 2001, a question arose whether debris flows could be initiated in rock fall masses during prolonged rainfalls, possibly as soon as in the first wet period of 2002. Therefore, the channel of the Brusnik Stream was enlarged. A parabolic cross

section was chosen to enable good conveyance for possible debris flows, and a small arch bridge in the village was replaced by a larger one.

After the rainfall in spring 2002, small debris flows made of clayey gravels, up to several  $100 \text{ m}^3$ , started to flow from the zone of accumulation of the rock fall over the landslide along the channel of the Brusnik Stream (Figure 9). The construction works in the Brusnik channel were completed just before the first debris flow reached the village of Koseč on April 22, 2002. More than 20 debris flow events, with volumes between some  $100 \text{ m}^3$  and  $1,000 \text{ m}^3$ , were registered to reach Koseč village in 2002 and passed through the new regulated Brusnik Stream channel towards the Soča River. The enlarged and regulated Brusnik channel successfully withstood all debris flows without any overtopping.



Figure 9. The enlarged parabolic channel of the Brusnik Stream in Koseč was protected using rip-rap and as such in 2002 it was conveying more than 20 debris flows with the magnitude from around  $100 \text{ m}^3$  to around  $1000 \text{ m}^3$ .

The statistical analysis showed that debris flows were initiated at daily rainfall between 20 to 30 mm, depending on the antecedent precipitation (Mikoš *et al.*, 2006a). This value may be taken as a specific hydrologic threshold for this site. The decrease of rock fall activity was studied by field measurements of erosion processes in the rock-fall deposits using laser scanner technique (Mikoš *et al.*, 2005a). Because in 2003 and 2004 no more debris flows were registered, the conclusion was drawn that debris flow events were rainfall-induced but governed also by the availability of rock fall debris in its zone of accumulation (Mikoš *et al.*, 2005a). Nevertheless in future, under extreme conditions, new debris flows from the same source may be expected to reach Koseč.

One- and two-dimensional mathematical modeling of debris flows (Mikoš *et al.*, 2006c) was used to prepare the hazard map for the village of Koseč. The same mathematical models were used as successfully applied for the Stože Landslide case (Četina *et al.*, 2006). For the determination of the designed debris-flow with the total volume of  $25,000 \text{ m}^3$ , hydrological modeling was applied (Sodnik and Mikoš, 2006).

Using the results of mathematical modeling, the proposed enlargement of the channel of the Brusnik Creek through the village of Koseč was optimized. In 2002, the major part of the reforming of a torrential channel to a parabolic shape has been successfully executed, and the channel withstood all debris flows in 2002. The debris-flow modeling showed that some minor corrections should be done in order to secure the village of Koseč the safety against the designed debris flow with the total volume of 25,000 m<sup>3</sup>. As an additional measure, two retention basins are planned to be built in 2009 in the lower reach of the Ročica Torrent (of which the Brusnik Creek is a tributary) to protect the village of Ladra from possible hyper-concentrated sediment flows.

### C. Macesnik Landslide

The Macesnik landslide above the village of Solčava in N Slovenia near the border with Austria was triggered in autumn 1990. Today, the landslide crown is at the altitude of 1360 m. Until 1994 there were no activities on the landslide. In the period between 1994 and 1998 the advancement of the landslide on the slope was utmost intense, even though the torrential agency was trying to stop the landslide by mainly executing surface drainage works that were soon after their completion out of function and in need of continuous repair. During its advancement phase in late 1990's the landslide destroyed the state road at the altitude of approximately 1110 m, and a new pontoon bridge had to be built instead. In 1996, the landslide advanced again and destroyed a turn on the same road at the altitude of 1000 and 980 m, respectively. In 1999, the landslide advancement was luckily stopped by a large rock outcrop, and the toe of the landslide is nowadays at the altitude of 840 m (Mikoš *et al.*, 2005b). Its further advancement will possibly destroy three farm houses near the toe and several more on the way down the valley towards the Savinja River. The damming of this large river would cause a catastrophic flooding.

### D. Slano Blato Landslide

The Slano Blato landslide is nowadays more than 1290 m long, 60 to 400 m wide and 3 to 12 m deep with a volume of more than 800,000 m<sup>3</sup> (Logar *et al.*, 2005). Its source area is located in the Eocene flysch formation on a slope below a large limestone high karst plateau, called the Trnovski gozd, which overlooks the Vipava River valley in western Slovenia (Figure 10). The landslide in this locality was first mentioned about 200 years ago and in 1887 it flowed as a fast moving earth flow and reached and destroyed the main road in the Vipava River valley 2 km away from its origin. The restoration of the landslide area (check dams, surface drainage works) was performed by the Austrian torrential service and took over 10 years – it was finished in 1906 (Logar *et al.*, 2005).

The landslide was triggered again after a wet autumn in November 2000, when a large slump was initiated within the old fossil landslide. It is ever since progressively enlarging behind the main scarp via retrogressive slumping of new and freshly weathered flysch material that due to high water pore pressures turns into a viscous earth flow. From this source area high on the slope, it has been moving down slope mainly as a slow moving viscous earth flow with occurrences, during rainy periods, of rapid mudflows initiated in wet

earth-flow masses. It exhibits periods of different activity. In dry periods or in freezing conditions it behaves as a group of several slow to moderately fast moving landslides. In rainy periods it moves much faster with maximum displacements of up to 90 meters a day. Today, it still presents a hazard to the relatively new residential houses in the village of Lokavec at the toe of the slope.



Figure 10. The Slano Blato landslide on the slopes of the Trnovski gozd plateau seen from the Vipava valley.

## V. General on Mitigation of Large Landslides in Slovenia

These four large landslides and their mitigation were the reason for proposing a special law that was adopted in 2002, and revised in 2005. Their final mitigation is planned to be finished before the end of 2010. According to an agreed decision, a landslide is called large when it directly threatens human lives and its estimated mitigation costs are close to 1 Mio € or more. Along with this arbitrary designation, three more landslides were proclaimed to be large and their mitigation was included into the special law on mitigation of large landslides in Slovenia. All these three landslides are rather slow (less than few cm/year) but they threaten several

houses or a part of a village. Their volumes, however, are much less than 1 Mio m<sup>3</sup> and are therefore not treated in this paper on mitigation of large landslides in Slovenia.

As defined by this law, a special governmental four-member professional committee (nominated experts from the fields of engineering geology, geotechnical engineering, and hydraulic engineering) supports all activities of the Ministry of the Environment and Spatial Planning on the mitigation of large landslides. A total sum to cover the costs for all the planned activities in terms of the final mitigation of these large landslides in Slovenia was estimated at 60.5 Mio €. This should be added to the estimated sum of 83.5 Mio € as the final remediation costs for other registered active smaller landslides in Slovenia. The majority of the financial sources will be used for measures on local and public roads.

Sediment production of these large landslides is comparable to the annual average sediment production in Slovenia (around 5 Mio m<sup>3</sup> on average a year on 20,273 km<sup>2</sup>). Nevertheless, the sediment delivery to the fluvial system from large landslides is very different. These may occasionally release large amounts of sediment debris, entering the fluvial network and increasing sediment supply from headwaters. An important point is whether or not the slid masses reach the watercourses. If the process of land sliding changes into faster moving mass wasting phenomena, such as mud flows (Slano Blato landslide) or debris flows (Stože and Strug landslides), the unstable landslide masses may contribute large amounts of sediment to the fluvial system (Mikoš *et al.*, 2006b).

The proposed non-structural and structural measures on large landslides before their final mitigation were defined in the special law adopted for their final mitigation, and can be divided into:

1. intervention measures (mechanical removal of landslide masses and debris deposits, temporary evacuation of endangered persons, daily field observations) to assure high level of protection in case of immediate emergency (heavy rainfall, fast or large landslide displacements) during the landslide mitigation phase before its final mitigation will be reached in the field, and
2. final mitigation measures, where these are a chain of very different activities: field and laboratory investigations (aero-photogrammetry, geological mapping, boreholes, inclinometers, geophysical methods, infiltration tests, discharge measurements, laboratory investigations on material properties ...); mathematical modeling (slope stability, debris flows, mud flows); recognizing/defining future hazards (possible hazard scenarios) and especially assessing the remaining risk after the completion of the proposed measures; planning and construction of mitigation measures (proposing acceptable solutions, preparation and acceptance of State Location Plans, project documentation, construction on site); post-mitigation observations (surveying and remote sensing, warning systems).

It is clear from the variety of possible mitigation measures and from the fact that each landslide is a story for itself to be treated individually, but taking into account the experiences gained on other landslides, that only an interdisciplinary team of highly experienced professionals may guide the lengthy mitigation process of several large landslides and redirect the mitigation activities under fast changing circumstances.

The mitigation of large and deep-seated landslides asks for heavy constructions that can stabilize such unstable slopes. Usually, this kind of large supporting structures, such as

supporting walls or similar concrete structures cannot be successfully built in fast moving landslide masses. One option is to build them during dormant phases of a landslide (i.e. during dry periods without rain or in cold winter time). In this case adequate financial support must be available, but this is not the case if the fiscal year ends in November and the budget for the next one is, for example, adopted in April. The other more robust option is to slow down the landslide movement. In order to slow down a fast moving landslide ( $> 10$  cm a day) it is often necessary first to drain surface waters by drainage works and then to lower groundwater level in the landslide. The latter measure can be done by digging deep drain trenches. They may go as deep as 6 to 8 meters in rather wet soils, where additional berms in order to dig deeper are not possible. In the case of deep-seated landslides ( $> 10$  m thick), wet soil conditions do not allow us to dig drain trenches all the way down to the sliding surface to efficiently slow down sliding. In such cases reinforced concrete (RC) deep wells (dowels) may come under consideration. This type of structure is known from road construction as a kind of supporting structure for large viaducts and bridges. Their advantage is that once they are built, they have the function of retaining (supporting) as well as draining.

We used RC wells as structural mitigation measures on two large deep-seated landslides in Slovenia: the Macesnik and the Slano Blato landslides, respectively (Pulko *et al.*, 2005). In 2004 we firstly built two wells on the Macesnik landslide and then in two phases we built altogether eight RC wells on the Slano Blato landslide in order to stabilize the upper part of these two deep-seated and over 1-km long landslides. The RC wells were made of reinforced concrete, 5 m in diameter and over 20 m in height in order to found them into the non-weathered rock below the sliding surface. For their design the field and laboratory data on geological conditions as well as landslide material properties were used in a numerical model to estimate design loads. Under such labile field conditions, their construction was a challenge, but they proved as an effective structural measure providing the stabilization of two large deep-seated landslides in their upper part. This fact was proven by a clear decrease of measured displacements of the landslide masses after their completion (Mikoš *et al.*, 2005b). Further RC wells are planned to be constructed on both landslides in order to gradually stabilize the whole landslide. Even though the RC wells were meant as a temporary measure, they are definitely part of the final remediation of these large deep-seated landslides. In the continuation of this paper, the experiences with the mitigation of the Macesnik landslide and the Slano Blato landslide will be given in more detail.

## VI. Mitigation of the Macesnik Landslides

The surface drainage works in the upper part of the landslide, executed in the period 1994–1998, were unsuccessful and did not help to stabilize the landslide. The first extensive engineering geologic and geotechnical investigations on the landslide started in 2001. From then on regular measurements of the landslide surface displacements in the selected cross sections have been performed on this rather long but deep landslide (Figure 11).

The usage of point data from the boreholes disclosed changes in the inclination of the landslide base (sliding surface), which explained the higher landslide thickness where the inclination changes and different landslide dynamics (relative displacements) as measured on its surface in the selected cross sections.



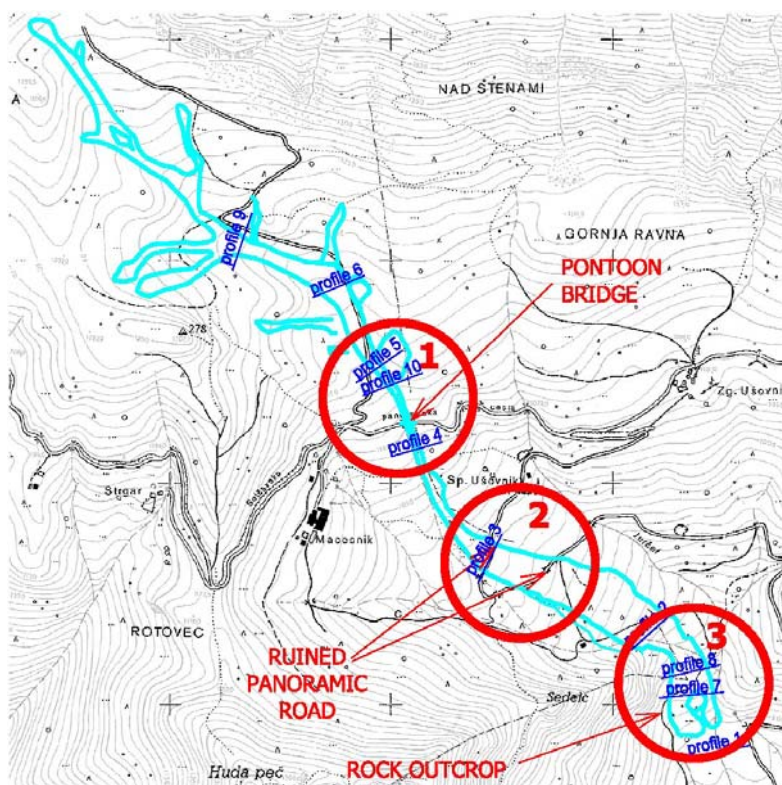


Figure 11. The three parts of the Macesnik landslide with the landslide contour and the cross sections for measurements of the landslide surface displacements (from Mikos *et al.*, *Natural Hazards and Earth System Sciences*, Vol. 5, No. 6, 2005, p. 949).



Figure 12. The Macesnik Landslide in its upper part showing the execution of surface drainage works in 2004 (from Mikos *et al.*, *Natural Hazards and Earth System Sciences*, Vol. 5, No. 6, 2005, p. 952).

Because the slid masses are heterogeneous (mainly dark-grey stiff clay with layers of more permeable clayey gravels of different thickness at different depths) and not knowing the

exact values of water pressures on the sliding surface, the remediation measures (lowering of water pressures and supporting structures) were planned only on the basis of »idealized« conditions prevailing in separate landslide reaches, as follows:

1. Lowering of water pressures by deep drainages is technologically possible (up to the depth of 8 m) only in the upper part of the landslide above the pontoon bridge.
2. The sequence of supporting structures on such a long landslide should be planned in such a way that no overtopping by slid masses from above or subsidence and sliding of masses away from the structures may occur.

On the basis of all executed field and study investigations, field measurements, and experiences the planned remediation of the Macesnik landslide will follow the division of the landslide by supporting and drainage structures into three areas (Figure 11):

1. Upper part of the landslide with the area above and around the pontoon bridge.
2. Middle part of the landslide with the area at the turn of the ruined road.
3. Lower part of the landslide around and above the rock outcrop that stopped further landslide advancement.
4. Supporting structures should be formed by grouping together several RC wells.

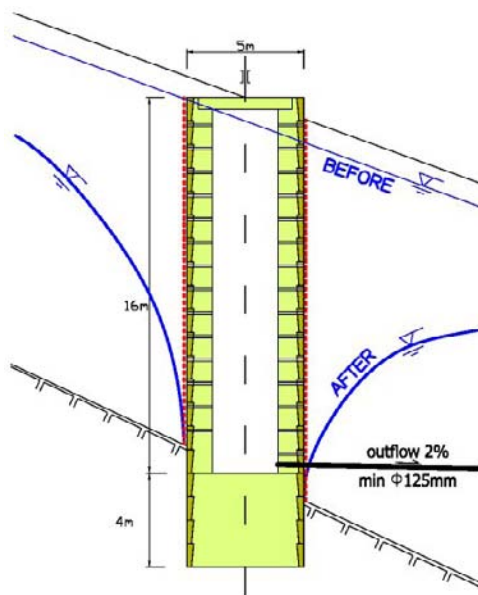


Figure 13. The drainage function of a RC well.

As the precaution measure, a mechanical warning system was established below the landslide toe. In 2002, the proposed remediation measures started to be executed from the upper part of the landslide in the down-slope direction. In the upper part of the landslide above the pontoon bridge peripheral surface drainage works were formed mainly on the stable ground outside the landslide (Figure 13). In summer 2003, above the pontoon bridge three parallel deep drainages were constructed to slow down the landslide displacements in the area



and to make possible the execution of two RC wells above the bridge. In spring 2004, in the upper part of the landslide two additional deep drainages were constructed. In late 2004, the landslide above the pontoon bridge was stopped so that between the pontoon bridge and the lower end of the deep drainage system two RC wells were built.

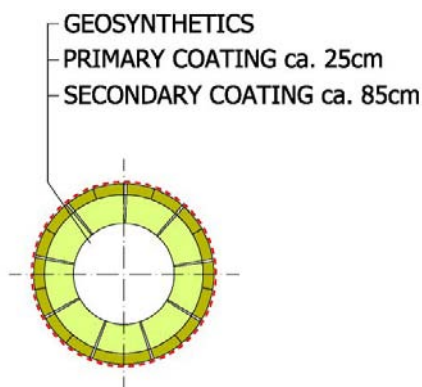


Figure 14. A horizontal section of the RC well.

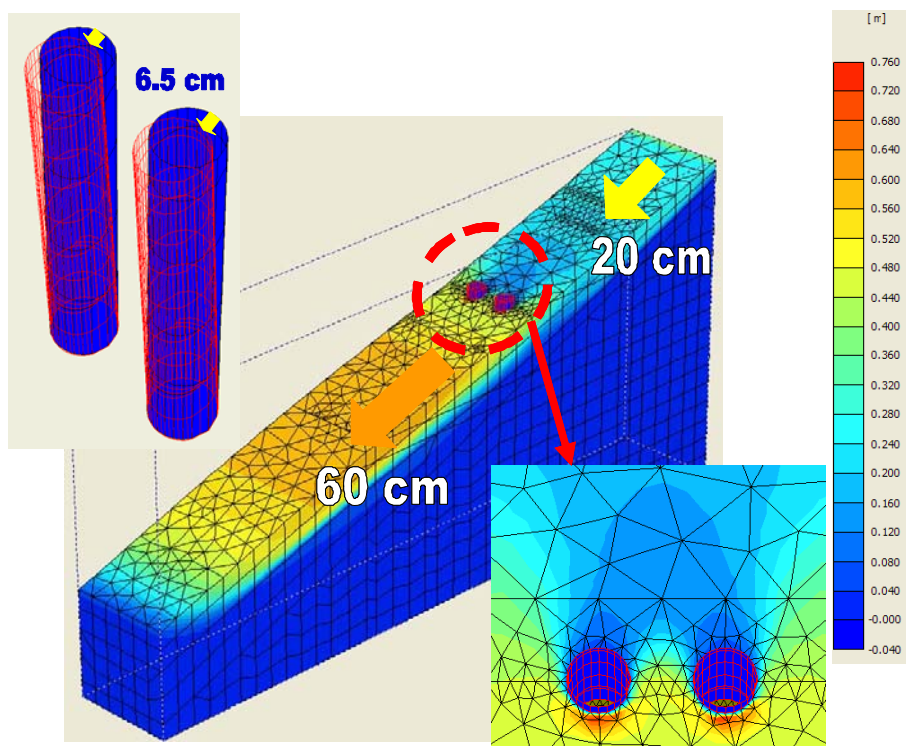


Figure 15. Displacements isolines (scale is given in meters) for two reinforced concrete wells on the Macesnik landslide, computed by PLAXIS® 3D.

If an RC well (dowel) should have supportive as well as drainage function (Figure 13), the following demands should be fulfilled:

1. The primary coating (during digging, Figure 14) should stand all loads of the landslide ( $F \cong 1.10$ ).
2. The primary coating of the well should be adequately perforated so that ground water could infiltrate into the central part of the well.
3. The primary coating of the well should be separated from the landslide masses by using an adequate geo-synthetic material. From it the water should be able to enter the central part of the well through the perforations of the primary coating.
4. After digging out the well and the execution of the primary coating with a thickness between 30 and 50 cm to the prescribed depth, the execution of a reinforced concrete foundation plate follows.
5. The prescribed safety factor for the well ( $F > 1.25$ ) will be reached only after the execution of the reinforced concrete secondary coating with a thickness of 80 cm is ensured.
6. From the central part of the well an outlet pipe (drainage) should be executed to make possible the gravitational outflow of the infiltrated water from the well.

On the basis of the stability analyses (using Plaxis<sup>®</sup> 3D, displacement isolines are given in Figure 15), for each RC well with a diameter of 5 m and a depth of 22 m (18 m of the landslide mass and 4 m of rock base) the following loads were determined: axial forces 4,350 kN; bending moments 37,650 kNm; shear forces 9,160 kN; and vertical total stresses 1,540 kN/m<sup>2</sup>.

The executed remediation (stabilization) measures in the upper part of the Macesnik landslide (above the pontoon bridge) made the landslide in this part to practically stop. Furthermore, the displacements in the other two parts of the landslide also effectively slowed down.

The landslide is rather deep in its middle part (area 2 on Figure 11), where it is crossed by the ruined panoramic road twice. In the place of the present upper road turn the landslide depth is more than 16 m, and in the place of the lower road turn the depth is more than 22 m, respectively. In this area, two lines of support structures made of RC wells are proposed – in 2007, the upper line above the upper road turn made of two RC has been finished. During such a step-wise mitigation of a large landslide in a down-slope approach it could happen that some of the initially proposed measures are left out or executed in a smaller extent. Nevertheless, the estimated costs for the final remediation of the Macesnik landslide are over 16.0 Mio €.

## VII. Mitigation of the Slano Blato Landslide

The mitigation started soon after the triggering of the landslide. In the first phase, i.e. in 2001 and 2002, around 260,000 m<sup>3</sup> of landslide masses were removed from the lower part close to the landslide toe and put to a dumping site in order to control the advancement of the viscous earth flow. Furthermore, the channel of the Grajšček stream that springs in the landslide area was enlarged downstream of the landslide toe in order to convey occasional very muddy flows from the bare landslide area through the village of Lokavec.

In the second phase of the landslide mitigation, we used the promising results, achieved with the execution of two deep RC wells on the Macesnik landslide. As a consequence of this

reasoning, at the end of the summer 2004, 3 such RC wells were started to be built using the same technology in the upper part (source area) of the Slano Blato landslide. The second reason for such a supporting structure in the upper part of the landslide was the expected large landslide displacement ( $> 10$  m) in late 2004 as a consequence of the forthcoming autumn rainfall (Mikoš *et al.*, 2005c).



Figure 16. The upper part of the Slano Blato landslide with partially finished reinforced concrete deep wells on its right-hand side (square is 100 x 100 m).

At the end of October 2004, two deep RC wells were already excavated to the depth of  $-9$  m (to the bottom of the landslide or to the top of the rock base), and the third deep RC well (on the far left side looking up the slope) was excavated to the depth of  $-6$  m. Its bottom reached only to the half of the depth of the landslide.

After intense rainfall at the end of October 2004 (monthly rainfall accumulation in October 2004 was 363 mm), and on 1 November 2004, large amounts of surface waters and strong inflow of groundwater into the rock depression below the landslide in its upper part, i.e. in below the area with RC wells, caused the fast landslide displacement that happened in the night between 1 and 2 November 2004. The translational displacement of the wells was nearly 20 m, and the wells also tilted backwards.

Despite the fact that they were displaced, the RC wells decreased the total landslide displacements in this area and captured large amounts of groundwater, which would turn the landslide masses into a viscous flow – a normal process observed during wet periods. In the period from 31 October to 6 November 2004, each well captured between 100 and 120 m<sup>3</sup> of water in 12 hours. The decreased displacements in the area were achieved to a large extent by the drainage effect of the RC wells under construction, even though they were excavated only to the contact between the landslide and the rock base.

At the end of 2004, two displaced but undamaged deep RC wells were finished using the same technology: their primary coating of 25 cm was in the inside finished by an 85 cm thick secondary coating. In March 2005, the third displaced and damaged deep RC well was rehabilitated using new technology. Using this new technology, at the same time 4 deep RC wells were built in 2005 in the right-hand side of the landslide (Figure 16).

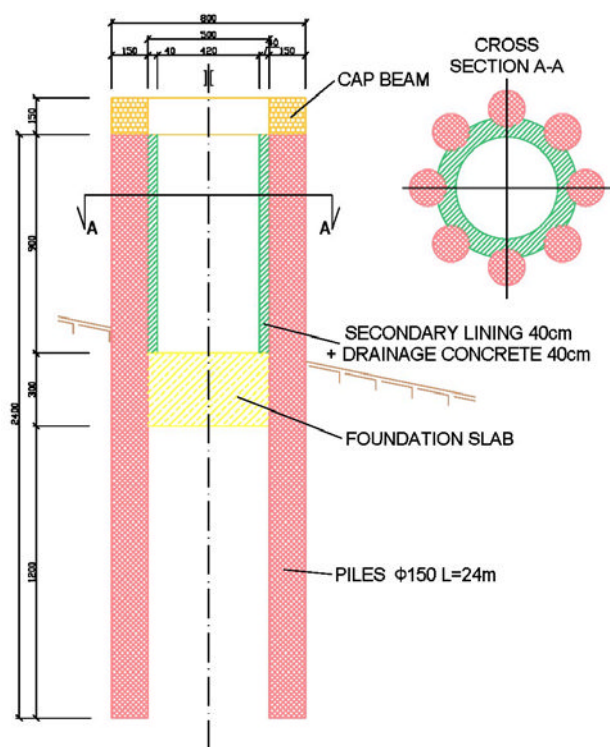


Figure 17. Details of RC wells on the Slano Blato landslide.

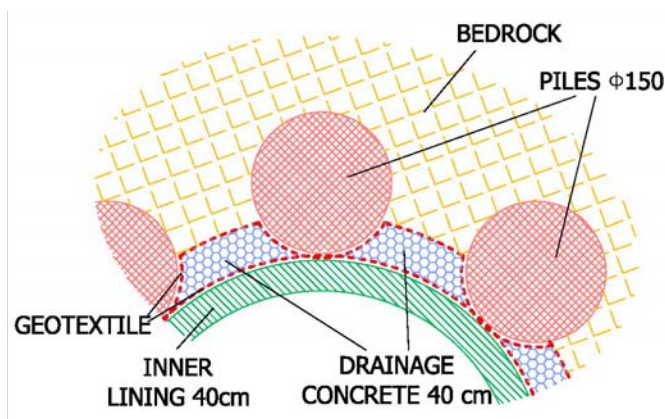


Figure 18. The detail of embedded draining concrete into the primary and secondary coating of the RC well.

In the first phase, the so called primary coating of the well was executed by drilling 8 RC Benotto piles with the diameter of 150 cm to the depth of 24 m (well below the sliding surface), which were then on their top connected by a reinforced concrete 2-m high beam. The centre of the piles was on a circle with the diameter of 6.5 m, so that the final inner diameter of the primary coating was 5.0 m (Figure 17). In the second phase, the excavation between the piles to the depth of -15 m followed. At this depth, a 3-m thick concrete

foundation plate was executed. Above its top there was a drainage pipe drilled out of the well to the landslide surface for gravitational outflow of the captured water infiltrating into the well through the drainage concrete (Figure 17) and thus securing not only the supporting but also the draining function of the well. As a final mitigation of the landslide in its upper part, the finalization of the curtain of more than 10 RC deep wells all together is planned to be finished until 2010.

All planned and executed deep RC wells were designed on the loads (bending moments, transversal and axial forces), given from numerical analyses using commercial software (Plaxis® 3D Foundation). For modeling the vicinity of the wells (soils, rocks) the Hardening Soil Model was applied, and the well was modeled as a shell.

## VIII. Conclusions

On the basis of this review paper, one can conclude that a major part of Slovenia is subjected to dangerous natural hazards, such as earthquakes, fires, landslides, floods, and rock falls. In the last decade the number of disasters is rising, handicapping state budget and budgets of over 200 local communities. These are in most cases incapable of covering economic damages, as well as organizing and financing mitigation of larger natural disasters (droughts, floods, large landslides). It is therefore legally regulated that mitigation in such cases goes to the debit of the state.

In 2009, Slovenia will celebrate 125 years of organized torrential service (started in the former Austrian-Hungarian monarchy in 1884). Several stony structures built 100 years ago and more are today still in good shape and in function – so far so good. What is troublesome in Slovenia is further historical development of the second half of the 20<sup>th</sup> century related to the planning and execution of torrential structures. In the 50's and 60's of the last century, labor-intensive manual work was still prevailing thus making possible the construction of a diffuse network of small but effective torrential measures such as check dams, gabions, dense drainage works, and reforestation. By using concrete more and more as the prevailing construction material, and thus also civil mechanization, the construction sites were limited to places easily reachable by machines. With this field practice, the maintenance of the existing dense network of torrential infrastructure was far more difficult to execute. The final blow to such a policy was given in 90's after Slovenia had become an independent democratic republic in 1991, when green ecologism prevented any substantial investments in the water management sector by decimating its financial resources for a decade. The protection of natural resources grew into overprotection, not acknowledging that a continuous maintenance of the existing protective infrastructure at a high level is essential to keep the protection of mankind and its property against natural hazards at least on the same level as the one reached in the past.

Upon its accession to the European Union, Slovenia was forced to adopt its legal and economic system to the common European values. In this respect, new Waters Act was adopted in 2002 that established a special Water Fund. This fresh approach should help to keep the relatively high level of safety against natural hazards in Slovenia, especially against floods. This new Waters Act also prescribes the preparation and acceptance of hazard and risk maps for different natural hazards as a prevention tool. These maps will then be used in spatial planning as a legal basis in the process issuing building permits. At this moment, the

preparation of methodologies how to prepare such hazard and risk maps under Slovenian conditions are under way and these methodologies will be given legal status. By doing that we are trying to catch up with the other alpine countries in Europe (Đurović and Mikoš, 2004).

In Slovenia, the RC deep wells, well known from road construction, were successfully used in two different designed forms for the first time as supportive and draining construction for large landslide mitigation. Before applying this mitigation technique, it was at utmost importance to stabilize a landslide to such an extent by e.g. deep drainage trenches and surface drainage works that the execution of deep wells was made possible.

In the last years, several debris flows (Stože, Strug) draw attention and as a response to them, torrent and river channels were optimized to convey water and sediment flows as well as rare debris flows using the results of one- and two-dimensional mathematical modeling of debris flows.

In Slovenia, the ongoing mitigation of the large landslides is subjected to a special law adopted in 2002 (revised in 2005). The final mitigation is planned to be finished before the end of 2010, with estimated total costs of 60.5 Mio € for all activities planned. These costs should be added to the estimated sum of 83.5 Mio € as the final remediation costs for all other registered active small-sized landslides in Slovenia. Because the mitigation process of large landslides is due to restricted financial resources not finished in a year or two, the organizational aspect becomes very important.

A special governmental (inter-ministerial) commission is leading all activities on large landslides, which is helped by a professional committee (experts in the fields of engineering geology, geotechnical and hydraulic engineering).

Possible measures on large landslides before their final mitigation can be divided into intervention measures (mechanical removal of landslide or debris-flow mass, temporary evacuation of inhabitants, and daily observations) in case of emergency (heavy rainfall, large landslide displacements) and final mitigation measures. The latter are a chain of very different activities:

- field and laboratory investigations (aerophotogrammetry, geological maps, boreholes, inclinometers, geophysical methods, infiltration tests, discharge measurements, material properties ...);
- modeling (slope stability, debris flows, mudflows);
- future hazard assessment (possible scenarios);
- mitigation measures (proposing solutions, project documentation, construction);
- post-mitigation observations (surveying and remote sensing, warning systems).

In Slovenia, practical experiences with mitigation of large landslides up to now show that only a strict and insightful co-ordination, interdisciplinary approach and adequate financial support may lead to successful large landslide mitigation.

Because the national legislation covering the mitigation of large landslides is not up-to-date, we suffer from long-lasting mitigation process. The main cause is on one hand the restrictive annual budget that can be applied, and on the other hand the rather complicated planning procedures needed for executing proposed structural mitigation measures in the field. Such an approach might help to carefully propose and design adequate structural

measures, but it also causes additional costs because landslides are active, they enlarge according to their own dynamics and ask for higher financial resources for their mitigation if the mitigation spreads over a longer period of several years.

## Acknowledgements

The mitigation of large landslides in Slovenia in all its phases is financed by the Ministry of the Environment and Spatial Planning of the Republic of Slovenia. Many data and details from research laboratory and field investigations, as well as planned and executed mitigation engineering measures presented in this paper, are taken from the archives of the Professional Committee for Mitigation of Large Landslides in Slovenia, of which the author is a member, and from the extensive project documentation prepared by different Slovenian engineering companies and planning bureaus. Partially were results presented in this paper also financed by the Research Agency of Slovenia through the research program “Hydrotechnics, Hydraulics, and Geotechnics”. The author acknowledges the proof-reading of the paper by Mojca Vilfan.

## References

- [1] ACPDR (2005), “Republic of Slovenia: National report and information on disaster reduction”, *World Conference on Disaster Reduction*, Kobe-Hyogo, Japan, January 18–22, 2005, 24 p. (<http://www.unisdr.org/eng/mdgs-drr/national-reports/Slovenia-report.pdf>)
- [2] Brilly, M., M. Mikoš, and M. Kobold (2002), “Catastrophe caused by debris flow in the village of Log pod Mangartom in autumn 2000”, *Mediterranean storms : proceedings of the 3rd EGS Plinius conference*, Baja Sardinia, Italy, October 1-3, 2001, pp. 367–370.
- [3] Chen, H. (2006), “Controlling factors of hazardous debris flow in Taiwan”, *Quaternary International*, **147**(1), pp. 3-15.
- [4] Chen, H., S. Dadson, and Y.G. Chi (2006), “Recent rainfall-induced landslides and debris flow in northern Taiwan”, *Geomorphology*, **77**(1-2), pp. 112–125.
- [5] Cheng, J.D., Y.C. Huang, H.L. Wu, J.L. Yeh, and C.H. Chang (2005), “Hydrometeorological and landuse attributed of debris flows and debris floods during typhoon Toraji, July 29-30, 2001 in central Taiwan”, *Journal of Hydrology*, **306**(1-4), pp. 161–173.
- [6] Četina, M., R. Rajar, T. Hojnik, M. Zakrajšek, M. Krzyk, and M. Mikoš (2006), “Case Study: Numerical Simulations of Debris Flow Below Stože, Slovenia”, *Journal of Hydraulic Engineering*, **132**(2), pp. 121–130.
- [7] Đurović, B. and M. Mikoš (2004), “Preventive Management of Risk due to Natural Hazards : Procedures in the Alpine Countries and in Slovenia”, *Acta hydrotechnica*, **22**(36), pp. 17–35.
- [8] Fazarinc, R. and M. Mikoš (1992), “Feststoffmobilisierung als Folge der extremen Niederschläge in Slowenien”, *Proceedings of the 7<sup>th</sup> INTERPRAEVENT Congress on*

- Protection of Habitat from Floods, Debris Flows and Avalanches*, Bern, Switzerland, Juni 29–3, 1992, pp. 377–388.
- [9] Fazarinc, R., B. Majes, and M. Mikoš (2006), “Using results of mathematical modeling of debris flows for optimization of a river channel form to convey debris flows and floods”, *Proceedings of the International Conference on Fluvial Hydraulics*, Taylor & Francis, London, pp. 2137–2146.
  - [10] Gosar, A., R. Stopar, M. Car, and M. Mucciarelli (2001), “The earthquake on 12 April 1998 in the Krn mountains (Slovenia): ground-motion amplification study using microtremors and modelling based on geophysical data”, *Journal of Applied Geophysics*, **47**(2), pp. 153–167.
  - [11] Komac, M. (2006), “A landslide susceptibility model using the Analytical Hierarchy Process method and multivariate statistics in perialpine Slovenia”, *Geomorphology*, **74**(1-4), pp. 17–28.
  - [12] Lin, M.L., and F.S. Jeng (2000), “Characteristics of hazards induced by extremely rainfall in Central Taiwan – Typhoon Herb”, *Engineering Geology*, **58**(2), pp. 191–207.
  - [13] Lin, C.W., C.L. Shieh, B.D. Yuan, Y.C. Shieh, S.H. Liu, and S.Y. Lee (2003), “Impact of Chi-Chi earthquake on the occurrence of landslides and debris flows: example from the Chenyulan River watershed, Nantou, Taiwan”, *Engineering Geology*, **71**(1-2), pp. 49–61.
  - [14] Lin, C.W., S.H. Liu, S.Y. Lee, and C.C. Liu (2006), “Impacts of the Chi-Chi earthquake on subsequent rainfall-induced landslides in central Taiwan”, *Engineering Geology*, **86**(2-3), pp. 87–101.
  - [15] Logar, J., K. Fifer Bizjak, M. Kočevár, M. Mikoš, M. Ribičič, and B. Majes (2005), “History and present state of the Slano blato landslide”, *Natural Hazards and Earth System Sciences*, **5**(3), pp. 447–457.
  - [16] Kolbezen, M. and J. Pristov (1998), *Surface Streams and Water Balance of Slovenia*, Ministry of the Environment and Physical Planning, Hydrometeorological Survey, Ljubljana, Slovenia.
  - [17] Mikoš, M. (1995), “Interdependence of erosion processes in space”, *Gozdarski vestnik*, **53**(9), pp. 342–351.
  - [18] Mikoš, M. (2000a), “Sediment budget of the Sava river from Jesenice to Mokrice”, *Gradbeni vestnik*, **49**(9), pp. 208–219.
  - [19] Mikoš, M. (2000b), “Sedimentation of retention basins on the Sava River”, *Gradbeni vestnik*, **49**(10), pp. 224–230.
  - [20] Mikoš, M. (2008), “Lakes in Slovenia”, *Encyclopedia of Lakes and Reservoirs – Geography, Geology, Hydrology and Paleolimnology*, Encyclopedia of Earth Sciences Series, Springer Verlag, Berlin, Germany (in press).
  - [21] Mikoš, M. and R. Fazarinc (2000), “Earthquake-induced erosion processes in two alpine valleys in Slovenia”, *Proceedings of the 9<sup>th</sup> INTERPRAEVENT Congress on Protection of Habitat from Floods, Debris Flows and Avalanches*, Villach, Austria, June 26–30, 2000, pp. 143–154.
  - [22] Mikoš, M. and V. Zupanc (2000), “Soil erosion on agricultural land”, *Sodobno kmetijstvo*, **33**(10), pp. 419–423.
  - [23] Mikoš, M., M. Brilly, and M. Ribičič (2004a), “Floods and Landslides in Slovenia”, *Acta hydrotechnica*, **22**(37), pp. 113–133.



- 
- [24] Mikoš, M., M. Četina, and M. Brilly (2004b), "Hydrologic conditions responsible for triggering the Stože landslide, Slovenia", *Engineering Geology*, **73**(3-4), pp. 193–213.
- [25] Mikoš, M., A. Vidmar, and M. Brilly (2005a), "Using a laser scanner measurement system for monitoring morphological changes on the Strug rock fall, Slovenia", *Natural Hazards and Earth System Sciences*, **5**(1), pp. 143–153.
- [26] Mikoš, M., Fazarinc R., Pulko B., Petkovšek A. and Majes B. (2005b), "Stepwise Mitigation of the Macesnik Landslide, N Slovenia", *Natural Hazards and Earth System Sciences*, **5**(6), pp. 947–958.
- [27] Mikoš, M., B. Majes, M. Brilly, and M. Ribičič (2005c), "Activity of the Slano Blato landslide as an example of a landslide behaviour in karstic hydrological conditions", *Abstracts of the Contributions of the EGU General Assembly 2005*, Vienna, Austria, April 24-29, 2005.
- [28] Mikoš, M., M. Brilly, R. Fazarinc, and M. Ribičič (2006a), "Strug landslide in W Slovenia: a complex multi-process phenomenon", *Engineering Geology*, **83**(1-3), pp. 22–35.
- [29] Mikoš, M., R. Fazarinc, and M. Ribičič (2006b), "Sediment Production and Delivery from Recent Large Landslides and Earthquake-Induced Rock Falls in the Upper Soča River Valley, Slovenia", *Engineering Geology*, **85**(3-4), pp. 198–210.
- [30] Mikoš, M., R. Fazarinc, B. Majes, R. Rajar, D. Žagar, M. Krzyk, T. Hojnik, and M. Četina (2006c), "Numerical Simulation of Debris Flows Triggered from the Strug Rock Fall Source Area, W Slovenia", *Natural Hazards and Earth System Sciences*, **6**(2), pp. 261–270.
- [31] Mikoš, M., R. Fazarinc, and B. Majes (2006d), "Delineation of risk area in Log pod Mangartom due to debris flows from the Stože landslide", *Acta geographica Slovenica*, **47**(2), pp. 171–198.
- [32] Pulko, B., M. Mikoš, R. Fazarinc, A. Petkovšek, and B. Majes (2005), "Deep shafts (dowels) as an effective structural mitigation measure on large landslides in Slovenia", *Abstracts of the Contributions of the EGU General Assembly 2005*, Vienna, Austria, April 24-29, 2005.
- [33] Repe, B. (2002), "Soil degradation threat to Slovenia's landscapes", *Acta geographica*, **42**, pp. 99–121.
- [34] Sodnik, J., and M. Mikoš (2006), "Estimation of magnitudes of debris flows in selected torrential watersheds in Slovenia", *Acta geographica Slovenica*, **46**(1), pp. 93–123.
- [35] SURS (2007), *Statistical yearbook of the Republic of Slovenia 2007*, Statistical Office of the Republic of Slovenia, Ljubljana, Slovenia (also on <http://www.stat.si/>).
- [36] van Steijn, H. (1996), "Debris-flow magnitude-frequency relationships for mountainous regions of Central and Northwest Europe", *Geomorphology*, **15**(3-4), pp. 259–273.
- [37] Vidrih, R., M. Ribičič, and P. Suhadolc (2001), "Seismogeological effects on rocks during the 12 April 1998 upper Soča Territory earthquake (NW Slovenia)", *Tectonophysics*, **330**(3), pp. 153–175.



*Chapter 4*

## **GEOMATIC METHODS FOR PUNCTUAL AND AREAL CONTROL OF SURFACE CHANGES DUE TO LANDSLIDE PHENOMENA**

***L. Borgatti, L. Vittuari and A. Zanutta\****

University of Bologna, Bologna, Italy

### **Abstract**

Landslides are one of the major causes of natural disasters worldwide. In the field of landslide studies, much effort has been put into investigating landslide causes and mechanisms. Geodetic and Remote Sensing methods, in addition to geological, geotechnical and geophysical techniques are fundamental to study and understand landslides. In fact, besides the use of geotechnical devices that are mainly devoted to on-site and punctual monitoring, Geomatics may play a relevant role in the assessment of superficial movements, especially on large and non accessible areas. Nowadays, the integration of several techniques allows a wide range of landslide types in different environmental contexts to be surveyed and controlled. Besides alerting and alarming purposes, the acquired data set may also serve in numerical modeling, from the set-up of 2D- and 3D-descriptions of the slope, up to the validation of the results.

Differential Leveling, GNSS, Total Station, Laser Scanning (both airborne and terrestrial), high resolution space-borne imagery, Photogrammetry and Radar Interferometry can be used in each step of landslide studies, from site characterization onwards: to detect and to map landslide areas; to classify landslide type, state and style of activity; to monitor landslide activity; to evaluate the probability of occurrence within a given area in landslide hazard assessment; in structural and non-structural mitigation of landslide risk.

The monitoring of surface displacement may be based on topographic punctual observations or on non-contact methods.

Point-based measurements are carried out on the field by means of GNSS (by static, fast static, kinematic, Real Time Kinematic methods) or by Total Stations (triangulation, trilateration, intersection - resection, traverses, radial sides hot methods and more generally 3D or 2D networks). The elevations are determined by spirit or trigonometric leveling. All these techniques deliver 1D, 2D or 3D coordinates of some isolated point on the landslide

---

\* E-mail address: antonio.zanutta@mail.ing.unibo.it (Prof. A. Zanutta). Tel: +39 051 2093102; fax: +39 051 2093114. (Corresponding author.)

body, and, therefore, an estimate of movement rates, along with the evaluation of their precision.

Non-contact methods are becoming a widespread technique to measure wide areas and to quantify landform changes, providing information on the displacement fields or on surface changes of point clouds. By the interpolation of point clouds, Digital Elevation Models (DEMs) are generated as support of geomorphological survey and mapping. Then, by multi-temporal DEMs comparisons, morphological changes can be assessed on a metrical basis.

This paper describes the classical and modern methods that may be adopted for analyzing superficial landslide movements, focusing on pros and cons of each method with respect to geological, geomorphological and environmental conditions.

**Keywords:** Landslide, Geomatics, superficial displacements, DEMs

## 1. Introduction

Observational methods are the sound bases of the study of natural hazards (Einstein and Sousa, 2007). Indeed, the assessment of spatial and temporal relationships between the frequency and magnitude of dangerous events and of their eventual predisposing, preparatory and triggering factors is essential in each hazard and/or risk management procedure (Glade et al., 2005). In particular, monitoring actions are an intrinsic part of any hazard scenarios assessment, providing the data sets to answer the fundamental questions on “where, when and how” a certain potentially dangerous phenomenon might occur.

Among natural hazards, in the field of landslide investigation and mitigation, monitoring activities are generally carried out during each phase of the risk management procedure, from site characterization onwards, i.e., in prevention, forecast, response, recovery phases (Canuti et al., 2007; Kienholtz, 1994). Immediately after a landslide, in the response period, which is generally limited from weeks to months, the evolution of the phenomenon is controlled and site conditions progressively updated during the event and in the recovery period, which comprises the residual development of the event and generally lasts for some months. During the prevention phase, which can last for years, the cause-effect relationships are analyzed in order to define future scenarios and design and implement risk mitigation actions. The preparedness phase foresees the set-up and the maintenance of structural and non structural mitigation measures. In each phase, monitoring allows the definition of hazard scenarios and at the same time, of damage scenarios (if, to which extent and at which economic and social cost a specific natural or man-made asset will be damaged by a specific dangerous landslide). Conceptually, during prevention and recovery phases, the collection of data can be in both near-real-time and non-real-time. For forecasting and response actions, monitoring activities have to provide real-time or near-real-time data, also for alerting and alarming purposes.

In this general framework, some landslide-specific key points have to be stressed. As most of natural phenomena, landslides show a great variability not only from the typological, but also from the geometrical and kinematical viewpoints. In this sense, each phenomenon is unique, being also characterized by its own evolution in space and time. Besides for example floods, the deterministic and statistical predictions of the timing and the frequency of instability events are concealed by complex triggering and reactivation mechanisms in both failure and post-failure behavior. In some cases, the only information that can be gathered is about present-day geological and geomorphological features.

In this context, monitoring is a fundamental tool to characterize and manage slope instability, at all the different spatial and temporal scales. Monitoring systems are a combination of sensors, devices for data storage and transmission, together with data processing procedures (Dunnicliff, 1988). A large number of different geotechnical monitoring systems have been developed in the last decades (Mikkelsen, 1996). In the best practice, several systems are joined in integrated monitoring networks, to obey the fundamental principles of coherence of measurements and redundancy of instrumentation.

Landslide monitoring is generally accomplished by field-based geotechnical, geophysical and geodetic techniques, complemented with the broad category of Remote Sensing. Monitoring methods can be used to investigate all the variables that can be regarded as the causes (predisposing, preparatory or triggering) or the effects (direct or indirect) of a landslide in a specific risk scenario. On the one hand, some of the possible causes are rainfall duration and/or intensity, snow melting, temperature fluctuations, groundwater level and pore pressure changes, etc. On the other hand, the effects of a landslide event can be ground deformations (cracks, bulging), displacements (at the surface or at the subsurface), etc.

Traditional geotechnical instruments (see Angeli et al., 2000; Mikkelsen, 1996 for comprehensive reviews) are exploited for decades to collect data on:

- surface or underground displacements and deformations (extensometers, inclinometers, Time Domain Reflectometry - TDR cables, etc.);
- hydrogeological and hydraulic parameters (piezometers, tensiometers, flowmeters, etc.);
- climatic variables (rainfall, snow cover, temperature, wind speed gauges, etc.).

It is worthy to stress that these monitoring systems gather significant and irreplaceable pieces of information to build up a geotechnical model of unstable slopes, providing on-site data. The major drawback is that this information is inherently punctual and has therefore to be generalized, mainly by means of expert knowledge and engineering-geological judgment. Furthermore, no information is usually gathered both on past events and in particular on the temporal and spatial evolution of the phenomena during these events. Finally, the costs of installation, maintenance and eventual replacement in case of loss are often high, so that sometimes stakeholders prefer to skip landslide monitoring going directly for a sort of “blind” consolidation of unstable slopes.

Besides geotechnical methods, geodetic and remote sensing techniques may play a relevant role in the collection of data concerning the superficial effects of landsliding phenomena, with reference to morphological changes, surface displacement data series, fields of velocity and acceleration, also on a continuous and multitemporal basis, and especially in the survey of large and non accessible areas (see Metternicht et al., 2005 for a review).

Surface velocity field displays both temporal and spatial heterogeneity. From the temporal evolution viewpoint, a landslide may be active or inactive, i.e., moving or not at the moment of observation (more specifically, inactive landslides can be suspended to dormant, depending on the timing of the last reactivation, see Cruden and Varnes, 1996). During a generic period of activity, that hypothetically could last from seconds up to even millennia (see for example Soldati et al., 2004), surface displacements can follow a multi-year trend (acceleration or deceleration and stop), can show seasonal variations or eventually undergo

surge episodes or local reactivations (Fig. 1). This temporal heterogeneity is controlled mainly by the regimes of external triggering causes (i.e., rainfall) and also by geomechanical and geotechnical properties of rock and soils, especially in post-failure behavior.

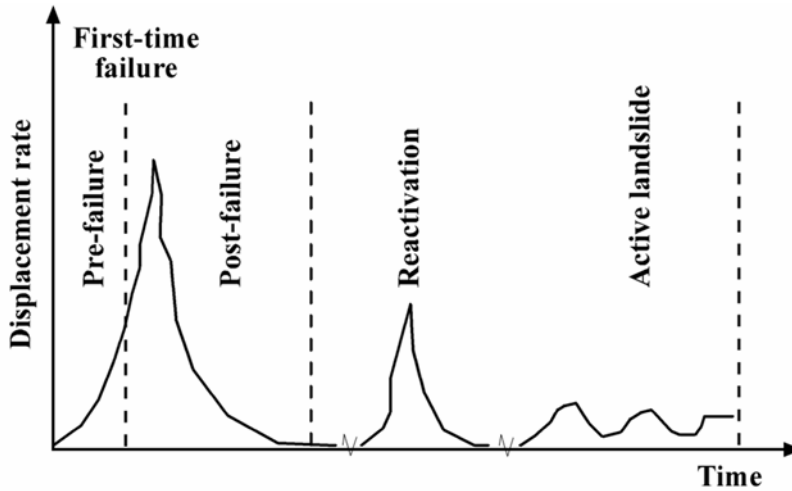


Figure 1. Different stages of slope movements (after Leroueil et al., 1996).

As far as spatial heterogeneity is concerned, displacement vectors may in general have different components (in magnitude, direction and sense) in different parts of the slope during a specific phase of activity. This may be due to slope geometry, to geotechnical properties of rock and soils, and also to the type, the style and the distribution of activity of the landslide (Cruden and Varnes, 1996). Therefore, a multitemporal and multiscale monitoring of kinematic features is fundamental to fully describe landsliding phenomena. The choice of the sensor (together with its accuracy and precision issues), of the number and the location of measurements points (spatial resolution), of the sampling frequency (temporal resolution) is actually a key task. In order to obtain relevant results, an ideal monitoring system should be selected not as an up-to-date product of modern technologies itself, but after a preliminary analysis of landslide features. In fact, a set of sensors placed randomly inside and around a landslide body will yield a series of measurements that will be neither easy to interpret, nor to exploit. The best results can be obtained if the position of the sensors is significant and representative. A proper design of the monitoring system and of the monitoring procedure results only from a previous understanding of the general behavior of phenomena, obtained after the collection and the analysis of all the available documentation and after field surveys. In particular, geomorphological mapping and monitoring of ground movements can be carried out with different techniques. First, by analyzing and comparing a series of documents (topographic maps, aerial photographs, cadastral maps, DEMs), an instantaneous view of an unstable slope in different periods can be obtained. These studies also enable the historical evolution of the phenomenon to be described and displacement vectors to be traced.

Then, to provide a full description of landslide kinematics with 3D displacement vectors, geomatic techniques (Global Positioning System - GPS, Total Station - TS, digital levels, Photogrammetry, Laser Scanning - LS, Radar Interferometry - InSAR etc.) can be used in each step of landslide investigations, from site characterization onwards. In general, the

monitoring of surface displacements may be based on on-site topographic punctual observations or on non-contact methods. On the basis of the frequency of measurements, both periodic geodetic surveys conducted at almost regular time intervals, and continuous monitoring through automatic data acquisition, such as by GPS or robotic total stations, can be performed fitting spatial and temporal resolutions to the type of landslides. If high risk conditions are expected, different procedures could be planned, with the exploitation of different sensors and different frequencies of measurement. In fact, geodetic techniques can be easily adapted to real time surveys. If the system is devoted to alerting and alarming purposes, which are inherently real-time activities, a proper design of an integrated platform of different sensor is advisable. For instance, the ideal system would integrate sensors that can acquire high frequency data without being influenced by visibility and meteorological issues.

Point-based measurements are carried out directly in the field by means of GPS (by static, rapid static, kinematic, Real Time Kinematic - RTK methods) or by TS (triangulation, trilateration, intersection - resection, traverses, radial side shot methods and more modern 3D or 2D networks). The elevation is determined by spirit or trigonometric leveling. These techniques deliver 1D, 2D or 3D coordinates of some isolated points on the slope, and therefore can provide an estimate of displacement rates, along with the evaluation of their precision.

Non-contact methods are becoming a widespread technique to appraise wide areas and to quantify landform changes, providing information on surface changes of point clouds and their displacement fields. By the interpolation of point clouds, Digital Elevation Models (DEMs) are generated primarily as support of geomorphological survey and mapping. Then, by multi-temporal DEMs comparisons, morphological changes can be assessed on a metrical basis. In particular, these techniques can be used:

- to detect and to map unstable areas, creating or improving multitemporal and multiscale landslide inventories;
- to classify landslide type, state, distribution and style of activity;
- to monitor long-term and short-term landslide kinematics;
- before and after the implementation of structural and non-structural mitigation actions.

For example, updated landslide inventories (Farina et al., 2006, 2008) have demonstrated to be a fundamental tool to assess local, regional and global landslide susceptibility and triggering thresholds, also with alerting and alarming purposes if the prediction is based on the analysis of rainfall as a possible triggering factor (Guzzetti et al., 2008). Continuous monitoring of displacements can for example allow the time of failure of slopes to be predicted days in advance, by analyzing displacement data, which are the effects of instability (Crosta and Agliardi, 2003). Surface monitoring data have also been used for the interpretation of landslide movement patterns (Petley et al., 2002; 2005). The modeling suggests that different landslide patterns are observed for different parts of the landslide, primarily as a result of groundwater conditions and of the inter-relationships between pore pressures, deformation and displacements, both shallow and deep. If geomatic products are exploited to generate high-resolution DEMs, three dimensional landslide features can be illustrated with great detail, together with their three-dimensional evolution over time. In fact,

the comparison of multitemporal DEMs has been demonstrated to be a powerful tool for the analysis of landslide processes (Baldi et al., 2008; Casson et al., 2005; Corsini et al., 2007; Dewitte et al., 2005, 2008; Mora et al., 2003; Van Westen et al., 2003; Zanutta et al., 2006).

Hereafter, a list of methods that can be used to monitor landslide kinematic features will be described, with reference to basic concepts, types of instruments and elaborates, precision and accuracy issues.

## **2. Point - Based Measurements**

Point-based measurements are carried out directly in the field by means of different measuring procedures with Levels, Total Stations and GPS instruments. The 1D, 2D or 3D coordinates of single points opportunely marked or identified on the area to be surveyed, together with evaluation of the accuracy of the measurements, are derived starting from in situ observations and applying post-processing computation methods.

A brief description of the most important “point based” methods that can be used to monitor and survey landslides is presented.

### **2.1. Differential Leveling**

Geometric and trigonometric levelling are traditional methods of geodetic surveying and they are used to measure differences of elevation between two points on the Earth surface. Nowadays modern digital levels and very high precision Total Stations have renewed and significantly improved the operational performances of these methods, allowing fast and accurate automatic reading and data recording.

In particular, these techniques may be exploited to assess rotational and translational movements along a slope as well as bulging at the toe of the slope itself. In any case, they gather datasets that allow the assessment of kinematic features on a quantitative basis and can be used both as boundary conditions and as geometric control points in numerical modelling. Differential levelling could be also applied for tilt measurements of rock blocks. For example, a well-spaced set of benchmarks can provide the estimation of the attitude of a plane solved by means of the least squares approach, to fit the surface to the measurements.

#### **2.1.1. Spirit and Trigonometric Levelling Basic Concepts**

Spirit and Trigonometric levelling allow for a high-precision estimation of elevation changes. In particular, adopting geometric levelling with modern digital levels, a precision in the order of 1 to 2 mm/km can be routinely reached. Normally, interconnected closed rings form the levelling network structure, and the presence of redundant data allows the estimation of elevations by means of a rigorous statistical data treatment. In this case, in fact, results are accomplished by a full variance-covariance matrix. For differential trigonometric levelling a high-precision total station is used. With this methodology a precision in the order of few mm/km can be reached, when measuring elevation differences.



### 2.1.2. Instruments and Elaborates

One of the most widespread techniques for the monitoring of vertical ground movements is high-precision geometric levelling. This technique is based on differential readings of two rigid invar staffs, positioned at a maximum distance of 30 m from the instrument; for best performance in terms of precision, foresight and backsight distances should be balanced within 0.5-1 m. At present, analogical automatic levels are used only in special monitoring activities of buildings and infrastructures or of inaccessible areas (lakes, rivers etc.). Conversely, in the repetition of levelling networks digital levels are mostly used. Digital instruments automatically read standard rigid staffs and record the data in an internal memory. This greatly enhances the efficiency of the method and minimizes the errors due to data transcription in the field.

The measurements are carried out with a classical scheme: the instrument performs a horizontal line of sight, tangent to the equipotential surface of the gravitational field that pass through the instrument's centre. The concept of carrying out each measurement from the centre of short distances allows symmetry of both the equipotential line curvature and of residual effects in the line of sight rectification be assumed in first approximation. At the same time, the elevation difference between the points where the staffs are positioned is obtained without measuring the instrument height.

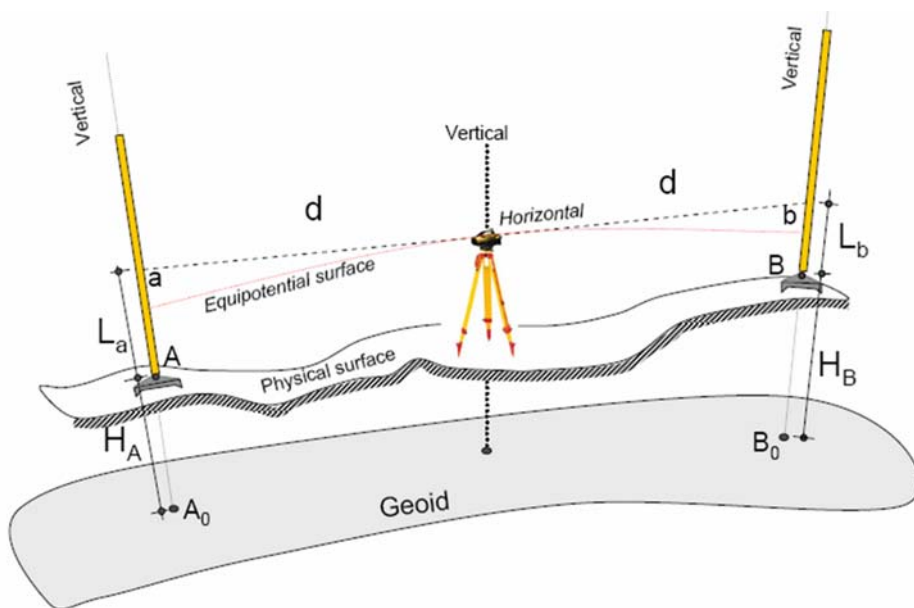


Figure 2. Scheme of a geometric levelling with single instrument set-up.

By means of a sequence of double-run section measurements, the elevation differences between a line of stable control points (benchmarks) are obtained (levelling lines). Single sections shall not exceed one kilometre in length. The lines are then closed to form polygons, which altogether make up monitoring leveling networks.

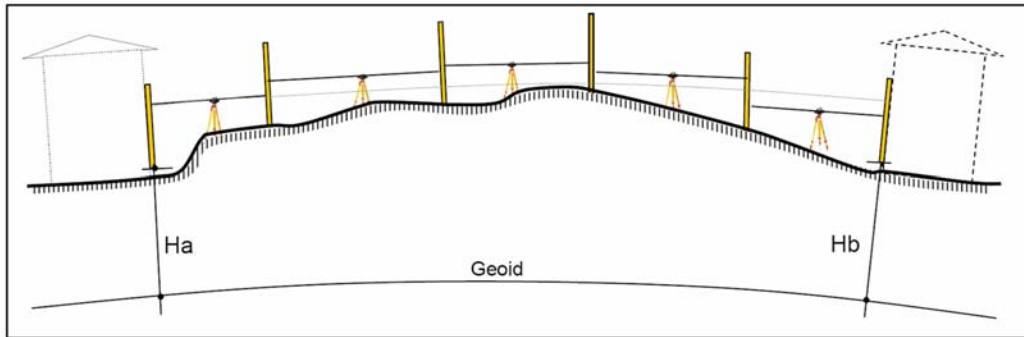


Figure 3. Scheme of a geometric levelling survey composed by successive instrument set-ups (single lines of sight not exceeding 30 m for high precision).

One of the major drawbacks comes from the necessity of carrying out measurements only over horizontal lines of sight. This requirement significantly limits the length of each single levelling segment, especially in rough terrains. To overcome this limitation, without losing the precision of few mm/km on each levelling section, the differential trigonometric levelling technique can be adopted.

The traditional leveling can be replaced thanks to the development of high-precision total stations, reaching angular resolutions lower than a sexagesimal second, equipped with phase shift Electronic Distance Meter (EDM) of millimetrical class (1mm + 1ppm). In this case, the collimations are carried out by means of staffs with calibrated height, equipped with a prism and an angular target on top. The length of each segment can be up to 150-200 m and the line of sight can be inclined. These characteristics considerably foster the survey of large elevation differences in sloping terrains, such as landslide prone areas.

If the station is placed symmetrically with respect to the staffs, the measurements consist of a series of readings in direct and reversed positions of the vertical circle and of slope distances for each target. In the calculations, a simple spherical hypothesis is assumed (local sphere with radius  $R$ ) to reduce the slope distances to the reference surface ( $S_1$ ,  $S_2$ ). In the equation used to calculate the elevation difference,  $k$  is refraction index, whereas the vertical angles  $V_1$  e  $V_2$  are the apparent zenithal angles averaged in the conjugated positions (direct and reversed modes) of the vertical circle (1).

$$\Delta H_{12} = S_2 \cot g(V_2) - S_1 \cot g(V_1) + \frac{1-k}{2R} (S_2^2 - S_1^2) \quad (1)$$

If an asymmetrical measurement scheme is required due to visibility constraints or in presence of unreachable areas (i.e., lakes, rivers or valleys), a different surveying procedure is advisable. A high precision total station has to be installed on a tripod (A) close to the point 1 (few meters, in order to be able to disregard the effects of the Earth curvature and of air refraction over a small distance). The vertical angles and the slope distances from the instrument towards both the prism over the staff installed at the benchmark 1, and toward a second target prism installed on tripod B located close to the second benchmark 2, have to be measured in direct and reversed modes of the vertical circle. Then, without moving the tribrachs installed on the tripods' top, the position of total station A and of the target B are changed reciprocally. The second set of measurements has to be collected as soon as possible,

in order to maintain the air refraction conditions the most similar as possible with respect to the first stationing (Fig. 5). If two total stations are available a similar measurement scheme can be applied simultaneously at both ends of the asymmetrical sections.

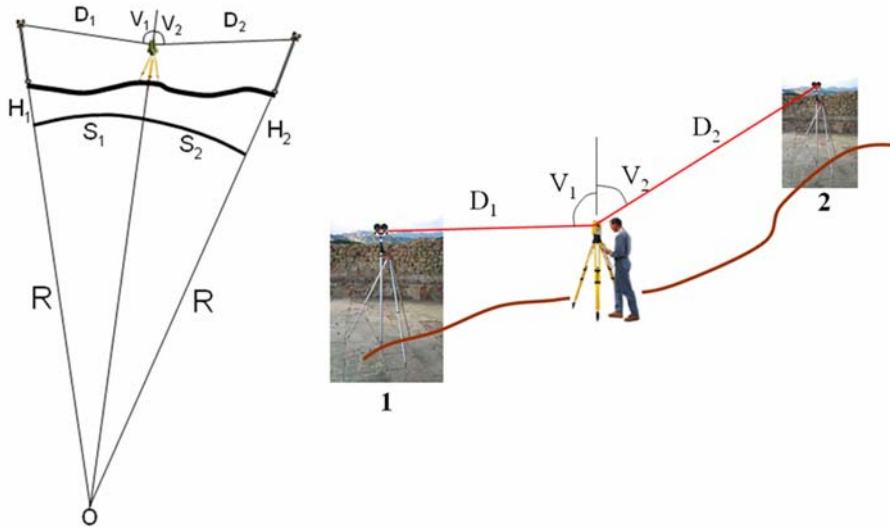


Figure 4. Scheme of single instrument set-up for differential trigonometric levelling.

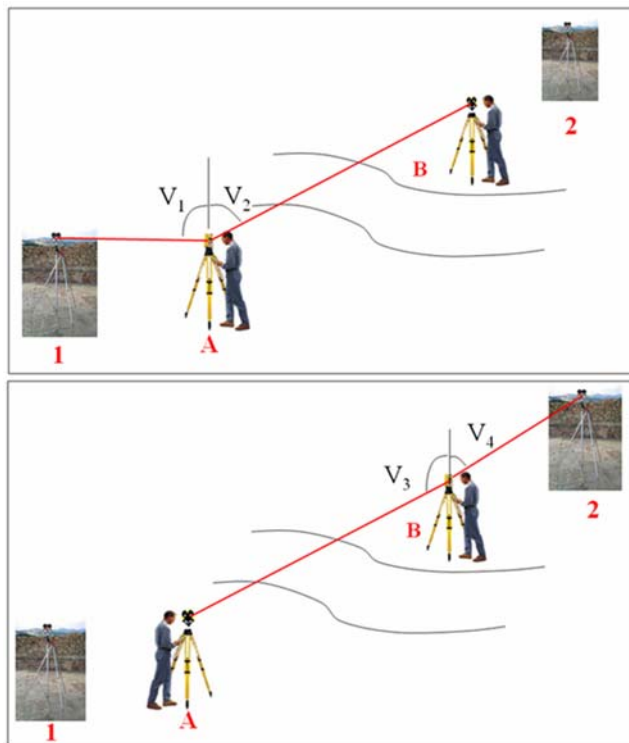


Figure 5. Scheme of an alternative method for asymmetrical differential trigonometric levelling.

## **2.2. Two- and Three-Dimensional Positioning Techniques**

Normally, to control with high precision both 2D and 3D superficial movements, the positions of single points are monitored. Here, GNSS satellite receivers and total stations (automated when the timing is semi-continuous or continuous) are usually adopted. When photogrammetric and remote sensing techniques as well as aerial or terrestrial LiDAR are used, the analysis of displacements and subsequent variations of the object shape is based on a large number of control points (see § 3).

The specific features of each case study (landslide type, geographic and topographic conditions, lithology, velocity etc.) rule the design of the monitoring system infrastructure, in order to reach compensation between users' needs, technological constraints and boundary conditions. The integration of different monitoring systems is often the only solution able to match all the prerequisites.

### **2.2.1. Basic Concepts about Topographic Surveys by Means of GNSS and Total Stations**

In the context of Geosciences, there is a growing awareness about the importance of integrated geodetic infrastructures able to define, the position of points on the Earth surface with millimetric precisions. Today, these tools are used for the study of geophysical phenomena, such as present-day geodynamics, and can be easily extended to the control of landslide movements.

Global Navigation Satellite System (GNSS) is the name used to describe the ensemble of navigation systems that provide autonomous geo-spatial positioning and timing with global coverage. It is composed of the United States NAVSTAR Global Positioning System (GPS) and the Russian GLONASS, while systems have been planned for future global service, including the European Union's Galileo positioning system, scheduled to be operational in 2012 and the Chinese navigation system Compass. In particular, these are passive, all-weather, 24-hour global precise positioning and timing satellite systems.

Thanks to satellite global positioning systems, the relative position of points on the Earth surface can be assessed with centimetric or even sub-centimetric precision without requiring the intervisibility between points as in classical surveying techniques. Conversely, an open sky visual is needed.

The positioning techniques are both static and kinematic and can be readily applied for the positioning of single points as well as to produce profiles. In the field of landslide monitoring, these techniques can be used:

- to verify the stability of control points;
- to measure the velocity field;
- to locate sensors and field surveys;
- to position ground control points for photogrammetric analysis or LiDAR point clouds;
- to survey 3D profiles of terrain.

Modern total stations integrate several sensors and are able to measure horizontal and vertical angles as well as slope distances. The lines of sight used to measure the angle and the distance are coaxial and it is therefore possible to assess 3D coordinates of measured points with respect to the coordinates of the station. Total stations are particularly useful for high precision monitoring of relative displacements between the station itself and well-defined points. In this case, a relative reference system is fixed a priori using specific points in the network. If integrated with GNSS, the position is globally framed and monitored on a continuous basis, thanks to the permanent stations maintained by the International GNSS Service (IGS). Before the development of GPS, long range single or dual color laser EDMs (Langbein, 2004) were the unique solution for measuring very long distances (up to several tens of km) with high accuracy. At present, large monitoring networks are mostly built up by means of spatial geodetic techniques.

### **2.2.2. Instruments and Elaborates of GNSS**

Various GNSS surveying methods are used in natural hazard monitoring (i.e. static, rapid static, kinematic, Real Time Kinematic - RTK).

Static and rapid static GPS surveys typically use a network of baselines. The survey may consist of an occupation of points using multiple receivers. A redundant number of baselines, with respect to the number of the unknowns, allows for a least squares evaluation of point coordinates, along with their variance-covariance matrix. The static method provides the highest accuracy, in particular through the analysis of long time series derived by continuous acquisition. A precise GNSS surveying is essentially the differential measure of the incoming carrier phase of the satellite signals with a few millimeters level of resolution. When two or more receivers observe the same set of satellites simultaneously, most of the systematic effects are eliminated. The observation time and the accuracy are mainly a function of the baseline length.

The kinematic term used in conjunction with GNSS positioning means that the data collection is made from a receiver moving with respect to a fixed reference station located within 10-15 km. This master station supplies data for relative processing and frames the surveyed path followed by the rover antenna. This method is widely used when other sensors need for a time referenced positioning. There are two principal types of kinematic surveying methods: Post Processed (PPK) and Real Time (RTK). To operate in real time mode with the simultaneous acquisition of GNSS signals from satellites at the master and rover receivers, a radio-link between the instruments (radio or mobile phone) is necessary. If instead of a single master station the RTK service is supplied by an active network of reference stations, the method can be extended to wide regions, and this positioning method is called Network-based Real Time Kinematic (NRTK).

Today, alongside to the positioning techniques derived by the carrier phase signal difference, an undifferentiated approach, the so-called Precise Point Positioning technique (PPP), is also used. This allows precise positioning time series starting from the observations of a single receiver to be realized.

Using a PPP approach, the datum is fixed by using precise estimates of satellite clock error and satellite ephemerides published by International geodetic services; hence, at the stage of application of the method it is not necessary to make any choice regarding the reference stations (inter-station distance is irrelevant). Besides furnishing a mean for framing

within the International Terrestrial Reference Frame (e.g., current ITRF2005), the PPP approach provides solutions of coordinates with accuracies that can vary depending on age of the data, time length of collection, satellite geometry, frequency of cycle slips, receiver type and measurement quality. Users can expect 5-40 cm kinematic accuracies and 1-10 cm static accuracies without using a base station.


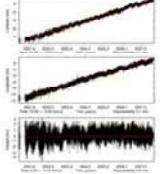
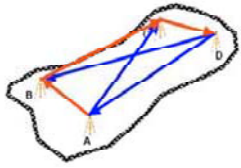
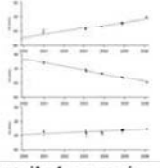
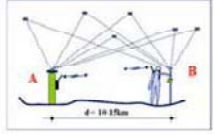
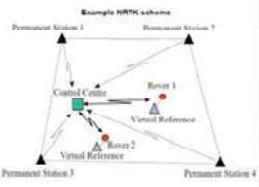

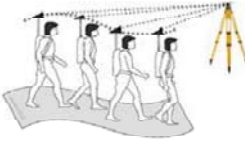

Surveying Method	Examples of products	Precision
<b>GNSS Permanent Station</b> 	<b>Continuous coordinate Time Series</b> 	<b>Position:</b> Horizontal $\pm 1\text{-}2\text{mm}$ Vertical $\pm 2\text{-}4\text{mm}$ <b>Velocity:</b> Horizontal $\pm 0.1\text{-}0.2\text{mm/yr}$ Vertical $\pm 0.4\text{-}0.5\text{mm/yr}$
<b>Static – Rapid Static</b> 	<b>Precise positioning and discontinuous coordinate Time Series</b> 	<b>Position:</b> $\pm (5\text{-}10\text{ mm} + 1\text{ppm})$  Precision of velocity determination depends from the number of repetitions and from the time-span between measurements  E.G. Vel (N-E) $+0.5\text{-}1\text{ mm/yr}$ Vel. (Up) $\pm 1\text{-}2\text{mm/yr}$
<b>RTK/NRTK</b>  	<b>Detailed surveying of surface features and near real time monitoring of movements</b> 	<b>Three-D <math>\pm (10\text{-}20\text{ mm} + 2\text{ppm})</math></b>
<b>Continuous PPK</b> 	<b>Digital Terrain Model</b> 	<b>Three-D profiles within 10-15 km from the reference station: <math>\pm 50\text{mm}</math></b>

Figure 6. Scheme of GNSS relative positioning methods along with their indicative precision (1 ppm means one part per million, or one additional mm per km of measured baseline).

### 2.2.3. Instruments and Elaborates of Total Stations

The survey of single points can be performed only in case of visibility and over short distances (normally less than 1 km, with sub-centimetric precision) by means of high-precision topographic total stations. The total station firmware interfaces through the onboard microprocessors with sensors, data collector, display, external computers etc. The instruments can be classified in two main types, considering the EDM operating modes:

- Total station that implements a strategy for the measurements of distances based on phase-shift between the emitted and the returned carrier wave modulated signal. It requires for retroreflector prisms installed in the collimated points;
- Total station that implements time-pulsed infrared EDM. It doesn't require for retroreflector prisms installed in the collimated points for short distances (reflectorless total station).

A third class of EDM has been recently developed that allows the combination of a reflectorless and reflector based EDM using a single laser beam emitter (Bayoud F. A., 2006).

The collimation can be preformed manually by the operator, or eventually by means of robotic total stations, which automatically detect and collimate retroreflector prisms.

The timing (frequency) of measurements is dictated by the type of phenomenon, up to a continuous monitoring in case of high risk conditions. If the surveys can be performed on a discontinuous basis, the monumentation of the stations and the collimation require a minimal configuration, even with a single total station placed on a number of pillars. On the contrary, if the measurements have to be performed with high frequency (i.e., monitoring), the system have to be designed for a permanent running, with a number of self-tracking robotic total station able to fulfill the monitoring scheme. The stations have to be protected from atmospheric agents, energy has to be provided and proper data storage and transmission system have to be planned. Nonetheless, the system has to be protected from robbery, vandalism and so on. One fundamental issue is the stability and repeatability of the instrument placement. The instruments have to be placed on pillars that ensure the three-dimensional stability of the point and provide a three-dimensional force centering. Modern instruments are often equipped with a dual-axis compensator, which numerically corrects horizontal and vertical angles for small deviations in the plumb line.

The monitoring network has to be designed for long-term exploitation, therefore the monumentation of station and control points have to be carefully carried out. In particular, the stability of stationing points has to be checked. In fact, displacements of the reference system lead to wrong estimates of landslide displacements. When continuous monitoring is performed, considering also the high precision of angular measurements, even very small displacements of the pillar can put in "out of range" position the biaxial compensator, leading to a re-verticalisation procedure of the general axis of the instrument. This procedure on the one hand causes a discontinuity in the measurement series. On the other hand, systematic errors could be expected (caused by the reference frame instability) in the interpretation of displacement data. GNSS techniques (using long data series acquired by permanent stations), together with biaxial inclination sensors fixed to the TS pillars can be adopted to verify the

actual stability of reference points or to define the velocity datum of the local reference frame to be considered in the calculations.

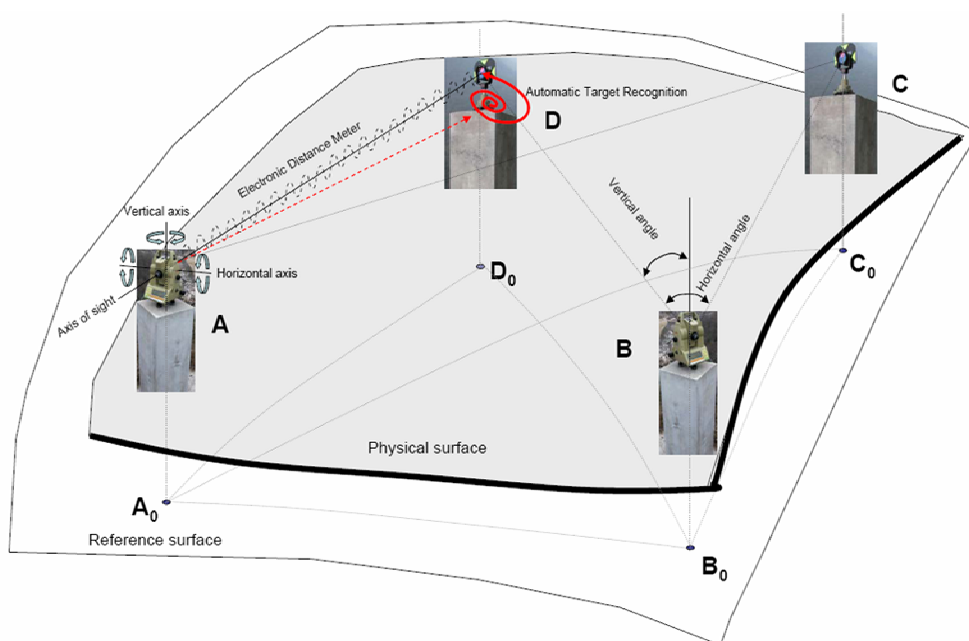


Figure 7. Scheme of measurement of angles (horizontal and vertical) and slope distances using self tracking robotic total stations.

The integration between TS and GNSS is particularly functional as satellite systems are able to fix a number of control points within a very high accurate geodetic global reference frames in a simple and reliable way by means of long series of continuous acquisitions. This allows for a precise control of actual local differential displacements with respect of absolute tectonic plate movements. At the same time, total stations can control with high precision the relative displacement (Table 1) of a large number of points placed in a radius of 1-2 km with respect to the station position itself (intrinsically controlled by GNSS).

**Table 1. Range of achievable accuracy of 3D coordinates derived by high precision TS**

Accuracy of 3D coordinates derived by high precision TS*	
Distance < 100 m	$\pm 0.5 \div 1$ mm
Distance < 500 m	$\pm 2 \div 5$ mm
Distance < 2500 m	$\pm 10 \div 15$ mm
* depends from several aspects :instrumental characteristics and calibration, measurement scheme robustness (geometry, redundancy), air refraction, centering device repeatability, etc.	

Atmospheric refraction is a critical issue in the measuring of distances and vertical angles and its modeling is necessary to overcome the induced errors. Therefore air temperature, barometric pressure, and relative humidity must be measured, using psychrometers and barometers at least at both sides of the measured distance. An error of 1 degree Celsius causes



an error of about 1 ppm for distances measured using infrared signals, while an error of 1 millimeters of mercury causes an error of about 0.2 ppm in distance. The refractive index of air with respect to infrared signals is thoroughly analyzed by Ciddor (2002).

#### 2.2.4. Monumentation

Regarding monumentation, the leveling benchmarks are often materialized by pegs fixed to rocky outcrops or to manmade structures. Once the points have been chosen, the movements of these points have to be representative of the investigated phenomena, so particular care have to be used in point selection. The same position can be measured using different instruments and approaches through interchangeable devices (i.e., leveling, GPS and TS - Fig. 8).



Figure 8. Example of pegs for horizontal and vertical placement (left), interchangeable device for leveling benchmark, GPS antenna and retro-reflecting prism installation (right).

Concrete pillars used to host total stations and GNSS antennas have to be designed in order to guarantee a 3D self-centering of the instruments. Moreover, in the choice of representative points, in the design and construction of the network, attention has to be paid to the inherent stability of the point themselves due to groundwater fluctuations, thermal expansion, soil geotechnical properties, suction phenomena etc.

Examples concerning the stability of concrete pillars and deep drilled braced monuments can be found in literature (Beavan, 2005; Wyatt, 1982, Wyatt, 1989, Wyatt et al., 1989).



Figure 9. Example of three-dimensional self-centring device for non permanent total stations set-up.



Figure 10. Monumentation (thermal non-insulated and insulated) of stationing points for discontinuous measurements and monitoring.

If the monument is represented by a simple reinforced concrete or steel pillar, especially in the case of high structures, the difference of temperature with respect to a reference value ( $T_0$ ) could induce significant vertical and, in some circumstances horizontal, instabilities on the pillar top. The first effect could be simply modelled recording the temperature of the monument during the measurement. To avoid horizontal displacements, it is advisable to install an external insulated shell in order to protect the monument from inhomogeneous temperature changes (i.e., due to sun radiation effects).

### 3. Non-contact Methods

The ground-based techniques described in Section 2 permit to acquire very precise information on displacements or deformations at specific locations within landslides bodies, but they do not provide information on displacement fields or on surface changes in wider areas.

Nowadays, airborne and terrestrial LiDAR, Satellite images processing, Photogrammetry and InSAR are becoming widespread techniques, which may provide the estimation of displacements and the detection of surface changes without requiring a physical contact with the object to be measured.

The following sections describe the classical non-contact methods which may be adopted for analyzing superficial movements of unstable slopes.

#### 3.1. Airborne LiDAR and Terrestrial Laser Scanner

Within the field of Geomatics, LiDAR (Light Detection And Ranging) is a relatively new technique, covering a broad range of different technologies and areas of applications (Ackermann, 1999; Baltsavias, 1999; Brinkman and O'Neill, 2000; Kilian et al., 1996; Hengl and Reuter, 2008; Wehr and Lohr, 1999). This technique offers the typical advantage of non-contact methods and is usually adopted in surface mapping, industry, piping, architecture,

archaeology and control of quarries (Bitelli et al., 2002, 2004; Bornaz et al., 2002; Chen et al., 2006; Fangi et al., 2001; French, 2003; Gutelius et al., 1998; Hsiao et al., 2004; McKean and Roering, 2004; Rowlands et al., 2003; White and Wang, 2003).

LiDAR, without the requirement of reflectors deployment, rapidly provides dense clouds of three dimensional points and a perspective image (complemented with intensity data and sometimes RGB data), fundamental to represent the morphology of irregular surfaces.

The collected data are brought in a unique reference system and merged to construct the shape and three dimensional model of the object.

Laser scanner records distances and angles to reflective objects; a GPS receiver furnishes the coordinates of the LiDAR device in a global reference system; the inertial navigation device acquires the angular position in space of the scanner with respect to the object coordinate system, defined by three angles (pitch, yaw and roll).

In terrestrial laser scanner, high density surveys are realised from the ground, putting the scanner on a fixed tripod and then moving it in other positions to cover up the entire object to be surveyed. With respect to the different types of laser scanning, different principles for distances measurement (phase difference, triangulation, Time of Flight) are available; long-range scanners based on Time of Flight (ToF) are mostly used in landslide surveying.

These instruments, called rangefinder lasers, measure distance, direction and elevations of points. The range is from hundreds of meters till a couple of km in the case of high performance long-range 3D scanner, with centimetric accuracy on short distances till several centimeters on long distances. Laser pulses are transmitted toward the object, reflected and detected from the laser nearly instantaneously.

### **3.1.1. Basic Concepts**

The most common type of laser rangefinder sends a laser pulse towards the object and measures the time taken to the pulse to return to the sender. Known the speed of light, object distance is determined; azimuth and elevation measurements are also provided by the instrument. These observations permit to calculate in near real-time the 3D position of a point, by means of a similar radial side shot topographic method (Ghilani and Wolf, 2008).

The scanning directions are changed horizontally and vertically, by moving the scanner itself or by the rotation of internal mirrors, to cover up the entire instrumental field of view; this automatic procedure permits the acquisition of 10,000-100,000 points per second, according to the technical characteristics of the scanner.

### **3.1.2. Instruments and Elaborates**

Several types of laser scanning are available and the main characteristics are the following:

- the strategies of laser measurements;
- the laser class;
- the number of observations per second;
- the object - instrument distance (range and range accuracy);
- the spacing between observed points (angular resolution and angular accuracy);

- the field of view;
- the availability of imaging cameras to be combined with the scans.

While terrestrial scanners register a unique laser pulse, airborne LiDAR systems are usually able to record multiple returns of the emitted pulse of light; thanks to this tool, during the post-processing step, it is possible to discriminate ground from vegetation, trees, building roofs, aerial electrical cables etc., delivering both Digital Surface Models (DSMs) and filtered Digital Elevation Models (DEMs; Sithole and Vosselman, 2004).

The resulting products are clouds of three-dimensional points referred to a local coordinate system or inserted in a global coordinate system, thanks to the presence of Ground Control Points (GCPs) or to the integration with GPS receivers. After data merging, the point clouds produced by 3D scanners have to be converted in a continuous surface in the “reconstruction” step, performed by means of common interpolation algorithms.

Reflectivity features are generated together with the vectorial data, while some instruments also yield raster images of the object. This radiometric information permits the elaboration in post processing of three dimensional raster models and orthophotos.

### **3.1.3. Accuracy of Point Clouds**

In the frame of landslide surveying, the possibility to collect hundreds or even thousands of 3D points per second in near real time is the main advantage of this technique, but at the same time the accuracy of the results is difficult to be estimated a priori (Alharthy et al., 2004; Boehler and Marbs, 2006; Bretar et al., 2003). This is an important issue, because laser scanning does not provide redundant information for the computation of 3D points (even if some instruments can supply the mean value of a number of measurements on single spots), so outliers can only be detected during the filtering step. It is clear that this is not an estimate of the actual accuracy, but improves the overall precision of results. Moreover, when surveying natural surfaces by means of non-homogeneous point clouds, in a sequence of repeated measurements the instrument may not acquire each time exactly the same point cloud, mainly because of surface roughness, perspective occlusion effects, canopy, air refraction etc. This is particularly applicable to airborne scans, where the position of the aircraft along strips inevitably changes in subsequent surveys, eventually generating somehow different point clouds. Nevertheless, the reference accuracy of airborne LiDAR is currently in the range of 10-15 cm (Ghilani and Wolf, 2008) on smooth surfaces, while few millimeters to decimeter range is available by means of terrestrial Laser Scanners.

The accuracy depends on several issues:

- the characteristics of GPS and IMU systems (for aerial LiDAR);
- the calibration of the integrated instruments (i.e. laser scanner and camera, etc.);
- the performance of the systems (angular and range laser accuracy);
- the laser clock accuracy;
- the dimension of the laser spot on the object;
- the geometry of multiple scans;
- the morphology of the surveyed area (topographic roughness);
- the surface color and reflectivity;

- the resolution of the scans (interdistance between points on the object; grid resolution);
- the presence and the type of vegetation;
- the environmental conditions (temperature, atmosphere etc).

Furthermore the quality of laser surfaces depends on the operator skills concerning GPS-IMU data post processing, and laser data treatment, with reference to the geo-referencing step, the alignment and the noise reduction filtering strategy adopted.

## 3.2. Optical Sensors

This section describes the branch of remote sensing methods that exploit optical sensors. The techniques that can be used to survey landslides and to measure displacements on landslide bodies comprise both the satellite imagery and aerial and ground-based photogrammetry.

### 3.2.1. Satellite Imagery

The exploitation of satellite imagery in the field of landslide study and surveying is profitable because of its intrinsically multitemporal, multiscale and multispectral qualities. At the moment, optical sensors for civil purposes do not reach the spatial resolutions of low-altitude, close-range and fixed camera photogrammetric surveys. At the same time, satellite imagery can improve the mapping of landslide phenomena from the regional to the catchment and the slope scale. An overall view of the geomorphological features of a large area can, in fact, be attained handling a relatively small number of images. Thanks to high resolution imagery, available from year 2000 onwards, both feature identification and tracking techniques can be applied to multitemporal series. The most common approach exploits pixel brightness patterns cross-correlation techniques. The motion tracking analysis allows surface velocity fields to be estimated (Bernstein 1983; Bitelli et al., 2008; Frezzotti et al., 1998; Scambos et al., 1992). Moreover, the availability of multispectral bands allows image classification and automatic and semi-automatic production of thematic maps (i.e., soil moisture distribution). With image enhancement techniques features can be detected even in shaded or dark areas.

As far as DEM generation is concerned, two different approaches can be used with reference to satellite products: the first is based on interferometric analysis of radar data (see section 3.3), while the second uses stereocouples acquired from optical sensors. Stereo pair imagery products are composed by two scenes with approximately 90% area overlap, which are acquired with specific look angles in order to attain an appropriate base to height ratio for stereo viewing. These stereo-pairs are usually acquired in-track, meaning that they are both collected in the same pass, allowing for a photogrammetric approach that can be applied also to raw data, if specific and dedicated algorithms have to be used.

Even if these DEMs are characterised by a lower resolution with respect to terrestrial and airborne laser scanning, they are particularly useful in the case of large and inaccessible areas and in the generation of high-resolution satellite orthoimagery. Up to now, the best geometrical resolution is available with the sensor GeoEye-1, launched successfully in

September 2008. It offers unprecedented spatial resolution by simultaneously acquiring 0.41-meter panchromatic at nadir and 1.65-meter multispectral imagery (pixel resolution varies across the image due to off-nadir viewing angle). Besides this, IKONOS, Quickbird and SPOT5 offer a wide range of high-resolution satellite imagery for surface change detection at a relatively low cost with respect to ad hoc photogrammetric flights, if the covered area and the temporal resolution are considered.

### **3.2.2. Photogrammetry**

Photogrammetry is one of the most interesting techniques which can be applied to landslides surveying, offering the possibility to detect and classify landslide type, state and style of activity (Baily et al., 2003; Baldi et al., 2008; Brunsden and Chandler, 1996; Brückl et al., 2006; Chadwick et al., 2005; Kääb, 2000; Lane and Chandler, 2003; Mantovani et al., 1996).

The first task of photogrammetry is to determine the position of 3D ground points from the measurement of 2D image coordinates, taken from remote sensing platforms. This step is called “restitution” which is, from a geometric point of view, a spatial intersection problem.

By means of image points measurement applied to at least two photos collected from different points of view, single or dense ground points can be obtained without a direct contact with the object

Otherwise, a single ground fixed camera may be used for mapping landslide displacements and to provide real time data. This is a very important application that allows information to be obtained in the prediction of landslide reactivations (Delacourt et al., 2007).

#### **3.2.2.1. Basic Concepts**

The basic mathematical model adopted to convert a two-dimensional system (photo) into a three-dimensional system (ground) is expressed by collinearity equations (Kraus, 1997), which define the correspondence between the image and the ground spaces.

In order to define the shape and the position of land portions, it is necessary to reconstruct the original geometric conditions under which the images were taken, removing the distortions due to the data acquisition system and to the central projection characteristics of a photograph. This is a spatial resection problem; the procedure that permits to calculate the space position and the angular orientation of an image (External Orientation Parameters - EOPs) may be performed thanks to the presence in the photos of ground points of known coordinates (Ground Control Points, GCPs). On the photo, a 2D coordinate system is defined, while the GCPs have also their 3D coordinates expressed in a local or global coordinate system. In the orientation procedure, the coordinates of the GCPs detected on the image have to be measured, then the image orientation is computed. Normally, at least three GCPs must be available for one pair of overlapping photos, so several points are needed to orient large blocks of photos. This is often the most expensive aspect of a photogrammetric survey.

The adoption of the photogrammetric Triangulation technique, originally developed for aerial surveys, based on tie points detection, can largely reduce the number of required GCPs. Traditionally, the coordinates of GCPs are measured at the same time of the photogrammetric survey using topographic techniques, but they may also be obtained afterwards from others photogrammetric surveys of the same area, identifying common tie points.

Once the transformation parameters between the image and the object space are known, the restitution problem has a solution. The assessment of the 3D coordinates of a point in the object space is carried out measuring image coordinates on at least two images collected from different points.

### 3.2.2.2. Instruments and Elaborates

A photogrammetric survey can be carried out by means of any type of camera (metric, semi-metric or amateur cameras) but the inner geometry of the camera, the characteristics of the camera lens and the film or pixel dimension (the so called, Inner Orientation Parameters - IOPs) have to be known to perform the restitution.

Metrical cameras are mostly employed in aerial surveys, while semi-metric (with réseau) or amateur cameras (nowadays very high resolution digital cameras) are largely used in close range surveys.

Alternatively, if the IOPs are unknown, they can be calculated in the laboratory or on the field by means of a procedure called "bundle adjustment with image self-calibration" (Kraus, 1997) based on the detection of high precision GCPs on multiple photos.

Analytical stereoplotters or modern Digital Photogrammetric Workstations may be adopted for the stereoscopic image measurements of points.

Alternative photogrammetric systems, called "non conventional", are designed for monoscopic multi-image measurements. By means of these systems, convergent, horizontal, vertical or oblique photos can be acquired by means of different cameras (semi-metric or non-metric) or lenses.

Using a Digital photogrammetric approach the space resection and intersection procedures have become relatively easy and quasi totally automatic (Image Matching algorithms - IM).

In photogrammetry, IM comprise a variety of sophisticated strategies, often combined (Hahn and Förstner, 1988; Heipke, 1996; Helava, 1988; Kraus, 1997) to produce accurate restitutions.

The points in the object space are always related to the points in the image system by means of the collinearity condition, but the digital image permits fast three-dimensional measurements.

The matching problem cannot be always solved and even the most sophisticated algorithms recently produced may fail; as a consequence, a specific expertise and a good knowledge of photogrammetric theory are necessary to achieve reliable results (geomatic engineers).

The results of the restitution procedures are coordinates of single points, three dimensional lines and polylines, contour lines, profiles, cross-sections and grids, which may be used to prepare maps and 3D models of the area.

The preparation of orthophoto mosaics, which reproduce the photo-texture in colors or grey tones of the original photographs, is another task of photogrammetry. This photographic metric product is indeed very interesting in supporting any kind of study, as it shows the complete radiometric content of the original image, without subjective interpretations. It is derived from perspective photographs by differential rectification. Each pixel of the image is transformed by means of an orthogonal projection scaling onto a horizontal plane, which

represents an element of, or the entire digital surface model of the object. Afterwards, image resampling is carried out using different kinds of transformations (Kraus, 1997).

### **3.2.2.3. Ground Fixed Single Digital Camera**

In the investigations of relatively small unstable areas automatic single camera systems are used together with simple and differential rectification products.

By means of a digital camera fixed on the ground, placed in front of an unstable area, the collection of images with high-frequency time step is very easy. The images may be oriented in the space thanks to the presence of Ground Control Points (spatial resection problem) detectable on the images. At the end of these orientation procedures, the correspondence between image and ground coordinates is defined.

The availability of a dense DEM permits to transform the images in orthogonal projections having a metric content. Instead, if the DEM is not used because the landscape may be considered as a plane, a simple image rectification may be generated and adopted for comparison purposes.

The analysis of the image time series is carried out applying image matching algorithms, which automatically identify displacements and surface changes (Harris et al., 2007; Jimenez et al., 2007).

### **3.2.2.4. About the Archival Photogrammetry**

Most field techniques only provide point-based measurements of landslides features. In addition, they do not give information on past movement episodes.

Thus, photographic archives represent a fundamental source of historical data that in some cases allow modeling the deformation of unstable areas and may help in predicting future failures.

In the case of historical image processing, a photogrammetric method known as Archival Photogrammetry has to be applied to extract metric information from historical photos (Baldi et al., 2008; Chandler and Brunsden, 1995; Chandler and Cooper, 1988a, b; D'Agata and Zanutta, 2007; Walstra et al., 2004; Zanutta et al., 2006).

Displacement vectors of points distributed in the studied area can also be obtained by measuring the positions of natural and artificial points recognized on multi-temporal images.

A recursive procedure (Zanutta et al., 2006) based on the use of homologous points located on multitemporal models has to be applied to evaluate the orientations of the photos and then insert all the final vectorial elaborations in a unique 3D reference system. Furthermore, differential photogrammetry can be employed to realize DEMs comparisons. In the study of landslide evolution during recent historical times, the appropriate comparison of 3D models obtained in different years allows a metrical identification of the geometric changes occurred during a specific time interval to be assessed.

### **3.2.2.5. Accuracy of Stereoscopic Data Capture**

The accuracy of photogrammetric measurements depends on several parameters, mainly: scale of photos; type of cameras; instruments used to carry out the measurements; density, distribution and quality of GCPs; pixel size.



These parameters also constrain the costs and are therefore to be correctly defined before performing the survey. Among these, the camera - object distance (flying height in aerial photogrammetry) plays a relevant role, affecting the final accuracy with a quadratic influence (2). At present, with a moderately low flying height, a few centimeters accuracy can be achieved.

Several approaches are available to evaluate the *a priori* accuracy of photogrammetric point restitutions, based on empirical relationships (Kraus, 1993; D'Agata and Zanutta, 2007) or on statistical methods (i.e., applying the variance propagation law to the simplified collinearity model). For instance, a simple relation to evaluate the final accuracy of points is provided by the equation (2) (Kraus, 1993):

$$\sigma = \left( \frac{Z^2}{c \cdot B} \right) \cdot \sigma_{P_\xi} \quad (2)$$

where:

$\sigma$  = theoretical Root Mean Square deviation expected;

$Z$  = relative distance from the object;

$c$  = focal length of the camera;

$B$  = distance between central points on subsequent images (photobase);

$\sigma_{P_\xi}$  = horizontal parallax measurement error (errors measuring image coordinates on the images).

Furthermore, for an accurate object description, the definition of the pixel dimension on the ground (Object Sampling Distance - OSD) is of great importance, because it constrains the detail of the scene (3):

$$OSD = l \cdot \frac{Z}{c} \quad (3)$$

where:

$l$  = pixel dimension;

$Z$  = relative distance to the object;

$c$  = focal length of the camera.

**Table 2. Characteristics of satellite aerial and terrestrial optical sensors**

	Optical sensor		
	Satellite	Aerial/balloon	Close range/Fixed camera
Spatial Resolution	0.42 m to 80 m	0.05 m to 2 m	0.01 m to few meters
Temporal Resolution	~ 1-30 days	On request	On request/1 s to 1 day
Spectral resolution	Pancromatic/Multispectral	Visible	Visible
Accuracy	1/5 to 1 pixel	1/5 to 2-3 pixel	1/5 pixel
Swath	10x10 km to 60x60 km	10x10 m to 5x5 km	10x10 m to 1x1 km
Historical data archive	SPOT 1-4 (1986); IKONOS (1999); QUICKBIRD (1999) SPOT 5 (2002); GEOEYE-1 (2008)	National and regional photogrammetric coverage	-

### 3.3. Radar Sensors

Radar satellite systems generate electromagnetic images (i.e. with frequency ranging from 500 MHz to 10 GHz) of the Earth surface with a spatial resolution of few meters. Besides optical ones, being active sensors, they can operate also in cloudy conditions and without daylight. The instrument focuses the electromagnetic target and measures its distance by means of the time lag between the transmission and the receiving of the signal. The target is located estimating the direction of the antenna in range. The direction parallel to the orbit is called azimuth. The longer is the antenna, the better is the location of the object also in azimuth, despite a reduction of the illuminated area. The approach adopted in the SAR (Synthetic Aperture Radar) allows a balance to be reached between the spatial resolution and the dimensions of the observed area.

The sensor-target direction (perpendicular to the orbit and inclined of the off-nadir angle with respect to the vertical, i.e.  $23^\circ$ ) is called slant-range. Range and azimuth represent the so-called SAR coordinates (Fig. 11).

The SAR technique (Bürgmann et al., 2000; Elachi, 1980; Graham, 1974; Jensen et al., 1977; Massonnet and Feigl, 1998) requires therefore an active illumination system in which reflected radar signals transmitted from antennas installed on aircrafts, spacecrafts or Ground-Based instruments, after being backscattered from object surface, are recorded (Curlander and McDonough, 1992; Luzi et al., 2006; Rudolf et al., 1999; Tarchi et al., 2000a, 2000b, 2003a, 2003b). The returning echoes generate a high resolution radar image in which each picture element registers both amplitude and phase signal information.

Radar images are generated with a focalization algorithm that associates to each single pixel its backscattered energy. The radar interferometry technique (InSAR) involves phase comparison of multiple SAR images of the same scene (Madsen and Zebker, 1999; Gens and Vangenderen, 1996).

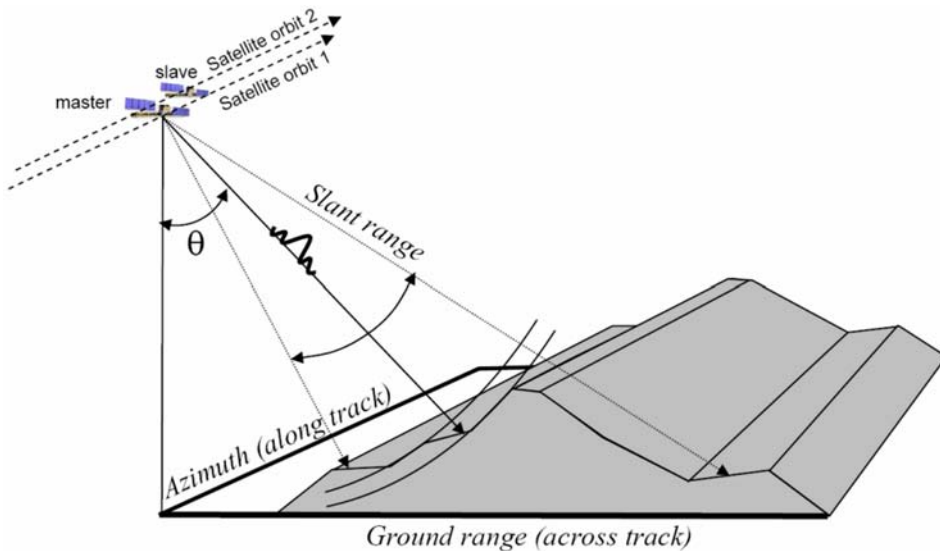


Figure 11. Basic scheme of the interferometric SAR system (after Li and Goldstein, 1990).

A SAR satellite can irradiate the same area from slightly different look angles. This can be done either simultaneously when two radars are mounted on the same satellite or at different times through successive satellites passes. The orbital separation between master and slave satellites in the plane perpendicular to the orbit is called interferometer baseline and, in particular, its normal component with respect to the master's slant range is the normal baseline. For each processing approach (considering the wavelength used), an optimum perpendicular baseline is defined. Because of the different positions of the sensor during subsequent acquisitions, the geometry may vary generating matrices that do not match exactly the same area on the ground. For this reason, a master image is chosen and the following images (slaves) are resampled with respect to it, so to obtain a reference grid for the whole stack of images to be analyzed.

The final elaborate of the processing of a couple of images is an interferogram, which can be converted to a very high-resolution topographic map with meter accuracy (Madsen et al., 1995). Adding more images the analysis will produce a displacement map with sub centimeter to sub millimeter level of accuracy; this latter level of precision is typical for Ground Based techniques (Antonello et al., 2004; Balan and Mather, 1999; Colesanti et al., 2003; Colesanti and Wasowski, 2006; Corsini et al., 2006; Crosetto, 2002; Moreira et al., 1995).

In the last decade, a new InSAR technique has been developed, based on the analyses of a sequence of interferograms. The technique, called Permanent or Persistent Scatterers (PS in Ferretti et al., 2001, 2005; Hilley et al., 2004; Kampes, 2006) is based on the detection of radar reflectors (outcrops, buildings etc.) on multiple images of the same scene, which maintain stable reflectivity values for long time intervals.

The use of the PS technique, based on large image datasets, permits to remove the atmospheric effects, and allows estimations of displacements with millimetric accuracy. To derive the absolute velocities of the radar reflectors contained in a scene, at least one fixed reference point has to be chosen, or if it is moving, the velocity of movement of this reference point has to be known in advance.

SAR Interferometry carried out by means of single-pass systems or repeat-pass systems has been applied in a variety of analyses, from environmental monitoring to global change studies (Inggs and Lord, 2000; Massonnet and Feigl, 1998).

### **3.3.1. Satellite/Airborne Dinsar: Basic Concepts**

The most exploited SAR technique in the study of topographical data and of ground movements is the Differential SAR Interferometry. This technique is based on the analysis of the interferometric phase evolution in three or more couples of images of the same area. The interferometric phase is the phase difference between two radar images (SLC - Single Look Complex) and it is influenced by topographical effects, from ground movements, from atmospheric conditions and from the intrinsic blunder of the measure itself. The backscattered radar signal is composed of two main parameters, amplitude and phase. In the framework of advanced studies on the nature of the target, signal polarization is used as well.

An interferogram may be generated using multiple images acquired from a single antenna in successive pass or by means of two simultaneous images collected by two separated antennas located at a proper normal baseline. The two techniques, based on spatial and/or temporal baseline approaches, may be applied to the same frame to achieve more accurate

results. The measured phases are differenced on a pixel-by-pixel basis: due the different distance from the radar, a different delay exists between transmission and reception of the radiation; therefore, the phase differences can be interpreted as pixel heights or as the radial velocity of the scatterer, when multitemporal radar images are analyzed (Allen, 1995; Li and Goldstein, 1990).

If no other changes occurred in the period between two acquisitions, the interferometric phase depends principally on the sensor-target distance and therefore on eventual movements of the target, plus the effects induced by variations of atmospheric refraction. As time passes by (temporal baseline) the electromagnetic content of the targets may vary (as a consequence of canopy, snow cover, soil moisture etc.) and a temporal decorrelation may be observed.

To reach a millimetric accuracy in the assessment of movements, the removal of atmospheric effects is of fundamental importance. This can be achieved with the PS approach, which is based on the analysis of a sub-set of reflectors with stable electromagnetic content (geometric and temporal correlation) in a large number of scenes of the same area (usually more than 30). The permanent scatterers are generally buildings, infrastructures, bare ground, rock outcrops etc. Among the possible PS, only the sub-set of points displaying a high coherence parameter is chosen. For each PS, the history of movements can be reconstructed: each acquisition is a point in the series of linear displacement in the Line of Sight (LoS) direction.

For small areas the “advanced” analysis can be carried out, that seeks for non-linear displacements in the PS time-series. This technique has been successfully used in urban areas, where the presence of a large number of artificial structures guarantees a large number of possible PS. On the contrary, if no buildings are available, or in vegetated areas, its application may give no results. In some cases, also for calibration purposes, dedicated reflectors may be appositely installed in the area to be surveyed (corner reflectors).

The precision in the assessment of movement rates depends on the number of scenes, on the electromagnetic content of the target and on the orientation of the satellite with respect to the direction of the displacement. Under specific conditions, the precision can be sub-millimetric. One of the major problems in landslide applications is the correct assessment of horizontal and vertical movements starting from the LoS displacements. For instance, if the movement is perpendicular to the LoS, the SAR won't reveal any displacement. The separation of the SAR displacement, that is originally almost subvertical, into specific topographic directions (i.e., maximum slope gradient) have to be carried out with great care and validated by means of elaboration of the same scenes in both ascendant and descendent orbits. In this sense, field observations, geotechnical instrumentations and complementary geodetic techniques can be used to interpret and validate satellite measures. Besides these geometric constrains, the velocity of the displacements have to be taken into account. In fact, if the amount of displacements occurred between two subsequent acquisitions exceed one half of the wavelength of the used signal, the system won't be able to compute the exact number of phase cycles. This implies a practical limitation: if the displacements are small, the system is applicable and yields accurate results; if the displacements are large (or the landslide is rapid), the results could be unrealistic.

The integer numbers of half wavelengths between the two way trips, called ambiguities, are therefore unknown and the interferogram is “wrapped” because registers the fractional part of the phase change between two radar images. Thus, it has to be unwrapped with the

goal to know at each point on the interferogram, the integer part of the phase cycles (Kim and Kim, 2005; Zebker and Lu, 1998).

If wavelengths in the order of 5.6 cm (ERS, ENVISAT) and revisiting time of 35 days are considered, a part from the uncertainty depending on the availability of scenes at specific times, displacements larger than 5-6 cm/y will not be evidenced. With Radarsat sensor the velocities have to be lower than 15 cm/y.

As geometric leveling, also PS InSAR can deliver only relative displacements, measured with reference to an origin located within the scene. In this sense, both techniques undergo the critical choice of benchmarks as reference points.

One key point of the interferometric techniques is the possibility to exploit historical archives dating back to 1992 (ERS sensors). Therefore, the evolution of slope instability phenomena can be followed for a long period, even in areas where no geotechnical instrumentation or other measurement/monitoring have been carried out. At present, the availability of satellites with shorter revisiting times (i.e., 6-12 days) allows innovative techniques to be exploited. In the case of landslide monitoring, it will be possible to analyze a subset of frequent acquisitions with a sufficient population of scatterers. In particular, also semi-permanent scatterers could be used. These are represented by temporary targets that display high coherence for a period long enough to yield information on displacements, at least for elevation changes.

### 3.3.2. Terrestrial Radar Interferometry

In the frame of the application of radar interferometry to the control of slope movements, a Ground Based acquisition platform has been developed recently. At present, two different configurations are possible. In the first, a simple radar interferometer can monitor at high frequency (i.e. 50-100 Hz) a number of corner reflectors or of natural scatterers conveniently placed inside the scene at conveniently separated range distances. The second is a SAR mode, which gathers bidimensional pieces of information on the reflectivity of the scene (Ground-Based Synthetic Aperture Radar sensors GB-SAR) by means of an antenna able to move on a calibrated rail. Normally, radar with Continuous Wave and with a Stepped Frequency (CW-SF) are adopted and with the classical SAR focalization technique, the radar response of the object is converted into images that contain both amplitude and phase of the signal. As in satellite SAR, in two images acquired with slightly different geometry the phases differ themselves, with the sensor-target distance (range). Then, the phase of the complex product of two images, calculated pixel by pixel, represents an interferogram. By means of a differential interferometry analysis, the displacements can be quantified.

The instrumental range is in the order of few km (3-4 km), with very high resolutions (up to 0.1 mm in range). The possibility to repeat the measurement at a high temporal resolution allows for the estimation of both displacements and velocities and, thus, to an effective estimation of hazard.

As in the case of satellite SAR, atmospheric refraction can affect the interferograms. These effects have to be modeled and removed by means of polynomial models calibrated on stable areas located inside the scene (Noferini et al., 2005) or through a statistical analysis of historical data series. Moreover, the effects of temperature changes on instruments have to be compensated by means of self-calibrating procedures. Mechanical deformations of the rail over long time spans and the positioning of the rail in case of repeated measurements may

affect the results of this surveying method and have to be taken into account and thoroughly understood.

GB-SAR coordinates are generally quoted in a Cartesian reference system in which the X-axis is the cross range resolution (scanning direction of the sensor) and the Y-axis is the range resolution (line of sight of the radar). The resolution in range does not depend on the distance sensor-object albeit the resolution in cross range is lessened with the distance. In fact, the resolution in range  $\Delta r$  e cross range  $\Delta x$  can be calculated by the following equations:

$$\Delta r = \frac{c}{2B}; \Delta x = \frac{\lambda}{2L} D \quad (4)$$

where  $c$  is the velocity of radar signal propagation,  $B$  is the band of frequency,  $\lambda$  is the wavelength,  $L$  is the length of the rail and  $D$  is the sensor-object distance.

Temporal decorrelation (due to atmospheric conditions) and image co-registration issues have to be taken into account. The choice of the pixels to be used to assess the displacements depends on the coherence parameter. The coherence of radar images indicates the time constancy of the amplitude of the scattered radar signal (varying from 0 to 1 and normalized to 1) and for best performances the coherence of radar images should be as high as possible.

After some years of experimental applications, commercial platforms are presently available for technical exploitation. Though, in this framework, nor a comprehensive description or a classification of these instrumentations is feasible at present.

## 4. Selection of the Monitoring System

The selection of monitoring methods should start from clear statements of the four “Ws” (see also Corsini, 2008):

- What? What is exactly the object to be observed?
- Why? Which is the operational purpose of the observation?
- When? Which is the period of interest and how long is it lasting?
- Where? Which are the specific environmental conditions that must be coped with during the whole period of observation?

The list of answers should lead to the set up of an integrated monitoring system, including or excluding possible devices on the basis of different limiting factors, besides the economic ones. The first step is to assess the type of instability phenomena. When designing a monitoring system devoted to the assessment of superficial displacement, besides the type of landslide (Cruden and Varnes, 1996), i.e., fall, topple, slide, flow and lateral spreading and the material involved (rock, debris and earth), the area, the depth and the velocity are the most important factors to be taken into account (Table 3). The areal extension of the site can stretch from a single slope to the whole catchment or the mountain chain, depending on the scale and the purpose of the analysis. The depth of the landslide, from shallow (less than 5 m) to deep is important to interpret the pattern of displacement vectors and the volumes involved. The

velocity, together with the volume is important in the assessment of landslide magnitude. In fact, the landslide velocity scale (in Cruden and Varnes, 1996, slow is less than 13 meters per month, rapid is more than 1.8 m per hour) defines the probable destructive significance of landslides.

**Table 3. General characteristics of monitoring methods with reference to the type of instability phenomena**

Measurement Technique		Type of landslide					
		Area		Depth		Velocity	
		small	large	shallow	deep	slow	fast
Differential leveling		X	-	X	X	X	1
Total Stations		X	X	X	X	2	2
GNSS		X	X	X	X	X	X
Laser sensors	Terrestrial LiDAR	X	-	X	X	X	X
	Airborne LiDAR	X	X	X	X	X	X
Optical sensors	Satellite imagery	3	X	4	X	X	X
	Aerial Photogrammetry	X	X	X	X	X	X
	Terrestrial Photogrammetry	X	-	X	X	X	5
Radar sensors	Satellite/airborne DInSAR	-	X	X	X	X	6
	Terrestrial DInSAR	X	X	X	X	X	X
1 Depending on benchmarks condition; 2 Depending on targets condition and visibility; 3 Depending on scale and timing of acquisition HR; 4 Depending on scale and timing of flights; 5 Depending on the number of acquisitions for fixed cameras; 6 Depending on scale and timing of acquisition and on decorrelation.							

In the second step, further site constraints have to be analyzed, with reference to each monitoring technique (Table 4).

Site constraints (i.e., relief, vegetation, land use etc.) are among the most important. In fact, a heavy logistics of sensor installation and of surveys (baseline lengths, multipaths, session durations) may impede the application of some specific techniques. At the same time, sensor functioning and expected efforts for system management and maintenance (i.e., alimentation and energy consumption, memory size of data storage system, radio, GSM or cable transmission facilities etc.) are to be considered.

The productivity of the system, the possibility to transfer and process data in real-time or near real-time, together with the flexibility of the configuration, condition the choice of a specific technique also with reference to landslide risk management phases.

With reference to data acquisition platform (Table 3), remote-sensing systems do not require the deployment of active sensors directly in the area of interest and can be subdivided in space-borne, aerial and terrestrial systems, depending on the position of the sensor. Conversely, on-site systems need the exploitation of active sensors directly in the area to be observed.

**Table 4. General characteristics of monitoring methods, with reference to possible limiting factors**

Measurement techniques	Data acquisition platform	Spatial distribution	Temporal resolution	Site accessibility	Site visibility	Meteorological and light conditions	Application	Data availability	Main risk mitigation purpose
	Terrestrial Aerial Space-borne	Point-based Areal	Discontinuous Continuous		From ground From air/space	No - Cloudy foggy, rainy Daylight	Measurement Monitoring	Real time Non real time	DEM generation Displacement measurement Alerting/alarming
Differential leveling	X	X	X	X		X	X	X	X
Total Stations	X	X	X X	X	X	X X	X X	X X	X X X
GNSS	X X	X	X X	X			X X	X X	X X X
Airborne LiDAR	X	X	X		X	X	X	X	X
Terrestrial LiDAR	X	X	X		X	X	X	X	X
Satellite imagery		X	X			X X	X	X	X
Aerial Photogrammetry	X	X	X		X	X X	X	X	X
Terrestrial Photogrammetry	X	X	X X		X	X X	X X	X	X X X
Satellite/airborne DInSAR	X X	X X	X		X		X	X	X X
Terrestrial DInSAR	X	X X	X X		X	X	X X	X X	X X X

Spatial resolution is a very important issue to describe displacement patterns. Measurement and monitoring can be performed on single or multiple points, or over a large area containing many point-like sites.

Concerning temporal resolution, continuous monitoring imply that the data acquisition frequency can be fixed principally on the basis of the type of phenomenon (i.e., displacement rate, velocity, acceleration) and on the risk conditions to be managed so to obtain a “continuous” description of the landslide evolution. In some cases measurement are automated and sampling frequency can be varied, also operating on a remote basis. In the case of discontinuous monitoring, the measurements are performed periodically, thus may not describe the displacement patterns, especially in case of eventual acceleration and deceleration phases. If the acquisition is not-automated, the frequency may also depend upon personnel availability.

With particular reference to risk management procedure, in the case of real-time monitoring, data are acquired with a frequency that describes the evolution of the landslide, eventually transmitted and processed immediately. In some cases the procedure can be automatic and also directly connected to an alert or alarm system. In the case of non real-time monitoring data can be acquired, transmitted and processed both automatically and manually, but the exploitation of data is guaranteed by expert knowledge.



Some typical situations can exemplify selection, logistics and maintenance issues of surface displacement monitoring systems. In the period of the observation the site could be temporarily inaccessible, for example because of loss of road connections, extreme meteorological conditions, hazardous conditions etc. In this case, on-site systems are to be discarded. This applies in particular to differential leveling and GNSS techniques (excluding in situ continuous tracking stations), if the operators are not able to work safely. In the case of terrestrial devices (LiDAR, GBInSAR), the site to be accessible is the place where the instrument has to be installed. This location may raise a series of problems itself. In fact, in the period of interest the landslide site has necessarily to be visible from a panoramic point. If this is not possible, due to topographic effects, canopy etc., terrestrial remote sensing systems are not viable. Total stations, terrestrial laser scanners or radars need a panoramic location whose distance from the slope to be monitored is constrained by the range of the instrument. Moreover, the presence of vegetation may conceal the bare ground, limiting the potentiality of the systems (Tarchi et al., 2003a, b).

Similarly, if in the period of interest, again for topographical effects, vegetation, clouds etc. the area is not visible from air, aerial or satellite remote sensing systems are not feasible. On the one hand, airborne LiDAR can operate and yield high-resolution DEMs even with a medium density vegetation, after a post-processing procedure that eliminates (also automatically) vegetation, buildings etc. On the other hand, satellite SAR interferometry suffers from loss of coherence because of vegetation (Corsini et al., 2006), even if L-band SAR data have proved to be less affected by canopy than C-band SAR data.

The rates of movement are a constraining factor themselves. If they exceed a certain threshold, some systems have to be excluded (for instance DInSAR). An evaluation of the range of expected displacements, velocities and accelerations is of fundamental importance in the choice of the system, with reference to its range, temporal and spatial resolution.

## 5. Discussion

A complete study of the kinematics of landslides and their monitoring can be realised by means of the integration of geophysical, geotechnical and geodetic methods. Geophysical profiles can reveal the geometry of landslides and can identify sliding surfaces. Borehole inclinometers, strainmeters, extensometers permit to monitor with high accuracy small deformations at depth or at the surface, being in some cases limited to a range of slip or deformation. On the other hand, geodetic methods provide displacements of single or of clouds of points on the surface of the landslide, and may contribute to a better understanding of the dynamics of landslides.

All numerical models analyzing landslide evolution and/or models aiming to predict time of failure incorporate the kinematic characteristics of the movements i.e., displacement, velocity and acceleration (see the pioneering works of Saito, 1969 and Fukuzono, 1985), or as input or as reference data for calibration purposes. These characteristics can be estimated by differentiation with respect to time of displacement data, eventually recorded by a monitoring system. Clearly, when the accuracy of the instrumentation is comparable to the range of the displacements, this procedure can yield unacceptable results and some authors have proposed statistical data treatments (Simeoni et al., 2003). However, to analyze in detail landslide kinematics, especially if the monitoring is included in a real-time early warning system, it is

necessary to obtain precise 3D positions (millimetric) and a fine temporal resolution (hourly to infrahourly, depending on the velocity).

Leveling techniques are used to determine height difference between benchmarks and permit to realize highly accurate 1D networks. Digital levels with automatic height readouts from encoded rods and high precision Total Stations can be used for Spirit Leveling and for Trigonometric heighting (the latter particularly in measuring inaccessible points).

Electronic distance measurements carried out by means of modern robotic survey instruments provide real-time dislocations of control points of a landslide at a few millimeter accuracy (Stiros et al., 2004).

Horizontal and vertical angles measurements together with slope distances are collected by Total Stations: triangulation, trilateration, intersection - resection, polygonal, radial sideshot methods and more modern 3D or 2D network can be done. These geodetic networks opportunely compared furnish point displacements on a discontinuous basis, but continuous monitoring can be realized relatively easily

It is now a common practice to monitor landslide displacements by GNSS (Coe et al., 2003; Gili et al., 2000; Malet et al., 2002; Moss, 2000; Squarzoni et al., 2003; 2005).

Several GPS survey techniques can be used (static, fast static, kinematic, Real Time Kinematic etc.). At the same time different methods of data processing (differenced or undifferenced) result in different accuracy of the data (Hofmann-Wellenhof et al., 2001).

With respect to conventional techniques, these approaches have proved efficient in depicting small ground displacements in 3D. GNSS has been used in repeated measurements (Gili et al., 2000; Hiura et al., 1996; Jackson et al., 1996) as a complement to conventional geodetic methods. At present, the continuous monitoring of landslide displacements with GNSS can be performed operationally, thanks to its cost reduction with respect to the recent past and some successful applications of low-cost instruments have been proposed (Corsini, 2008). GPS kinematic surveying proved efficient in providing a detailed and accurate topographic model. At least in open terrains, it should be considered complementary with precise point positioning in ground displacement monitoring.

In these cases, some errors have to be taken into account in the interpretation of the data set. In fact, GNSS measurements can reach a millimeter-level of accuracy for long observation sessions (typically continuous observations), but the accuracy tends to decrease with the duration of the observation sessions, because of errors introduced by satellite constellation variations and multipath effects (Genrich and Bock, 1992).

Terrestrial or air photogrammetry provides 3D coordinates of a number of points and supports the setting up of geomorphological maps and in particular of the generation of DEMs and associated cross-sections (Oka, 1998; Weber and Herrmann, 2000). Historical displacement data may be obtained from the stereophotogrammetric analysis of aerial photographs, a method pioneered by Chandler and Brunsden (1995) and recently much used (e.g. Baldi et al., 2008; D'Agata and Zanutta, 2007; Demoulin, 2006; Hapke, 2005; Kerle, 2002; Lantuit and Pollard, 2005; Zanutta et al., 2006). Stereophotogrammetry of historical aerial images is an indispensable data source for extending rate estimates over longer time spans.

LS technology has proved to be very interesting to monitor slope displacements, as it provides a quick collection of topographical data and allows the representation of large surfaces with dense spatial sampling (Abellan et al, 2006; Conforti et al, 2005; Glenn et al., 2006; Lim et al., 2005, Monserrat and Crosetto, 2008; Oppikofer et al, 2008; Rosser et al.,

2007). In particular, from a dense displacement field, the deformations of the ground surface of a landslide can be computed. In this way, the tensional state can be evaluated, together with a series of parameters useful for stability analyses. In particular, TLS is a powerful and cost-effective technology to detect slope movements. In fact, the comparison of multitemporal DEMs, controlled by a rigid geodetic network, can provide the reconstruction of the displacement field, by means of surface matching. Thanks to the high resolution, small topographic changes, that are relevant for understanding the landslide kinematics and dynamics, can be fruitfully detected and measured. Conversely, if the displacements are large, the development of complex surface changes may not allow displacements to be detected, even at a very short time resolution. In addition, recent works by Travelletti et al. (2008) demonstrate the need to calibrate the scans on stable areas to maximize the accuracy and propose different techniques to analyze topographical data. Cloud to cloud comparisons give a good approximation of the displacement magnitudes, with constraints due to the geometry of the slope and of displacement vectors. Relief image correlation has been proposed as an alternative, with successive scans systematically taken at the same point, chosen also in order to assure an adequate resolution to discriminate objects. The benchmark technique on rebuilt objects is the most reliable method to identify both the direction and magnitude of displacement vectors (Travelletti et al., 2008). It is clear that a cross-validation of these data with conventional geotechnical data is of great importance.

Synthetic Aperture Radar Interferometry (InSAR) from satellite is a powerful and established technique for mapping land surface deformation with cm to mm accuracy at fine spatial resolution over large areas (Berardino et al., 2003; Bulmer et al., 2006; Catani et al., 2005; Kimura and Yamaguchi, 2000; Werner et al., 2003). Surface deformations include subsidence, tectonic and volcanic activity, landslides and glaciers. Notwithstanding limitations due to temporal and geometric decorrelations, satellite line of sight and tropospheric path delay, in recent years InSAR was also successfully applied in mountainous areas to detect surface displacement of sparsely vegetated and built-up areas. Depending on data availability, displacement velocities, land cover and season, satellite SAR data from various sensors, with different acquisition time intervals and frequencies may be used. The exploitation of space-borne radar interferometry as an element in a warning system is however constrained by the specific space-borne radar imaging geometry, the typical multiple-week repeat interval, and several uncertainties in the data availability. Most of these limitations can be overcome with an in-situ radar imaging system. In fact, the so-called continuous GB-SAR has been confirmed to be an effective technique for retrieving movements over wide areas (Rowlands et al., 2003, Tarchi et al. 2003a, b). Terrestrial radar images are typically acquired in a few minutes and phase differences between successive images taken from the same location are used to determine millimetric line-of-sight displacements, on a continuous basis. These techniques can provide accurate results in different observational conditions but some limitations do exist. Firstly, no significant data can be acquired in case of extensive vegetation cover. Therefore, the development of specific tools in post-processing phase is necessary in order to overcome these problems.

A lot of pieces of information can be acquired by TLS and InSAR, with high spatial sampling. Therefore specific data-processing software and expertise are necessary in the elaboration and interpretation phases.

The InSAR spatial resolution is of a few meters. Instead, the corresponding TLS resolution could be centimetric, on the basis of observational conditions. The two techniques

are not interchangeable but complementary, and their integration could provide a detailed picture of displacement patterns. For instance, large displacement could be detected by multitemporal TLS observations, and a continuous detailed monitoring may be performed through InSAR. The TLS can be used in order to generate an accurate digital model on which the radar data can be rendered as textures (Teza et al., 2007; 2008). In perspective, the two techniques could be interfaced in order to obtain an effective and efficient monitoring and warning system for risk mitigation.

## 6. Final Remarks

In recent years, the development of remote sensing techniques has produced significant benefits for landslide risk management practices. The data obtained from different types of sensors have practical applications in all stages of landslide risk mitigation: from characterization, prediction and early warning, to post-crisis management. The strategic importance of remote sensing in natural hazard and risk management is emphasized by the large number of international initiatives sponsored by agencies such as the United Nations (UN), the European Space Agency (ESA), the World Meteorological Organization (WMO), the European Union (EU) and many others. Outstanding programs include the Global Landslides Observation Strategy of the International Consortium on Landslides (ICL), the International Global Observing Strategy – Geohazards (IGOS-G) and Global Monitoring for Environment and Security (GMES). Space-borne, aerial and terrestrial remote sensing techniques have allowed surface displacements to be detected at different scales, from a single slope to catchments and whole mountain chains, without the deployment of any active sensor in the study areas. Earth Observation (EO) data have been utilized on the one hand to update landslide inventories, with the identification of previously unknown landslides and the confirmation or modification of landslide boundaries and state of activity. On the other hand, landslide hazard and risk assessment procedures at regional scales have been improved.

Remote sensing systems are generally characterised by varying ground resolution, discontinuous data acquisition and non real time data availability. Moreover, the elaboration of images is generally complex and a specific expertise is needed. Ground-based systems, such as total stations, terrestrial radar and GNSS devices, on-demand spatial resolution, pseudo-continuous data and real time accessibility are feasible. In this sense, ground-based systems have shown to be innovative early warning systems especially for slow-moving landslides, while coupled techniques involving both optical and radar images can provide support also in the management of crisis and post-crisis phases.

GNSS, LS and InSAR techniques are not to be used as a substitute for traditional geodetic techniques, but are to be integrated with both a topographical network and in situ geotechnical instrumentation, also to be able to cross validate each data set. All these pieces of information are used to describe surface changes and consequently are the prime tool for the physical interpretation of the deformation field. In fact, a detailed geometric model of the ground surface and a dense displacement field acquired repeatedly, with a suitable recurring time, can be very well integrated in a numerical model both as input and as calibration.

## Acknowledgement

The authors wish to thank to Dr. Andrea Lugli for fruitful discussions about radar interferometry.

## References

- Abellan A., Vilaplana J.M., Martinez J., 2006. Application of a long-range Terrestrial Laser Scanner to a detailed rockfall study at Vall de Nuria (Eastern Pyrenees, Spain). *Engineering geology*, **88**, 3-4, 136-148.
- Ackermann F., 1999. Airborne Laser Scanning - Present Status and Future Expectations. International Society for Photogrammetry and Remote Sensing, *Journal of Photogrammetry & Remote Sensing*, Elsevier B.V., 54, 64-67.
- Alharthy A., Bethel J., Mikhail E.M., 2004. Analysis and accuracy assessment of airborne laserscanning system. In *International Archives of Photogrammetry, Remote Sensing and Spatial Information Sciences*, Istanbul, Turkey, XXXV, B2, 144-149.
- Allen C.T., 1995. Interferometric synthetic aperture radar (review article). *IEEE Geoscience and Remote Sensing Society Newsletter*, **96**, 6-13.
- Angeli M.C., Pasuto A., Silvano S., 2000. A critical review of landslide monitoring experiences. *Engineering Geology* **55**, 133-147.
- Antonello G., Casagli N., Farina P., Leva D., Nico G., Sieber A.J., Tarchi D., 2004. Ground-based SAR interferometry for monitoring mass movements. *Landslides*, **1**, 21-28.
- Baily B., Collier P., Farres P., Inkpen R., Pearson A., 2003. Comparative assessment of analytical and digital photogrammetric methods in the construction of DEMs of geomorphological forms. *Earth Surface Processes and Landforms, Wiley InterScience*, **28**, 307-320.
- Balan P., Mather P.M., 1999. *Evaluation of the accuracy on InSAR DEM as a function of baseline, wavelength and resolution*. Fringe'99 Workshop, Advancing ERS SAR Interferometry from Applications towards operations, Liège, Belgium, 10-12 November, 1-8.
- Baldi P., Cenni N., Fabris M., Zanutta A., 2008. Kinematics of a landslide derived from archival photogrammetry and GPS data. *Geomorphology* **102**, 3-4, 435-444.
- Baltsavias E.P., 1999. Airborne laser scanning: basic relations and formulas. International Society for Photogrammetry and Remote Sensing, *Journal of Photogrammetry & Remote Sensing*, Elsevier B.V., 54, 199-214.
- Bayoud F. A., 2006. Leica's Pinpoint EDM Technology with Modified Signal Processing and Novel Optomechanical Features. *Proceedings of XXIII FIG Congress INTERGEO*, 8-13 October 2006, Munich. <http://www.fig.net/pub/fig2006/techprog.htm>.
- Beavan J., 2005. Noise properties of continuous GPS data from concrete pillar geodetic monuments in New Zealand and comparison with data from U.S. deep drilled braced monuments. *Journal of Geophysical Research*, **110**, B08410, doi:10.1029/2005JB003642.
- Berardino P., Costantini M., Franceschetti G., Iodice A., Pietranera L., Rizzo V., 2003. Use of differential SAR interferometry in monitoring and modeling large slope instability at Maratea (Basilicata, Italy). *Engineering Geology*, **68**, 31-51.

- Bernstein R., 1983. Image geometry and rectification. In: R. N. Colwell (ed.), *Manual of Remote Sensing, American Society of Photogrammetry*, Falls Church (VA), 881-884.
- Bitelli G., Capra A., Zanutta A., 2002. Digital Photogrammetry and Laser Scanning in Surveying the "Nymphaea" in Pompeii. *Proceedings CIPA WG 6 International Workshop on Scanning for Cultural Heritage Recording*, Corfu (Greece), 1-2 september 2002, Wolfgang Boehler, ZITI, Thessaloniki (Greece), 115-120.
- Bitelli G., Dubbini M., Zanutta A., 2004. Terrestrial Laser Scanning and Digital Photogrammetry techniques to monitor landslide bodies. *International Archives of the Photogrammetry Remote Sensing and Spatial Information Sciences*, **35**, B, 246 – 251.
- Bitelli G., Gusella L., Mancini F., Pino I., Vittuari L. 2008. Analysis of multispectral satellite images for ice-streams velocity evaluation. *Terra Antartica Reports*, **14**, 1-7.
- Boehler W., Marbs A., 2006. Comparing different Laser Scanners. In *Laser Scanning terrestre*, Crosilla F., Dequal S., Eds, International Centre for Mechanical Sciences, CISM (ITA), Collana di Geodesia e Cartografia, ISBN: 8885137199, 19-37.
- Bornaz L., Rinaudo F; Lingua A., 2002. Engineering and environmental applications of laser scanner techniques. In *International Archives of Photogrammetry and Remote Sensing*, B, 40-43.
- Bretar F., Pierrot-Deseilligny M., Roux M., 2003. Estimating Intrinsic Accuracy of Airborne Laser Data with Local 3D-Offsets. In: International Society for Photogrammetry and Remote Sensing, III/3, 3-D reconstruction from airborne laser scanner and InSAR data, Dresden, Germany.
- Brinkman R., O'Neill C., 2000. LIDAR and Photogrammetric Mapping. *The Military Engineer*, 605.
- Brückl E., Brunner F.K., Kraus K., 2006. Kinematics of a deep-seated landslide derived from photogrammetric, GPS and geophysical data. *Engineering Geology*, **88**, 149-159.
- Brunsdon D., Chandler J.H., 1996. Development of an episodic landform change model based upon the Black Ven mudslide, 1946 -1995. In: Anderson, M.G., Brooks, S.M. Eds., *Advances in Hillslope Processes*. Wiley, Chichester, UK, 869- 896.
- Bulmer M.H., Petley D.N., Murphy W., Mantovani F., 2006. Detecting slope deformation using two-pass differential interferometry: Implications for landslide studies on Earth and other planetary bodies. *Journal of Geophysical Research*, **111**: E06S16, doi:10.1029/2005JE002593.
- Bürgmann R., Rosen P.A., Fielding E.J., 2000. Synthetic Aperture Radar Interferometry to measure Earth's surface topography and its deformation. *Annual Review of Earth and Planetary Sciences.*, **28**, 169-209.
- Canuti P., Casagli N., Catani F., Falorni G., Farina P., 2007. Integration of Remote Sensing Techniques in Different Stages of Landslide Response. *Progress in Landslide Science, Part III*. Springer Berlin Heidelberg, 251-260.
- Casson B., Delacourt C., Allemand P., 2005. Contribution of multi-temporal remote sensing images to characterize landslide slip surface - Application to the La Clapiere landslide (France). *Natural Hazards and Earth System Sciences*, **5**, 425-437.
- Catani F., Farina P., Moretti S., Nico G., Strozzi T., 2005. On the application of SAR interferometry to geomorphological studies: estimation of landform attributes and mass movements. *Geomorphology*, **66**, 1-4, 119-131.
- Chadwick J., Dorscha S., Glenna N., Thackraya G., Shillingb K., 2005. Application of multi-temporal high-resolution imagery and GPS in a study of the motion of a canyon rim

- landslide. International Society for Photogrammetry and Remote Sensing, *Journal of Photogrammetry & Remote Sensing*, Elsevier B.V., 59, 212- 221.
- Chandler J.H., Cooper M., 1988a. Monitoring the development of landslides using archival photography and analytical photogrammetry. *Land Miner Surveying Royal Institution of Chartered Surveyors* **6**, 576-584.
- Chandler J.H., Cooper M., 1988b. The extraction of positional data from historical photographs and their application in geomorphology. *Photogrammetric Record* **13**, 73, 69-78.
- Chandler J.H., Brunsden D., 1995. Steady state behaviour of the Black Ven mudslide: the application of archival analytical photogrammetry to study of landform change. *Earth Surface Processes and Landforms, Wiley InterScience*, **20**, 255-275.
- Chen R.F, Chang K.J., Angelier J., Chan Y.C., Deffontaines B., Lee C.T., Lin M.L., 2006. Topographical changes revealed by high-resolution airborne LiDAR data: The 1999 Tsaoling landslide induced by the Chi-Chi earthquake. *Engineering Geology*, **88**, 160-172.
- Ciddor P.E., 2002. Refractive index of air: 3. The roles of CO<sub>2</sub>, H<sub>2</sub>O, and refractivity virials. *Applied Optics* **41**, 12, 2292-2298.
- Coe J., Ellis W., Godt J., Savage W., Savage J., Michael J., Kibler J., Powers P., Lidke D., Debray S., 2003. Seasonal movement of the Slumgullion landslide determined from Global Positioning System surveys and field instrumentation, July 1998-March 2002. *Engineering Geology*, **68**, 67-101.
- Colesanti C., Ferretti A., Prati C., Rocca F., 2003. Monitoring landslides and tectonic motions with the Permanent Scatterers Technique. *Engineering Geology*, **68**, 3-14.
- Colesanti C., Wasowski J., 2006. Investigating landslides with satellite Synthetic Aperture Radar (SAR) interferometry. *Engineering Geology*, **88**, 3-4, 173-199.
- Conforti, D., Deline, P., Mortara, G., Tamburini, A., 2005. Report on the Joint ISPRS Commission VI, Workshop "Terrestrial scanning lidar technology applied to study the evolution of the ice-contact Miage Lake (Mont Blanc, Italy). [http://www.innovmetric.com/Surveying/english/pdf/miage\\_lake.pdf](http://www.innovmetric.com/Surveying/english/pdf/miage_lake.pdf) (accessed 11 Jan. 2008).
- Corsini A. 2008. Monitoring Methods: Systems Behind a Safer Environment. In. R. Mayer, A. Bohner, C. Plank, B. Marold (Eds), Results of the International conference monitor/08. Agricultural Research and Education-Centre Raumberg-Gumpenstein (Irdning, Austria), ISBN 978-3-902559-19-7, 47-54.
- Corsini A., Borgatti L., Caputo G., De Simone N., Sartini G., Truffelli G., 2006. Investigation and monitoring in support of the structural mitigation of large slow moving landslides: an example from Ca' Lita (Northern Apennines, Reggio Emilia, Italy). *Natural Hazards and Earth System Science*, **6**, 1, 55-61.
- Corsini A., Borgatti L., Coren F., Vellico M., 2007. Use of multitemporal airborne LiDAR surveys to analyse post-failure behaviour of earthslides. *Canadian Journal of Remote Sensing*, **33**, 2, 116-120.
- Corsini A., Farina P., Antonello G., Barbieri M., Casagli N., Coren F., Guerri L., Ronchetti F., Sterzai P., Tarchi D., 2006. Spaceborne and ground-based SAR interferometry as tools for landslide hazard management in civil protection. *International Journal of Remote Sensing* **27**, 12, 2351-2369.

- Crosetto M., 2002. Calibration and Validation of SAR interferometry for DEM generation, International Society for Photogrammetry and Remote Sensing, *Journal of Photogrammetry & Remote Sensing*, Elsevier B.V., 57, 213-227.
- Crosta G.B., Agliardi F., 2003. Failure forecast for large rock-slides by surface displacement measurements. *Canadian Geotechnical Journal*, **40**, 176-191.
- Cruden D.M., Varnes D.J., 1996. Landslides types and processes. In: *Landslides: Investigation and control, Special Report 247*. Transportation Research Board, Washington, 36-75.
- Curlander J.C., McDonough R.N., 1992. *Synthetic Aperture Radar: Systems and Signal Processing*. John Wiley, New York, ISBN: 978-0-471-85770-9.
- D'Agata C., Zanutta A., 2007. Reconstruction by indirect source of the recent changes of a debris covered glacier (Brenva, Mont Blanc Massif, Italy): methods, results and validation. *Global and Planetary Change* **56**, 57-68.
- Delacourt C., Allemand P., Berthier E., Raucoules D., Casson B., Grandjean P., Pambrun C., Varel E., 2007. Remote-sensing techniques for analysing landslide kinematics: a review. *Bulletin de la Societe Geologique de France* **178**, 2, 89-100.
- Demoulin A., 2006. Monitoring and mapping landslide displacements: a combined DGPS-stereophotogrammetric approach for detailed short- and long-term rate estimates. *Terra Nova*, **18**, 290-298.
- Dewitte O., Demoulin A., 2005. Morphometry and kinematics of land-slides inferred from precise DTMs in West Belgium. *Natural Hazards and Earth System Sciences*, **5**, 259-265.
- Dewitte O., Jasselette J.-C., Cornet Y., Van Den Eeckhaut M., Collignon A., Poesen J., Demoulin A., 2008. Tracking landslide displacements by multi-temporal DTMs: A combined aerial stereophotogrammetric and LIDAR approach in western Belgium. *Engineering Geology*, **99**, 11-22.
- Dunnicliff J., 1988. *Geotechnical Instrumentation for Monitoring Field Performance*. Wiley, New York.
- Einstein H., Sousa R., 2007. Warning Systems for Natural Threats. *Georisk: Assessment and Management of Risk for Engineered Systems and Geohazards*, **1**, 1, 3-20.
- Elachi C., 1980. Spaceborne imaging radar: geologic and oceanographic applications. *Science*, **209**, 1073-1082.
- Fangi G., Fiori F., Gagliardini G., Malinverni E.S., 2001. Fast And Accurate Close Range 3d Modelling By Laser Scanning System. *Proceedings of XVIII International Symposium of CIPA*, Postdam, 196-203.
- Farina P., Colombo D., Fumagalli A., Marks F., Moretti S., 2006. Permanent Scatterers for landslide investigations: outcomes from the ESA-SLAM project. *Engineering Geology* **88**, 200-217.
- Farina P., Casagli N., Ferretti A., 2008. Radar-interpretation of InSAR measurements for landslide investigations in civil protection practices. Proceedings of the First North American Landslide Conference in Vail, Colorado, 3-8 June 2007.
- Ferretti A., Prati C., Rocca F., 2001. Permanent scatters in SAR interferometry. *IEEE Transactions on Geoscience and Remote Sensing*, **39**, 1, 8-20.
- Ferretti A., Prati C., Rocca F., Casagli N., Farina P., Young B., 2005. Permanent Scatterers technology: a powerful state of the art tool for historic and future monitoring of landslides and other terrain instability phenomena. *Proceeding of 2005 International*



- Conference on Landslide Risk Management*, A.A. Balkema, Vancouver, Canada, CD-Rom.
- French J.R., 2003. Airborne LiDAR in support of geomorphological and hydraulic modeling. *Earth Surface Processes and Landforms, Wiley InterScience*, **28**, 321-335.
- Frezzotti M., Capra A., Vittuari L., 1998. Comparison between glacier ice velocities inferred from GPS and sequential satellite images. *Annals of Glaciology*, **27**, 54-60.
- Fukuzono T.A., 1985. New method for Predicting the Failure Time of a Slope. *Proceeding of the 4th International Conference and Field Workshop on Landslides*, Tokyo, 145-150.
- Genrich, J.F., Bock, Y., 1992. Rapid resolution of crustal motion at short ranges with Global Positioning System. *Journal of Geophysical Research* **96**, 3261– 3269.
- Gens R., Vangenderen J.L., 1996. SAR Interferometry - Issues, techniques, applications. *International Journal of Remote Sensing*, **17**, 10, 1803-1835.
- Ghilani C.D., Wolf P.R., 2008. *Elementary Surveying: An Introduction to Geomatics*, 12th edition, Pearson International Edition, Prentice Hall.
- Gili J.A., Corominas J., Rius J., 2000. Using Global Positioning System techniques in landslide monitoring. *Engineering Geology*, **55**, 167-192.
- Glade T., Anderson M., Crozier M.J., 2005. *Landslide hazard and risk*. Wiley.
- Glenn N.F., Streutker D.R., Chadwick D.J., Thackray G.D., Dorsch S.J., 2006. Analysis of LiDAR-derived topographic information for characterizing and differentiating landslide morphology and activity. *Geomorphology*, **73**, 1-2, 131-148.
- Graham L.C., 1974. Synthetic Interferometer Radar for Topographic Mapping. *Proceeding of the IEEE*, **62**, 2, 763-768.
- Gutelius W., Carter W., Shrestha R., Medvedev E., Gutierz R., Gibeaut J., 1998. Engineering applications of airborne scanning lasers: reports from the field. *Photogrammetric Engineering & Remote Sensing*, **64**, 246-253.
- Guzzetti F., Peruccacci S., Rossi M., Stark C.P., 2008. The rainfall intensity-duration control of shallow landslides and debris flows: an update. *Landslides*, **5**, 1, 3-17.
- Hahn M., Förstner W., 1988. The Applicability of a Feature Based Matching and a Least Squares Matching Algorithm for DTM Acquisition. *International Archives of Photogrammetry and Remote Sensing, Kyoto*, **27**, B9, III, 137-150.
- Hapke C., 2005. Estimation of regional material yield from coastal landslides based on historical digital terrain modelling. *Earth Surface Process Landforms*, **3**, 679-697.
- Harris C., Luetschg M., Davies M.C.R., Smith F., Christiansen H.H., Isaksen K., 2007. Field instrumentation for real-time monitoring of periglacial solifluction. *Permafrost and Periglacial Processes*, **18**, 1, 105-114.
- Heipke C., 1996. Overview of image matching techniques. In: Kölbl O., Editor, *OEEPE - Workshop on Application of Digital Photogrammetric Workstations, The European Organization for Experimental Photogrammetric Research Official Publications*, **33**, 173–189.
- Helava U.V., 1988. Object space least square correlation. *Photogrammetric Engineering & Remote Sensing*, **54**, 6, 711-714.
- Hilley G.E., Burgmann R., Ferretti A., Novali F., Rocca F., 2004. Dynamics of slow-moving landslides from Permanent Scatterer analysis. *Science*, **304**, 5679, 1952-1955.
- Hiura, H., Sassa, K., Fukuoka, H., 1996. Monitoring system of a crystalline schist-landslide: three dimensional displacement meters and underground erosion. VIIth International Symposium on Landslides, Trondheim, vol. 3. Balkema, Rotterdam, pp. 1141– 1146.

- Hengl T., Reuter H.I., 2008. Geomorphometry: Concepts, Software, Applications. *Developments in Soil Science*, vol. 33, Elsevier, 772.
- Hofmann-Wellenhof B., Lichtenegger H., Collins J., 2001. *GPS: Theory and Practice* (Fifth Revised Edition). Springer-Verlag Wien, 370 pgs, ISBN 978-3211835340.
- Hsiao K.H., Liu J.K., Yu M.F., Tseng Y.H., 2004. Change detection of landslide terrains using ground-based LiDAR data. *International Society for Photogrammetry and Remote Sensing*, Istanbul, Turkey, VII/5.
- Inggis M.R., Lord R.T., 2000. Applications of Satellite Imaging Radar. In *Proceedings of the Satellite 2000 Symposium, Marshalltown, South Africa*, South African Institute of Electrical Engineers, 1-8.
- Jackson, M.E., Bodin, P.W., Savage, W.Z., Nel, E.M., 1996. Measurement of local horizontal velocities on the Slumgullion landslide using the Global Positioning System. *U.S. Geological Survey Bulletin* **2130**, 93–95.
- Jensen H., Graham L.C., Pocello L.J., Leith E.N., 1977. Side-looking airborne radar. *Scientific American*, **237**, 84-95.
- Jimenez A., Osorio A., Marino-Tapia I., Davidson M., Medina R., Kroon A., Archetti R., Ciavola P., Aarninkhof S., 2007. Beach recreation planning using video-derived coastal state indicators. *Coastal Engineering*, **54**, 6-7, 504 - 522.
- Kääb A., 2000. Photogrammetry for early recognition of high mountain hazards: new techniques and applications. *Physics and Chemistry of the Earth*, **25**, 9, 765-770.
- Kampes B.M., 2006. Radar Interferometry: Persistent Scatterer Technique. Series: *Remote Sensing and Digital Image Processing*, 12, Springer, Germany, XVI, 211, ISBN: 978-1-4020-4576-9.
- Kerle N., 2002. Volume estimation of the 1998 flank collapse at Casita volcano, Nicaragua: a comparison of photogrammetric and conventional techniques. *Earth Surface Processes and Landforms, Wiley InterScience*, **27**, 759-772.
- Kienholz H., 1994. Naturgefahren - Naturrisiken im Gebirge. *Schweizerische Zeitschrift für Forstwesen*, 145, 1-25.
- Kilian J., Haala N., Englich M., 1996. Capture and Evaluation of airborne laser scanner data. *Int. Arch. Photogramm. Remote Sensing* **31**, B3, 383-388.
- Kim S.B., Kim Y.S., 2005. Least squares phase unwrapping in wavelet domain. *IEE Proceedings - Vision, Image and Signal Processing*, **152**, 3, 261-267.
- Kimura H., Yamaguchi Y., 2000. Detection of landslide areas using satellite radar interferometer. *Photogrammetric Engineering and Remote Sensing, Journal of the American Society for Photogrammetry and Remote Sensing*, **66**, 3, 337-344.
- Kraus K., 1993. *Photogrammetry, volume 1: Fundamentals and standard processes*. Dümmlers Verlag, Bonn.
- Kraus K., 1997. *Photogrammetry, volume 2: Advanced methods and applications*. Dümmlers Verlag, Bonn.
- Lane S.N., Chandler J.H., 2003. Editorial: The generation of high quality topographic data for hydrology and geomorphology: new data source, new applications and new problems. *Earth Surface Processes and Landforms, Wiley InterScience*, **28**, 229-230.
- Langbein J., 2004. Noise in two-color electronic distance meter measurements revisited. *Journal of Geophysical Research*, **109**, B04406, doi:10.1029/2003JB002819.

- Lantuit H., Pollard W., 2005. Temporal stereophotogrammetric analysis of retrogressive thaw slumps on Herschel Island, Yukon Territory. *Natural Hazards and Earth System Sciences*, **5**, 413-423.
- Leroueil S., Locat J., Vaunat J., Picarelli L., Lee H., Faure R., 1996. Geotechnical characterization of slope movements. In: K. Senneset, Editor, *Landslides*, Balkema, Rotterdam, 53-74.
- Li F.K., Goldstein R.M., 1990. Studies of Multibaseline Spaceborne Interferometric Synthetic Aperture Radars. *IEEE Transactions on Geoscience and Remote Sensing*, **28**, 1, 88-97.
- Lim M., Petley D.N., Rosser N.J., Allison R.J., Long A.J., Pybus D., 2005. Combined digital photogrammetry and time-of-flight laser scanning for monitoring cliff evolution. *The Photogrammetric Record*, **20**, 109-129.
- Luzi G., Pieraccini M., Mecatti D., Noferini L., Macaluso G., Galgaro A., Atzeni C., 2006. Advances in ground-based microwave interferometry for landslide survey: a case study. *International Journal of Remote Sensing*, **27**, 2331-2350.
- Madsen S.N., Martin J.M., Zebker H. A., 1995. Analysis and evaluation of the NASA/JPL TOPSAR across track interferometric SAR system. *IEEE Transactions on Geoscience and Remote Sensing*, **33**, 2, 383-391.
- Madsen S.N., Zebker H.A., 1999. Synthetic aperture radar interferometry: Principles and applications. In *Manual of Remote Sensing*, Boston, MA, Artech House, 3, 6.
- Malet J.P., Maquaire O., Calais E., 2002. The use of Global Positioning System for the continuous monitoring of landslides. Application to the Super Sauze earthflow (Alpes-de-Haute-Provence, France). *Geomorphology*, **43**, 33-54.
- Mantovani F., Soeters R., Van Westen C.J., 1996. Remote sensing techniques for landslide studies and hazard zonation in Europe. *Geomorphology*, **15**(3-4), 213-225.
- Massonnet D., Feigl K., 1998. Radar interferometry and its application to changes in the earth's surface. *Reviews of Geophysics*, **36**, 4, 441-500.
- McKean J., Roering J., 2004. Objective landslide detection and surface morphology mapping using high-resolution airborne laser altimetry. *Geomorphology*, **57**, 331-351.
- Metternicht G., Hurni L., Gogu R., 2005. Remote sensing of landslides: An analysis of the potential contribution to geo-spatial systems for hazard assessment in mountainous environments. *Remote Sensing of Environment*, **98**, 284-303.
- Mikkelsen P.E., 1996. Field instrumentation. In: Turner, A.K., Schuster, R.L. (Eds.), *Landslides Investigation and Mitigation, TRB Special Report 247*, National Academy Press, Washington DC, 278-316.
- Monserat, O. and Crosetto, M., 2008. Deformation measurement using terrestrial laser scanning data and least squares 3D surface matching. *ISPRS Journal of Photogrammetry and Remote Sensing*, **63**(1), 142-154.
- Mora P., Baldi P., Casula G., Fabris M., Ghirotti M., Mazzini E., Pesci A., 2003. Global positioning systems and digital photogrammetry for the monitoring of mass movements: application to the Ca' di Malta landslide (northern Apennines, Italy). *Engineering Geology* **68**, 103-121.
- Moreira J., Schwabisch M., Fornaro G., Lunari R., Bamler R., Just D., Steinbrecher U., Breit H., Eineder M., Franceschetti I.G., Geudtner D., Rinkel H., 1995. X-SAR interferometry: first results. *IEEE Transactions on Geoscience and Remote Sensing*, **33**, 950-956.

- Moss J., 2000. Using the Global Positioning System to monitor dynamic ground deformation networks on potentially active landslides. *International Journal of Applied Earth Observation and Geoinformation* **2**, 24-32.
- Noferini L., Pieraccini M., Mecatti D., Luzi G., Atzeni C., Tamburini A., Broccolato M., 2005. Permanent scatterers analysis for atmospheric correction in ground-based SAR interferometry. *IEEE Transactions on Geoscience and Remote Sensing*, **43**, 7, 1459-1471.
- Oka, N., 1998. Applications of photogrammetry to the field observation of failed slopes. *Engineering Geology* **50**, 85– 100.
- Oppifofer, T., Jaboyedoff, M., Blikra, L.H., Derron, M.-H., 2008. Characterization and monitoring of the Aknes Rockslide using terrestrial laser scanning. 4th Geohazards Canadian Congress, University of Laval, Quebec, 20-24 May 2008.
- Petley D.N., Bulmer M.H., Murphy W., 2002. Patterns of movement in rotational and translational landslides. *Geology*, **30**, 719-722.
- Petley D.N., Mantovani F., Bulmer M.H., Zannoni A., 2005. The use of surface monitoring data for the interpretation of landslide movement patterns. *Geomorphology*, **66**, 133-147.
- Rosser, N.J., Petley, D.N., Dunning, S.A., Lim, M. and Ball, S., 2007. The surface expression of strain accumulation in failing rock masses. In: Eberhardt, E., Stead, D. and Morrison, E. (Editors), *Rock mechanics: Meeting Society's challenges and demands*. Proceedings of the 1st Canada–U.S. Rock Mechanics Slob, S. and Hack, R. 2004. 3D Terrestrial Laser Scanning as a New Field Measurements and Monitoring Technique. In Hack, R., Azzam, R. and Charlier, R. (Ed): *Engineering Geology for Infrastructure Planning in Europe. A European Perspective*. Lecture Note in Earth Sciences. Springer, Berlin / Heidelberg, pp. 179-190.
- Rowlands K., Jones L., Whitworth M., 2003. Landslide laser scanning: a new look at an old problem. *Quarterly Journal of Engineering Geology and Hydrogeology* **36**, 155- 157.
- Rudolf H., Leva D., Tarchi D., Sieber A.J., 1999. A Mobile and Versatile SAR System. In *Proceedings of Geoscience and Remote Sensing Symposium, IEEE International*, **1**, 592-594.
- Saito M., 1969. Forecasting time of slope failure by tertiary creep. *Proceeding of the 7th International Conference of Soil Mechanics and Foundation Engineering, Mexico*, **I**, 291-340.
- Scambos T.A., Dutkiewicz M.J., Wilson J.C., Bindshadler R.A., 1992. Application of image crosscorrelation to the measurement of glacier velocity using satellite image data. *Remote Sensing of Environment*, **42**, 3, 177-186.
- Simeoni L., Proietti T., Mongiovì L., 2003. Analysis and prediction of slow landslide evolutions by using automatic displacement monitoring systems. *ISRM 2003 - Technology roadmap for rock mechanics*, South African Institute of Mining and Metallurgy, Gauteng, South Africa, 1077-1082.
- Sithole G., Vosselman G., 2004. Experimental comparison of filter algorithms for bare—Earth extraction from airborne laser scanning point clouds. International Society for Photogrammetry and Remote Sensing, *Journal of Photogrammetry & Remote Sensing*, Elsevier B.V., 59, 85-101.
- Stiros S., Vichas C., Skourtis C., 2004. Landslide Monitoring based on Geodetically Derived Distance Changes. *Journal of Surveying Engineering*, **130**, 4, 156 –162.
- Soldati M., Corsini A., Pasuto A., 2004. Landslides and climate change in the Italian Dolomites since the Lateglacial. *Catena* **55**, 2, 141-161.

- Squarzoni C., Delacourt T., Allemand P., 2003. Nine years of spatial and temporal evolution of the La Valette landslide observed by SAR interferometry. *Engineering Geology*, **68**, 53-66.
- Squarzoni C., Delacourt T., Allemand P., 2005. Differential single frequency GPS monitoring of the La Valette landslide (French Alps). *Engineering Geology*, **79**, 215-229.
- Tarchi D., Casagli N., Moretti S., Leva D., Luzi G., Pasuto A., Pieraccini M., Silvano S., 2003a. Landslide monitoring using round-based SAR interferometry: an example of application to the Tessina landslide in Italy. *Engineering Geology*, **68**, 15-30.
- Tarchi D., Casagli N., Moretti S., Leva D., Luzi G., Pieraccini M., Sieber A.J., 2003b. Monitoring landslide displacements by using ground-based differential SAR interferometry: application to the Ruinon landslide in the Italian Alps. *Journal of Geophysical Research*, **108**, B8, 2387, doi: 10.1029/2002JB002204.
- Tarchi D., Ohlmer E., Sieber A.J., 2000a. Monitoring of structural changes by radar interferometry. *Research Nondestructive Evaluation*, 213-215.
- Tarchi D., Rudolf H., Pieraccini M., Atzeni C., 2000b. Remote monitoring of buildings using a ground-based SAR: application to cultural heritage survey. *International Journal of Remote Sensing*, **21**, 18, 3545-3551.
- Teza G., Atzeni C., Balzani M., Galgaro A., Galvani G., Genevois R., Luzi G., Mecatti D., Noferini L., Pieraccini M., Silvano S., Uccelli F., Zaltron N., 2008. Ground-based monitoring of high-risk landslides through joint use of laser scanner and interferometric radar. *International Journal of Remote Sensing*, **29**, 16, 4735-4756.
- Teza G., Galgaro A., Zaltron N., Genevois R., 2007. Terrestrial laser scanner to detect landslide displacement fields: a new approach. *International Journal of Remote Sensing*, **28**, 3425-3446.
- Travelletti J., Oppikofer T., Delacourt C., Malet J.P., Jaboyedoff M., 2008. Monitoring landslide displacements during a controlled rain experiment using a long-range terrestrial laser scanning (TLS). *The International Archives of the Photogrammetry, Remote Sensing and Spatial Information Sciences*, **XXXVII**, B5, 485-490.
- Van Westen C.J., Lulie Getahun F., 2003. Analyzing the evolution of the Tessina landslide using aerial photographs and digital elevation models. *Geomorphology*, **54**, 77-89.
- Walstra J., Chandler J.H., Dixon N., Dijkstra T.A., 2004. Extracting landslide movements from historical aerial photographs. In: Lacerda W., Erlich M., Fontoura S.A.B., Sayao A.S.F. Eds., *Landslides: Evaluation and Stabilization*, Taylor & Francis, London, 843-850.
- Weber, D., Herrmann, A., 2000. Reconstitution de l'évolution géomorphologique de versants instables par photogrammétrie numérique: l'exemple du glissement de terrain de Super-Sauze (Alpes-de-Haute-Provence, France). *Bulletin Societe Geologique de France*, **171**, 637-648.
- Wehr A., Lohr U., 1999. Airborne Laser Scanning - An Introduction and Overview. International Society for Photogrammetry and Remote Sensing, *Journal of Photogrammetry & Remote Sensing*, Elsevier B.V., **54**, 68-82.
- Werner C., Wegmuller U., Strozzi T., Wiesmann A., 2003. Interferometric point target analysis for deformation mapping. In *Proceedings of IEEE International Geoscience and Remote Sensing Symposium*, Toulouse, France, INT\_F11\_09, 7, 4362-4364.

- White S.A., Wang Y., 2003. Utilizing DEMs derived from LiDAR data to analyze morphologic change in the North Carolina coastline. *Remote Sensing of Environment* **85**, 39-47.
- Wyatt F.K., 1982. Displacements of surface monuments: Horizontal motion. *Journal of Geophysical Research*, **87**, 979- 989.
- Wyatt F.K., 1989. Displacements of surface monuments: Vertical motion. *Journal of Geophysical Research*, **94**, 1655-1664.
- Wyatt FK., Bolton H., Bralla S., Agnew D.C., 1989. New designs of geodetic monuments for use with GPS. *EOS Transactions American Geophysical Union*, **70**, 1054.
- Zebker H.A., Lu Y.P., 1998. Phase unwrapping algorithms for radar interferometry — Residue-cut, least-squares, and synthesis algorithms. *Journal of the Optical Society of America A*, **15**, 3, 586-598.
- Zanutta A., Baldi P., Bitelli G., Cardinali M., Carrara A., 2006. Qualitative and quantitative photogrammetric techniques for multi-temporal landslide analysis. *Annals of Geophysics*, **49**, 4/5, 1067-1079.

*Chapter 5*

## **USING LARGEST SEISMICALLY INDUCED LANDSLIDES FOR ESTIMATING EARTHQUAKE MAGNITUDES AND TOPOGRAPHY CHANGES**

***A.R. Agatova\* and R.K. Nepop***

Institute of Geology and Mineralogy SB RAS, Novosibirsk, Russia

### **Abstract**

Earthquake triggered landslides are widespread phenomena in tectonically active mountain provinces. Their abundant occurrence and large volumes of displaced soil indicate great influence on the topography changes. Using such an informative object as the largest seismically induced paleolandslide we broadened the paleoseismogeological method developed in Russia since the 1960s. So far most of research has focused on coseismic fault motion. The seismogravitational dislocations have been used mainly for establishing epicentral zones and the timing of old earthquakes. Using the parameters of the largest landslides allow us to estimate magnitudes of prehistoric earthquakes, calculate the total volume of earthquake triggered landslides, the contribution of landslides caused by aftershocks and erosion rate due to seismically induced landslides. This approach was tested in the mountainous, seismically active southeastern part of Russian Altai – an area of numerous giant Holocene seismically induced landslides where the Chuya earthquake ( $M_S = 7.3$ ) took place in 2003.

Despite several objective difficulties including: 1) establishing the seismic origin of paleolandslides; 2) estimating the typical size of the largest landslides for particular region and time period; 3) determination of the landslide parameters where the joining of several detachments or considerable change of landslide's body has occurred, this approach demonstrates the principle possibility of using the largest seismically induced landslides for estimating the paleoseismicity and earthquake induced topography changes.

---

\* E-mail address: [agatr@mail.ru](mailto:agatr@mail.ru)

## Introduction

Coseismic slope failures often caused most of the global damage and most of all casualties related to the strong earthquakes all over the world. Seismically induced landslides, which are widespread phenomena within tectonically active mountain regions, represent the highest risk to both construction and life. Corroborated examples of this abound. A well-known catastrophic Huascarán rock debris avalanche triggered by the 1970 Peru earthquake ( $M = 7.7$ ) killed more than 18000 people (Plafker et al., 1971), giant loess landslide induced by the 1920 Haiyuan earthquake, NW China ( $M = 8.5$ ) – about 100000 casualties (Schuster and Highland, 2001), a long run out rock avalanche caused by the 1949 Khait earthquake ( $M = 7.7$ ) (Leonov, 1960) buried the Khait town with thousands of inhabitants etc.

Seismically induced landslides are also especially important agents of denudation in tectonically active zones. In spite of diversity in climatic, geological, geomorphological conditions and peculiarities of seismic process for different areas, landslides of various types can be triggered even by the moderate seismic shocks with the smallest approximate magnitudes 4 - 5. Since about 1/5 of the Earth's surface is affected by earthquakes, evaluating of seismic risk hazard and associated topography changes is a matter of vital importance.

Estimating earthquake magnitudes and earthquake induced topography changes using instrumental data and historic accounts can give information about the seismicity of mountain provinces during relatively short time period. The suggested approach which develops the method of paleoseismogeology (Solonenko, 1966) can give this information for the time period of about  $10^4$  years. Examination of longer time period is not proved due to significant changes in seismic regimen at the edge of Pleistocene-Holocene. For Altai Mountains (Russia) we consider the Holocene as the corresponding time period for several reasons. First of all in comparison with the Pleistocene the oscillations of mountain glaciers were not so extremal and the total glacier intensity was much less. This led to intensification of gravitational mass movements including that with the seismic origin on the outcropped trough slopes. Moreover, Holocene landslides are morphologically “fresh” and so make it possible to estimate the erosion rate more correctly. Strong Holocene earthquakes leave the most enduring imprint on landforms in the giant landslides which are well preserved in topography due to arid climate. Finally duration of the Holocene noticeably exceeds the recurrence interval of strong earthquakes (about 500-900 years for the southeastern part of Russian (Gorny) Altai (Rogozhin et al., 2007)).

The leading factor in the generation of giant landslides in the arid SE part of Russian Altai is seismic excitation. Our field observations of the impact of large modern and prehistoric earthquakes reveal several criteria that indicate seismic origin for paleolandslides in SE Altai. Their wide-spread occurrence and large volumes of displaced soil indicate the great influence of earthquake-induced landslide on the topography changes.

In this paper we calculated the Holocene erosion rate due to seismically induced landslides for the Chagan-Uzun basin (SE Altai, Russia) - an area of numerous large earthquake induced paleolandslides where the 2003 Chuya earthquake took place. We also calculated the contribution of aftershock triggered landslides to erosion and suggested a regional coefficient considering the contribution of aftershock induced landslides to Holocene erosion rate for SE Altai. Moreover for the first time we use the parameters of seismically induced paleolandslides for numerical estimating magnitudes of their triggers. That allows



amplifying and refining available seismic risk zoning. These estimates can form the basis for this zoning in poorly studied regions with the shortage of seismological and historical data.

## **The Method of the Paleoseismogeology and Evolution of Paleoseismological Investigations**

The evolution of paleoseismological study clearly demonstrates that in order to properly understand the seismic potential of a region, and to assess the associated topography changes, extensive studies are necessary to take full advantage from the geological evidence of past earthquakes. A major line of paleoseismic investigation is detailed study of coseismic effects in the natural environment and quantitative assessment of the topography changes depending on earthquake magnitude.

The idea of interconnection between seismicity and existent earthquake induced topography changes is quite old. Thus early speculations on the long-term importance of seismically induced landslides were presented by J. Muir (1912) after field trip that began in 1868 and after the 1872 Owens Valley earthquake. He was impressed by massive talus deposits that were largely the result of earthquake induced rock falls in Yosemite Valley, California. On another hemisphere one of the founders of the paleoseismogeological method V.P. Solonenko considered that the real birthday of paleoseismicity studies is the 6<sup>th</sup> of September 1757 when on the session of Russian Academy of Sciences M.V. Lomonosov gave a report "About birth of metals from the Earth shaking". In particular he said: "Wherever you see the rock mountains with clefts and faults which were stay after earthquakes the more drastic the more unsteady is the essence of ruin, chute or abyss". His thoughts about the earthquake role in forming Earth topography and crust structure were caused by the strong 1745-1746 Peru earthquake and the 1745 Lisbon disaster.

In the middle of 20<sup>th</sup> century there was a rapid development of paleoseismogeological researches (or paleoseismology studies) all over the world. But the main contribution to the theory and methodology of these investigations was done by Soviet and American scientists. In USA preference is traditionally given to stratigraphical approach. As a result the method of trenching was well developed after the beginning of atomic power stations and great artificial dams constructing (Hatheway and Leighton, 1979). Already in the 70<sup>th</sup> in California engineering geologists estimated earthquake magnitudes and an average recurrence interval of the strongest shocks using excavations in tectonically active urban areas. On the other hand in the USSR geomorphological and morphostructural approaches were more popular (Gerasimov, 1954). The presence of just a few American papers that used geomorphological features to identify paleoseismodislocations (Slemmons, 1957; Plafker and Rubin, 1967; Wallace, 1970) did not lead to formulating a new method. That was done by Soviet geologists after the 1957 Gobi-Altai earthquake. The resulted monograph was translated into English (Florensov and Solonenko, 1965) and was generally recognized by specialists. Later the method of paleoseismogeology was formulated by N.A. Florensov and V.P. Solonenko (Solonenko, 1966; Solonenko, 1973; Florensov, 1978).

By now there are some well developed approaches, estimated the seismic risk hazard, which are based on seismological data (Gubin, 1950; Belousov, 1954; Gzovskij, 1957a; Gzovskij, 1957b). But along with all advantages these approaches have some weaknesses too.

Thus for forecasting the intensity of seismic shocks for specific active area it is necessary to extrapolate the registered seismicity from one seismically active area to another. The applicability of these methods is limited by the seismostatistical data. There are also difficulties in revealing the correlation between seismicity and geological structure of a region. Moreover, estimating earthquake magnitudes using instrumental data and historic accounts can only give information about the seismicity of mountain provinces during relatively short time period. Using these methods it is practically impossible estimate the seismic risk hazard for unstudied areas, evaluate the upper bound of seismic potential of specific seismogenerative structures and obtain information about location of epicenters and recurrence time period for strong earthquakes.

The method of paleoseismogeology (Solonenko, 1966; Solonenko, 1973; Florensov, 1978), which was mentioned above, can fill the gap in this knowledge and give such information for the time period of about  $10^4$  years. The key point of the method is analysis of geomorphically expressed surface displacement (slope failure or fault scarps) of evidently seismic origin. Each strong earthquake source creates a signature on the geology and the geomorphology of an area. The sizes and patterns of prehistoric and historic ground failure have direct implications for the magnitude of their triggers. So detailed study on relations between various categories of coseismic effects in the natural environment and earthquake magnitude can provide the assessment of associated seismic risk hazards, estimating the paleoseismicity and topography changes in mountain provinces. In the classification by Solonenko (1973), earthquakes can cause surface ruptures (tectonic effects), slope movements such as landslides, rockfalls, debris flows, etc. (gravity effects), or events of mixed gravity-tectonic origin.

So far most of research has focused on coseismic fault motion, and a number of empirical correlations have been obtained for the earthquake magnitudes and rupture parameters (Tocher, 1958; Solonenko, 1973; Khromovskikh et al., 1979; Nikonov et al., 1983; Wells and Coppersmith, 1994 and many others). This opened up possibilities to make seismic risk zoning on the basis of estimated earthquake magnitudes. There are, however, natural problems in rupture studies (Nikonov et al., 1983): it is difficult to predict the origin and geometry of old ruptures in rugged terrains, to time and distinguish prehistoric events in multiple ruptures, or to discriminate between ruptures produced by the main shock, foreshocks, or aftershocks. The latter objective is critical for empirical relationships used to estimate the magnitudes of paleoearthquakes.

The largest earthquake-induced landslides rarely pose such problems, and are the most interesting target for paleoseismicity study in mountain provinces for several reasons. First, they leave the most persistent imprint on landforms and thus represent the longest period of seismic activity. Second, each specific seismic event can produce many smaller landslides and only a single largest one. Our data on strong modern and prehistoric earthquakes for Altai-Sayan mountain province (Russia) show that the largest landslide volume is several times or even orders of magnitude greater than the volume of the next one. Thus in this case, the largest landslide each stands for a separate trigger unlike faults or smaller landslides. Another advantage, especially important for hardly accessible terrains, is that large landslides are well resolved in remote sensing imagery.

Using such informative object as the largest earthquake triggered paleolandslide we broadened the scope of the paleoseismogeological method. Our approach within this method allows using the largest seismically induced landslide data not only for possible timing of

prehistoric events and locating of their epicenters as it was earlier but also for numerical evaluation of paleoearthquake magnitudes and earthquake induced topography changes (Fig. 1).

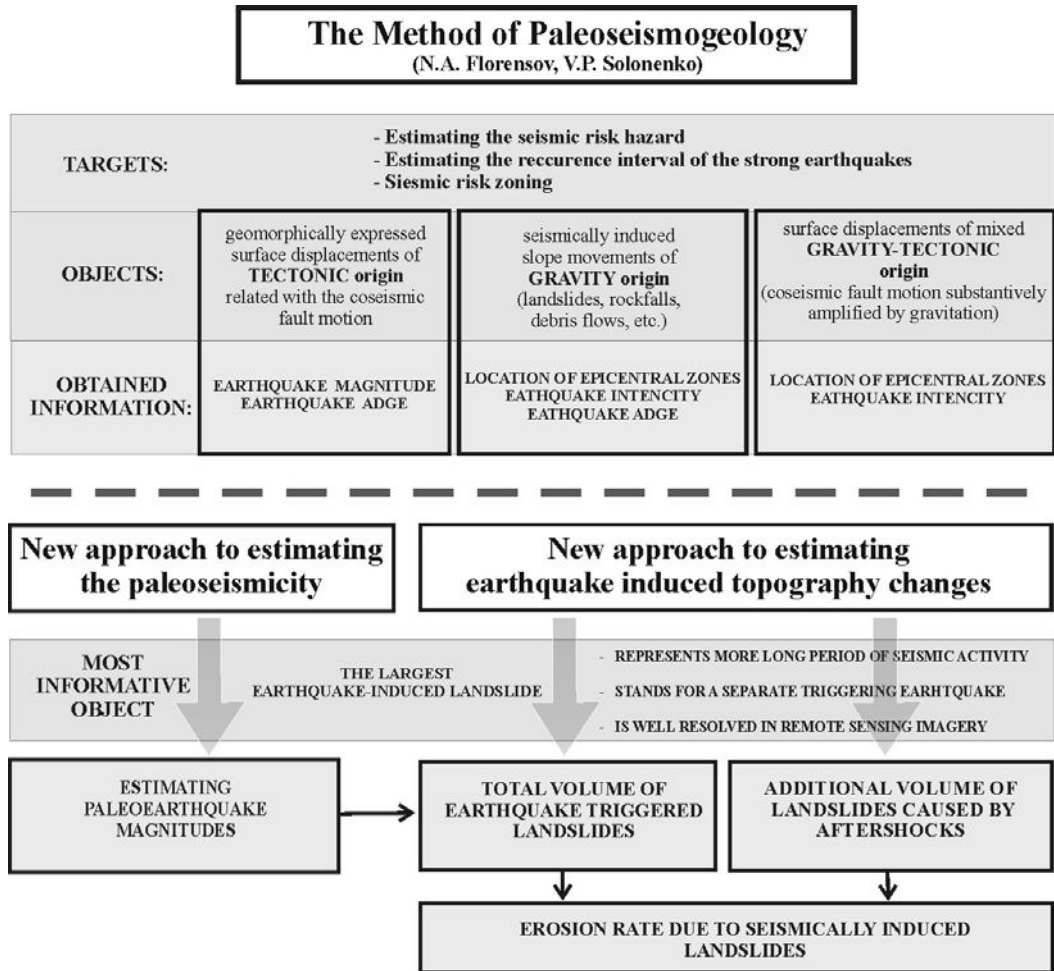


Figure 1. New approach within the Paleoseismogeological method to estimating the paleoseismicity and seismically induced topography changes on the basis of the largest earthquake induced landslide data.

## Study Area and Historic Background

The suggested approach was developed and tested in the course of the paleoseismicity study of the SE Altai (Russia) (Fig.2), an area of numerous large Holocene earthquake induced landslides (Devyatkin, 1965; Rogozhin and Platonova, 2002; Agatova et al., 2006). The Altai neotectonic uplift is the part of Central-Asian collision belt and is a transpressional zone formed due to oblique thrusting (Molnar P., Tapponnie P., 1975; Dobretsov et al 1996). It has a complicated regular fold-block structure (Ufimcev, 2002; Novikov, 2004). The southeastern part of Russian Altai is the northern extension of the Mongolian Altai, which is

known for its high modern seismicity. As a result, SE Altai is the most seismically active part of Russian Altai. This was evidenced by the 2003 Chuya earthquake ( $M_S = 7.3$ ), which triggered giant landslide in Taldura valley (Fig. 3). Unconsolidated Cenozoic sediments are widely presented here in the most active areas at the depression-range transition along fault boundaries of landforms and provide geological conditions to produce earthquake-induced landslides.

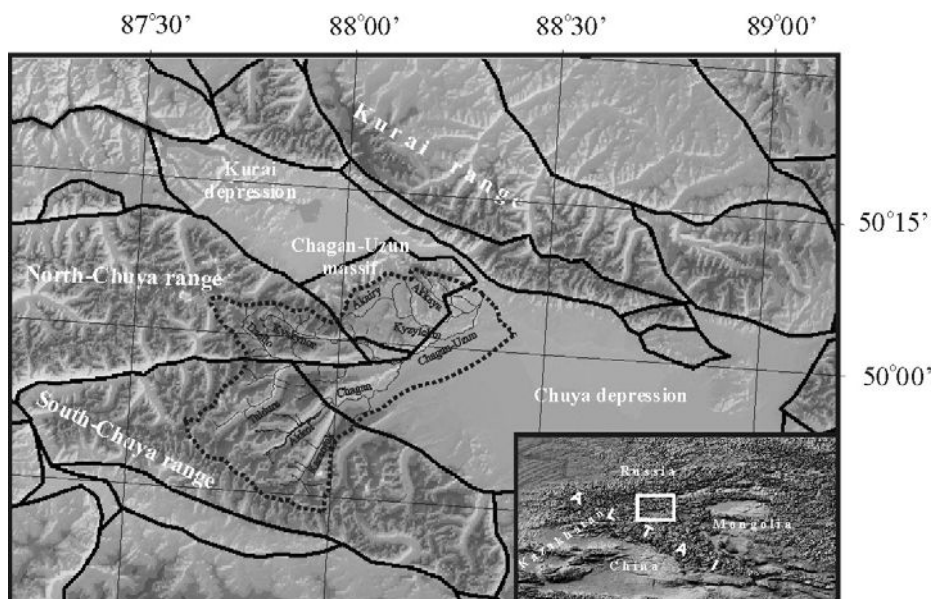


Figure 2. Location map of the Altai mountains, the study area – SE part of Russian Altai, and Chagan-Uzun river basin (dotted) - representative region for estimating earthquake induced topography changes.



Figure 3. The largest landslide triggered by the 2003 Chuya earthquake.

The seismicity of the Altai region has been largely studied (Masarsky and Moiseenko, 1962; Chernov, 1978; Zhalkovsky et al., 1978; Zhalkovsky et al., 1995 and others). Since recently, the earthquake data from the Altai-Sayan mountain province, including total energy, have been systematized in annual catalogs (Filina, 1985, 1987, 1991, 1997; Filina and Kuchai, 1990). First historic accounts of earthquakes in the Altai date back to the 18th century and the first Earthquake Catalog of the Russian Empire which mentioned Altai events came out in the 19th century, but instrumental seismicity has been documented since as late as 1959 - 1960 (Masarsky and Moiseenko, 1962). Many historic earthquakes were poorly located and remained missing in the seismicity map (Maloletko, 1978). The earliest instrumental data had come from remote stations that provided reliable records of  $M > 5$  or larger events (Kirnos et al., 1961) before a regional seismological network was set up in 1962 (Zhalkovsky et al., 1995). Numerous instrumental records of  $M \approx 1.66$  to 5.5 ( $K = 7 - 14$ ) events collected by the regional network allowed earthquake relocating and estimating the recurrence intervals for events of different magnitudes. The results were applied to seismic risk mapping (Zhalkovsky et al., 1978), where the northwestern part of Russian Altai, except for the Lake Teletskoye basin, was a zone of shaking intensity VI (according MSK-64 intensity scale) with a low seismic activity ( $A_{10} < 0.01$ ) and low frequency of intensity VII events; areas of the South Katun', Charysh-Terekta, and Teletsk faults were the intensity VII zone; the southeastern Russian Altai with abundant active faults and high general seismicity was an intensity VIII zone ( $A_{10} \leq 0.1$ ) with a 1 - 3 kyr recurrence of large earthquakes. The intensity IX zone was restricted to a small area including the southern Chuya basin. It was outlined proceeding from the authentic seismic origin of failure in the Chagan-Uzun and Djasater valleys (Devyatkin, 1965) and from the neighborhood of the highly active ( $A_{10} = 0.2$ ) area of Mongolia shocked by several strong earthquakes in the 20th century.

All our calculations for estimating the topography changes were made for Chagan-Uzun river basin (SE Altai, Russia) (Fig.2) with a surface area of about 1 400 km<sup>2</sup>. It includes parts of the largest in Altai Chuya intermontane depression and frame ridges. This is an area of numerous prehistoric earthquake-triggered landslides (Devyatkin, 1965; Agatova et al., 2006). Moreover, the epicenter zone of the 2003 Chuya earthquake ( $M_S = 7.3$ ) is located there.

For estimating magnitudes of prehistoric earthquakes we selected four largest and best preserved old landslides (Fig. 4, 5, 6) in the Taldura, Chagan, and Elangash rivers valleys at the transition from the South Chuya range to the Chuya basin (Agatova et al. 2006, Nepop and Agatova 2006a) located within the epicenter zone of the 2003 Chuya event. The fault boundary between the South Chuya range and the Chuya basin, together with other WE and NW large faults, is the principal seismogenic structure of the area. The foothill of the South Chuya range is a block of the Chuya basin periphery which has been involved in uplift and is expressed geomorphically as an eroded transverse high in the valley floor (Fig. 5). It extends from the Irbistu valley to the Taldura valley along a fault scarp that separates the range from the piedmont part of the Chuya basin. It was the front of the basin-range transition that was reactivated by the 2003 Chuya earthquake. Moreover the borders of this block are marked by numerous disturbances of slopes formed by both rocks and unconsolidated Neogene and Pleistocene sediments.

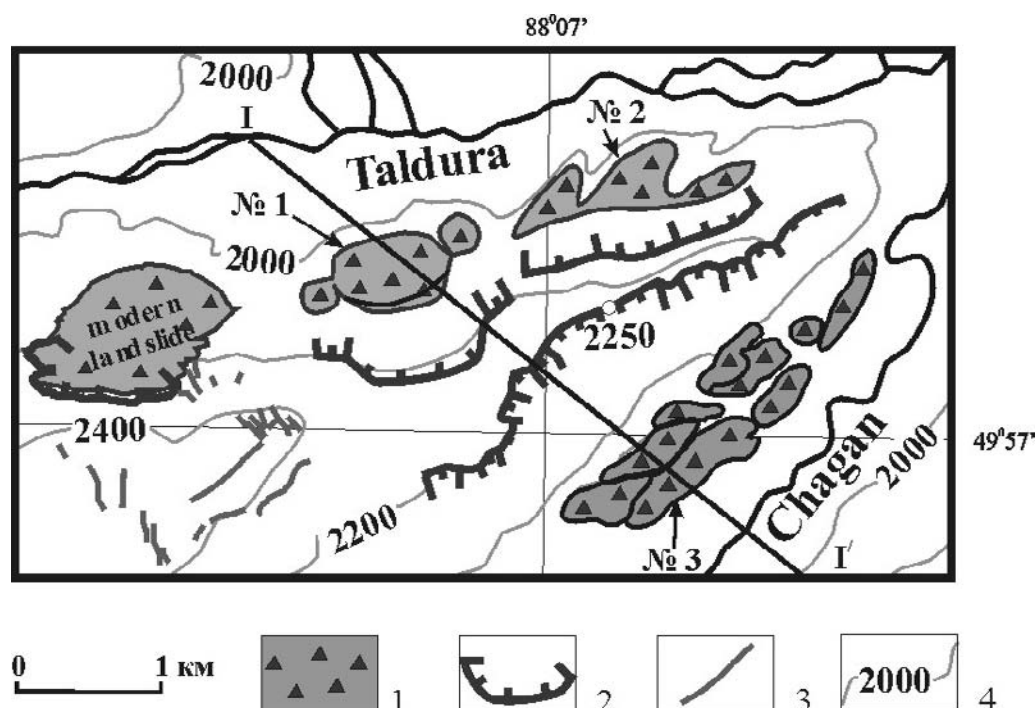


Figure 4. Location map of the largest earthquake-induced landslides in Taldura-Chagan divide (modified after (Nepop and Agatova, 2008)). 1 - landslide bodies; 2 – detachment surfaces; 3 - faults caused by the 2003 Chuya earthquake; 4 - elevation contour lines (m a.s.l.). Studied landslides are marked with numbers.

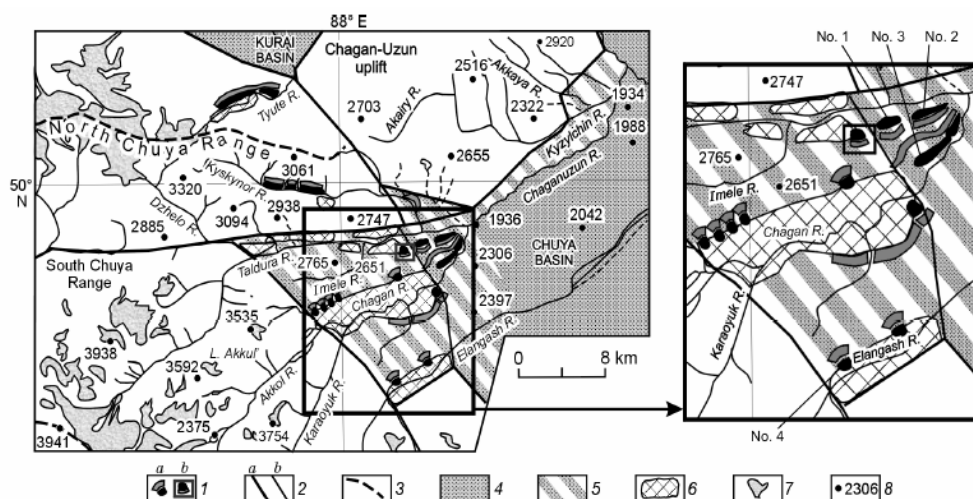


Figure 5. Prehistoric earthquake-induced landslides in epicentral zone of the 2003 Chuya earthquake, modified after (Agatova et al. 2006). 1 - prehistoric landslides (a) and the largest landslide triggered by the 2003 Chuya earthquake (b); 2 - faults that bound basin and range blocks (a) and blocks at basin-range transition (b); 3 - range axes; 4 - intermontane basins; 5 - submontane periphery of Chuya basin; 6 - glacially eroded basement uplifts in valley floors; 7 - glaciers; 8 - elevations above sea level (in m). See inset for the largest Holocene landslides under study (marked with numbers).

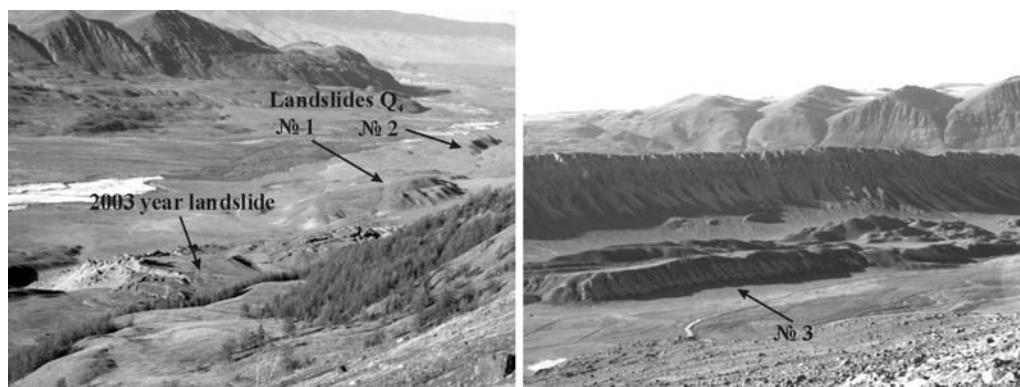


Figure 6. Modern landslide and prehistoric landslides 1-3 in Taldura-Chagan watershed.

All studied slope failures apparently have the Holocene ages because the youngest displaced rocks are Late Pleistocene moraines and fluvioglacial deposits that cover the watersheds at the basin-range transition (Agatova, 2005). The observed mass movements were interpreted as *landslides events* (rock slumps and rock block slides according to (Keefer, 1984; 2002)) for several reasons. The coexistence of hills at the foot of valley sides with cirque-shaped scarps and the characteristics of sediments in the landslide body and in the scarp provide reliable evidence of landsliding (Agatova et al., 2006; Nepop and Agatova, 2008). It was quite difficult to identify the rocks in the deposition area with those in the detachment surfaces because the latter are mantled with talus. However, the presence of fauna-bearing frozen greenish-gray lacustrine clay of the Tueryk Formation exhumed in the right flank of the modern landslide (Agatova et al., 2004) argues that these rocks take part in the forming of the eastern part of the Taldura-Chagan watershed and explain their presence in the nearby paleolandslide 1 which scarp is mantled by talus fans (Fig. 7). We also discovered brown patches of soft sand-clay detritus of the same color and composition as the cement of lacustrine pebbles in landslide 3 between the talus fans covering the detachment surface below moraine deposits. The bedding of sediments in a landslide body indicates rotation of the blocks during the landslide events and argues against their tectonic (Shchukina, 1960) or *in situ* erosional origin.

As mentioned by Keefer (1984, 2002), Jibson (1996) and others all types of landslides triggered by earthquakes also can occur without seismic triggering. Therefore, identifying surface features as landslides with a seismic origin is an important problem especially for old, more degraded landslides. Our field observations of the impact of large modern and prehistoric earthquakes reveal several criteria that indicate *seismic origin* of landslides in the studied area:

1. The great extent of ground failures upon strongly cemented Neogene and Pleistocene permafrost sediments;
2. Location of the landslides in the most active area at the basin-range transition along fault boundaries of landforms;
3. The relative positions of the detachment surfaces in the Taldura and Chagan valleys and the prehistoric fault scarps in the Taldura-Chagan divide are the same as the fault scarps and landslide detachment associated with the 2003 Chuya earthquake;





## Estimating Earthquake Magnitudes and Topography Changes on the Basis of Landslide Study

### Estimating Magnitudes of Prehistoric Earthquakes from Landslide Data

Recently, complete landslide-event inventories have become possible due to advanced methods and facilities, including analysis of high resolution satellite images, interpretation of aerial photographs and extensive field investigations that use a variety of techniques and tools pertaining to geomorphology, engineering geology and geotechnical engineering (Wieczorek, 1984). Using these complete inventories Malamud et al. (2004a) suggested a statistical landslide probability distribution function. The new data made it possible to relate the landslide parameters to the trigger magnitude. Relationship (1) shows the correlation between  $M$  - earthquake magnitude<sup>1</sup>, and  $V_{Lmax}$  - the volume of the largest landslide it causes (Malamud et al. 2004b):

$$\log V_{Lmax} = 1.36M - 11.58(\pm 0.49) \quad (1)$$

with  $V_{Lmax}$  in  $\text{km}^3$ . The error bounds represent the standard deviations of the fit.

Equation (1) is valid for medium and large earthquakes that generate at least one landslide. There are a number of papers which report the relation between earthquake magnitude and landslide triggering. Thus on the basis of intensity reports from several hundred small earthquakes in USA Keefer (1984, 2002) suggests the minimum magnitude 4.0 for earthquakes causing all types of landslides. Bommer and Rodrigues (2002) have considered 62 earthquakes in Central America and the smallest one that generated landslides had a surface wave magnitude 4.8. Solonenko (1973) described some common characteristics of seismically induced landslides in Mongol-Baikal active zone. He reported that earthquakes with the magnitude more than 5 trigger landslides which can be preserved in topography for a long time (Holocene). Using landslide probability density function Malamud et al. (2004b) calculated a threshold moment magnitude  $4.3 \pm 0.4$  responsible for the onset of earthquake-triggered landsliding.

It should be noted that the volume of the largest earthquake induced landslide just as other landslide parameters: total volume of triggered landslides, area affected by landslides etc., is not simply a function of earthquake magnitude. There are additional factors related both to geomorphic and earthquake's mechanism considerations such as roughness of topography, rock type, hydrological conditions, earthquake type and depth, direction of energy focusing, regional morphotectonic structure and so on. Some of them were considered by Keefer (1984, 1994, 2002) who inferred that in spite of their importance as far as could be determined from the available data, regional variations in seismic attenuation was not a significant factor.

The applicability of the empirical correlation (1) to the Altai has been proved due to the 2003 Chuya earthquake ( $M_S = 7.3$ ) which triggered a great landslide (Fig. 3). The GPS-

<sup>1</sup> Kanamori (1983) shows approximately equality of  $M_S$  - surface wave, and  $M_W$  - moment magnitudes, within the range of  $M_S$  5.0 to 7.5. On the basis of 176 historical earthquakes worldwide Wells and Coppersmith (1994) report no systematic difference in the range of 5.7 to 8.0 with the standard deviation approximately 0.19. So we suppose that the difference between magnitude scales ( $M_S$  and  $M_W$ ) is insignificant for the earthquakes on magnitude greater than 5.7 and we mean the moment magnitude everywhere unless mentioned another.

contoured landslide area measured using the ArcView software was  $0.66 \text{ km}^2$  and the landslide volume was  $0.027 \text{ km}^3$ . This data as well as data of the 1957 Gobi-Altai earthquake ( $M_S = 8.1$ ) (Florensov and Solonenko, 1965) show a perfect fit to Eq.(1): the corresponding points in the landslide volume - magnitude coordinates falls within the error band (Fig. 9). At present, seismostatistical data base for Russian Altai is quite limited. The 2003 event has been historical the only instance in the SE Altai when the magnitude of a large earthquake could be numerically correlated with the associated ground failure. Perhaps future researches can give new opportunities to test this relation. Anyway, it would be unwise to neglect relationships reported from other seismically active areas because the recurrence of large earthquakes in the mountains flanking the Kurai-Chuya system of intermontane depressions (SE part of Russian Altai) is 500-900 yr (Rogozhin et al., 2007).

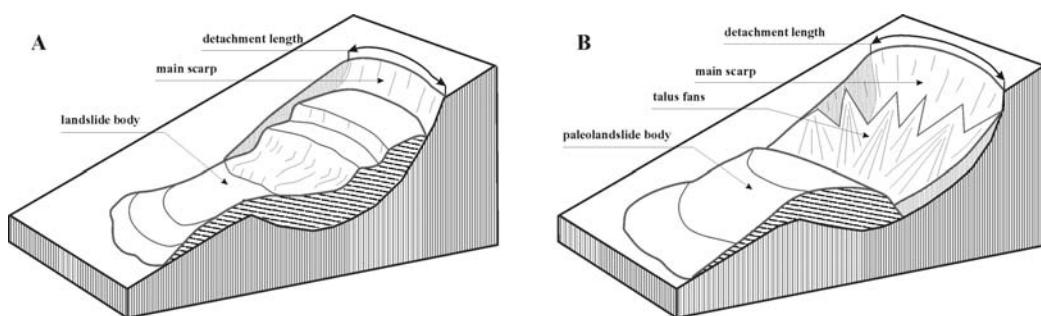


Figure 9. Modern landslide (A) and its transformation during a long time period (B).

While estimating paleoearthquake magnitudes from the largest landslides data equation (1) provides the low-bound limit of the value as immediately following the event the landslide size begins to reduce by wasting processes (ice degradation in permafrost, erosion, etc.) (Fig. 1). Therefore, deriving the upper-bound limit of the paleoearthquake trigger magnitude for old landslides, which have different ages and have been wasted to different degrees, requires a parameter not involved in the landslide deposition area. The detachment length can be used as this parameter. According to the landslide type the detachment length has its own size defined by the landslide surface area. Landslide body naturally tends to a certain geometry, more or less isometric depending on the slope inclination, geologic environments etc., and thus cannot stretch too far in any dimension (Vazhenin, 2000; Burbank, 2002). Inasmuch as later surface processes most often increase the length of the initial detachment surface, the magnitude derived from detachment length corresponds to the upper limit.

For estimating magnitudes of prehistoric earthquakes from landslide data, the deposition areas and detachment lengths of studied landslides were quantified with the ArcView software using the 1:25000 topographic base map. The deposition areas were measured excluding later small rockfall and landslides. The landslide volumes can be also estimated with the empirical relationship (Hovius et al., 1997):

$$V_L = \varepsilon \cdot S_L^{1.5}$$

where  $S_L$  and  $V_L$  are the landslide area and volume, respectively and  $\varepsilon = 0.05 \pm 0.02$ .

The time succession of the landslide events was inferred from the morphology of the deposited landslide bodies and their distances from the detachment surfaces. Note that this distance in areas of frozen ground largely depends on the slope gradient and corresponds rather to the rates of permafrost degradation and landslide descent than to the magnitude and direction of seismic shocks.

The minimum magnitudes were estimated using equation (1). Proceeding from the 2003 Chuya earthquake data, we estimated the maximum magnitudes of prehistoric earthquakes using a linear relationship. This approach is applicable for the greatest prehistoric landslides in the immediate vicinity of the largest Chuya earthquake landslide because they share similar origin and evolution patterns. It should be emphasized that this simplification may work only for paleoearthquakes of a comparable magnitude, and its applicability to other active areas requires a special study. Table 1 lists the parameters of the landslides and the derived maximum and minimum magnitudes of their triggers.

**Table 1. Parameters of the largest prehistoric earthquake-induced landslides and calculated magnitudes of respective paleoearthquakes.  $S_{Lmax}$  and  $V_{Lmax}$  are the area and the volume of the largest landslides,  $L_{Det}$  is the landslide detachment length,  $M_{min}$  and  $M_{max}$  are minimum and maximum magnitudes.**

Landslide	$S_{Lmax}$ [km <sup>2</sup> ]	$V_{Lmax}$ [10 <sup>-3</sup> km <sup>3</sup> ]	$L_{Det}$ [km]	$M_{min}$	$M_{max}$
1	0.35	10.44	1.4	7.1	9.3
2	0.23	5.44	1.20	6.9	8.0
3	0.33	9.48	1.22	7.0	8.1
4	0.30	8.22	1.1	7.0	7.3
Modern	0.66	27.0	1.1	7.3	7.3

The paleoearthquake magnitudes obtained from the largest landslide data, from 6.9 to 9.3, indicate high seismic activity of SE Altai through the Holocene and its seismotectonic identity with the Mongolian Altai. The intensity of the earthquakes that triggered all the studied giant landslides, by analogy with the consequences of the 2003 Chuya earthquake ( $M_S = 7.3$ ,  $I = 9-10$ ), can be estimated 9 - 12 units on the MSK-64 scale. This fact, along with recent discoveries, argues for the greater seismic activity of this region than it was supposed before. All these allow the marking out of not only the southern part of Chuya intermontane depression as a highly seismically active zone with the recurrence of large earthquakes 500-900 yr but also all the mountain ridges framing the Kurai-Chuya system of intermontane depressions (not including Sailjugem range). The northern border of this zone lies along the Kurai range axis. The marked zone coincides with the morphotectonic area which is characterized by the highest for Russian Altai altitudes (up to 4000-4500 m a.s.l.) and relative tectonic block displacements up to 2500-3000 m in height. It is caused by two major reasons. First, there is an abrupt step of base-leveled surface (surface joining beds of principal fault valleys and depressions) here (Agatova et al., 2006). Second, main dextral zones change their direction here from NW to sublatitudinal that lead to vertical component of slipping on faults. This area is the oldest (Oligocene) orogen in the Altai mountain province. It was also seismically active in Holocene, which is confirmed by studied giant Holocene seismically induced landslides and the estimated magnitudes of their triggers.

## Estimating Topography Changes from Landslide Data

Quantitative assessment of earthquake induced topography changes can be done using the total volume of associated landslides -  $V_{LT}$ . The relationship between  $V_{LT}$  and earthquake magnitude  $M$  (Eq. 2) is given in Malamud et al. (2004a) on the basis of total volume of landslide material generated by 15 historical earthquakes (Keefer, 1994) along with the 1994 Northridge earthquake data (Harp and Jibson, 1996):

$$\log V_{LT} = 1.42M - 11.26(\pm 0.52), \quad (2)$$

with  $V_{LT}$  in  $\text{km}^3$ . This equation gives the best fit for modern earthquakes with instrumental measured magnitude, but the historical database of strong earthquakes in SE Altai is quite poor and the period of seismological regional studies is short. Along with old ruptures, the only evidences of the high Holocene seismicity in this area are the giant earthquake induced paleolandslides which have being preserved in topography for a long time period. These landslides are the records of strong prehistoric earthquakes and keep information about the regional seismicity.

Using the general landslide distribution (Malamud et al., 2004a) allows extrapolating of an inventory that contains just the largest landslide to correlate the volume of the largest landslide -  $V_{Lmax}$  with the magnitude of its trigger (Eq. (1)). Thus equation (1) has important paleoseismological implications for mountain provinces where there are giant earthquake induced landslides. Combining Eqs. (1) and (2) we can obtain the correspondence between  $V_{LT}$  and  $V_{Lmax}$ :

$$\log V_{LT} = 1.04 \log V_{Lmax} + 0.83, \quad (3)$$

with the expected standard deviations less than 1.03. Both  $V_{LT}$  and  $V_{Lmax}$  are in  $\text{km}^3$ . This relation (Eq. (3)) is best applied for prehistoric earthquakes that caused the largest landslides in SE Altai.

Equations (2) and (3) define the destructive effect of earthquakes leading to topography changes, which can be evaluated by erosion due to seismically induced landslides. The rate at which earthquakes contribute to erosion can be estimated on the basis of different approaches. To make a calculation for the Holocene earthquakes in SE Altai we use Eq. (4):

$$\dot{h} = \frac{\sum V_{LT}}{S \cdot T}. \quad (4)$$

Here  $\dot{h}$  is the erosion rate due to seismically induced landslides,  $\sum V_{LT}$  is the sum of total volume of landslides triggered by each individual earthquake in a region with the surface area  $S$ , during time interval  $T$ . For more accurate estimating all strong earthquakes over this time period should be taken into account. Moreover  $T$  should be much longer than the recurrence interval for strong earthquakes. As was mentioned above we can take the Holocene as the corresponding time period for SE Altai because the recurrence interval here is about 500-900 years (Rogozhin et al., 2007). Another reason is that Holocene landslides are

morphologically “fresh” and so make it possible to estimate the erosion rate more correctly. It should be also taken into account that there is certain area affected by landslides triggered by a single earthquake. Although there are a lot of factors such as focal depth, specific ground motion characteristics of individual earthquake, geological conditions and so on, this area correlates with the earthquake magnitude and so can be estimated (Keefer, 2002; Keefer and Wilson, 1989). Therefore when calculating erosion rate it should be compared in a proper way with the studied area  $S$ .

We consider only strong earthquakes that give as a result the low-bound estimation of erosion rate. But this estimation closely relates to the real value because of the much more significant influence of strong earthquakes on mountain topography in comparison with the same of moderate seismic shaking. Our calculations show the difference in corresponding erosion produced by strong and moderate seismic shocks of about 2 orders. The main problem under such an approach is ascertaining the typical size of the largest paleolandslides for a specified active area over concerned time period.

The overwhelming majority of landslides are triggered by the main shock with the largest magnitude. But aftershocks which accompany powerful earthquakes can also generate landslides. The influence of aftershock induced landslides on mountain topography is poorly investigated and for the Altai mountain province such investigations are absent.

To quantify the relative contribution of aftershocks to erosion due to the associated landslides we can use the equation (2), which shows the consequences of a single shock, and the recurrence of aftershocks generally satisfying the Gutenberg-Richter frequency-magnitude relation (Gutenberg and Richter, 1954):

$$\lg N = -b \cdot M + \lg a. \quad (5)$$

Here  $N$  is cumulative number of earthquakes in a region with magnitudes greater than  $M$ . Constant  $a$  is a measure of the intensity of the regional seismicity. Constant  $b$  is known as the  $b$ -value and has a near-universal value  $b = 0.90 \pm 0.14$  (Evernden, 1970). Coefficient  $b$  is one of the major seismic parameter which is calculated for each separate active area or set of seismic events. Thus for the Altai-Sayan mountain province  $b = 0.882 \pm 0.018$  (Zhalkovsky et al., 1978) and for the 2003 Chuya earthquake aftershocks which occurred in June – September 2004,  $b = 0.977 \pm 0.015$  and  $b = 0.947 \pm 0.014$  (least-squares and maximum-likelihood methods accordingly) (Arefiev et al., 2006). Generally,  $b$  is in the range  $0.8 \leq b \leq 1.2$  with the most frequent value  $b = 0.9$  (Frohlich and Davis, 1993).

Good correlation of Eq. (5) in magnitude range  $5.2 \leq M \leq 7.5$  is shown for the worldwide earthquakes from the Harvard Centroid-Moment Tensor Data Base (1997) for the period 1977-1994 (Turcotte, 1999). The deviation of the data from the Gutenberg-Richter law at magnitudes less than 5.2 can be attributed to the resolution limits of the global seismic network. Regional studies (Aki, 1987) indicate this correlation down to at least  $M = 2.0$ . Applicability of Eq. (5) at magnitudes greater than  $M = 7.5$  is more controversial (Scholz, 1997). On the one hand, the duration of seismological study is too short in comparison with the recurrence interval for strong earthquakes. On the other hand, this deviation can be fundamental and can have a physical basis (Pacheco et al., 1992). But magnitudes of the 2003

Chuya earthquake and its aftershocks fit the range which allows confidence in using the Gutenberg-Richter frequency-magnitude relation.

The total volume of aftershock triggered landslides -  $V_A$ , depends mainly on magnitude difference between the main shock and the largest aftershock -  $\Delta M$  (Nepop and Agatova, 2006b).

$$\frac{V_A}{V_{LT}} = \frac{b}{1.42 - b} \cdot 10^{-1.42 \cdot \Delta M} \quad (6)$$

where  $V_{LT}$  is the total volume of landslides triggered by the main shock.

Eq. (6) shows what part of the total landslide volume derives from the aftershock induced landslides. So it allows calculating the contribution of aftershocks to erosion due to seismically triggered landslides. In this calculation, beside the value of  $V_{LT}$  (which can be estimated using main shock magnitude (Eq. (1)) or the volume of the largest landslide (Eq. (3))), only two values - parameter  $b$  and typical magnitude difference between the main shock and the largest aftershock  $\Delta M$  are used. These values ( $b$  and  $\Delta M$ ) enable all regional diversity to be considered and calculations to be made for different seismically active areas.

As can be seen from Eq. (6), the lower  $\Delta M$ , the more the contribution of aftershock induced landslides to erosion. If  $\Delta M = 1.2$  according to the Bath Law (Bath 1965), the contribution of all aftershocks is only about 4% of the  $V_{LT}$ . But if  $\Delta M = 0.6$  (as it is for the 2003 Chuya earthquake), this contribution is about 22% - the value that should be taken into account. The peculiarity of the 2003 Chuya earthquake, similar to other strong earthquakes of Altai-Sayan mountain province (Russia) (the 1970 Ureg-Nur ( $M_S = 7.0$ ) and the 1991 Busingol ( $M_S = 6.5$ ) earthquakes) is that their aftershock activity does not fit the Omori law. So it is necessary to consider aftershock induced landslides while estimating the topography changes for this area.

Paleolandslides close location in the modern earthquake's epicenter zone show that the source areas of large earthquakes in SE Altai were repeatedly reactivated. Strong prehistoric earthquakes with magnitudes of 6.9 to 9.3 (Nepop and Agatova, 2006a, Agatova et al., 2006, Nepop and Agatova, 2008) occurred here. All these argue for the identity of historic and Holocene earthquake's mechanisms in this region. So  $\alpha$  - regional coefficient that considers the contribution of aftershock induced landslides, should be introduced to modify the Eq. (4):

$$\dot{h} = \alpha \cdot \frac{\sum V_{LT}}{S * T}, \quad (7)$$

where

$$\alpha = \left(1 + \frac{V_A}{V_{LT}}\right) = \left(1 + \frac{b}{1.42 - b} \cdot 10^{-1.42 \cdot \Delta M}\right).$$

Assuming the identity of historic and Holocene earthquake's mechanisms we can estimate  $\alpha = 1.2$  on the analogy of the 2003 Chuya earthquake (Nepop and Agatova,

2006b). Thus Eq. (4) does not take into account the contribution of aftershock triggered landslides and represents the low-bound estimation of erosion rate.

The suggested approach allows us to calculate Holocene erosion rate due to seismically induced landslides  $\dot{h} = 3 \cdot 10^{-5}$  m year<sup>-1</sup> for Chagan-Uzun river basin. As shown above, this is the low-bound estimation. It is in agreement with estimates obtained with different techniques for other seismically active regions with arid and semiarid climate.

Thus Keefer (1994), using his empirical relationship between landslides volume and earthquake magnitudes, determined the total landslide volume triggered by historic earthquakes in southern California. He obtained an erosion rate due to seismically induced landslides for a surface area of about 70 000 km<sup>2</sup> of  $\dot{h} = (4 - 8) \cdot 10^{-5}$  m year<sup>-1</sup>. Malamud et al. (2004b) studied the seismicity of southern California over an area of about 240 000 km<sup>2</sup> using parameters of Gutenberg-Richter frequency-magnitude relation, and estimated this rate to be over the range  $\dot{h} = (2 - 20) \cdot 10^{-5}$  m year<sup>-1</sup>. They also gave the inferred regional erosion rate due to landslides for the 1994 Northridge earthquake, California ( $M_S = 6.7$ ) (Harp and Jibson, 1996) of  $\dot{h} = 10 \cdot 10^{-5}$  m year<sup>-1</sup>. This estimation was obtained for the area of about 1 000 km<sup>2</sup>. For seismically active regions with humid climate this rate is generally higher. Thus for Papua New Guinea  $\dot{h} = (50 - 70) \cdot 10^{-5}$  m year<sup>-1</sup> (Pain and Bowier, 1973).

## Difficulties and Limitations of Suggested Approach

The suggested approach to estimating paleoseismicity and earthquake induced topography changes using the largest landslide data has some essential limitations and difficulties.

In spite of the fact that the paleoseismogeological method can give information about the regional seismicity for much longer time period then the period of seismological researches usually in mountain provinces it is limited by the Holocene. One of the reasons is more intensive and expanded Pleistocene glaciations which exceed the stadial glacier variations in the Holocene. Thus more ancient landforms have been mostly erased. Moreover erosion and further degradation of seismically induced landslides in non glacier areas depends mainly on climate. Landforms preserve better in arid and semiarid conditions.

Because all correlations were obtained for landslide inventories with the area of the largest earthquake triggered landslide about 1 km<sup>2</sup> (Malamud et al., 2004a, b) in the strict sense the suggested approach can be used for mountain provinces where this typical area doesn't exceed 1 km<sup>2</sup>. Using this approach for active regions with larger seismically induced landslides demands calculating landslide distribution function for such landslide inventories or determining functional dependence between landslide volume (area) and such factors as type of rock material, degree of internal fissuring, slope inclination, water content etc.

The separate problem is revealing the typical size of the largest landslide body for specific seismically active area. Not very strong earthquake can trigger the largest landslide comparable in size with the ordinary landslide caused by actually strong earthquake. As a result this necessitate determining for particular area exactly the largest paleolandslides taking into account their age and preservation. There are no special studies of the landslide size distribution for Russian Altai due to lack of historic accounts and difficulties of correlating of

the largest slope failures with particular paleoearthquakes. For the 2003 Chuya earthquake the volume of the largest landslide exceeds about 2 orders of magnitude the volume of the next one. So we suggest that each studied giant seismically induced paleolandslide (comparable with the largest landslide caused by the 2003 Chuya earthquake considering their age and preservation) stands for a separate trigger. For seismically active regions where strong earthquake could generate several largest landslides with comparable volumes paleolandslide dating is required to distinguish prehistoric events.

There are some problems with absolute dating of paleolandslides. It is quite difficult to find buried or covered soils, organic matter, dammed lake sediments or culture layers especially for the areas with arid climate. Nevertheless such kind of dating is the only way to expand the seismological data about the repetition of the strongest shocks because an average recurrence interval of strong earthquakes much more exceeds the time period of seismological researches.

For the active mountain provinces of repeatedly occurred earthquakes the landslide bodies of the second and even the third generations are often concentrated practically on the same area. Sometimes they overlay each other. In this situation the suggested approach can give the opportunity to estimate the magnitude of the youngest paleoearthquake which triggered the upper landslide. At the same time while estimating the total volume of triggered landslides using Eq. (3) the error caused by wrong number of determined events doesn't exceed 5 % (in case of three landslides with the volume of  $V_{Lmax}/3$  instead of one with  $V_{Lmax}$ ) which can be ignored in calculating erosion rate.

There are also some local difficulties in establishing the seismic origin of landslide events and determining of the landslide parameters where the joining of several detachments has occurred.

And finally it should be emphasized that in order to properly evaluate the seismic potential of a region, and to assess the associated topography changes all available methods and approaches are necessary to be used. Despite of mentioned difficulties and limitations the suggested approach can improve the fault studies and form the basis for seismic hazard zoning in poorly studied regions with the shortage of seismological and historical data.

## Conclusion

Estimating earthquake magnitudes and topography changes using instrumental data and historic accounts can give information about the seismicity of mountain provinces during relatively short time period. The method of paleoseismogeology developed in Russia since the 1960s can give this information for the time period of  $10^4$  years. The key point of the method is analysis of geomorphically expressed surface displacement of evidently seismic origin. So far most of research has focused on coseismic fault motion and the seismogravitational dislocations have been used mainly for establishing epicentral zones and the timing of old earthquakes. At the same time using the parameters of seismically induced landslides for estimating earthquake's magnitudes can essentially improve the analysis of seismotectonic dislocations. In this case, the largest earthquake-induced landslide is the most interesting target.



Using parameters of the largest seismically induced landslides allow us to calculate magnitudes of prehistoric earthquakes which caused these giant slope failures, the total volume of earthquake triggered landslides, the contribution of landslides caused by aftershocks and finally the Holocene regional erosion rate due to seismically induced landslides by the example of Chagan-Uzun river basin (SE Altai, Russia).

It should be noted that different parameters of earthquake triggered landslides are not simply a functions of earthquake magnitude. There are additional factors related both to geomorphic and earthquake mechanism considerations such as roughness of topography, rock type, hydrological conditions, earthquake type and depth, direction of energy focusing, regional morphotectonic structure and so on. We believe that all of them play important role in seismic triggering of landslides but as soon as landslide event has occurred the statistical approach appears to be the most promising tool. It gives universal laws for landslide events in any conditions and allows correlating different parameters irrespective of their functional links.

The suggested approach (Fig. 1) was tested for the mountainous, seismically active SE part of Russian Altai where there are many large Holocene seismically induced landslides and the 2003 Chuya earthquake ( $M_S = 7.3$ ) took place. Despite several objective difficulties including: 1) establishing the seismic origin of paleolandslides; 2) estimating the typical size of the largest landslides for particular region and time period; 3) determination of the landslide parameters where the joining of several detachments or considerable change of landslide's body has occurred, this approach demonstrates the principle possibility of using the largest seismically induced landslides for estimating the paleoseismicity and earthquake induced topography changes.

## References

- Agatova, A.R. Geomorphologic mapping of the Chagan-Uzun river basin: a key for reconstructing history of Pleistocene glaciations in the Southeastern Altai. *Stratigraphy and Geological Correlation*. 2005, 13(6), 656-666.
- Agatova, A.R.; Novikov, I.S.; Vysotsky, E.M.; Gibsher, A.S. Geomorphologic effects of the 27 September and 1 October 2003 earthquakes in Gorny Altai. *Geomorfologiya*. 2004, 3, 3-12 (in Russian).
- Agatova, A.R.; Nepop, R.K.; Vysotsky, E.M. Seismogravitational paleodislocations in Chagan-river valley (SE Altai, Russia). *Geomorfologiya*. 2006, 4, 53-62 (in Russian).
- Aki, K. Magnitude-frequency relation for small earthquakes; a clue to the origin of large earthquakes. *J. Geophys. Res.* 1987, 92, 1349-1355.
- Arefev, S.S.; Aptekman, Zh.Ya.; Bykova, V.V.; Matveev, I.V.; Mikhin, A.G.; Molotkov, S.G.; Pletnev, K.G.; Pogrebchenko, V.V. Seismic focus and aftershocks of the 2003 Altai (Chuya) earthquake. *Fizika Zemli*. 2006, 2, 85-96 (in Russian).
- Bath, M. Lateral inhomogeneities in upper mantle. *Tectonophysics*. 1965, 2, 483-514.
- Belousov, V.V. Concerning the methods of seismic risk zoning. *Izvestiya AN SSSR, Ser. Geophysics*. 1954, 3, 209-222 (in Russian).
- Bommer, J.J.; Rodriguez, C.E. Earthquake-induced landslides in Central America. *Eng. Geol.* 2002, 63, 189-220.

- Bulatov, V.I.; Dik, I.P.; Revjakin, V.S. Glaciological observations in Akkol-river basin. *Glyatsiologiya Altaya*. 1967, 5, 178-183 (in Russian).
- Burbank, D.W. Rates of erosion and their implications for exhumation. *Miner. Mag.* 2002, 66(1), 25-52.
- Chernov, G.A.. Seismogeological and neotectonic studies in the Altai-Sayan area. In *Seismogeology of the Eastern Altai-Sayan Area*; Solonenko, V.P.; Nikolaev, V.A.; Eds.; Nauka, Novosibirsk, 1978; pp. 6-27 (in Russian).
- Devyatkin, E.V. *Cenozoic sediments and neotectonics of the SE Altai*; USSR Academy of Science, Moscow, (GIN Transactions, Issue 126), 1965, 244 p (in Russian).
- Dobretsov, N.L.; Buslov, M.M.; Delvaux, D.; Berzin, N.A.; Ermikov, V.D. Meso- and Cenozoic tectonics of the Central Asian mountain belt: effects of lithospheric plate interaction and mantle plume. *International Geology Review*. 1996, 38, 430-466.
- Evernden, J.F. Study of regional seismicity and associated problems. *Seis. Soc. Am. Bull.* 1970, 60, 393-446.
- Filina, A.G. Earthquakes in the Altai and Sayan regions. In *Earthquakes in the USSR in 1982. Annual Catalog*; Kondorskaya, N.V.; Ed.; Nauka, Moscow, 1985 (in Russian).
- Filina, A.G. Earthquakes in the Altai and Sayan regions. In *Earthquakes in the USSR in 1984. Annual Catalog*; Kondorskaya, N.V.; Ed.; Nauka, Moscow, 1987 (in Russian).
- Filina, A.G. Earthquakes in the Altai and Sayan regions. In *Earthquakes in the USSR in 1988. Annual Catalog*; Kondorskaya, N.V.; Ed.; Nauka, Moscow, 1991 (in Russian).
- Filina, A.G. Earthquakes in the Altai and Sayan regions. In *Earthquakes in the USSR in 1989. Annual Catalog*; Kondorskaya, N.V.; Ed.; Nauka, Moscow, 1993 (in Russian).
- Filina, A.G. Earthquakes in the Altai and Sayan regions. In *Earthquakes in the USSR in 1991. Annual Catalog*; Kondorskaya, N.V.; Ed.; Nauka, Moscow, 1997 (in Russian).
- Filina, A.G.; Kuchai, O.A. Earthquakes in the Altai and Sayan regions. In *Earthquakes in the USSR in 1987. Annual Catalog*; Kondorskaya, N.V.; Ed.; Nauka, Moscow, 1990 (in Russian).
- Florensov, N.A. *Treaties in Structural Geomorphology*; Nauka, Moscow, 1978; 238 p (in Russian).
- Florensov, N.A.; Solonenko, V.P. (Eds.) *The Gobi-Altai Earthquake*; U.S. Department of Commerce, D.C., 1965, 424 p.
- Frohlich, C.; Davis, S.D. Teleseismic b values; or, much ado about 1.0. *J. Geophys. Res.* 1993, 98, 631-644.
- Gerasimov, I.P. Using geomorphological methods in seismotectonic researches (by the example of the hollow of the Issyk-Kul' Lake). *Problems of the earthquake prediction* (Institute of Geophysical Researches, AN SSSR, Transactions), 1954, 25(152), 9-15 (in Russian).
- Gubin, I.E. *Seismotectonic method of seismic risk zoning*; USSR Academy of Science, Moscow, (Institute of Geophysics Transactions 13(140)), 1950; 63 p (in Russian).
- Gutenberg, B.; Richter, C.F. *Seismicity of the Earth and Associated Phenomenon*; 2<sup>nd</sup> ed. Princeton University Press, Princeton, NJ, 1954; 310 p.
- Gzovskij, M.V. Tectonophysics bases of geological criteria of seismicity (1). *Izvestiya AN SSSR, Ser. Geophysics*. 1957a, 2, 141-160 (in Russian).
- Gzovskij, M.V. Tectonophysics bases of geological criteria of seismicity (2). *Izvestiya AN SSSR, Ser. Geophysics*., 1957b, 3, 273-283 (in Russian).

- Harp, E.L.; Jibson, R.W. Landslides triggered by the 1994 Northridge, California, Earthquakes. *Bulletin of the Seismological Society of America*. 1996, 86(1B), S319-S332.
- Hatheway, A.W.; Leighton, F.B. Trenching as an exploratory method. In *Geology in the Siting of Nuclear Power Plants*; Hatheway, A.W.; McClure C.R.; Eds.; Geol. Soc. Am. Rev. Eng. Geol. 1979; V, IV, 169-196.
- Hovius, N.; Stark, C.P.; Allen, P.A. Sediment flux from a mountain belt derived by landslide mapping. *Geology*. 1997, 25, 801-804.
- Jibson, R.W. Use landslides for paleoseismic analysis. *Engineering Geology*, 1996, 43, 291-323.
- Kanamori, H. Magnitude scale and quantification of earthquakes. *Tectonophysics*. 1983, 93, 185-199.
- Keefer, D.K. Landslides caused by earthquakes. *Geological Society of America Bulletin*. 1984, 95, 406-421.
- Keefer, D.K. The importance of earthquake-induced landslides to long-term slope erosion and slope-failure hazards in seismically active regions. *Geomorphology*. 1994, 10, 265-284.
- Keefer, D.K. Investigating landslides caused by earthquakes - a historical review. *U.S. Surveys in Geophysics*. 2002, 23, 473-510.
- Keefer, D.K.; Wilson R.S. Predicting earthquake-induced landslides, with emphasis on arid and semi-arid environments. In *Landslides in Semi-arid Enviroments*; Sadler P.M.; Morton D.M.; Eds.; Inland Geological Society of Southern California Publications, Riverside, Ca, 1989; Vol. 2, part 1, pp. 118-149.
- Khromovskikh, V.S.; Solonenko, V.P.; Semenov, R.M.; Zhilkin, V.M. *Paleoseismogeology of the Great Caucasus*; Nauka, Moscow, 1979; 178 p (in Russian).
- Kirnos, D.P.; Kharin, D.A.; Shebalin, N.V. History of instrumental seismology in the USSR. In *Earthquakes in the USSR*; Vvedenskaya, N.A.; Kondorskaya, N.V.; Eds.; AN SSSR, Moscow, 1961; pp. 9-66 (in Russian).
- Leonov, N.N. The Khait, 1949 earthquake and geological conditions of its origin. *Proceedings of Academy of Sciences of the USSR, Geophysics*, 1960, Series 3, 409-424 (in Russian).
- Malamud, B.D.; Turcotte, D.L.; Guzzetti, F.; Reichenbach, P. Landslides inventories and their statistical properties. *Earth Surface Processes and Landforms*. 2004a, 29, 687-711.
- Malamud, B.D.; Turcotte, D.L.; Guzzetti, F.; Reichenbach, P. Landslides, earthquakes and erosion. *Earth and Planetary Science Letters*. 2004b, 229, 45-59.
- Maloletko, O.M. (Ed.) *Atlas of the Altai Territory. Book 1*; GUGK, Moscow-Barnaul, 1978 (in Russian).
- Masarsky, S.I.; Moiseenko, F.S. Seismicity of the Altai. *Soviet Geology and Geophysics*. 1962, 3 (8), 104-106.
- Molnar, P.; Tapponnie, P. Cenozoic tectonics of Asia: Effects of a continental collision. *Science*. 1975, 189, 419-426.
- Muir, J. *The Yosemite*; Doubleday, New York, 1912; 1962 Reprint ed., 225 p.
- Nepop, R.K.; Agatova, A.R. Estimation of magnitudes of old earthquakes in the Gornyi Altai region based on analysis of seismogravitational dislocations. *Doklady Earth Sciences*. 2006a, 411(8), 1212-1214.
- Nepop, R.K.; Agatova, A.R. Influence of aftershocks upon erosion due to seismically induced landslides. In *Geodynamic evolution of lithosphere of the Central Asian mobile belt*;

- Sklyarov, E.V.; Ed.; Institute of Earth Crust, Irkutsk, 2006b; Issue 4, V.2, pp.61-64 (in Russian).
- Nepop, R.K.; Agatova, A.R. Estimating magnitudes of prehistoric earthquakes from landslide data: first experience in southeastern Altai. *Russian Geology and Geophysics*. 2008, 49, 144-151.
- Nikonov, A.A.; Vakov, A.V.; Veselov, I.A. *Seismotectonics and earthquakes of the Pamir-Tien-Shan collision zone*; Nauka, Moscow, 1983; 240 p. (in Russian).
- Novikov, I.S. *Morphotectonic of Altai*; SB RAS Geo, Novosibirsk, 2004; 313 p. (in Russian).
- Pacheco, J.F.; Scholz, C.H.; Sykes, L.R. Changes in frequency - size relationship from small to large earthquakes. *Nature. (Gr. Brit.)* 1992, 355, 71-73.
- Pain, C.F.; Bowier, J.M. Denudation following the November 1970 earthquake at Magang, Papua New Guinea. *J. Geomorph.* 1973, 18, 92-104.
- Plafker, G.; Ericksen, G.E.; Fernández Concha, J. Geological Aspects of the May 31, 1970, Perú Earthquake. *Bulletin of the Seismological Society of America*. 1971, 61, 543-578.
- Plafker, G.; Rubin, M. Vertical tectonic displacements in south-central Alaska during and prior to the great 1964 earthquake. *Journal of Geosciences*. 1967, 10(19), 53-66.
- Rogozhin, E.A.; Platonova, S.G. *Strong earthquake focal zones of Russian Altai in Holocene*; UIPE RAS, Moscow, 2002; 130 p. (in Russian).
- Rogozhin, E.A.; Ovsyuchenko, A.N.; Marahanov, A.V.; Ushanova, E.A. The tectonic setting and geological consequences of the Altai earthquake. *Geotektonika*. 2007, 2, 3-22.
- Schuster, R.L.; Highland, L.M. Socioeconomic and environmental impacts of landslides in the western hemisphere. *USGS Open-File Report*, 2001, 01-276.
- Shchukina, E.N. Geography and stratigraphy of Quaternary deposits in the Altai Territory. In *Stratigraphy of Quaternary (Anthropogene) Deposits in the Asian USSR and their Correlation with Deposits in the European USSR*; Gromov, V.I.; Ed.; Nauka, Moscow, 1960; 127-165 p. (in Russian).
- Slemmons, D.B. Geological effects of the Dixie Valley-Fairview Peak, Nevada, earthquakes of December 16, 1954. *Bull. Seis. Soc. Am.* 1957, 47, 353-375.
- Solonenko, V.P.. Paleoseismogeological metod. In *Active Tectonics, Volcanism, and Seismicity of the Stanovoi Upland*; Solonenko, V.P.; Ed.; Nauka, Moscow, 1966; pp. 15-35 (in Russian).
- Solonenko, V.P. Earthquakes and relief. *Geomorfologiya*. 1973, 4, 3-13 (in Russian).
- Tocher, D. Earthquake energy and ground breakage. *Bulletin of the Seismological Society of America*. 1958, 48, 147-153.
- Turcotte, D.L. Self-organized criticality. *Reports on Progress in Physics*. 1999, 62, 1377-1429.
- Ufimcev, G.F. *Morphotectonic of Eurasia*; Irkutsk State University, Irkutsk, 2002; 494 p. (in Russian).
- Vazhenin, B.P. *The principles, methods, and results of paleoseismic-geologic studies in the North-East of Russia*; NEISRI FEB RAS, Magadan, 2000; 205 p. (in Russian).
- Wallace, R.E. Earthquake recurrence intervals on the San Andreas fault. *Geological Society of America Bulletin*. 1970, 81(10), 2875-3889.
- Wells, D.L.; Coppersmith, K.J. New empirical relationships among magnitude, rupture length, rupture width, rupture area and surface displacement. *Bulletin of the Seismological Society of America*. 1994, 84(4), 974-1002.

- 
- Wieczorek, G.F. Preparing a detailed landslide -inventory map for hazard evaluation and reduction. *Bulletin Association of Engineering Geologists*. 1984, 21, 337–342.
- Zhalkovsky, N.D.; Chernov, G.A.; Muchnaya, V.I.. Seismic risk mapping in the Altai-Sayan mountain province. In: *Seismogeology of the Eastern Altai-Sayan Mountain Province*; Solonenko, V.P.; Nikolaev V.A.; Eds.; Nauka, Novosibirsk, 1978; pp. 79-90 (in Russian).
- Zhalkovsky, N.D.; Kuchai, O.A.; Muchnaya, V.I. Seismicity and some characteristics of the stress state of the Earth's crust in the Altai-Sayan region. *Russian Geology and Geophysics*. 1995, 36(10), 16-26.



*Chapter 6*

## **RECOGNITION OF LIKELY LARGE-SCALE LANDSLIP FAILURE SURFACES THROUGH GEOTECHNICAL CORE LOGGING METHODS**

*Nick Thompson<sup>1</sup> and Robert J. Watters<sup>2</sup>*

<sup>1</sup>School of Conservation Sciences, Bournemouth University, United Kingdom

<sup>2</sup>Mackay School of Earth Sciences and Engineering,  
University of Nevada, Reno, United States

### **Abstract**

The Hawaiian Scientific Drilling Project (HSDP) Phase 1 deep drilling project produced a continuous rock core extending 3.1 km into Mauna Kea volcano on the island of Hawaii. This core generally consisted of lithified but often unconsolidated subaerial and submarine lava flows (basalts) with minor amounts of ash, soil and sedimentary rocks. The primary intention for this project was to provide information about the origin and geochemical, magnetic and hydrologic conditions of the volcano but subsequent geotechnical analysis of the rock core has identified a significant natural hazard may also be present through recognition of a potential large-scale landslide failure surface.

Commonly used qualitative geotechnical logging methods, including RQD and limited GSI and RMR techniques, were initially performed. This effort identified a significant weak zone beginning at a depth of approximately 1.1 km below the ground surface, the location of a particularly unconsolidated region of hyaloclastite, or rapidly quenched basaltic glass. Subsequent strength testing of the core (point load) allowed a quantitative strength profile to be created for the entire depth of the core, thus representing the vertical strength of the volcanic edifice. Though this profile characterizes only a minute area of the overall edifice, this analysis has shown how geotechnical rock core logging methods may be implemented to identify otherwise unseen hazards or significant changes in rock mass quality.

### **1. Introduction**

Though rock cores may represent only a small fraction of an area being studied, their ability to reveal otherwise unobservable rock mass characteristics can be indispensable. Such

is the case with the study presented here where the great depth of region in question likely means it may have gone unrecognized.

The Hawaii Scientific Drilling Project (HSDP) Phase 1 deep drilling project was developed as a venture of the International Continental Scientific Drilling Program (ICDP), a multinational organization designed to promote and fund continental scientific drilling (ICDP, 2008). This phase of the HSDP project produced a 9.7 cm diameter, generally continuous rock core to a depth of 3.1 km into Mauna Kea volcano for a number of exploratory purposes (see De Paolo et al., 2000). The initial 1.1 km of drilling penetrated various types subaerial lava flows (basalts) with minor amounts of soil, ash and sedimentary rocks. The remainder of the core consists of rocks formed below sea level. From 1.1 km, the following 0.9 km of the core generally consists of poorly consolidated basaltic glass, or hyaloclastite, a granular medium formed from the rapid quenching of molten lava flows. These hyaloclastites are altered to various degrees, which generally promotes consolidation, lithification and strength with depth (Walton and Schiffman, 2003; Schiffman et al., 2006). Minor intrusive basalts are also present. The remaining 1.1 km of the HSDP core is mostly comprised of indurated and competent pillow basalts.

The poorly consolidated hyaloclastite zone at 1.2-2 km depths is of particular concern as Hawaiian Island flanks are notoriously unstable on a dangerously large scale (Moore et al., 1994). In fact, past slope failures associated with these precarious flanks are recognized as the largest landslide-type events on Earth, having traveled up to 235 km from their sources and covered areas of over 23000 km<sup>2</sup> (Canon-Tapia et al., 2002). An event of this magnitude today would not doubt have devastating consequences, even more so when the added threat of an associated tsunami is considered. Recognition of the conditions that promote these instabilities is therefore of the utmost importance.

The rock core produced by the HSDP project, though not originally acquired for this purpose, was used by Schiffman et al. (2006) and Thompson et al. (2008) with this goal in mind. Common geotechnical techniques typically performed in mining and construction activities were not performed on the HSDP core during its extraction; these methods were applied subsequently by these authors to develop both a qualitative and quantitative understanding of the weaknesses present in the HSDP core. A summary of the core logging methods used in these studies is presented here. These methods were used to identify areas along the core where laboratory samples could be selected from to obtain data usable in stability analyses, as presented by Thompson et al. (2008).

## **2. Geotechnical Rock Core Logging**

### **2.1. Qualitative Rock Mass Descriptions**

Several qualitative studies were applied to the HSDP core, the first of which was Rock Quality Designation (RQD) procedure. Though the end result of an RQD analysis is a numerical value, and could therefore be considered a quantitative method, this number falls in a broad range of values which describe general rock mass *quality*. As such, it is considered a qualitative approach in this study. This notion also applies to the GSI and RMR results described later.



RQD is a standard method for describing the degree of fracturing of a rock mass, as described by Deere (1963). RQD is calculated as the percentage ratio of the sum of core fragments greater than 10 cm to the total drilled length per run. Therefore, RQD is considered a general estimate of rock mass quality which can be related to more descriptive terms as follows (Deere, 1963):

<b>RQD</b>	<b>ISRM rock classification</b>
0-25%	very poor
25-50%	Poor
50-75%	Fair
75-90%	Good
90-100%	excellent

Because measuring the RQD for each of the 1083 core boxes that contain the HSDP would not doubt be a laborious and time-consuming task, a more efficient method had to be developed due to time constraints. As descriptions and high quality photographs of each of the HSDP core boxes was made available online (Fig. 1), the RQD study was performed remotely using a laptop computer and a scaled measuring device (ICDP, 2008). To establish the accuracy of this approach, the traditional RQD method was applied to a limited number of core runs at the HSDP storage facility, the results of which were compared to RQD results determined remotely (Table 1).

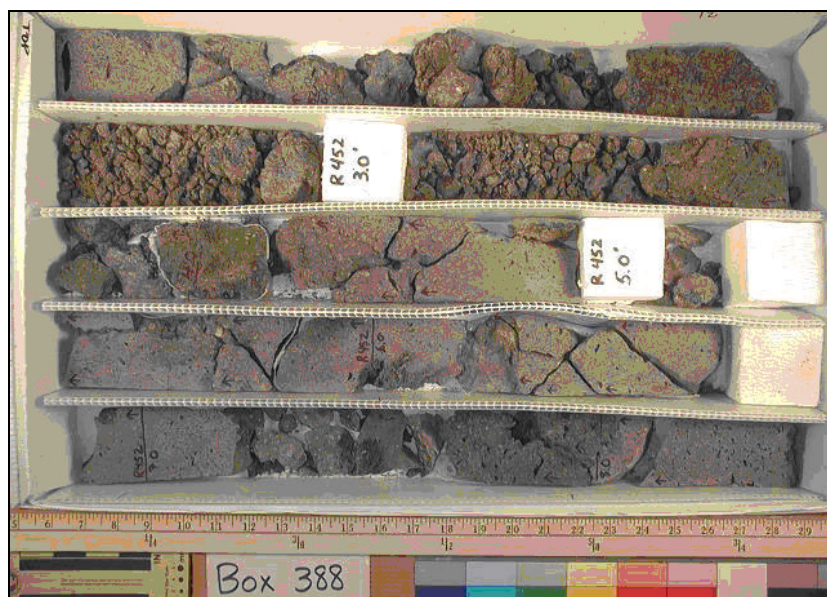


Figure 1. HSDP Box 388. Basaltic hyaloclastite and massive submarine flows, moderately-to-highly olivine phyric basalt.

As observed in Table 1, the differences between the RQD values determined remotely and traditionally were generally quite small. The large discrepancies seen in the RQD values of boxes 396 and 539 is likely due to the difficulty in identifying small-scale fractures remotely. All other differences are sufficiently small enough to be considered negligible. This

is particularly true when the 25% increments of the descriptive rock mass quality terms are considered.

**Table 1. Comparison of RQD values determined remotely to RQ determined traditionally. (Large discrepancies in remote and traditional results were tested a second time)**

Box	RQD determined remotely (%)	RQD determined traditionally (%)	Percent difference	RQD determined traditionally, trial 2 (%)
189	97.7	92.9	4.9	
393	0	0	0	
396	42.7	23.3	45.4	41.7
420	52.6	57.8	9.0	
448	90.0	89.4	0.7	
473	87.6	88.6	1.1	
508	28.9	27.4	5.2	
539	62.2	75.7	17.8	67.1
627	85.6	93.1	8.1	
837	32.0	30.4	5.0	

Because of the results of the RQD analysis is too lengthy to be given in detail here. A brief summary of the trends observed in the RQD values is as follows:

- Inconsistent RQD values and subsequent rock classification in the subaerial portion of the core (<1.1 km depth). This is thought to be due to the high lithologic variability present in this section.
- Abundance of very low RQD values (0-25%) beginning at the top of the submarine section of the core, the first location of poorly consolidated hyaloclastites.
- General increase in RQD values and associated rock mass quality on going deeper and away from the poorly consolidated hyaloclastites.
- Decrease in RQD towards the bottom of the cored hole. The decrease in rock mass quality in all rock types is suspected to be a result of stress relief as rocks from great depths are relieved of overburden pressures. Signs of stress relief, such as diskings, were present in rock core from great depths.

The most significant observation of the RQD analysis is the abundance of low values at the top of the submarine portion of the HSDP core, beginning at approximately 1.1 km. These low values correlate to the location of the poorly consolidated hyaloclastites.

Geological Strength Index (GSI) is an additional numerical description of rock mass quality performed on the HSDP core. This method describes rock mass condition based on fracture spacing and condition (roughness, clay lining, etc.) and is estimated by qualitative visual inspection and compared to the chart of Hoek et al. (1995) to assign a numerical value. For this study, only a proportional number of core boxes for each lithologic zone present in the HSDP core. Due to the highly variable nature of the HSDP core, the results of this exercise are also variable for each rock type considered, though they do represent the general relative strengths of each lithology (Table 2).

Also observed in Table 2 are Rock Mass Rating (RMR) values estimated for the same core boxes for which the GSI analysis was performed. RMR is a more thorough description of rock mass quality than RQD or GSI as it considers uniaxial compressive strength, RQD, discontinuity spacing and condition and groundwater conditions. It is also generally relatable to GSI and used here as a validation of the GSI results which were needed in subsequent slope stability analyses as discussed by Thompson et al. (2008) (Bieniawski, 1999). RMR values here were obtained by using the RQD values obtained as discussed above, uniaxial compressive strength values for each rock type, and core descriptions from the initial logging reports. As seen in Table 2, RMR and GSI value estimations are very closely matched in range and mean values confirming both the reliability of the estimation methods and *overall* high quality of the HSDP core, taking into exception the poorly consolidated hyaloclastite zone below 1.1 km.

**Table 2. GSI and RMR estimation results**

Rock type	GSI range	Mean GSI value	RMR range	Mean RMR value
Subaerial basalt flows	25 – 70	49	35 - 67	51
Hyaloclastites <sup>a</sup>	23 – 40	32	24 - 44	36
	25 – 57	40	25 - 49	38
	35 – 65	56	36 - 60	49
Submarine basalt flows	35 – 63	46	37 - 61	50

<sup>a</sup>The four different hyaloclastite value rows represent various degrees of alteration present, as discussed by Schiffman et al., (2006) and Thompson et al. (2008). The alteration zones from top to bottom are incipient, smectitic and palagonitic, which also represents their relative location in the core.

## 2.2. Quantitative Rock Mass Strength Characterization

The HSDP core was split length-wise along its entire span, one half as a working section, the other reserved for archival purposes. Because of this, typical methods such as uniaxial and triaxial strength testing could not easily be used to quantify the strength of the HSDP rock types. To accommodate this unusual shape, point load testing was therefore employed, an indirect measure of the tensile strength of a rock specimen. This method is also portable and efficient, allowing a large amount of data to be collected easily in the field. Because the core generally retains a consistent shape with length/diameter ratios typically greater than the suggested value of 1.4, the diametral method of specimen orientation was used in this study (Hoek and Brown, 1988).

In the point load test, a rock specimen is placed between two 60° conical platens with a 5 mm radius. The specimen is then broken within 10-60 s by the application of a concentrated load. The maximum pressure at the time of failure,  $P_{gauge}$ , is recorded and converted to a load at failure,  $P$ :

$$P = P_{gauge} * A_e$$

where  $A_e$  = effective piston area = 9.67 cm<sup>2</sup>.

The load at failure,  $P$ , is then converted to an uncorrected point load strength index,  $I_s$ :

$$I_s = P/D_e^2$$

where  $D_e$  = equivalent core diameter. For the diametral test,  $D_e = D$  = platen separation at the time of failure. The corrected point load strength index, or  $I_{s(50)}$ , is defined as the point load strength value for a sample of diameter  $D = 50$  mm (ISRM, 1985). Therefore, for specimens where  $D \neq 50$  mm, the value of  $I_s$  is normalized to  $I_{s(50)}$  by the following equation:

$$I_{s(50)} = F * I_s$$

where  $F = 0.79$  (as obtained graphically from ISRM [1985] based on  $D = 30$  mm).

302 point load tests were conducted at regular intervals along the length of the HSDP core, though higher concentrations of tests were performed in weak hyaloclastite zone discussed in Section 2.1 (Table 3). The following key observations were made:

- Increase in median hyaloclastite  $I_{s(50)}$  values with increasing depth and degree of alteration (0.5, 0.8 and 1.9 MPa for the incipient, smectitic and palagonitic alteration zones, respectively).
- Large differences between the median values of the hyaloclastites (1.1 MPa) and the subaerial and submarine basalts (6.5 and 8.0 MPa, respectively).

**Table 3. Point load  $I_{s(50)}$  values for the various HSDP rock types. S.D. – standard deviation**

Rock Type (n=number of tests)	Depth range of samples tested (m)	Range of $I_{s(50)}$ Values (MPa)	Mean (S.D.) $I_{s(50)}$ values (MPa)	Median (S.D.) $I_{s(50)}$ values (MPa)
Subaerial basalt flows, aa (n=55)	+1.8-1080 <sup>b</sup>	1.1-17.6	7.3 (4.0)	6.8
Subaerial basalts, pahoe-hoe (n=22)	+1.8-1080 <sup>b</sup>	2.0-13.5	6.7 (2.9)	6.3
Subaerial basalts, transitional (n=10)	+1.8-1080 <sup>b</sup>	0.1-7.4	3.9 (2.3)	4.5
Incipient altered hyaloclastite (n=41)	1080-1335	0.0-1.4	0.5 (0.4)	0.5
Smectitic altered hyaloclastite (n=45)	1405-1573	0.1-2.1	0.9 (0.5)	0.8
Palagonitic altered hyaloclastite (n=87)	1573-3098	0.3-5.8	2.0 (1.0)	1.9
Submarine basalt flows (n=5)	1885-3098	6.2-10.2	7.5 (1.6)	7.2
Submarine intrusive basalts (n=2)	1885-3098	6.3-9.9	8.1 (2.6)	8.1
Submarine pillow basalts (n=35)	1885-3098	2.9-23.6	10.1 (4.4)	8.2

<sup>b</sup>Positive value of 1.8 indicates coring began at 1.8 m above mean sea level, 1080 m indicates depth below mean sea level

In summary, the key observations made here are the clear differences in strength between the various degrees of altered hyaloclastites and hyaloclastites in general in comparison to the surrounding subaerial/submarine basalts.

### 3. Further Characterization and Implications

As evident by the RQD, GSI and RMR analyses, an inherent weakness exists in the HSDP core beginning at a depth of 1.1-2 km, particularly so in the upper, poorly consolidated section of this zone. This observation is substantiated by the strength values provided from point load testing; low point load values typically correlate to low RQD, GSI and RMR estimations.

For a more in-depth analysis, point load  $I_{s(50)}$  values are converted to rock specimen uniaxial compressive strength (UCS), a more accurate representation of rock strength. This is done this done easily by multiplying point load  $I_{s(50)}$  values by suggested conversion factors, typically in the range of 20-25 (Bieniawski, 1975; ISRM, 1985; Goodman, 1989). For this study, however, these larger conversion factors did not apply to the often poorly consolidated nature of the tested rock samples. To accommodate similar limitations in previous studies, authors have suggested adopting conversion factors based on UCS values for the same material on which point load values were obtained (Read et al., 1980; AEWES, 1990; Leung and Radhakrishnan, 1990; Smith, 1997; Bowden et al., 1998). As several successful UCS tests were in fact conducted on the HSDP core for this study, a similar conversion factor calibration process could be implemented. As discussed by Thompson et al. (2008), two separate  $I_{s(50)}$ /UCS conversion factors were recognized, one for the poorly consolidated hyaloclastites (5.0) and one for the subaerial/submarine basalts (18.4). The rather low conversion factor found for the hyaloclastites is in good general agreement with those suggested by the previously mentioned authors.

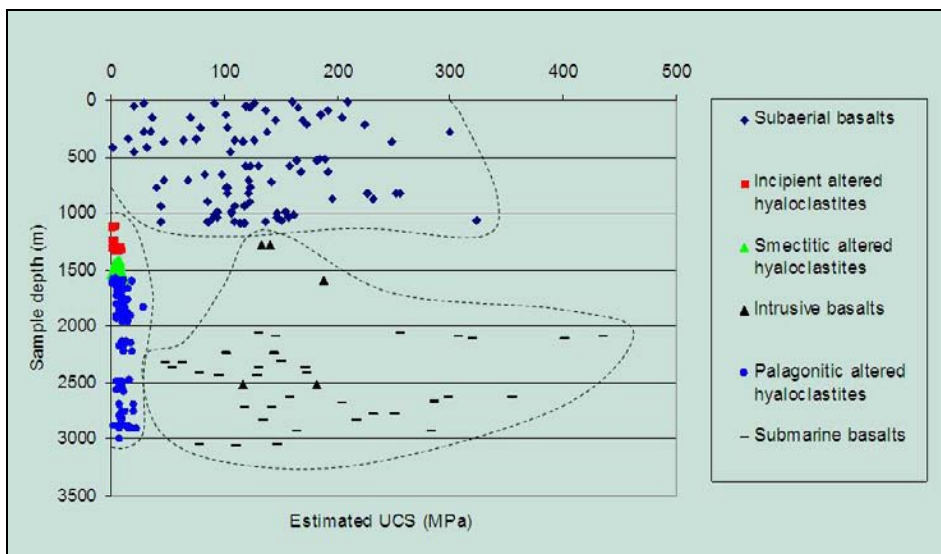


Figure 2. Unconfined compressive strength estimations with depth.

This conversion procedure allows the point load strength data collected in the field to now be presented as UCS values and for informative graphic strength profiles to be created (Figs. 2 and 3). Observable in Figure 2 are the marked differences in estimated rock mass UCS for the various lithologies along the HSDP core. This difference is most noticeable

beginning at 1.1 km. Consistent with the RQD analysis, rock strength is highly variable in the submarine section of the core, decreases at the hyaloclastites and increases dramatically in the submarine basalts. Figure 3 is a zoom view of the hyaloclastite section of Figure 2 and displays the general increase in consolidation and associated strength with increasing alteration. The poorly consolidated incipient altered hyaloclastites are recognized as by far the weakest area in the HSDP core and therefore a definite zone where a large-scale flank failure may originate.

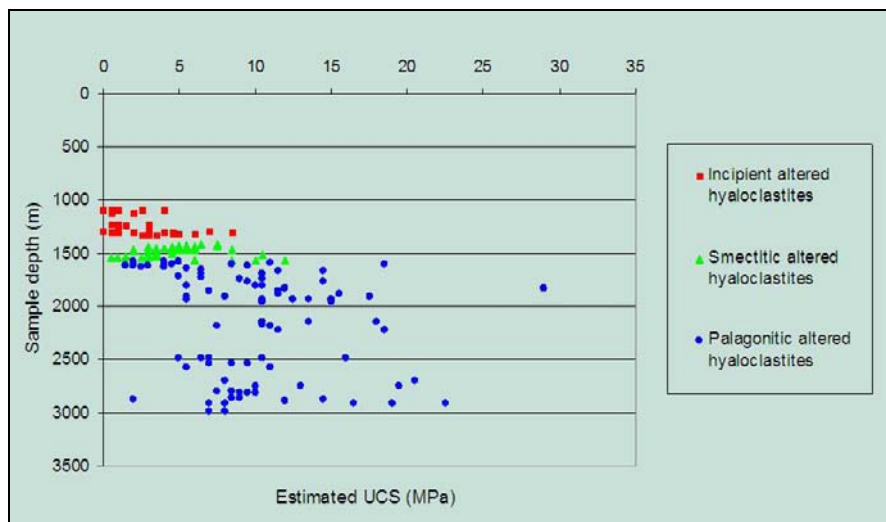


Figure 3. Estimated UCS values for the hyaloclastites specifically. Incipient altered hyaloclastites are the least consolidated.

## 4. Conclusion

The core logging methods described, though simple in their approach and application, have yielded important clues to the mass wasting events that may perhaps facilitate the large-scale collapse of oceanic island flanks. It is reasonable to assume that the poorly consolidated hyaloclastites recognized in this study may extend laterally for some distance, which would define a potential large-scale failure surface. It is again important to note that this core represents only a small part of an extremely large area. Additional coring of similar nature to the HSDP Phase 1 project and subsequent logging similar to the methods presented here would be invaluable in defining such a hazard. Furthermore, the remote technique applied here to define the RQD classifications may also be applied in similar future scenarios where this type of information is required but not recorded upon initial logging.

## Acknowledgements

The author would like to thank Dr. Robert Watters for his guidance throughout this project. Special thanks are also given to Dr. Peter Schiffman, Dr. Jaak Daemen, Kurt Katzenstein, Dr. Steve Bowman, Lumin Ma, and Rock Blitz for their assistance in rock

strength testing methods. Additionally, acknowledgements are given to Ed Mathez and Njoki Gitahi at the American Museum of Natural History in New York, New York for their help and hospitality in accessing the HSDP core.

## References

- AEWES (Army Engineer Waterways Experiment Station, Vicksburg, MS), 1990, Suggested methods for use of the point load tester in dredging applications. *AUG Technical Note* DRP-2-01, 1-6.
- Bieniawski, Z.T. *Eng. Geol.* 1975, 9, 1-11.
- Bieniawski, Z.T. *Engineering rock mass classifications*; John Wiley and Sons: New York, 1989, 251 pp.
- Bowden, A. J.; Lamont-Black, J.; Ulliyott, S. *Quart. J. Eng. Geol.* 1998, 31, 95-103.
- Canon-Tapia, E.; Guerrero-Garcia, J. C.; Herrero-Bervera, E.; Walker, G. P. L. *Phys. Earth and Plan. Int.* 2002, 129, 83-98.
- Deere, D.U. *R. Mech. Eng. Geol.* 1963, 1, 17-22.
- De Paolo, D. J.; Thomas, D. M.; Stolper, E. M.; Garcia, M. O. *Scientific Drilling Project: core logs and summarizing data*; California Institute of Technology: Pasadena, 2000.
- Goodman, R. E. *Introduction to Rock Mechanics*; John Wiley & Sons: New York, 1989, second edition.
- Hoek, E., Brown, E. T., 1988, The Hoek-Brown failure criterion – A 1988 update. In: Curran, J.C. (ed.), *Rock Engineering for Underground Excavations*, Proceedings of the 15th Canadian Rock Mechanics Symposium, Department of Civil Engineering, University of Toronto, Canada, 31-38.
- Hoek, E.; Kaiser, P. K.; Bawden, W. F. *Support of underground excavations in hard rock*; A.A. Balkema: Rotterdam, 1995, 215 pp.
- ICDP (2008). International Continental Scientific Drilling Program. [www.icdp-online.org](http://www.icdp-online.org).
- ISRM (International Society for Rock Mechanics), 1985, Suggested methods for determining point load strength. *International Journal for Rock Mechanics, Mineral Science and Geomechanical Abstracts*, 22, 51-61.
- Leung, C. F.; Radhakrishnan, R. *Geotech. Eng. Thai.* 1990, 21, 29-48.
- Moore, J.G.; Normark, W.R.; Holcomb, R.T. *Ann. Rev. Earth Plan. Sci.* 1994, 22, 119-144.
- Read, J. R. L., Thornton, P. N., Regan, W. M., 1980, A rational approach to the point load test. *Proceedings of the 3rd Australian and New Zealand Conference on Geomechanics*, Wellington, 2, 25-39.
- Schiffman, P.; Watters, R.J.; Thompson, N.; Walton, A. J. *Volc. Geoth. Res.* 2006, 151, 217-228.
- Smith, H. J. *Int. J. Rock Mech. Min. Sci.* 1997, 34, 702.
- Thompson, N.; Watters, R.J.; Schiffman, P. J. *Volc. Geoth. Res.* 2008, 171, 163-177.
- Walton, A.W.; Schiffman, P. *Geochem. Geophys. Geosys.* 2003, 4, 5, 8709. doi:10.1029/2002GC000368.





*Chapter 7*

# **MULTI-SCALE ANALYSIS FOR ESTIMATING STRONG GROUND MOTION AND STRUCTURE RESPONSES**

*Tsuyoshi Ichimura<sup>1</sup> and Muneo Hori<sup>2</sup>*

<sup>1</sup> Dept. Civil and Environmental Eng., Tokyo Institute of Technology

<sup>2</sup> Earthquake Research Institute, University of Tokyo, Japan

## **Abstract**

While full three-dimensional (3D) numerical simulation is a solution to estimate strong ground motion and a seismic structure response for a given earthquake, it is difficult to carry out numerical computation because of its huge computational cost; the order of a target domain size is  $10^4 \sim 5$  m and the target resolution required is  $10^{-2} \sim 0$  m. In this article, we present an efficient approach which is based upon multi-scale analysis to make a 3D simulation of wave propagation and amplification as well as seismic responses of an infrastructure. The formulation of the multi-scale analysis is presented, and it is validated by comparing a strong ground motion and a seismic structure response which is obtained by directly analyzing the whole system. The usefulness and applicability of this multiscale approach are also discussed.

## **1. Introduction**

It is necessary to increase spatial resolution in predicting strong ground motion and seismic structure response for a given earthquake, in order to advance design and construction of large structures such as long-span bridges and underground tunnels. Seismic responses of such structures are influenced considerably by local differences in the amplitude and phase of input strong ground motion, in particular when the structures are of complicated configuration or located in several non-flattened ground layers. A full three-dimensional (3D) numerical simulation will be a useful tool to estimate the strong ground motion and structure response in higher spatial resolution; the simulation is made for earthquake wave propagation from fault to infrastructure, as depicted in Fig. 1-a). Advancement of computational seismology and earthquake engineering accelerates research into developing such a tool.

However, it is difficult to carry out such 3D simulation since it requires its huge computational cost; the spatial resolution required for the structure analysis is in the engineering length-scale, say,  $10^{-2\sim 0}$  m, while the target domain size is in the geological length scale, say,  $10^{2\sim 5}$  m. In most cases, an approximate simulation is made which computes wave propagation in the geological length scale neglecting soft surface layers and then input resulting waves into the surface layers to analyze structure responses. This approximation is rather crude, and hence the analysis of soil-structure interaction is often simplified; a simple parallel layer model is used for surface layers, and two-dimensional state of plane strain is assumed. By its own nature, the approximate simulation is not applicable to a large-scale structure as mentioned above.

Recently, studies of earthquake motion prediction are conducted for practical engineering purposes (e.g., [1]), and remarkable progress of 3D seismic wave propagation simulation is being achieved (e.g., [2, 3, 4, 5, 6, 7, 8]). Also, in the field of computational mechanics, 3D numerical simulation with finer spatial discretization is being studied to analyze dynamic response of structures (e.g., [9, 10, 11]). Therefore, it can be expected that an efficient approach to carry out 3D numerical simulation of strong ground motion and structure response can be made by combining these two advanced simulations.

In this article, we present a multi-scale analysis for the 3D numerical simulation. The key idea of this analysis is to rationally link numerical simulation in the geological length-scale to that in the engineering length-scale; see Fig. 1-b). The rationality of the link is due to the mathematical theory that takes advantages of the singular perturbation expansion; this theory is established for analysis of general heterogeneous media [8, 12, 13]. Separately carrying out two numerical computations, the multi-scale analysis drastically reduces computational cost for the 3D simulation of strong ground motion and seismic structure responses.

The contents of this article are as follows: First, in section 2., multi-scale analysis is formulated for the 3D simulation of strong ground motion and seismic structure response. Next, we present an example of applying the multi-scale analysis in section 3.. The target problem is an underground shaft which connects a large-scale tunnel to the ground; the shaft runs through soft soil deposit. The results of the multi-scale analysis are compared with the *direct* analysis that is obtained by the huge-scale numerical computation, and it is shown that the agreement of the multi-scale analysis with the direct analysis is more than satisfactory. Some discussions are made for the potential usefulness of the multi-scale analysis in order to estimate strong ground motion and seismic structure responses of large infrastructures.

## 2. Formulation of Multi-Scale Analysis

In this section, we present the multi-scale analysis for the 3D numerical simulation of strong ground motion and seismic structure responses. The target problem is a fault-infrastructure system, denoted by  $D$ , as shown in Fig. 1-a). Since the formulation is used for the numerical computation, we start from a discretized wave equation by a finite element method (FEM) in spatial domain, i.e.,

$$[M][\ddot{u}] + [C][\dot{u}] + [K][u] = [0] \quad (\text{for } D). \quad (1)$$

where  $[M]$ ,  $[C]$  and  $[K]$  are mass, damping and stiffness matrices, respectively, and  $[u]$  is displacement vectors. Since  $[u]$  include displacement of both ground and the infrastructure, the spatial length-scale of Eq. (1) is in the engineering length scale and hence the dimension of the matrices and vector is huge.

Now, we formulate the multi-scale analysis proposed by the authors[8, 12, 13]. If viewed in the geological length-scale, local stiffness (which is determined in the engineering length-scale) is *averaged* so that it represents *effective* stiffness. In this manner, a stiffness matrix in the geological length-scale, denoted by  $[\bar{K}]$ , is constructed. Similarly,  $[\bar{C}]$  and  $[\bar{M}]$  are constructed using  $[M]$  and  $[C]$ , respectively. The dimension of  $[\bar{K}]$  is much smaller than that of  $[K]$ , and hence displacement viewed in the geological length-scale,  $[u^{(0)}]$ , is obtained by numerically solving

$$[\bar{M}][\ddot{u}^{(0)}] + [\bar{C}][\dot{u}^{(0)}] + [\bar{K}][u^{(0)}] = [0] \quad (\text{for } D). \quad (2)$$

The boundary conditions for  $[u^{(0)}]$  are easily derived from those of  $[u]$ . We should mention that the construction of  $[\bar{K}]$  is not trivial. Several averaging schemes which estimate effective properties are proposed, and we make use the scheme that is based on stochastic modeling[12].

We refine  $[u^{(0)}]$  so that displacement in the engineering length-scale is obtained. By suitably interpolating  $[u^{(0)}]$  (which is discretized in the geological length-scale), we can make a new displacement vector (which is discretized in the engineering length scale). This displacement, denoted by  $[u^{(0)*}]$ , is of the same dimension as  $[u]$ , but its spatial variation is in the geological length-scale. Thus, we need correction which changes in the engineering length-scale. The correction is needed only for a sub-domain of  $D$  which includes an infrastructure in it, in order to estimate the strong ground motion and seismic structure response. We choose a sub-domain, denoted by  $D_S$ , and determine the correction  $[u^{(1)}]$  by solving Eq. (1), as follows:

$$[M_S](\ddot{u}_S^{(0)*}) + [\ddot{u}_S^{(1)}] + [C_S](\dot{u}_S^{(0)*}) + [\dot{u}_S^{(1)}] + [K_S](u_S^{(0)*}) + [u^{(1)}] = [0] \quad (\text{for } D_S), \quad (3)$$

where  $[M_S]$ ,  $[C_S]$ ,  $[K_S]$  and  $[u_S^{(0)*}]$  are obtained by extracting  $[M]$ ,  $[C]$ ,  $[K]$  and  $[u^{(0)*}]$  for  $D_S$ , respectively. The dimension of  $[K_S]$  and others is much smaller than  $[K]$ , and hence Eq. (3) is numerically solved. Dispersion boundary conditions (or absorbing boundary conditions) must be posed for  $[u^{(1)}]$  since it is the correction of  $[u^{(0)}]$ .

The analysis of solving Eqs. (2) and (3) for  $[u^{(0)}]$  and  $[u^{(1)}]$  is respectively called the macro-analysis and the micro-analysis, and the multi-scale analysis combines the macro-analysis and the micro-analysis. This is called the macro-micro analysis. Denoting  $[u_S^{(0)*}] + [u^{(1)}]$  by  $[u_S]$ , we can rewrite Eq. (3) as

$$[M_S][\ddot{u}_S] + [C_S][\dot{u}_S] + [K_S][u_S] = [0] \quad (\text{for } D_S).$$

Thus, the macro-micro analysis is similar to the sub-structure method that solves Eq. (1) separating  $D$  into a set of sub-domains. The boundary conditions of the above differential equation are determined by connecting the solution of each neighboring sub-domains so that Eq. (1) is solved. The macro-micro analysis method, however, obtains the solution  $[u_S]$  only for  $D_S$ , since it uses  $[u_S^{(0)*}]$ , displacement which is discretized in the engineering length scale but changes in the geological length-scale, as an approximation of the boundary conditions on  $\partial D_S$ .

### 3. Numerical Experiments

In this section, we solve an example problem using the multi-scale analysis. The results of the 3D simulation of strong ground motion and structure responses are compared with those of the 3D simulation of analyzing the whole domain in the engineering length-scale by using huge numerical computation; from now on, the analysis that directly solves the whole domain is called direct analysis. As mentioned in the preceding section, the multi-scale analysis approximates the boundary conditions for the sub-domain, and hence the validity of this approximation is verified from the comparison.

First, we explain the example problem. The target domain is located above a basin; see Fig. 2-a). The dimension of the domain is  $9000 \times 9000 \times 2000$  m. This domain is of the largest size that can be numerically solved in the authors' computational environment with the accuracy being ensured up to 2 Hz. A fault is not included in this underground structure model. The domain consists of two layers, namely, bedrock and basement; the thickness of the both layers is 1000 m. Soft soil deposit of slightly complicated geometry is put at the center on the top surface; see Fig. 2-b). The material properties of the two layers and soil deposits are summarized in Table 1.

A large-scale structure is located in the basement at the center of the domain, as shown in Fig. 2. The structure is an underground tunnel which is connected to a vertical shaft; there is a small duct which connects the main tunnel and the shaft. Our major concern is the vertical shaft, since it goes through the basement and the soft soil deposit; the wave amplification characteristics is considerably different in these two layers and the seismic response of the shaft is complicated near the interface between them. The shaft is modeled as a cylinder of the radius 22.4 m and the height 99 m, and the connecting duct as smoothly curved tube. The main tunnel is modeled as a cylinder with the radius 5.2 m and length 170 m. The configuration of the shaft and the connecting ducts is shown in Fig. 2-b). For simplicity, we assume that all structures are made of reinforced concrete (RC) and its material property is linear elasticity; see Table 1.

While the macro-micro analysis is developed for a fault-infrastructure system, the domain of the present example problem is not so large as to be called a fault-infrastructure system; the domain size is reduced so that displacement in the engineering length-scale is obtained by the direct analysis. Instead of emitting earthquake waves from the fault, we assume that an ideal Ricker wave of the center time and frequency being 2.0 s and 1.0 Hz is input to the bottom surface; see Fig. 3 for the waveform of the input Ricker wave. The direction of the wave is vertical to the main tunnel so that it is shaken transversely. We should mention that the use of the Ricker wave is a standard practice in computational seismology, in order to examine the performance of a numerical analysis method of solving wave propagation problems.

Now, we explain the multi-scale analysis for the 3D simulation of the target problem. Models made for the macro-analysis and micro-analysis are shown in Fig. 4. The macro-analysis model is of the same configuration as the original domain, although the structures and the soil deposits are excluded since they are negligible if viewed in the geological length-scale. The micro-analysis model is a surface sub-domain of  $1000 \times 1000 \times 300$  m; this depth is needed in order to make the multi-scale analysis results coincide with those of the direct analysis. As mentioned, we seek to ensure the accuracy of numerical computation

up to 2 Hz. Since a FEM is applied to numerically solve Eqs. (2) and (3) for the multi-scale analysis, an ordinary criterion that the description of one wavelength requires 15 elements is used. Thus, the macro-analysis uses elements of 40 m and 20 m for the bedrock and the basement layers, respectively. The micro-analysis uses elements of  $0.5 \sim 20$  m.

Newmark  $\beta$  method ( $\delta = 1/2$ ,  $\beta = 1/4$ ) is applied for time integration of solving Eqs. (2) and (3) for the multi-scale analysis or Eq. (1) for the direct analysis. Simple explicit time integrations cannot be used since Courant's condition of the present example is too severe; fine meshes are used around the main tunnel and the impedance contrast between the tunnel and the basement is high. For instance, the direct analysis solves

$$([K] + \frac{2}{\delta t}[C] + \frac{4}{\delta t^2}[M])[u_{n+1}] = (\frac{2}{\delta t}[C] + \frac{4}{\delta t^2}[M])[u_n] + ([C] + \frac{4}{\delta t}[M])[v_n] + [M][a_n]. \quad (4)$$

Here,  $[v]$  and  $[a]$  are velocity and acceleration vectors, suffix indicates the time increment number, and  $\delta t$  is the time increment. Note that this discretized equation is rewritten as

$$[M](2[a^{ap}] - [a_n]) + [C]([v_n] + [a^{ap}]\delta t) + [K][u_{n+1}] = [0],$$

where  $[a^{ap}] = 2(([u_{n+1}] - [u_n])/\delta t - [v_n])/\delta t$ ; the vectors for  $[M]$  and  $[C]$  correspond to  $[\ddot{u}]$  and  $[\dot{u}]$ , respectively, measured at  $t = n\delta t$ .

We use the Rayleigh damping matrix,  $[C] = a[K] + b[M]$ . The parameters  $a$  and  $b$  are determined so that the material damping characteristics is reproduced. The values of  $a$  and  $b$  used in the numerical computation as well as the damping constant are presented in Table 1; these values are determined by minimum error fitting to the damping constant.

Now, we present the results of the 3D simulation. First, we study the 3D simulation of strong ground motion. The distribution of the maximum norm for surface displacement is plotted in Fig. 5; a) is for the direct analysis (or  $[u]$ ), which is regarded to provide a numerically exact solution, and b) and c) are for the macro-analysis and the multi-scale analyses (or  $[u^{(0)}]$  and  $[u_s]$ , respectively). The direct analysis shows larger amplification of strong ground motion in the soil deposit. This amplification is fully neglected in  $[u^{(0)}]$ , but  $[u^{(1)}]$  succeeds to correct  $[u^{(0)}]$  and the distribution of  $[u_s]$  is quite similar to  $[u]$ ; see Figs. 5-a) and 5-c).

In order to study the detail of the synthesized strong ground motion, we choose 12 observation points on the top surface and compare the waveform; these points, denoted by a–m, are set at equal intervals and cross the soft soil deposit, as shown in Fig. 6-a). A displacement component parallel to the input Ricker wave is analyzed. For the response displacement waveform and Fourier amplitude spectrum of these 12 points, the comparison of the macro-analysis and the multi-scale analysis with the direct analysis is presented in Figs. 7 and 8, respectively; solid lines are for the direct analysis and dotted lines are for the macro-analysis and the multi-scale analysis. Like Fig. 5-a), the direct analysis shows larger amplification of strong ground motion in the soil deposit (points j–c), and the multi-scale analysis succeeds to produce waveform and Fourier spectrum obtained from the direct analysis for all 12 points. It is transparent that  $[u^{(1)}]$  corrects the geological length-scale solution  $[u^{(0)}]$ . As mentioned, this  $[u^{(0)}]$  is regarded as the boundary conditions for the sub-domain to obtain  $[u_s]$ . The thickness of the sub-domain is 300 m. Thus, it is remarkable that this thickness is needed to use the geological length-scale solution as artificial boundary conditions at the bottom surface of the sub-domain.

Next, we study the 3D simulation of the seismic structure response. The target structure is the vertical shaft which runs in the basement and the soft soil deposit. Fig. 9 shows the maximum deformation of the shaft, together with a contour map of the displacement norm; a) and b) are for the direct analysis ( $[u]$ ) and the multi-scale analysis ( $[u_S]$ ). As is seen, an upper part of the shaft has larger deformation, which is caused by the soil-structure interaction effect. The multi-scale analysis is able to produce this deformation concentration. This is not surprising since the waves synthesized by the multi-scale analysis are in almost perfect agreement with those synthesized by the direct analysis, as shown in Fig. 8. In Fig. 10, the mode of deformation at the primary natural frequency of the structure (0.98 Hz) is plotted, together with a contour map of the frequency component norm. The result of the multi-scale analysis agrees with that of the direct analysis.

We choose 12 observation points, n–z, at an equal interval along a vertical line on the surface of the shaft, to examine the waveform of the structure response; see Fig. 6-b) for the location of the observation points. The points n–p are located in the soft soil deposit. Like Fig. 8, we compare the response wave profiles and Fourier spectra computed by the 3D simulation of the direct analysis and the multi-scale analysis. The results are shown in Fig. 11. While the structure response is drastically amplified near the surface, the multi-scale analysis succeeds to compute the structure response obtained by the direct analysis.

For the present example problem, it is clearly shown that the multi-scale analysis is able to make a full 3D simulation of strong ground motion and seismic response, as accurately as the direct analysis. The multi-scale analysis requires much smaller computational environment since Eqs. (2) and (3) are for a vector of smaller dimension. We should mention that the computation cost of solving Eq. (4) by a conjugate gradient method is  $O(N \log N)$  where  $N$  is the vector dimension. Thus, reducing the vector size is essential to increase the numerical efficiency. Similar efficiency is expected even for the case when non-linear materials are used for structures.

As mentioned, the sub-domain used for the micro-analysis is deeper than usual; the clearance of the main tunnel to the bottom model surface is more than 100 m. This implies that the strong ground motion of the engineering length-scale does not vanish at the depth of 100 m for the present example. Thus, the use of the geological length-scale solution produces non-negligible errors, when the clearance is smaller. While further investigation is surely needed, we need to clarify the requirement for the strong ground motion input to a shallow underground structure model.

## 4. Conclusion

In this article, we present the multi-scale analysis for the 3D simulation of strong ground motion and seismic response. While the present analysis solves two problems, the required computational cost is much reduced. The comparison with the direct analysis shows that the accuracy of the multi-scale analysis is satisfactory.

In closing this article, we should mention that the determination of the effective matrices ( $[\bar{K}]$ ,  $[\bar{C}]$  or  $[\bar{M}]$ ) is essential in order to determine a solution in the geological length-scale ( $[u^{(0)}]$ ). A well-established mathematical theory and advanced averaging schemes have been proposed; see [8, 12, 13].

Table 1. Material properties.

	primary wave (m/sec)	secondary wave (m/sec)	unit weight (tf/m <sup>3</sup> )	damping constant <i>h</i>	damping coefficient <i>a</i>	damping coefficient <i>b</i>
soil	300	100	1.7	0.15	0.3642	0.029
basement	1260	600	1.8	0.04	0.0971	0.008
bedrock	2950	1700	2.0	0.005	0.0121	0.001
RC	3373	2127	2.5	0.005	0.0121	0.001

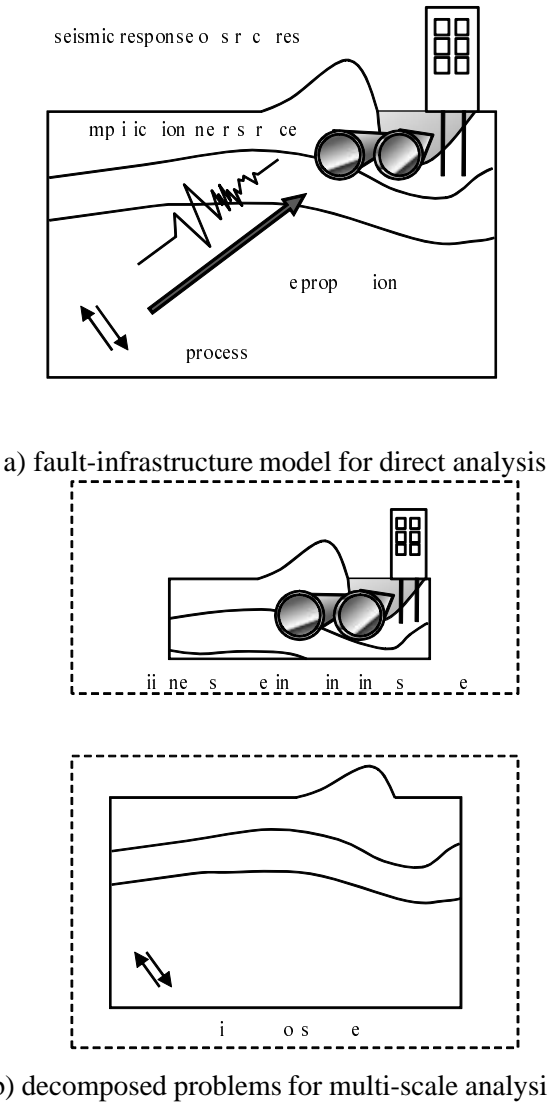
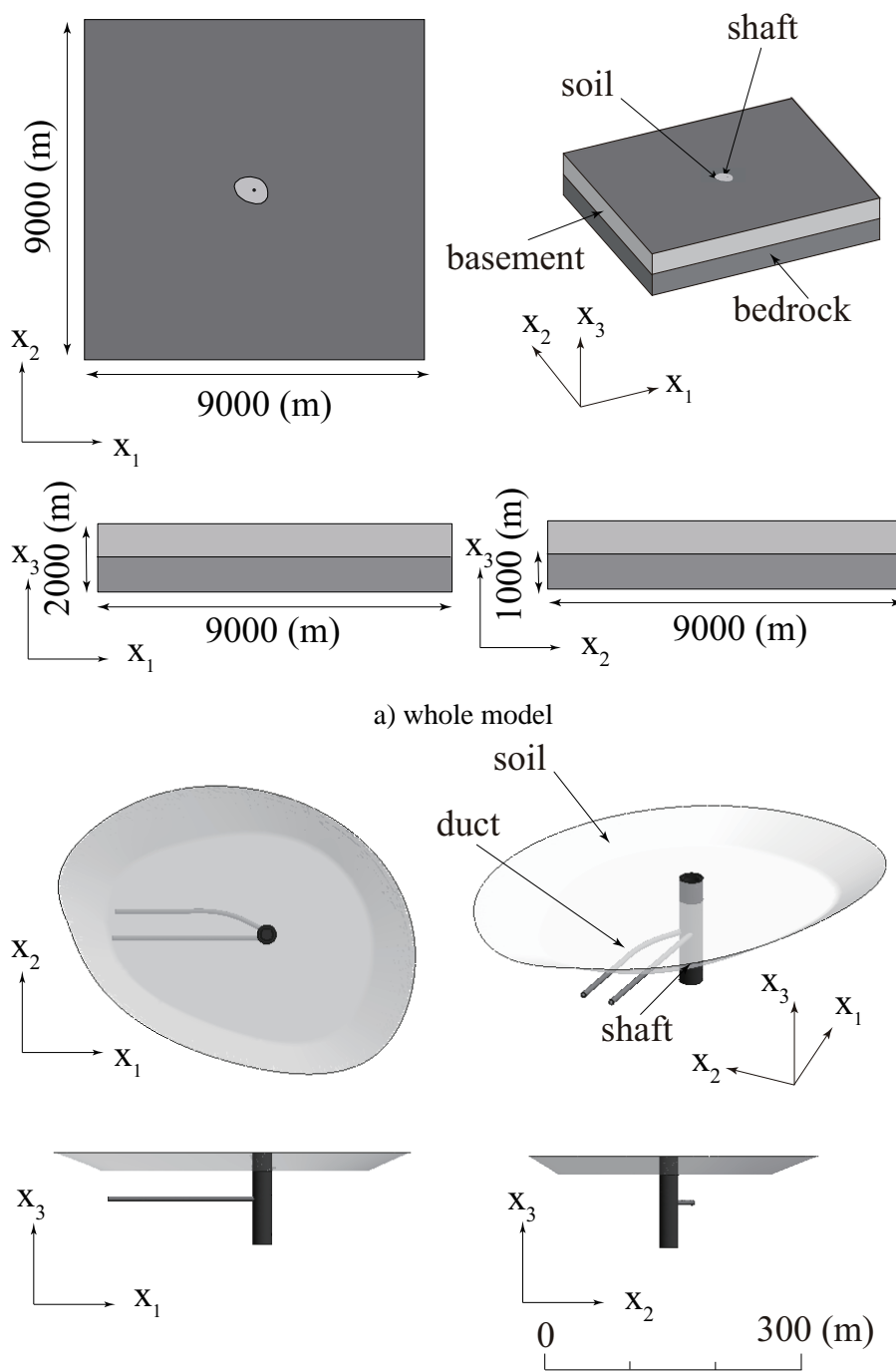


Figure 1. Schematic view of direct analysis and multi-scale analysis.



b) shaft model and soil layer model

Figure 2. Target problem.



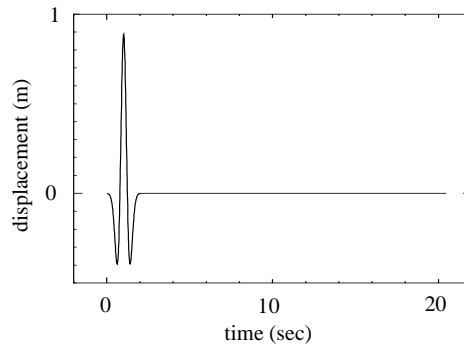


Figure 3. Waveform of input Ricker wave.

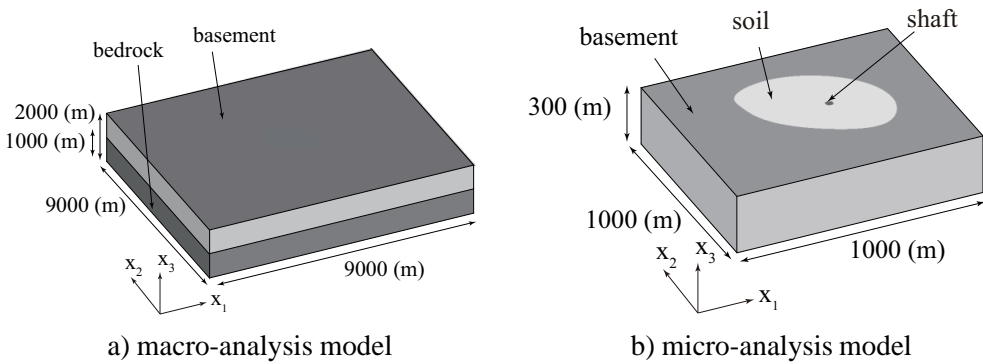


Figure 4. 3D models for multi-scale analysis; a) is a 3D model from fault to surface for macro-analysis, and b) is a 3D model around target infrastructure for micro-analysis.

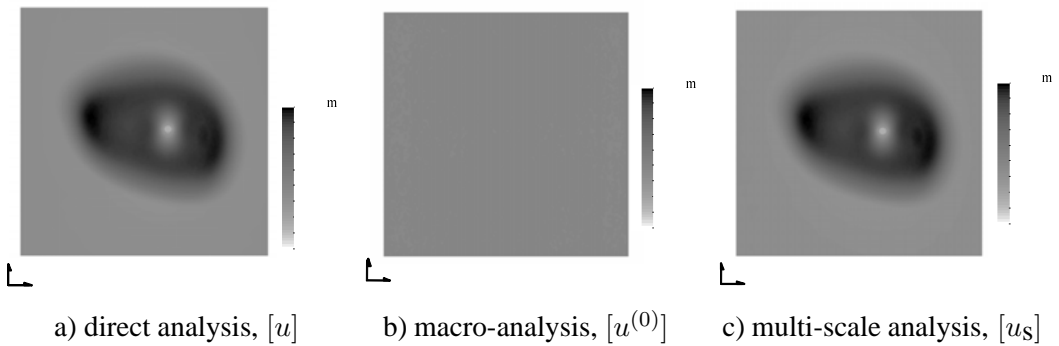


Figure 5. Distribution of maximum displacement norm on top surface.

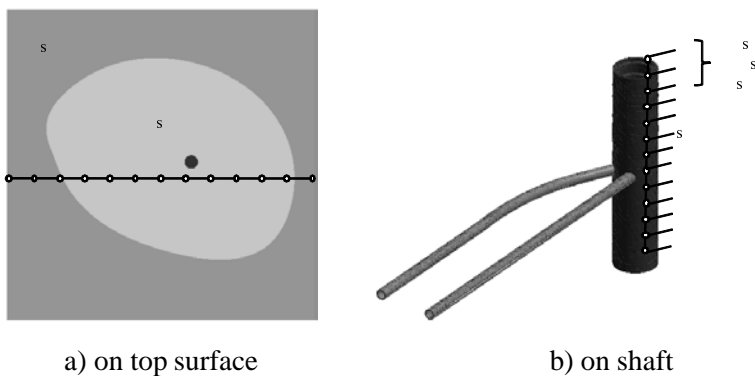
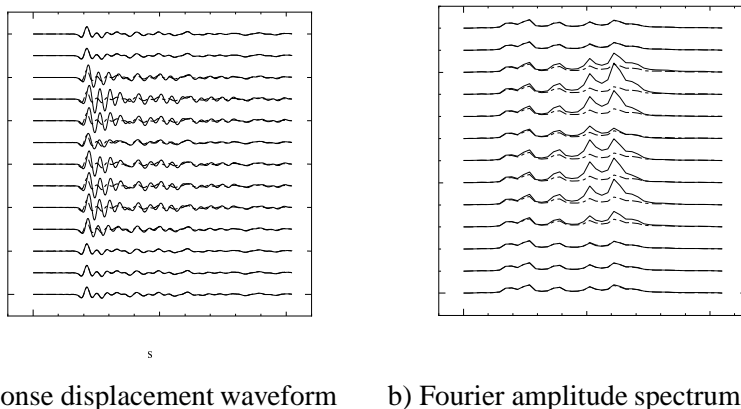
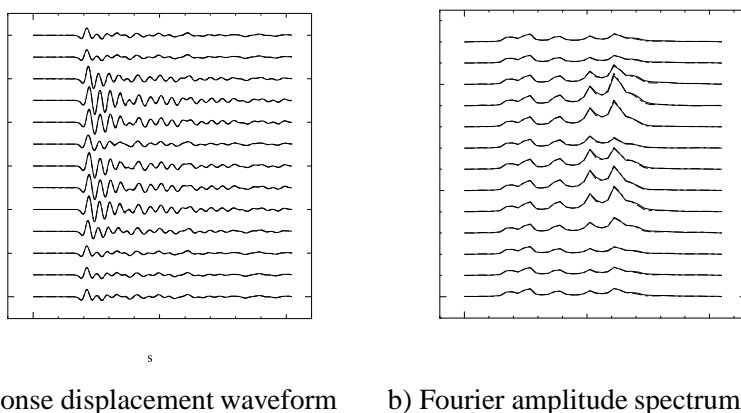


Figure 6. Locations of observation points.

Figure 7. Comparison of wave component in the  $x_2$  direction at points a–m shown in Fig. 6-a); macro-analysis,  $[u^{(0)}]$ , (dotted) and direct analysis,  $[u]$ , (solid).Figure 8. Comparison of wave component in the  $x_2$  direction at point a–m shown in Fig. 6-a): multi-scale analysis,  $[u_S]$ , (dotted) and direct analysis,  $[u]$ , (solid).

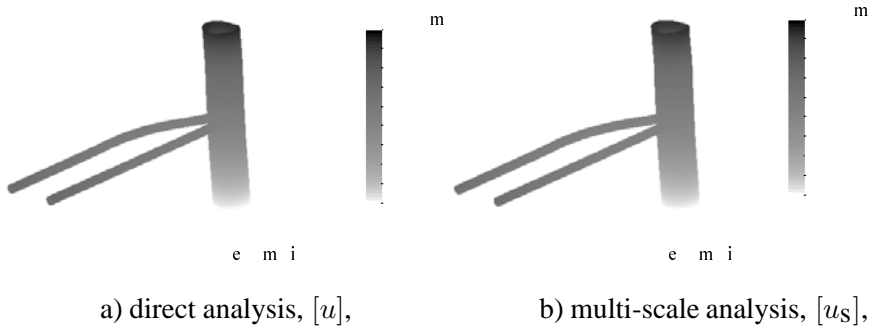


Figure 9. Distribution of maximum displacement norm with deformation on shaft.

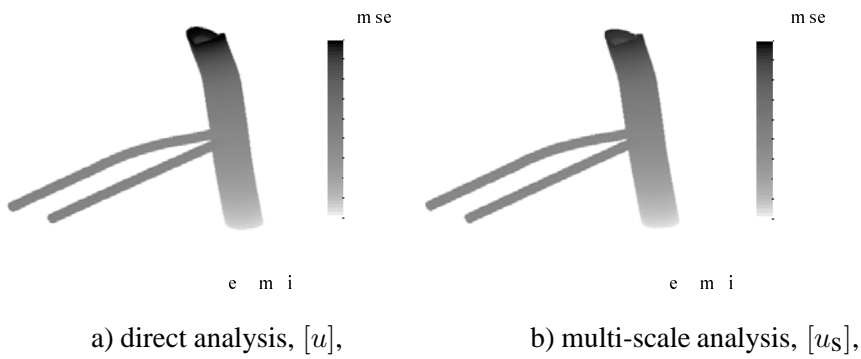


Figure 10. Distribution of frequency component norm on shaft on 0.98 Hz.

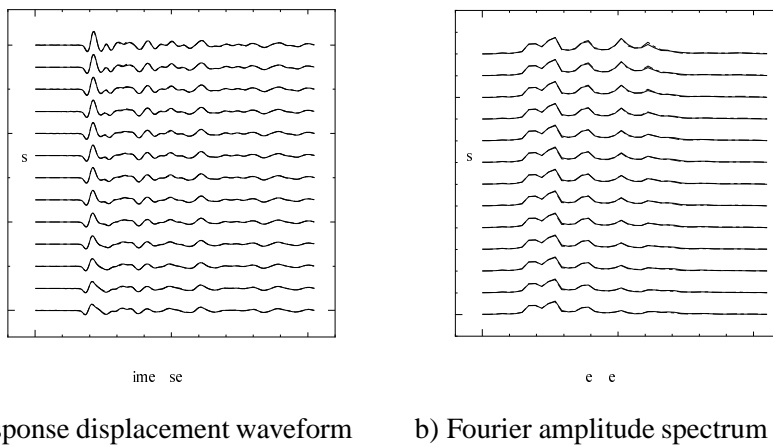


Figure 11. Comparison of structure response in the  $x_2$  direction at points n-z shown in Fig. 6-b); multi-scale analysis,  $[u_S]$ , (dotted) and direct analysis,  $[u]$ , (solid).

## Acknowledgement

The authors would like to express appreciation to Mr. Yohei Yamaki for his helpful support.

## References

- [1] Irkura K, Miyake H, Iwata T, Kamae K, Kawabe H, Dalguer LA. Recipe for predicting strong ground motion from future large earthquake. *Proc. of the 13th World Conference on Earthquake Engineering* 2004; 1371.
- [2] Koketsu K, Fujiwara H, Ikegami Y. Finite-element simulation of seismic ground motion with a voxel mesh. *Pure Appl. Geophys.* 2004; 161: 2463-2478.
- [3] Komatitsch D, Liu Q, Tromp J, Suss P, Stidham C, Shaw JH. Simulations of ground motion in the Los Angeles Basin based upon the spectral element method. *Bulletin of the Seismological Society of America* 2004; 94: 187-206.
- [4] Bielak J, Ghattas O, Kim EJ. Parallel octree-based finite element method for large-scale earthquake ground motion simulation. *Computer Modeling in Engineering and Sciences* 2005; 10: 99-112.
- [5] Furumura T. Large-scale parallel simulation of seismic wave propagation and strong ground motions for the past and future earthquakes in Japan. *Journal of the Earth Simulator* 2005; 3: 29-38.
- [6] Kaeser M, Dumbser M. An arbitrary high-order discontinuous Galerkin method for elastic waves on unstructured meshes – I. The two-dimensional isotropic case with external source terms. *Geophys. J. Int.* 2006; 166: 855-877.
- [7] Ma S, Liu P. Modeling of the perfectly matched layer absorbing boundaries and intrinsic attenuation in explicit finite-element methods. *Bulletin of the Seismological Society of America* 2006; 96:1779-1794.
- [8] Ichimura T, Hori M, Kuwamoto H. Earthquake Motion Simulation with Multiscale Finite Element Analysis on Hybrid Grid. *Bulletin of the Seismological Society of America* 2007; 97: 1133-1143.
- [9] Ogino M, Shioya R, Kawai H, Yoshimura S. Seismic Response Analysis of Nuclear Pressure Vessel Model with ADVENTURE System on the Earth Simulator. *Journal of the Earth Simulator* 2005; 2: 41-54.
- [10] Elgamal A, Lu J, He L, Law K, Yang Z. Techniques for Simulation of Large-Scale Nonlinear Soil-Structure Systems. *International Workshop on Constitutive Modelling, Development, Implementation, Evaluation, and Application* 2007.
- [11] Dobashi H, Ochiai E, Ichimura T, Yamaki Y, Hori M, Yamada T, Ohbo N, Moriguchi M. 3D FE Analysis for Seismic Response of Complicated Large-Scale Ramp Tunnel Structure. *ECCOMAS Thematic Conference on Computational Methods in Structural Dynamics and Earthquake Engineering* 2007.

- 
- [12] Ichimura T, Hori M. Macro-Micro Analysis Method for Wave Propagation in Stochastic Media. *Earthquake Engineering & Structural Dynamics* 2006; 35: 419-432.
  - [13] Ichimura T, Hori M. Strong Ground Motion Prediction using Macro-Micro Analysis Method, *Earthquake Engineering & Structural Dynamics* 2006, 35: 395-417.



## *Chapter 8*

# **PREDICTION OF THE SEISMIC DISPLACEMENT OF LANDSLIDES USING A MULTI-BLOCK MODEL**

*Constantine A. Stamatopoulos*

Athens, Greece

## **Abstract**

Newmark's sliding-block model is usually employed to predict the seismic displacement of slopes. Yet, when displacement is large, the conventional sliding-block model predicts displacements that are larger than expected for the given input motion and soil strength. Alternatively, to simulate slope movement when the displacement is large, a multi-block sliding model has been proposed. Similarly to the Sarma (1979) stability method, a general mass sliding on a slip surface that consists of  $n$  linear segments is considered. In order for the mass to move, interfaces where resisting forces are exerted must be formed between nodes of the slip surface. Thus, the mass is divided into  $n$  blocks sliding in  $n$  different inclinations. For landslides, the masses and lengths of each block entering the calculation are updated in terms of the distance moved. In addition, constitutive equations that simulate strength degradation along the slip surface coupled with the multi-block model are proposed in order to simulate the triggering of the slides. The chapter first describes the multi-block model and its extensions for the prediction of the seismic displacement of landslides outlined above. Then, it validates the above method by predicting the response of a well-documented earthquake-induced landslide.

## **1. Introduction**

Newmark's sliding-block model (Newmark, 1965), shown in Fig. 1, is usually employed to predict the seismic displacement of slopes (Kramer, 1996, Modaressi et al., 1995, Stark and Contreras, 1998). Newmark's model consists of a block on an inclined plane. Critical acceleration factor,  $k_{c-sl}$ , is the minimum factor that when multiplied by the acceleration of gravity,  $g$ , gives the horizontal acceleration which is just sufficient to cause movement of the block. Every time during the earthquake that the applied horizontal acceleration is larger than

the critical acceleration ( $k_{c-sl}$  g), the block slides downwards. The total displacement of the block is equal to the sum of these partial displacements that are caused by the momentary slides. The seismic displacement of slopes is estimated using the sliding-block model with similar critical and applied seismic acceleration.

When the displacement of slopes is large, the conventional sliding-block model has shortcomings. It predicts displacements that are larger than expected for similar input motion and soil strength (Stamatopoulos, 1996). The reason is that it does not model the change of geometry of the sliding mass with displacement towards a gentler configuration. In addition, ordinary computer codes based on the Finite Element Method cannot be applied when displacement is very large. To overcome the problem, mesh-free techniques have been proposed (Foester and Modaressi, 2001). Yet, such approaches are still in a developing stage.

Alternatively, to simulate slope movement when the displacement is large, a multi-block sliding model has been proposed (Stamatopoulos, 1992, Ambraseys and Srbulov, 1995, Stamatopoulos et al. 2000, Sarma and Chlimintzas, 2001a, b). Similarly to the Sarma (1979) stability method (Fig. 2), a general mass sliding on a slip surface that consists of  $n$  linear segments is considered. In order for the mass to move, at the nodes of the slip surface, interfaces where resisting forces are exerted must be formed (Fig. 2). Thus, the mass is divided into  $n$  blocks sliding in  $n$  different inclinations. At the interface between two consecutive blocks, the velocity must be continuous. This principle gives that the relative displacement of the  $n$  blocks is related to each other and the governing equation of motion is reduced to have only one displacement as variable. For large displacement, the masses and lengths of each block are updated during calculation in terms of the distance moved. Furthermore, constitutive equations that simulate strength degradation along the slip surface coupled with the multi-block model are needed in order to simulate the triggering of the slides. A constitutive model that predicts the continuous change of resistance along the slip surface due to build-up of pore pressures has been developed and implemented in the multi-block model.

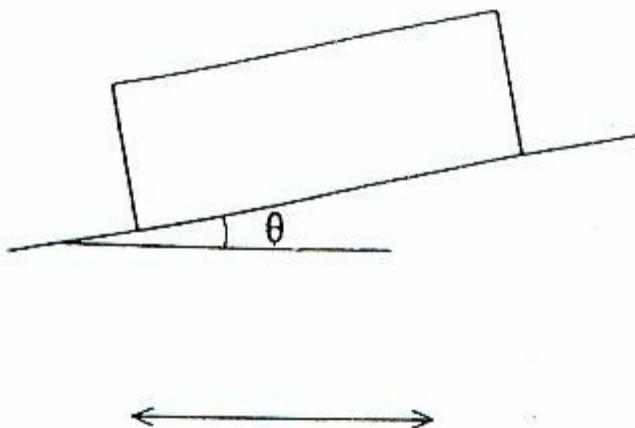


Figure 1. Newmark's sliding-block model.



The chapter first describes the multi-block model and its extensions for the prediction of the seismic displacement of landslides outlined above. Then, it validates the above method by predicting the response of a well-documented earthquake-induced landslide.

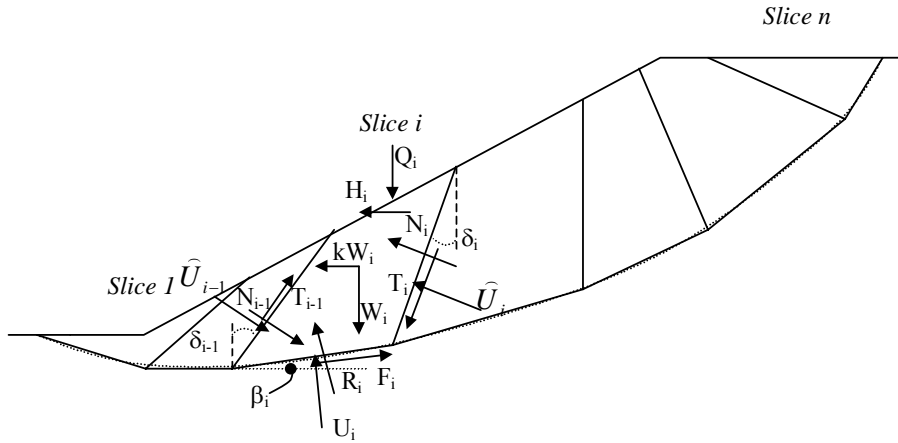


Figure 2. The multi-block stability method proposed by Sarma (1979).

## 2. The Multi-block Model

Similarly to the Sarma (1979) stability method, shown in Fig. 2, a general mass sliding on a slip surface that consists of  $n$  linear segments is considered. In order for the mass to move, interfaces where resisting forces are exerted must be formed between the nodes of the slip surface (Fig. 2). Thus, the mass is divided into  $n$  blocks sliding in different inclinations. At the interface between two consecutive blocks, the velocity must be continuous. This principle gives that the relative displacement of the  $n$  blocks is related to each other as:

$$u_i/u_{i+1} = du_i/du_{i+1} = \cos(\delta_i + \beta_{i+1}) / \cos(\delta_i + \beta_i) \quad (1)$$

where  $u$  is the displacement moved along a segment of the slip surface, the subscripts  $i$  and  $i+1$  refer to blocks  $i$  and  $i+1$  counting uphill,  $d$  refers to increment and  $\beta_i$  and  $(90 - \delta_i)$  are the inclinations of the segment and interface  $i$  respectively, shown in Fig. 2.

The forces that are exerted in block “ $i$ ” are given in Fig. 2. Soil is assumed to behave as a Mohr-Coulomb material. As the body moves, the Mohr Coulomb failure criterion applies at both the slip surface and the interfaces. The equation of motion of block ( $i$ ) along the direction of motion, when a horizontal component of acceleration  $a(t)$ , is applied, is :

$$\begin{aligned} m_i \left( \frac{d^2 u_i}{dt^2} \right) \cos \varphi_i = & -U_i l_i \sin \varphi_i + (m_i g Q_i) v_i - (m_i a(t) + H_i) x_i + c_i l_i \cos \varphi_i \\ & + (1 / \cos \varphi_{i-1}) N_{i-1} d_i - (1 / \cos \varphi_i) N_i f_i \\ & + s a_i (c_{i-1} b_{i-1} - \tan \varphi_{i-1} U_{i-1} b_{i-1}) - s b_i (c_i b_i \sin \varphi_i - \tan \varphi_i U_i b_i) \end{aligned} \quad (2)$$

where

$$\begin{aligned} v_i &= \sin(\varphi_i - \beta_i), & x_i &= \cos(\varphi_i - \beta_i), \\ d_i &= \cos(\delta_{i-1} + \beta_i - \varphi_i - \varphi_{in_{i-1}}), & f_i &= \cos(\delta_{i-1} + \beta_i - \varphi_i - \varphi_{in_{i-1}}), \\ sa_i &= \sin(\delta_{i-1} + \beta_i - \varphi_i), & sb_i &= \sin(\delta_i + \beta_i - \varphi_i), \\ q_i &= \prod_{j=i}^{n-1} [ \cos(\delta_i + \beta_{i+1}) / \cos(\delta_i + \beta_i) ] \end{aligned}$$

and  $m_i$  is the mass of block  $i$ ,  $\varphi_i$ ,  $c_i$ ,  $\varphi_{in_i}$ ,  $c_{in_i}$  are the frictional and cohesional components of resistance at the  $i$  slip segment and interface respectively,  $l_i$  and  $d_i$  are the lengths of the  $i$  slip segment and interface respectively,  $U_i$ ,  $U_{in_i}$  are the pore pressures at the  $i$  slip segment and interface respectively and  $Q_i$  and  $H_i$  are the vertical and horizontal external loads of block  $i$  respectively. To eliminate the interslice forces,  $N_i$ , the (i) equation is multiplied by a factor. Summing all equations and expressing displacement of all blocks in terms of the displacement of the upper block,  $u_n$ , the equation of motion is obtained. It is a single second-order differential equation in terms of time. As it is very long, it is not presented here. It is given by Sarma and Chlimitzas (2001 a and b). When a horizontal component of acceleration  $a(t)$  is applied, it has the general form

$$du_n^2/dt^2 = A (a(t) - a_c) \text{ for } du_n/dt > 0 \quad (3)$$

where  $A$  is a factor and  $a_c$  is the critical acceleration, defined as the horizontal acceleration which is just sufficient to start movement of the mass. The factors  $A$  and  $a_c$  depend of the geometry, the pore pressure and the strength of the  $n$  blocks of the sliding mass. The factor  $a_c$  is positive and negative when the sliding mass is stable and unstable respectively. According to the principle of limit equilibrium, the inclinations of the interfaces  $\delta_i$  correspond to the inclinations that produce failure at a minimum value of  $a_c$ .

### 3. Extension of the Multi-block Model to Predict the Response of Landslides

#### Sliding System Model for Large Displacement

When slide displacement is large, to solve accurately equation (3), the masses and lengths of each block  $i$  are updated during calculations in terms of the distance moved. The location of the interfaces does not change. The transformation rule, that states that when each block is displaced by  $d\tilde{u}_i$ , each point of the block including the ground surface at the top of the block is also displaced by  $d\tilde{u}_i$ , is applied. Incremental application is needed because a point may move from one block to the previous, and thus its incremental displacement for given  $d\tilde{u}_n$  will change from  $d\tilde{u}_i$  to  $d\tilde{u}_{i-1}$ . The deformation that this rule predicts in a two-block system is illustrated in Fig. 3a.

Separation of blocks occurs when an interslice force,  $N_i$ , is negative. Fig. 3b illustrates a typical case where this occurs: when the angle  $\beta_{m,1}$  representing the initial inclination of the first block of the system, is less than the angle  $\beta_{m,0}$  representing the slope of the free ground

surface immediately preceding the first block. In this case, the increased soil mass of the first block cannot maintain contact with the rest of the material and is detached from the system. For frictional materials, the angle of the internal sub-plane at the node of separation can be obtained from the resistance of the material inside block  $i$ ,  $\phi_{in_i}$ , according to what stability predicts as:

$$\delta_{i-separ} = 90^\circ - \phi_{in_i} \quad (4)$$

In addition, earthquake-induced slides usually occur due to generation of large excess pore pressures (Sassa et al., 1996, Stark and Contreras, 1998). With constant strength, the multi-block model can be applied in back analyses of slides to approximately estimate the residual soil strength (Stamatopoulos et al., 2000). Yet, constitutive equations that simulate strength degradation along the slip surface coupled with the multi-block model are needed in order to simulate the triggering of the slides and predict accurately the seismic displacement. Such models should predict the continuous change of resistance along the slip surface from its initial value to the peak strength and then at the large displacement residual value.

Constitutive models of various complexities simulating the response of localized discontinuities in saturated soils have been proposed and are used in both finite element codes and sliding-block models. In the context of numerical approaches using finite elements, if the interface is to represent strain at localized or failure zones in a soil medium, the constitutive model of the interface should be compatible and derived from the constitutive model of the surrounding materials. Based on this concept, Aubry et al. (1990) and Modaressi et al. (1998) relate stresses to displacement along and normal to the slip surface. In association with the sliding-block model, Sarma (1975) proposed a simplified model predicting pore pressures build-up based on Skempton's A and B parameters. A more elaborate model predicting the continuous change of resistance along a slip surface has been developed by Modaressi H. et al. (1995). The model is based on the elasto-plastic model by Aubry et al. (1993), relates shear stress to shear displacement, and requires only five parameters. The model has not been calibrated with soil response measured along slip surfaces for different soils. Recently, Gerolymos and Gazetas (2007) have proposed a constitutive model for grain-crushing-induced pore-water pressures. The model extends Hardin's theory for crushing of soil particles and has 12 parameters.

The purpose of the sections below are (a) to propose and validate a constitutive model simulating the change of resistance along a slip surface due to generation of excess pore pressures, (b) to implement it at the multi-block sliding system model and (c) based on this improved model to propose a methodology predicting the triggering and the final displacement of earthquake-induced slides. The best testing device to simulate soil response along slip surfaces is the ring shear test. In this test, similarly to field conditions, relative displacement at the slip surface can be very large, larger than a few centimeters, or even meters. The first objective is to propose a general model that simulates the soil response due to pore pressures build-up in these tests with a small number of model parameters.

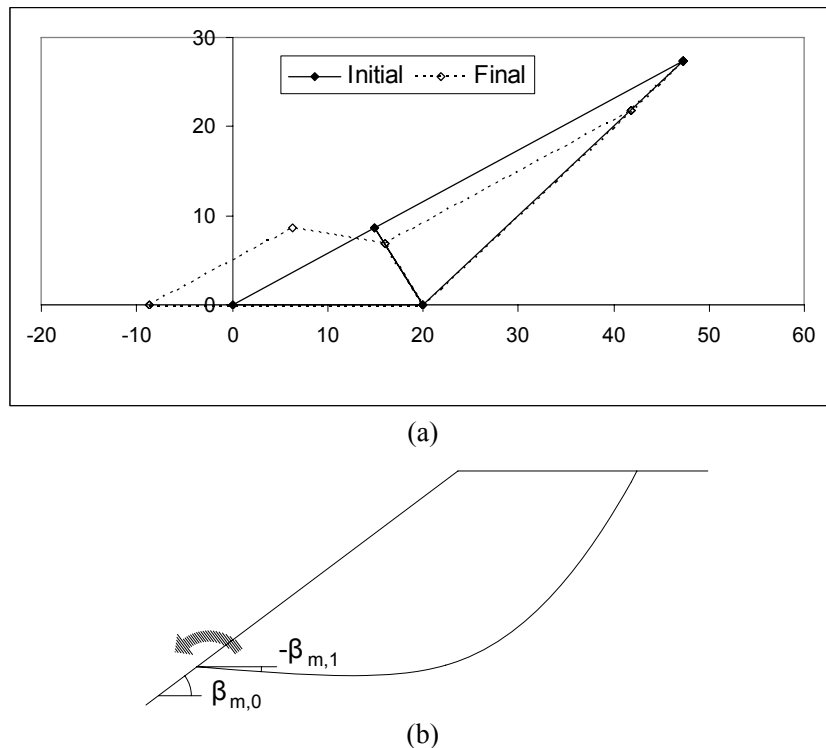


Figure 3. The case of landslides. (a) Deformation assumed in the multi-block model. A case of two blocks is given. (b) Typical case where separation of blocks occurs (Sarma and Chlimintzas, 2001).

## Constitutive Model Predicting the Response along Slip Surfaces due to Pore Pressure Build-Up

### Soil Response

Extensive ring shear testing of soils from (a) the 4th Avenue – Alasca slide (Stark and Contreras, 1998), (b) the Nikawa slide (Sassa et al., 1996) and (c) the Vaiont slide (Tika and Hutchinson, 1999) are reported in the bibliography. Table 1 gives the main classification characteristics of the soils of the three slides. Typical results of the ring shear tests are given in Figs 4 to 6. In the cases of the 4th Avenue – Alasca and Nikawa slides, both the shear stress and the excess pore pressure versus shear displacement relationships exist. In the case of the Vaiont slide only the shear stress versus shear displacement relationship exists. Table 1 presents the main characteristics of the shear stress-shear displacement relationships. In addition, the main characteristics of the shear stress-shear displacement relationship from ring shear tests on other soils together with the main classification characteristics of these soils are given in table form by Stark and Contreras (1998). They are presented in table 2.

All test results indicate that as shear displacement increases, the shear stress increases, reaches a peak and then progressively decreases towards a limit value. At large displacement, as displacement increases further, soil shear strength remains more-or-less constant. Accordingly, as shear displacement increases, the excess pore pressure increases at a steadily

decreasing rate towards a limit value. An exception is only one test, where negative excess pore pressure is measured at the initial stages of loading of an overconsolidated sample from Nikawa slope.

Quantitatively, large differences in the values of the measured maximum ( $\tau_m$ ) and residual ( $\tau_r$ ) soil strengths are observed:  $\tau_m$  varies from 11 to 392kPa, while  $\tau_r$  from 7 to 98kPa. The corresponding ratios (a)  $\tau_m/\sigma'_o$  and (b)  $\tau_r/\sigma'_o$ , where  $\sigma'_o$  is the initial effective normal stress, vary (a) from 0.20 to 0.61 and (b) from 0.05 to 0.17, respectively. Also, the ratio  $\tau_m/\tau_r$  varies from 1.4 to 5.4. In addition, differences in the shear displacement at peak and residual strength are observed: At  $\tau_m$  shear displacement varies from 0.3mm to 10mm, while at  $\tau_r$  from 19mm to 24mm.

Yet, results of tables 1 and 2 illustrate that for given soil layer and speed of shearing,  $\tau_r$  is more-or-less proportional to the vertical consolidation stress. Additional data illustrating this for the soil of the Vaiont slide is given in Fig. 6b by Tika and Hutchinson (1999). It is inferred that the total residual friction angle,  $\phi_r$ , is a parameter more-or-less-independent of the applied stress. It should be noted that  $\phi_r$  is related to the final generated excess pore pressure,  $P_f$ , as

$$\tan\phi_r = \tan\phi_{CS} (1 - P_f/\sigma'_o) \quad (5)$$

where  $\phi_{CS}$  is the final effective friction angle. Equation (5) is relevant especially for sands, where, according to discussion above, a small  $\phi_r$  value may be a result of excess pore pressure generation due to grain crushing.

### Proposed Model

As discussed previously, ring shear tests illustrate that at large displacement, as displacement increases further, soil strength and excess pore pressure remain more-or-less constant. Consistently, a steady-state (or critical state) model is proposed. The steady-state is that measured in constant-volume ring shear tests, that may be different to that measured in triaxial tests.

The model uses the following equations

$$\tau = \sigma' r f \quad (6)$$

$$dP = -d\sigma' = du K (\tan\phi_{CS} - \tau/\sigma') \quad (7)$$

where

$$f = 1 - b \ln [\tan\phi_{CS} \sigma' / (\sigma'_o \tan\phi_{res})] \quad (8)$$

$$r = \tan\phi_{CS} u / (a + u) \quad (9)$$

$$K = k_1 (\sigma'/Pa)^{k_2} \quad (10)$$

In the above equations  $\tau$  is the shear stress,  $\sigma'$  is the effective normal stress, compressive positive,  $\sigma'_o$  is the initial effective normal stress,  $P$  is the excess pore pressure,  $K$  is the elastic

normal stiffness coefficient,  $u$  is the shear displacement along the slip surface,  $P_a$  is the atmospheric pressure (equals about 100kPa),  $\varphi_{cs}$  is the final (critical-state) effective friction angle,  $\varphi_{res}$  is the final (critical-state) total friction angle and  $a$ ,  $k_1$ ,  $k_2$ ,  $b$  are fitting parameters. Displacement is in m and stresses and pressures in kPa. Unloading is not modelled, as it is assumed that relative motion of slides is only downslope.

### Discussion of the Model and Its Parameters

The model is based on (a) the critical state theory that predicts that (i) as shear strain increases soil gradually reaches a steady-state and (ii) the response is affected by the distance from the critical state (The factor  $f$  gives the effect of the distance from the critical state), (b) the fact that plastic shear strain depends on the  $\tau / \sigma'$  ratio, (c) a Roscoe type dilation equation and (d) the proposition that the constitutive model of displacement and stress of an interface should be of the same form as the constitutive model of shear strain and shear stress of soils.

The model structure is similar with the previous model by Modaressi H. et al. (1995). It differs from this previous model in (a) the form of the factors  $f$  and  $K$  and (b) taking the dilation angle equal to  $\varphi_{cs}$ . The form of the factor  $f$  in terms of  $\tan\varphi_{res}$  is critical for the ability of the model to predict the measured response, because, as discussed above, for given soil deposit and speed of shearing, laboratory tests have shown that the residual soil strength is more-or-less proportional to the vertical consolidation stress. Taking  $K$  as  $[k_1 (\sigma'/Pa)^{k_2}]$  is consistent with the assumption often used in soil models (e.g. Papadimitriou et al, 2001) that the elastic moduli of soils may be affected by the confining stress. Taking the dilation angle equal to  $\varphi_{cs}$  is consistent with sophisticated critical state models (e.g. Papadimitriou et al, 2001) for samples with final shear stress less than that at the critical state ( $\varphi_{res} < \varphi_{cs}$ ). This condition clearly exists in the cases considered in the present study.

The model has six parameters:  $\varphi_{cs}$ ,  $\varphi_{res}$ ,  $b$ ,  $a$ ,  $k_1$ ,  $k_2$ . These parameters can be estimated from constant-volume ring shear tests. In particular, the parameters  $\varphi_{res}$  and  $\varphi_{cs}$  can be estimated from the final (residual) shear stress and effective vertical stress: The parameter  $\varphi_{res}$  equals  $\arctan(\tau_r/\sigma'_o)$  where  $\tau_r$  is the residual shear stress and  $\sigma'_o$  is the initial effective normal stress. The angle  $\varphi_{cs}$  equals  $\arctan(\tau_r/\sigma'_r)$  where  $\sigma'_r$  is the final effective normal stress. The angle  $\varphi_{cs}$  for sands typically equals  $30^\circ$  and for clays  $26^\circ$  (Modaressi and Lopez-Caballero, 2001). The remaining parameters  $k_1$ ,  $k_2$ ,  $b$ ,  $a$  are fitting parameters. The parameter  $k_1$  affects primarily the displacement where the residual value of strength is reached. It decreases as the displacement where the residual strength is reached increases. The parameter  $k_2$  describes the effect of the confining stress on the displacement where the residual value of strength is reached. It can be obtained when for a given soil, ring shear tests with different confining stresses exist. The parameter  $b$  indicates the manner that the distance from the critical state affects the shear stress. The parameter  $a$  affects mainly the shape of the stress-displacement curve.

### Calibration of the Model Parameters, Comparison between Measurements and Predictions and Discussion

As in the multi-block model the shear stress - displacement relationship is of primary importance, the focus is the prediction of this relationship. Prediction of the excess pore

pressure generation versus displacement validates the model assumptions. Model parameters were varied for each soil type, and not for each individual test.

First the ring shear tests of table 1, where the shear stress-shear displacement relationships are available, were considered. The obtained model parameters that better fit the shear stress - shear displacement curves are given in table 3. Fig. 7 gives typical predictions of tests from the soil from (a) the 4th Avenue – Alasca, (b) the Nikawa and (c) the Vaiont slides. Table 4 compares the measured with the predicted response. The ratio of predicted to measured values for shear stress at different shear displacements is between 0.7 and 1.5 in all cases. It is inferred that the accuracy of the predictions is satisfactory.

**Table 1. Summary of constant volume ring shear tests found in the bibliography (Sassa et al., 1996, Stark and Contreras, 1998, Tika and Hutchinson, 1999) where much data is available, and partial results**

No	Soil deposit	Liquid limit (%)	Plastic limit (%)	Clay size fraction (% < 0.002m)	$\sigma'_o$ (kPa)	$\tau_m/\sigma'_o$	u at $\tau_m$ (mm)	$\tau_r/\sigma'_o$	u at $\tau_r$ (mm)
1.1a	4th Avenue – Alasca	40	20	59	100	0.28	1.2	0.07	55
1.1b	"	34	19	57	230	0.28	1.1	0.07	75
1.1c	"	36	21	56	300	0.24	1.3	0.06	75
1.1d	"	38	21	55	400	0.23	1.8	0.06	120
1.1e	"	39	20	62	500	0.23	1.8	0.06	130
1.2a	Nikawa - (OCR=1)	-	-	0	300	0.47	4.0	0.17	24300
1.2b	Nikawa - (OCR=1.9)	-	-	0	230	0.61	1.0	0.15	28400
1.3a	Vaiont - sample 4 -slow	49	30	20	500	0.48	5	0.22	600
1.3b	Vaiont - sample 3 - slow	50	28	20	500	0.47	5	0.20	600
1.4a	Vaiont - sample 4 - fast	49	30	20	505	0.42	5	0.15	600
<b>1.4b</b>	Vaiont - sample 4 - fast	49	30	20	980	0.38	5	0.10	600
<b>1.4c</b>	Vaiont - sample 3 - fast	50	28	20	505	0.43	10	0.15	700
<b>1.4d</b>	Vaiont - sample 3 - fast	50	28	20	980	0.40	5	0.10	900

slow= speed 0.0145 mm/s

fast= speed 2600 mm/s

Regarding pore pressures, such data exist only for the soil from (a) the 4th Avenue – Alasca and (b) the Nikawa slides (cases 1.1 and 1.2 of table 1). Fig. 7 gives typical predictions of pore pressure response from these two slides. Table 4 compares the measured with the predicted response. The model qualitatively does not predict the dilation that occurs

at the initial stages of test No1.2b and underpredicts or overpredicts the pore pressure that develops at the initial stages of tests No 1.1b, 1.1d, 1.1e, 1.2a. Beyond the initial stage, the ratio of predicted to measured values of pore pressure at different shear displacements of all samples is between 0.8 and 1.1. It is inferred that the accuracy of the predictions is reasonable.

**Table 2. Summary of other constant volume ring shear tests and partial results (Stark and Contreras, 1998)**

No	Soil deposit and location	Liquid limit (%)	Plastic limit (%)	Clay size fraction (% < 0.002m)	Vertical consolidation stress $\sigma'_o$ (kPa)	$\tau_m/\sigma'_o$	Shear displ. at $\tau_m$ (mm)	Undrained residual strength ratio $\tau_r/\sigma'_{v-0}$	Shear displ. at $\tau_r$ (mm)
2.1a	Drammen clay,	47	23	70	95	0.27	1.1	0.09	19
2.1b	Danvik-gate,	48	24	72	255	0.22	1.3	0.11	16
2.1c	Drammen, Norway	47	25	65	400	0.20	1.1	0.11	60
2.2a	Bootlegger Cove clay,	42	23	47	150	0.31	1.5	0.11	95
2.2b	outside Fourth Ave.	40	21	42	225	0.32	1.6	0.10	110
2.2c	landslide, Anchorage,	42	23	49	400	0.31	1.7	0.11	125
2.2d	Alaska	41	22	45	500	0.30	1.7	0.11	140
2.3a	Cohesive alluvium,	30	22	19	95.8	0.19	2.2	0.10	52
2.3b	Enid Dam,	28	22	20	147	0.27	1.1	0.05	77
2.3c	Enid, Mississippi	23	19	17	191	0.24	1.1	0.07	70
2.3d		25	22	20	287	0.23	1.2	0.07	72
2.3e		30	22	20	383	0.23	1.2	0.06	75
2.4a	Cohesive alluvium,	59	31	51	51.8	0.21	0.50	0.13	36
2.4b	Jackson, Alabama	59	31	51	79.4	0.23	0.35	0.16	50
2.4c		59	31	51	100	0.23	0.37	0.14	38
2.5a	Upper Bonneville clay,	46	23	33	47.9	0.32	0.30	0.11	39
2.5b	Salt Lake City, Utah	46	23	33	95.8	0.36	0.60	0.15	25
2.5c		46	23	33	191.5	0.31	1.2	0.12	29
2.5d		46	23	33	383	0.34	2.0	0.14	36

Finally, the cases of table 2, where only the values of peak and residual shear stress with the corresponding displacements were found, were considered. As soils are fine-grained, according to the previous discussion, the friction angle  $\phi_{cs}$  is assumed  $26^\circ$ . The model parameters obtained that better predict the measured response are given in table 3. Table 5



compares the measured with the predicted response. The ratio of predicted to measured values of the peak and residual shear stress is between 0.7 and 1.5 in all cases. The ratio of predicted to measured values of the shear stress when the displacement takes the measured peak and residual shear stress is between 0.8 and 1.5. It is inferred that the accuracy of the predictions is satisfactory.

Table 3 indicates that for all cases the model parameter  $a$  equals  $10^{-4}$ , the parameter  $\phi_{cs}$  varies between 26 and 31°, the parameter  $\phi_{res}$  takes values between 4 and 10°, the parameter  $k_1$  takes values between  $4 \times 10^2$  and  $15 \times 10^4$  kPa/m, the parameter  $k_2$  equals to 1 except for two cases and the parameter  $b$  varies between 0.01 and 0.24. Statistical analyses, shown in Fig. 8, indicate that as clay size fraction increases,  $\phi_{res}$  decreases,  $k_1$  increases and  $b$  increases. Yet, the coefficient of correlation of these relationships is small. Statistical analysis in terms of the Plasticity Index produces even smaller correlation.

The value of the model parameter  $a$  used ( $10^{-4}$ ) is within the range of the values  $10^{-5}$  to  $10^{-3}$  suggested by the previous similar model by Modaressi H et al. (1995). The typical value of  $k_1$  given for clays in the previous model by Modaressi H et al. (1995) of  $61(10^4)$  kPa\*m is somewhat larger than the range of values of the present model. According to Modaressi and Lopez-Caballero (2001) under conventional triaxial loading the parameter  $b$  typically equals 0.1 for sands and 1 for clays. Consistently, the obtained values of the parameter  $b$  increase with fines content. The obtained values are smaller than those proposed by Modaressi and Lopez-Caballero (2001). The difference can be attributed to the fact that soil response of the current model is of a lower value of residual strength mobilized in ring-shear tests as compared to triaxial tests. For example, in clays in triaxial tests  $\tau_r/\sigma'_o$  typically equals 0.2 (Modaressi and Lopez-Caballero, 2001), while as previously discussed, in ring-shear tests it can be as low as 0.07.

**Table 3. Model parameters predicting the response of the tests of tables 1 and 2**

Case	$\phi_{cs}$ (°)	$\phi_{res}$ (°)	$b$	$a$ ( $10^{-4}$ m)	$k_1$ kPa/m	$k_2$
1.1	26	4	0.12	1	100000	1
1.2	31	8.5	0.07	1	400	4
1.3	28	10	0.03	1	90000	1
1.4	28	8.5	0.01	1	70000	1
2.1	26	6	0.22	1	130000	1
2.2	26	6	0.2	1	25000	1
2.3	26	4	0.24	1	30000	1
2.4	26	8	0.3	1	150000	1
2.5	26	8	0.15	1	130000	0.7

Concluding, the proposed model simulates the excess pore pressure generation and subsequently the small value of residual shear strength measured in constant-volume ring shear tests. In particular, it simulates well the shear stress - displacement curves and the middle and final stages of the pore pressure - displacements curves of ring shear tests. From the six parameters of the proposed model, the parameter  $a$  does not change, the parameter  $\phi_{cs}$  can be approximately obtained according to the sand/clay differentiation and the parameter  $k_2$  equals 1 for most cases. It is inferred that in the proposed model the parameters that vary

considerably are only three:  $\phi_{\text{res}}$ ,  $k_1$  and  $b$ . The constitutive model does not simulate the effect of strain rate on the residual soil strength that has been measured in ring shear tests (e.g. Tika and Hutchinson, 1999). Thus, when estimating the residual soil strength, the laboratory tests should have similar strain rate to that at the field during the landslides.

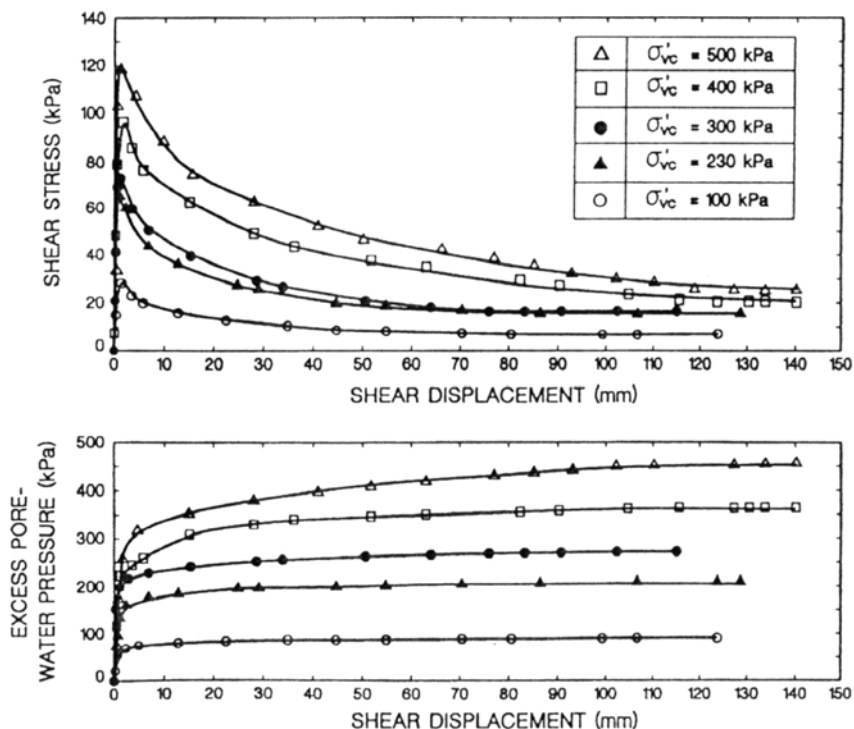


Figure 4. Measured response of ring shear tests on a sample from the 4th Avenue – Alasca slide (Stark and Contreras, 1998).

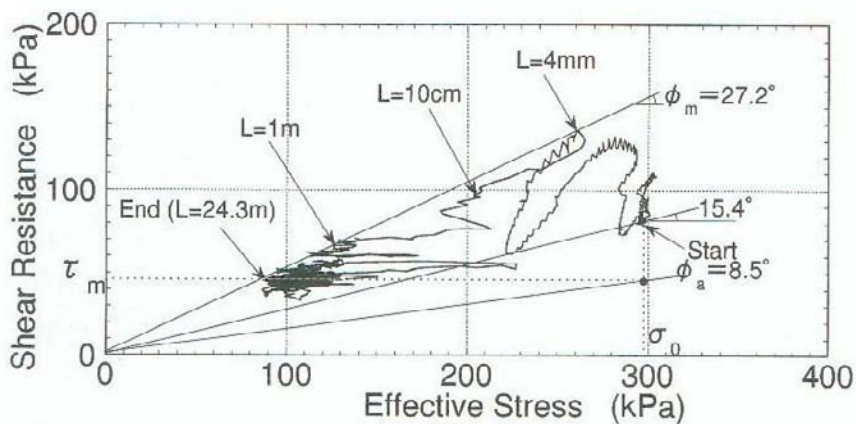


Figure 5. Measured response of ring shear tests on a normally-consolidated sample from the Nikawa slide (Sassa et al, 1995).

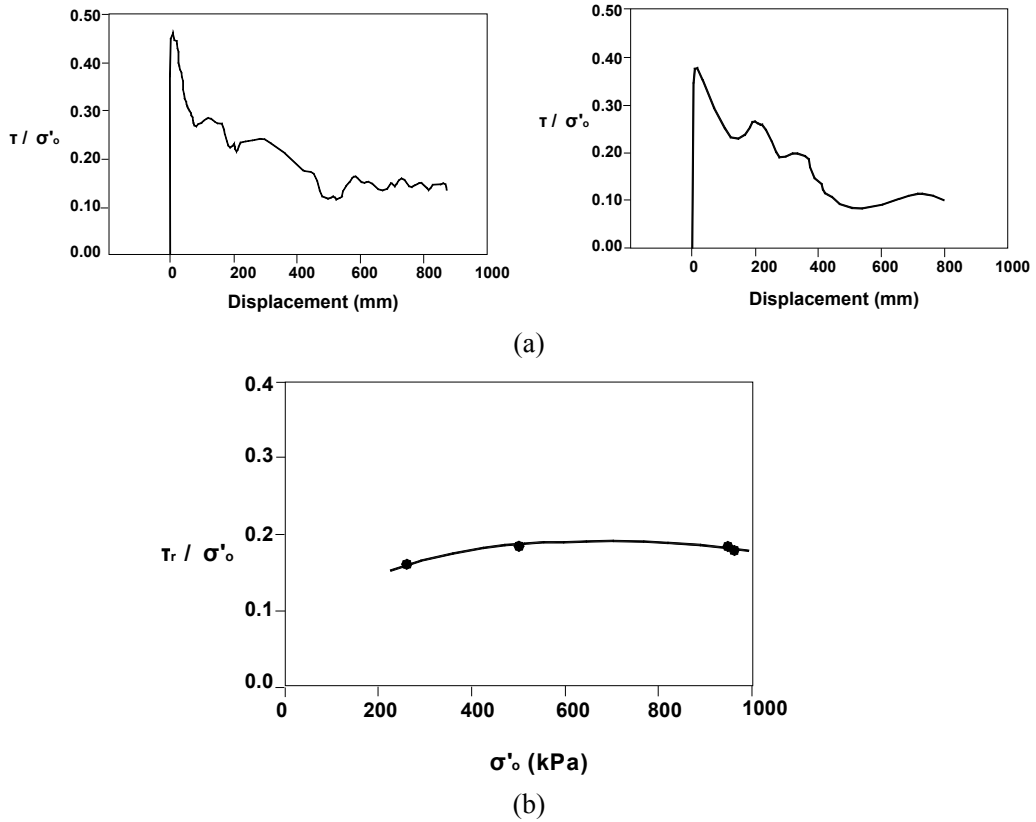


Figure 6. (a) Measured response of ring shear tests on sample 4 from the Vaiont slide. (b) Measured effect of vertical consolidation stress on the residual shear strength ratio ( $\tau_r / \sigma'_0$ ) on sample 3 from Vaiont slide (Tika and Hutchinson, 1999).

**Table 4. The accuracy of the model predictions. Cases of table 1. The ratio of predicted to measured values for shear stress and pore pressures at different shear displacements**

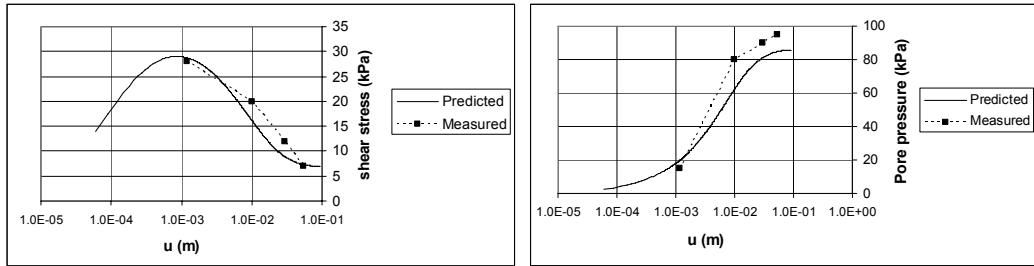
No	u (m)	Predicted / Measured		No	u (m)	$\tau$
		$\tau$	P			
1.1a	0.0012	1.03	1.33	1.3a	0.005	0.85
	0.01	0.81	0.78		0.05	1.12
	0.03	0.74	0.90		0.2	0.86
	0.055	1.04	0.89		0.6	0.87
1.1b	0.0011	1.04	2.19	1.3b	0.002	0.89
	0.01	0.93	0.84		0.05	1.16
	0.03	0.68	1.04		0.6	0.87
	0.075	1.01	0.98	1.4a	0.01	1.02
1.1c	0.0013	1.19	2.09		0.1	0.87
	0.01	0.97	0.89		0.2	0.88
	0.03	0.67	0.97		0.4	0.92
	0.075	1.17	0.99		0.7	1.14

**Table 4. Continued**

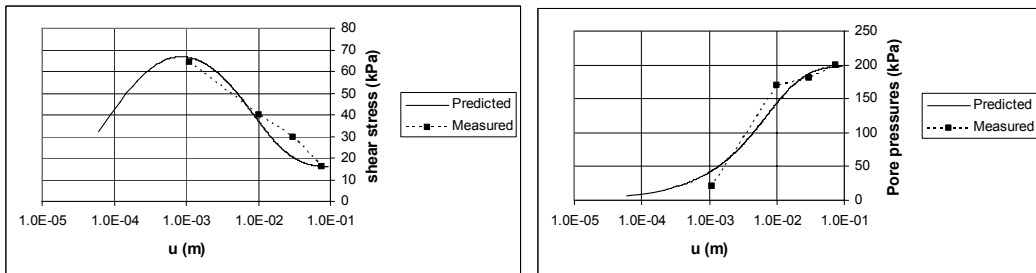
		Predicted / Measured				Predicted / Measured	
No	u (m)	$\tau$	P	No	u (m)	$\tau$	
1.1d	0.0018	1.20	2.05	1.4b	0.005	1.15	
	0.01	0.86	0.92		0.2	0.95	
	0.03	0.76	1.01		0.4	1.22	
	0.075	0.88	0.98		0.6	1.43	
	0.12	1.16	0.98	1.4c	0.01	0.99	
1.1e	0.0018	1.20	0.51		0.2	0.95	
	0.01	0.95	0.89		0.4	0.92	
	0.03	0.74	1.10		0.6	1.14	
	0.075	1.00	0.99	1.4d	0.005	1.10	
	0.13	1.16	0.95		0.2	0.95	
1.2a	0.004	1.09	0.25		0.4	0.92	
	0.1	1.19	0.95		0.8	1.14	
	1	1.09	1.05				
	24.3	1.50	0.89				
1.2b	0.001	0.80	0.99				
	0.1	0.80					
	1	1.38	1.09				
	28.4	1.37	0.87				

**Table 5. The accuracy of the model predictions. Cases of table 2. The ratio of predicted to measured values of (a) the peak and residual shear stress and (b) the shear stress when the displacement takes the measured peak and residual shear stress**

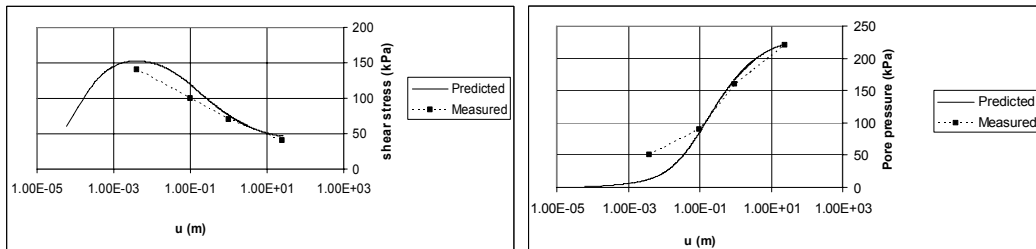
		Predicted / Measured					Predicted / Measured		
No	$\tau_{\max}$	$\tau_r$	$\tau$ at u of $\tau_{m-MEAS}$	$\tau$ at u of $\tau_{r-MEAS}$	No	$\tau_{\max}$	$\tau_r$	$\tau$ at u of $\tau_{m-MEAS}$	$\tau$ at u of $\tau_{r-MEAS}$
2.1a	0.89	1.11	0.87	1.16	2.4a	1.09	1.03	1.07	1.03
2.1b	1.11	0.95	1.07	1.04	2.4b	1.03	0.85	0.97	0.85
2.1c	1.21	0.95	1.19	0.95	2.4c	1.01	0.99	0.96	0.99
2.2a	0.98	1.38	0.98	1.38	2.5a	0.92	1.32	0.86	1.32
2.2b	0.94	1.10	0.94	1.16	2.5b	0.84	0.95	0.83	0.96
2.2c	0.97	1.08	0.97	1.11	2.5c	1.00	1.16	1.00	1.19
2.2d	1.00	0.98	1.00	0.99	2.5d	0.94	0.99	0.91	1.02
2.3a	1.22	0.68	1.21	0.84					
2.3b	0.84	1.50	0.83	1.51					
2.3c	0.84	1.35	0.83	1.50					
2.3d	0.99	1.01	0.99	1.12					
2.3e	0.99	1.20	0.99	1.28					



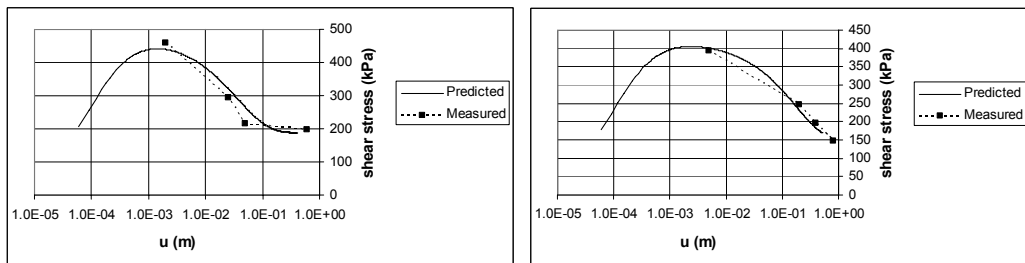
(a)



(b)



(c)



(d)

Figure 7. Predicted by the proposed model versus measured response of ring shear tests.. Tests (a) 1.1a, (b) 1.1b, (c) 1.2a and (d) 1.3b and 1.4d of table 1.

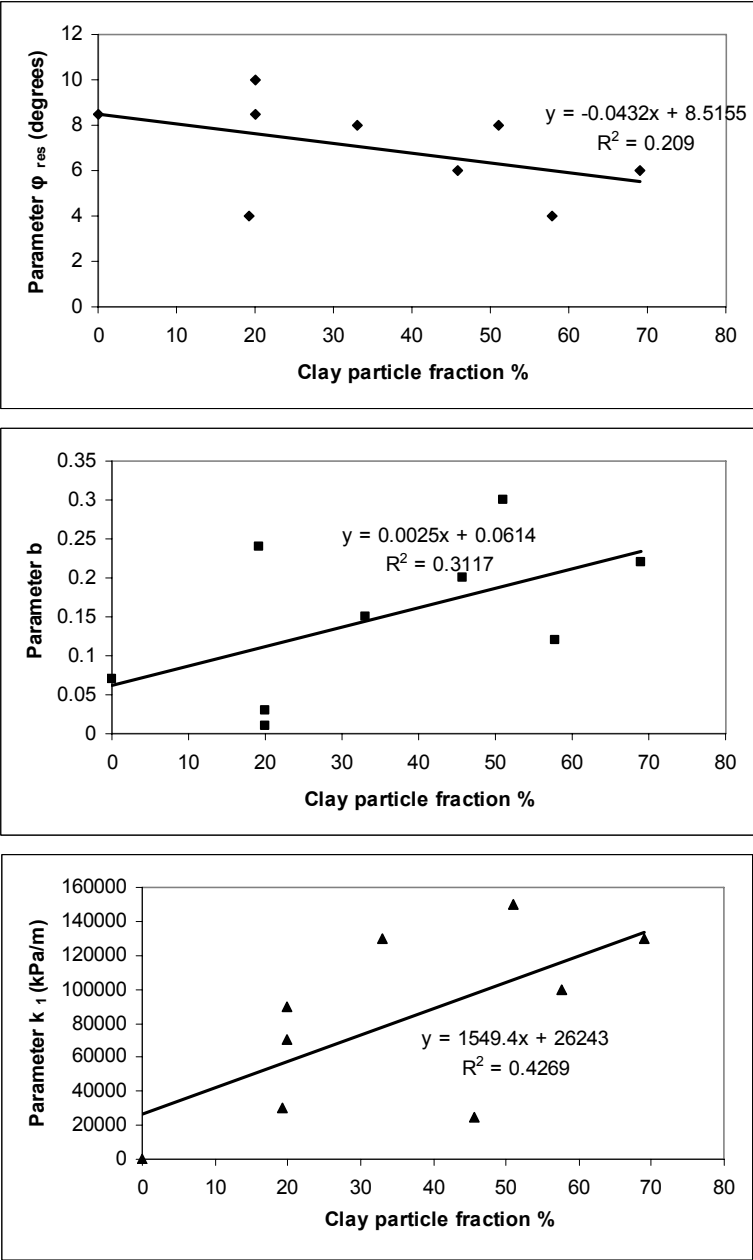


Figure 8. Variation of the estimated model parameters  $\phi_{res}$ ,  $b$  and  $k_1$  in terms of clay particle fraction.

Implementation

In equation (2), the multi-block sliding system model was based on both the frictional and cohesive resistance of the Mohr-Coulomb model. The proposed constitutive model is coupled with the multi-block sliding system by varying only the friction angle at the base of each block 'i' as

$$\varphi_i = \arctan(\tau_i / \sigma'_{o-i}) \quad (11)$$

In equation (11)  $\sigma'_{o-i}$  is the effective normal stress at the base block  $i$  without considering the excess pore pressures. At each increment,  $\tau_i$  is predicted from equations (6) to (10) (by taking  $u$  and  $\sigma'_o$  of these equations equal to  $u_i$  and  $\sigma'_{o-i}$  respectively).

Furthermore, when the proposed constitutive model is applied, it is needed first to estimate (a)  $\sigma'_{o-i}$  and (b) the initial equilibrium shear stress along the slip surface, or equivalently the equilibrium friction angle at zero displacement. The stresses  $\sigma'_{o-i}$  equal  $(R_i/l_i - U_i)$  where  $R_i$  and  $l_i$  are the normal force at the base of block  $i$  and the length of the base of block  $i$ , respectively and  $U_i$  is the initial pore pressure at the base of block  $i$ . The forces  $R_i$  are estimated from the equilibrium equations of the multi-block model. The initial equilibrium friction angle is estimated by finding the friction angle consistent with a critical acceleration value equal to zero (or equivalently a factor of safety equal to unity) at the initial slide configuration, using iterations. It may be noted that this implies uniform stress ratio along the slip surface. This is reasonable, as the slip surface is initially stable with more-or less uniform strength. Generation of excess pore pressures that may cause failure and may be non-uniform, will develop at a later stage, when the earthquake is applied.

A computer program that solves equations (2) and (6) to (11) has been developed by the author. Equation (2) is a second order differential equation. It is solved numerically by the Euler method (e.g. Dahliquist and Bjorck, 1974). At each time step, the masses and lengths are updated according to the transformation rule described above. Parametric analyses using different time steps illustrated that a time step of 0.01s, typically used in earthquake records found in the literature, produces adequate accuracy. The input geometry is specified as the nodes of the linear segments defining the slip, ground and water table surfaces. The inclinations of the internal slip surfaces must also be specified. The parameters of the constitutive soil model are specified in each segment of the slip surface. The computer program includes graphics that illustrate (a) the initial and final deformed configurations of the slope, (b) the applied acceleration, the critical acceleration and the mass of each block of the slide, all versus time and (c) the excess pore pressure, the equivalent resistance (specified as the friction angle of equation (11)) and the acceleration, velocity and displacement of each block versus time.

### Steps Needed to Apply the Model

The steps required to apply the multi-block model to investigate if triggering will occur and to predict the final displacement of earthquake-induced slides are:

- (a) The soil strength and a representative seismic motion of the problem under consideration are established. For the Mohr-Coulomb model, both the peak and residual strength values of the soil layers of the problem must be specified. In addition, along the potential slip surface the parameters of the proposed constitutive model must be specified.
- (b) The potential slip surface of maximum displacement is located by stability analyses using the Mohr-Coulomb model for strength of the soil layers of the problem considering also the inertia seismic forces. Stability analysis that locates a slip surface consisting of linear segments can be performed by the procedure developed

recently by Sarma and Tan (2006) in terms of the minimum critical acceleration value. In addition, it can be performed by the procedure described by Dawson et al. (1999) and implemented in the code FLAC (Itasca Consultants, 2005). The method performs a full solution of the coupled stress/displacement equilibrium and constitutive equations. For a given set of properties, the system is determined to be stable or unstable. By automatically performing simulations for different strength properties, the critical slip surface can be located.

- (c) The slip surface is simulated as a series of linear segments according to (b). Then, a first estimate of the inclination of the internal linear segments is obtained according to the condition of minimum critical acceleration value of the initial slide configuration using the Mohr-Coulomb model. For this first estimate, along the slip surface the residual value of soil strength should be used. At the interfaces the peak value of soil strength should be used. The reason is that at the interfaces different material is sheared at each time increment, and thus the residual strength value is not relevant.
- (d) The slide triggering is investigated and the potential slide deformation is estimated using the multi-block model. The representative seismic motion is applied. At the slip surface the proposed constitutive model is used. At the interfaces, similarly to (c), the Mohr-Coulomb model with peak values of strength is used. Model parameters are specified. If the displacement is large compared to the length of the slip surface, a better estimate of the interslice angle is obtained according to criterion of maximum displacement using iterations.

## **4. Validation of the Multi-block Model for the Prediction of the Triggerring and Deformation of Landslides**

### **The Nikawa Slide**

One the most well-documented slides directly related to an earthquake is the Nikawa slide. Knowledge of (a) the initial and final slide configurations, (b) the soil response along the slip surface, and (c) the applied seismic motion exists. In this section the multi-block model for landslides is validated by the prediction of this slide.

The slide was triggered by the 1995 Hyogoken-nambu earthquake with magnitude  $M_w$  equal to 7. With a landslide volume in the order of  $110,000 \text{ m}^3$ , moving rapidly over a distance of about 100 m, it destroyed 11 residential buildings causing 34 fatalities (Sassa et al. 1995, 1996). Fig. 9a shows the plan of the slope before the landslide and the outline of the landslide area (Sassa et al., 1996). A cross-section of the landslide is given in Fig. 9b (Sassa et al., 1996). The water table level at the region (measured about a month after the earthquake) is also given. Seismic records do not exist at the site. However, accelerations have been recorded on nearby sites. Kallou and Gazetas (2001) indicate that the accelerogram of Skinkobe, given in Fig. 10a, is possibly the most representative of the site. In addition the seismic shaking at the Nikawa slope was perhaps accentuated by topographic amplification (Kallou and Gazetas, 2001).



The region has two formations: the soil and the underlying rock at a depth of about 35m from the crest of the slope (Sassa et al., 1995). Geotechnical data of the soil formation includes cyclic ring shear tests. About one third of the slip surface was below the water table at time of landslide. Sassa et al. (1996) performed two fast cyclic ring shear tests on samples with a degree of saturation of 0.35, to simulate average field conditions. The results are given in Fig. 3 and table 1. They illustrate that as a result of cyclic loading, the sand resistance first increases and then drastically decreases. The peak total friction angle is  $25^\circ$  and  $31^\circ$  in the two tests and the residual total friction angle is only  $8.5^\circ$ . The residual strength value occurs at very large shear displacement, about 25m. Yet, at 1m displacement most of the soil strength has already been lost.

### Establishment of the Soil Strength and Density

As described above, the region has two formations: the soil and the underlying rock at a depth of about 35m from the crest of the slope. For the soil, for the Mohr-Coulomb model the two ring shear tests gave average total peak strength parameters  $c=0$ ,  $\phi=28^\circ$  and average residual total strength parameters  $c=0$ ,  $\phi=8.5^\circ$ . For the proposed soil model, the parameters that better fit the two ring shear tests and should be used are those given in table 3 (case 1.2). Finally, the total unit density of the soil was taken as  $1.8\text{T/m}^3$ , a typical value for sands

### Prediction of the Location of the Slip Surface

Rigorous stability analysis to obtain the slip surface consisting of linear segments cannot be performed in the present case study. The reason is that only the "average" value of residual soil strength along the slip surface is known. It is expected that the residual soil strength decreases as the degree of saturation increases (Gerolymos and Gazetas, 2007). The variation of the residual soil strength with degree of saturation, and thus versus depth is not known. Yet, it should be noted that stability analyses using the code FLAC (Itasca consultants, 2005) were performed. These analyses illustrated that the location of the observed slip surface can be predicted when non-uniform soil conditions, with a considerably smaller friction angle below the water table, are assumed.

### Multi-block Predictions

The slide is represented by a five-block system, where the front two blocks (left of the node B of Fig. 11) are dummy with zero area and their purpose is to define the trajectory of the slide outside the original slip surface (Fig. 11a). The water table of Fig. 9b was applied. First, an estimate of the inclination of the critical interfaces at the initial configuration is made. According to the previous discussion, along the slip surface, the strength is simulated as  $\phi=8.5^\circ$  and at the interfaces  $\phi' = 28^\circ$  was used. Figure 12a shows the obtained variation of the critical acceleration versus each of the interface angles  $\delta_C$  and  $\delta_D$ , shown in Fig. 11. Any of these two graphs is produced by holding constant the critical value of the other angle. It is inferred that an initial estimate of the critical values of  $\delta_C$  and  $\delta_D$  are  $-20^\circ$  and  $-25^\circ$  respectively.

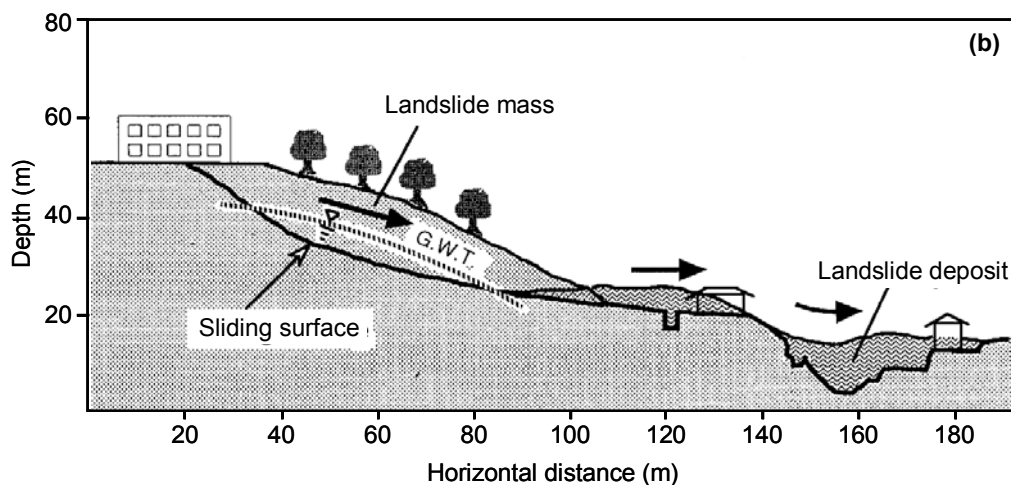
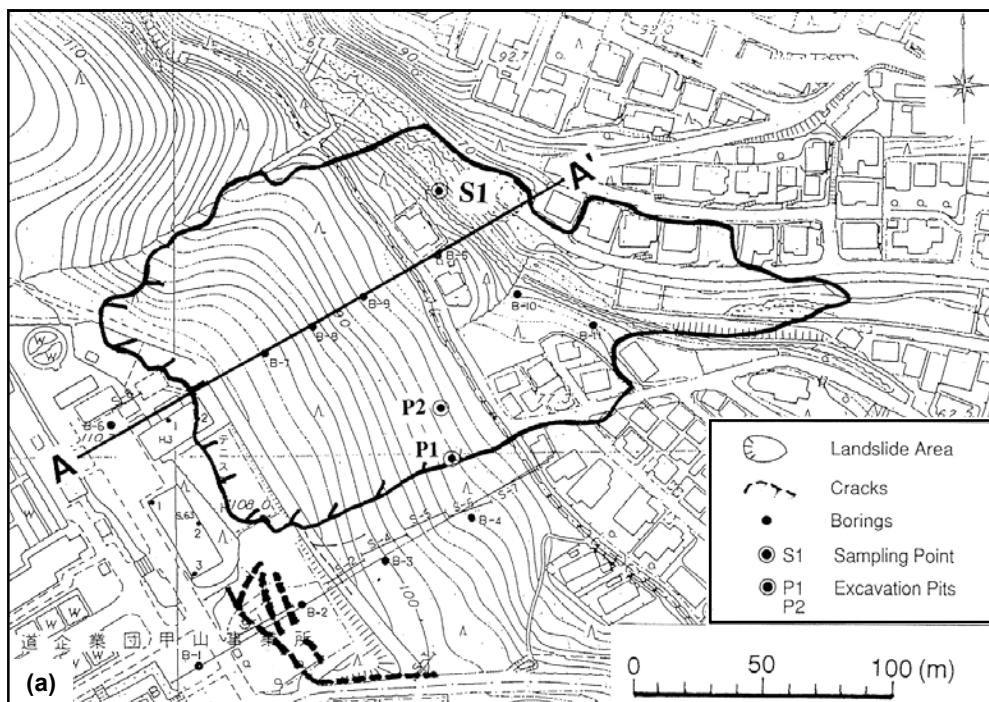
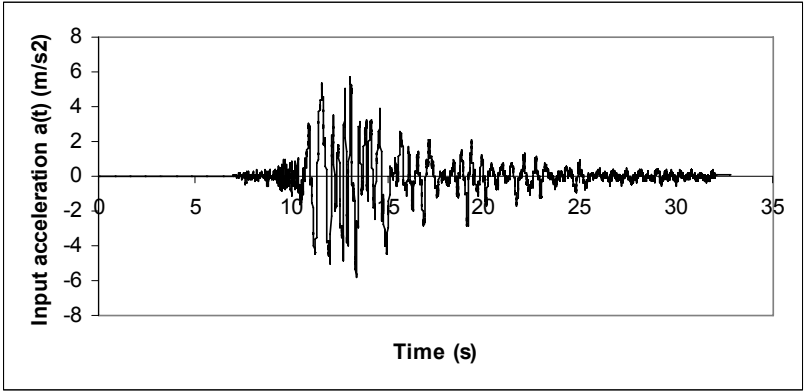
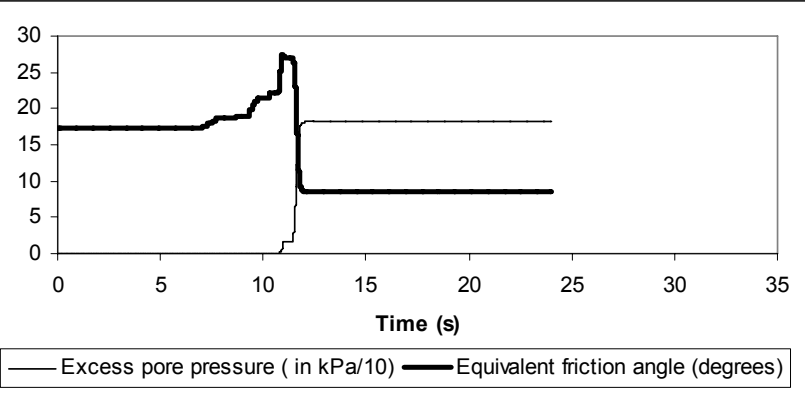


Figure 9. The Nikawa landslide: (a) plan view, and (b) cross section (Sassa et al, 1996)

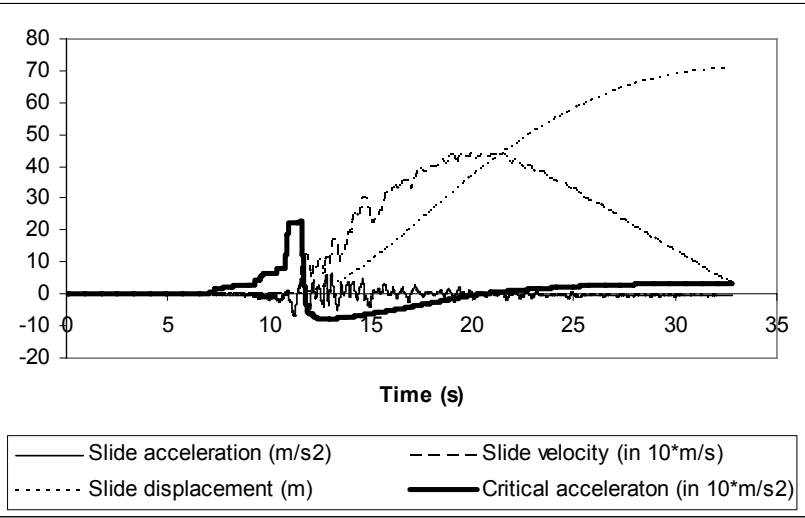
Once an initial estimate of the critical values of the angles  $\delta$  is established, the multi-block model is applied. At the slip surface the proposed constitutive model is used. At the interfaces, again a frictional resistance of  $\phi' = 28^\circ$  was used. The angle  $\delta_A$  is obtained according to equation (4). The reason is that the inclination of the slip surface at the left of node A is greater than the inclination at the right. Thus, the mass to the left of node A cannot maintain contact with the rest of the slide and was subsequently detached from the system.



(a)



(b)



(c)

Figure 10. Nikawa slide predictions: (a) Applied acceleration, (b) computed excess pore pressure and equivalent friction angle (given by equation (11)) of block 2 and (c) computed slide acceleration, velocity, distance moved, as well as critical acceleration, of block 2 block, in terms of time.

According to the previous discussion, the acceleration history of Fig. 10a, was applied. The seismic shaking was perhaps accentuated by topographic amplification (Kallou and Gazetas, 2001). Yet, to demonstrate conservatively that the proposed model predicts the triggering mechanism, this effect is not considered. To estimate the angle  $\delta_B$  (see Fig. 11) and establish a better estimate of  $\delta_C$  and  $\delta_d$  the criterion of maximum displacement is applied, using iterations. Fig. 10b gives the displacement of block 2 (from bottom to top, defined by nodes B and C of Fig. 11) in terms of the interface angles. Any of these graphs is produced by holding constant the critical value of the other angle. It is noted that the critical value of angles  $\delta_B$ ,  $\delta_C$  and  $\delta_d$  are  $-38^\circ$ ,  $-45^\circ$  and  $-48^\circ$  respectively.

For these values of  $\delta$ , Fig. 10b gives the computed excess pore pressure and equivalent friction angle (given by equation (11)) of block 2, in terms of time. Fig. 10c gives the computed slide acceleration, velocity and distance moved of the same block, as well as the critical acceleration of the slide, in terms of time. From Fig. 10 it can be observed that as the earthquake is applied, some shear displacement accumulates. This causes excess pore pressure to be generated and the friction angle to increase. Once the peak friction angle is reached, due to material softening, the friction angle decreases drastically, at about  $t=12s$ , to its residual value. At this point, the critical acceleration of the sliding system is negative (this means that the slide is unstable) and the slide velocity starts to increase and displacement to accumulate rapidly. As the slide moves, the mass slides at a progressively smaller average inclination. The critical acceleration of the system gradually increases and at  $t=17s$  becomes positive. Then, the slide velocity starts to decrease, and becomes zero, at  $t=32s$ . According to the above discussion, when the slide reached node A (Fig. 11), the model predicts that some mass is lost. The obtained deformed geometry is given in Fig. 11. As separation occurs, only the final top part of the slide is given. In the same figure, a comparison is made between the computed deformation and the measured deformation at the top part of the slide.

From the above it is inferred that the proposed multi-block model predicted the triggering of Nikawa slide. In addition, the computed deformed geometry agrees reasonably with that measured. Furthermore, the computed time duration of motion (about 20s) agrees with the observed rapid occurrence of the slide.

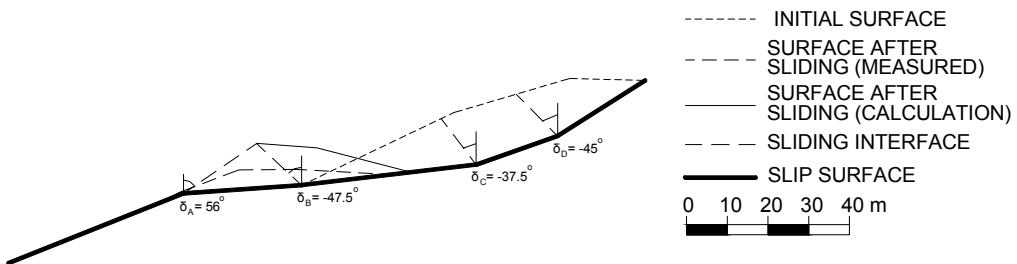
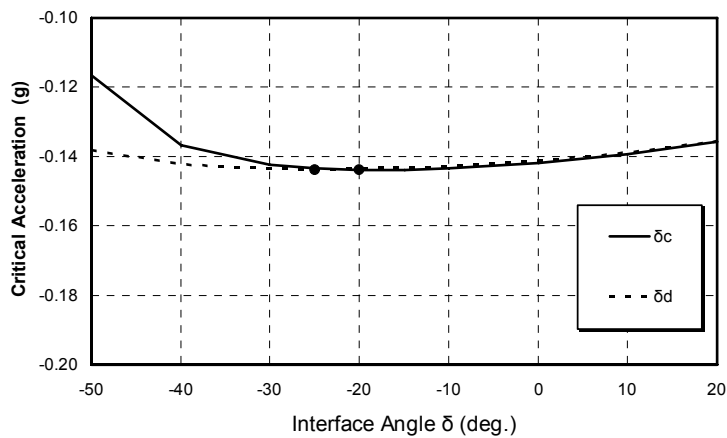
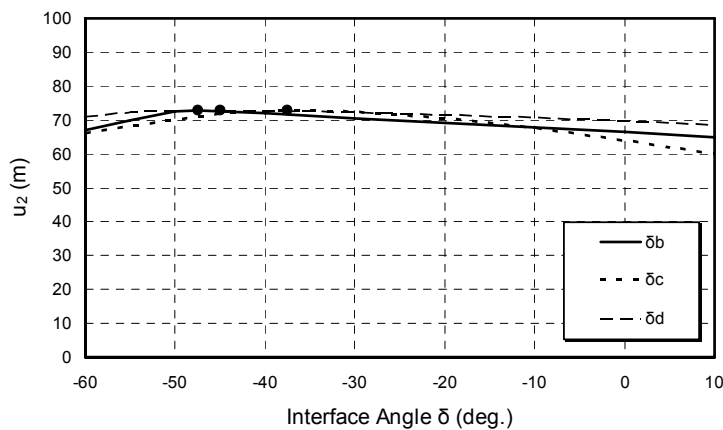


Figure 11. Nikawa slide predictions: Initial slide configuration assumed and computed and measured final configuration.



(a)



(b)

Figure 12. Nikawa slide predictions: (a) Critical acceleration coefficient for relative motion at the initial configuration and (b) the displacement of block 2 in terms of the interface angles.

## 5. Conclusions

A multi-block sliding system model has been developed. Similarly to the Sarma (1979) stability method, a general mass sliding on a slip surface that consists of  $n$  linear segments is considered. In order for the mass to move, interfaces where resisting forces are exerted must be formed at the nodes of the slip surface. Thus, the mass is divided into  $n$  blocks sliding in  $n$  different inclinations.

To simulate slope movement when the displacement is large, the masses and lengths of each block are updated during calculations in terms of the distance moved. Furthermore, constitutive equations that simulate strength degradation along the slip surface coupled with the multi-block model are needed in order to simulate the triggering of the slides and predict accurately the seismic displacement. A constitutive model that predicts the continuous change

of resistance along the slip surface due to build-up of pore pressures has been developed and implemented in the multi-block model.

The chapter first describes the multi-block model and its extensions for the prediction of the seismic displacement of landslides and gravity walls, outlined above. Then, it validates these methods by predicting the response of a well-documented earthquake-induced landslide.

## Acknowledgements

This work was supported by (a) the European Commission, DG XII for Science, Research and Development (projects ENV4-CT97-0392 and GOCE-CT-2003-505448) and (b) the Hellenic Organization of Seismic Protection (OASP). The author wishes to thank Prof. S. Sarma, Prof. A. Modaressi, Mr Aris Stamatopoulos, Mr Stavros Aneroussis and Mr Petros Petridis who contributed in parts of the research work described in the chapter.

## References

- Ambroseys, N. and Menu, J. (1988). "Earthquake induced ground displacements, *Earthquake engineering and structural dynamics*, **16**, 7, 985-1006.
- Ambraseys N., Srbulov M. (1995). "Earthquake induced displacements of slopes," *Soil Dynamics and Earthquake Engineering*; **14**, pp. 59-71.
- Aubry, D., A., Modaressi, H., Modaressi, A. (1990). Constitutive model for cyclic behaviour of interfaces with variable dilatancy, *Computers and Geotechnics*, **9**, pp. 47-58.
- Aubry, D., Benzenati, I., and Modaressi, A. (1993). Numerical predictions for model No. 1, Verification of numerical procedures for the analysis of liquefaction problems. Arulanandan K. and Scott R. F. (editors), Balkema, Rotterdam, pp. 45-54.
- Dahlquist, G. and Bjorck, A., translated by Andeson, N. (1974) "Numerical methods", Prentice-Hall Inc., New Jersey.
- Dawson, E. M., Roth W.H., Drescher A. (1999) "Slope Stability Analysis by Strength Reduction", *Geotechnique*, **49**(6), pp 835-840.
- Foerster E. and Modaressi H. (2001). Large motion assessment in soils under dynamic loading. *Fourth International Conference on Recent Advances in Geotechnical Earthquake Engineering and Soil Dynamics*, San Diego, California. (on CD, 6 pages)
- Gerolymos N. and Gazetas G. (2007). A model for grain-crushing-induced landslides - Application to Nikawa, Kobe 1995, *Soil Dynamics and Earthquake Engineering*; **27**, Iai, S. (2001). "Recent studies on seismic analysis and design of retaining structures", Fourth International Conference on Recent Advances in Geotechnical Earthquake Engineering and Soil Dynamics, San Diego, California, March 26-31.
- Kallou P.B., and Gazetas G., (2001). "Dynamic Analysis of Nikawa Landslide, Kobe 1995". *Proceedings of the 4 th Hellenic Conference on Geotechnical and Geoenvironmental Engineering*, Athens, Vol. 2, pp.171-178.
- Kramer S. (1996). *Geotechnical Earthquake Engineering*. Prentice-Hall, pp 438-447
- Modaressi, A. and Lopez-Caballero, F. (2001). Final Report for the project "Seismic Ground Displacements as a tool for town planning, design and mitigation", Work performed by Ecole Centrale Paris, European Commission, DG12.

- Modaressi, H., Aubry, D., Faccioli, E., Noret, C. (1995). Numerical modelling approaches for the analysis of earthquake triggered landslides. *Proceedings: Third International Conference on Recent Advances in Geotechnical Earthquake Engineering and Soil Dynamics*, April 2-7, Volume II, St. Louis, Missouri.
- Modaressi, A., and Lopez-Caballero, F. (2001). Global methodology for soil behavior identification and its application to the study of site effects. *Proceedings: Fourth International Conference of Recent Advances in Geotechnical earthquake engineering*, San Diego, California, March (CD-ROM).
- Modaressi, A. (1998). Second Progress Report, performed under the grant of the European Commission Project ENV4-CT97-0392, November.
- Newmark, N. M. (1965). "Effect of earthquakes on dams and embankments", *Geotechnique*, Vol. 15, No. 2, London, England, June, pp. 139-160.
- Papadimitriou A., Bouckovalas G., Dafalias Y. (2001). Plasticity model for sand under small and large cyclic strains. *Journal of Geotechnical and Geoenvironmental Engineering*, ASCE; Vol.127, No. 11, pp. 973-983.
- Stark, T.-D., Contreras, I.-A. (1998) Fourth Avenue Landslide during 1964 Alaskan Earthquake. *Journal of Geotechnical and Geoenvironmental Engineering*, Vol. 124, No. 2, pp. 99-109.
- Sarma S.K. and Chlimitzas G. (2001a) Co-seismic & post-seismic displacements of slopes, 15th ICSMGE TC4 Satellite Conference on "Lessons Learned from Recent Strong Earthquakes", 2001, 25 August, Istanbul, Turkey
- Sarma, S. K. and Chlimitzas, G. (2001b) Analysis of seismic displacement of slopes using multi-block model. Final report performed under the grant of the European Commission Project ENV4-CT97-0392, 2001, January.
- Sarma S.K. (1979). Stability analysis of embankments and slopes. *Journal of Geotechnical Engineering ASCE*; Vol.105, No. 12, pp. 1511-1524.
- Sarma, S.K. (1975). Seismic Stability of Earth Dams and Embankments", *Geotechnique*, Vol. 25, No. 4, pp.743-761
- Sarma S. K. , Tan D. (2006). Determination of critical slip surface in slope analysis *Geotechnique*, Vol 56, No 8, pp 539 - 550.
- Sarma, S. K. (1999). "Seismic slope stability - The critical acceleration", *Proceedings of the Second International Conference on Earthquake Geotechnical Engineering*, Balkema, Lisbon, 1999, pp. 1077-1082.
- Sassa, K., Fukuoka, H., Scarascia-Mugnozza, G., Evans, S. (1996) "Earthquake-induced landslides: Distribution, motion and mechanisms" Special Issue of Soils and Foundations, *Japan Geotechnical Society*, pp. 53-64.
- Sassa, K., Fukuoka, H., Sakamoto, T. (1995). The rapid and disastrous Nikawa landslide," *Landslide News*, No. 9, pp 6-9.
- Stamatopoulos, C. A. (1996). Sliding System Predicting Large Permanent Co-Seismic Movements of Slopes. *Earthquake Engineering and Structural Dynamics*, Vol. 25, No, 10, pp 1075-1093.
- Stamatopoulos C. (1992). Analysis of a slide parallel to the slope. *Proc. 2nd Greek National Conference of Geotechnical Engineering*. Vol. 1, pp. 481-488. (in Greek)
- Stamatopoulos C., Velgaki E., and Sarma S. (2000) "Sliding-block back analysis of earthquake induced slides". *Soils and foundations*, *The Japanese Geotechnical Society*, Vol. 40, No. 6, pp 61-75.

- Stamatopoulos, C. A., Stamatopoulos A. C., Aneroussis S. and Velgaki, E. G., (2001). Final Report for the project “Seismic Ground Displacements as a tool for town planning, design and mitigation”, Work performed by Kotzias-Stamatopoulos Co., European Commission, DG12.
- Tika, T.-E., and Hutchinson, J.-N (1999). Ring shear tests on soil from the Vaiont landslide slip surface, *Geotechnique*, pp. 59-74.
- Vucetic, M. and Dobry, R. (1991). “Effect of soil plasticity on cyclic response, *Journal of the Geotechnical Division, ASCE*, **117** (1).



## *Chapter 9*

# **FAULTS ACTIVITY, LANDSLIDES AND FLUVIAL CATCHMENTS TRIGGERED BY THE 28 DECEMBER 1908 MESSINA STRAIT EARTHQUAKE (ITALY)**

*Pierpaolo Guarnieri\**

Department of Geological Sciences, University of Catania, Catania, Italy

## **Abstract**

The 28 December 1908 Messina Strait earthquake ranks among the most disastrous historical events in the Mediterranean, causing more than 100,000 fatalities and the nearly total devastation of the cities of Messina and Reggio Calabria.

In recent years, one of the most debated issues in this context has been the definition of the source of the 1908 earthquake. Numerous studies have dealt with the subject, and given the lack of evidence of surface faulting, the most plausible hypotheses propose a source model with a blind fault fitting the concepts of rupturing and with the inversion of the historical levelling data.

This work presents a synthesis of geological field work associated with geomorphological analysis that define a tectonically active fault system, to which can be attributed fluvial catchments and landslides.

The novel aspect of this work comes from the comparison made between the present topography and 19th century topographic map. The analysis reveals that the modifications of the drainage network and the landslide activity, located in correspondence of some active faults, have occurred after the 1877, probably triggered by the 1908 earthquake.

**Keywords:** Active tectonics, Geomorphic indices, Holocene, Messina Strait.

## **1. Introduction**

The paper shows some results of a study on active tectonics in a sector lying to the north of the city of Messina on the Sicilian side of the Messina Strait (Figure 1a). The study carried

---

\* E-mail address: guarnier@unict.it, mobile: +39 3395348359

out in this area has for the first time revealed the presence of a fault system capable of modifying not only the hydrographic network of streams on the Ionian side, but also the morphology of the landscape, triggering landslides. In fact, by means of a digital reconstruction of a topographic map realized at the end of the 19th century and its comparison with the present topography, it has been possible to reconstruct the morphology in proximity of the active structures, showing the substantial coseismic modifications of the landscape provoked by the 1908 event.

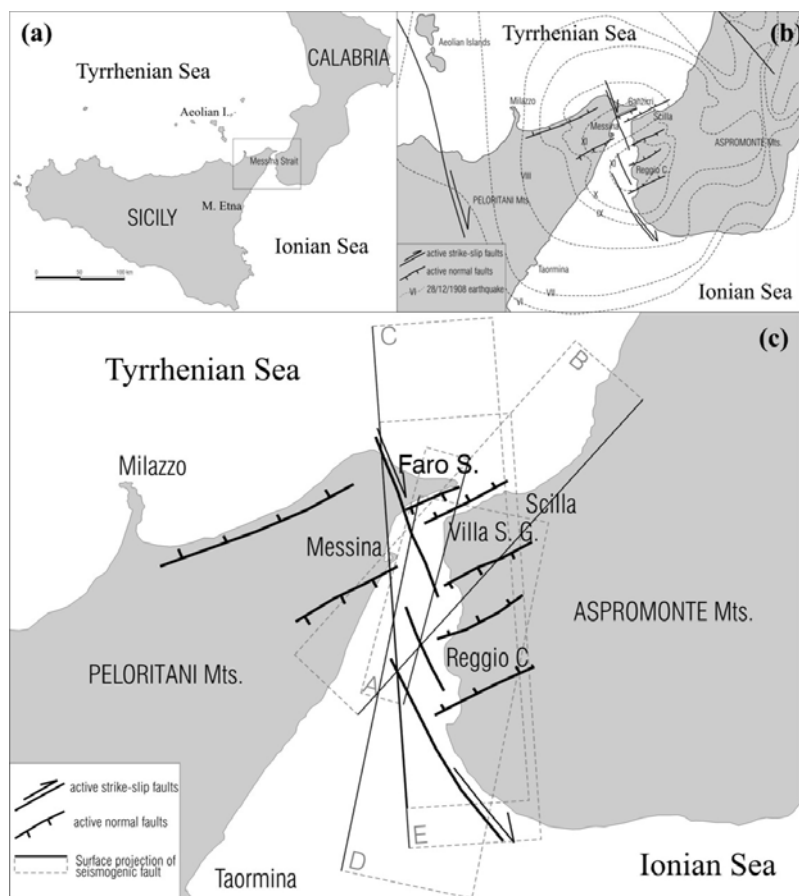


Figure 1. (a) Location map of the Messina Strait; (b) Isoseismal map of the 28 December 1908 Messina Strait earthquake (Barbano et al., 1980). The elongated direction of the maximum damage zone depicts some correspondence with minor faults (Guarnieri, 2006); (c) relationships between the surface projection of the seismogenic faults (A-from Schick, 1977; B-from Bottari et al. 1986; C-from Capuano et al. 1988; D-from Boschi et al. 1989; E-from De Natale and Pingue 1991) and the superficial active fault systems (Guarnieri, 2006). Thick sides are the upper ones.

The village of Faro Superiore, which was also totally destroyed during the 28 December 1908 earthquake, lies in the central part of this sector (Figure 1b, 1c). Observations made after the earthquake, besides describing the destruction caused by the earthquake, also note landslides and subsidence near to the village (Baratta, 1910).

## 2. The 28 December 1908 Messina Strait Earthquake: Source Parameters

The last 20 years have led to a better knowledge of the 1908 earthquake, after some of the fundamental concepts had been elaborated since the end of the 1970s.

All recent studies have led to a reduction of the magnitude compared to that originally proposed by Gutenberg and Richter (1954) ( $M_s$  7 1/2). The value of 7.1 ( $M_w$ ) proposed by Pino et al. (2000) coincides well with the estimates made by authors based on dislocation data.

Geodetic analysis, on the other hand, has been essential for the definition of the overall geometry of the seismic source and of the eastward dip of  $30^\circ$ - $40^\circ$  of the fault plane.

In contrary, the fault strike oscillates around a N-S trend, with a range of about  $30^\circ$ . Models privileging purely geodetic data (Capuano et al., 1988; De Natale and Pingue, 1991; Amoruso et al., 2002) tend to prefer a N-S orientation, whereas models that link the geodetic observations to geological data give preferences to a orientation of  $N10^\circ$ - $30^\circ$  (Valensise, 1988; Boschi et al., 1989; Valensise and Pantosti, 1992; Bottari et al., 1986) (Figure 1c).

The rake of the 1908 earthquake varies from purely normal (Boschi et al., 1989; Shick, 1977; Mulargia and Boschi, 1983) to normal with a subordinate dextral component (Capuano et al., 1988; De Natale and Pingue, 1991; Amoruso et al., 2002). The overall dimensions of the fault oscillate within a quite narrow range of 35-40 km for the length, and 15-22 km for the width of the fault plane, coherent with the estimates of the seismic moment that indicate a total area of the fault plane of 500-800 km<sup>2</sup>.

The location of the fault has been determined exclusively on the base of geodetic observations with little reference to the geology and, in part, supported by seismological investigation. The fault is thus believed to lie on the bottom of the Strait, with its extremities coinciding, to the north, with the Ganzirri peninsula, and, to the south, roughly halfway between Messina and Taormina in the Ionian Sea (Figure 1c).

All geodetic models agree on the fact that there has been a blind rupture, that is, the plane of rupturing has not intersected the topographic surface but stopped at a depth of 2-4 km below the surface. This well-established opinion is taken as a definitive explanation why it has been so difficult to define the localisation and characteristics of the 1908 fault on the base of conventional geological data.

Finally, the different types of analysis of the distribution of co-seismic slip have shown the existence of a zone of maximum release lying offshore of Reggio Calabria and a secondary zone lying before Villa San Giovanni (Figure 1b). Recently, Amoruso et al. (2002) proposed the existence of zones of significant moment release at the two extremities of the fault, that is, north of Ganzirri and south of the Calabrian coast.

Research on the active tectonics in the area of the Strait have seen a strong impulse during the 1980s, when various authors proposed the identification of the main tectonic elements in the area, and of the the dominant stress field (Bousquet et al., 1980a; Bousquet et al., 1980b; Ghisetti, 1980; Ghisetti, 1981; Ghisetti and Vezzani, 1982; Ghisetti, 1984; Cristofolini et al., 1985; Barrier, 1987). From the end of the 1990s several detailed geological maps have been published, which began to identify some active fault systems showing evidence for a remarkable recent activity (Gargano, 1994; Lentini, 2000; Guarnieri et al., 2005).

It has, however, to be underlined that the seismological analyses place several constraints on the fault responsible for the 1908 earthquake:

- [1] blind fault;
- [2] it emerges on the Sicilian side of the Strait;
- [3] the fault length coincides with the length estimated for the co-seismic rupture at depth (about 40 km);
- [4] the region of the Strait is dominated by vertical movement of opposed directions, regional uplift (Bordoni and Valensise, 1998) and subsidence determined by the activity of major faults.

Up to now, one of the possible interpretations of the geological problem was offered by the geodetic and seismological evidence, according to which the faults in the Strait described as active were envisaged to respond in a passive and selective manner to deformation guided by the underlying seismogenetic fault. This observation is true also for the so-called Reggio Calabria fault. Following some authors (Tortorici et al., 1995), this fault has a length of 15 km and dips toward W, and is believed to be part of a system active between the middle Pleistocene and the Holocene. This system is interpreted as having controlled the recent evolution of the Strait and being characterized by a minimum slip rate of 0.6 mm/yr. According to Tortorici et al. (1995) the 1908 earthquake was generated by the offshore continuation of the Reggio Calabria fault. Unfortunately, there is evidence, both from geological field data and from a geodynamic standpoint, that this fault cannot have produced that large earthquake. For example, there is disagreement with the geodetic observations of Loperfido (1909), which cannot be justified with the activation of a fault of such characteristics, localisation and dimensions. The values of coseismic coastal subsidence to the south of Reggio Calabria, which paradoxically coincides with the footwall of the fault.

All the aforementioned data leads us to categorically exclude that any of the faults mapped in surface within the Strait can be considered the source of the 1908 earthquake. Yet the field of deformation within the Strait, derived from the combination of regional uplift and movement along the large fault identified from the instrumental analysis (Valensise and Pantosti, 1992), determines conditions that may allow important modifications of the geology and landscape, and the selective reactivation of the surface faults (Figure 1c).

### **3. Evidence of Tectonic Controls on Drainage Basins**

The organisation and development of a hydrographic network are dictated by a series of factors including climate, lithology, bedding characteristics of the strata, but also structural factors such as fault activity, and tectonics, such as regional uplift or subsidence. Geomorphological analysis permits to analyse the modifications affecting the hydrographic basins, and to describe, in numerical terms, the landscape forms. Numerical calculations of the geomorphological indices is capable of determining the influence of faults on the hydrographic network (Guarnieri and Pirrotta, 2007).

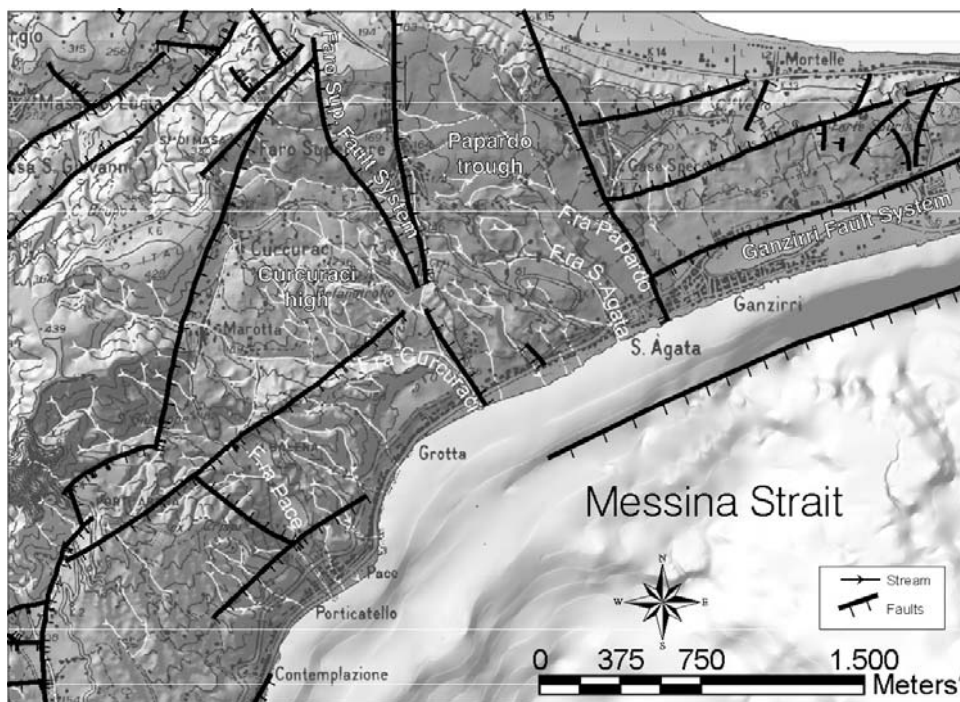


Figure 2. DEM of the onland and offshore Messina Strait area and distribution of the analysed basins. The figure shows the particular trends of the Fiumare. The first part is WNW-ESE-oriented then rotating to the SE, towards the modern coastline. The ENE-WSW-oriented faults are the Ganzirri Fault System (Guarnieri et al., 2005) that controls the modern coastline as it is evident from the slope break in the bathymetry. The NNW-SSE-oriented faults are the Faro Superiore Fault System that controls the Curcuraci High and the Papardo trough.

In Sicily and Calabria the water courses are named “fiumare”. A fiumara constitutes a particular typology of rivers, in that it presents an elevated slope, limited length, within deep valleys and characterized by a torrential regime. Recently a geomorphological analysis was carried out on the fluvial networks of four fiumare that flow into the northern portion of the Messina Strait: the Fiumara Pace, Curcuraci, S. Agata and Papardo (Guarnieri and Pirrotta, 2007) (Figure 2).

This analysis was not only carried out to show the recent activity of some of the fault systems recognised in the area, but it has also allowed to define the evolution of the fluvial network that extends, with a drainage towards ENE, since 90-100 ky to subsequently rotate towards SE, following the direction of the present fiumare (Guarnieri and Pirrotta, 2007) (Figure 2). Furthermore, the northern portion of the Messina Strait is seen to be controlled by systems of dip-slip faults oriented ENE-WSW and dextral strike-slip faults trending NNW-SSE, which are responsible for the recent deformation (Guarnieri, 2006) and for the modification of the present hydrographic network (Guarnieri and Pirrotta, 2007) (Figure 2).

The starting point for this kind of analysis was field mapping on a scale of 1:5000 and the construction of a DEM that has allowed to observe the landscape forms for morphological and morphostructural analysis. Then, by means of photo interpretation including the use of vertical photos on a scale of 1:10.000, the present drainage system has been reconstructed, and a geomorphological map has been created (Guarnieri and Pirrotta, 2007) (Figure 4a).

The upper part of the basin of the Fiumara Pace initially evolves on top of the metamorphic basement to continue on middle Pleistocene clastic deposits (Guarnieri et al., 2005) (Gravels and Sands of Messina Fm.), traversing the NE-SW trending fault system (Figure 2). The basin presents a slight asymmetry ( $AF=55$ ), which can be associated to the action of the NE-SE trending structures. The hypsometric curve shows a marked rejuvenation in the terminal portion provoked by the activity of the faults. The hierarchical parameters of the hydrographic network show a good organisation of the drainage.

Also the Fiumara Curcuraci develops on the metamorphic basement in its upper part, then passing onto the Gravels and Sands of Messina Fm. (Gargano, 1994; Lentini, 2000; Guarnieri et al., 2005). The fiumara Curcuraci shows a strong asymmetry of its drainage basin ( $AF=27$ ). The lack of SL anomalies leads to consider the NNE-SSW trending Curcuraci fault not active (Figure 2), whereas there are strong SL anomalies that can be associated with the activity of the Faro Superiore faults (Figure 2). The hypsometric curve shows a strong rejuvenation in its central and terminal parts, which indicates fault activity; all hierarchical parameters of the hydrographic network reflect the tectonic influence.

The drainage of the fiumara S. Agata develops on the Gravels and Sands of Messina Fm. within the Papardo Trough, a structural depression formed by the Faro Superiore and Papardo faults (Figure 2), while the hydrographic basin is nearly perfectly symmetrical. The SL index does not show any anomalies and the hypsometric curve has the typical character of a mature state with a well-organized network.

The Fiumara Papardo, which also lies on the Gravels and Sands of Messina Fm., is cut by the Faro Superiore faults and presents a notable basin asymmetry ( $AF=30$ ) whereas the SL index does not show particular anomalies. In contrast, the hypsometric curve has the typical trend of a mature state with an increase in convexity in the central portion and an anomalous trend in the terminal part.

The courses of the studied fiumare show, with the exception of the Papardo, the characteristics of bedrock channels. The first half of the course of that fiumara lies on the footwall of the Faro Superiore faults, where it is incised into bedrock constituted by the Gravels and Sands of Messina Fm., whereas the second half lies on the hanging wall and beyond the two structures, assumes the characteristics of an alluvial river with an alluvial deposit that in places reaches thicknesses of 10 m, probably facilitated by an accommodation space created by tectonic subsidence.

#### **4. Modifications of Landscape Induced by the 1908 Fault Rupture**

During the second half of the 19th century a geological map of the Messina Strait was published by Giuseppe Seguenza (1878) who worked as a naturalist, pharmacist, university teacher, and author of studies on the geology in the Messina territory (Figure 3).

In the same period (1877-1892) in Italy the project of a national geological map was launched, which aimed at the covering of the entire territory on a scale of 1:100.000, reduced from a scale of 1:25.000. The creation of the Geological Map of Italy was planned to proceed from the realisation of a good topographic base, which, in that period, was lacking for the major part of southern Italy. A similar experience had been made a few years earlier in Sardinia, where a topographic map had been published in 1845, but the corresponding geological map was published only in 1857. On that occasion military experts were charged with the

topographic surveys. For the map of Italy, the Corps of Engineers of Mines was charged with leading the work, which continued from 1873 until the second decade of the 20<sup>th</sup> century. The topographic map was realised at a scale of 1:25.000 with contour intervals of 10 m.

The geological map of Seguenza (Seguenza, 1878), is important because it was published at the same time that the topographic base was realised in 1877. It was made meticulously and, in certain aspects, innovatively, since its author distinguishes a marine from a continental lithofacies in the quaternary clastic deposits, now grouped together under the name Formation of the Gravels and Sands of Messina.



Figure 3. The 1878 Geological Map of the Messina Strait (Seguenza, 1878).

To evaluate the possible modifications to the landscape after the 1908 earthquake, the 1877 map has been acquired in digital format and georeferenced, using a series of man-made constructions and infrastructures as control points, which appear both in this map as well as in the present cartography. Subsequently it has been digitalized transforming contour lines and hydrographic network as drawn by the 19th century cartographers into vector format.

Figure 4a shows the geomorphological map of the surroundings of the village of Faro Superiore (Messina) (Guarnieri and Pirrotta, 2007). This little centre lies on one of the NNW-SSE trending faults that form the western limit of the Papardo trough (Figure 2). In this area it is possible to observe an example of fluvial catchment due to headwall erosion in correspondence with the fault scarp. The SW-NE direction of the fiumara Papardo provokes the abandonment of the WNW-ESE oriented stream, confluent into the basin of the fiumara S. Agata. The vertical displacement of the fault can be measured a little to the south of the catchment, where the deposits of a fluvial terrace are displaced by about 10 m. This line as well as the one slightly to the north, the latter also trending roughly W-E, show a migration of their direction of drainage towards north, as testified by the development of asymmetrical terraces on the right slope of the two small valleys. The same watercourse presents a double elbow in correspondence with the fault testifying to a dextral strike-slip component along the structure.



The most particular aspect revealed by this geomorphological analysis lies in two landslide bodies that are present on the hanging wall of the fault, for which it has also been possible to recognize the detachment scar on the footwall. Their location leads us to consider them a superficial expression of the deformation along this fault.

Finally, the superposition of the two topographic bases of 1877 and 2000 (Figure 4a), has revealed that the two landslide bodies and the respective detachment scar are not present in the older map. Moreover, it has been possible to verify that the morphology of this small valley has changed notably. In fact, in 1877 it was oriented W-E whereas it now follows a tortuous course, with a double elbow corresponding to the fault, and it appears completely displaced towards the northern slope of the valley, besides having been strongly modified by the emptying due to the landslide.

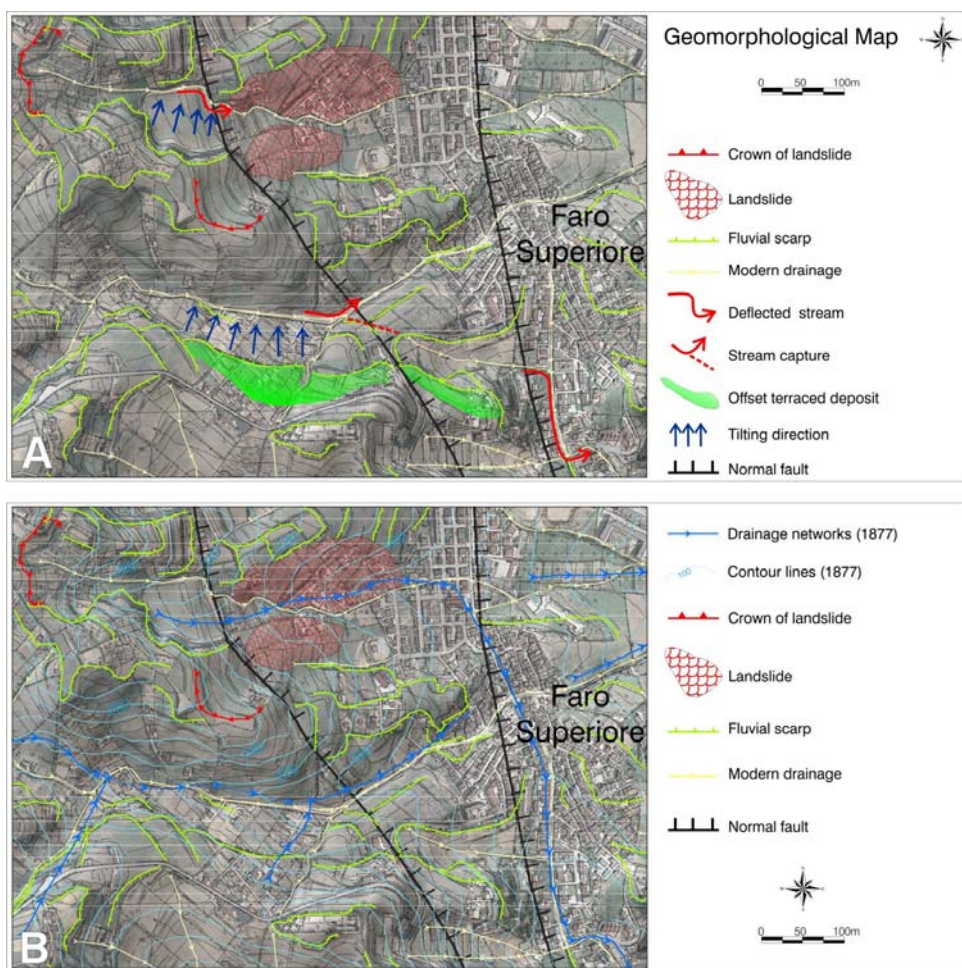


Figure 4 (a) Geomorphological Map of the Faro Superiore area (modify after Guarnieri and Pirrotta, 2007); (b) superposition between the modern topography and that of 1877, with the elements of the Geomorphological Map. It is evident that the landscape modifications are linked to the activity of the fault, with some features located on the footwall (detachment scars) and others on the hanging wall (landslide bodies). The stream belonging to the Fiumara Papardo develops as a bedrock channel on the footwall of the Faro Superiore faults and becomes an alluvial river on the hanging wall.



## Conclusion

In recent years the area of the Messina Strait has been subject of numerous studies aimed at a better understanding of its present dynamics. Many of these studies, some of which have been carried out in the framework of the planned construction of a permanent bridge across the Strait, have been primarily focused on the 1908 earthquake.

The characteristic structure attributed to the Messina earthquake and well-known from a geophysical standpoint, is envisaged in the most accredited models in the literature to be a large, blind fault lying within the Messina Strait, with an orientation about N-S.

In contrast, the secondary deformation linked to minor structures has never received serious consideration and has been neglected for many years. However, the presence of tectonically active faults is of fundamental importance in the evaluation of the geological risk as they are capable of interacting profoundly with the human framework, such as lifelines and population centers.

In conclusion, this paper shows how:

- (1) it has been possible to define the active faults in the area of the Messina Strait by means of a multidisciplinary geological-geomorphological-geophysical study;
- (2) the modifications of the landscape that occurred during little more than 100 years are of notable dimensions and impact on the human environment;
- (3) for the first time the secondary effects induced by the 28 December 1908 earthquake have been identified, describing the superficial faulting, landsliding and changes in the fluvial network.

## Acknowledgment

Reviewed by Maria Srafinà Barbano, Dipartimento di Scienze Geologiche, Università di Catania, Corso Italia 55 95129, Catania, Italy.

## References

- Amoruso, A., Crescentini, L. and Scarpa, R., (2002). Source parameters of the 1908 Messina Straits, Italy, earthquake from geodetic and seismic data. *J. Geophys. Res.*, doi:10.1029/2001JB000434, ESE 4-1 to ESE 4-11.
- Baratta, M., (1910). La catastrofe sismica calabro-messinese (28 dicembre 1908), *Rel. Soc. Geogr. It.*, 1-496.
- Barbano, M. S., Cosentino, M., Lombardo, G. and Patanè, G., (1980). Isoleismal maps of Calabria and Sicily earthquakes (Southern Italy), Consiglio Nazionale delle Ricerche, Progetto finalizzato Geodinamica, Gruppo di Lavoro "Catalogo dei Grandi Terremoti". Pub. n 341.
- Barrier, P. (1987). Stratigraphie des depots pliocenes et quaternaires du Detroit de Messine, *Doc. et Trav. IGAL*, **11**, 59-81.

- Bordoni, P. and Valensise, G. (1998). Deformation of the 125 ka marine terrace in Italy: tectonic implications, in: I. Stewart e C. Vita-Finzi (Eds), Coastal Tectonics, *Geol. Soc. London Spec. Pub.* **146**, 71-110.
- Boschi, E., Pantosti, D. and Valensise, G., (1989). Modello di sorgente per il terremoto di Messina del 1908 ed evoluzione recente dell'area dello Stretto. *Atti 8° Meeting G.N.G.T.S.*, 245-258.
- Bottari, A., Carapezza, E., Carapezza, M., Carveni, P., Cefali, F., Lo Giudice, E., and Pandolfo, C., (1986). The 1908 Messina Strait earthquake in the regional geosstructural framework. *J. Geodynamics*, **5**, 275-302.
- Bousquet, J. C., Carveni, P., Lanzafame, G., Philip, H. and Tortorici, L. (1980a). La distension pléistocène sur le bord oriental du détroit de Messine: analogies entre les résultats microtectoniques et le mécanisme au foyer du séisme de 1908, *Bull. Soc. Géol. Fr.* **7**, XXII, 3, 327-336.
- Bousquet, J. C., Lanzafame, G., Tortorici, L., Sauret, B. and Abou Bekr, N. (1980b). Mise en evidence d'un episode tectonique de distension pendant le Quaternaire ancien sur le bord sud-oriental du detroit de Messine, *C. R. Somm. Soc. Geol. Fr.* **3**, 88-91.
- Capuano, P., De Natale, G., Gasparini, P., Pingue, F. and Scarpa, R., (1988). A model for the 1908 Messina Straits (Italy) earthquake by inversion of levelling data. *Bull. Seism. Soc. Am.* **78**, 1930-1947.
- Cristofolini, R., Ghisetti, F., Scarpa, R. and Vezzani, L. (1985). Character of the stress field in the Calabrian Arc and southern Apennines (Italy) as deduced by geological, seismological and volcanological information, *Tectonophysics*, **117**, 39-58.
- De Natale, G. and Pingue, F., (1991). A variable slip fault model for the 1908 Messina Straits (Italy) earthquake, by inversion of levelling data. *Geophys. J. Int.*, **104**, 73-84.
- Gargano, C. (1994). *Carta Geologica di Messina e del settore nord-orientale dei Monti Peloritani (Sicilia Nord-orientale) alla scala 1:25.000*. S.El.Ca. Eds.
- Ghisetti, F. (1980). *Caratterizzazione dei blocchi della Calabria meridionale in base alle velocità di sollevamento nel Plio-Pleistocene: una proposta di zonazione neotettonica*, C.N.R., Contributi conclusivi per la realizzazione della Carta Neotettonica d'Italia, Progetto Finalizzato Geodinamica.
- Ghisetti, F. (1981). L'evoluzione strutturale del bacino plio-pleistocenico di Reggio Calabria nel quadro geodinamico dell'arco calabro, *Boll. Soc. Geol. It.* **100**, 433-466.
- Ghisetti, F. (1984). Recent deformations and the seismogenic source in the Messina Strait (Southern Italy), *Tectonophysics*, **109**, 191-208.
- Ghisetti, F., and Vezzani, L. (1982). The recent deformation mechanism of the Calabrian Arc. *Earth Evolution. Sciences.* **3**, 197-206.
- Guarnieri, P. (2006). Plio-Quaternary segmentation of the South Tyrrhenian Forearc basin. *Int. J. of Earth Sciences (Geologisch. Rundsc.)*, **95**, 107-118.
- Guarnieri, P., Di Stefano, A., Carbone, S., Lentini, F. and Del Ben, A. (2005). A Multidisciplinary approach for the reconstruction of the Quaternary evolution of the Messina Strait (with Geological Map of the Messina Strait 1:25.000 scale). In G. Pasquarè and C. Venturini (Ed.), *Mapping Geology in Italy*, pp 43-50, Roma, Italy: APAT.
- Guarnieri P. and Pirrotta C. (2007) - The response of drainage basins to the late Quaternary tectonics in the Sicilian side of the Messina Strait (NE Sicily). *Geomorphology* doi:10.1016/j.geomorph.2007.06.013.

- Gutenberg, B. and C.F., (1954). Richter, Seismicity of the Earth and associated phenomena, *Princeton Univ. Press*, New Jersey, 1-310.
- Lentini, F. (2000). *Carta geologica della Provincia di Messina* (1:50.000). S.El.Ca. Eds.
- Loperfido, A. (1909). Livellazione geometrica di precisione eseguita dall'I.G.M. sulla costa orientale della Sicilia, da Messina a Catania, a Gesso ed a Faro Peloro e sulla costa occidentale della Calabria da Gioia Tauro a Melito di Porto Salvo, *Relaz. Comm. Reale Acc. Naz. Lincei*, 1-35.
- Mulargia, F. and Boschi, E. (1983). The 1908 Messina earthquake and related seismicity, *Atti Int. School Phys. "E. Fermi" on "Earthquakes: observation, theory and interpretation"*, *North Holland Publ. Co.*, pp. 493-518.
- Pino, N.A., Giardini, D. and Boschi, E., (2000). The December 28, 1908, Messina Straits, southern Italy, earthquake: waveform modeling of regional seismograms, *J. Geophys. Res.*, **105**, 25.473-25.492.
- Schick, R. (1977). Eine seismotektonische Bearbeitung des Erdbebens von Messina im Jahre 1908. *Geol. Jahrb., R.E., H. 11*, 1-74.
- Seguenza, G. (1878). Carta Geologica dello Stretto di Messina (1:25.000), *Regio Com. Geol. D'It.*, 2.
- Tortorici, L., Monaco, C., Tansi, C., Cocina, O. (1995). Recent and active tectonics in the Calabrian arc (Southern Italy), *Tectonophysics*, **243**, 37-55.
- Valensise, G., (1988). Low angle normal faulting during the 1908 Messina earthquake revealed by geodetic data analysis. *EOS Transactions A.G.U., 1988 Fall Meeting*. **69**, 1.433.
- Valensise, G. and Pantosti, D., (1992). A 125 kyr-long geological record of seismic source repeatability: the Messina Straits (southern Italy) and the 1908 earthquake (Ms 7.1/2), *Terra Nova*, **4**, 472-483.



*Chapter 10*

## **SPECIAL PROBLEMS IN LANDSLIDE MODELLING: MATHEMATICAL AND COMPUTATIONAL METHODS**

*Jiří Nedoma*

Institute of Computer Science,  
Academy of Sciences of the Czech Republic, Czech Republic

### **1. The Role of Mathematical Methods in Simulations of Landslide Movements**

#### **1.1. General Motivation**

Regions with great mountain landslides, regions with bigger climatic events (i.e. hurricanes and deluges) and regions with frequental seismic events (i.e. bigger earthquakes) with ensuing landslides represent one of the most detrimental natural hazards. These events have been responsible for some of most destructive natural disasters in terms of human and economical losses.

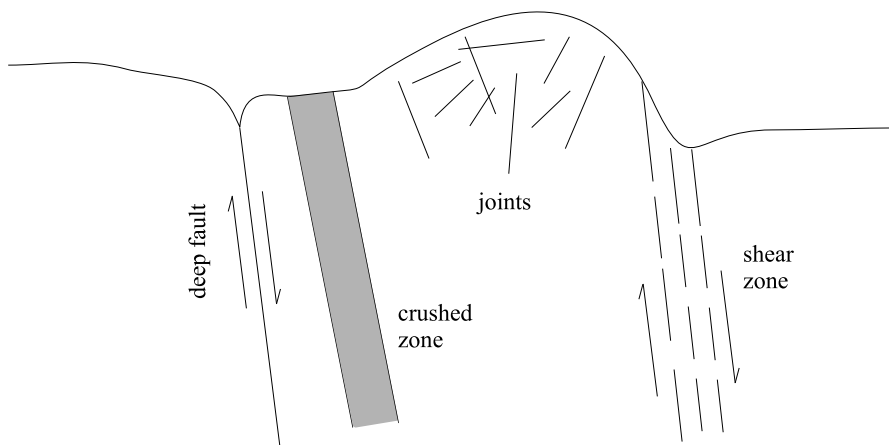


Figure 1. Different types of joints, shear and crushed zones.

In this part of the book we will deal with some mathematical and computational meth-

ods for numerical studies of potential landslides originated in different regions in the world as results of geodynamic and seismic effects or creep movements on wetting slopes and of most water-saturated masses of soils and rocks after the bigger torrential rains and ensuing bigger deluges. The geological structure is obviously one of the most important factors governing the stability of slopes. By the term geological structure is meant both rock type and discontinuities which together form the rock mass. Discontinuities are presented in great scales, from microcracks which have lengths less than 10 mm, to the deep faults in the earth crust with lengths of thousands of kilometers. Boundaries between different types of rocks can be also viewed as discontinuities. Similarly, bedding planes which can extend for kilometers and schistosity which can be several tens of meters long can be viewed as discontinuities. Other geological discontinuities include joints which vary in size from approx. 1 meter to 100 meters and faults which can be from approx. tens of meters to several hundreds of kilometers in length. Faults are distinguished from joints in that faults have undergone shear movements. Several parallel joints and faults form a shear zone (see Fig. 1). The actual shapes of discontinuities are not well known and in reality all discontinuities are two- or three-dimensional surfaces. Failures occur when the loads or stresses acting on the rocks exceed the (compressive or tensile) strength of the rock materials. By the failure mode is meant a macroscopic description of the manner in which failure occurs. Based on the geological structure and the stress state in the rock mass, certain failure modes appear to be more likely than others in large scale slopes. The failure surface, defined as the surface along which failure develops, could be a single discontinuity (plane failure) or the so-called wedge failure when two discontinuities intersect each other and the so-called step path and step wedge failures when a combination of several discontinuities are connecting together. A common feature of most failure modes is the formation of a tension crack at the slope crest. The significant group of failure modes are rotational shear failures, which occur in slopes without critically oriented discontinuities or planes of weakness. These types of failures are the typical modes of failures in soils. Furthermore, blasting-induced failures are a marginal problem for large scale slopes. Seismic events, and similarly other low frequency vibrations, could be more dangerous for large scale slopes. Several seismic-induced failures of natural slopes have been observed in great mountains, like the large landslide in the Huascaran area in the North Andes forty years ago. The interesting question is where such failures are initiated and the question about the mechanisms of such failures (see [26, 75]). In some cases the failure is initiated at the toe of the slope, where the highest shear stresses are found. In many cases the failure surface forming at the crest of the slope will be a tension crack. Failure initiation in clayey soils depends also upon the groundwater conditions. For more details see [26, 70, 75]. A few failures are presented in Figs 2-7.

The facts, which should be necessary mentioned here, will also show how to obtain approximately the geometry of the investigated areas, the dimensions of the potential failure masses and the mechanisms of landslide origins. The investigated slope mainly consists of intact up to weathered or otherwise destroyed rocks and has been affected by recurrent instability phenomena.

In order to analyse and evaluate the potential hazard related to unstable rock slopes, related to effects of weather like the great torrential rains with resulting great deluges and, moreover, related to consequences of geodynamic and geomechanic processes in these regions with ensuing earthquakes or shocks, it is essential to understand the processes and

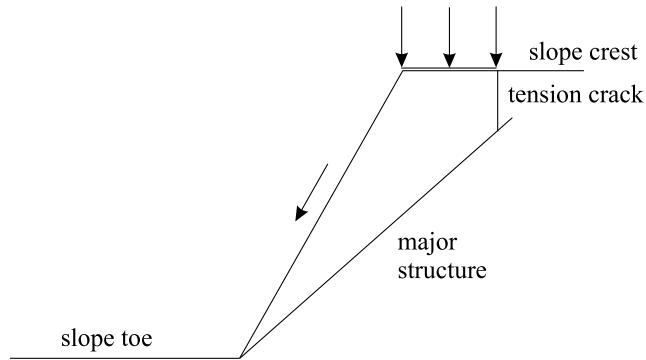


Figure 2. Plane failure with tension crack.

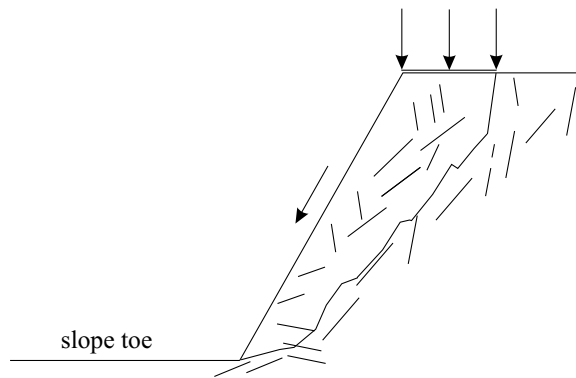


Figure 3. Step path failure.

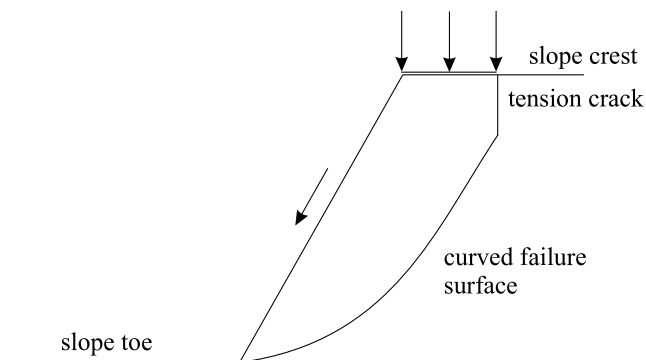


Figure 4. Rotational shear with tension crack.

mechanisms driving the slope instability. Therefore, the research about the trigger mechanism of landslides and the behaviour of landslides is of the significant importance. Such research are predominantly focused on fast and slow landslides. Creep movements may also represent an initial stage of slow and fast landslides or earth flows. Slow creep movements are typical for soils built by cohesive soils, which can be described, from a geological point

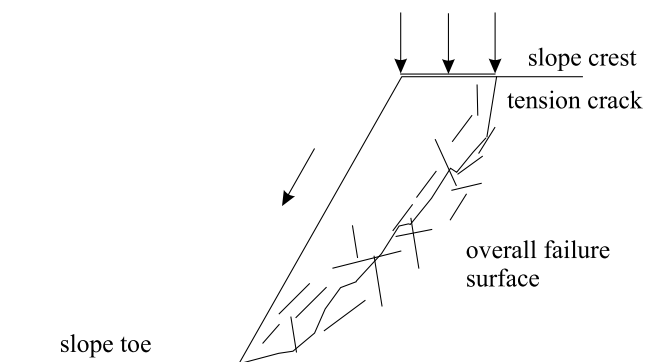


Figure 5. Combination of failure through intact rock and along discontinuities.

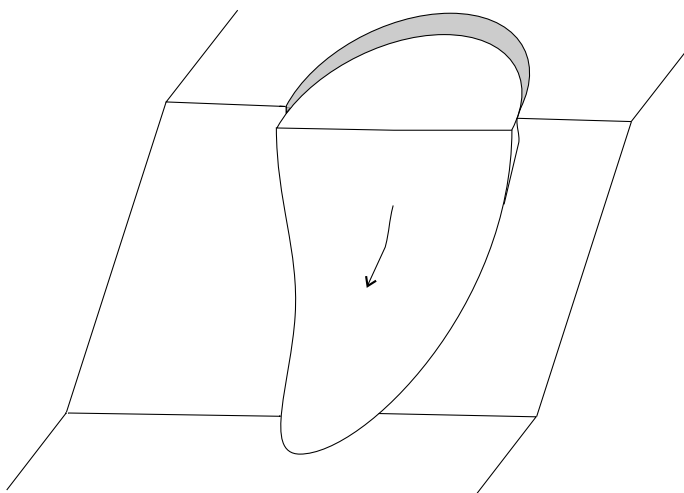


Figure 6. The 3D model of rotational shear failure.

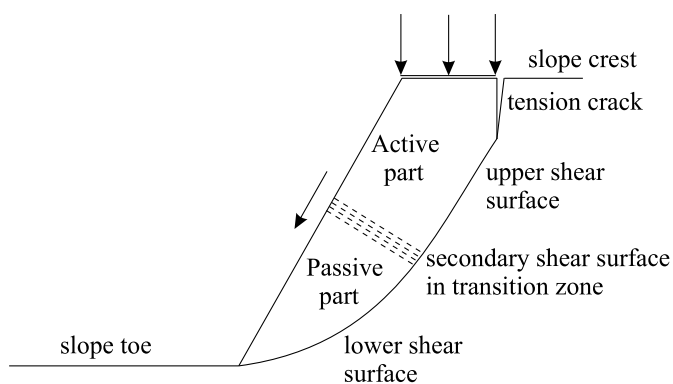


Figure 7. Large scale slope failure - transition zone.

of view, as soils characterized by a high clay content. Therefore, it is important to be able to understand the mechanisms by which large slopes gradually move downhill and to be able



to simulate and to determine their actual displacements, velocities as well as distribution of stresses in these regions. In the case, if the landslides have the origin in a consequence of earthquakes or in originated fractures in the rock massif with resulting shocks, it is important to describe, to understand and to simulate their coupling mechanism.

A landslide is characterized by the gravity-driven downslope movement of a slide mass composed of the rock, soil and vegetation. Landslides occur when the downslope weights of the slide masses exceed the strength of the soil along the slip surfaces, i.e., when the driving forces exceed the resisting forces. The stability of a slope depends on (i) the steepness of the slope and the slope aspects, (ii) composition of the soil and the rock, (iii) saturation soils and rocks by water and the further groundwater conditions, (iv) recent precipitation patterns, (v) situation of the vegetation on the slope, (vi) anthropomorphous properties of rocks (grading of rocks, clearing of the land, etc.). Landslide movements may be also considered as falls, slides, spreads or flows. These mechanisms are often complex and act at different depth, making the investigation characterization of contributing factors very difficult.

The landslide hazard can be identified as (i) debris flows, characterized by fast moving of the rock mass, by water-saturated masses of the soil, rocks and debris of vegetation that move down through steep slopes and channels, (ii) shallow bluff failures - the small landslide with limited area which can move slowly or very quickly, (iii) deep seated, large landslides, which can be reactivations of older and prehistoric, failure, and they are typically slow moving, (iv) submarine landslides, characterized by unstable slopes of rapid sedimentation, of bottom current erosion of the materials at the base of the delta slope, additional loading at the top of the delta slope as well as of the earthquake shaking causing loss of the soil strength and increasing in the downslope force on the soil mass. These large submarine landslides typically occur on the deltas of major rivers or streams. Submarine landslides may produce waves large enough to cause damage, destruction and life-loss to the communities along the shoreline. The submarine landslides are also associated with earthquakes and can evoke the great waves, the so-called tsunami.

The assessment of the hazard posed by a large unstable rock slope requires information about (i) state of stability, (ii) anticipated failure mechanism, (iii) potential failure volume, (iv) deformation behaviour at failure, (v) determination of post-failure values of distances and velocities in devastated region. It is evident that a prediction of landslides and estimation of the ensuing devastation of the region is needed and desirable. The prediction of creep movements concerns the prediction of both displacements and velocities as well as their evolution over time. From a soil mechanical point of view, cohesive soil materials can be defined as materials that can creep (i.e. strain rate is nonzero and stress rate is zero), relaxate (i.e. strain rate is zero and stress rate is nonzero) and that must be rate-dependent, i.e., stress evolution and stiffness depend on the strain rate. Such materials can be described by visco-elastic, elasto-plastic, elasto-visco-plastic or visco-hypoplastic rheologies, respectively. Therefore, a wide variety of constitutive relations for soils has been used for slope stability analysis in literature represent very simple linear elastic laws, visco-elastic, up to elasto-visco-plastic laws. Moreover, for these studies different approaches based on a great number of rheologies, mathematical models and methods are known from the literature. In our study we will limit ourselves to the (thermo-)visco-elastic rheology and the contact theory for the dynamic evolution of landslides originated by geodynamic processes, earth-

quakes or shocks and to the (thermo-)visco-plastic rheology of Bingham type for landslides for dynamic evolution of landslides evoked by great rainfalls, hurricanes and deluges.

A wide variety of geological and geomechanical engineering systems are connected with coupled thermo-hydro-mechanical processes (THM processes). The thermo-hydro-mechanical coupling processes involve processes connected with heat, water and mechanical properties of loaded and fractured rocks. Moreover, the THM coupling processes involve many pairwise mechanisms as a flow water through a saturated - unsaturated rocks, consolidation processes, water - chemical processes in rocks, water movements, pore water pressures, etc., and many special properties like poro-elastic, elasto-plastic, poro-elasto-plastic properties of rocks, etc. When all of the connecting mechanism links are present, then the system is fully-connected or fully-coupled; if mechanism links are missing, the system is not fully-coupled. In our consideration in the second part of this study we limit ourselves to heat, water and mechanical aspects of thermo-hydro-mechanical processes. The nature is three dimensional and non-linear in general. Therefore, for a description of the above aspects of thermo-hydro-geomechanical processes the coupled thermo-visco-plastic Bingham rheology can be used with a great merit. The best advantage of this rheology is its extensive spectrum of material properties covered up incompressible rocks, rocks saturated by water up to the liquid, as if the threshold of plasticity in the Bingham's stress-strain rate relation is equal to zero, the constitutive relation is identical with the viscous Newtonian liquid. Therefore, the Bingham rheology is also useful for studies and analyses of the thermo-hydro-geomechanical processes, including the landslides evoked by enormous climatic changes accompanied by great cloud-bursts and catastrophic deluges.

The main objective is to simulate and predict the THM processes in and around the engineered barrier system of the overground and the underground geotechnical structures and constructions. Therefore, the THM phenomena are subjects of great interests, e.g. in the projects of great water dams, High Level Waste Repositories, etc.. On the other hand the THM coupling processes, based on the (thermo-)visco-plastic Bingham rheology, also describe hydrological problems and problems of unstable slopes connected with consequences of deluges.

Moreover, the main aim is also to simulate and to predict all effects of the thermo-hydro-mechanical and thermo-hydro-dynamical processes in the unsafed regions, intervened by hurricanes, deluges (etc.) in critical situations. The introduced 3D mathematical model will be based on the thermo-visco-plastic rheology of the Bingham type coupled with climatic and hydro-geological models (for the project see APPENDIX).

The last years have been through the tragedy in the Czech Republic, in New Orleans, in the Iowa region, in the Asian regions as well as in other regions in the world. Further, we would like to present some idea and algorithms connected with future security of some parts of countries which are endangered by great rainfalls and by bigger hurricanes with great catastrophic consequences as those in the case of the Katrina hurricane and ensuing bigger deluges.

The idea of the proposal how to predict the future situation in the endangered regions is based on the mathematical simulation of coupled thermo-hydro-mechanical and thermo-hydro-dynamical processes together with the climatic processes in the endangered region during the strong hurricane and the consequences of the enormous quantity of water in such regions onto the stability of slopes and onto the security of such regions (see [54, 57, 60]).

The main goal of the presented idea is to connect the climatic, hydro-mechanic and geological observations and the corresponding climatic models with the thermo-hydro-dynamic and the thermo-hydro-mechanic models, with the possibility to estimate future destruction of these endangered regions with landslides of the non-stable slopes. The integral part of this idea is to determine the causes of risks in endangered regions and the determination of characteristic parameters for their evaluations and analyses. The goal is to help with specification and categorization of all these causes with aims at removal relevant risks and symptoms of a crisis in such critical situations. Such complex evaluations of the future situation start then to be an important foundation for elaboration of the “Analyses of risks” for critical situations in such endangered regions.

Since the rheology used in the model can describe the situations in the endangered regions with respect to all effects of great hurricanes, to bigger storms with great fallout of water, resulting deluges and the ensuing relevant landslides. The main goal of the presented idea is to connect the climatic observations and the corresponding climatic models with the thermo-hydro-dynamic and the thermo-hydro-mechanic models, with the possibility to estimate future destruction of these endangered regions with landslides of the non-stable slopes. The integral part of this idea is to determine the causes of risks in endangered regions and the determination of characteristic parameters for their evaluations and analyses. The goal is to help with specification and categorization of all these causes with aims at removal relevant risks and symptoms of a crisis in such critical situations. Such complex evaluations of the future situation start then to be an important foundation for elaboration of the “Analyses of risks” for critical situations in such endangered regions.

It is evident that cooperation of specialists from climatology, geology, hydrology, physics and mathematics as well as of specialists from the workplace of the Meteorological Centres (like the National Hurricane’s Center in Miami, etc.) are fundamental for successfully close of this part of project.

In this part of the book we limit ourselves to only small part of the above presented project, to the analysis of the mathematical model of hydro-mechanical problem of non-stable slopes in connection with great deluge. Moreover, in this part of the book the mathematical models and the useful numerical methods and algorithms for modelling and simulation of landslides evoked by geodynamic processes, earthquakes, shocks and creep movements will be also investigated and discussed.

In the first part of this study we limit ourselves to coupling processes between geodynamic processes in the upper parts of the Earth lithosphere, the ensuing earthquakes and the evoked landslides. The theory will be based on the dynamic and quasi-static contact and impact mechanics. The presented theory renders possible to understand and to clear up the origin and the mechanism of the earthquake as a consequence of geodynamic processes in the upper parts of the Earth and the ensuing landslides on the Earth surface.

This study proposes a computational efficient methodology for combining multibody static, quasi-static and dynamic simulation methods with a deformable contact models. Recent trends in geomechanics and geodynamics have provided a strong impetus for the development of accurate stress analyses in the part of the Earth. The success of geomechanic processes in the upper parts of the Earth depend on many factors. The mechanical factor is an important one.

Mechanical loadings, static and especially dynamic loadings, are presupposed to play

an important role in the deformation of the upper parts of the Earth. Besides the loading (i.e. contact pressures) also motion (i.e. kinematics) contributes to an interactive effect of progression of deformation of areas near the Earth surface. A complex relation exists between this mechanism and the magnitude and direction of the loads, the geometry of the areas configuration, the elastic properties of the materials and the physical connections at the material connections, where motion and loads influence landslides.

It can be shown that the static, quasi-static and dynamic contact problems in a suitable rheology and their finite element approximations are a very useful tools for analyzing the deformation of upper parts of the Earth. Such problems lead to solving variational inequalities, which physically describe the principle of virtual work in its inequality form. But our contemporary knowledges concerning the analysis of multibody contact theory with respect to prevailing problems in geomechanics are still very limited. Therefore, one of the main goals of this study is to disclose the limitation of validity of our model problems used in practice.

## 1.2. Formulation of Model Problems Based on the Multibody Contact Theory

### 1.2.1. Models Based on the Multibody Contact Theory in Thermo-visco-elasticity

In this section we will investigate the dynamic and/or the quasi-static and static multibody contact problems with Coulomb friction in linear thermo-elasticity, thermo-visco-elasticity with short and long memories and damping in  $N$ -dimensions.

Let  $I = (0, t_p)$  be a time interval. Let  $\Omega \subset \mathbb{R}^N$ ,  $N = 2, 3$ , be a region occupied by a system of  $r$  geological bodies of arbitrary shapes  $\Omega^\iota$  such that  $\Omega = \bigcup_{\iota=1}^r \Omega^\iota$ . We will assume that all  $\Omega^\iota$  have Lipschitz boundaries  $\partial\Omega^\iota$  and that  $\partial\Omega = \Gamma_\tau \cup \Gamma_u \cup \Gamma_c$ , where the disjoint parts  $\Gamma_\tau$ ,  $\Gamma_u$ ,  $\Gamma_c$  are open subsets. Assume that a system of geological bodies occupying the region  $\Omega$  consists of  $r$  geological bodies  $\Omega^\iota$ ,  $\iota = 1, \dots, r$ , and let several neighbouring geological bodies, say  $\Omega^k$  and  $\Omega^l$ , are in a mutual contact. Denote the common contact boundary between both geological bodies  $\Omega^k$  and  $\Omega^l$  before deformation by  $\Gamma_c^{kl}$ . Let  $\mathbf{n}$  denote the unit outer normal vector and  $\mathbf{t} = (t_i)$  denote the unit tangential vector to the contact boundary  $\Gamma_c^{kl}$ . Further, denote  $\mathbf{u} = (u_i)$  the displacement vector,  $\mathbf{v} = (v_i) = (u'_i)$  the velocity vector and  $\boldsymbol{\tau} = (\tau_i)$ ,  $\tau_i = \tau_{ij}n_j$ ,  $i, j = 1, \dots, N$ , the stress vector, its normal and tangential components by  $\tau_n = \tau_i n_i = \tau_{ij}n_i n_j$ ,  $\boldsymbol{\tau}_t = \boldsymbol{\tau} - \tau_n \mathbf{n}$ , and the normal and tangential components of displacement vector by  $u_n = u_i n_i$  and  $\mathbf{u}_t = \mathbf{u} - u_n \mathbf{n}$  and  $v_n = v_i n_i$  and  $\mathbf{v}_t = \mathbf{v} - v_n \mathbf{n}$  the normal and tangential components of velocity vector. Denote by  $\mathbf{u}^k, \mathbf{u}^l, \mathbf{v}^k, \mathbf{v}^l, T^k, T^l$  (indices  $k, l$  correspond with the neighbouring geological bodies being in contact) the displacements, velocities and the temperatures in the neighbouring geological bodies. All these quantities are functions of spatial coordinates. Moreover, we will assume that  $\Gamma_u = {}^1\Gamma_u \cup {}^2\Gamma_u$ ,  $\Gamma_\tau = {}^1\Gamma_\tau \cup {}^2\Gamma_\tau$  and  $\Gamma_c = \bigcup_{k,l} \Gamma_c^{kl}$ ,  $\Gamma_c^{kl} = \partial\Omega^k \cap \partial\Omega^l$ ,  $k \neq l$ ,  $k, l \in \{1, \dots, r\}$ . We denote by  $\Omega_t = I \times \Omega$  the time-space domain and by  $\Gamma_\tau(t) = \Gamma_\tau \times I$ ,  $\Gamma_u(t) = \Gamma_u \times I$ ,  $\Gamma_c(t) = \Gamma_c \times I$  the parts of its boundary  $\partial\Omega_t = \partial\Omega \times I$ .

The stress-strain relation will be defined by the Hooke's or the Duhamel-Neumann's

laws

- (a)  $\tau_{ij} = \tau_{ij}(\mathbf{u}) = c_{ijkl}^{(0)}(\mathbf{x})e_{kl}(\mathbf{u}), i, j, k, l = 1, \dots, N$ , in the elastic rheology,
  - (b)  $\tau_{ij} = \tau_{ij}(\mathbf{u}, T) = c_{ijkl}^{(0)}(\mathbf{x})e_{kl}(\mathbf{u}) - \beta_{ij}(T - T_0) = {}^e\tau_{ij} + {}^T\tau_{ij}, i, j, k, l = 1, \dots, N$ , in the thermo-elastic rheology,
  - (c)  $\tau_{ij} = \tau_{ij}(\mathbf{u}, \mathbf{u}') = c_{ijkl}^{(0)}(\mathbf{x})e_{kl}(\mathbf{u}) + c_{ijkl}^{(1)}(\mathbf{x})e_{kl}(\mathbf{u}'), i, j, k, l = 1, \dots, N$ , in the visco-elastic rheology with short memory,
  - (d)  $\tau_{ij} = \tau_{ij}(\mathbf{u}, \mathbf{u}', T) = c_{ijkl}^{(0)}(\mathbf{x})e_{kl}(\mathbf{u}) + c_{ijkl}^{(1)}(\mathbf{x})e_{kl}(\mathbf{u}') - \beta_{ij}(T - T_0) = {}^e\tau_{ij} + {}^v\tau_{ij} + {}^T\tau_{ij}, i, j, k, l = 1, \dots, N$ , in the thermo-visco-elastic rheology with short memory, (1)
  - (e)  $\tau_{ij} = c_{ijkl}^{(0)}e_{kl}(\mathbf{u}(t, \cdot)) + \int_0^t b_{ijkl}(t - \tau)e_{kl}(\mathbf{u}(\tau, \cdot))d\tau - \beta_{ij}(T - T_0) = {}^e\tau_{ij} + {}^v\tau_{ij} + {}^T\tau_{ij}, i, j, k, l = 1, \dots, N$ , in the thermo-visco-elastic rheology with long memory,
- and where  $e_{ij}(\mathbf{u}) = \frac{1}{2} \left( \frac{\partial u_i}{\partial x_j} + \frac{\partial u_j}{\partial x_i} \right), e_{ij} = e_{ji}, i, j = 1, \dots, N$ ,

where  $c_{ijkl}^{(n)}(\mathbf{x}), n = 0, 1$ , are elastic (for  $n = 0$ ) and viscous (for  $n = 1$ ) coefficients,  $b_{ijkl} = b_{ijkl}(\mathbf{x}, t)$  represents the material memory coefficients, depending on  $t$  and  $\mathbf{x}$ , bounded in  $\mathbf{x}, t$  and satisfying the symmetry and regularity conditions and  $e_{ij}(\mathbf{u})$  are components of the small strain tensor,  $N$  is the space dimension. For the tensors  $c_{ijkl}^{(n)}(\mathbf{x}), n = 0, 1$ , we assume the properties of symmetry, ellipticity and boundedness and for  $\beta_{ij}$  the symmetry conditions, i.e. we assume that

$$\begin{aligned}
 c_{ijkl}^{(n)} &\in L^\infty(\Omega), c_{ijkl}^{(n)} = c_{jikl}^{(n)} = c_{klij}^{(n)} = c_{ijlk}^{(n)}, n = 0, 1, i, j, k, l = 1, \dots, N, \\
 c_{ijkl}^{(n)}e_{ij}e_{kl} &\geq c_0^{(n)}e_{ij}e_{ij} \quad \forall e_{ij}, \quad e_{ij} = e_{ji} \quad \text{and a.e. } \mathbf{x} \in \Omega, \quad c_0^{(n)} > 0, \\
 c_{ijkl}^{(n)} &= \lambda^{(n)}\delta_{ij}\delta_{kl} + \mu^{(n)}(\delta_{ik}\delta_{jl} + \delta_{il}\delta_{jk}) \quad \text{for the isotropic materials,} \\
 b_{ijkl} &= b_{jikl}, b_{ijkl}, \partial b_{ijkl}/\partial t, \partial^2 b_{ijkl}/\partial t^2 \in L^\infty(\Omega \times I), i, j, k, l = 1, \dots, N, \\
 \beta_{ij} &\in C^1(\overline{\Omega}), \beta_{ij} = \beta_{ji}, \beta_{ij} \geq \beta_0 > 0, i, j = 1, \dots, N,
 \end{aligned} \tag{2}$$

where  $\lambda^{(n)}, \mu^{(n)}$  for  $n = 0$  are the Lamé elastic coefficients and for  $n = 1$  the viscous coefficients for isotropic materials,  ${}^e\tau_{ij}, {}^v\tau_{ij}, {}^T\tau_{ij}$  are the elastic, viscous and thermal stresses. A repeated index implies summation from 1 to  $N$ .

Let  $\mathbf{F}(t, \mathbf{x}), \mathbf{P}(t, \mathbf{x})$  be the body and surface forces,  $\rho(\mathbf{x})$  the density,  $\alpha(\mathbf{x}) \geq 0$  physically mean the damping,  $W$  be the thermal sources,  $c_e(\mathbf{x})$  be the specific heat and  $c(\mathbf{x}) = \rho(\mathbf{x})c_e(\mathbf{x})$  the thermal capacity and  $\beta_{ij}$  the coefficient of linear thermal expansion. The respective time derivatives is denoted by “ $\prime$ ”. We denote by  $\mathbf{u}' = (u'_i)$  the velocity vector. Let on  $\Gamma_c^{kl}$  the positive direction of the outer normal vector  $\mathbf{n}$  be assumed with respect to  $\Omega^k$ . Further, we denote by  $[u_n]^{kl} = u_n^k - u_n^l$  the jump of the normal displacement across the contact zone between neighbouring geological bodies  $\Omega^k$  and  $\Omega^l$  and similarly we put  $[\mathbf{u}_t]^{kl} = \mathbf{u}_t^k - \mathbf{u}_t^l$  for the tangential component of displacement vector. If one of the colliding bodies is absolutely rigid, say  $\Omega^l$ , then  $[u_n]^{kl} \equiv u_n^k$ , and similarly, we put  $[\mathbf{u}_t]^{kl} = \mathbf{u}_t^k$ .

From the momentum conservation law and the entropy density law the equation of motion in dynamic case, the equilibrium equation in static and quasi-static cases and the expanded equation of heat conduction in the form

$$\begin{aligned} \rho^\iota \frac{\partial^2 u_i^\iota}{\partial t^2} + \alpha^\iota \frac{\partial u_i^\iota}{\partial t} &= \frac{\partial \tau_{ij}^\iota(\mathbf{u}^\iota, \mathbf{u}^\iota, T^\iota)}{\partial x_j} + F_i^\iota \quad \text{in the dynamic case,} \\ \frac{\partial \tau_{ij}^\iota(\mathbf{u}^\iota, \mathbf{u}^\iota, T^\iota)}{\partial x_j} + F_i^\iota &= 0 \quad \text{in the static and quasi-static cases,} \\ \rho^\iota c_e^\iota \frac{\partial T^\iota}{\partial t} - \frac{\partial}{\partial x_j} (\kappa_{ij}^\iota \frac{\partial T^\iota}{\partial x_i}) &= W^\iota - \rho^\iota \beta_{ij}^\iota T_0^\iota e_{ij}(\mathbf{u}^\iota) + c_{ijkl}^{(1)\iota} e_{kl}(\mathbf{u}^\iota) e_{ij}(\mathbf{u}^\iota), \\ \text{where } i, j &= 1, \dots, N, \iota = 1, \dots, r, (t, \mathbf{x}) \in \Omega_t^\iota = I \times \Omega^\iota, \iota = 1, \dots, r, \end{aligned} \quad (3)$$

hold, where  $T_0^\iota$  are the initial temperatures of nondeformable parts of the system of geological bodies,  $\kappa_{ij}^\iota(\mathbf{x})$ ,  $\iota = 1, \dots, r$ , the coefficients of thermal conductivity that are symmetric and uniformly positive definite, i.e.

$$\kappa_{ij}^\iota(\mathbf{x}) = \kappa_{ji}^\iota(\mathbf{x}), \quad \kappa_{ij}^\iota(\mathbf{x}) \zeta_i \zeta_j \geq \kappa_0^\iota |\zeta|^2, \quad \kappa_0^\iota = \text{const.} > 0, \quad \zeta \in \mathbb{R}^N, \quad N = 2, 3 \quad (4)$$

and where the term  $\rho^\iota \beta_{ij}^\iota T_0^\iota e_{ij}(\mathbf{u}^\iota)$  represents the deformation energy which changes into a heat, the so-called deformation heat and the term  $c_{ijkl}^{(1)\iota} e_{ij}(\mathbf{u}^\iota) e_{kl}(\mathbf{u}^\iota)$  is the additional viscous dissipation and represents one of heat sources in the heat equation, the so-called viscous heat, in order to satisfy the first thermodynamic law.

### Boundary and contact conditions:

We will assume that the system of geological bodies is loaded, and moreover, that their parts are in mutual contacts. Further, we will assume that the volume forces and surface tractions change in time and the movements of geological bodies change also in time. Then we impose the conditions in displacements (or in velocities) and temperature. Here we limit ourselves in the formulation in displacements, the formulation in velocities will be formulated in the next chapters, where the problems will be analysed in details.

Let us assume that the boundary  $\Gamma_\tau$  is divided in two parts, say  ${}^1\Gamma_\tau$  and  ${}^2\Gamma_\tau$ , such that  $\Gamma_\tau = {}^1\Gamma_\tau \cup {}^2\Gamma_\tau$ . Let a portion of the examined system of geological bodies on one part of this boundary is loaded, we denote it as  ${}^1\Gamma_\tau$ , while on the second one is unloaded, we denote it as  ${}^2\Gamma_\tau$ . Moreover, we will introduce the external temperature  $Y$ . Then we will assume the condition in the form

$$\begin{aligned} \kappa_{ij} \frac{\partial T(\mathbf{x}, t)}{\partial x_i} n_j &= K(Y(\mathbf{x}, t) - T(\mathbf{x}, t)), \quad \tau_{ij} n_j = P_i, \quad (P_i \geq 0), \quad i, j = 1, \dots, N, \\ \text{for } (t, \mathbf{x}) \in \Gamma_\tau(t) &= I \times \cup_{i=1}^r (\Gamma_\tau \cap \partial\Omega^\iota), \quad \text{meas } {}^i\Gamma_\tau \geq 0, \quad i = 1, 2. \end{aligned} \quad (5)$$

Let the boundary  $\Gamma_u$  be divided in two parts, say  ${}^1\Gamma_u$  and  ${}^2\Gamma_u$ , i.e.  $\Gamma_u = {}^1\Gamma_u \cup {}^2\Gamma_u$ . Let us assume that the temperature and the displacement vector are prescribed at a part of the boundary  $\Gamma_u$ , we denoted it by  ${}^1\Gamma_u$ . Thus, we will assume e.g. the conditions

$$\begin{aligned} T(\mathbf{x}, t) &= T_1(\mathbf{x}, t), \quad u_i = u_{2i}, \quad i = 1, \dots, N, \\ \text{for } (t, \mathbf{x}) \in {}^1\Gamma_u(t) &= I \times \cup_{i=1}^r ({}^1\Gamma_u \cap \partial\Omega^\iota), \quad \text{meas } {}^1\Gamma_u > 0. \end{aligned} \quad (6)$$

Let us assume that a portion of the examined system of geological bodies is fixed at a certain part of the boundary  ${}^2\Gamma_u$  and that the heat flow is nonzero at this part of the boundary

$$\begin{aligned} \kappa_{ij} \frac{\partial T(\mathbf{x}, t)}{\partial x_i} n_j &= q, \quad u_i = 0, \quad i = 1, \dots, N, \\ \text{for } (t, \mathbf{x}) \in {}^2\Gamma_u(t) &= I \times \cup_{i=1}^r ({}^2\Gamma_u \cap \partial\Omega^i), \quad \text{meas } {}^2\Gamma_u > 0. \end{aligned} \quad (7)$$

From Eqs (1), (3) and (5) it follows that the effect of a change of temperature due to the deformation is equivalent to the replacement of mass forces by forces  $F_i - \frac{\partial}{\partial x_j}(\beta_{ij}(T - T_0))$  and of surface loading by surface forces  $P_i + \beta_{ij}(T - T_0)n_j$ .

To describe the contact between geological bodies we need to consider the normal approach and the tangential process. By **contact conditions** we understand conditions which describe the tangential process, that is a relation involving the tangential stress  $\tau_t$  and the tangential displacements  $\mathbf{u}_t$  (or the tangential velocity  $\mathbf{v}_t = \mathbf{u}'_t$ , where we denote  $\mathbf{u}' = \frac{\partial \mathbf{u}}{\partial t}$ ). The nature of friction forces acting between geological bodies is extremely complex and depends on several factors, like as the constitution of the interface, the time scales, the response of the interface to normal forces, the presence of some lubrications, inertia and thermal effects, roughness of the contacting surfaces, history of loadings, etc. (see e.g. [72]). These conditions can be formulated as nonlinear equalities or inequalities.

Let  $u_n = \mathbf{u} \cdot \mathbf{n}$ ,  $\mathbf{u}_t = \mathbf{u} - u_n \mathbf{n}$ ,  $v_n = \mathbf{v} \cdot \mathbf{n}$ ,  $\mathbf{v}_t = \mathbf{v} - v_n \mathbf{n}$ ,  $\boldsymbol{\tau} = (\tau_{ij} n_j)$ ,  $\tau_n = \tau_{ij} n_j n_i$ ,  $\boldsymbol{\tau}_t = \boldsymbol{\tau} - \tau_n \mathbf{n}$  be the normal and tangential components of the displacement, velocity and stress vectors defined above. The component  $\boldsymbol{\tau}_t$  is connected with friction forces on the contact surface  $\cup \Gamma_c^{kl}$ . Generally, a mathematical theory of friction would be a generalization of experiments and it must be in agreement with the knowledges of thermodynamics. In the case if there are no loss of the contacts during the process, thus the normal displacements or normal velocities vanish, i.e.  $u_n = 0$  or  $v_n = 0$  and tangential component of stresses are equal to zero or are nonzero. Then we speak about **bilateral contact conditions**. This bilateral conditions can be also defined in the form with Coulombian or viscous friction and/or without friction. In some problems the bilateral contact conditions with or without friction can be used, e.g. for the case without friction

$$u_n = 0, \quad \tau_{tj} = 0, \quad j = 1, \dots, N, \quad \text{on } \Gamma_0. \quad (8)$$

This type of condition describes also e.g. the symmetry condition.

On the contact boundary for the case of bilateral contact with Coulombian friction we have the conditions

$$\left\{ \begin{array}{l} [u_n]^{kl} = 0 \quad \text{and} \quad |\boldsymbol{\tau}_t^{kl}| \leq \mathcal{F}_c^{kl} |\boldsymbol{\tau}_n^{kl}| \equiv g_c^{kl}, \\ \left\{ \begin{array}{l} \text{if } |\boldsymbol{\tau}_t^{kl}| < g_c^{kl} \quad \text{then} \quad [\mathbf{u}_t]^{kl} = 0, \\ \text{if } |\boldsymbol{\tau}_t^{kl}| = g_c^{kl} \quad \text{then there exists } \lambda \geq 0 \\ \text{such that} \quad [\mathbf{u}_t]^{kl} = -\lambda \boldsymbol{\tau}_t^{kl}, \end{array} \right. \end{array} \right\} \quad \text{on } \cup_{k,l} \Gamma_c^{kl} \times I, \quad (9)$$

in displacements and

$$\left\{ \begin{array}{l} [v_n]^{kl} = 0 \quad \text{and} \quad |\boldsymbol{\tau}_t^{kl}| \leq \mathcal{F}_c^{kl} |\boldsymbol{\tau}_n^{kl}| \equiv g_c^{kl}, \\ \left\{ \begin{array}{l} \text{if } |\boldsymbol{\tau}_t^{kl}| < g_c^{kl} \quad \text{then} \quad [\mathbf{v}_t]^{kl} = 0, \\ \text{if } |\boldsymbol{\tau}_t^{kl}| = g_c^{kl} \quad \text{then there exists } \lambda \geq 0 \\ \text{such that} \quad [\mathbf{v}_t]^{kl} = -\lambda \boldsymbol{\tau}_t^{kl}, \end{array} \right. \end{array} \right\} \quad \text{on } \cup_{k,l} \Gamma_c^{kl} \times I, \quad (10)$$

in velocities. The relations (9) and (10) represent the Coulombian law of friction.

Another contact conditions must be used in the case if the geological bodies are strongly loaded. These conditions are represented by the **unilateral contact conditions of Signorini types** with or without friction. In such cases during the deformation process in the system of geological bodies the contact points will be displaced in different ways, but colliding parts of geological bodies can not penetrate, i.e.

$$[u_n]^{kl} \leq d^{kl} \quad \text{in displacements or} \quad [v_n]^{kl} \leq 0 \quad \text{in velocities on} \quad \Gamma_c^{kl} \times I \quad (11)$$

where the positive direction of the outward normal to the contact boundary  $\mathbf{n}$  is related to the domain  $\Omega^k$  occupying by the  $k$ -th part of the investigated geological system and, where  $d^{kl}$  denotes the gap between the neighbouring colliding geological bodies. The relation (11) is known as the condition of nonpenetration.

For contact forces from the law of action and reaction it follows that  $\tau_n^k = -\tau_n^l = \tau_n^{kl}$  and  $\tau_t^k = \tau_t^l = \tau_t^{kl}$ . Since normal components cannot be positive (tractions) then

$$\tau_n^{kl} \leq 0 \quad \text{on} \quad \Gamma_c^{kl} \times I. \quad (12)$$

During the deformation of both neighbouring colliding geological bodies the colliding geological bodies are in a contact, i.e.  $[u_n]^{kl} = d^{kl}$  in displacements or  $[v_n]^{kl} = 0$  in velocities or are not in a contact i.e.  $[u_n]^{kl} < d^{kl}$  in displacements or  $[v_n]^{kl} < 0$  in velocities. If the geological bodies are in contact, i.e.  $[u_n]^{kl} = d^{kl}$  in displacement or  $[v_n]^{kl} = 0$ , then there may exist non zero contact forces  $\tau_n^k = -\tau_n^l \equiv \tau_n^{kl} < 0$ . If geological bodies are not in contact i.e. if  $[u_n]^{kl} < 0$ , then the contact forces are zero, i.e.  $\tau_n^k = -\tau_n^l \equiv \tau_n^{kl} = 0$ . These cases are included in the following condition

$$[u_n]^{kl} \tau_n^k \leq d^{kl} \quad \text{in displacements or} \quad [v_n]^{kl} \tau_n^k \leq 0 \quad \text{in velocities on} \quad \Gamma_c^{kl} \times I. \quad (13)$$

Equations (11)-(13) are known as the **Signorini type conditions**. In some real cases a gap  $d^{kl}$  between the colliding parts of geological bodies measured along the outward normal are observed.

Further, if both bodies are in contact, then on the contact boundary the Coulombian type of friction acts. The frictional forces  $g_c^{kl}$  acting on the contact boundary  $\Gamma_c^{kl}$  are, in their absolute value, proportional to the normal stress component, where the coefficient of proportionality is the coefficient of Coulombian friction  $\mathcal{F}_c^{kl}(\mathbf{u}_t)$  in displacements and  $\mathcal{F}_c^{kl}(\mathbf{u}_t')$  in velocities, i.e.

$$\begin{aligned} g_c^{kl}(\mathbf{x}, t) &= \mathcal{F}_c^{kl}(\mathbf{u}_t) |\tau_n^{kl}(\mathbf{x}, t)| \quad \text{in displacements,} \\ g_c^{kl}(\mathbf{x}, t) &= \mathcal{F}_c^{kl}(\mathbf{u}_t') |\tau_n^{kl}(\mathbf{x}, t)| \quad \text{in velocities.} \end{aligned} \quad (14)$$

Due to the acting and frictional forces we have the following cases:

If the absolute value of tangential forces  $\tau_t^{kl}$  is less than the frictional forces  $g_c^{kl}$ , then the frictional forces preclude the mutual shifts of both geological bodies being in contact. If the tangential forces  $\tau_t^{kl}$  are equal in their absolute value to the frictional forces, so that are no forces which can preclude the mutual, i.e. bilateral, motion of both geologic bodies. Thus the contact points change their position in the direction opposite to that in



which the tangential stress component acts. These conditions are described by the following conditions:

- a) if  $[u_n]^{kl} = 0$  then  $|\tau_t^{kl}(\mathbf{x}, t)| \leq g_c^{kl}(\mathbf{x}, t)$  in displacements,  
if  $[v_n]^{kl} = 0$  then  $|\tau_t^{kl}(\mathbf{x}, t)| \leq g_c^{kl}(\mathbf{x}, t)$  in velocities,
  - b) if  $|\tau_t^{kl}(\mathbf{x}, t)| < g_c^{kl}(\mathbf{x}, t)$  then  $[\mathbf{u}'_t(\mathbf{x}, t)]^{kl} = 0$ ,  
which means that the friction forces are sufficient to preclude  
the mutual shifting between the assumed bodies and
  - c) if  $|\tau_t^{kl}(\mathbf{x}, t)| = g_c^{kl}$  then there exists a function  $\vartheta \geq 0$  such that  
 $[\mathbf{u}'_t(\mathbf{x}, t)]^{kl} = -\vartheta \tau_t^{kl}(\mathbf{x}, t)$ ,  
which means that the friction forces are not sufficient to preclude  
the mutual-bilateral shifting of both assumed geologic bodies. This  
shift acts in an opposite direction to the acting tangential forces .
- (15)

On the contact boundary between the geological bodies we will assume that the temperatures and heat flow are continuous, i.e.

$$T^k = T^l, \kappa_{ij} \frac{\partial T}{\partial x_j} n_{i|(k)} - \kappa_{ij} \frac{\partial T}{\partial x_j} n_{i|(l)} = \mathcal{F}_c^{kl} |\tau_n| \left| [\mathbf{u}'_t]^{kl} \right| \quad \text{on } \Gamma_c^{kl}. \quad (16)$$

When  $\mathcal{F}_c^{kl} = 0$  then  $g_c^{kl} = 0$  and then  $\tau_t^{kl} = 0$ , and we speak about the case of contact problems without friction. In the case if  $r = 1$ , i.e. if the second body is approximated by an absolutely rigid material and the frictional forces are equal to zero, then Eqs (11),(12),(13) reduce to

$$u_n \leq 0, \quad \tau_n \leq 0, \quad u_n \tau_n = 0. \quad (17)$$

The amplitude of the Coulombian coefficient of friction is not known, but for the existence of a solution it can be estimated (see [31, 23, 17]) for the elastic case and [32, 10, 43, 48]) for thermo-elastic case and in the literature presented here) e.g. for the isotropic and for the anisotropic cases by

$$\|\mathcal{F}_c^{kl}\| < (\mu/(\lambda + 2\mu))^{\frac{1}{4}} \sim (c_s/c_p)^{\frac{1}{2}} \quad \text{or} \quad \|\mathcal{F}_c^{kl}\| < a_0/(2A_0) \quad (18)$$

where  $\lambda$  and  $\mu$  are the Lamé coefficients,  $c_s^2 = \mu\rho^{-1}$ ,  $c_p^2 = (\lambda + 2\mu)\rho^{-1}$  the velocities of  $S$  and  $P$  waves,  $a_0$  and  $A_0$  are constants, the so-called coefficients of ellipticity and upper bound of the Hooke tensor, i.e.  $a_0 \xi_{ij} \xi_{ij} \leq c_{ijkl} \xi_{ij} \xi_{kl} \leq A_0 \xi_{ij} \xi_{ij}$  holds. We see that the coefficient of friction depends on the material properties only.

The problem investigated will be coercive if  $\Gamma_u^\iota \neq \emptyset$  for all  $\iota = 1, \dots, r$  and semi-coercive if at least one part of  $\Gamma_u = \cup_{\iota=1}^r \Gamma_u^\iota$ , say  $\Gamma_u^j$ , is empty. The problem is coupled due to the coupling terms  $\frac{\partial}{\partial x_j}(\beta_{ij}^\iota(T^\iota - T_0^\iota))$  following from Eqs (1b), (3) and  $\rho^\iota \beta_{ij}^\iota T_0^\iota e_{ij}(\mathbf{u}^{\iota'})$  in Eq. (3c). In the case if the term  $\rho^\iota \beta_{ij}^\iota T_0^\iota e_{ij}(\mathbf{u}^{\iota'})$  is omitted, then we speak about the quasi-coupled model problem.

Then we introduce the following contact problems

**(A) Multibody contact problems in (thermo-visco-)elastic rheology with short memory:**

**Problem** ( $\mathcal{P}_{sm}$ ): Let  $N = 2, 3$ ,  $r \geq 2$ . Find a pair of functions  $(T, \mathbf{u}) : \Omega \times I \rightarrow (\mathbb{R} \times \mathbb{R}^N) \times I$ ,  $N = 2, 3$ , satisfying (3) with (1d), (2), (4) and boundary value and contact conditions

$$\begin{aligned} \kappa_{ij} \frac{\partial T(\mathbf{x}, t)}{\partial x_i} n_j &= K(Y(\mathbf{x}, t) - T(\mathbf{x}, t)), \quad \tau_{ij} n_j = P_i, \quad i, j = 1, \dots, N, \\ \text{for } (t, \mathbf{x}) \in \Gamma_\tau(t) &= I \times \cup_{i=1}^r (\Gamma_\tau \cap \partial\Omega^i), \end{aligned} \quad (19)$$

$$\begin{aligned} \kappa_{ij} \frac{\partial T(\mathbf{x}, t)}{\partial x_i} n_j &= K(Y(\mathbf{x}, t) - T(\mathbf{x}, t)) \quad \left( \text{or } \kappa_{ij} \frac{\partial T(\mathbf{x}, t)}{\partial x_i} n_j = q \right), \\ u_i &= u_{2i}, \quad i = 1, \dots, N, \quad \text{for } (t, \mathbf{x}) \in {}^1\Gamma_u(t) = I \times \cup_{i=1}^r ({}^1\Gamma_u \cap \partial\Omega^i), \end{aligned} \quad (20)$$

$$T(\mathbf{x}, t) = T_1(\mathbf{x}, t), \quad u_i = 0, \quad i = 1, \dots, N, \quad \text{on } {}^2\Gamma_u(t) = I \times \cup_{i=1}^r ({}^2\Gamma_u \cap \partial\Omega^i), \quad (21)$$

$$\begin{aligned} \kappa_{ij} \frac{\partial T(\mathbf{x}, t)}{\partial x_i} n_j &= q \quad \left( \text{or } \kappa_{ij} \frac{\partial T(\mathbf{x}, t)}{\partial x_i} n_j = K(Y(\mathbf{x}, t) - T(\mathbf{x}, t)) \right), \\ u_n &= 0, \quad \boldsymbol{\tau}_t = 0 \quad \text{on } \Gamma_0(t) = I \times \cup_{i=1}^r (\Gamma_0 \cap \partial\Omega^i) \end{aligned} \quad (22)$$

$$\left. \begin{aligned} (a) \quad & T^k = T^l, \\ (b) \quad & \left. \begin{aligned} \kappa_{ij} \frac{\partial T}{\partial x_i} n_j|^{(k)} - \kappa_{ij} \frac{\partial T}{\partial x_i} n_j|^{(l)} &= \mathcal{F}_c^{kl} |\tau_n^{kl}| |[\mathbf{u}'_t]^{kl}|, \\ [u_n]^{kl} \leq d^{kl}, \quad \tau_n^k = -\tau_n^l \equiv \tau_n^{kl} \leq 0, \\ ([u_n]^{kl} - d^{kl}) \tau_n^{kl} &= 0, \end{aligned} \right\} \\ (c) \quad & \left. \begin{aligned} [\mathbf{u}'_t]^{kl} = 0 &\implies |\boldsymbol{\tau}_t^{kl}| \leq \mathcal{F}_c^{kl}(0) |\tau_n^{kl}|, \\ [\mathbf{u}'_t]^{kl} \neq 0 &\implies \boldsymbol{\tau}_t^{kl} = -\mathcal{F}_c^{kl}([\mathbf{u}'_t]^{kl}) |\tau_n^{kl}| \frac{[\mathbf{u}'_t]^{kl}}{|[\mathbf{u}'_t]^{kl}|}, \end{aligned} \right\} \end{aligned} \quad (t, \mathbf{x}) \in I \times \cup_{k,l} \Gamma_c^{kl}, \quad (23)$$

$$T(\mathbf{x}, 0) = T_0(\mathbf{x}), \quad \mathbf{u}(\mathbf{x}, 0) = \mathbf{u}_0(\mathbf{x}), \quad \mathbf{u}'(\mathbf{x}, 0) = \mathbf{u}_1(\mathbf{x}), \quad \mathbf{x} \in \Omega, \quad (24)$$

where  $q = q(\mathbf{x}, t)$  is the heat flux,  $K$  the heat transition coefficient,  $Y(\mathbf{x}, t)$  the external temperature,  $T_0(\mathbf{x})$ ,  $T(\mathbf{x}, t)$  the initial and actual temperatures and the term  $\mathcal{F}_c^{kl} |\tau_n^{kl}| |[\mathbf{u}'_t]^{kl}|$  represents the frictional heatings on the contact surfaces  $\Gamma_c^{kl}$ ,  $\mathbf{u}(\mathbf{x}, t)$ ,  $\boldsymbol{\tau}(\mathbf{x}, t)$  are the displacement and the stress vectors,  $u_n$ ,  $\mathbf{u}_t$ ,  $\tau_n$ ,  $\boldsymbol{\tau}_t$  the normal and tangential components of displacement and stress vectors,  $\mathbf{n}$  the outward normal to the boundary  $\partial\Omega$  and where  $\mathbf{u}_0$ ,  $\mathbf{u}_1$ ,  $\mathbf{u}_2$  are given functions,  $\mathbf{u}_2$  has a time derivative  $\mathbf{u}'_2$ , and  $\mathbf{u}_0$ ,  $\mathbf{u}_1$  satisfy static contact problem in linear elasticity with or without Coulombian friction and on  $\cup \Gamma_c^{kl}$  due to the equilibrium of forces  $\tau_{ij}(\mathbf{u}^k) n_j^k = -\tau_{ij}(\mathbf{u}^l) n_j^l$ .

**Remark 1** In the case if the Hooke law is taken in the form (1a) or in the form (1c) or if the thermal field changes only little, thus the thermal part of the problem can be omitted and then we have the multibody contact problems in the elastic rheology or in the visco-elastic rheology with short memory. Next, such type of problems will be also investigated and discussed.

**(B) Multibody contact problems in thermo-visco-elastic rheology with long memory:**

**Problem** ( $\mathcal{P}_{lm}$ ): Find a pair of functions  $(T, \mathbf{u}) : \Omega \times I \rightarrow (\mathbb{R} \times \mathbb{R}^N) \times I$ ,  $N = 2, 3$ , and a stress tensor  $\tau_{ij} : \Omega \times I \rightarrow \mathbb{R}^{N \times N} \times I$  satisfying (3) with (1e), (2), (4) and the boundary value conditions

$$T(\mathbf{x}, t) = T_1(\mathbf{x}, t) (= 0), \quad \tau_{ij} n_j = P_i \quad \text{on } \Gamma_\tau \times I, \quad (25)$$

$$\kappa_{ij} \frac{\partial T(\mathbf{x}, t)}{\partial x_i} n_j = 0, \quad \mathbf{u}(\mathbf{x}, t) = \mathbf{u}_2(\mathbf{x}, t) (= 0) \quad \text{on } \Gamma_u \times I, \quad (26)$$

$$T^k = T^l,$$

$$\kappa_{ij} \frac{\partial T}{\partial x_i} n_{j|(k)} - \kappa_{ij} \frac{\partial T}{\partial x_i} n_{j|(l)} = \mathcal{F}_c^{kl} |\tau_n^{kl}| |[\mathbf{u}_t']^{kl}| (\mathbf{x}, t) \in \cup_{k,l} \Gamma_c^{kl} \times I, \quad (27)$$

and the bilateral contact condition with Coulombian friction on  $\Gamma_c^{kl} \times I$  of the form

$$\left. \begin{aligned} &u_n^k - u_n^l = 0 \quad \text{and} \quad |\tau_t^{kl}| \leq \mathcal{F}_c^{kl} |\tau_n^{kl}| \equiv g_c^{kl}, \\ &\left\{ \begin{array}{l} \text{if } |\tau_t^{kl}| < g_c^{kl} \text{ then } [\mathbf{u}_t']^{kl} = 0, \\ \text{if } |\tau_t^{kl}| = g_c^{kl} \text{ then there exists } \lambda \geq 0 \\ \text{such that } [\mathbf{u}_t']^{kl} = -\lambda \tau_t^{kl}, \end{array} \right\} (\mathbf{x}, t) \in \cup_{k,l} \Gamma_c^{kl} \times I, \end{aligned} \right\} \quad (28)$$

and the initial conditions

$$T(\mathbf{x}, 0) = T_0(\mathbf{x}), \quad \mathbf{u}(\mathbf{x}, 0) = \mathbf{u}_0(\mathbf{x}), \quad \mathbf{u}'(\mathbf{x}, 0) = \mathbf{u}_1(\mathbf{x}), \quad (29)$$

where  $T_0(\mathbf{x})$ ,  $T_1(\mathbf{x}, t)$ ,  $T(\mathbf{x}, t)$  the initial, the given and the actual temperatures,  $\mathbf{u}(\mathbf{x}, t)$ ,  $\tau(\mathbf{x}, t)$  the displacement and the stress vectors,  $\tau_{ij}$  the stress tensor,  $u_n$ ,  $\mathbf{u}_t$ ,  $\tau_n$ ,  $\tau_t$  normal and tangential components of displacement and stress vectors,  $\mathbf{n}$  the outward normal to the boundary  $\partial\Omega$ ,  $\mathbf{u}_1$  and  $\mathbf{u}_2$  the given functions and where  $g_c^{kl}(\mathbf{x}, t)$  is a slip limit.

The coefficient of friction  $\mathcal{F}_c^{kl} \equiv \mathcal{F}_c^{kl}(\mathbf{x}, \mathbf{u}')$  is globally bounded, non-negative and satisfies the Carathéodory property, i.e.  $\mathcal{F}_c^{kl}(\cdot, \mathbf{v})$  is measurable,  $\mathbf{v} \in \mathbb{R}^N$ , and  $\mathcal{F}_c^{kl}(\mathbf{x}, \cdot)$  is continuous for a.e.  $\mathbf{x} \in \Gamma_c^{kl}$ . Moreover, it has a compact support

$$\mathcal{SF}_c \equiv \sup_x \text{p}(\mathcal{F}_c) = \overline{\{(\mathbf{x}, t) \in \Gamma_c(t) = \Gamma_c \times I \mid \exists \mathbf{u}_t' \quad \mathcal{F}_c^{kl}(\mathbf{x}, \mathbf{u}_t') \neq 0\}}, \quad (30)$$

which depends on the space variable  $\mathbf{x}$  and since we model also the difference between the coefficients of friction and of stick as well as slip, it depends also on the tangential displacement rate component  $\mathbf{u}_t'$  (see Fig. 8).

Furthermore, we denote by  $(y)_+ \equiv \max\{y, 0\}$  the positive part of  $y$ . Let us denote by  ${}^a\Gamma_c^{kl} \subset \Gamma_c^{kl}$  the actual contact set, i.e. for which  $[u]^{kl} - d^{kl} = 0$  on  ${}^a\Gamma_c^{kl}$  and  $[u_n]^{kl} - d^{kl} < 0$  on  ${}^c\Gamma_c^{kl} = \Gamma_c^{kl} \setminus {}^a\Gamma_c^{kl}$ , where  $d^{kl}$  is a gap. For the continuous displacement  $\mathbf{u}$  the actual contact zone  ${}^a\Gamma_c^{kl}$  is well-defined and closed subset of  $\cup \Gamma_c^{kl}$ .

Moreover, in our model we will assume that we have a certain information about a behaviour of thermal field in the neighbourhood of the investigated part of the geological system of bodies and that the initial temperature  $T_0(\mathbf{x})$  before deformation is known.

For more details about mathematical problems of (quasi-)static and dynamic contact problems with or without friction in (thermo-) elasticity, visco-elasticity and viscoplasticity, see e.g. [8, 41, 31, 43, 23, 61, 49, 69, 73, 33, 59, 24, 14, 72, 10, 4, 18, 21, 29, 33, 65, 67, 68, 47, 50] and in the references presented here.

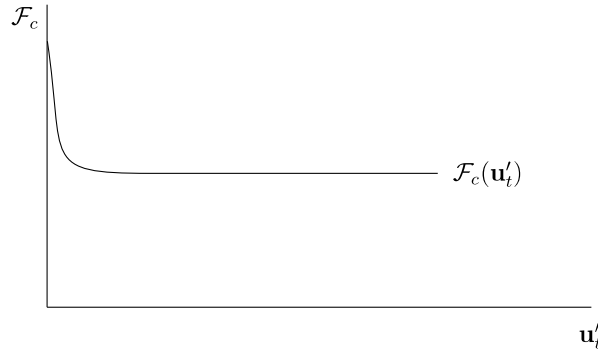


Figure 8. Coefficient of friction as a function of tangential velocity component.

Since all input data, i.e. coefficients of stress-strain laws, coefficients of thermal conductivity, body and surface forces, thermal sources, initial temperature, friction coefficients, density, etc., are in general uncertain, then method of worst scenario can be applied to find the most “dangerous” admissible input data. By uncertain data we mean input data (physical coefficients, right-hand sides, boundary values, friction coefficients, etc.), which cannot be determined uniquely but only in some intervals with errors determined by their measurement errors. The notation reliable solution denotes the worst case among a set of possible solutions of investigated problems, where possibility is given by uncertain input data, and the degree of badness is measured by a criterion-functional. For more details see [25].

### 1.2.2. Models Based on the Multibody Contact Theory in Thermo-visco-plasticity

In the second part of this study we limit ourselves to only small part of the presented project, to analysis of the mathematical model of hydro-mechanical problem of non-stable slopes in connection with bigger flood.

#### Rheology and the constitutive relations:

Let  $\Omega \subset \mathbb{R}^N$ ,  $N = 2, 3$ ,  $\Omega = \cup_{l=1}^r \Omega^l$ , be a union of bounded domains occupied by visco-plastic bodies with a smooth boundary  $\partial\Omega = \Gamma_u \cup \Gamma_\tau \cup \Gamma_0 \cup \Gamma_c$ , where  $\Gamma_u$  represents one part of the boundary, where the velocity is prescribed;  $\Gamma_\tau$  is the part of the boundary, where the loading is prescribed;  $\Gamma_0$  is the part of the boundary, where the symmetry condition or the bilateral contact condition are given and  $\Gamma_c (= \cup_{k,l} \Gamma_c^{kl}, \Gamma_c^{kl} = \partial\Omega^k \cap \partial\Omega^l, k \neq l, k, l \in \{1, \dots, r\})$  represents the contact boundary. Assume the Eulerian coordinate system as a spatial variable system. Any repeated index implies summation from 1 to  $N$ . Let  $t \in I \equiv (0, t_p)$ ,  $t_p > 0$ , where  $t_p$  is the duration of the geological processes. Let  $u_n = \mathbf{u} \cdot \mathbf{n}$ ,  $\mathbf{u}_t = \mathbf{u} - u_n \mathbf{n}$ ,  $\boldsymbol{\tau} = (\tau_{ij} n_j)$ ,  $\tau_n = \tau_{ij} n_j n_i$ ,  $\boldsymbol{\tau}_t = \boldsymbol{\tau} - \tau_n \mathbf{n}$  be the normal and tangential components of the velocity and stress vectors.

The Bingham rheology has the following property: the rock material starts to flow if and only if the applied forces exceed a certain limit, the so-called yield limit. We speak also about Bingham solid/fluid media. We assume that the rocks are incompressible.

Let  $\mathbf{u} = (u_i)$  be the material velocity, let  $D = (D_{ij})$  denote the strain rate tensor and

$D^D = (D_{ij}^D)$  the strain rate deviator defined by

$$D_{ij} = D_{ij}(\mathbf{u}) = \frac{1}{2} \left( \frac{\partial u_i}{\partial x_j} + \frac{\partial u_j}{\partial x_i} \right), \quad D_{ij}^D = D_{ij} - \frac{1}{3} D_{kk} \delta_{ij}, \quad (31)$$

where  $\delta_{ij}$  is the Kronecker symbol. Denote by  ${}^B\tau = ({}^B\tau_{ij})$  the Cauchy stress tensor and its deviator  ${}^B\tau^D = ({}^B\tau_{ij}^D)$  by

$${}^B\tau_{ij}^D = {}^B\tau_{ij} - \frac{1}{3} {}^B\tau_{kk} \delta_{ij} \quad \text{i.e.} \quad {}^B\tau^D = {}^B\tau + pI_3,$$

where  $-p$  denotes the spherical part of the stress tensor and has a meaning of the pressure and  $I_3$  is the identity tensor. Besides the deviators  $D_{ij}^D$  and  ${}^B\tau_{ij}^D$  another tensor deviator  $S^D = (S_{ij}^D)$  can be introduced, which corresponds to the plastic properties of the rock material, where  $S_{ij}^D = \hat{g} D_{ij} D_{II}^{-\frac{1}{2}}$ ,  $D_{II} = \frac{1}{2} D_{ij} D_{ij}$ .

In the rheology by a process we mean a collection of sufficiently smooth functions  $t \rightarrow D_{ij}^D(t)$ ,  $t \rightarrow {}^B\tau_{ij}^D(t)$ ,  $t \rightarrow S_{ij}^D(t)$  for  $t \in [0, t_p]$ , where  $t_p$  is the duration of the rheological process in the medium. In the Bingham rheology for any process we find

$${}^B\tau^D = S^D + 2\hat{\mu} D^D, \quad (32)$$

$$f(S^D) = |S^D|^2 - \hat{g}^2 \leq 0 \quad (33)$$

the so-called Mises relation or the yield condition,

$$D^D = 2\lambda S^D, \quad (34)$$

where  $|S^D| = S_{ij}^D S_{ij}^D$ ,  $\hat{\mu} > 0$  is the threshold of viscosity,  $\hat{g}$  the threshold of plasticity or the yield limit,  $\hat{g}/\sqrt{2}$  is the yield stress in pure shear and  $\lambda$  is a scalar function defined by

$$\text{if } f(S^D) < 0 \quad \text{or} \quad \left( f(S^D) = 0 \quad \text{and} \quad \frac{\partial f(S^D(t))}{\partial t} < 0 \right) \quad \text{then} \quad \lambda(t) = 0,$$

$$\text{if } f(S^D) = 0 \quad \text{and} \quad \frac{\partial f(S^D(t))}{\partial t} = 0 \quad \text{then} \quad \lambda(t) > 0. \quad (35)$$

The Mises relation yields that the invariant  $S_{II} = \frac{1}{2} S_{ij}^D S_{ij}^D = \frac{1}{2} |S^D|^2$  cannot exceed the square of the yield stress in pure shear  $\hat{g}/\sqrt{2}$ . Relations (34) and (35) yield that the deviator of the strain rate tensor can change in the case if  $S_{ij}^D$  rests on the surface  $f(S^D) = 0$ , moving along it. In other cases  $D_{ij}^D = 0$ , which represents the argument why the relation  $|S^D| = \hat{g}$  is called the yield condition.

Moreover, (32) and (34) yield

$${}^B\tau_{ij}^D = (1 + 4\hat{\mu}\lambda) S_{ij}^D, \quad |{}^B\tau^D| = (1 + 4\hat{\mu}\lambda) |S^D|. \quad (36)$$

Let  $|{}^B\tau^D| > \hat{g}$  then from (36b) and (33) we find  $\lambda > 0$  and from (35) we have  $|S^D| = \hat{g}$ . Then (36b) yields

$$\lambda = (4\hat{\mu})^{-1}(|^B\tau^D|\hat{g}^{-1} - 1). \quad (37)$$

Hence and from (34) and (36a) we obtain

$$D_{ij}^D = (2\hat{\mu})^{-1}(1 - \hat{g}|^B\tau^D|^{-1}) ^B\tau_{ij}^D. \quad (38)$$

For incompressible rocks and any duration of the process  $t_p > 0$

$$D_{ij} = (2\hat{\mu})^{-1}(1 - \hat{g}|^B\tau^D|^{-1}) ^B\tau_{ij}^D. \quad (39)$$

Assume that  $|^B\tau^D| \leq \hat{g}$ . Then if  $|S^D| = \hat{g}$  from (36b) we find that  $\lambda = 0$  and if  $|S^D| < \hat{g}$ , then (35) yields also  $\lambda = 0$ . Hence, by using (34) and the incompressibility condition, i.e.  $D_{kk} = 0$ , we have  $D_{ij} = 0$ .

Summarizing, the constitutive law in the Bingham rheology can be written as

$$\begin{aligned} D_{ij} &= (2\hat{\mu})^{-1}(1 - \hat{g}|^B\tau^D|^{-1}) ^B\tau_{ij}^D \quad \text{if } |^B\tau^D| > \hat{g}, \\ D_{ij} &= 0 \quad \text{if } |^B\tau^D| \leq \hat{g}, \end{aligned} \quad (40)$$

where  $\frac{1}{2}|^B\tau^D|^2 = ^B\tau_{II}$ ,  $^B\tau_{II} = \frac{1}{2} ^B\tau_{ij}^D ^B\tau_{ij}^D$  is an invariant of the stress tensor.

In order to invert relations (40) we have: let  $|D| = 0$ , then from (40) we find  $|^B\tau^D| < \hat{g}$ ; if  $|^B\tau^D| \neq 0$  then from (40) we obtain  $|^B\tau^D| > \hat{g}$  and  $|^B\tau^D| = 2\hat{\mu}|D| + \hat{g}$ . Then using the incompressibility condition and (31) from (40) we find

$$^B\tau_{ij} = -p\delta_{ij} + \hat{g}D_{ij}D_{II}^{-1/2} + 2\hat{\mu}D_{ij} = -p\delta_{ij} + 2^{\frac{1}{2}}\hat{g}D_{ij}|D|^{-1} + 2\hat{\mu}D_{ij}, \quad (41)$$

representing the constitutive stress-strain rate relation in the Bingham rheology. For  $\hat{g} = 0$ , we have a classical viscous incompressible (Newtonian) fluid; for small  $\hat{g} > 0$ , we have strongly visco-plastic materials close to the classical viscous fluid and for  $\hat{g} \rightarrow \infty$ , we have absolutely rigid rock materials. If  $\hat{g}$  is strictly positive, we can observe rigid zones inside the flow; when  $\hat{g}$  further increases, these rigid zones become larger and larger and start completely rigid when  $\hat{g}$  is sufficiently large. In this case, when these rigid zones block the flow, we speak about blocking property of the Bingham fluid. From these point of view the Bingham rheology is useful for solidification, recrystallization and melting processes inside the Earth's mantle and in volcanic areas and also for modelling of landslide stability [48, 53, 56].

The thermal stresses are defined by the well-known relation

$$^T\tau_{ij} = -\beta_{ij}(T - T_0), \quad (42)$$

where  $\beta_{ij}$  is the coefficient of thermal expansion,  $T, T_0$  are the actual and initial temperatures.

The stress-strain rate relation in thermo-Bingham rheology is as follows:

$$\tau_{ij} = ^B\tau_{ij} + ^T\tau_{ij}. \quad (43)$$

**Boundary and contact conditions:**

We will assume that the boundary  $\partial\Omega$  is divided into disjoint parts  $\Gamma_u, \Gamma_\tau, \Gamma_0$  and  $\Gamma_c$ , such that  $\partial\Omega = \Gamma_u \cup \Gamma_\tau \cup \Gamma_0 \cup \Gamma_c$ . We will assume that on the part of boundary  $\Gamma_\tau$  the investigated geological body is loaded and the temperature is prescribed  $\tau_{ij}n_j = P_i, T(\mathbf{x}, t) = T_1(\mathbf{x}, t)$ , and on the part of boundary  $\Gamma_u$  we assume that the velocity  $\mathbf{u}_1$  is given and the heat flux is zero, i.e.  $\mathbf{u}(\mathbf{x}, t) = \mathbf{u}_1(\mathbf{x}, t)$  and  $\kappa_{ij} \frac{\partial T(\mathbf{x}, t)}{\partial x_j} n_j = 0$ . On the part of the boundary  $\Gamma_0$ , about it we will assume to be a boundary of symmetry, the heat flux is prescribed so that on  $\Gamma_0$  we have the conditions  $u_n(\mathbf{x}, t) = 0, \tau_t(\mathbf{x}, t) = 0$  and  $\kappa_{ij} \frac{\partial T(\mathbf{x}, t)}{\partial x_j} n_j = q(\mathbf{x}, t)$ . Moreover, about the contact boundary  $\Gamma_c$  we assume that it is a bilateral contact boundary, then the bilateral contact condition in velocities of the type (10) is used.

Thus, we will solve the following problem:

**Problem (P):** Find a pair of functions  $(T, \mathbf{u}) : \Omega \times I \rightarrow (\mathbb{R} \times \mathbb{R}^N) \times I, N = 2, 3$ , temperature  $T$  and velocity vector  $\mathbf{u}$ , and a stress tensor  $\tau_{ij} : \Omega \times I \rightarrow \mathbb{R}^{N \times N} \times I$  satisfying

$$\rho \left( \frac{\partial u_i}{\partial t} + u_k \frac{\partial u_i}{\partial x_k} \right) = \frac{\partial}{\partial x_j} \tau_{ij} + f_i \quad \text{in } \Omega \times I; \quad (44)$$

$$\text{div } \mathbf{u} = 0 \quad \text{in } \Omega \times I; \quad (45)$$

$$\rho c_e \left( \frac{\partial T}{\partial t} + u_k \frac{\partial T}{\partial x_k} \right) - \rho \beta_{ij} T_0 D_{ij}(\mathbf{u}) = \frac{\partial}{\partial x_j} \left( \kappa_{ij} \frac{\partial T}{\partial x_i} \right) + W \quad \text{in } \Omega \times I; \quad (46)$$

$$\tau_{ij} = -p\delta_{ij} + \hat{g} D_{ij} D_{II}^{-1/2} + 2\hat{\mu} D_{ij} - \beta_{ij}(T - T_0); \quad (47)$$

provided  $D_{II} \neq 0, |\tau^D| \leq 2^{\frac{1}{2}} \hat{g}$  if  $D_{II} = 0$ , with the boundary value and contact conditions

$$T(\mathbf{x}, t) = T_1(\mathbf{x}, t), \quad \tau_{ij}n_j = P_i \quad \text{on } \Gamma_\tau \times I, \quad (48)$$

$$\kappa_{ij} \frac{\partial T(\mathbf{x}, t)}{\partial x_j} n_j = 0, \quad \mathbf{u}(\mathbf{x}, t) = \mathbf{u}_1(\mathbf{x}, t) \quad \text{on } \Gamma_u \times I, \quad (49)$$

$$\kappa_{ij} \frac{\partial T(\mathbf{x}, t)}{\partial x_j} n_j = q(\mathbf{x}, t), \quad u_n(\mathbf{x}, t) = 0, \quad \tau_t(\mathbf{x}, t) = 0 \quad \text{on } \Gamma_0 \times I, \quad (50)$$

$$T^k(\mathbf{x}, t) = T^l(\mathbf{x}, t),$$

$$\kappa_{ij} \frac{\partial T(\mathbf{x}, t)}{\partial x_j} n_{j|(k)} - \kappa_{ij} \frac{\partial T(\mathbf{x}, t)}{\partial x_j} n_{j|(l)} = \mathcal{F}_c^{kl} |S^{Dk}| |[\mathbf{u}_t(\mathbf{x}, t)]^{kl}| \quad \text{on } \Gamma_c \times I, \quad (51)$$

and the bilateral contact condition with local friction law of the form

$$[u_n]^{kl} = 0 \quad \text{and} \quad |\tau_t^k| \leq \mathcal{F}_c^{kl} S^{Dk},$$

$$\text{if } |\tau_t^k| < \mathcal{F}_c^{kl} S^{Dk} \quad \text{then } [\mathbf{u}_t]^{kl} = 0,$$

$$\text{if } |\tau_t^k| = \mathcal{F}_c^{kl} S^{Dk} \quad \text{then there exists } \lambda \geq 0 \quad \text{such that} \quad [\mathbf{u}_t]^{kl} = -\lambda \tau_t^k, \quad (52)$$

where  $\mathcal{F}_c^{kl}$  is a coefficient of friction,  $u_n^k = u_i^k n_i^k$ ,  $u_n^l = -u_i^l n_i^l = u_i^l n_i^k$  and  $\tau_n^k = -\tau_n^l \leq 0$ ,  $\tau_t^k = \tau_t^l$

$$T(\mathbf{x}, t_0) = T_0(\mathbf{x}), \quad \mathbf{u}(\mathbf{x}, t_0) = 0. \quad (53)$$

If  $S^D = |\tau_n|$ , then (52) is the classical Coulombian law of friction. Such model problems describe the geodynamical processes in upper parts of the Earth discussed in the previous part of the study. The processes in the landslide zones can also be described by a local visco-plastic friction law. If we set  $S^D = |B\tau^D|$  and if we determine  $|B\tau^D|$  from (41) we obtain  $|B\tau^D| = \hat{g} + 2\hat{\mu}|D(\mathbf{u})|$ . Then the contact condition (52) depends on the solution of the investigated problem.

### 1.2.3. Preliminaries and Notations

Let  $\Omega = \cup_{i=1}^r \Omega^i \subset \mathbb{R}^N$ ,  $N = 2, 3$ , be an open bounded subset in Euclidean space  $\mathbb{R}^N$ ,  $N = 2, 3$ , with a sufficiently smooth boundary  $\partial\Omega = \cup_r \Gamma_r$  ( $\in C^{1,1}$ ),  $r = \tau, u, c$ , whose generic point is denoted by  $\mathbf{x} = (x_i)$ ,  $i = 1, \dots, N$ . Let  $I = (0, t_p)$  be the time interval.

As usual we define the Hilbert spaces  $L^2(M)$ ,  $L^{2,N}(M) = [L^2(M)]^N$ ,  $M = \Omega$  or  $\Gamma_r$ ,  $r = u, \tau, c$ ,  $N = 2, 3$ , as the spaces of all square integrable functions endowed with the inner product  $(u, v) = \int_M u(\mathbf{x})v(\mathbf{x})dM$  such that  $\|u\|_{L^2(M)} = (\int_M |u(\mathbf{x})|^2 dM)^{\frac{1}{2}} < \infty$ . We introduce the space  $C_0^\infty(\Omega)$  as a space of all functions in  $C^\infty(\Omega)$  with a compact support in  $\Omega^i$ ,  $i = 1, \dots, r$ . The space is equipped with the ordinary countable system of seminorms and as usual  $C_0^\infty(\Omega, \mathbb{R}^N) = [C_0^\infty(\Omega)]^N$ . We introduce the space  $L^p(\Omega)$ ,  $1 \leq p \leq \infty$ , as the space of all measurable functions such that  $\|u\|_{L^p(\Omega)} = n(\int_\Omega |u(\mathbf{x})|^p d\mathbf{x})^{1/p} < +\infty$ . By  $L^\infty(M)$  we denote the set of all measurable functions  $u$  defined almost everywhere on  $M$ , such that  $\|u\|_{L^\infty(M)} = \|u\|_\infty = \text{ess sup}_M |u(\mathbf{x})|$  are finite.

We denote by  $W^{k,2}(M)$ ,  $M = \Omega$  or  $\Gamma_r$ , the Sobolev space of  $L^2(M)$ -functions having the derivatives in all directions of the order  $k$  such that these derivatives belong to  $L^2(M)$ . We also write  $W^{k,2}(M) \equiv H^k(M)$  and we define  $[H^k(M)]^N \equiv H^{k,N}(M)$ ,  $H^{0,N}(M) = L^{2,N}(M)$ , the corresponding norm is denoted by  $\|\cdot\|_{k,N}$  and the scalar product and the dual pairing are denoted by  $(\cdot, \cdot)_{k,M}$  and  $\langle \cdot, \cdot \rangle_{k,M}$  (for each integer  $N$ ). The duals of the spaces will be marked by using the symbol “'”. The dual space of  $H^{k,N}(M)$  we denote by  $(H^{k,N}(M))' = H^{-k,N}(M)$  and the corresponding norms by  $\|\cdot\|_{H^{-k,N}(M)} \equiv \|\cdot\|_{-k,N}$ . It is known, that values on  $\Gamma_r$  for a function in  $H^1(\Omega)$  can be interpreted as the values of its  $H^{\frac{1}{2}}(\Gamma_r)$  image through the linear, continuous trace mapping. The norm on the topological dual space  $H^{-\frac{1}{2}}(\Gamma_r)$  is defined by  $\|u\|_{H^{-\frac{1}{2}}(\Gamma_r)} = \sup_{v \in H^{\frac{1}{2}}(\Gamma_r)} \frac{\langle u, v \rangle_{-1/2, 1/2, \Gamma_r}}{\|v\|_{H^{1/2}(\Gamma_r)}}$ , where  $\langle \cdot, \cdot \rangle_{-1/2, 1/2, \Gamma_r}$  denotes the dual pairing between  $H^{-\frac{1}{2}}(\Gamma_r)$  and  $H^{\frac{1}{2}}(\Gamma_r)$ . For  $\rho \neq 1$ ,  $\alpha \neq 1$ , but  $\rho, \alpha \in L^\infty(M)$  with  $\rho \geq \rho_0 > 0$ ,  $\alpha \geq \alpha_0 > 0$  a.e.  $\mathbf{x} \in M$ , by  $(\cdot, \cdot)_{k,M}$  we also denote the inner product in weighted spaces  $L^{2,N}(M)$  and by  $\|\cdot\|_{k,M}$  the corresponding norms.

Furthermore, we introduce the Bochner spaces  $L^2(I; X)$ ,  $W^{k,2}(I; X)$ ,  $X$  being Hilbert spaces, by the usual way (see [1, 10]). The space  $L^2(I; X)$  is the space of all measurable functions  $v : I \rightarrow X$  such that  $\int_I \|v(t)\|_X^2 dt < \infty$ , and its norm is defined by  $\|v(t)\|_{L^2(I; X)} = (\int_I \|v(t)\|_X^2 dt)^{\frac{1}{2}}$ . The space  $W^{k,2}(I; X)$ ,  $k \in \mathbb{N}$ , is defined as  $W^{k,2}(I; X) = \{v \in L^2(I; X) | \|v^{(j)}\|_{L^2(I; X)} < \infty \forall j \leq k\}$  and its norm by



$\|v\|_{W^{k,2}(I;X)} = \left( \int_I \sum_{0 \leq j \leq k} \|v^{(j)}\|_{L^2(I;X)}^2 dt \right)^{\frac{1}{2}}$  and for  $W^{k,\infty}(I;X)$  by  $\|v\|_{W^{k,\infty}(I;X)} = \max_{0 \leq j \leq k} \operatorname{ess\,sup}_{t \in I} \|v^{(j)}\|_X$ .

The space  $B(I;X)$ ,  $X$  being a Banach space, is the space of all continuous and bounded functions from  $I$  into  $X$  with the sup-norm  $\|v\|_{B(I;X)} = \|v\|_{L^\infty(I;X)} = \sup_{t \in I} \|u(t)\|_X$ .

The Sobolev space of fractional order  $k$ ,  $k > 0$  non-integer (the so-called Sobolev-Slobodetskii space, see e.g [40, 1]), where  $k = [k] + \lambda$ ,  $0 < \lambda < 1$ ,  $[k]$  denotes the integer part of  $k$  and  $\lambda$  the rest, is then defined by the usual way, the norm is defined by

$$\|u\|_{W^{k,2}(\Omega)}^2 = \|u\|_{W^{[k],2}(\Omega)}^2 + \sum_{|\alpha|=[k]} \int_{\Omega} \int_{\Omega} \frac{|D^\alpha u(\mathbf{x}) - D^\alpha u(\mathbf{y})|^2}{|\mathbf{x} - \mathbf{y}|^{N+2\lambda}} d\mathbf{x} d\mathbf{y}.$$

If  $\mathbf{k} = (k_1, \dots, k_N)$ ,  $k_i > 0$  and  $k_i = [k_i] + \lambda_i$ ,  $0 \leq \lambda_i < 1$ ,  $i = 1, \dots, N$ , then we speak about anisotropic spaces. If  $\mathbf{k} = (k_1, k_2)$  then the first component defines the smoothness with respect to the time variable and the second one the regularity with respect to the space variables.

If  $\Omega = \cup_{\ell=1}^r \Omega^\ell$ , where  $\Omega^\ell$ ,  $\ell = 1, \dots, r$ , are assumed domains with sufficiently smooth boundaries  $\partial\Omega^\ell$ , then we can introduce the trace space  $H^{\frac{1}{2},N}(\cup_{k,l} \Gamma_c^{kl})$ , being the trace space of Hilbert space  $V$  restricted to  $\cup_{k,l} \Gamma_c^{kl}$ , where  $\Gamma_c^{kl}$  is a contact boundary between neighbouring domains  $\Omega^k$  and  $\Omega^l$ , and its dual is denoted as  $H^{-\frac{1}{2},N}(\cup_{k,l} \Gamma_c^{kl})$ . In the case if  $\bar{\Gamma}_c^k = \partial\Omega^k \cap (\Gamma_u \cup \partial\Omega^k)$  (where  $\Gamma_u$  is a part of the boundary  $\partial\Omega$  with Dirichlet condition), we introduce the space  $H_{00}^{\frac{1}{2},N}(\Gamma_c^{kl})$ , where  $H_{00}^{\frac{1}{2},N}(\Gamma_c^{kl})$  is the Hilbertian interpolation space between  $L^{2,N}(\Gamma_c^{kl})$  and  $H_0^{1,N}(\Gamma_c^{kl})$ . Its dual is denoted by  $H_{00}^{-\frac{1}{2},N}(\Gamma_c^{kl}) = (H_{00}^{\frac{1}{2},N}(\Gamma_c^{kl}))'$  and  $H_{00}^{\frac{1}{2},N}(\Gamma_c^{kl})$  is a proper and continuously embedded subspace of  $H^{\frac{1}{2},N}(\Gamma_c^{kl})$  (see [39]), and is assigned with the norm

$$\|\mathbf{z}\|_{H_{00}^{\frac{1}{2},N}(\Gamma_c^{kl})} = \left( \|\mathbf{z}\|_{H^{\frac{1}{2},N}(\Gamma_c^{kl})}^2 + \int_{\Gamma_c^{kl}} \frac{\mathbf{z}^2(\mathbf{x}t)}{\rho(\mathbf{x})} ds \right)^{\frac{1}{2}},$$

where  $\rho$  is the distance to extreme points of  $\Gamma_c^{kl}$ .

Let us denote by  $H^{\gamma,1,1,N}(I \times \Omega)$ ,  $0 < \gamma < 1$ , the anisotropic Sobolev space corresponding to time-space-continuum space  $I \times \Omega$  ( $\Omega - \dim N$ ) with the norm

$$\|v\|_{\gamma,1,1,Q}^2 = \|v\|_{L^2(Q)}^2 + \sum_{i=1}^N \left\| \frac{\partial v}{\partial x_i} \right\|_{L^2(Q)}^2 + \int_{\mathbb{R}} \int_{\mathbb{R}} \frac{\|v(t_1, \cdot) - v(t_2, \cdot)\|_{0,N}^2}{|t_1 - t_2|^{1+2\gamma}} dt_2 dt_1,$$

where we denote by  $L^2(Q) = L^2(I \times \Omega) = L^2(I; L^2(\Omega))$ . For  $\gamma, \beta \geq 0$  and an interval  $I$ , we introduce the notation  $H^{\gamma,\beta}(I \times M) = H^\gamma(I; L^2(M)) \cap L^2(I; H^\beta(M))$ .

## 2. The Model Based on the Contact Problem with Given Friction in Thermo-Elasticity: Static Case

### 2.1. Introduction

Geomechanics belongs to the numerous fields where mathematical simulation and mathematical modelling are broadly applied and where strong demands appear for efficient

methods and algorithms. Moreover, there are strong requirements concerning reliability of the input material data and of the computed numerical results. This means a control of the discretization error arising from the use of the numerical analysis and an assesment of the errors caused by inexact input data for material parameters, material distribution, boundary conditions and initial stress data. The stress-strain analysis can be based on the theory of contact problems in linear (thermo-)elasticity, (thermo-)visco-elasticity or the other rheologies.

In this part we will deal with the solvability of a generalized static semi-coercive contact problem in linear thermo-elasticity, describing the system of geological bodies being in mutual contacts. The present problem studied will be formulated as a primary variational inequality problem, i.e., in term of displacements, arising from the variational formulation of the contact problem with friction in linear thermo-elasticity. We will assume the generalized case of bodies of arbitrary shapes which are in mutual contacts. On one part of the boundary, the system of geological bodies are loaded and on the second one they are fixed and therefore, as a result, some of the bodies can also shift and rotate.

## 2.2. Models Based on the Contact Problem with Given Friction (The so-called Tresca Model) in Thermo-elasticity

### 2.2.1. Formulation of the Problem

Let  $\Omega = \cup_{\iota=1}^r \Omega^\iota \subset \mathbb{R}^N$ ,  $N = 2, 3$ , be a union of domains with Lipschitz boundaries  $\partial\Omega$ , occupied by geological bodies about which we assume to be elastic and of arbitrary shapes. Let the boundary  $\partial\Omega$  consist of parts  $\Gamma_\tau, \Gamma_u, \Gamma_c, \Gamma_0$ ,  $\partial\Omega = \Gamma_\tau \cup \Gamma_u \cup \Gamma_c \cup \Gamma_0$ , where  $\Gamma_c = \cup_{k,l} \Gamma_c^{kl}$  represents the boundary between geological bodies being in contact (Fig. 9). Moreover, we denote the temperature by  $T$ , the displacement vector by  $\mathbf{u} = (u_1, \dots, u_N)$ . Let  $W$  be the thermal sources,  $\mathbf{F}$  be the body forces,  $\mathbf{P}$  be the surface loads,  $\mathbf{u}_0$  the given displacement vector on  $\Gamma_u$ ,  $T_0, T_1$  the initial (in  $\Omega$ ) and the given (on  ${}^2\Gamma_u$ ) temperatures,  $q$  the heat flow,  $g_c^{kl}$  the given slip limits. Next, the landslide model can be described by the following problem:

**Problem (P):** Find a pair of function  $(T, \mathbf{u})$ , a scalar function  $T$  and a vector function  $\mathbf{u}$ , satisfying

$$\frac{\partial}{\partial x_i} \left( \kappa_{ij}^\iota \frac{\partial T^\iota}{\partial x_j} \right) + W^\iota + \rho^\iota \beta_{ij}^\iota T_0^\iota e_{ij}(\mathbf{u}^\iota) = 0, \quad \frac{\partial \tau_{ij}(\mathbf{u}^\iota)}{\partial x_j} + F_i^\iota = 0, \\ i, j = 1, \dots, N, \quad \iota = 1, \dots, r, \quad \text{in } \Omega^\iota, \quad (54)$$

$$\tau_{ij}^\iota = c_{ijkl}^\iota e_{kl}(\mathbf{u}^\iota) - \beta_{ij}^\iota (T^\iota - T_0^\iota), \quad i, j, k, l = 1, \dots, N, \quad \iota = 1, \dots, r, \quad (55)$$

$$\kappa_{ij} \frac{\partial T}{\partial x_i} n_i = q (= 0), \quad \tau_{ij} n_j = P_i, \quad i, j = 1, \dots, N \quad \text{on } \Gamma_\tau, \quad (56)$$

$$\kappa_{ij} \frac{\partial T}{\partial x_i} n_i = q (= 0), \quad u_i = {}^1u_{0i} (= 0), \quad i, j = 1, \dots, N \quad \text{on } {}^1\Gamma_u, \quad (57)$$

$$T = T_1 (= 0), \quad u_i = {}^2u_{0i} (\neq 0), \quad i = 1, \dots, N \quad \text{on } {}^2\Gamma_u, \quad (58)$$

$$T^k = T^l, \quad \kappa_{ij} \frac{\partial T}{\partial x_i} n_{i|(k)} - \kappa_{ij} \frac{\partial T}{\partial x_i} n_{i|(l)} = g_c^{kl} |[\mathbf{u}_t]^{kl}|, \quad i, j = 1, \dots, N \quad \text{on } \Gamma_c^{kl}, \quad (59)$$

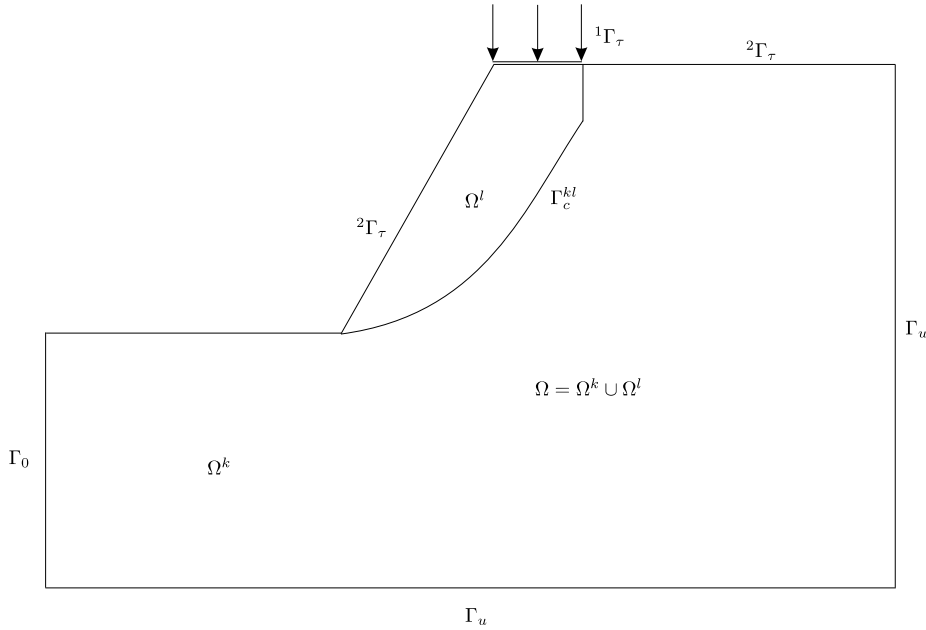


Figure 9. The model of the statically loaded landslide.

$$\begin{aligned}
 & [u_n]^{kl} \leq 0 \text{ (or } d^{kl}), \quad \tau_n^k = -\tau_n^l \equiv \tau_n^{kl} \leq 0, \\
 & [u_n]^{kl} \tau_n^{kl} = 0, \quad (\text{or } ([u_n]^{kl} - d^{kl}) \tau_n^{kl} = 0) \\
 & \text{if } [u_n]^{kl} = 0 \text{ (or } d^{kl}) \text{ then } |\tau_t^{kl}| \leq g_c^{kl}, \\
 & \text{if } |\tau_t^{kl}| < g_c^{kl} \text{ then } [\mathbf{u}_t]_t^{kl} = 0, \quad \text{on } \Gamma_c^{kl} \\
 & \text{if } |\tau_t^{kl}| = g_c^{kl} \text{ then there exists a function } \vartheta \geq 0 \text{ such} \\
 & \quad \text{that } [\mathbf{u}_t]^{kl} = -\vartheta \boldsymbol{\tau}_t^{kl}(\mathbf{x}),
 \end{aligned} \tag{60}$$

where  $d^{kl}$  denotes a gap between both neighbouring geological bodies, and moreover,

$$u_n = 0, \quad \tau_{tj} = 0, \quad j = 1, \dots, N \quad \text{on } \Gamma_0, \tag{61}$$

where the last condition represents the bilateral contact condition without friction, and it can be suitable for numerical computation as it represents the condition of symmetry. As we see above the problem is coupled due to the coupling terms  $\frac{\partial}{\partial x_j}(\beta_{ij}^\iota(T^\iota - T_0^\iota))$  following from Eqs (54), (55) and  $\rho^\iota \beta_{ij}^\iota T_0^\iota e_{ij}(\mathbf{u}^\iota)$  in Eq. (54a) and is quasi-coupled if the term  $\rho^\iota \beta_{ij}^\iota T_0^\iota e_{ij}(\mathbf{u}^\iota)$  in Eq. (54a) is neglected. The problem is coercive if all  ${}^j\Gamma_u^\iota \neq \emptyset$  and semi-coercive for  $\Gamma_u = \emptyset$  or if at least one part of  $\Gamma_u = \cup_{j=1}^2 \cup_{\iota=1}^r {}^j\Gamma_u^\iota$ , say  ${}^2\Gamma_u^m$ , is empty.

**Definition 1** A pair of functions  $(T^\iota, \mathbf{u}^\iota)$ ,  $\iota = 1, \dots, r$ , is called a classical solution of the problem  $(\mathcal{P})$ , if  $T^\iota \in C^2(\Omega^\iota) \cap C^1(\Omega^\iota)$ ,  $\mathbf{u}^\iota \in [C^2(\Omega^\iota)]^N \cap [C^1(\Omega^\iota)]^N$  and satisfy Eqs (54), (55) in every point of  $\Omega$ , boundary conditions (56)-(58) in every point of  $\Gamma_\tau$  or  ${}^1\Gamma_u$  or  ${}^2\Gamma_u$ , respectively, contact conditions and conditions of the Coulombian law of friction (59)-(60) on  $\cup_{k,l} \Gamma_c^{kl}$  and conditions (61) on  $\Gamma_0$ .

### 2.2.2. Variational (Weak) Solution of the Problem

In the following we will consider the  $N$ -dimensional (semi-)coercive case with the unilateral contact conditions (60) on  $\cup_{k,l} \Gamma_c^{kl}$ ,  $k \neq l$  and with bilateral contact conditions (61) on  $\Gamma_0$ .

Let  $\Omega \subset \mathbb{R}^N$ ,  $N = 2, 3$  be a union of domains, occupied by a body, with a Lipschitz boundaries  $\partial\Omega^\ell$ , consisting of four parts  $\Gamma_\tau$ ,  $\Gamma_u$ ,  $\Gamma_0$ ,  $\Gamma_c$ ,  $\partial\Omega = \Gamma_\tau \cup \Gamma_u \cup \Gamma_0 \cup \Gamma_c$ , all defined above. Let  $\mathbf{x} = (x_i)$ ,  $i = 1, \dots, N$ , be the Cartesian co-ordinates and let  $\mathbf{n} = (n_i)$ ,  $\mathbf{t} = (t_i)$  be the outward normal and tangential vectors to  $\partial\Omega$ . Let us look for the temperature  $T \in H^1(\Omega)$  and the displacement vector  $\mathbf{u} = (u_i) \in \mathbf{W}(\Omega) = [H^1(\Omega)]^N$ , where  $H^1(\Omega)$  is the Sobolev space in the usual sense. Let  $e_{ij}(\mathbf{u})$ ,  $\tau_{ij}(\mathbf{u})$  be the small strain tensor and the stress tensor, respectively,  $T_0 = T_0(\mathbf{x})$  the initial temperature at which the bodies are in an initial strain and stress state,  $\beta_{ij}^\ell(\mathbf{x}) \in C^1(\overline{\Omega}^\ell)$  the coefficient of thermal expansion, satisfying (2e) and  $\rho^\ell = \rho^\ell(\mathbf{x}) \in C(\overline{\Omega}^\ell)$  the density. Let  $W \in L^2(\Omega)$ ,  $F_i \in L^2(\Omega)$  be the heat sources and components of the body forces and  $c_{ijkl}^\ell, \kappa_{ij}^\ell \in C^1(\overline{\Omega}^\ell)$  the coefficients of elasticity and of heat conductivity, respectively, satisfying the usual symmetry conditions and the usual ellipticity and continuity conditions, i.e. Eqs (2) and (4). Let  $g_c^{kl} \in L^2(\Gamma_c^{kl})$ ,  $g_c^{kl} \geq 0$  a.e. on  $\Gamma_c^{kl}$ , be the given slip limits.

Since the problem  $(\mathcal{P})$  is static the dissipative term  $\rho^\ell \beta_{ij}^\ell T_0^\ell e_{ij}(\mathbf{u}'')$  can be omitted, so that we will investigate the quasi-coupled problem. We will assume that (we adopt the same notation)  $F_i^\ell = F_i^\ell - \frac{\partial}{\partial x_j}(\beta_{ij}^\ell(T^\ell - T_0^\ell)) \in L^2(\Omega^\ell)$ ,  $W^\ell \in L^2(\Omega^\ell)$   $q \in L^2(\Gamma_\tau \cup {}^1\Gamma_u)$  is the heat flow,  $P_i \in L^2(\Gamma_\tau)$  (or  $H^{-1/2}(\Gamma_\tau)$ ),  $u_{0i} \in H^{\frac{1}{2}}(\Gamma_u)$ ,  $T_1 \in L^2(\Gamma_\tau)$ ,  $T_0 \in H^1(\Omega)$ . Let us denote by  $(\cdot, \cdot)$  the scalar product in  $[L^2(\Omega)]^N$ , by  $\langle \cdot, \cdot \rangle$  the scalar product in  $[L^2(\Gamma_c)]^N$ , by  $\|\cdot\|_k$  the norm in  $[H^k(\Omega)]^N$ ,  $k$  being an integer, where  $H^k(\Omega)$  denotes the Sobolev space in the usual sense. Let us denote by

$$\begin{aligned} {}^1V_0 &= \{z | z \in {}^1W \equiv H^1(\Omega^1) \times \dots \times H^1(\Omega^r), z = 0 \text{ on } {}^2\Gamma_u\}, \\ {}^1V &= \{z | z \in {}^1W, z = T_1 \text{ on } {}^2\Gamma_u\}, \\ V_0 &= \{\mathbf{v} | \mathbf{v} \in \mathbf{W} \equiv [H^1(\Omega^1)]^N \times \dots \times [H^1(\Omega^r)]^N, \mathbf{v} = \mathbf{0} \text{ on } \\ &\quad {}^1\Gamma_u \cup {}^2\Gamma_u, v_n = 0 \text{ on } \Gamma_0\}, \\ V &= \{\mathbf{v} | \mathbf{v} \in \mathbf{W}, \mathbf{v} = \mathbf{u}_0 \text{ on } {}^1\Gamma_u \cup {}^2\Gamma_u, v_n = 0 \text{ on } \Gamma_0\}, \end{aligned}$$

the spaces and sets of virtual temperatures and virtual displacements, resp.,

$$K = \{\mathbf{v} | \mathbf{v} \in V, [u_n]^{kl} \leq 0 \text{ (or } d^{kl}) \text{ on } \cup_{k,l} \Gamma_c^{kl}\},$$

the set of all admissible displacements, which for  $\mathbf{u}_0 = 0$  is a convex cone with vertex at the origin.

As our quasi-coupled problem investigated is indeed not coupled, then both the problems in thermics and elasticity can be solved separately (see [43]) and the additional term  $\frac{\partial}{\partial x_j}(\beta_{ij}^\ell(T^\ell - T_0^\ell))$  has a meaning of body forces. Since we assume that  $\beta_{ij}^\ell \in C^1(\overline{\Omega}^\ell)$ ,  $T^\ell, T_0^\ell \in H^1(\Omega^\ell)$ , then  $\beta_{ij}^\ell(T^\ell - T_0^\ell) \in H^1(\Omega^\ell)$  and therefore  $\frac{\partial}{\partial x_j}(\beta_{ij}^\ell(T^\ell - T_0^\ell)) \in L^2(\Omega^\ell)$ .

**Definition 2** By a variational (weak) solution of the problem  $(\mathcal{P})$  we mean a pair of functions  $(T, \mathbf{u})$ ,  $T \in {}^1V$ ,  $\mathbf{u} \in K$ , such that

$$b(T, z - T) \geq s(z - T) \quad \forall z \in {}^1V, \quad (62)$$

$$a(\mathbf{u}, \mathbf{v} - \mathbf{u}) + \left\langle g_c^{kl}, \left| [\mathbf{v}_t]^{kl} \right| - \left| [\mathbf{u}_t]^{kl} \right| \right\rangle \geq S(\mathbf{v} - \mathbf{u}) \quad \forall \mathbf{v} \in K, \quad (63)$$

where for  $T, z \in H^1(\Omega)$ ,  $\mathbf{u}, \mathbf{v} \in \mathbf{W}$  we put

$$\begin{aligned} b(T, z) &= \sum_{\iota=1}^r b^\iota(T^\iota, z^\iota) = \int_{\Omega} \kappa_{ij} \frac{\partial T}{\partial x_j} \frac{\partial z}{\partial x_i} d\mathbf{x}, \\ s(z) &= \sum_{\iota=1}^r s^\iota(z^\iota) = \int_{\Omega} W z d\mathbf{x} + \int_{\Gamma_\tau \cup {}^1\Gamma_u} q z ds + \int_{\cup \Gamma_c^{kl}} g_c^{kl} |[\mathbf{u}_t]^{kl}| z ds, \\ a(\mathbf{u}, \mathbf{v}) &= \sum_{\iota=1}^r a(\mathbf{u}, \mathbf{v}) = \int_{\Omega} c_{ijkl} e_{ij}(\mathbf{u}) e_{kl}(\mathbf{v}) d\mathbf{x}, \\ S(\mathbf{v}) &= \sum_{\iota=1}^r S^\iota(\mathbf{v}^\iota) = \int_{\Omega} F_i v_i d\mathbf{x} + \int_{\Gamma_\tau} P_i v_i ds, \\ j_{gn}(\mathbf{v}) &= \int_{\cup_{k,l} \Gamma_c^{kl}} g_c^{kl} |[\mathbf{v}_t]^{kl}| ds = \langle g_c^{kl}, |[\mathbf{v}_t]^{kl}| \rangle. \end{aligned}$$

The problem (62)-(63) is equivalent to the following variational formulation:

Find a pair of functions  $(T, \mathbf{u})$ ,  $T \in {}^1V$ ,  $\mathbf{u} \in K$ , such that

$$l(T) \leq l(z) \quad \forall z \in {}^1V, \quad (64)$$

$$L(\mathbf{u}) \leq L(\mathbf{v}) \quad \forall \mathbf{v} \in K, \quad (65)$$

where  $l(z)$ ,  $L(\mathbf{v})$  are defined by

$$\begin{aligned} l(z) &= \frac{1}{2} b(z, z) - s(z), \\ L(\mathbf{v}) &= L_0(\mathbf{v}) + j_{gn}(\mathbf{v}), \quad L_0(\mathbf{v}) = \frac{1}{2} a(\mathbf{v}, \mathbf{v}) - S(\mathbf{v}). \end{aligned}$$

**Remark 2** The problem with the non-homogeneous boundary conditions (Dirichlet) can be transformed to one with homogeneous boundary conditions. In the equations (54) let us replace  $T$  by  $T + z$   $\mathbf{u}$  by  $\mathbf{u} + \mathbf{w}$ , where  $z$  is a sufficiently smooth scalar function in  $\overline{\Omega}$  satisfying (58) and  $\mathbf{w}$  is a sufficiently smooth vector function in  $\overline{\Omega}$  satisfying (57), (58) and  $\mathbf{w} = \mathbf{0}$  on  $\cup \Gamma_c^{kl}$ . Then due to this transformation we have the equivalent problem with the homogeneous boundary conditions, where (the same notations are used)  $W^\iota = W^\iota + \frac{\partial}{\partial x_i} \left( \kappa_{ij}^\iota \frac{\partial z^\iota}{\partial x_j} \right)$ ,  $F_i^\iota = F_i^\iota - \frac{\partial}{\partial x_j} (\beta_{ij}^\iota (T^\iota - T_0^\iota)) + \frac{\partial}{\partial x_j} (c_{ijkl}^\iota e_{kl}(\mathbf{w}^\iota))$ ,  $P_i = P_i - c_{ijkl} e_{kl}(\mathbf{w}) n_j$ , etc.

As the set  $K$  is a nonempty, closed and convex subset of  $V_0$ , the functional  $L_0(\mathbf{v})$  is (similarly as in [42]) convex and differentiable, the functional  $j_{gn}(\mathbf{v})$  is convex and non-differentiable, then due to [5], (62)-(63) and (64)-(65) are equivalent.

It can be proved that any classical solution of the problem  $(\mathcal{P})$  is a weak solution and conversely, if the weak solution is smooth enough, it represents a classical solution.

The next theorem gives the existence and uniqueness of the weak solution of the coercive problem investigated and an estimate of it. The theorem states that there exists a

unique solution and that the problem is well-posed. By the well-posedness we will mean the existence, uniqueness, and continuous dependence of the solution on the given data  $(T_0, T_1, W, q, \mathbf{u}_0, \mathbf{F}, \mathbf{P})$ . From the physical point of view, it reflects the fact that the solution only changes a little for little changes in the displacements and surface body forces and temperatures.

**Theorem 1** *Let (2), (4) hold. Let  $W^\iota \in L^2(\Omega^\iota)$ ,  $q \in L^2(\Gamma_\tau)$ ,  $F_i^\iota \in L^2(\Omega^\iota)$ ,  $P_i \in L^2(\Gamma_\tau)$ ,  $u_{0i} \in H^{\frac{1}{2}}(\Gamma_u)$ ,  $T_1 \in L^2(\Gamma_u)$ ,  $T_0 \in H^1(\Omega)$ ,  $g_c^{kl} \in L^2(\Gamma_c^{kl})$  then there exists one weak solution of the problem with or without friction (62)-(63). Furthermore, there exist constants  $c_0, c_1$  independent of  $g_c^{kl}$  such that*

$$\begin{aligned} \|T\|_1 &\leq c_0(\|q\|_{L^2(\Gamma_\tau \cup \Gamma_u)} + \|W\|_{L^2(\Omega)} + \|T_1\|_{L^2(\Gamma_u)} + \|T_0\|_1), \\ \|\mathbf{u}\|_1 &\leq c_1(\|\mathbf{P}\|_{L^{2,N}(\Gamma_\tau)} + \|\mathbf{F}\|_{L^{2,N}(\Omega)} + \|\mathbf{u}_0\|_1) \end{aligned}$$

The proof is similar of that of [42, 43, 48].

To prove the existence and uniqueness of the variational (weak) solution for the semi-coercive case we introduce the set of all rigid displacements and rotations

$$P = \cup_{\iota=1}^r P^\iota, \quad P^\iota = \{\mathbf{v}^\iota | \mathbf{v}^\iota = \mathbf{a} + b \times \mathbf{x}\},$$

where  $a_i^\iota \in \mathbb{R}^1$ ,  $b^\iota \in \mathbb{R}^1$ ,  $i = 1, \dots, N$ ,  $\iota = 1, \dots, r$ , are arbitrary and the set of bilateral admissible rigid displacements

$$\begin{aligned} P_0 &= \{\mathbf{v} \in K \cap P | \mathbf{v} \in P_0 \Rightarrow -\mathbf{v} \in P_0\} = \\ &= \{\mathbf{v} \in P_V = P \cap V | [v_n]^{kl} = 0 \text{ on } \cup_{k,l} \Gamma_c^{kl}\}. \end{aligned}$$

**Lemma 1** *Let  $\Omega^\iota \subset \mathbb{R}^N$ ,  $\mathbf{u}^\iota \in [H^1(\Omega^\iota)]^N$ ,  $\iota = 1, \dots, r$ . Then*

$$e_{ij}(\mathbf{u}^\iota) = 0, \quad \forall i, j = 1, \dots, N \iff \mathbf{u}^\iota = \mathbf{a}^\iota + (b^\iota \times \mathbf{x}), \quad (66)$$

where  $\mathbf{a}^\iota$  is a vector and  $b^\iota$  is a real constant.

**Lemma 2** *Let  $\Gamma_u \neq \emptyset$ . Then*

$$P_V \equiv P \cap V_0 = \{0\},$$

i.e. only the zero function lies in the intersection  $P \cap V_0$ .

For the proof see [41].

**Lemma 3** *Since  $e_{ij}(\mathbf{v}) = 0 \forall \mathbf{v} \in P$ ,  $\forall i, j$ , then*

$$a(\mathbf{u}, \mathbf{v}) = 0 \quad \forall \mathbf{v} \in P. \quad (67)$$

Moreover, if  $\mathbf{w} \in \mathbf{W}$ ,  $e_{ij}(\mathbf{w}) = 0 \forall i, j$ , then  $\mathbf{w} \in P$ .

**Lemma 4** *Let there exist a weak solution of the problem  $(\mathcal{P})$ . Then*

$$\begin{aligned} S(\mathbf{w}) &\leq j_{gn}(\mathbf{w}) \quad \forall \mathbf{w} \in K \cap P, \quad \text{i.e.} \\ \int_{\Omega} F_i w_i d\mathbf{x} + \int_{\Gamma_\tau} P_i w_i ds - \int_{\cup_{k,l} \Gamma_c^{kl}} g_c^{kl} |[\mathbf{w}_t]^{kl}| ds &\leq 0 \quad \forall \mathbf{w} \in K \cap P. \end{aligned} \quad (68)$$

The proof is similar of that of [24].

**Remark 3** Eq. (68) represents the condition of the total equilibrium and is the necessary condition for the existence of the solution.

**Theorem 2** Assume that

$$P_0 = \{0\}, \quad P \cap K \neq \{0\} \quad (69)$$

and

$$S(\mathbf{w}) < j_{gn}(\mathbf{w}) \quad \forall \mathbf{w} \in P \cap K \setminus \{0\}. \quad (70)$$

Then  $L$  is coercive on  $K$  and there exists a weak solution of Problem  $(\mathcal{P})$ . If

$$S(\mathbf{w}) > j_{gn}(\mathbf{w}) \quad \forall \mathbf{w} \in P \cap K \setminus \{0\}. \quad (71)$$

then the solution is unique. If

$$|S(\mathbf{w})| \leq j_{gn}(\mathbf{w}) \quad \forall \mathbf{w} \in P_V$$

then for any two solutions  $\mathbf{u}, \mathbf{u}^*$  we have

$$\mathbf{w} \equiv \mathbf{u}^* - \mathbf{u} \in P_V, \quad S(\mathbf{w}) = j_{gn}(\mathbf{u}^*) - j_{gn}(\mathbf{u}). \quad (72)$$

For the proof see [24].

### 2.2.3. Finite Element Solution of the Problem

Let the domain  $\Omega \subset \mathbb{R}^N$  be a bounded domain and let it be approximated by a polygonal (for  $N = 2$ ) or polyhedral (for  $N = 3$ ) domain  $\Omega_h$ . Let the domain  $\Omega_h$  be “triangulated”, i.e. the domain  $\overline{\Omega}_h = \Omega_h \cup \partial\Omega_h$  is divided into a system of  $m$  triangles  $T_{h_i}$  in the 2D case and into a system of  $m$  tetrahedra  $T_{h_i}$  in the 3D case, generating a triangulation  $\mathcal{T}_h$  such that  $\overline{\Omega}_h = \cup_{i=1}^m T_{h_i}$  and such that two neighbouring triangles have only a vertex or an entire side common in the 2D case, and that two neighbouring tetrahedra have only a vertex or an entire edge or an entire face common in the 3D case. Denote by  $h = \max_{1 \leq i \leq m} (\text{diam } T_{h_i})$  the maximal side of the triangle  $T_{h_i}$  in the 2D case and/or the maximal edge of the tetrahedron in the 3D case in  $\mathcal{T}_h$ . Let  $\rho_{T_i}$  denote the radius of the maximal circle (for 2D case) or maximal ball (for 3D case), inscribed in the simplex  $T_{h_i}$ . A family of triangulation  $\{\mathcal{T}_h\}$ ,  $0 < h \leq h_0 < \infty$ , is said to be regular if there exists a constant  $\vartheta_0 > 0$  independent of  $h$  and such that  $h/\rho_{T_i} \leq \vartheta_0$  for all  $h \in (0, h_0)$ . We will assume that the sets  $\overline{\Gamma}_u \cap \overline{\Gamma}_\tau, \overline{\Gamma}_u \cap \overline{\Gamma}_c, \overline{\Gamma}_u \cap \overline{\Gamma}_0, \overline{\Gamma}_c \cap \overline{\Gamma}_\tau, \overline{\Gamma}_c \cap \overline{\Gamma}_0, \overline{\Gamma}_\tau \cap \overline{\Gamma}_0$  coincide with the vertices or edges of  $T_{h_i}$ .

Let  $R_i \in \Omega_h$  be an arbitrary interior vertex of the triangulation  $\mathcal{T}_h$ . Generally the basis function  $w_h^i$  (where  $w_h^i$  is a scalar or vector function) is defined to be a function linear on each element  $T_{h_i} \in \mathcal{T}_h$  and taking the values  $w_h^i(R_j) = \delta_{ij}$  at the vertices of the triangulation, where  $\delta_{ij}$  is the Kronecker symbol. The function  $w_h^i$  represents a pyramid of height 1 with its vertex above the point  $R_i$  and with its support ( $\text{supp } w_h^i$ ) consisting of those triangles or tetrahedra which have the vertex  $R_i$  in common. The basis function has small support since  $\text{diam}(\text{supp } w_h^i) \leq 2h$  and the parameter  $h \rightarrow 0$ .

Let  ${}^1V_h$  and  $V_h$  be the spaces of linear finite elements, i.e. the spaces of continuous scalar and/or vector functions in  $\bar{\Omega}_h$ , piecewise linear over  $\mathcal{T}_h$ , i.e.

$$\begin{aligned} {}^1V_h &= \{z \in C(\bar{\Omega}_h^1) \times \cdots \times C(\bar{\Omega}_h^r) \cap {}^1V \mid z|_{T_{h_i}} \in P_1 \quad \forall T_{h_i} \in \mathcal{T}_h\}, \\ V_h &= \{\mathbf{v} \in [C(\bar{\Omega}_h^1)]^N \times \cdots \times [C(\bar{\Omega}_h^r)]^N \cap V \mid \mathbf{v}|_{T_{h_i}} \in [P_1]^N \quad \forall T_{h_i} \in \mathcal{T}_h\}, \\ K_h &= \{\mathbf{v} \in V_h \mid [v_n]^{kl} \leq 0 \text{ (or } d^{kl}) \text{ on } \cup \Gamma_c^{kl}\} = K \cap V_h. \end{aligned}$$

It is evident that  $K_h$  is convex and closed subset of  $V_h \forall h$  and  $K_h \subset K$  for all  $h$ .

**Definition 3** A pair of functions  $(T_h, \mathbf{u}_h)$ ,  $T_h \in {}^1V_h$ ,  $\mathbf{u}_h \in K_h$ , is said to be a finite element approximation of the problem  $(\mathcal{P})$ , if

$$l(T_h) \leq l(z) \quad \forall z \in {}^1V_h, \quad (73)$$

$$L(\mathbf{u}_h) \leq L(\mathbf{v}) \quad \forall \mathbf{v} \in K_h. \quad (74)$$

**Theorem 3** There exist unique solutions of the finite element approximations (73)-(74) for  $\forall h$ .

The proof is parallel of that of Theorem 3.1 of [43].

To find the relation between the solutions of Problems (64)-(65) and (73)-(74) we have to prove the following theorem:

**Theorem 4** Let  ${}^1V_h \subset {}^1V$  and let  $K_h \subset K$  satisfying the following conditions:

- (i)  $\forall \mathbf{v} \in K \exists \mathbf{v}_h$  such that  $\|\mathbf{v} - \mathbf{v}_h\|_{1,N} \rightarrow 0$  for  $h \rightarrow 0_+$ ,
- (ii) let  $\mathbf{v}_h \in K_h$ ,  $\mathbf{v}_h \rightarrow \mathbf{v}$  weakly for  $h \rightarrow 0_+$  in the space  $V \Rightarrow \mathbf{v} \in K$ .

Then

$$\|T - T_h\|_1 \rightarrow 0, \quad \|\mathbf{u} - \mathbf{u}_h\|_{1,N} \rightarrow 0 \quad \text{for } h \rightarrow 0_+.$$

The proof for the thermal part is based on the general theorem about convergence of the Ritz-Galerkin approximation and for the elastic part is based on the results of [22, 24, 44].

To find an estimate for the error of the solution  $(T_h - T, \mathbf{u}_h - \mathbf{u})$ , a modification of the Falk's technique (see e.g. [42, 43]) will be used. Since the problem is quasi-coupled the method will be based on the following lemma:

**Lemma 5** Let  $|\cdot|$  be the semi-norm defined by

$$|\mathbf{v}|^2 = \int_{\cup_{i=1}^r \Omega_h^i} e_{ij}(\mathbf{v}) e_{ij}(\mathbf{v}) d\mathbf{x}. \quad (75)$$

Then it holds

$$\begin{aligned} \|T - T_h\|_1 &\leq c \{b(T_h - T, z_h - T) + b(T, z_h - T) - s(z_h - T)\}^{\frac{1}{2}} \\ &\quad \text{for any } z_h \in {}^1V_h, \quad c = \text{const.} > 0, \\ c_0 |\mathbf{u} - \mathbf{u}_h|^2 &\leq a(\mathbf{u} - \mathbf{u}_h, \mathbf{u} - \mathbf{u}_h) \leq \{a(\mathbf{u}_h - \mathbf{u}, \mathbf{v}_h - \mathbf{u}) + \\ &\quad + a(\mathbf{u}, \mathbf{v} - \mathbf{u}_h) + a(\mathbf{u}, \mathbf{v}_h - \mathbf{u}) + j_{gn}(\mathbf{v}_h) - j_{gn}(\mathbf{u}) + j_{gn}(\mathbf{v}) - j_{gn}(\mathbf{u}_h) + \\ &\quad + S(\mathbf{u} - \mathbf{v}_h) + S(\mathbf{u}_h - \mathbf{v})\} \text{ for any } \mathbf{v} \in K, \mathbf{v}_h \in K_h, \quad c_0 = \text{const.} > 0. \end{aligned} \quad (76)$$



For the proof see [42, 43, 44, 48].

**Corollary 1** *Let  $K_h \subset K$ . Then substituting  $\mathbf{v} = \mathbf{u}_h$  in (76b) we have*

$$|\mathbf{u} - \mathbf{u}_h| \leq c\{a(\mathbf{u}_h - \mathbf{u}, \mathbf{v}_h - \mathbf{u}) + a(\mathbf{u}, \mathbf{v}_h - \mathbf{u}) + j_{gn}(\mathbf{v}_h) - j_{gn}(\mathbf{u}) - S(\mathbf{v}_h - \mathbf{u})\}^{\frac{1}{2}} \quad \forall \mathbf{v}_h \in K_h, \quad c = \text{const.} > 0. \quad (77)$$

**Theorem 5** *Let  $\partial\Omega$  and its parts  $\Gamma_u, \Gamma_\tau, \Gamma_0, \Gamma_c$  be piecewise polygonal. Let  $T^\iota \in H^2(\Omega^\iota)$ ,  $\mathbf{u}^\iota \in [H^2(\Omega^\iota)]^N$ ,  $\iota = 1, \dots, r$ , be the solutions of (64)-(65) and such that the stress components  $\tau_{ij}(\mathbf{u}^\iota) \in H^1(\Omega^\iota)$ ,  $i, j = 1, 2$ ,  $\iota = 1, \dots, r$ ,  $\tau_n^{kl} \in L^\infty(\Gamma_c^{kl})$ ,  $u_n^{k(l)} \in H^2(\Gamma_c \cap \Gamma_{ci}^{kl})$  holds for any of the boundary  $\partial\Omega$ ,  $g_c^{kl} \in L^\infty(\Gamma_c^{kl})$ . Let  ${}^1V_h \subset {}^1V$ ,  $K_h \subset K$  and let the changes  $[u_n]^{kl} < 0$  ( $d^{kl}$ )  $\rightarrow$   $[u_n]^{kl} = 0$  ( $d^{kl}$ ) and  $[\mathbf{u}_t]^{kl} = 0 \rightarrow [\mathbf{u}_t]^{kl} \neq 0$  occur at finitely many points of  $\cup_{k,l} \Gamma_c^{kl}$  only. Then*

$$\|T - T_h\|_1 = O(h), |\mathbf{u} - \mathbf{u}_h| = O(h). \quad (78)$$

The proof is based on [42, 43, 44, 48, 24].

## 2.2.4. Algorithm

Since the studied problem is quasi-coupled the algorithm is divided into two parts. The algorithm of the thermal part of the problem is based on the classical finite element algorithm. The algorithm of the elastic part of the problem leads to solving the contact problem with friction by using the numerical approximation of a saddle point (see e.g. [5, 43, 48]). Sufficient conditions for the existence of a saddle point can be found in [11]. An approximate saddle point means a point  $(\mathbf{u}_{sh}, \lambda_h) \in K_h \times \Lambda_h \subset K \times \Lambda$  of functional  $\mathcal{L}$ , the so-called Lagrangian, on  $K_h \times \Lambda_h$  if a saddle point  $(\mathbf{u}_s, \lambda) \in K \times \Lambda$  exists and if  $\mathcal{L}(\mathbf{u}_{sh}, \mu_h) \leq \mathcal{L}(\mathbf{u}_{sh}, \lambda_h) \leq \mathcal{L}(\mathbf{v}_h, \lambda_h)$  for all pairs of functions  $(\mathbf{v}_h, \mu_h) \in K_h \times \Lambda_h$ .

Then the studied problem is equivalent to the following problem:

find  $\mathbf{u}_h \in K_h$  such that

$$L(\mathbf{u}_h) = \min_{\mathbf{v} \in K_h} \sup_{\mu_h \in \Lambda_h} \mathcal{L}(\mathbf{v}_h, \mu_h), \quad \mathcal{L}(\mathbf{v}_h, \mu_h) = L_0(\mathbf{v}_h) + \int_{\cup \Gamma_c^{kl}} \mu_h^{kl} g_c^{kl}([\mathbf{v}_{ht}]^{kl}) ds,$$

where  $\Lambda_h = \cup \{\mu_h^{kl} | \mu_h^{kl} \in L^2(\Gamma_c^{kl}), |\mu_h^{kl}| \leq 1 \text{ a.e. on } \Gamma_c^{kl}\}$  and where the non-differentiable functional  $j_{gn}(\mathbf{v}_h)$  is replaced by

$$j_{gn}(\mathbf{v}_h, \mu_h) = \int_{\cup \Gamma_c^{kl}} \mu_h^{kl} g_c^{kl}([\mathbf{v}_{ht}]^{kl}) ds,$$

where  $\mu_h^{kl}$  are the Lagrange multipliers. The existence of a saddle point follows from Proposition 1.2 and 2.2 of [11] and the Korn inequality. By Proposition 2.2 we also obtain uniqueness of its approximation  $(\mathbf{u}_{sh}, \lambda_h) \in K_h \times \Lambda_h$ . For more details see [43, 48, 59].

For the realization of a saddle point the Uzawa or the Arrow-Hurwicz algorithms can be used [48]). The Uzawa algorithm is the following:

Choose  $\lambda_h^0 \in \Lambda_h$ , e.g.  $\lambda_h^0 = 0$ . Let  $\lambda_h^i$  be known, then we find  $\mathbf{u}_h^i$  solving the following problem

$$\min_{\mathbf{v}_h \in K_h} \left\{ L(\mathbf{v}_h) = L_0(\mathbf{v}_h) + \int_{\cup \Gamma_c^{kl}} \lambda_h^{i,kl} g_c^{kl}([\mathbf{v}_{ht}]^{kl}) ds \right\}, \quad (79)$$

and  $\lambda_h^{i+1,kl}$  we find from the relation

$$\lambda_h^{i+1,kl} = \mathcal{P}(\lambda_h^{i,kl} + \rho_i g_c^{kl}((\mathbf{u}_{ht}^k)^i - (\mathbf{u}_{ht}^l)^i)), \quad (80)$$

where  $\mathcal{P}$  is a projection  $\mathcal{P} : L^2(\Gamma_c^{kl}) \rightarrow \Lambda_h$  defined by

$$\begin{aligned} \mu &\in L^2(\Gamma_c^{kl}), \quad y \in \Gamma_c^{kl} \\ \mathcal{P}\mu(y) &= \mu(y) \quad \text{for } |\mu(y)| \leq 1, \\ \mathcal{P}\mu(y) &= 1 \quad \text{for } \mu(y) > 1, \\ \mathcal{P}\mu(y) &= -1 \quad \text{for } \mu(y) < -1, \end{aligned}$$

and where  $0 < \rho_1 \leq \rho_i \leq \rho_2$ ,  $\rho_1, \rho_2$  are sufficiently small numbers, which follow from the convergence theorem of Uzawa algorithm (see [11, 48]).

The finite element approximation of the problem investigated leads to minimization of the functional  $L(\mathbf{v}_h)$  on the set  $K_h$ . This problem is equivalent to the problem

$$\begin{aligned} f(\mathbf{w}) &= \frac{1}{2} \mathbf{w}^T C \mathbf{w} + \mathbf{b}^T \mathbf{w}, \\ \text{with linear constraints } A \mathbf{w} &\leq \mathbf{d}, \end{aligned} \quad (81)$$

where  $f(\mathbf{w})$  is generated from the functional  $L(\mathbf{v}_h)$ ,  $C$  is the stiffness matrix ( $\dim n \times n$ ), which is positive (semi-)definite and generated by the term  $\frac{1}{2} \int_{\Omega} c_{ijkl}(\mathbf{x}) e_{ij}(\mathbf{v}_h) e_{kl}(\mathbf{v}_h) d\mathbf{x}$ ,  $\mathbf{b}$  ( $\dim n$ ) is the vector generated by the body and surface forces, i.e. by the term  $\int_{\Omega} F_i v_{hi} d\mathbf{x} + \int_{\Gamma_{\tau}} P_i v_{hi} ds$  and by friction forces  $\int_{\cup \Gamma_c^{kl}} \lambda_h g_c^{kl}([\mathbf{v}_{ht}]^{kl}) ds$  and it changes due to the friction forces in every step of the Uzawa algorithm,  $A$  is the matrix of constraints ( $\dim m \times n$ ) generated by condition  $[u_{hn}]^{kl} \leq 0$  (or  $d^{kl}$ ) on  $\Gamma_c^{kl}$  in the definition of the admissible set of displacements  $K_h$ ,  $\mathbf{d} \equiv \mathbf{0}$ , for a zero gap,  $n$  represents double or triple the number of points of triangulation in which the displacement is not prescribed and  $m$  is the number of points of triangulation on the contact boundary  $\Gamma_c^{kl}$ . Stiffness matrix  $C$  and vector  $\mathbf{b}$  are generated by the standard techniques. By a similar technique the frictional forces are also approximated.

Constrained optimization methods often derive from unconstrained ones. The conjugate gradient methods with constraints can be generally efficient. We will further give some useful algorithm.

The problem (81) represents the problem of minimization of a quadratic function with constraints, which will be written in the form

$$\begin{aligned} f(\mathbf{x}) &= \frac{1}{2} \mathbf{x}^T C \mathbf{x} + \mathbf{b}^T \mathbf{x} \equiv \frac{1}{2} (\mathbf{x}, C \mathbf{x}) + (\mathbf{b}, \mathbf{x}), \\ \left. \begin{aligned} (\mathbf{a}_i, \mathbf{x}) &\leq d_i, \quad i \in J^-, \\ (\mathbf{a}_i, \mathbf{x}) &= d_i, \quad i \in J^0, \end{aligned} \right\} \text{ or in the matrix form } A \mathbf{x} &\leq \mathbf{d}, \end{aligned} \quad (82)$$

where  $\mathbf{x} \in \mathbb{R}^n$ ,  $\mathbf{a}_i \in \mathbb{R}^n$ ,  $\mathbf{b} \in \mathbb{R}^n$ ,  $\mathbf{d} = (d_i) \in \mathbb{R}^m$ ,  $d_i$  are numbers,  $C$  is  $n \times n$  symmetric, positive (semi-)definite matrix,  $A = (a_{ij})$  is the matrix of constraints ( $\dim m \times n$ ),  $\underline{J} = J^- \cup J^0$ ,  $J^-$ ,  $J^0$  are finite sets of indices.

The main idea of the method is the following: we minimize (82a) on certain facets (faces of the polyhedral set defined by linear inequalities (82b,c)) created by constraints (82b,c) among which the equalities are satisfied. We find the minimum of (82a) on each such facet by using the conjugate gradient method, which converges after a finite number of iteration steps. Hence, and since the number of facets is limited, the algorithm for (82a,b,c) also converges after a finite number of steps. For more details see [62, 48, 49, 59].

Let  $J = J(\mathbf{x})$  be a subset of  $\underline{J}$  defined by  $J(\mathbf{x}) = \{i | (\mathbf{a}_i, \mathbf{x}) = d_i, i \in J^- \cup J^0\}$ , where  $\mathbf{a}_i$  are linearly independent vectors. Let  $J^0 \neq \emptyset$  then  $J(\mathbf{x})$  is non-empty and  $\mathbf{x}$  satisfies (82b,c). Take a set of indices  $J = J(\mathbf{x})$  and construct matrix  $A_J$  in such a way that its rows are vectors  $\mathbf{a}_i$ ,  $i \in J$ . Matrix  $A_J$  is  $m \times n$ -dimensional, where  $m$  is the number of elements of set  $J$ , which corresponds to the number of all nodal points on  $\cup \Gamma_c^{kl}$  and  $n$  is the dimension of  $\mathbf{x}$ . Since vectors  $\mathbf{a}_i$ ,  $i \in J$ , are linearly independent, then matrix  $A_J A_J^T$  is regular. Moreover, we construct operator  $P_J = A_J^T (A_J A_J^T)^{-1} A_J$  and vectors  $\mathbf{u}(\mathbf{x}) = -(A_J A_J^T)^{-1} A_J f'(\mathbf{x})$ , where  $f'(\mathbf{x})$  is the gradient of  $f(\mathbf{x})$ . Operator  $P_J$  is an orthogonal projection into the subspace spanned by vectors  $\mathbf{a}_i$ ,  $i \in J$ .

We introduce the transformation  $\mathbf{x} = \mathbf{x}_0 + (I - P_J)\mathbf{y}$ , thus the quadratic functional  $f(\mathbf{x})$  can be rewritten as  $\varphi(\mathbf{y}) = f(\mathbf{x}_0 + (I - P_J)\mathbf{y})$ . Then the initial problem with constraints reduces to the minimization of quadratic functional  $\varphi(\mathbf{y})$  without constraints. Then we apply the conjugate gradient algorithm, which is convergent. In the  $\mathbf{x}$  variable we then have the following convergent CG process:

Let  $\mathbf{x}_0$  be given, then

$$\begin{aligned} \text{(i)} \quad & \mathbf{p}_1 = -(I - P_J)f'(\mathbf{x}_0) \\ \text{(ii)} \quad & \mathbf{x}_{k+1} = \mathbf{x}_k + \alpha_{k+1} \mathbf{p}_{k+1}, \\ \text{(iii)} \quad & \mathbf{p}_{k+1} = -(I - P_J)f'(\mathbf{x}_k) + \frac{\|(I - P_J)f'(\mathbf{x}_k)\|^2}{\|(I - P_J)f'(\mathbf{x}_{k-1})\|^2} \mathbf{p}_k, \end{aligned} \quad (83)$$

where  $\alpha_{k+1} = -\frac{(f'(\mathbf{x}_k), \mathbf{p}_{k+1})}{(\mathbf{p}_{k+1}, C \mathbf{p}_{k+1})}$ ,  $k = 0, 1, 2, \dots$

Then the algorithm minimizing  $f(\mathbf{x})$  under constraints (82b,c) is as follows:

**Algorithm 2.1** (conjugate gradient method with constraints – CGMC).

- (1) Let us choose  $\mathbf{x}_0 \in \mathbb{R}^n$  satisfying (82b,c),
- (2) we determine a set  $J(\mathbf{x}_0) = \{i | (\mathbf{a}_i, \mathbf{x}_0) = d_i, i \in J^- \cup J^0\}$ , and form matrix  $A_{J(\mathbf{x}_0)}$ ,
- (3) we calculate vector  $(I - P_J)f'(\mathbf{x}_0)$ , where  $f'(\mathbf{x}_0) = C\mathbf{x}_0 + \mathbf{b}$ ,  $P_J = A_{J(\mathbf{x}_0)}^T (A_{J(\mathbf{x}_0)} A_{J(\mathbf{x}_0)}^T)^{-1} A_{J(\mathbf{x}_0)}$ ,
- (4) there are two cases:
  - (a)  $(I - P_J)f'(\mathbf{x}_0) \neq 0$  then we apply the algorithm (83), then for every  $k = 0, 1, 2, \dots$  we calculate (i.e. we check whether the points obtained are feasible

or not)

$$\alpha_{k+1} = -\frac{(f'(\mathbf{x}_k), \mathbf{p}_{k+1})}{(\mathbf{p}_{k+1}, C\mathbf{p}_{k+1})} \quad \text{and} \quad \underline{\alpha}_{k+1} = \min_{i, (\mathbf{a}_i, \mathbf{p}_{k+1}) > 0} \frac{d_i - (\mathbf{a}_i, \mathbf{x}_i)}{(\mathbf{a}_i, \mathbf{p}_{k+1})}.$$

Then we put  $\mathbf{x}_{k+1} = \mathbf{x}_k + \alpha_{k+1}\mathbf{p}_{k+1}$  provided  $\alpha_{k+1} \leq \underline{\alpha}_{k+1}$  and then continue in (83).

In the case when  $\mathbf{x}_{i+1}$  is the minimum of  $f(\mathbf{x})$  with constraints (82b,c),  $i \in J$ , we put  $\mathbf{x}_0 = \mathbf{x}_{k+1}$  and go to (5).

If  $\alpha_{k+1} > \underline{\alpha}_{k+1}$ , we put  $\mathbf{x}_{k+1} = \mathbf{x}_k + \underline{\alpha}_{k+1}\mathbf{p}_{k+1}$  and the algorithm continues onto (2),

(b)  $(I - P_J)f'(\mathbf{x}_0) = 0$  then we continue on (5).

(5) we calculate  $\mathbf{u}(\mathbf{x}_0) = -(A_J A_J^T)^{-1} A_J f'(\mathbf{x}_0)$ .

If  $(\mathbf{u}(\mathbf{x}_0))_i \geq 0 \forall i \in J(\mathbf{x}_0) \cap J^-$  we find the minimum point of  $f(\mathbf{x})$  and the process stops.

If there exists an index  $j \in J(\mathbf{x}_0) \cap J^-$  such that  $(\mathbf{u}(\mathbf{x}_0))_j < 0$ , we put  $J(\mathbf{x}_0) = J(\mathbf{x}_0) - \{j\}$  and go to (3).  $\square$

Sequence  $\{f(\mathbf{x}_k)\}$ ,  $k = 0, 1, 2, \dots$ , generated by Algorithm 2.1 from the sequence  $\{\mathbf{x}_k\}$ , is strictly decreasing. Then there exists a number  $n_0$  such that  $f(\mathbf{x}_{n_0})$  minimizes  $f(\mathbf{x})$  with constraints (82b,c). For more details see [48, 49, 59, 62].

The above algorithm can be preconditioned. For more details see [49, 59]. The convergence of such methods is faster than the above CGMC without preconditioning.

Since the stiffness matrix remains the same throughout the whole iteration process, the number of the approximated displacement vector  $\mathbf{u}_h$  subject to the condition on the contact boundaries  $\Gamma_c^{kl}$  is small as compared to the total number of components of  $\mathbf{u}_h$ , then in [15, 44, 48] the modified algorithm is presented. The algorithm renders possible to eliminate the free components of  $\mathbf{u}_h$  corresponding to the nodes not belonging to  $\cup \Gamma_c^{kl}$ , and to carry out the iteration process with only the other components of  $\mathbf{u}_h$ .

### 3. The Models Based on the Dynamic and Quasi-Static Contact Problems with Coulombian Friction in Visco-Elasticity with Short and Long Memories Formulated in Velocities and Displacements

#### 3.1. Introduction

Geomechanic processes in upper parts of the Earth and intensive large-scale mining with a lot of quarry blasts produce ground shocks of microseismic character or even local tremors. Together with certain possibility of local natural earthquakes there is often a high risk potential for landslides and the slope may be considered as hazardous. The information on geometrical properties of discontinuous rock mass are available from surface outcrops, excavations in the vicinity and core drills. It is not enough to predict a position of all discontinuities in the investigated areas of our interest. The shape, size and spatial position

of rock blocks depend on the spatial position of discontinuities. Knowledge of the stress state in a slope is essential in order to understand the mechanics of the slope behaviour. The stresses acting upon a structure in comparison to the strength of the structure govern the stability of that structure. The initial stresses before loading or excavation in the case of engineering applications, in the rock masses are (in almost all cases) compressive, and are primarily a combination of (i) gravitational stresses arising from the weight of the overlying rocks, (ii) tectonic stresses arising from the external tectonic forces and arising from geodynamic processes taking place in the investigated region and cumulated in this region, (iii) stresses caused by a previous glaciation, (iv) residual stresses. The gravitational and tectonic stresses are the major contributors to the overall virgin stress state. The virgin vertical stresses are usually assumed to be solely due to the weight of the overlying rock masses. The virgin horizontal stresses are difficult to quantify due to the geodynamic processes taking place in these regions. The tectonic stresses (horizontal, shear and vertical) are different in every region of the world in dependence on the properties and structure of rocks and on geodynamic processes acting in this region.

In this study we deal with numerical studies of (i) the potential landslides originated in different regions in the world as results of geodynamic processes and seismic effects or creep movements on wetting slopes and (ii) of gravity type of the landslides. The consequences of the geodynamic processes in the upper parts of the Earth onto the processes on the Earth surface, resulting also earthquakes and shocks, will be discussed. This study proposes a computational efficient methodology for combining multibody quasi-static and dynamic simulation methods with deformable contact models. The objective of this study reported here will obtain approximately the geometry of the area and the dimensions of the potential failure mass as well as the mechanisms of their origins. The investigated slope mainly consists of intact up to weathered rock and has been affected by recurrent instability phenomena.

In this part we will deal with a new methodology for simulating deformable contact in the system of colliding geological bodies within a multibody dynamics, based on the analyses of the quasi-static and dynamic contact multibody problems in visco-elastic rheology with short memory. The approach for the existence proof is similar to that of [10] and is similar to that in the static case, i.e. the original problem is approximated by a sequence of auxiliary problems, the solvability and some limited regularity of the solutions of the auxiliary problems are proved, and a transition to the original problem is done. The unilateral contact conditions are formulated in the displacement velocities, which corresponds to a first order approximation of the physically more realistic unilateral conditions formulated in the displacements. This approximation is not suitable for all type of geomechanical problems, but it can be suitable for special model problems in geomechanics only. In despite of their practical applications, dynamic contact problems with Coulomb friction still belong to the underdeveloped problems in the present theoretical and applied mathematics. At present the models respecting the nonpenetrability of mass only the static multibody contact problems are well investigated. For the dynamic contact problems the existence theorems are proved for bodies having smooth contact parts of their boundaries with a rigid undeformable support, i.e., in the applications we must assume that one of the colliding geological body is absolutely rigid. Such approximation seems to be geophysically realistic for the cases of very small distances between the body and the rigid foundations and for very small time in-

tervals. The coefficient of friction, which can be solution-dependent, must be smaller than a definite upper bound (for its estimation see [31, 32, 43, 48, 10]). Recently the dynamic contact problems are studied for visco-elastic rheologies with short and long memories and rigid undeformable supports under the assumption that the Signorini conditions are formulated in velocities. The extension of these results to the multibody contact problems is possible but with limited applications. But the determination of couples of points which are in actual or potential contact in varying times during the geological process seems to be very complicated problem, and therefore, the generalized dynamic multibody contact problem with Coulombian friction is up-to-date from the present knowledges and from the mathematical analysis point of view still an open problem. At present the problem can be solved under the additional assumptions about the regularity conditions and about the requirement on the sufficient smoothness of contact boundaries in varying times  $t \in I$ , where the duration of the geological process (i.e. the time interval  $I$ ) is sufficiently small, which from the geological point of view is satisfied. These assumptions mean the requirement that the above mentioned regularity and smoothness properties keep the values of the initial state or values very near the initial state. It is evident that the quality of such geomechanical models has a certain limit. The above assumptions are also valid for contact problems where the Signorini contact conditions are formulated in displacements. This type of models analysed mathematically in the continuous domain, due to the above discussed difficulties, can realistically describe the early state of the landslide evolution (i.e. before downslope movement of a slide mass) only. On the contrary the corresponding discrete models can describe the landslide mechanism in all phases of its evolution, as the changes of geometry of the colliding geological bodies and their contact zones can be determined in every time step.

## 3.2. Models Based on the Dynamic Contact Problems Formulated in Velocities

### 3.2.1. Formulation of the Problem

In the study we will investigate the dynamic multibody contact problem with Coulomb friction in linear visco-elasticity with short memory and damping in  $N$ -dimensions formulated in velocities.

Let  $I = (0, t_p)$  be the time interval. Let  $\Omega \subset \mathbb{R}^N$ ,  $N = 2, 3$ , be the region occupied by a system of bodies of arbitrary shapes  $\Omega^l$  such that  $\Omega = \bigcup_{l=1}^r \Omega^l$  (Fig. 10). Let  $\Omega^l$  have Lipschitz boundaries  $\partial\Omega^l$  and let us assume that  $\partial\Omega = \Gamma_\tau \cup \Gamma_u \cup \Gamma_c$ , where the disjoint parts  $\Gamma_\tau$ ,  $\Gamma_u$ ,  $\Gamma_c$  are open subsets. Moreover, let  $\Gamma_u = {}^1\Gamma_u \cup {}^2\Gamma_u$  and  $\Gamma_c = \bigcup_{k,l} \Gamma_c^{kl}$ ,  $\Gamma_c^{kl} = \partial\Omega^k \cap \partial\Omega^l$ ,  $k \neq l$ ,  $k, l \in \{1, \dots, r\}$ . Let  $Q = I \times \Omega$  denote the time-space domain and let  $\Gamma_\tau(t) = \Gamma_\tau \times I$ ,  $\Gamma_u(t) = \Gamma_u \times I$ ,  $\Gamma_c(t) = \Gamma_c \times I$  denote the parts of its boundary and  $\partial Q = \partial\Omega \times I$ .

Furthermore, let  $\mathbf{n}$  denote the outer normal vector of the boundary,  $u_n = u_i n_i$ ,  $\mathbf{u}_t = \mathbf{u} - u_n \mathbf{n}$ ,  $\tau_n = \tau_{ij} n_j n_i$ ,  $\boldsymbol{\tau}_t = \boldsymbol{\tau} - \tau_n \mathbf{n}$  be normal and tangential components of displacement and stress vectors  $\mathbf{u} = (u_i)$ ,  $\boldsymbol{\tau} = (\tau_i)$ ,  $\tau_i = \tau_{ij} n_j$ ,  $i, j = 1, \dots, N$ . Let  $\mathbf{F}$ ,  $\mathbf{P}$  be the body and surface forces,  $\rho$  the density,  $\alpha(\mathbf{x}) \geq 0$  physically have a meaning of damping. Let us denote by  $\mathbf{u}' = (u'_k)$  the velocity vector. Let on  $\Gamma_c^{kl}$  the positive direction of the outer normal vector  $\mathbf{n}$  be assumed with respect to  $\Omega^k$ . Let us denote by  $[u'_n]^{kl} = u'^k_n - u'^l_n$  the jump of the normal velocity across the contact zone between neighbouring geological

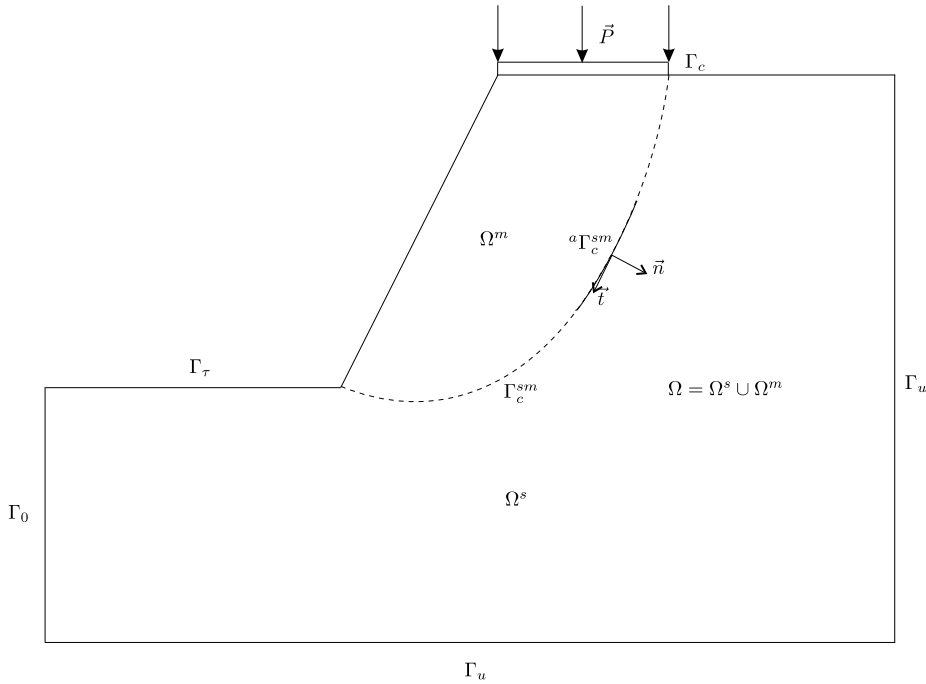


Figure 10. The model of the landslide – the evolution of the curved failure surface.

bodies  $\Omega^k$  and  $\Omega^l$ . Similarly, we denote  $[\mathbf{u}'_t]^{kl} \equiv \mathbf{u}'_t{}^k - \mathbf{u}'_t{}^l$ . If one of the colliding bodies is absolutely rigid, say  $\Omega^l$ , then  $[u'_n]^{kl} \equiv u'_n{}^k$  and  $[\mathbf{u}'_t]^{kl} \equiv \mathbf{u}'_t{}^k$ .

The stress-strain relation will be defined by the Hooke's law

$$\begin{aligned} \tau_{ij} &= \tau_{ij}(\mathbf{u}, \mathbf{u}') = c_{ijkl}^{(0)}(\mathbf{x}) e_{kl}(\mathbf{u}) + c_{ijkl}^{(1)}(\mathbf{x}) e_{kl}(\mathbf{u}'), \\ e_{ij}(\mathbf{u}) &= \frac{1}{2} \left( \frac{\partial u_i}{\partial x_j} + \frac{\partial u_j}{\partial x_i} \right), \quad i, j, k, l = 1, \dots, N, \end{aligned} \quad (84)$$

where  $c_{ijkl}^{(n)}(\mathbf{x})$ ,  $n = 0, 1$ , are elastic and viscous coefficients and  $e_{ij}(\mathbf{u})$  are components of the small strain tensor,  $N$  is the space dimension. For the tensors  $c_{ijkl}^{(n)}(\mathbf{x})$ ,  $n = 0, 1$ , we assume

$$\begin{aligned} c_{ijkl}^{(n)} &\in L^\infty(\Omega), \quad n = 0, 1, \quad c_{ijkl}^{(n)} = c_{jikl}^{(n)} = c_{klij}^{(n)} = c_{ijlk}^{(n)}, \\ c_{ijkl}^{(n)} e_{ij} e_{kl} &\geq c_0^{(n)} e_{ij} e_{ij} \quad \forall e_{ij}, \quad e_{ij} = e_{ji} \quad \text{and a.e. } \mathbf{x} \in \Omega, \quad c_0^{(n)} > 0. \end{aligned} \quad (85)$$

A repeated index implies summation from 1 to  $N$ .

The dynamic contact problems with Coulombian friction, where the Signorini conditions are formulated in displacements, are up-to-date unsolved. Therefore, for the mathematical analysis the Signorini conditions are formulated in velocities, i.e. we will assume the following contact conditions:

$$[u'_n]^{kl} \leq 0, \quad \tau_n^k = -\tau_n^l \equiv \tau_n^{kl} \leq 0, \quad [u'_n]^{kl} \tau_n^{kl} = 0 \quad \text{on } \cup \Gamma_c^{kl}.$$

If one of the colliding bodies is absolutely rigid, say  $\Omega^l$ , then  $[u'_n]^{kl} \equiv u_n'^k \equiv u'_n$  and the Signorini conditions are as follows:

$$u'_n \leq 0, \quad \tau_n \leq 0, \quad u'_n \tau_n = 0 \quad \text{on } \Gamma_c^k.$$

The problem to be solved has the following classical formulation:

**Problem (P):** Let  $N = 2, 3, s \geq 2$ . Find a vector function  $\mathbf{u} : \bar{\Omega} \times I \rightarrow \mathbb{R}$ , satisfying

$$\begin{aligned} \rho^\iota \frac{\partial^2 u_i^\iota}{\partial t^2} + \alpha^\iota \frac{\partial u_i^\iota}{\partial t} &= \frac{\partial \tau_{ij}^\iota(\mathbf{u}^\iota, \mathbf{u}^{\iota'})}{\partial x_j} + F_i^\iota, \quad i, j = 1, \dots, N, \quad \iota = 1, \dots, s, \\ (t, \mathbf{x}) &\in Q^\iota = I \times \Omega^\iota, \end{aligned} \quad (86)$$

$$\begin{aligned} \tau_{ij}^\iota &= \tau_{ij}^\iota(\mathbf{u}^\iota, \mathbf{u}^{\iota'}) = c_{ijkl}^{(0)\iota}(\mathbf{x}) e_{kl}(\mathbf{u}^\iota) + c_{ijkl}^{(1)\iota}(\mathbf{x}) e_{kl}(\mathbf{u}^{\iota'}), \\ i, j, k, l &= 1, \dots, N, \quad \iota = 1, \dots, s, \end{aligned} \quad (87)$$

$$\tau_{ij} n_j = P_i, \quad i, j = 1, \dots, N, \quad (t, \mathbf{x}) \in \Gamma_\tau(t) = I \times \cup_{\iota=1}^s (\Gamma_\tau \cap \partial\Omega^\iota), \quad (88)$$

$$u_i = u_{2i}, \quad i = 1, \dots, N, \quad (t, \mathbf{x}) \in {}^1\Gamma_u(t) = I \times \cup_{\iota=1}^s ({}^1\Gamma_u \cap \partial\Omega^\iota), \quad (89)$$

$$u_i = 0, \quad i = 1, \dots, N, \quad \text{on } {}^2\Gamma_u(t) = I \times \cup_{\iota=1}^s ({}^2\Gamma_u \cap \partial\Omega^\iota), \quad (90)$$

the Signorini type contact conditions

$$[u'_n]^{kl} \leq 0, \quad \tau_n^k = -\tau_n^l \equiv \tau_n^{kl} \leq 0, \quad [u'_n]^{kl} \tau_n^{kl} = 0,$$

in the multibody geological system or

$$u_n'^k \leq 0, \quad \tau_n^k \leq 0, \quad u_n'^k \tau_n^k = 0$$

for the case with rigid foundation, and

$$[\mathbf{u}'_t]^{kl} = 0 \implies |\boldsymbol{\tau}_t^{kl}| \leq \mathcal{F}_c^{kl}(0) |\tau_n^{kl}|, \quad (t, \mathbf{x}) \in \Gamma_c(t) = I \times \cup_{k,l} \Gamma_c^{kl},$$

$$[\mathbf{u}'_t]^{kl} \neq 0 \implies \boldsymbol{\tau}_t^{kl} = -\mathcal{F}_c^{kl}([\mathbf{u}'_t]^{kl}) |\tau_n^{kl}| \frac{[\mathbf{u}'_t]^{kl}}{|[\mathbf{u}'_t]^{kl}|},$$

the Coulombian law of friction, (91)

and the initial conditions

$$\mathbf{u}(\mathbf{x}, 0) = \mathbf{u}_0(\mathbf{x}), \quad \mathbf{u}'(\mathbf{x}, 0) = \mathbf{u}_1(\mathbf{x}), \quad \mathbf{x} \in \Omega, \quad (92)$$

where  $\mathbf{u}_0, \mathbf{u}_1, \mathbf{u}_2$  are the given functions,  $\mathbf{u}_2$  has a time derivative  $\mathbf{u}'_2$ , and  $\mathbf{u}_0, \mathbf{u}_1$  satisfy the static linear contact problems in elasticity with or without Coulombian friction  $\mathcal{F}_c^{kl}$  (see [42, 43, 48] or can be equal to zero.

The coefficient of friction  $\mathcal{F}_c^{kl} \equiv \mathcal{F}_c^{kl}(\mathbf{x}, \mathbf{u}')$  is globally bounded, non-negative and satisfies the Carathéodory property, i.e.  $\mathcal{F}_c^{kl}(\cdot, \mathbf{v})$  is measurable,  $\mathbf{v} \in \mathbb{R}$ , and  $\mathcal{F}_c^{kl}(\mathbf{x}, \cdot)$  is continuous for a.e.  $\mathbf{x} \in \Gamma_c^{kl}$ . Moreover, it has a compact support  $\mathcal{SF}_c$  defined by (30), which depends on the space variable  $\mathbf{x}$  and since we model also the difference between the coefficients of friction and of stick as well as slip, it depends also on the tangential displacement rate component  $\mathbf{u}'_t$  (see Fig. 8). Furthermore, we denote by  $(y)_+ \equiv \max\{y, 0\}$  the positive part of  $y$ .



### 3.2.2. Weak Solution of the Problem

#### Variational formulation of the problem and the penalty approximation

The existence of the solution will be proved under the following assumptions:

**Presumption 1** Let  $N \geq 2$  and let  $\Omega = \cup_{i=1}^s \Omega^i$  be a bounded and connected set with Lipschitz boundary  $\partial\Omega = \Gamma_\tau \cup \Gamma_u \cup \Gamma_c$ , where the disjoint parts  $\Gamma_\tau, \Gamma_u, \Gamma_c$  are open subsets. Let  $\Gamma_u = {}^1\Gamma_u \cup {}^2\Gamma_u$  and  $\Gamma_c = \cup_{k,l} \Gamma_c^{kl}$ ,  $\Gamma_c^{kl} = \partial\Omega^k \cap \partial\Omega^l$ ,  $k \neq l$ ,  $k, l \in \{1, \dots, r\}$ . Let  $t_p > 0$  and let  $I = (0, t_p)$  be a sufficiently small time interval. Let  $Q = \Omega \times I$  denote the time-space domain and let  $\Gamma_\tau(t) = \Gamma_\tau \times I$ ,  $\Gamma_u(t) = \Gamma_u \times I$ ,  $\Gamma_c(t) = \Gamma_c \times I$  denote the parts of its boundary  $\partial Q = \partial\Omega \times I$ . The coefficients  $c_{ijkl}^{(n)}(\mathbf{x})$ ,  $n = 0, 1$ , satisfy (85). The given input data satisfy  $\rho \in C(\Omega)$ ,  $\mathbf{F}, \mathbf{F}' \in L^2(I; L^{2,N}(\Omega))$ ,  $\mathbf{P}, \mathbf{P}' \in L^2(I; L^{2,N}(\Gamma_\tau))$ ,  $\mathbf{u}_1 \in H^{1,N}(\Omega)$ ,  $u_{1n}^k - u_{1n}^l = 0$  on  $\cup_{k,l} \Gamma_c^{kl}$ ,  $\mathbf{u}_0 \in H^{1,N}(\Omega)$ , the coefficient of friction  $\mathcal{F}_c^{kl} \equiv \mathcal{F}_c^{kl}(\mathbf{x}, \mathbf{u}_t')$  is assumed to be bounded, non-negative and satisfies the Carathéodory property. Let  $m$  be an integer, then  $k = t_p/m$  is a time step. Moreover, we will assume that for every  $t \in I$  the regularity condition and the Lipschitzian property on  $\partial\Omega^i$  and  $\Gamma_c^{sm}$  are satisfied.

The contact problem (86) – (92) has a weak formulation in terms of a hyperbolic variational inequality. Let us introduce the set of virtual displacements and the set of admissible displacements by

$$\begin{aligned} \mathcal{V}_0 &= \{ \mathbf{v} | \mathbf{v} \in L^2(I; \cap_{i=1}^r H^{1,N}(\Omega^i)), \mathbf{v} = 0 \text{ on } \Gamma_u(t), \\ &\quad [v_n]^{kl} = 0 \text{ a.e. on } I \times \cup_{k,l} \Gamma_c^{kl} \}, \\ \mathcal{V} &= \mathbf{u}_2' + \mathcal{V}_0, \\ \mathcal{K} &= \{ \mathbf{v} | \mathbf{v} \in L^2(I; \cap_{i=1}^r H^{1,N}(\Omega^i)), \mathbf{v} = \mathbf{u}_2' \text{ on } \Gamma_u(t), \\ &\quad [v_n]^{kl} \leq 0 \text{ a.e. on } I \times \cup_{k,l} \Gamma_c^{kl} \}. \end{aligned}$$

Multiplying (86) by  $\mathbf{v} - \mathbf{u}'$ , where  $\mathbf{v}$  are suitable test functions, integrating over  $I \times \Omega$ , using the Green's theorem and boundary and contact conditions, then we obtain the following variational problem:

**Problem**  $(\mathcal{P})_v$ : Find a vector function  $\mathbf{u}$  with  $\mathbf{u}' \in \mathcal{K} \cap B(I; L^{2,N}(\Omega))$  and  $\mathbf{u}(0, \cdot) = \mathbf{u}_0$ ,  $\mathbf{u}'(0, \cdot) = \mathbf{u}_1$ , such that

$$\begin{aligned} &\int_I \{ (\mathbf{u}''(t), \mathbf{v} - \mathbf{u}'(t)) + (\alpha \mathbf{u}'(t), \mathbf{v} - \mathbf{u}'(t)) + a^{(0)}(\mathbf{u}(t), \mathbf{v} - \mathbf{u}'(t)) + \\ &\quad + a^{(1)}(\mathbf{u}'(t), \mathbf{v} - \mathbf{u}'(t)) + j(\mathbf{v}) - j(\mathbf{u}'(t)) \} dt \geq \int_I (\mathbf{f}(t), \mathbf{v} - \mathbf{u}'(t)) dt \quad \forall \mathbf{v} \in \mathcal{K}, \end{aligned} \quad (93)$$

where we assume that the initial data  $\mathbf{u}_0, \mathbf{u}_1$  satisfies the static contact multibody linear

elastic problem (see e.g. [42, 43]), and where

$$\begin{aligned}
 (\mathbf{u}'', \mathbf{v}) &= \sum_{\iota=1}^s (\mathbf{u}''^{\iota}, \mathbf{v}^{\iota}) = \int_{\Omega} \rho u_i'' v_i d\mathbf{x}, \\
 (\alpha \mathbf{u}', \mathbf{v}) &= \sum_{\iota=1}^s (\alpha^{\iota} \mathbf{u}'^{\iota}, \mathbf{v}^{\iota}) = \int_{\Omega} \alpha u_i' v_i d\mathbf{x}, \\
 a^{(n)}(\mathbf{u}, \mathbf{v}) &= \sum_{\iota=1}^s a^{(n)\iota}(\mathbf{u}^{\iota}, \mathbf{v}^{\iota}) = \int_{\Omega} c_{ijkl}^{(n)} e_{kl}(\mathbf{u}) e_{ij}(\mathbf{v}) d\mathbf{x}, \\
 (\mathbf{f}, \mathbf{v}) &= \sum_{\iota=1}^s (\mathbf{f}^{\iota}, \mathbf{v}^{\iota}) = \int_{\Omega} F_i v_i d\mathbf{x} + \int_{\Gamma_{\tau}} P_i v_i ds, \\
 j(\mathbf{v}) &= \sum_{\iota=1}^s j^{\iota}(\mathbf{v}^{\iota}) = \int_{\cup_{k,l} \Gamma_c^{kl}} \mathcal{F}_c^{kl}([\mathbf{u}'_t]^{kl}) |\tau_n^{kl}(\mathbf{u}, \mathbf{u}')| |[\mathbf{v}_t]^{kl}| ds \equiv \\
 &\equiv \langle \mathcal{F}_c^{kl}([\mathbf{u}'_t]^{kl}) |\tau_n^{kl}(\mathbf{u}, \mathbf{u}')|, |[\mathbf{v}_t]^{kl}| \rangle_{\Gamma_c},
 \end{aligned} \tag{94}$$

where the bilinear forms  $a^{(n)}(\mathbf{u}, \mathbf{v})$ ,  $n = 0, 1$ , are symmetric in  $\mathbf{u}, \mathbf{v}$  and satisfy  $a^{(n)}(\mathbf{u}, \mathbf{u}) \geq c_0^{(n)} \|\mathbf{u}\|_{1,N}^2$ ,  $c_0^{(n)} = \text{const.} > 0$ ,  $|a^{(n)}(\mathbf{u}, \mathbf{v})| \leq c_1^{(n)} \|\mathbf{u}\|_{1,N} \|\mathbf{v}\|_{1,N}$ ,  $c_1^{(n)} = \text{const.} > 0$ ,  $\mathbf{u}, \mathbf{v} \in V_0 = \{\mathbf{v} | \mathbf{v} \in \cap_{\iota=1}^s H^{1,N}(\Omega^{\iota}), \mathbf{v} = 0 \text{ on } \Gamma_u = {}^1\Gamma_u \cup {}^2\Gamma_u \text{ and } [v_n]^{kl} = 0 \text{ a.e. on } \Gamma_c\}$ .

It can be shown similarly as in [10] that every solution  $\mathbf{u} \in C^{2,N}(I \times \overline{\Omega})$  of (86)-(92) is a solution of (93) and that every sufficiently smooth solution  $\mathbf{u} \in C^{2,N}(I \times \overline{\Omega})$  of (93) is also a solution of (86)-(92).

The proof of the existence of the solution is based on the penalization and regularization techniques. In the first step, the penalty method will be used. This leads to a contact problem of normal compliance type. The contact condition (91a) will be replaced by the nonlinear boundary condition putting  $\tau_n(\mathbf{u}, \mathbf{u}') = -\frac{1}{\delta} [[u'_n]^{kl}]_+$  with  $[\cdot]_+ := \max\{\cdot, 0\}$ ,  $\delta > 0$ . Then we have to solve the following variational problem:

**Problem**  $(\mathcal{P})_{vp}$ : Find a function  $\mathbf{u}_{\delta}$  with  $\mathbf{u}'_{\delta} \in (\mathbf{u}'_2 + \mathcal{V}_0) \cap B(I; L^{2,N}(\Omega))$  and  $\mathbf{u}_{\delta}(0, \cdot) = \mathbf{u}_0$ ,  $\mathbf{u}'_{\delta}(0, \cdot) = \mathbf{u}_1$ , such that for all  $\mathbf{v} \in \mathcal{V}$ , there holds

$$\begin{aligned}
 &\int_I \{ (\mathbf{u}_{\delta}''(t), \mathbf{v} - \mathbf{u}'_{\delta}(t)) + (\alpha \mathbf{u}'_{\delta}(t), \mathbf{v} - \mathbf{u}'_{\delta}(t)) + a^{(0)}(\mathbf{u}_{\delta}(t), \mathbf{v} - \mathbf{u}'_{\delta}(t)) + \\
 &+ a^{(1)}(\mathbf{u}'_{\delta}(t), \mathbf{v} - \mathbf{u}'_{\delta}(t)) + \left\langle \frac{1}{\delta} [u'_{\delta n}(t)]^{kl}_+, [v_n]^{kl} - [u'_{\delta n}(t)]^{kl} \right\rangle_{\Gamma_c} + \\
 &+ \left\langle \mathcal{F}_c^{kl}([\mathbf{u}'_{\delta}(t)]^{kl}) [u'_{\delta n}(t)]^{kl}_+, |v_n|^{kl} - |[u'_{\delta n}(t)]^{kl}| \right\rangle_{\Gamma_c} \} dt \geq \\
 &\geq \int_I (\mathbf{f}(t), \mathbf{v} - \mathbf{u}'_{\delta}(t)) dt.
 \end{aligned} \tag{95}$$

Here we assume that  $\mathbf{u}'_2$  is extended onto the whole domain  $\Omega$ .

In the second step the regularization technique will be used. The functional  $j(\mathbf{v})$  is not Gâteaux differentiable, therefore we have to consider the function  $\varphi_{\varepsilon} : \mathbb{R} \rightarrow \mathbb{R}$  defined by

$$\varphi_{\varepsilon}(x) = \sqrt{x^2 + \varepsilon^2} - \varepsilon,$$

which regularizes the function  $x \rightarrow |x|$ . The function  $\varphi_\varepsilon$  is twice differentiable and the following inequality

$$||x| - \varphi_\varepsilon(|x|)| \leq \varepsilon, \quad \forall x \in \mathbb{R}, \varepsilon \geq 0,$$

holds.

Then we have the penalized-regularized problem:

**Problem**  $(\mathcal{P})_{vpr}$ : Find  $\mathbf{u}_{\delta\varepsilon}$  with  $\mathbf{u}'_{\delta\varepsilon} \in \mathcal{V} \cap B(I; L^{2,N}(\Omega))$  and  $\mathbf{u}_{\delta\varepsilon}(\mathbf{x}, 0) = \mathbf{u}_0(\mathbf{x})$ ,  $\mathbf{u}'_{\delta\varepsilon}(\mathbf{x}, 0) = \mathbf{u}_1(\mathbf{x})$ , such that for all  $\mathbf{v} \in \mathcal{V}$ , there holds

$$\begin{aligned} & \int_I \{(\mathbf{u}''_{\delta\varepsilon}(t), \mathbf{v} - \mathbf{u}'_{\delta\varepsilon}(t)) + (\alpha \mathbf{u}'_{\delta\varepsilon}(t), \mathbf{v} - \mathbf{u}'_{\delta\varepsilon}(t)) + a^{(0)}(\mathbf{u}_{\delta\varepsilon}(t), \mathbf{v} - \mathbf{u}'_{\delta\varepsilon}(t)) + \\ & + a^{(1)}(\mathbf{u}'_{\delta\varepsilon}(t), \mathbf{v} - \mathbf{u}'_{\delta\varepsilon}(t)) + \int_{\cup_{k,l} \Gamma_c^{kl}} \frac{1}{\delta} [u'_{\delta\varepsilon n}(t)]_+^{kl} ([v_n]^{kl} - [u'_{\delta\varepsilon n}(t)]^{kl}) ds + \\ & + \int_{\cup_{k,l} \Gamma_c^{kl}} \frac{1}{\delta} \mathcal{F}_c^{kl}([u'_{\delta\varepsilon t}(t)]^{kl}) [u'_{\delta\varepsilon n}(t)]_+^{kl} (\varphi_\varepsilon([v_t']^{kl}) - \varphi_\varepsilon([u'_{\delta\varepsilon t}(t)]^{kl})) ds \} dt \geq \\ & \geq \int_I (\mathbf{f}(t), \mathbf{v} - \mathbf{u}'_{\delta\varepsilon}(t)) dt. \end{aligned} \quad (96)$$

In order to investigate the existence solutions to (93) we introduce the equivalent problem:

**Problem**  $(\mathcal{P})_{vpre}$ : Find  $\mathbf{u}_{\delta\varepsilon}$  with  $\mathbf{u}'_{\delta\varepsilon} \in \mathcal{V} \cap B(I; L^{2,N}(\Omega))$  and  $\mathbf{u}_{\delta\varepsilon}(\mathbf{x}, 0) = \mathbf{u}_0(\mathbf{x})$ ,  $\mathbf{u}'_{\delta\varepsilon}(\mathbf{x}, 0) = \mathbf{u}_1(\mathbf{x})$ , such that for all  $\mathbf{v} \in \mathcal{V}_0$ , there holds

$$\begin{aligned} & \int_I \{(\mathbf{u}''_{\delta\varepsilon}(t), \mathbf{v}) + (\alpha \mathbf{u}'_{\delta\varepsilon}(t), \mathbf{v}) + a^{(0)}(\mathbf{u}_{\delta\varepsilon}(t), \mathbf{v}) + a^{(1)}(\mathbf{u}'_{\delta\varepsilon}(t), \mathbf{v}) + \\ & + \int_{\cup_{k,l} \Gamma_c^{kl}} \frac{1}{\delta} [u'_{\delta\varepsilon n}(t)]_+^{kl} [v_n]^{kl} ds + \int_{\cup_{k,l} \Gamma_c^{kl}} \frac{1}{\delta} \mathcal{F}_c^{kl}([u'_{\delta\varepsilon t}(t)]^{kl}) [\mathbf{u}'_{\delta\varepsilon t}(t)]_+^{kl} \cdot \\ & \cdot \nabla \varphi_\varepsilon([u'_{\delta\varepsilon t}(t)]^{kl}) [\mathbf{v}_t]^{kl} ds \} dt = \int_I (\mathbf{f}(t), \mathbf{v}) dt, \end{aligned} \quad (97)$$

since  $\nabla \varphi_\varepsilon([u_t']^{kl}) ([v_t]^{kl} - [u_t']^{kl}) \leq \varphi_\varepsilon([v_t]^{kl}) - \varphi_\varepsilon([u_t']^{kl})$ .

### Existence results

The existence of  $\mathbf{u}_{\delta\varepsilon}$  will be proved by means of the finite-dimensional approximation (Faedo-Galerkin) by the usual way. For simplicity we put  $\mathbf{u} = \mathbf{u}_{\delta\varepsilon}$ . We construct the Galerkin basis  $\{\mathbf{v}_i\}$  of the space  $V_0$  as usual, then  $V_m = \text{span}\{\mathbf{v}_1, \dots, \mathbf{v}_m\}$ ,  $\cup_{m=1}^\infty V_m$  is dense in  $V_0$ . Let us put

$$\mathbf{u}_m(t, \mathbf{x}) = \mathbf{u}_2(t, \mathbf{x}) + \sum_{j=1}^m c_{mj}(t) \mathbf{v}_j(\mathbf{x}), \quad t \in I, \mathbf{x} \in \Omega, m \in \mathbb{N}.$$

Then the approximate solution of order  $m$  satisfies the system

$$\begin{aligned} & (\mathbf{u}''_m(t), \mathbf{v}_j) + (\alpha \mathbf{u}'_m(t), \mathbf{v}_j) + a^{(0)}(\mathbf{u}_m(t), \mathbf{v}_j) + a^{(1)}(\mathbf{u}'_m(t), \mathbf{v}_j) + \\ & + \left\langle \frac{1}{\delta} [u_{mn}^k(t) - u_{mn}^l(t)]_+, v_{jn}^k - v_{jn}^l \right\rangle_{\cup_{k,l} \Gamma_c^{kl}} + \int_{\cup_{k,l} \Gamma_c^{kl}} \frac{1}{\delta} \mathcal{F}_c^{kl}(\mathbf{u}_{mt}^k(t) - \mathbf{u}_{mt}^l(t)) \cdot \\ & \cdot [u_{mn}^k(t) - u_{mn}^l(t)]_+ \nabla \varphi_\varepsilon(\mathbf{u}_{mt}^k(t) - \mathbf{u}_{mt}^l(t)) (\mathbf{v}_{jt}^k - \mathbf{v}_{jt}^l) ds = \\ & = (\mathbf{f}(t), \mathbf{v}_j) \quad j = 1, \dots, m, \quad \text{a.e. } t \in I, \end{aligned} \quad (98)$$

with approximate initial conditions

$$\langle \mathbf{u}_m(\mathbf{x}, 0) - \mathbf{u}_0(\mathbf{x}), \mathbf{v}_j \rangle_\Omega = 0, \langle \mathbf{u}'_m(\mathbf{x}, 0) - \mathbf{u}_1(\mathbf{x}), \mathbf{v}_j \rangle_\Omega = 0. \quad (99)$$

The system represents an initial value problem for a system of ordinary differential equations of the second order for a.e.  $t \in I$ . The solvability of such a system follows from the theory of systems of ordinary differential equations. The global existence follows from the a priori estimates.

### A priori estimates:

Firstly the term

$$\int_0^t \int_{\cup_{k,l} \Gamma_c^{kl}} \frac{1}{\delta} \mathcal{F}_c^{kl}([\mathbf{u}'_{mt}(\tau)]^{kl}) [u'_{mn}(\tau)]_+^{kl} \cdot \nabla \varphi_\varepsilon([\mathbf{u}'_{mt}(\tau)]^{kl}) [\mathbf{v}_{jt}]^{kl} ds d\tau \geq 0.$$

In order to pass to the limit  $m \rightarrow \infty$  of the Faedo-Galerkin parameter we need suitable a priori estimates.

Multiplying (98) by  $c'_{mj}(t)$ , summing over  $j$ , integrating over  $[0, t]$ ,  $t \in I$ , and putting

$$\mathbf{u}'_m(t) - \mathbf{u}'_2(t) = \sum_{j=1}^m c'_{mj}(t) \mathbf{v}_j,$$

then we have

$$\begin{aligned} & \int_0^t \{ (\mathbf{u}''_m(\tau), \mathbf{u}'_m(\tau)) + (\alpha \mathbf{u}'_m(\tau), \mathbf{u}'_m(\tau)) + a^{(0)}(\mathbf{u}_m(\tau), \mathbf{u}'_m(\tau)) + \\ & + a^{(1)}(\mathbf{u}'_m(\tau), \mathbf{u}'_m(\tau)) + \left\langle \frac{1}{\delta} [u'_{mn}(\tau)]_+^{kl}, [u'_{mn}(\tau)]^{kl} \right\rangle_{\cup_{k,l} \Gamma_c^{kl}} + \\ & + \int_{\cup_{k,l} \Gamma_c^{kl}} \frac{1}{\delta} \mathcal{F}_c^{kl}([\mathbf{u}'_{mt}(\tau)]^{kl}) [u'_{mn}(\tau)]_+^{kl} \cdot \nabla \varphi_\varepsilon([\mathbf{u}'_{mt}(\tau)]^{kl}) [\mathbf{u}'_{mt}(\tau)]^{kl} ds \} d\tau = \\ & = \int_0^t \{ (\mathbf{f}(\tau), \mathbf{u}'_m(\tau) - \mathbf{u}'_2(\tau)) + (\mathbf{u}''_m(\tau), \\ & \mathbf{u}'_2(\tau)) + a^{(0)}(\mathbf{u}_m(\tau), \mathbf{u}'_2(\tau)) + a^{(1)}(\mathbf{u}'_m(\tau), \mathbf{u}'_2(\tau)) \} d\tau. \end{aligned} \quad (100)$$

We estimate separate terms in (100). In respect of the definition of the space  $\mathcal{V}$  we have  $[u_{2n}]^{kl} = 0$  on  $\cup_{k,l} \Gamma_c^{kl}$ , and furthermore, we have  $\mathbf{u}'_m(0) = \mathbf{u}_1$  and as  $\nabla \varphi_\varepsilon([\mathbf{u}'_{mt}]^{kl}) [\mathbf{u}'_{mt}]^{kl} \geq 0$  then the last term on the left-hand side is  $\geq 0$ . Completing all estimates, then after some modification, using the Korn inequality and the Gronwall lemma, there exists a constant  $C$ , which does not depend on the Faedo-Galerkin index  $m$  and parameters  $\delta$  and  $\varepsilon$ , such that we have

$$\begin{aligned} & \|\mathbf{u}'_m(t)\|_{L^\infty(I; L^{2,N}(\Omega))}^2 + \|\mathbf{u}_m(t)\|_{L^\infty(I; H^{1,N}(\Omega))}^2 + \|\mathbf{u}'_m(t)\|_{0,1,Q}^2 \\ & + \frac{1}{\delta} \| [u'_{mn}(t) - u''_{mn}(t)]_+ \|_{0,\Gamma_c(t)}^2 \leq C, \end{aligned} \quad (101)$$

which proves the existence of the solution  $\mathbf{u}_m(t)$  for all  $t \in I$ . Moreover, it holds

$$\|\mathbf{u}_m(t)\|_{0,1,Q}^2 = \int_0^{t_p} \|\mathbf{u}_m(t)\|_{1,N}^2 dt \leq t_p \|\mathbf{u}_m(t)\|_{L^\infty(I;H^{1,N}(\Omega))}^2 \leq t_p C_0 = C. \quad (102)$$

In the limit process  $m \rightarrow \infty$  of the Faedo-Galerkin parameter  $m$ , where  $\varepsilon, \delta$  being fixed, besides the subsequence  $\{\mathbf{u}_{m_j}\}$ , the solutions of the Faedo-Galerkin equation, the strong convergence of  $\{\mathbf{u}'_{m_j}\}$  in  $L^2(\mathcal{SF}_c)$  is needed. The existence of such subsequence can be achieved with the help of compact imbedding theorems for Sobolev spaces and a priori estimates for  $\mathbf{u}'_m$ .

Let us put in (98) as the test function  $\mathbf{v}_k = \mathbf{u}'_m(t_2) - \mathbf{u}'_m(t_1) - \mathbf{u}'_2(t_2) + \mathbf{u}'_2(t_1)$  for a.e.  $t$ , integrate over  $t$  from  $t_1$  to  $t_2$ , multiplying the result by  $|t_2 - t_1|^{-2(1-\gamma)}$ ,  $0 < \gamma < \frac{1}{2}$  and then integrate over  $t_1$  and  $t_2$ ,  $t_1 < t_2$ ,  $0 < t_1 < t_p$ ,  $0 < t_2 < t_p$ . Then we obtain

$$\begin{aligned} & \int_0^{t_p} \int_{t_1}^{t_p} \int_{t_1}^{t_2} \{(\mathbf{u}''_m(t), \mathbf{u}'_m(t_2) - \mathbf{u}'_m(t_1) - \mathbf{u}'_2(t_2) + \mathbf{u}'_2(t_1))|t_2 - t_1|^{-2(1-\gamma)} + \\ & + (\alpha \mathbf{u}'_m(t), \mathbf{u}'_m(t_2) - \mathbf{u}'_m(t_1) - \mathbf{u}'_2(t_2) + \mathbf{u}'_2(t_1))|t_2 - t_1|^{-2(1-\gamma)} + \\ & + a^{(0)}(\mathbf{u}_m(t), \mathbf{u}'_m(t_2) - \mathbf{u}'_m(t_1) - \mathbf{u}'_2(t_2) + \mathbf{u}'_2(t_1))|t_2 - t_1|^{-2(1-\gamma)} + \\ & + a^{(1)}(\mathbf{u}'_m(t), \mathbf{u}'_m(t_2) - \mathbf{u}'_m(t_1) - \mathbf{u}'_2(t_2) + \mathbf{u}'_2(t_1))|t_2 - t_1|^{-2(1-\gamma)} + \\ & + \left\langle \frac{1}{\delta} [u'_{mn}(t)]_+^{kl}, u'_{mn}(t_2) - u'_{mn}(t_1) - u'_{mn}(t_2) + u'_{mn}(t_1) \right\rangle_{\cup_{k,l} \Gamma_c^{kl}}} \\ & |t_2 - t_1|^{-2(1-\gamma)} + \int_{\cup_{k,l} \Gamma_c^{kl}} \frac{1}{\delta} \mathcal{F}_c^{kl}([u'_{mt}(t)]^{kl})[u'_{mn}(t)]_+^{kl} \nabla \varphi_\varepsilon([u'_{mt}(t)]^{kl} \cdot \\ & \cdot (\mathbf{u}'_{mt}(t_2) - \mathbf{u}'_{mt}(t_1) - \mathbf{u}'_{mt}(t_2) + \mathbf{u}'_{mt}(t_1)))|t_2 - t_1|^{-2(1-\gamma)} ds\} dt dt_2 dt_1 = \\ & = \int_0^{t_p} \int_{t_1}^{t_p} \int_{t_1}^{t_2} (\mathbf{f}(t), \mathbf{u}'_m(t_2) - \mathbf{u}'_m(t_1) - \mathbf{u}'_2(t_2) + \\ & + \mathbf{u}'_2(t_1))|t_2 - t_1|^{-2(1-\gamma)} dt dt_2 dt_1. \end{aligned} \quad (103)$$

Next, using the technique of [9] and [10] we find

$$\begin{aligned} & |\mathbf{u}'_m|_{H^{\frac{1}{2}-\gamma}(I;L^{2,N}(\Omega))}^2 + |\mathbf{u}_m|_{H^{\frac{1}{2}-\gamma}(I;L^{2,N}(\Omega))}^2 \leq \\ & \leq C_1 |\mathbf{u}'_m|_{H^{\frac{1}{2}-\gamma}(I;L^{2,N}(\Omega))}^2 + C_2 |\mathbf{u}_m|_{H^{\frac{1}{2}-\gamma}(I;L^{2,N}(\Omega))}^2 + C_3(t_p, \gamma, \delta), \end{aligned} \quad (104)$$

where  $C_1, C_2, C_3$  are constants independent of  $\varepsilon$  and  $m$ .

From the interpolation theorem [10] follows, that the space  $H^{\frac{1}{2}-\gamma}(I;L^{2,N}(\Omega)) \cap L^2(I;H^{1,N}(\Omega))$  is continuously embedded in  $H^{(\frac{1}{2}-\gamma)^2}(I;H^{\frac{1}{2}+\gamma,N}(\Omega))$ . Since  $H^{\frac{1}{2}+\gamma,N}(Q)$  is continuously embedded in  $L^{2,N}(\Gamma_c(t))$ , then

$$|\mathbf{u}'_m|_{H^{(\frac{1}{2}-\gamma)^2}(\Gamma_c(t))} + |\mathbf{u}_m|_{H^{(\frac{1}{2}-\gamma)^2}(\Gamma_c(t))} \leq C(t_p, \gamma, \delta), \quad (105)$$

where the constant  $C(t_p, \gamma, \delta) > 0$  is independent of  $m$  and  $\varepsilon$ .

From the estimates (101), (102) and (105) there exists a subsequence  $\{\mathbf{u}_j\} \equiv \{\mathbf{u}_{m_j}\}$ ,  $\lim_{j \rightarrow \infty} m_j = 0$ , such that

$$\begin{aligned} \mathbf{u}_j &\rightharpoonup \mathbf{u} \quad \text{in } L^2(I; H^{1,N}(\Omega)), \\ \mathbf{u}'_j &\rightharpoonup \mathbf{u}' \quad \text{weakly in } L^2(I; H^{1,N}(\Omega)) \text{ and strongly in } L^2(\mathcal{SF}_c), \\ \frac{1}{\delta}[u'_{jn}]^{kl} &\rightharpoonup \frac{1}{\delta}[u'_n]^{kl} \quad \text{in } L^2(\cup_{k,l} \Gamma_c^{kl} \times I) \\ &\text{and} \\ \mathcal{F}_c^{kl}(\mathbf{u}'_{jt}) &\rightharpoonup \mathcal{F}_c^{kl}(\mathbf{u}'_t) \quad \text{weakly-* in } L^\infty(\mathcal{SF}_c). \end{aligned}$$

Let us put instead of  $\mathbf{v}_j$  the test function  $\mathbf{v}(t) \in C_0^1(I; V_m)$  in (98) for  $m = m_j$ . Then integrate the obtained result over  $t$  from 0 to  $t_p$  and let  $j \rightarrow \infty$ . After some modifications, we then find

$$\begin{aligned} \|\mathbf{u}'\|_{0,1,\Omega \times I} &\leq C_1, \quad \|\mathbf{u}\|_{0,1,\Omega \times I} \leq C_2, \\ \|\mathbf{u}''\|_{\mathcal{V}'_0} &\leq C_3(\delta), \quad |\mathbf{u}_m|_{H(\frac{1}{2}-\gamma)_{(\Gamma_c(t))}^2} \leq C_4(t_p, \gamma, \delta). \end{aligned} \quad (106)$$

where we denoted the function  $\mathbf{u}_{\delta,\varepsilon} \equiv \mathbf{u}$ .

Now we will prove the limit over  $\varepsilon$ , so that (97) converges to (95) for  $\varepsilon \rightarrow 0$ . Then from the above estimates (106) for every  $\delta > 0$  there exists a subsequence  $\{\mathbf{u}_j\} \equiv \{\mathbf{u}_{\delta,\varepsilon_j}\}$  of a sequence  $\{\mathbf{u}_{\delta,\varepsilon}\}$ ,  $\lim_{j \rightarrow \infty} \varepsilon_j = 0$ , such that

$$\begin{aligned} \mathbf{u}_j &\rightharpoonup \mathbf{u} \quad \text{in } L^2(I; H^{1,N}(\Omega)), \\ \mathbf{u}'_j &\rightharpoonup \mathbf{u}' \quad \text{weakly in } L^2(I; H^{1,N}(\Omega)) \text{ and strongly in } L^2(\mathcal{SF}_c), \\ \mathbf{u}''_j &\rightharpoonup \mathbf{u}'' \quad \text{weakly-* in } \mathcal{V}'_0, \\ \frac{1}{\delta}[u'_{jn}t]^{kl} &\rightharpoonup \frac{1}{\delta}[u'_n]^{kl} \quad \text{in } L^2\left(\cup_{k,l} \Gamma_c^{kl} \times I\right), \\ \mathcal{F}_c^{kl}([\mathbf{u}'_{jt}]^{kl}) &\rightharpoonup \mathcal{F}_c^{kl}([\mathbf{u}'_t]^{kl}) \quad \text{weakly-* in } L^\infty(\mathcal{SF}_c). \end{aligned}$$

Let  $\mathbf{u} \equiv \mathbf{u}_\delta$  be the solution of (95) and  $\mathbf{u}_j \equiv \mathbf{u}_{\delta,\varepsilon_j}$  be the solution of (97). Then firstly from (97), putting  $\mathbf{v} \in \mathcal{V}_0 \cap B(I; L^{2,N}(\Omega))$ , it follows

$$\begin{aligned} \lim_{j \rightarrow \infty} \int_0^{t_p} \left[ (\mathbf{u}''_j, \mathbf{v}) + a^{(0)}(\mathbf{u}_j, \mathbf{v}) + a^{(1)}(\mathbf{u}'_j, \mathbf{v}) + \int_{k,l} \Gamma_c^{kl} \frac{1}{\delta} [u'_{jn}]^{kl} [v_n]^{kl} ds \right] dt = \\ = \int_0^{t_p} \left[ (\mathbf{u}'', \mathbf{v}) + a^{(0)}(\mathbf{u}, \mathbf{v}) + a^{(1)}(\mathbf{u}', \mathbf{v}) + \int_{k,l} \Gamma_c^{kl} \frac{1}{\delta} [u'_n]^{kl} [v_n]^{kl} ds \right] dt. \end{aligned}$$

Hence, in the limit for  $j \rightarrow \infty$  we find

$$\|\mathbf{u}'_\delta\|_{0,1,Q} \leq c, \quad \|\mathbf{u}_\delta\|_{0,1,Q} \leq c. \quad (107)$$

At the end we must prove the convergence  $\mathbf{u}_\delta \rightarrow \mathbf{u}$ , where  $\mathbf{u}$  is the solution of (93). The convergence procedure can be repeated for penalty parameter  $\delta \rightarrow 0$ . From (107) there follows the existence of sequences  $\{\delta_j\}$ ,  $\lim_{j \rightarrow \infty} \delta_j = 0$  and  $\{\mathbf{u}_j\}$  such that the following convergence properties

$$\begin{aligned} \delta_j &\rightarrow 0, \quad \mathbf{u}'_j \rightharpoonup \mathbf{u}' \quad \text{weakly in } L^2(I; H^{1,N}(\Omega)) \text{ and strongly in } L^2(\mathcal{SF}_c), \\ -\frac{1}{\delta}[u'_{jn}]^{kl} &= \tau_n(\mathbf{u}_j) \rightharpoonup \tau_n(\mathbf{u}) \quad \text{in } L^2\left(\cup_{k,l} \Gamma_c^{kl} \times I\right) \end{aligned}$$

are valid. Performing the limit  $\delta \rightarrow 0$  in the penalized problem (95) then it can be shown that the limit  $\mathbf{u}$  is a solution of the original contact problem with friction.

Then we proved the following theorem:

**Theorem 6** *Let the assumptions concerning  $\Omega, \Gamma_r, r = \tau, u, c$  and physical data given in Presumption 1 be satisfied. Then there exists at least one weak solution of the dynamic contact problem with friction and damping in visco-elasticity with short memory.*

**Remark 4** *It can be shown, similarly as in [8], that the case in the classical linear elasticity is the special case of the problem in the linear visco-elasticity with short memory. Let  $\mathbf{u}_\lambda(t)$  and  $\mathbf{u}(t)$  be the solutions of the investigated problem (P) with  $\tau_{ij} = c_{ijkl}^{(0)} e_{kl}(\mathbf{u}(t)) + \lambda c_{ijkl}^{(1)} e_{kl}(\mathbf{u}(t))$ ,  $\lambda \rightarrow 0$ , in the first case and  $\tau_{ij} = c_{ijkl}^{(0)} e_{kl}(\mathbf{u}(t))$  in the second one, then it can be shown that  $\mathbf{u}_\lambda(t) \rightarrow \mathbf{u}(t)$  for  $\lambda \rightarrow 0$ .*

**Remark 5** *If the geodynamic processes are assumed to be run very slowly, then the rock masses are deformed very slowly, or if the geodynamic processes are assumed to be run with constant rate of motion, therefore, the inertia forces can be neglected. Then we speak about the quasi-static contact problems. Next, such type of problems will be studied numerically together with the dynamic contact problems both formulated in displacements.*

### 3.3. Models Based on Quasi-static and Dynamic Contact Problems Formulated in Displacements

#### 3.3.1. Introduction

In this part of the study we will propose a computational efficient methodology for combining multibody quasi-static and dynamic simulation methods with a deformable contact model formulated in displacements. We will deal with a new methodology for simulating deformable contact in the colliding geological bodies within a multibody dynamics, based on the analyses of the quasi-static and dynamic contact multibody problems in (visco-)elastic rheology. In both these problems the contact Signorini conditions will be formulated with the displacements while the Coulombian friction condition is formulated in the displacement velocities. Therefore, the variational formulation of the quasi-static contact problem is a little more complicated than in the static case, while the original dynamic contact problems with Coulombian friction for the contact conditions formulated in displacements are from the present day analyze technique point of view an open problem. Therefore, the original quasi-static and the original dynamic contact problems will be reformulated to the contact problems with a given friction. The great problem represents the determination of couples of points which are in actual or potential contact in different times during the geological process. Therefore, similarly as in the previous case the assumptions about the smoothness of contact parts of the boundaries of the multibody geological system, about the coefficients of friction and about the short time duration of the geological process are necessary.

The model considered will describe a cracked geological body(ies) (with nonpenetration conditions), which will clearly appear as including the case of the contact between two different bodies, say the  $s$  and  $m$  bodies and describing the first phase of the landslide

evolution. In the classical fracture mechanics analytical approaches were based on linear boundary value problem formulation on non-Lipschitzian domains, and therefore, the aim was to study solution singularities caused by the non-smooth boundary of the investigated domain and then to construct corresponding singular solution. Recent variational methods are based on unilaterally constrained crack problems. The variational formulations lead to variational inequalities and provide the acceptable spaces for the solutions to crack problems that are singular at the crack tip. Numerically the problems are solved by finite element and boundary element methods ([19, 37], etc.).

In the study the quasi-static and the dynamic multibody contact problems with Coulomb friction in linear visco-elasticity with short memory and damping in  $N$ -dimensions, formulated in displacements, will be reformulated for numerical solutions to contact problems with given frictions and we will speak about the approximate multibody contact problems. The notation used in the mortar approach will be used.

### 3.3.2. Formulation of the Dynamic Model Problems

In this formulation the Signorini conditions are formulated in displacements, while the Coulombian law of friction is formulated in velocities, i.e. the time derivative  $\mathbf{u}'$  (displacement velocity) occurs in the friction law only.

Let  $I = (0, t_p)$  be a time interval. Let  $\Omega \subset \mathbb{R}^N$ ,  $N = 2, 3$ , be a region occupied by a system of geological bodies of arbitrary shapes  $\Omega^\iota$  such that  $\Omega = \bigcup_{\iota=1}^r \Omega^\iota$ . Let  $\Omega^\iota$  have Lipschitz boundaries  $\partial\Omega^\iota$  and let us assume that  $\partial\Omega = \Gamma_\tau \cup \Gamma_u \cup \Gamma_c$ , where the disjoint parts  $\Gamma_\tau, \Gamma_u, \Gamma_c$  are open subsets with nonzero measures. Moreover, let  $\Gamma_u = {}^1\Gamma_u \cup {}^2\Gamma_u$  and  $\Gamma_c = \bigcup_{s,m} \Gamma_c^{sm}$ ,  $\Gamma_c^{sm} = \partial\Omega^s \cap \partial\Omega^m$ ,  $s \neq m$ ,  $s, m \in \{1, \dots, r\}$ . Let  $\Omega_t = I \times \Omega$  denote the time-space domain and let  $\Gamma_\tau(t) = \Gamma_\tau \times I$ ,  $\Gamma_u(t) = \Gamma_u \times I$ ,  $\Gamma_c(t) = \Gamma_c \times I$  denote the parts of its boundary  $\partial\Omega_t = \partial\Omega \times I$ .

Furthermore, let  $\mathbf{n}$  denote the outer unit normal vector of the boundary,  $u_n = u_i n_i$ ,  $\mathbf{u}_t = \mathbf{u} - u_n \mathbf{n}$ ,  $\tau_n = \tau_{ij} n_j n_i$ ,  $\boldsymbol{\tau}_t = \boldsymbol{\tau} - \tau_n \mathbf{n}$  be normal and tangential components of displacement and stress vectors  $\mathbf{u} = (u_i)$ ,  $\boldsymbol{\tau} = (\tau_i)$ ,  $\tau_i = \tau_{ij} n_j$ ,  $i, j = 1, \dots, N$ . Let  $\mathbf{F}, \mathbf{P}$  be the body and surface forces,  $\rho$  the density,  $\alpha(\mathbf{x}) \geq 0$  physically have a meaning of damping. Let us denote by  $\mathbf{u}' = (u'_k)$  the velocity vector. Let on  $\Gamma_c^{sm}$  the positive direction of the outer normal vector  $\mathbf{n}$  be assumed with respect to  $\Omega^s$ . Let us denote by  $[u_n]^{sm} = u_n^s - u_n^m$  the jump of the normal displacement across the contact zone between neighbouring geological bodies  $\Omega^s$  and  $\Omega^m$ . If one of the colliding bodies is absolutely rigid, say  $\Omega^m$ , then  $[u_n]^{sm} \equiv u_n^s$ . If the jump  $u_n^s - u_n^m \neq 0 \equiv d^{sm}$ , then we speak about a gap.

Let us denote by  ${}^a\Gamma_c^{sm} \subset \Gamma_c^{sm}$  the actual contact set, i.e. for which  $[u_n]^{sm} - d^{sm} = 0$  on  ${}^a\Gamma_c^{sm}$  and  $[u_n]^{sm} - d^{sm} < 0$  on  ${}^c\Gamma_c^{sm} = \Gamma_c^{sm} \setminus {}^a\Gamma_c^{sm}$ , where  $d^{sm}$  is a gap. In the crack case  $\Gamma_c^{sm}$  may be considered as a virtual interface between  $\Omega^s$  and  $\Omega^m$  (see the model described in Fig. 10).

**Remark 6** *The crack case: Let us introduce an open subset  $\Sigma \subset \mathbb{R}^{N-1}$  and let us assume that two faces of the crack can be parametrized by two  $C^1$  functions, say  $\varphi^s$  and  $\varphi^m$ , defined on  $\Sigma$ . We assume that  $\varphi^s(y) - \varphi^m(y) \geq 0$ ,  $\forall y \in \Sigma$  and we define each face  ${}^a\Gamma_c^\iota$ ,  $\iota = s, m$ , of the crack as the graph of  $\varphi^\iota$  on  $\Sigma$  that is  ${}^a\Gamma_c^\iota = \{(y, \varphi^\iota(y)); y \in \Sigma\}$ ,  $\iota = s, m$ . The gap between the two faces is given by  $\tilde{d}^{sm}(\xi) = \varphi^s(\xi) - \varphi^m(\xi)$  and the unit outward normal to*



${}^a\Gamma_c^\iota$  will be denoted  $\mathbf{n}^\iota : \Sigma \rightarrow \mathbb{R}^N$ , where the positive direction of the unit normal will be assumed to  ${}^a\Gamma_c^s$ . We introduce the following notation for normal and tangential components of the corresponding relative displacement vector  $\mathbf{u}^\iota$  and of the stress vector  $\boldsymbol{\tau}^\iota$ ,  $\iota = s, m$ :

$$\begin{aligned} u_n^\iota &= u_n^\iota(t, \xi) = \mathbf{u}^\iota(t, \xi, \varphi^\iota(\xi)) \cdot \mathbf{n}^\iota(\xi), \quad \mathbf{u}_t^\iota = \mathbf{u}_t^\iota(t, \xi) = \mathbf{u}^\iota - u_n^\iota \mathbf{n}^\iota, \quad \iota = s, m, \\ [u_n]^{sm} &= [u_n(t, \xi)]^{sm} = u_n^s - u_n^m, \quad [\mathbf{u}_t]^{sm} = [\mathbf{u}_t(t, \xi)]^{sm} = \mathbf{u}_t^s - \mathbf{u}_t^m, \\ \tau_n^\iota &= \tau_n^\iota(t, \xi) = (\boldsymbol{\tau}^\iota \mathbf{n}^\iota) \cdot \mathbf{n}^\iota, \quad \boldsymbol{\tau}_t^\iota = \boldsymbol{\tau}_t^\iota(t, \xi) = \boldsymbol{\tau}^\iota \mathbf{n}^\iota - (\boldsymbol{\tau}^\iota \mathbf{n}^\iota) \cdot \mathbf{n}^\iota = \boldsymbol{\tau}^\iota \mathbf{n}^\iota - \tau_n^\iota \mathbf{n}^\iota. \end{aligned}$$

For the normalized gap  $d^{sm} (\geq 0)$  between the two faces of the crack we find

$$d^{sm}(\xi) = (\varphi^s(\xi) - \varphi^m(\xi))(1 + |\nabla \varphi^s(\xi)|^2)^{-\frac{1}{2}}$$

and then the unilateral contact condition has the form

$$[u_n(t, \xi)]^{sm} \leq d^{sm}(\xi) \quad \forall \xi \in \Sigma,$$

and  $d^{sm} \in H_{00}^{\frac{1}{2}}(\Sigma)$ ,  $d^{sm} \geq 0$  almost everywhere on  $\Sigma$ . If in the crack case  ${}^c\Gamma_c^{sm} = 0$ , then the problem  $(\mathcal{P})$  defined below is a classical multibody unilateral contact problem. Then the landslide evolution can be also comprehended like the evolution of the crack during time. The problem of dynamic unilateral contact problems with friction for the cracked geological bodies in (visco-)elastic rheology was studied e.g. in [19, 6]. In [6] the existence of the solution of problems with nonlocal friction between two cracked visco-elastic bodies was proved.

The stress strain relation will be defined by the Hooke's law in the usual sense,

$$\begin{aligned} \tau_{ij} &= \tau_{ij}(\mathbf{u}, \mathbf{u}') = c_{ijkl}^{(0)}(\mathbf{x}) e_{kl}(\mathbf{u}) + c_{ijkl}^{(1)}(\mathbf{x}) e_{kl}(\mathbf{u}'), \\ e_{ij}(\mathbf{u}) &= \frac{1}{2} \left( \frac{\partial u_i}{\partial x_j} + \frac{\partial u_j}{\partial x_i} \right), \quad i, j, k, l = 1, \dots, N, \end{aligned} \quad (108)$$

where  $c_{ijkl}^{(n)}(\mathbf{x})$ ,  $n = 0, 1$ , are elastic and viscous coefficients and  $e_{ij}(\mathbf{u})$  are components of the small strain tensor,  $N$  is the space dimension. For the tensors  $c_{ijkl}^{(n)}(\mathbf{x})$ ,  $n = 0, 1$ , we assume

$$\begin{aligned} c_{ijkl}^{(n)} &\in L^\infty(\Omega), \quad n = 0, 1, \quad c_{ijkl}^{(n)} = c_{jikl}^{(n)} = c_{klij}^{(n)} = c_{ilkj}^{(n)}, \\ c_{ijkl}^{(n)} e_{ij} e_{kl} &\geq c_0^{(n)} e_{ij} e_{ij} \quad \forall e_{ij}, \quad e_{ij} = e_{ji} \quad \text{and a.e. } \mathbf{x} \in \Omega, \quad c_0^{(n)} > 0. \end{aligned} \quad (109)$$

A repeated index implies summation from 1 to  $N$ .

The problem to be solved has the following classical formulation:

**Problem  $(\mathcal{P})$ :** Let  $N = 2, 3$ ,  $r \geq 2$ . Find a vector function  $\mathbf{u} : \bar{\Omega} \times I \rightarrow \mathbb{R}$ , satisfying

$$\begin{aligned} \rho^\iota \frac{\partial^2 u_i^\iota}{\partial t^2} + \alpha^\iota \frac{\partial u_i^\iota}{\partial t} &= \frac{\partial \tau_{ij}^\iota(\mathbf{u}^\iota, \mathbf{u}^{\iota'})}{\partial x_j} + F_i^\iota, \\ i, j &= 1, \dots, N, \quad \iota = 1, \dots, r, \quad (t, \mathbf{x}) \in \Omega_t^\iota = I \times \Omega^\iota, \end{aligned} \quad (110)$$

$$\tau_{ij}n_j = P_i, \quad i, j = 1, \dots, N, \quad (t, \mathbf{x}) \in \Gamma_\tau(t) = I \times \cup_{l=1}^r (\Gamma_\tau \cap \partial\Omega^l), \quad (111)$$

$$u_i = u_{2i}, \quad i = 1, \dots, N, \quad (t, \mathbf{x}) \in {}^1\Gamma_u(t) = I \times \cup_{l=1}^r ({}^1\Gamma_u \cap \partial\Omega^l), \quad (112)$$

$$u_i = 0, \quad i = 1, \dots, N, \quad \text{on } {}^2\Gamma_u(t) = I \times \cup_{l=1}^r ({}^2\Gamma_u \cap \partial\Omega^l), \quad (113)$$

$$\left. \begin{aligned} [u_n]^{sm} &\leq d^{sm}, \quad \tau_n^s = -\tau_n^m \equiv \tau_n^{sm} \leq 0, \\ ([u_n]^{sm} - d^{sm})\tau_n^{sm} &= 0, \\ [u_n]^{sm} = 0, \quad \text{then } |\tau_t^{sm}| &\leq \mathcal{F}_c^{sm}(0)|\tau_n^{sm}|, \\ [\mathbf{u}'_t]^{sm} = 0 &\implies |\tau_t^{sm}| < \mathcal{F}_c^{sm}(0)|\tau_n^{sm}|, \\ [\mathbf{u}'_t]^{sm} \neq 0 &\implies \tau_t^{sm} = -\mathcal{F}_c^{sm}([\mathbf{u}'_t]^{sm})|\tau_n^{sm}| \frac{[\mathbf{u}'_t]^{sm}}{||[\mathbf{u}'_t]^{sm}||}, \end{aligned} \right\} (t, \mathbf{x}) \in I \times \cup_{k,l} \Gamma_c^{kl}, \quad (114)$$

$$\mathbf{u}(\mathbf{x}, 0) = \mathbf{u}_0(\mathbf{x}), \quad \mathbf{u}'(\mathbf{x}, 0) = \mathbf{u}_1(\mathbf{x}), \quad \mathbf{x} \in \Omega, \quad (115)$$

where  $\mathbf{u}_0, \mathbf{u}_1, \mathbf{u}_2$  are given functions,  $\mathbf{u}_2$  has a time derivative  $\mathbf{u}'_2$ , and  $\mathbf{u}_0, \mathbf{u}_1$  satisfy static linear contact problem in elasticity with or without Coulombian friction and on  $\cup \Gamma_c^{sm}$  due to the equilibrium of forces  $\tau_{ij}(\mathbf{u}^s)n_j^s = -\tau_{ij}(\mathbf{u}^m)n_j^m$ .

The coefficient of friction  $\mathcal{F}_c^{sm} \equiv \mathcal{F}_c^{sm}(\mathbf{x}, \mathbf{u}')$  is globally bounded, non-negative and satisfies the Carathéodory property, i.e.  $\mathcal{F}_c^{sm}(\cdot, \mathbf{v})$  is measurable,  $\mathbf{v} \in \mathbb{R}$ , and  $\mathcal{F}_c^{sm}(\mathbf{x}, \cdot)$  is continuous for a.e.  $\mathbf{x} \in \Gamma_c^{sm}$ . Moreover, it has a compact support

$$\mathcal{SF}_c \equiv \sup_x p(\mathcal{F}_c) = \overline{\{(\mathbf{x}, t) \in \Gamma_c(t) = \Gamma_c \times I \mid \exists \mathbf{u}_t \quad \mathcal{F}_c^{sm}(\mathbf{x}, \mathbf{u}'_t) \neq 0\}}, \quad (116)$$

which depends on the space variable  $\mathbf{x}$  and since we model also the difference between the coefficients of friction and of stick as well as slip, it depends also on the tangential displacement rate component  $\mathbf{u}'_t$  (see Fig. 8). Furthermore, we denote by  $(y)_+ \equiv \max\{y, 0\}$  the positive part of  $y$ . Let us denote by  ${}^a\Gamma_c^{sm} \subset \Gamma_c^{sm}$  the actual contact set, i.e. for which  $[u_n]^{sm} - d^{sm} = 0$  on  ${}^a\Gamma_c^{sm}$  and  $[u_n]^{sm} - d^{sm} < 0$  on  ${}^c\Gamma_c^{sm} = \Gamma_c^{sm} \setminus {}^a\Gamma_c^{sm}$ , where  $d^{sm}$  is a gap. For the continuous displacement  $\mathbf{u}$  the actual contact zone  ${}^a\Gamma_c^{sm}$  is well-defined and closed subset of  $\cup \Gamma_c^{sm}$ .

In the quasi-static contact problems the system of geological bodies is assumed to be deformed very slowly and the damping coefficient of rock materials is assumed very small, therefore the inertia forces and the damping term in (110) can be neglected.

It is evident that for different model problems that simulate the moving landslides the boundary conditions can be modified.

### 3.3.3. The Quasi-static Multibody Contact Problems

In the case if the system of geological bodies is assumed to be deformed very slowly, then the inertia forces in the initial dynamic formulation can be neglected, and moreover, if we assume that the damping is also very small, then the damping term in dynamic formulation can be also neglected. In this formulation the Signorini conditions are formulated in displacements, while the Coulombian law is formulated in velocities, i.e. the time derivative  $\mathbf{u}'$  occurs in the friction law only, and moreover, the initial condition is formulated in displacements only, i.e.

$$\mathbf{u}(0, \mathbf{x}) = \mathbf{u}_0 \quad \text{for } \mathbf{x} \in \Omega. \quad (117)$$

Let

$$V = V(\Omega) = \{\mathbf{v} \in H^{1,N}(\Omega), \mathbf{v} = 0 \text{ on } \Gamma_u\} \quad \text{and} \quad \mathcal{V} = \mathbf{u}'_2 + V,$$

$$\mathcal{K}(t) = \{\mathbf{v} \in H^{1,N}(\Omega), \mathbf{v} = \mathbf{u}_2(t, \cdot) \text{ on } \Gamma_u \quad \text{and} \quad [v_n]^{sm} \leq d^{sm} \text{ on } \cup \Gamma_c^{sm}\}.$$

Then we have to solve the following variational problem:

**Problem** ( $\mathcal{P}$ ): Find a function  $\mathbf{u} \in \mathbf{u}_2 + H^1(I; V(\Omega))$  with  $\mathbf{u}(t, \cdot) \in \mathcal{K}(t)$  for a.e.  $t \in I$  such that for a.e.  $t \in I$  and every  $\mathbf{w} \in \mathcal{K}(t)$

$$a(\mathbf{u}, \mathbf{w} - \mathbf{u}) + \int_{\cup \Gamma_c^{sm}} \mathcal{F}_c^{sm} |\tau_n^{sm}(\mathbf{u})| (|[ \mathbf{w}_t ]^{sm} - [ \mathbf{u}_t ]^{sm} + [ \mathbf{u}'_t ]^{sm} | - |[ \mathbf{u}'_t ]^{sm} |) ds \geq$$

$$\geq (\mathbf{f}, \mathbf{w} - \mathbf{u}) \quad (118)$$

holds, where

$$a(\mathbf{u}, \mathbf{w}) = \int_{\Omega} \tau_{ij}(\mathbf{u}) e_{ij}(\mathbf{w}) d\mathbf{x}, \quad (\mathbf{f}, \mathbf{w}) = \int_{\Omega} \mathbf{F} \cdot \mathbf{w} d\mathbf{x} + \int_{\Gamma_{\tau}} \mathbf{P} \cdot \mathbf{w} ds.$$

Using the decomposition

$$\mathbf{w} - \mathbf{u} = (\mathbf{w} - \mathbf{u} + \mathbf{u}') - \mathbf{u}' = \mathbf{v} - \mathbf{u}',$$

then (118) can be rewritten as

$$a(\mathbf{u}, \mathbf{v} - \mathbf{u}') + \int_{\cup \Gamma_c^{sm}} \mathcal{F}_c^{sm} |\tau_n^{sm}(\mathbf{u})| (|[ \mathbf{v}_t ]^{sm} | - |[ \mathbf{u}'_t ]^{sm} |) ds \geq$$

$$\geq (\mathbf{f}, \mathbf{v} - \mathbf{u}'), \quad (119)$$

where  $[ \mathbf{v}_t ]^{sm} \equiv \mathbf{v}_t^s - \mathbf{v}_t^m$ .

The existence of such problem is analyzed in [2, 10]. The proof is based on the Rothe method. The frictionless case in viscoelasticity is analyzed in [14]. Here the analysis of solvability is based on the theory of monotone operators. The numerical approximations can be based on the semi-discrete and the fully discrete techniques as well as on the Rothe method. All these problems were studied for unilateral contact of a visco-elastic body with a rigid foundation.

### 3.3.4. The Approximate Multibody Dynamic Contact Problems

The dynamic problem with damping and Coulombian friction ( $\mathcal{P}$ ), i.e. (110)-(115), where the Signorini conditions are formulated in velocities is analyzed in [55] and in this chapter. The dynamic contact problem with Coulombian friction where the Signorini conditions are formulated in displacements is up-to-date unsolved. Further, we will solve the other problem in which in every time level we will solve the contact problem with Tresca's friction, i.e. we will assume that the Coulombian law of friction depends in every time level on its value  $g_c^{kl}$  from the previous time level(s). For simplicity we can write  $g_c^{kl} \equiv (\mathcal{F}_c^{sm}([ \mathbf{u}'_t ]^{sm}) | \tau_n^{sm}(\mathbf{u}, \mathbf{u}') |)(t - \delta t)$ , where  $g_c^{kl}$  is non-negative function and has a meaning of a given friction limit (or a given friction bound, i.e., the magnitude of the limiting friction traction at which slip originates) and  $-g_c^{kl}$  is a given frictional force and  $\delta t$  is a

time element. In this section the problem will be solved by using the semi-implicit scheme in time and the FEM method in space. The other possibilities are represented by the explicit and fully-implicit schemes in time and the FEM method in space or by the Rothe or the Newmark methods.

Multiplying (110) by  $\mathbf{v} - \mathbf{u}$ , integrating the result over  $\Omega$ , using the Green theorem, the boundary conditions and contact conditions in displacements, then we have

**Problem**  $(\mathcal{P})_v$ : Find a displacement field  $\mathbf{u} : \bar{I} \rightarrow V$  such that  $\mathbf{u}(t) \in K$  for a.e.  $t \in I$ , and

$$\begin{aligned} & (\mathbf{u}''(t), \mathbf{v} - \mathbf{u}(t)) + (\alpha \mathbf{u}'(t), \mathbf{v} - \mathbf{u}(t)) + a^{(0)}(\mathbf{u}(t), \mathbf{v} - \mathbf{u}(t)) + \\ & + a^{(1)}(\mathbf{u}'(t), \mathbf{v} - \mathbf{u}(t)) + j(\mathbf{v}) - j(\mathbf{u}(t)) \geq (\mathbf{f}(t), \mathbf{v} - \mathbf{u}(t)) \\ & \forall \mathbf{v} \in K, \text{ a.e. } t \in I, \end{aligned} \quad (120)$$

$$\mathbf{u}(\mathbf{x}, 0) = \mathbf{u}_0(\mathbf{x}), \mathbf{u}'(\mathbf{x}, 0) = \mathbf{u}_1(\mathbf{x}), \quad (121)$$

where we assume that the initial data  $\mathbf{u}_0, \mathbf{u}_1$  satisfies the static contact multibody linear elastic problem (see e.g. [42, 43], where

$$\begin{aligned} (\mathbf{u}'', \mathbf{v}) &= \sum_{\iota=1}^r (\mathbf{u}''^\iota, \mathbf{v}^\iota) = \int_{\Omega} \rho u_i'' v_i d\mathbf{x}, \\ (\alpha \mathbf{u}', \mathbf{v}) &= \sum_{\iota=1}^r (\alpha^\iota \mathbf{u}'^\iota, \mathbf{v}^\iota) = \int_{\Omega} \alpha u_i' v_i d\mathbf{x}, \\ a^{(n)}(\mathbf{u}, \mathbf{v}) &= \sum_{\iota=1}^r a^{(n)\iota}(\mathbf{u}^\iota, \mathbf{v}^\iota) = \int_{\Omega} c_{ijkl}^{(n)} e_{kl}(\mathbf{u}) e_{ij}(\mathbf{v}) d\mathbf{x}, \quad n = 0, 1, \\ (\mathbf{f}, \mathbf{v}) &= \sum_{\iota=1}^r (\mathbf{f}^\iota, \mathbf{v}^\iota) = \int_{\Omega} F_i v_i d\mathbf{x} + \int_{\Gamma_\tau} P_i v_i ds, \\ j(\mathbf{v}) &= \sum_{\iota=1}^r j^\iota(\mathbf{v}^\iota) = \int_{\cup_{k,\iota} \Gamma_c^{kl}} g_c^{kl} |[\mathbf{v}_t]^{sm}| ds \equiv \langle g_c^{kl} |[\mathbf{v}_t]^{sm}| \rangle_{\cup \Gamma_c^{kl}}, \end{aligned}$$

where the bilinear forms  $a^{(n)}(\mathbf{u}, \mathbf{v})$ ,  $n = 0, 1$ , are symmetric in  $\mathbf{u}, \mathbf{v}$  and satisfy  $a^{(n)}(\mathbf{u}, \mathbf{u}) \geq c_0^{(n)} \|\mathbf{u}\|_{1,N}^2$ ,  $c_0^{(n)} = \text{const.} > 0$ ,  $a^{(n)}(\mathbf{u}, \mathbf{v}) \leq c_1^{(n)} \|\mathbf{u}\|_{1,N} \|\mathbf{v}\|_{1,N}$ ,  $c_1^{(n)} = \text{const.} > 0$ ,  $\mathbf{u}, \mathbf{v} \in V_0$ .

The problem  $(\mathcal{P})_v$  is equivalent with the following weak formulation:

**Problem**  $(\mathcal{P})_W$ : A weak solution of (110)-(115) is a function  $\mathbf{u} \in B(I; H^{1,N}(\Omega))$  with  $\mathbf{u}(t, \cdot) \in K$  for a.e.  $t \in I$ ,  $\mathbf{u}' \in L^2(I; H^{1,N}(\Omega)) \cap L^\infty(I; L^{2,N}(\Omega))$ ,  $\mathbf{u}'(t_p, \cdot) \in L^{2,N}(\Omega)$  such that for all  $\mathbf{v} \in H^{1,N}(\Omega(t))$  with  $\mathbf{v}(t, \cdot) \in K$  a.e. in  $I$  the following inequality holds

$$\begin{aligned} & \int_I \{ (\mathbf{u}''(t), \mathbf{v} - \mathbf{u}(t)) + (\alpha \mathbf{u}'(t), \mathbf{v} - \mathbf{u}(t)) + a^{(0)}(\mathbf{u}(t), \mathbf{v} - \mathbf{u}(t)) + \\ & + a^{(1)}(\mathbf{u}'(t), \mathbf{v} - \mathbf{u}(t)) + j(\mathbf{v}) - j(\mathbf{u}'(t)) \} dt \geq \int_I (\mathbf{f}(t), \mathbf{v} - \mathbf{u}(t)) dt, \\ & \mathbf{u}(\mathbf{x}, 0) = \mathbf{u}_0(\mathbf{x}), \quad \mathbf{u}'(\mathbf{x}, 0) = \mathbf{u}_1(\mathbf{x}). \end{aligned} \quad (122)$$

To prove the existence of the solution the following decomposition

$$\mathbf{v} - \mathbf{u} = \mathbf{v} - \mathbf{u} + \mathbf{u}' - \mathbf{u}' = \mathbf{w} - \mathbf{u}'$$

or, if the physical units are considered, the decomposition

$$\mathbf{v} - \mathbf{u} = \mathbf{v} - \mathbf{u} + c\mathbf{u}'c\mathbf{u}' = c\mathbf{w} - c\mathbf{u}',$$

are used, where  $c > 0$  is an arbitrary parameter that may be used to transformation of the physical units. Then the analysis is similar of that of [10], Chap. 4. For the proof of the existence theorem the techniques of penalization and regularization were used.

### 3.4. Numerical Solutions of Dynamic Model Problems Formulated in Displacements

Let  $\Omega$  be approximated by  $\Omega_h$ , being a polygon for the 2D case and a polyhedron for the 3D case, with the boundary  $\partial\Omega_h = \Gamma_{\tau h} \cup \Gamma_{uh} \cup \Gamma_{ch}$ . Let  $I = (0, t_p)$ ,  $t_p > 0$ , let  $m > 0$  be an integer, then  $\Delta t = t_p/m$ ,  $t_i = i\Delta t$ ,  $i = 0, \dots, m$ . Let  $\{\mathcal{T}_h\}$  be a regular family of finite element partitions  $\mathcal{T}_h$  of  $\overline{\Omega_h}$  compatible to the boundary subsets  $\overline{\Gamma}_{\tau h}$ ,  $\overline{\Gamma}_{uh}$  and  $\overline{\Gamma}_{ch}$ . Let  $V_h \subset V$  be the finite element space of linear elements corresponding to the partition  $\mathcal{T}_h$ . Then  $K_h = V_h \cap K$  is the set of continuous piecewise linear functions that vanish at the nodes of  $\overline{\Gamma}_{uh}$  and whose normal components are non-positive at the nodes on  $\cup_{k,l} \Gamma_c^{kl}$ . It is evident that  $K_h$  is a nonempty, closed, convex subset of  $V_h \subset V$ . Let  $\mathbf{u}_{0h} \in K_h$ ,  $\mathbf{u}_{1h} \in K_h$  be an approximation of  $\mathbf{u}_0$  or  $\mathbf{u}_1$ . Let us assume that  $\mathbf{u}_2 = 0$ . Further, we assume that the end points  $\overline{\Gamma}_{\tau h} \cup \overline{\Gamma}_{uh}$ ,  $\overline{\Gamma}_{uh} \cup \overline{\Gamma}_{ch}$ ,  $\overline{\Gamma}_{\tau h} \cup \overline{\Gamma}_{ch}$  coincide with the vertices of  $T_{hi}$ . Moreover, we will assume that the frictional term is approximated by its value in the previous time level(s), so that the frictional term at every  $t \in I$  is approximated by a given friction limit. Then we have the following semi-discrete problem:

**Problem  $(\mathcal{P})_h$ :** Find a displacement field  $\mathbf{u}_h : \overline{I} \rightarrow V_h$  with

$$\mathbf{u}_h(0) = \mathbf{u}_{0h}, \mathbf{u}'_h(0) = \mathbf{u}_{1h}, \quad (123)$$

such that for a.e.  $t \in I$ ,  $\mathbf{u}_h(t) \in K_h$  and

$$\begin{aligned} & (\mathbf{u}''_h(t), \mathbf{v}_h - \mathbf{u}_h(t)) + (\alpha \mathbf{u}'_h(t), \mathbf{v}_h - \mathbf{u}_h(t)) + a^{(0)}(\mathbf{u}_h(t), \mathbf{v}_h - \mathbf{u}_h(t)) + \\ & + a^{(1)}(\mathbf{u}'_h(t), \mathbf{v}_h - \mathbf{u}_h(t)) + j(\mathbf{v}_h) - j(\mathbf{u}_h(t)) \geq (\mathbf{f}(t), \mathbf{v}_h - \mathbf{u}_h(t)) \\ & \forall \mathbf{v}_h \in K_h, \end{aligned} \quad (124)$$

holds, where

$$\begin{aligned}
(\mathbf{u}_h'', \mathbf{v}_h) &= \sum_{\ell=1}^s (\mathbf{u}_h''^\ell, \mathbf{v}_h^\ell) = \int_{\Omega} \rho u_{hi}'' v_{hi} d\mathbf{x}, \\
(\alpha \mathbf{u}_h', \mathbf{v}_h) &= \sum_{\ell=1}^s (\alpha^\ell \mathbf{u}_h'^\ell, \mathbf{v}_h^\ell) = \int_{\Omega} \alpha u_{hi}' v_{hi} d\mathbf{x}, \\
a^{(n)}(\mathbf{u}_h, \mathbf{v}_h) &= \sum_{\ell=1}^s a^{(n)\ell}(\mathbf{u}_h^\ell, \mathbf{v}_h^\ell) = \int_{\Omega} c_{ijkl}^{(n)} e_{kl}(\mathbf{u}_h) e_{ij}(\mathbf{v}_h) d\mathbf{x} \quad n = 0, 1, \\
(\mathbf{f}, \mathbf{v}_h) &= \sum_{\ell=1}^s (\mathbf{f}^\ell, \mathbf{v}_h^\ell) = \int_{\Omega} F_i v_{hi} d\mathbf{x} + \int_{\Gamma_\tau} P_i v_{hi} ds, \\
j(\mathbf{v}_h) &= \sum_{\ell=1}^s j^\ell(\mathbf{v}_h^\ell) = \int_{\cup_{k,l} \Gamma_c^{kl}} g_c^{kl} |[\mathbf{v}_t]^{sm}| ds \equiv \langle g_c^{kl}, |[\mathbf{v}_t]^{sm}| \rangle_{\Gamma_c}. \quad (125)
\end{aligned}$$

and where we remark that the frictional term is approximated by the given frictional functional in the previous time level.

To prove the existence of the discrete (FEM) solution  $\mathbf{u}_h$  of the Problem  $(\mathcal{P})_h$  the decomposition

$$\mathbf{v}_h - \mathbf{u}_h = \mathbf{v}_h - \mathbf{u}_h + \mathbf{u}_h' - \mathbf{u}_h' = \mathbf{w}_h - \mathbf{u}_h'$$

and the penalty and regularization techniques are used. Then the proof will be similar to that as in the continuous case (and parallel to that of [10]). We remark that in the next the test function  $\mathbf{v}$  will correspond with the test function  $\mathbf{v} + \mathbf{u}' - \mathbf{u}$  in (122) and  $\mathbf{v}_h$  with the test function  $\mathbf{v}_h + \mathbf{u}_h' - \mathbf{u}_h$  in (124) after the used decompositions.

### 3.5. Algorithms

The algorithm can be based on the explicit, semi-implicit and fully-implicit schemes in time variable and the FE approximation in the space variables as well as on the Newark, Houbolt, Wilson, etc. schemes in time variable and FE approximation in the space variables. We limit ourselves to the semi-implicit FE method and the Newark method only.

It is evident that in every time step  $t \in I$  the system of geological bodies being in mutual contacts is deformed and the opposite bodies on the contact boundaries mutually move. Therefore, the initial geometry of the system of geological bodies changes, the geometry of the contact boundaries between them also changes. Thus, during the calculation the geometry of the system must be newly determined in every time step of the algorithm.

#### 3.5.1. Semi-implicit Scheme

Next, we shortly present derivation of the algorithm.

The algorithm is based on the semi-implicit scheme and on the assumption that the frictional term is approximated by its value in the previous time level(s). Such problem leads to the case with given friction.

Let  $m > 0$  be integer, then  $\Delta t = t_p/m$ ,  $t_i = i\Delta t$ ,  $i = 0, 1, \dots, m$ . Then

$$\begin{aligned} & (\Delta t^{-2}(\mathbf{u}_h^{i+1} - 2\mathbf{u}_h^i + \mathbf{u}_h^{i-1}), \mathbf{v}_h - \mathbf{u}_h^{i+1}) + (\Delta t^{-1}\alpha(\mathbf{u}_h^{i+1} - \mathbf{u}_h^i), \mathbf{v}_h - \mathbf{u}_h^{i+1}) + \\ & + a^{(0)}(\mathbf{u}_h^{i+1}, \mathbf{v}_h - \mathbf{u}_h^{i+1}) + a^{(1)}(\Delta t^{-1}(\mathbf{u}_h^{i+1} - \mathbf{u}_h^i), \mathbf{v}_h - \mathbf{u}_h^{i+1}) + \\ & + \int_{\cup_{s,m}\Gamma_c^{sm}} g_{ch}^{sm} |[\mathbf{v}_{th}]^{sm}| ds - \int_{\cup_{s,m}\Gamma_c^{sm}} g_{ch}^{sm} |[\mathbf{u}_{th}(t_{i+1})]^{sm}| ds \geq \\ & \geq (\mathbf{F}(t_{i+1}), \mathbf{v}_h - \mathbf{u}_h^{i+1}) \quad \forall \mathbf{v}_h \in K_h, \end{aligned}$$

where

$$\begin{aligned} \mathbf{u}_h^i &= \mathbf{u}_h(t_i), \quad \Delta \mathbf{u}_h^i = \mathbf{u}_h(t_i) - \mathbf{u}_h(t_{i-1}), \quad \mathbf{u}_h^0 = \mathbf{u}_{0h}, \\ \mathbf{u}_h^{-1} &= \mathbf{u}_{0h} - \Delta t \cdot \mathbf{u}_{1h}. \\ (\mathbf{F}(t_{i+1}), \mathbf{v}_h) &= \Delta t^2 (\mathbf{f}(t_{i+1}), \mathbf{v}_h) + (2\mathbf{u}_h^i - \mathbf{u}_h^{i-1}, \mathbf{v}_h) + \\ & + \Delta t (\alpha \mathbf{u}_h^i, \mathbf{v}_h) + \Delta t a_h^{(1)}(\mathbf{u}_h^i, \mathbf{v}_h), \end{aligned}$$

$$g_{ch}^{sm} = g_{ch}^{sm}(t_i) = \mathcal{F}_c^{sm}(\Delta t^{-1}([\Delta \mathbf{u}_{th}(t_i)]^{sm})) \left| \tau_n^{sm} \left( \mathbf{u}_h(t_i), \frac{\Delta \mathbf{u}_h(t_i)}{\Delta t} \right) \right|.$$

Then

$$\begin{aligned} & (\mathbf{u}_h^{i+1}, \mathbf{v}_h - \mathbf{u}_h^{i+1}) + \Delta t (\alpha \mathbf{u}_h^{i+1}, \mathbf{v}_h - \mathbf{u}_h^{i+1}) + \Delta t^2 a^{(0)}(\mathbf{u}_h^{i+1}, \mathbf{v}_h - \mathbf{u}_h^{i+1}) + \\ & + \Delta t a^{(1)}(\mathbf{u}_h^{i+1}, \mathbf{v}_h - \mathbf{u}_h^{i+1}) + \\ & + \Delta t^2 \int_{\cup_{s,m}\Gamma_c^{sm}} g_{ch}^{sm}(t_i) (|[\mathbf{v}_{th}]^{sm}| - |[\mathbf{u}_{th}(t_{i+1})]^{sm}|) ds \geq \\ & \geq (\mathbf{F}(t_{i+1}), \mathbf{v}_h - \mathbf{u}_h^{i+1}). \end{aligned} \tag{126}$$

The semi-discrete scheme is stable and converges.

For simplicity we set  $\mathbf{u}_h^{i+1} \equiv \mathbf{u}_h$ ,  $\tilde{g}_{ch}^{sm} = g_{ch}^{sm}(t_i)$ ,  $\mathbf{F}(t_{i+1}) \equiv \mathbf{f}_h$ , then (126) can be rewritten as

$$\begin{aligned} & (\mathbf{u}_h, \mathbf{v}_h - \mathbf{u}_h) + \Delta t (\alpha \mathbf{u}_h, \mathbf{v}_h - \mathbf{u}_h) + \Delta t^2 a^{(0)}(\mathbf{u}_h, \mathbf{v}_h - \mathbf{u}_h) + \\ & + \Delta t a^{(1)}(\mathbf{u}_h, \mathbf{v}_h - \mathbf{u}_h) + \Delta t^2 \int_{\cup_{s,m}\Gamma_c^{sm}} \tilde{g}_{ch}^{sm} (|[\mathbf{v}_{th}]^{sm}| - |[\mathbf{u}_{th}]^{sm}|) ds \geq \\ & \geq (\mathbf{f}_h, \mathbf{v}_h - \mathbf{u}_h), \quad t = t_{i+1} \in I. \end{aligned} \tag{127}$$

Let us define the bilinear form  $A(\mathbf{u}_h, \mathbf{v}_h)$  and the functional  $j(\mathbf{v}_h)$  by

$$\begin{aligned} A(\mathbf{u}_h, \mathbf{v}_h) &= (\mathbf{u}_h, \mathbf{v}_h) + \Delta t (\alpha \mathbf{u}_h, \mathbf{v}_h) + \Delta t^2 a^{(0)}(\mathbf{u}_h, \mathbf{v}_h) + \Delta t a^{(1)}(\mathbf{u}_h, \mathbf{v}_h), \\ j(\mathbf{v}_h) &= \Delta t^2 \int_{\cup_{k,l}\Gamma_c^{kl}} \tilde{g}_{ch}^{sm} |[\mathbf{v}_{th}]^{sm}| ds, \end{aligned} \tag{128}$$

where  $\tilde{g}_{ch}^{sm}$  represents the approximate given frictional limit.

Since we assumed that  $\rho \geq \rho_0 > 0$ ,  $\alpha \geq \alpha_0 > 0$  and since bilinear forms  $a_h^{(n)}(\mathbf{u}_h, \mathbf{v}_h)$ ,  $n = 0, 1$ , are symmetric in  $\mathbf{u}_h$  and  $\mathbf{v}_h$  and satisfy  $a^{(n)}(\mathbf{u}_h, \mathbf{u}_h) \geq c_0^{(n)} \|\mathbf{u}_h\|_{1,N}^2$ ,  $c_0^{(n)} =$

const.  $> 0$ ,  $|a^{(n)}(\mathbf{u}_h, \mathbf{v}_h)| \leq c_1^{(n)} \|\mathbf{u}_h\|_{1,N} \|\mathbf{v}_h\|_{1,N}$ ,  $c_1^{(n)} = \text{const.} > 0$ ,  $n = 0, 1$ ,  $\mathbf{u}_h, \mathbf{v}_h \in V_h$ , then the bilinear form  $A(\mathbf{u}_h, \mathbf{v}_h)$  is also symmetric in  $\mathbf{u}_h$  and  $\mathbf{v}_h$  and

$$\begin{aligned} A(\mathbf{u}_h, \mathbf{v}_h) &\geq a_0 \|\mathbf{u}_h\|_{1,N}^2, \quad c_0^{(n)} = \text{const.} > 0, \\ |A(\mathbf{u}_h, \mathbf{v}_h)| &\leq a_1 \|\mathbf{u}_h\|_{1,N} \|\mathbf{v}_h\|_{1,N}, \quad a_1 = \text{const.} > 0, \quad \mathbf{u}_h, \mathbf{v}_h \in V_{0h}, \end{aligned} \quad (129)$$

hold.

Then we have to solve in every time level the equivalent problem (we remark that we denoted  $\mathbf{u}_h \equiv \mathbf{u}_h^{i+1}$  for  $t = t_{i+1}$ ):

**Problem**  $(\mathcal{P}_A)_h$ : find  $\mathbf{u}_h \in K_h$ , a.e.  $t = t_{i+1} \in I$ , such that

$$A(\mathbf{u}_h, \mathbf{v}_h - \mathbf{u}_h) + j(\mathbf{v}_h) - j(\mathbf{u}_h) \geq (\mathbf{f}_h, \mathbf{v}_h - \mathbf{u}_h), \quad \forall \mathbf{v}_h \in K_h, \quad t = t_{i+1} \in I. \quad (130)$$

Let us introduce the functional  $\mathcal{L}(\mathbf{v}_h)$  by

$$\mathcal{L}(\mathbf{v}_h) = \mathcal{L}_0(\mathbf{v}_h) + j(\mathbf{v}_h),$$

where

$$\mathcal{L}_0(\mathbf{v}_h) = \frac{1}{2} A(\mathbf{v}_h, \mathbf{v}_h) - (\mathbf{f}_h, \mathbf{v}_h).$$

Then Problem  $(\mathcal{P}_A)_h$  is equivalent with the following problem:  
find  $\mathbf{u}_h \in K_h$  such that

$$\mathcal{L}(\mathbf{u}_h) \leq \mathcal{L}(\mathbf{v}_h), \quad \forall \mathbf{v}_h \in K_h, \quad t = t_{i+1} \in I. \quad (131)$$

### 3.5.2. Approximate Mixed Variational Formulation of the Tresca Model: The Saddle Point-Uzawa/CGM Approach - the Matching Case

Since the term  $j(\mathbf{v}_h)$  is not smooth then we introduce the approximate mixed variational formulation of the problem discussed, which employs the Lagrange multipliers. The Lagrange multipliers will be identified with normal and tangential components of contact stress vector. Problem (131) can be reformulated (see [17, 35, 48, 49, 59] in the form of an approximate saddle point problem. Piecewise linear finite elements will be used for the approximation of displacements and the Lagrange multipliers will be approximated by piecewise constant functions.

We introduce the standard spaces of linear elements on the regular division  $\mathcal{T}_h = \cup_{\iota=1}^r \mathcal{T}_h^\iota$  of polygonal (for  $N = 2$ ) or polyhedral (for  $N = 3$ ) domains  $\overline{\Omega}^\iota$ ,  $\iota = 1, \dots, r$ . Let

$$V_h = V_h^1 \times \dots \times V_h^r = \prod_{\iota=1}^r V_h^\iota, \quad K_h = K_h^1 \times \dots \times K_h^r = \prod_{\iota=1}^r K_h^\iota,$$

where

$$\begin{aligned} V_h^\iota &= \{ \mathbf{v}_h \in [C(\overline{\Omega}^\iota)]^N : \mathbf{v}_h|_{T_{hi}} \in [P_1(T_{hi})]^N \quad \forall T_{hi} \in \mathcal{T}_h^\iota, \quad \mathbf{v}_h = 0 \text{ on } \Gamma_u \cap \partial\Omega^\iota \}, \\ K_h^\iota &= \{ \mathbf{v}_h \in V_h^\iota : [\mathbf{v}_h \cdot \mathbf{n}]^{sm}(a_i) \leq 0 \quad \text{on } \Gamma_c^{sm}, \quad \forall i \}, \end{aligned}$$

where by  $T_{hi}$  we denote any triangle (for  $N = 2$ ) and any tetrahedron (for  $N = 3$ ) of the division  $\mathcal{T}_h^\iota$ ,  $\iota = 1, \dots, r$ , and  $a_i$ ,  $i = 1, \dots, q$ , denote the nodes of  $\mathcal{T}_h^\iota$  laying on  $\Gamma_c^{sm}$ .



Let us introduce the approximate Lagrange spaces  $W_h = W_{hn} \times W_{ht}$  and  $M_h = M_{hn} \times M_{ht}$  as follows:

$$\begin{aligned} W_h &= W_h(\cup \Gamma_c^{sm}) = \{(\varphi_n, \varphi_t) \mid \exists \mathbf{v}_h \in V_h \text{ such that } [v_{hn}] = \varphi_n, [\mathbf{v}_{ht}] = \varphi_t\}, \\ M_{hn} &= \{\mu_{hn} \in W_{hn} \mid \mu_{hn} \geq 0\}, \\ M_{ht} &= \{\mu_{ht} \in W_{ht} \mid (\mu_{ht}, \varphi_{ht})_{0, \cup \Gamma_c^{sm}} \leq (\tilde{g}_c^{sm}, |\varphi_{ht}|)_{0, \cup \Gamma_c^{sm}} \quad \forall \varphi_{ht} \in W_{ht}\}. \end{aligned}$$

We will assume that any division  $\mathcal{T}_h$  is compatible with end-points of  ${}^1\Gamma_u, {}^2\Gamma_u, \Gamma_\tau, \Gamma_c$  and that the nodes of  $\mathcal{T}_h^s$  and  $\mathcal{T}_h^m$  coincide on  $\Gamma_c^{sm}$ . Evidently,

$$j(\mathbf{v}_h) = \sup_{M_h} (\tilde{g}_c^{sm} \mu_h, [\mathbf{v}_{ht}]^{sm})_{0, \cup \Gamma_c^{sm}}.$$

Then the problem (131) leads to solve the saddle point problem:

find a pair  $(\mathbf{u}_h, \boldsymbol{\lambda}_h) \in K_h \times M_h$  such that

$$\mathcal{H}_h(\mathbf{u}_h, \boldsymbol{\mu}_h) \leq \mathcal{H}_h(\mathbf{u}_h, \boldsymbol{\lambda}_h) \leq \mathcal{H}_h(\mathbf{v}_h, \boldsymbol{\lambda}_h) \quad \forall (\mathbf{v}_h, \boldsymbol{\mu}_h) \in K_h \times M_h, \quad (132)$$

where

$$\begin{aligned} \mathcal{H}_h(\mathbf{v}_h, \boldsymbol{\mu}_h) &= \frac{1}{2} A(\mathbf{v}_h, \mathbf{v}_h) - (\mathbf{f}_h, \mathbf{v}_h) + b_h(\boldsymbol{\mu}_h, \mathbf{v}_h), \\ b_h(\boldsymbol{\mu}_h, \mathbf{v}_h) &= (\mu_{hn}, [v_{hn}])_{0, \cup \Gamma_c^{sm}} + (\mu_{ht}, [\mathbf{v}_{ht}])_{0, \cup \Gamma_c^{sm}}. \end{aligned}$$

or in the equivalent form: find  $(\mathbf{u}_h, \boldsymbol{\lambda}_h) \in K_h \times M_h$  such that

$$\begin{aligned} A(\mathbf{u}_h, \mathbf{v}_h - \mathbf{u}_h) + (\tilde{g}_c^{sm} \boldsymbol{\lambda}_h, [\mathbf{v}_{ht}]^{sm} - [\mathbf{u}_{ht}]^{sm})_{0, \cup \Gamma_c^{sm}} &\geq \\ &\geq (\mathbf{f}_h, \mathbf{v}_h - \mathbf{u}_h), \quad \forall \mathbf{v}_h \in K_h, \quad t = t_{i+1} \in I. \\ \tilde{g}_c^{sm}(\boldsymbol{\mu}_h - \boldsymbol{\lambda}_h, [\mathbf{u}_{ht}]^{sm})_{0, \cup \Gamma_c^{sm}} &\leq 0 \quad \forall \boldsymbol{\mu}_h \in M_h, \end{aligned} \quad (133)$$

For the local matrix representation then for every element  $T_{hi}$  (with appropriate boundary segments - sides for  $N = 2$  and faces for  $N = 3$ ) we find the local functional of the form

$$f_n(\mathbf{y}_n, \boldsymbol{\mu}_n) = \frac{1}{2} \mathbf{y}_n^T C_n \mathbf{y}_n - \mathbf{y}_n^T \mathbf{d}_n + \mathbf{y}_n^T G_n^T \boldsymbol{\mu}_n,$$

where in the 3D case  $C_n$  is the local stiffness matrix of the dimension  $12 \times 12$ ,  $\mathbf{y}_n$  is the vector (a representation of  $\mathbf{v}_h$  on  $T_{hi}$ ) of the dimensions  $12 \times 1$ ,  $\mathbf{d}_n$  is the local load vector of the dimensions  $12 \times 1$ , dimensions of  $G_n$  and  $\boldsymbol{\mu}_n$  depend on the number of faces, we denote it as  $p_n$ . Then  $\boldsymbol{\mu}_n$  is the vector of the dimension  $3p_n \times 1$  and  $G_n$  is the constraint matrix of the dimension  $3p_n \times 12$ . Similarly for  $N = 2$ .

The global matrix representation of the problem (133) for every  $t = t_{i+1} \in I$  leads to the following problem:

find  $(\mathbf{x}, \boldsymbol{\lambda}) \in K_d \times M_d$  such that

$$\begin{aligned} \mathcal{H}(\mathbf{x}, \boldsymbol{\mu}) &\leq \mathcal{H}(\mathbf{x}, \boldsymbol{\lambda}) \leq \mathcal{H}(\mathbf{y}, \boldsymbol{\lambda}) \quad \forall (\mathbf{y}, \boldsymbol{\mu}) \in K_d \times M_d, \\ \mathcal{H}(\mathbf{y}, \boldsymbol{\mu}) &= \frac{1}{2} \mathbf{y}^T C \mathbf{y} - \mathbf{y}^T \mathbf{d} + \mathbf{y}^T G^T \boldsymbol{\mu}, \\ K_d &= \{\mathbf{y} \in \mathbb{R}^N \mid A\mathbf{y} \leq 0\}, \\ M_d &= \{\boldsymbol{\mu} \in \mathbb{R}^{3P} \mid \boldsymbol{\mu}_{3i-2}^2 + \boldsymbol{\mu}_{3i-1}^2 + \boldsymbol{\mu}_{3i}^2 \leq 1, \quad i = 1, \dots, P\}, \end{aligned} \quad (134)$$

where  $C$  is the global stiffness matrix ( $\dim n \times n$ ), block diagonal every block of it is sparse, symmetric positive (semi-)definite matrix,  $A$  is the constraint matrix representing the non-penetration condition ( $\dim m \times n$ ),  $G$  is the matrix representing the friction forces ( $\dim 3P \times n$ ),  $\mathbf{d}$  is the global load vector ( $\dim n \times 1$ ), moreover, it holds  $m \ll n$ ,  $3P \ll n$ .

The problem (133) for every  $t = t_{i+1} \in I$  will be solved by the modified Uzawa algorithm with the preconditioning conjugate gradient method (CGM) with constraints (see [35, 49, 59, 34]). The algorithm for every  $t = t_{i+1} \in I$  will be the following:

Let  $\lambda_H^0$  be an initial approximation, then knowing  $\lambda_H^k \in M_d$ , we calculate  $\mathbf{x}^k$  as a solution of the minimization problem

$$\mathcal{H}(\mathbf{x}, \lambda_H^k) \rightarrow \min. \quad (135)$$

Then replace  $\lambda_H^k$  by  $\lambda_H^{k+1}$  by using the process

$$\lambda_H^{k+1} = \Pi_{M_d}(\lambda_H^k + \rho(\mathbf{x}^k)^T G^T), \rho > 0 \quad (136)$$

and return to (135). The value of  $\lambda_H^0 \in M_d$  is chosen arbitrarily. The symbol  $\Pi_{M_d}$  is the projection  $\mathbb{R}^{3P}$  into a convex set  $M_d$ , i.e.  $\Pi_{M_d}(\mathbf{y}) = [(\Pi_{M_d})_1^T, \dots, (\Pi_{M_d})_P^T]^T$ , where for  $i = 1, \dots, P$

$$(\Pi_{M_d}(\mathbf{y}))_i = \begin{cases} (\mathbf{y}_{3i-2}^2 + \mathbf{y}_{3i-1}^2 + \mathbf{y}_{3i}^2)^T & \text{for } |\mathbf{y}|_i \leq 1, \\ (\mathbf{y}_{3i-2}^2 + \mathbf{y}_{3i-1}^2 + \mathbf{y}_{3i}^2)^T / |\mathbf{y}|_i & \text{for } |\mathbf{y}|_i > 1, \end{cases} \quad \text{for } N = 3,$$

where

$$\begin{aligned} |\mathbf{y}|_i &= (\mathbf{y}_{3i-2}^2 + \mathbf{y}_{3i-1}^2 + \mathbf{y}_{3i}^2)^{\frac{1}{2}}, & \text{for } N = 3, \\ &= \begin{cases} \mathbf{y}_i & \text{for } |\mathbf{y}|_i \leq 1, \\ \text{sgn } \mathbf{y}_i & \text{for } |\mathbf{y}|_i > 1, \end{cases} & \text{for } N = 2, \end{aligned}$$

From the proof of the convergence of the Uzawa algorithm there exists the parameter  $\rho$  such that  $\rho \in (\rho_1, \rho_2) \sim (10^3, 10^4)$ .

Minimization problem (135) leads to

$$\begin{aligned} f(\mathbf{x}) &= \frac{1}{2} \mathbf{x}^T C \mathbf{x} - \mathbf{x}^T \mathbf{d}_0 \rightarrow \min \\ \mathbf{x}^T \mathbf{a}_i &\leq 0, \quad 1 \leq i \leq m, \end{aligned}$$

where  $\mathbf{x}, \mathbf{a}_i, \mathbf{d}_0 \in \mathbb{R}^N$ . The idea of the algorithm is based on the sequential minimization of  $f(\mathbf{x})$  on sides, determined by such rows  $\mathbf{a}_i$  for which the equality is set in. On every side we solve the minimization process by the conjugate gradient method with constraints (for details see [48, 59, 34] and Section 2 of this chapter). Since the number of steps in the conjugate gradient method is finite, and moreover, since the number of sides is also finite, the algorithm converges after the finite steps of Uzawa's iterations. For a better convergence the preconditioned Uzawa/CGM techniques can be used (see e.g. [48, 59, 35]), where there is shown that the preconditioning incomplete and complete Choleski method are the best methods and that converge quickly.

**Remark 7** Since the stiffness matrix remains the same throughout the whole iteration process, the number of the approximated displacement vector  $\mathbf{u}_h$  subject to the condition on  $\cup \Gamma_c^{sm}$  is small as compared to the total number of components of  $\mathbf{u}_h$  we can use the effective algorithm of the problem discussed. The linear term of the Lagrangian  $\mathcal{H}$  changes during the iteration process only those components, which correspond to the components of  $\mathbf{u}_h$  on  $\cup \Gamma_c^{sm}$ . Therefore, it is possible to eliminate the free components of  $\mathbf{u}_h$  corresponding to the nodes not belonging to  $\cup \Gamma_c^{sm}$ , and to carry out the iteration process with only the other components of  $\mathbf{u}_h$  (for details see [15, 44, 48]).

### 3.5.3. The Mortar Approach - the Non-matching Case

We reformulate the problem (130) as a saddle point (mixed) problem. To give a saddle point formulation, we introduce a Lagrange multiplier space  $M$ . Since  $\Omega^\iota$ ,  $\iota = 1, \dots, r$ , are assumed domains with sufficiently smooth boundaries  $\partial\Omega^\iota$ , then we can introduce the trace space  $W = H^{\frac{1}{2},N}(\cup_{s,m} \Gamma_c^{sm})$ , being the trace space of  $V_0$  restricted to  $\cup_{s,m} \Gamma_c^{sm}$ , and its dual as  $W' = H^{-\frac{1}{2},N}(\cup_{s,m} \Gamma_c^{sm})$ . In the case if  $\bar{\Gamma}_c^s = \partial\Omega^s \cap (\Gamma_u \cap \partial\Omega^s)$ , we will use  $H_{00}^{\frac{1}{2},N}(\Gamma_c^{sm})$  instead of  $H^{\frac{1}{2},N}(\Gamma_c^{sm})$ , where  $H_{00}^{\frac{1}{2},N}(\Gamma_c^{sm})$  is the Hilbertian interpolation space between  $L^{2,N}(\Gamma_c^{sm})$  and  $H_0^{1,N}(\Gamma_c^{sm})$ . We define its dual as  $H_{00}^{-\frac{1}{2},N}(\Gamma_c^{sm}) = (H_{00}^{\frac{1}{2},N}(\Gamma_c^{sm}))'$  and we remind that  $H_{00}^{\frac{1}{2},N}(\Gamma_c^{sm})$  is a proper and continuously embedded subspace of  $H^{\frac{1}{2},N}(\Gamma_c^{sm})$ .

We introduce the Lagrange multiplier space  $M = M_n \times M_t \subseteq W'$ , where  $W'$  is the dual space to  $H^{\frac{1}{2},N}(\cup_s \Gamma_c^s)$  or  $H_{00}^{\frac{1}{2},N}(\cup_s \Gamma_c^s)$  defined above. The norm  $\|\cdot\|_{-\frac{1}{2},N,\Gamma_c^s}$  on  $H^{-\frac{1}{2},N}(\Gamma_c^s)$  is defined by

$$\|\mathbf{w}\|_{-\frac{1}{2},N,\Gamma_c^s} \equiv \|\mathbf{w}\|_{H^{-1/2,N}(\Gamma_c^{sm})} = \sup_{0 \neq \mathbf{z} \in H^{\frac{1}{2},N}(\Gamma_c^s)} \frac{\langle \mathbf{w}, \mathbf{z} \rangle_{\frac{1}{2},N,\Gamma_c^s}}{\|\mathbf{w}\|_{\frac{1}{2},N,\Gamma_c^s}}.$$

Next, we will introduce the problem in elastic and visco-elastic rheologies separately.

#### Mixed variational formulation - elastic case

Let  $\mathbf{u}_h, \mathbf{v}_h \in \mathbf{V}_{0h} = \{\mathbf{v}_h \in H^{1,N}(\Omega) | \mathbf{v}_h = \mathbf{0} \text{ on } \Gamma_{uh}, v_{hn} = 0 \text{ on } \Gamma_{0h}\}$ ,  $\boldsymbol{\mu}_{hH} = (\mu_{nh}, \boldsymbol{\mu}_{tH}) \in H^{-\frac{1}{2}}(\Gamma_c^s) \times L^{2,N-1}(\Gamma_c^s)$ . We define

$$\begin{aligned} a(\mathbf{u}_h, \mathbf{v}_h) &= \int_{\Omega} c_{ijkl}(\mathbf{x}) e_{kl}(\mathbf{u}_h) e_{ij}(\mathbf{v}_h) d\mathbf{x}, \\ (\mathbf{f}, \mathbf{v}_h) &= \int_{\Omega} \mathbf{F} \cdot \mathbf{v}_h d\mathbf{x} + \int_{\Gamma_{\tau}} \mathbf{P} \cdot \mathbf{v}_h ds, \\ j(\mathbf{v}_h) &= \int_{\cup_s \Gamma_c^s} g_c^{sm} |\mathbf{v}_{ht}^s - \mathbf{v}_{ht}^m| ds \equiv \int_{\cup_s \Gamma_c^s} g_c^{sm} |[\mathbf{v}_{ht}]^{sm}| ds \end{aligned}$$

and

$$b(\boldsymbol{\mu}_{hH}, \mathbf{v}_h) = \langle \mu_{nh}, [\mathbf{v}_h \cdot \mathbf{n}]^s - d^{sm} \rangle_{\cup_s \Gamma_c^s} + \int_{\cup_s \Gamma_c^s} g_c^{sm} \boldsymbol{\mu}_{hHt} \cdot [\mathbf{v}_{ht}]^s ds,$$

where

$$[\mathbf{v} \cdot \mathbf{n}]^s = v_n^s(\mathbf{x}) - v_n^m(\mathcal{R}^{sm}(\mathbf{x})), [\mathbf{v}_t]^s = \mathbf{v}_t^s(\mathbf{x}) - \mathbf{v}_t^m(\mathcal{R}^{sm}(\mathbf{x})),$$

where  $\mathcal{R}^{sm} : \Gamma_c^s(t) \mapsto \Gamma_c^m(t)$ , at  $t \in I$ , is a bijective map satisfying  $\Gamma_c^m(t) \subset \mathcal{R}^{sm}(\Gamma_c^s(t))$ ,  $t \in I$ , i.e.  $\mathcal{R}^{sm}$  at  $t \in I$  may be defined by mapping any  $\mathbf{x}(t) \in \Gamma_c^s(t)$  to the interaction of the normal to  $\Gamma_c^s(t)$  at  $\mathbf{x}(t)$  with  $\Gamma_c^s(t)$ ,  $t \in I$ , and therefore,  $\Gamma_c^m(t)$  is defined as the image of  $\mathcal{R}^{sm}(\mathbf{x}(t))$ . Furthermore, let  $\langle \cdot, \cdot \rangle_{\Gamma_c^s}$  denote the duality pairing between  $W_{hH}$  and  $M_{hH} = M_{hn} \times M_{Ht}$ , where

$$\begin{aligned} M_{hn} &= \{\mu_{hn} \in W'_{hH}; \mu_{hn} \geq 0\}, \\ M_{Ht} &= \{\boldsymbol{\mu}_{Ht} \in L^{2,N-1}(\cup_{sm} \Gamma_c^{sm}) \mid \|\boldsymbol{\mu}_{Ht}\| \leq 1 \text{ a.e.}, \boldsymbol{\mu}_{Ht} = 0 \\ &\quad \text{on } \cup_{sm} \Gamma_c^{sm} \setminus \sup \text{pg}_c^{sm}\}. \end{aligned}$$

We will assume that  $\mathbf{F} \in L^2(I; L^{2,N}(\Omega))$ ,  $\mathbf{P} \in L^2(I; L^{2,N}(\Gamma_\tau))$ ,  $c_{ijkl}(\mathbf{x}) \in L^\infty(\Omega)$  and that  $\Gamma_u, \Gamma_\tau, \Gamma_c$  have positive surface measures.

Then in every time level the mixed formulation of the Signorini problem with given friction consists of finding  $\mathbf{u}_h \in V_h = \mathbf{u}_{2h} + V_{0h}$  and  $\boldsymbol{\lambda}_{hH} = (\lambda_{hn}, \boldsymbol{\lambda}_{Ht}) \in M_{hH}$  such that

$$\begin{aligned} a(\mathbf{u}_h, \mathbf{v}_h) + b(\boldsymbol{\lambda}_{hH}, \mathbf{v}_h) &= (\mathbf{f}_h, \mathbf{v}_h) \quad \forall \mathbf{v}_h \in V_h, t \in I, \\ b(\boldsymbol{\mu}_{hH} - \boldsymbol{\lambda}_{hH}, \mathbf{u}_h) &\leq \langle d^{sm}, (\mu_{hn} - \lambda_{hn}) \rangle_{\cup \Gamma_c^{sm}} \\ \forall \boldsymbol{\mu}_{hH} \in M_{hH} &= M_{hn} \times M_{Ht}, t \in I. \end{aligned} \quad (137)$$

The existence and uniqueness of  $(\boldsymbol{\lambda}_{hH}, \mathbf{u}_h)$  of this saddle-point problem has been stated e.g. in [17, 16]. Thus, we have

**Proposition 1** *Let  $-\tau_n(\mathbf{u}_h) \in M_{hn}$ . Then the problem (137) has a unique solution  $(\boldsymbol{\lambda}_{hH}, \mathbf{u}_h) \in M_{hH} \times V_h$ , a.e.  $t \in I$ . Moreover, we have*

$$\lambda_{hn}^s = -\tau_n^s(\mathbf{u}_h) \quad \text{and} \quad g_c^s \boldsymbol{\lambda}_{Ht}^s = -\boldsymbol{\tau}_t^s(\mathbf{u}_h),$$

where  $\mathbf{u}_h$  is the solution of the primal problem and we put

$$g_c^s = \mathcal{F}_c^s(\mathbf{u}^s(t_i - \Delta t, \dots, t_i - k\Delta t)) | \tau_n(\mathbf{u}^s(t_i - \Delta t, \dots, t_i - k\Delta t)) |, \quad k \geq 1.$$

The problem is equivalent to that of the Lagrangian formulation:

$$\begin{aligned} \text{Find a pair } (\boldsymbol{\lambda}_{hH}, \mathbf{u}_h) &\in (M_{hn} \times M_{Ht}) \times V_h, \text{ a.e. } t \in I, \text{ such that} \\ \mathcal{H}(\mathbf{u}_h, \boldsymbol{\mu}_{hH}) &\leq \mathcal{H}(\mathbf{u}_h, \boldsymbol{\lambda}_{hH}) \leq \mathcal{H}(\mathbf{v}_h, \boldsymbol{\lambda}_{hH}) \\ \forall (\mathbf{v}_h, \boldsymbol{\mu}_{hH}) &\in V_h \times (M_{hn} \times M_{Ht}), t \in I, \end{aligned}$$

where

$$\mathcal{H}(\mathbf{u}_h, \boldsymbol{\mu}_{hH}) = \frac{1}{2} a(\mathbf{u}_h, \mathbf{v}_h) + b(\boldsymbol{\mu}_{hH}, \mathbf{v}_h) - (\mathbf{f}_h, \mathbf{v}_h). \quad (138)$$

**Remark 8** *It can be verified that  $g_c^s \boldsymbol{\lambda}_{Ht}^s = -\boldsymbol{\tau}_t^s(\mathbf{u}_h^s)$  on  $\Gamma_{ch}^s$ .*

**Remark 9** *The problem (137), (138) is equivalent to the following problem*

$$\mathbf{u}_h \in K_h, \quad a(\mathbf{u}_h, \mathbf{v}_h - \mathbf{u}_h) + j(\mathbf{v}_h) - j(\mathbf{u}_h) \geq (\mathbf{f}_h, \mathbf{v}_h - \mathbf{u}_h) \quad \forall \mathbf{v}_h \in K_h, t \in I, \quad (139)$$

where  $K_h = V_h \cap K$ ,  $K = \{\mathbf{v} \in V, [\mathbf{v} \cdot \mathbf{n}]^{sm} \leq d^{sm} \text{ on } \cup_{sm} \Gamma_c^{sm}\}$ .

**Remark 10** If  $\gamma_a^{sm} \subset \Gamma_c^{sm}$  is the actual set and if the displacement  $\mathbf{u}$  is a continuous function, then the actual contact zone  $\gamma_a^{sm}$  is a well-defined and closed subset of  $\Gamma_c^{sm}$ .

### Mixed variational formulation - visco-elastic case

Let  $M_{hH} = M_{hn} \times M_{Ht}$  be the discrete approximation of the Langrange multiplier space  $M = M_n \times M_t$ . We introduce the spaces describing the degree of the polynomial approximation

$$M_{hn}^1 = \left\{ \mu_{hn} \in W_{hn}^1(\cup_s \Gamma_c^s), \int_{\Gamma_c^s} \mu_{hn} \psi_h ds \geq 0, \forall \psi_h \in W_{hn}^1, \psi_h \geq 0 \text{ a.e. on every } \Gamma_c^s \right\},$$

$$M_{Ht}^1 = \left\{ \mu_{Ht} \in W_{Ht}^1(\cup_s \Gamma_c^s), \int_{\Gamma_c^s} \mu_{Ht} \psi_H ds - \int_{\Gamma_c^s} g_c^{sm} |\psi_H| ds \leq 0, \forall \psi_H \in W_{Ht}^1(\Gamma_c^s) \right\},$$

where

$$W_{hH}^1(\cup_s \Gamma_c^s) = W_{hn}^1(\cup_s \Gamma_c^s) \times W_{Ht}^1(\cup_s \Gamma_c^s) = \{ \mathbf{v}_h|_{\cup_s \Gamma_c^s}, \mathbf{v}_h \in V_h \},$$

$$M_{hn}^0 = \{ \mu_{hn} \in W_{hn}^0(\cup_s \Gamma_c^s), \mu_{hn} \geq 0, \text{ a.e. on } \Gamma_c^s \},$$

$$M_{Ht}^0 = \left\{ \mu_{Ht} \in W_{Ht}^0(\cup_s \Gamma_c^s), \int_{\Gamma_c^s} \mu_{Ht} \psi_H ds - \int_{\Gamma_c^s} g_c^{sm} |\psi_H| ds \leq 0, \forall \psi_H \in W_{Ht}^0(\Gamma_c^s) \right\},$$

where

$$W_{hH}^0(\cup_s \Gamma_c^s) = W_{hn}^0(\cup_s \Gamma_c^s) \times W_{Ht}^0(\cup_s \Gamma_c^s) = \{ \mu_{hH} |_{\Delta_r} \in [P_0(\Delta_r)]^N, 0 \leq r \leq n(h^s) \},$$

and where  $\Gamma_c^s$  is created by a finite number parts  $\Gamma_c^{sp}, p = 1, \dots, \bar{p}$ ,

$$\Gamma_c^{sp} = \cup_s \Delta_r, \quad \Delta_r \equiv q_r = (s_r, s_r + h_p), \quad r = 0, 1, \dots, m-1, \quad m = m(h_p) \text{ for } N = 2,$$

and

$$\Gamma_c^{sp} = \cup_s \Delta_r,$$

where  $\Delta_r$  are sides of polyhedra of the given partition for  $N = 3$ .

We have the following problem:

In every time level find  $\mathbf{u}_h \in V_h, \lambda_{hH} \in M_{hH}$ , (i.e. for a.e.  $t \in I$ ), satisfying

$$A(\mathbf{u}_h, \mathbf{v}_h) + b(\lambda_{hH}, \mathbf{v}_h) = (\mathbf{f}, \mathbf{v}_h) \quad \mathbf{v}_h \in V_h \equiv \prod_{l=1}^r V_{h^l}^s,$$

$$b(\mu_{hH} - \lambda_{hH}, \mathbf{v}_h) \leq \langle d^{sm}, (\mu_{hn} - \lambda_{hn}) \rangle_{\cup \Gamma_c^{sm}} \quad \forall \mu_{hH} \in M_{hH}, \quad (140)$$

where  $M_{hH} = M_{hH}^1$  (or  $M_{hH}^0$ ).

To ensure the existence and uniqueness of a solution to (140), it is necessary to verify that

$$\{ \mu_{hH} \in M_{hH}, \quad b(\mu_{hH}, \mathbf{v}_h) = 0 \quad \forall \mathbf{v}_h \in V_h \} = \{0\},$$

which is obvious when  $M_{hH} = M_{hH}^1$ ; for  $M_{hH} = M_{hH}^0$  see [17], where the discrete Babuška-Brezzi “inf-sup” condition is of the form

$$\inf_{\mu_{hH} \in W_{hH}(\cup_s \Gamma_c^s)} \sup_{\mathbf{v}_h \in V_h} \frac{b(\mu_{hH}, \mathbf{v}_h)}{\| \mu_{hH} \|_{-\frac{1}{2}, \cup_s \Gamma_c^s} \| \mathbf{v}_h \|_1} \geq \beta,$$

where

$$\|\mathbf{v}_h\|_1 = \left( \sum_{\iota=1}^r \|\mathbf{v}_h^\iota\|_{1,\Omega^\iota}^2 \right)^{\frac{1}{2}}.$$

**Proposition 2** *Let  $-\tau_n(\mathbf{u}_h) \in M_{hn}$ . Then the problem (140) has a unique solution  $(\boldsymbol{\lambda}_{hH}, \mathbf{u}_h) \in M_{hH} \times V_h$ , a.e.  $t \in I$ . Moreover we have*

$$\lambda_{hn}^s = -\tau_n^s(\mathbf{u}_h) \quad \text{and} \quad g_c^s \boldsymbol{\lambda}_{Ht} = -\boldsymbol{\tau}_t^s(\mathbf{u}_h),$$

where  $\mathbf{u}_h$  is the solution of the discrete primal problem and where we put  $g_c^s \equiv \tilde{g}_{ch}^{sm}$ .

We define the Lagrangian

$$\mathcal{H}(\mathbf{v}, \boldsymbol{\mu}) = \frac{1}{2} A(\mathbf{u}_h, \mathbf{v}_h) + b(\boldsymbol{\mu}_{hH}, \mathbf{v}_h) - (\mathbf{f}_h, \mathbf{v}_h).$$

The problem (140) is equivalent to that of the Lagrangian formulation: find for every time level (i.e.  $t \in I$ ) a pair  $(\mathbf{v}_h, \boldsymbol{\lambda}_{hH}) \in V_h \times M_{hH}$ , such that

$$\mathcal{H}(\mathbf{u}_h, \boldsymbol{\mu}_{hH}) \leq \mathcal{H}(\mathbf{u}_h, \boldsymbol{\lambda}_{hH}) \leq \mathcal{H}(\mathbf{v}_h, \boldsymbol{\lambda}_{hH}) \quad \forall (\mathbf{v}_h, \boldsymbol{\mu}_{hH}) \in V_h \times M_{hH}, \quad t \in I \quad (141)$$

**Remark 11** *It is evident that similar remarks as above is valid also in this case.*

### 3.5.4. Matrix Formulation and the Primal-dual Active Set Strategy Method (PDAS): The Frictionless Case in (Visco-)elasticity with Short Memory

In this section, we will derive the matrix formulation of (130) for the case without friction, and then we will apply the primal-dual active set strategy to the investigated multibody contact problem. It is evident that the previous case in linear elasticity is the special case of that in linear visco-elasticity with short memory.

In [74] it was shown that standard basis of the space of linear finite elements  $X_h(\Omega^\iota, \mathcal{T}_{h,\Omega^\iota})$ ,  $\iota = s, m$ , satisfying homogeneous Dirichlet boundary conditions on  $\Gamma_u$ , is not a good choice. The acceptable idea is to modify the nodal basis functions on the mortar side in such a way that we introduce the space with a weak condition on  $\cup \Gamma_c^{sm}$

$$\hat{V}_h = \left\{ \mathbf{v} \in \cap_{\iota=1}^r X_h(\Omega^\iota, \mathcal{T}_{h,\Omega^\iota}) \mid \int_{\cup \Gamma_c^{sm}} [\mathbf{v} \cdot \mathbf{e}_i]^s \psi ds = 0, \quad 1 \leq i \leq N, \quad \psi \in M_{hH} \right\},$$

where  $\mathbf{e}_i$  denotes the  $i$ -th unit vector. The definition of  $\hat{V}_h$  yields

$$\int_{\cup \Gamma_c^s} [\mathbf{v} \cdot \mathbf{n}_p]^s \psi_s ds \leq d_p^s$$

for all vertices on the slide (non-mortar) side.

Then the strong form of the non-penetration condition  $[\mathbf{u} \cdot \mathbf{n}]^s \leq d^{sm}$  will be replaced by its weak discrete form

$$\int_{\cup \Gamma_c^s} [\mathbf{u} \cdot \mathbf{n}]^s \psi_p ds \leq \int_{\cup \Gamma_c^s} d_p^s \psi_p ds, \quad p \in S, \quad (142)$$

where  $S$  is the set of all vertices in the potential contact part on the slave side. The constraints (142) give a coupling between the vertices on the slave side and the master side. We introduce now a basis transformation of the basis of  $V_h$  in such a way that the weak non-penetration condition (142) in the new basis only deals with the vertices on the slave side. Thus the non-penetration condition is satisfied for all elements in  $\hat{V}_h$ , and  $\hat{V}_h$  is a subspace of  $K_h$ .

**The discrete mortar formulation of the saddle point problem** (141) for every time level for frictionless case is defined as follows:

**Problem**  $(\mathcal{P}_{sp})_{dm}$ : In every time level find  $\mathbf{u}_h \in V_h$ ,  $\lambda_{hn} \in M_{hn}$ , a.e.  $t \in I$ , satisfying

$$\begin{aligned} A(\mathbf{u}_h, \mathbf{v}_h) + b(\lambda_{hn}, \mathbf{v}_h) &= (\mathbf{f}_h, \mathbf{v}_h) \quad \forall \mathbf{v}_h \in V_h, \\ b(\mu_{hn} - \lambda_{hn}, \mathbf{v}_h) &\leq \langle d^{sm}, (\mu_{hn} - \lambda_{hn}) \rangle_{\cup \Gamma_c^{sm}} \quad \forall \mu_{hn} \in M_{hn}, \end{aligned} \quad (143)$$

where  $M_{hn} = M_{hn}^1$  (or  $M_{hn}^0$ ) defined

$$M_{hn}^1 = \left\{ \mu_{hn} \in W_{hn}^1(\cup_s \Gamma_c^s), \int_{\Gamma_c^s} \mu_{hn} \psi_h ds \geq 0, \forall \psi_h \in W_{hn}^1, \psi_h \geq 0 \text{ a.e. on every } \Gamma_c^s \right\},$$

where

$$\begin{aligned} W_{hH}^1(\cup_s \Gamma_c^s) &= W_{hn}^1(\cup_s \Gamma_c^s) \times W_{Ht}^1(\cup_s \Gamma_c^s) = \{ \mathbf{v}_h |_{\cup_s \Gamma_c^s}, \mathbf{v}_h \in V_h \}, \\ M_{hn}^0 &= \{ \mu_{hn} \in W_{hn}^0(\cup_s \Gamma_c^s), \mu_{hn} \geq 0, \text{ a.e. on } \Gamma_c^s \}, \end{aligned}$$

where

$$W_{hH}^0(\cup_s \Gamma_c^s) = W_{hn}^0(\cup_s \Gamma_c^s) \times W_{Ht}^0(\cup_s \Gamma_c^s) = \{ \mu_{hH} |_{\Delta_r} \in [P_0(\Delta_r)]^N, 0 \leq r \leq n(h^s) \},$$

and where  $\Gamma_c^s$  is created by a finite number parts  $\Gamma_c^{sp}$ ,  $p = 1, \dots, \bar{p}$ ,

$$\Gamma_c^{sp} = \bigcup_s \Delta_r, \quad \Delta_r \equiv q_r = (s_r, s_r + h_p), \quad r = 0, 1, \dots, m-1 \quad m = m(h_p) \text{ for } N = 2,$$

and  $\Gamma_c^{sp} = \bigcup_s \Delta_r$ , where  $\Delta_r$  are sides of polyhedra of the given partition for  $N = 3$ , and in addition, where

$$A(\mathbf{u}_h, \mathbf{v}_h) = (\rho \mathbf{u}_h, \mathbf{v}_h) + \Delta t (\alpha \mathbf{u}_h, \mathbf{v}_h) + \Delta t^2 a^{(0)}(\mathbf{u}_h, \mathbf{v}_h) + \Delta t a^{(1)}(\mathbf{u}_h, \mathbf{v}_h),$$

for the dynamic case in visco-elastic rheology with short memory, and

$$A(\mathbf{u}_h, \mathbf{v}_h) = \Delta t a^{(0)}(\mathbf{u}_h, \mathbf{v}_h) + a^{(1)}(\mathbf{u}_h, \mathbf{v}_h)$$

for the quasi-static case without damping in visco-elastic rheology with short memory,

$$A(\mathbf{u}_h, \mathbf{v}_h) = (\rho \mathbf{u}_h, \mathbf{v}_h) + \Delta t (\alpha \mathbf{u}_h, \mathbf{v}_h) + \Delta t^2 a^{(0)}(\mathbf{u}_h, \mathbf{v}_h)$$

for the dynamic case in elasticity, and

$$A(\mathbf{u}_h, \mathbf{v}_h) = a^{(0)}(\mathbf{u}_h, \mathbf{v}_h)$$

for the quasi-static case without damping in elasticity, and

$$b(\mu_{hn}, \mathbf{v}_h) = \int_{\cup \Gamma_c^{sm}} \mu_{hn} [\mathbf{v}_h \cdot \mathbf{n}]^s ds = \langle \mu_{hn}, [\mathbf{v}_h \cdot \mathbf{n}]^s \rangle_{\cup \Gamma_c^{sm}} \quad \forall \mathbf{v}_h \in V_h, \mu_{hn} \in M_{hn}.$$

The condition (143b) is equivalent with the following conditions

$$\begin{aligned} b(\lambda_{hn}, \mathbf{u}_h) &= \langle d^{sm}, \lambda_{hn} \rangle_{\cup \Gamma_c^{sm}} \\ b(\mu_{hn}, \mathbf{u}_h) &\leq \langle d^{sm}, \mu_{hn} \rangle_{\cup \Gamma_c^{sm}} \quad \forall \mu_{hn} \in M_{hn}. \end{aligned} \quad (144)$$

Since the space  $M_{hn}$  is the convex cone, then putting  $\mu_{hn} = 0$  and  $\mu_{hn} = 2\lambda_{hn}$  in (143b), we have  $b(\lambda_{hn}, \mathbf{u}_h) \geq \langle d^{sm}, \lambda_{hn} \rangle_{\cup \Gamma_c^{sm}}$  and  $b(\lambda_{hn}, \mathbf{u}_h) \leq \langle d^{sm}, \lambda_{hn} \rangle_{\cup \Gamma_c^{sm}}$ , therefore (144a) follows immediately. From (144b) using (144a) the condition (144b) follows.

The Lagrange multipliers  $\lambda_{hn}$  are approximations of the contact forces  $-\boldsymbol{\tau}(\mathbf{u}_h) \cdot \mathbf{n} = -(n_j n_k \tau_{jk}(\mathbf{u}_h))$  which are necessary to adjust the contact displacements on the contact boundary  $\cup \Gamma_c^{sm}$ .

Let the space  $V_h = \text{span} \{\varphi_p, p = 1, \dots, n_V\}^N$ ,  $N = 2, 3$ ,  $n_V$  denotes the number of degrees of freedom of the space  $V_h$  and  $n_{cn}$  denotes the number of degrees of freedom of the space  $M_{hn}$  in each component.  $\varphi_p$  and  $\psi_q$  are the scalar basis functions associated with the node  $p$  resp. the node  $q$ , and satisfying the biorthogonality relation (145) (for 2D case see Fig. 11). The biorthogonality condition for the basis functions is defined as

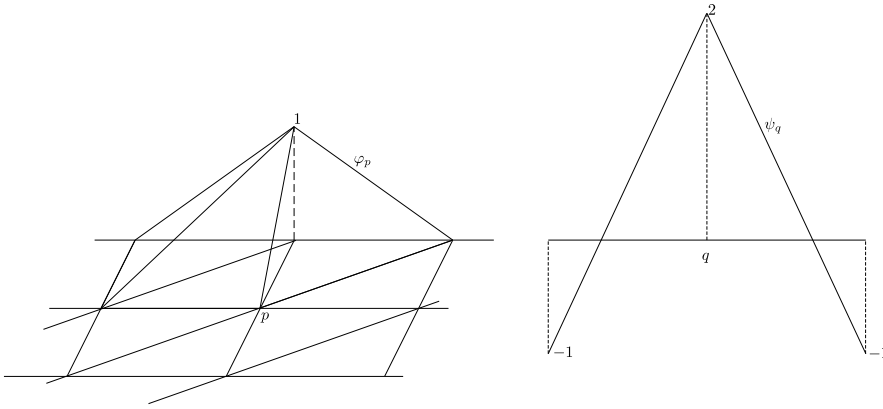


Figure 11. Shape functions.

$$\int_{\cup \Gamma_c^s} \varphi_p \psi_q ds = \delta_{pq} \int_{\cup \Gamma_c^s} \varphi_p ds, \quad (145)$$

where  $\delta_{pq}$  is the Kronecker symbol, and

$$\delta_{pq} = \begin{cases} 1 & \text{where the structure node } p \text{ coincides with potential node } q, \\ 0 & \text{otherwise.} \end{cases}$$

Let us denote the nodal parameters  $\mathbf{u}_h$  by  $\mathbf{U}$ , of  $\lambda_{hn}$  by  $\boldsymbol{\Lambda}_{hn}$ , and since for the frictionless case the tangential stress component on the contact boundary  $\cup \Gamma_c^{sm}$  is zero, then



$\lambda_{Ht} = 0$ , and thus  $\Lambda_{Ht} = 0$ . For the discretization of the space  $M_{hH} \equiv M_{hn}$ , the dual Lagrange multipliers will be used (see [28, 29, 4]).

The Eq. (143a) for every  $t \in I$  in the matrix form is the following

$$\mathbb{A}_h \mathbf{U} + \mathbb{B}_h \Lambda_h = \mathbb{F}_h. \quad (146)$$

To examine the structure of  $\mathbb{B}_h$ , we introduce three sets of indices  $\mathcal{N}$ ,  $\mathcal{M}$ ,  $\mathcal{S}$ . We decompose the set of all vertices in every time  $t \in I$  into three disjoint parts  $\mathcal{N}$ ,  $\mathcal{M}$  and  $\mathcal{S}$ , where by  $\mathcal{S}$  ( $\dim n_{cn}$ ) we denote all vertices on the possible contact part on the slave side, by  $\mathcal{M}$  ( $\dim n_{cn}$ ) all vertices of the possible contact part of the master side, and by  $\mathcal{N}$  all the other one. Then the strong formulation of the non-penetration condition (i.e.  $[\mathbf{u} \cdot \mathbf{n}]^{sm} \leq d^{sm}$  on  $\cup \Gamma_c^{sm}$ ) will be replaced by its weak discrete form

$$\int_{\cup \Gamma_c^{sm}} [\mathbf{U} \cdot \mathbf{n}]^s \psi_p ds \leq \int_{\cup \Gamma_c^{sm}} d^{sm} \psi_p ds, \quad p \in \mathcal{S}. \quad (147)$$

This condition connects points of sets  $\mathcal{S}$  and  $\mathcal{M}$ . We introduce a basis of new transformation of the basis of the space  $V_h$  in such a way that the weak non-penetration condition (147) in the new basis only deals with the vertices on the slave side (see [27, 28, 74]).

Let us introduce the transformation  $\varphi = (\varphi_{\mathcal{N}}, \varphi_{\mathcal{M}}, \varphi_{\mathcal{S}})^T$ . The matrices and vectors in (148) can be decomposed in the sense of decomposition of the set of all vertices into three disjoint parts  $\mathcal{N}$ ,  $\mathcal{M}$  and  $\mathcal{S}$ , i.e.

$$\begin{bmatrix} \mathbb{A}_{\mathcal{N}\mathcal{N}} & \mathbb{A}_{\mathcal{N}\mathcal{M}} & \mathbb{A}_{\mathcal{N}\mathcal{S}} & \mathbb{O} \\ \mathbb{A}_{\mathcal{M}\mathcal{N}} & \mathbb{A}_{\mathcal{M}\mathcal{M}} & \mathbb{A}_{\mathcal{M}\mathcal{S}} & -\mathbb{M}^T \\ \mathbb{A}_{\mathcal{S}\mathcal{N}} & \mathbb{A}_{\mathcal{S}\mathcal{M}} & \mathbb{A}_{\mathcal{S}\mathcal{S}} & \mathbb{D} \end{bmatrix} \begin{bmatrix} \mathbf{U}_{\mathcal{N}} \\ \mathbf{U}_{\mathcal{M}} \\ \mathbf{U}_{\mathcal{S}} \\ \Lambda_{\mathcal{S}} \end{bmatrix} = \begin{bmatrix} \mathbb{F}_{\mathcal{N}} \\ \mathbb{F}_{\mathcal{M}} \\ \mathbb{F}_{\mathcal{S}} \end{bmatrix}, \quad (148)$$

where elements of  $\mathbb{B}_h$  are defined by  $\mathbb{B}_h[p, q] = \int_{\cup \Gamma_c^{sm}} \varphi_p \psi_q ds \mathbb{I}_N = \delta_{pq} \int_{\cup \Gamma_c^{sm}} \varphi_p ds$ ,  $p = 1, \dots, n_V$ ,  $q = 1, \dots, n_{cn}$ , and where  $\mathbb{I}_N$  denotes the identity matrix in  $\mathbb{R}^{N \times N}$ . The basis functions satisfy the biorthogonality condition (145). Further, the matrix  $\mathbb{M}$  represents the matrix coupling the trace of the finite element shape functions on the master side “ $m$ ” and the shape functions for the Lagrange multiplier on the slave side “ $s$ ” defined by

$$\mathbb{M}[p, q] = \int_{\cup \Gamma_c^{sm}} \varphi_p \psi_q ds \mathbb{I}_N, \quad p \in \mathcal{S}, q \in \mathcal{M}, \quad (149)$$

where  $\mathbb{I}_N$  denotes the identity matrix in  $\mathbb{R}^{N \times N}$ . The matrix  $\mathbb{M}$  is the block matrix and  $\mathbb{D}$  is the block diagonal matrix. Due to (145), the entries of  $\mathbb{D}$  are given by

$$\mathbb{D}[p, q] = \delta_{pq} \mathbb{I}_N \cdot \int_{\cup \Gamma_c^{sm}} \varphi_p ds, \quad p = q \in \mathcal{S} \equiv \{1, \dots, n_{cn}\}. \quad (150)$$

The structure of the matrix  $\mathbb{B}_h$  in every time level  $t \in I$ , using an approximate node numbering, is thus of the form  $\mathbb{B}_h = (\mathbb{O}, -\mathbb{M}^T, \mathbb{D})^T$ . The block matrices associated with the basis functions of the free structure nodes (i.e.  $\mathcal{N}$ ), the potential contact nodes of the master side (i.e.  $\mathcal{M}$ ) and the potential contact nodes on the slide side (i.e.  $\mathcal{S}$ ) are denoted by  $\mathbb{A}_{k,l}$ ,

$k, l \in \{\mathcal{N}, \mathcal{M}, \mathcal{S}\}$ . The entries of vectors  $\mathbb{U}$  and  $\mathbb{F}$  for  $k \in \{\mathcal{N}, \mathcal{M}, \mathcal{S}\}$  are denoted by  $\mathbb{U}_k$  and  $\mathbb{F}_k$ , respectively.

Our goal is now to introduce a new modified basis  $\Phi = (\Phi_{\mathcal{N}}, \Phi_{\mathcal{M}}, \Phi_{\mathcal{S}})^T$  instead of the basis  $\varphi = (\varphi_{\mathcal{N}}, \varphi_{\mathcal{M}}, \varphi_{\mathcal{S}})^T$ . We introduce the matrix  $\hat{\mathbb{M}} = \mathbb{D}^{-1}\mathbb{M}$ , then the matrix  $\hat{\mathbb{M}}$  is sparse and then  $\Phi$  can be defined by

$$V_h \ni \Phi = (\Phi_{\mathcal{N}}, \Phi_{\mathcal{M}}, \Phi_{\mathcal{S}})^T = \begin{bmatrix} \mathbb{I}_N & \mathbb{O} & \mathbb{O} \\ \mathbb{O} & \mathbb{I}_N & \hat{\mathbb{M}}^T \\ \mathbb{O} & \mathbb{O} & \mathbb{I}_N \end{bmatrix} \begin{bmatrix} \varphi_{\mathcal{N}} \\ \varphi_{\mathcal{M}} \\ \varphi_{\mathcal{S}} \end{bmatrix} = Q\varphi. \quad (151)$$

Then

$$\mathbb{U} = Q^T \hat{\mathbb{U}},$$

where  $\hat{\mathbb{U}}$  is the vector of coefficients with respect to the transformed basis  $\Phi$ .

Next we give the algebraic representation of (151). The modified stiffness matrix  $\hat{\mathbb{A}}_h$  associated with the transformed basis  $\Phi$  is the following

$$\begin{aligned} \hat{\mathbb{A}}_h &= \begin{bmatrix} \mathbb{I}_N & \mathbb{O} & \mathbb{O} \\ \mathbb{O} & \mathbb{I}_N & \hat{\mathbb{M}}^T \\ \mathbb{O} & \mathbb{O} & \mathbb{I}_N \end{bmatrix} \begin{bmatrix} \mathbb{A}_{\mathcal{N}\mathcal{N}} & \mathbb{A}_{\mathcal{N}\mathcal{M}} & \mathbb{A}_{\mathcal{N}\mathcal{S}} \\ \mathbb{A}_{\mathcal{M}\mathcal{N}} & \mathbb{A}_{\mathcal{M}\mathcal{M}} & \mathbb{A}_{\mathcal{M}\mathcal{S}} \\ \mathbb{A}_{\mathcal{S}\mathcal{N}} & \mathbb{A}_{\mathcal{S}\mathcal{M}} & \mathbb{A}_{\mathcal{S}\mathcal{S}} \end{bmatrix} \begin{bmatrix} \mathbb{I}_N & \mathbb{O} & \mathbb{O} \\ \mathbb{O} & \mathbb{I}_N & \mathbb{O} \\ \mathbb{O} & \hat{\mathbb{M}} & \mathbb{I}_N \end{bmatrix} = Q\mathbb{A}_hQ^T = \\ &= \begin{bmatrix} \mathbb{A}_{\mathcal{N}\mathcal{N}} & \mathbb{A}_{\mathcal{N}\mathcal{M}} + \mathbb{A}_{\mathcal{N}\mathcal{S}}\hat{\mathbb{M}} & \mathbb{A}_{\mathcal{N}\mathcal{S}} \\ \mathbb{A}_{\mathcal{M}\mathcal{N}} + (\hat{\mathbb{M}})^T\mathbb{A}_{\mathcal{S}\mathcal{N}} & \mathbb{A}_{\mathcal{M}\mathcal{M}} + \mathbb{A}_{\mathcal{M}\mathcal{S}}\hat{\mathbb{M}} + (\hat{\mathbb{M}})^T\mathbb{A}_{\mathcal{S}\mathcal{M}} + (\hat{\mathbb{M}})^T\mathbb{A}_{\mathcal{S}\mathcal{S}}\hat{\mathbb{M}} & \mathbb{A}_{\mathcal{M}\mathcal{S}} + (\hat{\mathbb{M}})^T\mathbb{A}_{\mathcal{S}\mathcal{S}} \\ \mathbb{A}_{\mathcal{S}\mathcal{N}} & \mathbb{A}_{\mathcal{S}\mathcal{M}} + \mathbb{A}_{\mathcal{S}\mathcal{S}}\hat{\mathbb{M}} & \mathbb{A}_{\mathcal{S}\mathcal{S}} \end{bmatrix} \end{aligned}$$

and the modified vector of the right hand side  $\hat{\mathbb{F}}_h$  is the following

$$\hat{\mathbb{F}}_h = Q\mathbb{F}_h = \begin{bmatrix} \mathbb{F}_{\mathcal{N}} \\ \mathbb{F}_{\mathcal{M}} + (\hat{\mathbb{M}})^T\mathbb{F}_{\mathcal{S}} \\ \mathbb{F}_{\mathcal{S}} \end{bmatrix}.$$

The algebraic representation of the weak non-penetration condition associated with the transformed basis  $\Phi$  is the following:

$$\begin{aligned} [\mathbb{U}_n]^s &= \sum_{p \in \mathcal{S}} \hat{\mathbb{U}}_p [\Phi_{pn}]^s + \sum_{q \in \mathcal{M}} \hat{\mathbb{U}}_q [\Phi_{qn}]^s = \\ &= \left( \sum_{p \in \mathcal{S}} \hat{\mathbb{U}}_p \varphi_p \right) \cdot \mathbf{n}_p^s + \sum_{q \in \mathcal{M}} \hat{\mathbb{U}}_q \left( -\varphi_q + \sum_{p' \in \mathcal{S}} \hat{\mathbb{M}}[p', q] \varphi_{p'} \right) \cdot \mathbf{n}_p^s. \end{aligned}$$

By multiplying this equation with  $\psi_p$ ,  $p \in \mathcal{S}$  and integrating the resulting equation over  $\cup_s \Gamma_c^s$ , we have due to the biorthogonality condition (148) and the definition of the matrix  $\hat{\mathbb{M}}$  and (151)

$$\hat{\mathbb{U}}_{n,p} \equiv (\mathbf{n}_p^s)^T \mathbb{D}[p, p] \hat{\mathbb{U}}_p \leq d_p^{sm} \quad \forall p \in \mathcal{S}, \quad (152)$$

where  $d_p^{sm} = \int_{\cup_s \Gamma_c^s} d_h^{sm} \psi_p ds$ ,  $p \in \mathcal{S}$ , as the coefficients at  $\hat{\mathbb{U}}_q$ ,  $q \in \mathcal{M}$ , are nullified. This basis transformation glues the vertices of the slave (non-master) side and on the master side together. The displacements of the glued vertices are given by  $\hat{\mathbb{U}}_{\mathcal{M}}$  and the relative

displacements between the vertices on the slave side and on the master side are given by  $\hat{\mathbf{U}}_{\mathcal{S}}$ .

The modified matrix  $\hat{\mathbb{B}}_h$  associated with the transformed basis  $\Phi$  has the form

$$\hat{\mathbb{B}}_h = Q\mathbb{B}_h = \begin{bmatrix} \mathbb{I}_N & \mathbb{O} & \mathbb{O} \\ \mathbb{O} & \mathbb{I}_N & \mathbb{M}^T \\ \mathbb{O} & \mathbb{O} & \mathbb{I}_N \end{bmatrix} \begin{bmatrix} \mathbb{O} \\ -\mathbb{M}^T \\ \mathbb{D} \end{bmatrix} = (\mathbb{O}, \mathbb{O}, \mathbb{D})^T.$$

Then we will solve in every time level the following problem

$$\begin{aligned} \hat{\mathbf{A}}_h \hat{\mathbf{U}} + \hat{\mathbb{B}}_h \boldsymbol{\Lambda}_{hH} &= \hat{\mathbf{F}}_h, \\ \hat{\mathbf{U}}_{n,p} &\leq d_p^{sm}, \boldsymbol{\Lambda}_{hn,p} \geq 0, (\hat{\mathbf{U}}_{n,p} - d_p^{sm}) \boldsymbol{\Lambda}_{hn,p} = 0, \quad \forall p \in \mathcal{S}, t \in I, \\ \boldsymbol{\Lambda}_{Ht,p} &= 0, \quad \forall p \in \mathcal{S}, t \in I, \end{aligned} \quad (153)$$

where in (153) the second line represents the Karush-Kuhn-Tucker conditions of a constrained optimization problem for inequality constraints,

$$\begin{aligned} \boldsymbol{\Lambda}_{hn,p} &= \mathbf{n}_p^{sT} \hat{\mathbb{D}}[p, p] \boldsymbol{\Lambda}_{hH}(p), \quad \boldsymbol{\Lambda}_{hH}(p) \in \mathbb{R}^N, \\ \boldsymbol{\Lambda}_{Ht,p} &= \boldsymbol{\Lambda}_{hH}(p) - (\boldsymbol{\Lambda}_{hH}(p) \cdot \mathbf{n}_p^s) \mathbf{n}_p^s = (\boldsymbol{\Lambda}_{hH}(p) \cdot \mathbf{t}_p^s) \mathbf{t}_p^s. \end{aligned}$$

In [18] the method how to find the correct subset  $\mathcal{A}$  of vertices from  $\mathcal{S}$ , for which the structures are in the mutual contact, is presented. To find it, we decompose the set  $\mathcal{S}$  as  $\mathcal{S} = \mathcal{A} \cup \mathcal{I}$ , where  $\mathcal{A}$  is the active set and  $\mathcal{I}$  is the inactive set. Let at each vertex the function

$$C(\hat{\mathbf{U}}_{n,p}, \boldsymbol{\Lambda}_{hn,p}) = \boldsymbol{\Lambda}_{hn,p} - \max\{0, \boldsymbol{\Lambda}_{hn,p} + c_1(\hat{\mathbf{U}}_{n,p} - d_p^{sm})\}, c_1 = \text{const.} > 0$$

be defined. Then (153b-d) can be expressed as

$$C(\hat{\mathbf{U}}_{n,p}, \boldsymbol{\Lambda}_{hn,p}) = 0, \quad p \in \mathcal{S},$$

and therefore, in every time level (153) can be rewritten as

$$\begin{aligned} \hat{\mathbf{A}}_h \hat{\mathbf{U}} + \hat{\mathbb{B}}_h \boldsymbol{\Lambda}_{hH} &= \hat{\mathbf{F}}_h, \\ C(\hat{\mathbf{U}}_{n,p}, \boldsymbol{\Lambda}_{hn,p}) &= 0, \\ \boldsymbol{\Lambda}_{Ht,p} &= 0 \end{aligned} \quad (154)$$

for all vertices  $p \in \mathcal{S}$  and  $t \in I$ .

This leads to **the primal-dual active set algorithm**, which is as follows:

#### Algorithm PDAS:

**STEP 1.** Initiate the sets  $\mathcal{A}_1$  (active set) and  $\mathcal{I}_1$  (inactive set), such that  $\mathcal{S} = \mathcal{A}_1 \cup \mathcal{I}_1$  and  $\mathcal{A}_1 \cap \mathcal{I}_1 = \emptyset$ , put the initial value  $(\hat{\mathbf{U}}^0, \boldsymbol{\Lambda}_{hH}^0)$ ,  $c_1 \in (10^3, 10^4)$  and set  $k = 1$ .

**STEP 2.** If  $(\hat{\mathbf{U}}^{k-1}, \boldsymbol{\Lambda}_{hH}^{k-1})$  is known, find the primal-dual pair  $(\hat{\mathbf{U}}^k, \boldsymbol{\Lambda}_{hH}^k)$  such that

$$\hat{\mathbf{A}}_h \hat{\mathbf{U}}^k + \hat{\mathbb{B}}_h \boldsymbol{\Lambda}_{hH}^k = \hat{\mathbf{F}}_h, \quad (155)$$

$$\hat{\mathbf{U}}_{n,p}^k = d_p^{sm} \quad \text{for all } p \in \mathcal{A}_k,$$

$$\boldsymbol{\Lambda}_{hn,p}^k = 0 \quad \text{for all } p \in \mathcal{I}_k,$$

$$\boldsymbol{\Lambda}_{Ht,p}^k = 0 \quad \text{for all } p \in \mathcal{S}. \quad (156)$$

**STEP 3.** Set  $\mathcal{A}_{k+1}$  and  $\mathcal{I}_{k+1}$  to

$$\begin{aligned}\mathcal{A}_{k+1} &= \left\{ p \in \mathcal{S} : \mathbf{\Lambda}_{hn,p}^k + c_1(\hat{\mathbf{U}}_{n,p}^k - d_p^{sm}) > 0 \right\}, \\ \mathcal{I}_{k+1} &= \left\{ p \in \mathcal{S} : \mathbf{\Lambda}_{hn,p}^k + c_1(\hat{\mathbf{U}}_{n,p}^k - d_p^{sm}) \leq 0 \right\}.\end{aligned}$$

**STEP 4.** If  $\mathcal{A}_{k+1} = \mathcal{A}_k$  and  $\mathcal{I}_{k+1} := \mathcal{I}_k$ ; **then STOP else**  $k = k + 1$ ; **goto** STEP 2.  $\square$

Then we can apply in every time level the PDAS algorithm with modified system in STEP 2 of the Algorithm PDAS, i.e. the system

$$\begin{aligned}\hat{\mathbf{A}}_h \hat{\mathbf{U}}^k + \hat{\mathbf{B}}_h \mathbf{\Lambda}_{hH}^k &= \hat{\mathbf{F}}_h^k, \\ \hat{\mathbf{U}}_{n,p}^k &= d_p^{sm}, \quad \forall p \in \mathcal{A}_k, \quad t \in I, \\ \mathbf{\Lambda}_{hn,p}^k &= \mathbf{0}, \quad \forall p \in \mathcal{I}_k, \quad t \in I, \\ \mathbf{\Lambda}_{Ht,p}^k &= \mathbf{0}, \quad \forall p \in \mathcal{S}, \quad t \in I,\end{aligned}\tag{157}$$

and where the active ( $\mathcal{A}_k$ ) and inactive ( $\mathcal{I}_k$ ) sets are associated with the transformed basis  $\Phi$ .

The system (157) can be rewritten if we decompose the set of vertices  $\mathcal{S}$  on the slave side in each step  $k$  of the PDAS algorithm into the disjoint active and inactive sets  $\mathcal{S} = \mathcal{A}_k \cup \mathcal{I}_k$ . Since  $\hat{\mathbf{B}}_h = (\mathbb{O}, \mathbb{O}, \mathbb{D})^T$ , we decompose the diagonal matrix  $\mathbb{D}$  into

$$\mathbb{D} = \begin{bmatrix} \mathbb{D}_{\mathcal{I}_k} & \mathbb{O} \\ \mathbb{O} & \mathbb{D}_{\mathcal{A}_k} \end{bmatrix}.$$

According to the definition of  $\hat{\mathbf{U}}_{n,p}$  in (152), we introduce the matrix  $\mathbb{N}_{\mathcal{A}_k} \in \mathbb{R}^{|\mathcal{A}_k| \times N|\mathcal{A}_k|}$ , where  $|\mathcal{A}_k|$  denotes the number of vertices in  $\mathcal{A}_k$ , by

$$\mathbb{N}_{\mathcal{A}_k} = \begin{bmatrix} \ddots & \mathbb{O}_{1 \times N} & & \\ \mathbb{O}_{1 \times N} & w_{pp} \mathbf{n}_p^s & & \\ & & \ddots & \end{bmatrix}, \quad p \in \mathcal{A}_k,$$

where  $w_{pp}$  denotes an abbreviation for  $\mathbb{D}[p, p]_{1,1} = \dots = \mathbb{D}[p, p]_{N,N} = \int_{\Gamma_c^s} \varphi_p ds$ ,  $N = 2, 3$ , having the meaning of a weighting factor. The associated tangential vectors are then given by  $\mathbf{t}_p^s \perp \mathbf{n}_p^s$ , i.e.  $\mathbf{t}_p^s = (-n_{p2}^s, n_{p1}^s)^T$  for the  $N = 2$  case and by  $\mathbf{t}_p^\xi \perp \mathbf{n}_p^s$  and  $\mathbf{t}_p^\eta = \mathbf{t}_p^\xi \times \mathbf{n}_p^s$  with  $\|\mathbf{n}_p^s\| = \|\mathbf{t}_p^\xi\| = \|\mathbf{t}_p^\eta\| = 1$  for the  $N = 3$  case. We define the matrix  $\mathbb{T}_{\mathcal{A}_k} \in \mathbb{R}^{|\mathcal{A}_k| \times 2|\mathcal{A}_k|}$ , by

$$\mathbb{T}_{\mathcal{A}_k} = \begin{bmatrix} \ddots & \mathbb{O}_{1 \times 2} & & \\ \mathbb{O}_{1 \times 2} & \mathbf{t}_p^{(s)} & & \\ & & \ddots & \end{bmatrix} = \begin{bmatrix} \ddots & \ddots & & \\ & -n_{p,2}^s & n_{p,1}^s & \\ & 0 & \ddots & \ddots \end{bmatrix}, \quad p \in \mathcal{A}_k$$

for the  $N = 2$  case, and

$$\mathbb{T}_{\mathcal{A}_k} = \begin{bmatrix} \ddots & \mathbb{O}_{1 \times 3} & & \\ \mathbb{O}_{1 \times 3} & \mathbf{t}_p^{(m)} & & \\ & & \ddots & \end{bmatrix} \in \mathbb{R}^{|\mathcal{A}_k| \times 3|\mathcal{A}_k|}, \quad m = \xi, \eta, \quad p \in \mathcal{A}_k$$

for the  $N = 3$  case.

Then the algebraic representation of (157) is given by

$$\begin{bmatrix} \hat{\mathbb{A}}_{\mathcal{N}\mathcal{N}} & \hat{\mathbb{A}}_{\mathcal{N}\mathcal{M}} & \hat{\mathbb{A}}_{\mathcal{N}\mathcal{I}_k} & \hat{\mathbb{A}}_{\mathcal{N}\mathcal{A}_k} & 0 & 0 \\ \hat{\mathbb{A}}_{\mathcal{M}\mathcal{N}} & \hat{\mathbb{A}}_{\mathcal{M}\mathcal{M}} & \hat{\mathbb{A}}_{\mathcal{M}\mathcal{I}_k} & \hat{\mathbb{A}}_{\mathcal{M}\mathcal{A}_k} & 0 & 0 \\ \hat{\mathbb{A}}_{\mathcal{I}_k\mathcal{N}} & \hat{\mathbb{A}}_{\mathcal{I}_k\mathcal{M}} & \hat{\mathbb{A}}_{\mathcal{I}_k\mathcal{I}_k} & \hat{\mathbb{A}}_{\mathcal{I}_k\mathcal{A}_k} & \mathbb{D}_{\mathcal{I}_k} & 0 \\ \hat{\mathbb{A}}_{\mathcal{A}_k\mathcal{N}} & \hat{\mathbb{A}}_{\mathcal{A}_k\mathcal{M}} & \hat{\mathbb{A}}_{\mathcal{A}_k\mathcal{I}_k} & \hat{\mathbb{A}}_{\mathcal{A}_k\mathcal{A}_k} & 0 & \mathbb{D}_{\mathcal{A}_k} \\ 0 & 0 & 0 & 0 & \mathbb{I}_{\mathcal{I}_k} & 0 \\ 0 & 0 & 0 & \mathbb{N}_{\mathcal{A}_k} & 0 & 0 \\ 0 & 0 & 0 & 0 & 0 & \mathbb{T}_{\mathcal{A}_k} \end{bmatrix} \cdot \begin{bmatrix} \hat{\mathbb{U}}_{\mathcal{N}}^k \\ \hat{\mathbb{U}}_{\mathcal{M}}^k \\ \hat{\mathbb{U}}_{\mathcal{I}_k}^k \\ \hat{\mathbb{U}}_{\mathcal{A}_k}^k \\ \hat{\Lambda}_{\mathcal{I}_k}^k \\ \hat{\Lambda}_{\mathcal{A}_k}^k \end{bmatrix} = \begin{bmatrix} \hat{\mathbb{F}}_{\mathcal{N}} \\ \hat{\mathbb{F}}_{\mathcal{M}} \\ \hat{\mathbb{F}}_{\mathcal{I}_k} \\ \hat{\mathbb{F}}_{\mathcal{A}_k} \\ 0 \\ d_{\mathcal{A}_k}^{sm} \\ 0 \end{bmatrix}, \quad (158)$$

with  $\mathbb{T}_{\mathcal{A}_k} = (\mathbb{T}_{\mathcal{A}_k}^\xi, \mathbb{T}_{\mathcal{A}_k}^\eta)^T$  in the 3D-case, where  $k$  denotes the index of the active set step,  $d_{\mathcal{A}_k}^{sm}$  denotes the vector containing the entries  $d_p^{sm}$  associated with the active vertex  $p \in \mathcal{A}_k$ . The system (158) cannot be solved directly. Due to the dual Lagrange multiplier space,  $\hat{\Lambda}_{hH}$  can be locally eliminated. Since  $\hat{\mathbb{B}} = Q\mathbb{B}_h = (0, 0, \mathbb{D})^T$ , then

$$\hat{\mathbb{B}}_h \Lambda_{hH}^k = (0, 0, \mathbb{D}\Lambda_{hHS}^k)^T,$$

then  $\hat{\Lambda}_{hHS}^k$  can be eliminated locally, i.e.

$$\Lambda_{hHS}^k = \mathbb{D}^{-1}[\hat{\mathbb{F}}_{\mathcal{S}} - \hat{\mathbb{A}}_{\mathcal{S}\mathcal{N}}\hat{\mathbb{U}}_{\mathcal{N}}^k - \hat{\mathbb{A}}_{\mathcal{S}\mathcal{S}}\hat{\mathbb{U}}_{\mathcal{S}}^k - (\hat{\mathbb{A}}_{\mathcal{S}\mathcal{M}} + \hat{\mathbb{A}}_{\mathcal{S}\mathcal{S}}\hat{\mathbb{M}})\hat{\mathbb{U}}_{\mathcal{M}}^k]. \quad (159)$$

The system (158) can be reduced. We can eliminate the fifth row and column in (158), since  $\Lambda_{\mathcal{I}_k}^k = 0$ . Applying the matrix  $\mathbb{T}_{\mathcal{A}_k}$  to the fourth row, then

$$\mathbb{T}_{\mathcal{A}_k}\mathbb{D}_{\mathcal{A}_k}\Lambda_{\mathcal{A}_k} = 0 \text{ since } \mathbb{T}_{\mathcal{A}_k}\Lambda_{\mathcal{A}_k} = 0 \text{ and } \mathbb{D}_{\mathcal{A}_k} \text{ is a diagonal matrix, } p \in \mathcal{A}_k.$$

Hence  $\Lambda_{\mathcal{A}_k} = 0$ . Now we can rewrite the sixth row and then we obtain

$$\begin{bmatrix} \hat{\mathbb{A}}_{\mathcal{N}\mathcal{N}} & \hat{\mathbb{A}}_{\mathcal{N}\mathcal{M}} & \hat{\mathbb{A}}_{\mathcal{N}\mathcal{I}_k} & \hat{\mathbb{A}}_{\mathcal{N}\mathcal{A}_k} \\ \hat{\mathbb{A}}_{\mathcal{M}\mathcal{N}} & \hat{\mathbb{A}}_{\mathcal{M}\mathcal{M}} & \hat{\mathbb{A}}_{\mathcal{M}\mathcal{I}_k} & \hat{\mathbb{A}}_{\mathcal{M}\mathcal{A}_k} \\ \hat{\mathbb{A}}_{\mathcal{I}_k\mathcal{N}} & \hat{\mathbb{A}}_{\mathcal{I}_k\mathcal{M}} & \hat{\mathbb{A}}_{\mathcal{I}_k\mathcal{I}_k} & \hat{\mathbb{A}}_{\mathcal{I}_k\mathcal{A}_k} \\ 0 & 0 & 0 & \mathbb{N}_{\mathcal{A}_k} \\ \mathbb{T}_{\mathcal{A}_k}\hat{\mathbb{A}}_{\mathcal{A}_k\mathcal{N}} & \mathbb{T}_{\mathcal{A}_k}\hat{\mathbb{A}}_{\mathcal{A}_k\mathcal{M}} & \mathbb{T}_{\mathcal{A}_k}\hat{\mathbb{A}}_{\mathcal{A}_k\mathcal{I}_k} & \mathbb{T}_{\mathcal{A}_k}\hat{\mathbb{A}}_{\mathcal{A}_k\mathcal{A}_k} \end{bmatrix} \cdot \begin{bmatrix} \hat{\mathbb{U}}_{\mathcal{N}}^k \\ \hat{\mathbb{U}}_{\mathcal{M}}^k \\ \hat{\mathbb{U}}_{\mathcal{I}_k}^k \\ \hat{\mathbb{U}}_{\mathcal{A}_k}^k \end{bmatrix} = \begin{bmatrix} \hat{\mathbb{F}}_{\mathcal{N}} \\ \hat{\mathbb{F}}_{\mathcal{M}} \\ \hat{\mathbb{F}}_{\mathcal{I}_k} \\ d_{\mathcal{A}_k}^{sm} \\ \mathbb{T}_{\mathcal{A}_k}\hat{\mathbb{F}}_{\mathcal{A}_k} \end{bmatrix}.$$

Hence, we determine  $(\hat{\mathbb{U}}_{\mathcal{N}}^k, \hat{\mathbb{U}}_{\mathcal{M}}^k, \hat{\mathbb{U}}_{\mathcal{I}_k}^k, \hat{\mathbb{U}}_{\mathcal{A}_k}^k)^T$  and by (159) we determine  $\hat{\Lambda}_{hH}^k$ , where  $\hat{\Lambda}_h$  and  $\hat{\mathbb{F}}_h$  were defined above.

### 3.5.5. The Newmark Method

Since the discrete approximation of the dynamic problem leads to the system of ordinary differential equations, then the problem can be solved numerically by some of methods solving systems of ordinary equations. Moreover, the primal-dual active set algorithm can be extended for these cases. In practice the Newmark method is frequently used. The other possibilities are represented by the central difference method, the Houbolt method, the Wilson  $\Theta$  method, etc.

The discrete approximation of the problem for  $t \in I$  leads to the system

$$\overline{\mathbb{M}}_h \mathbf{u}_h''(t) + \mathbb{C}_h \mathbf{u}_h'(t) + \mathbb{A}_h \mathbf{u}_h(t) + \mathbb{B}_h(t) \boldsymbol{\Lambda}_h(t) = \mathbb{F}_h(t), \quad (160)$$

where  $\overline{\mathbb{M}}_h$  is the mass matrix having connection with the density  $\rho$  of the material,  $\mathbb{C}_h$  is a damping matrix,  $\mathbb{A}_h$  is a stiffness matrix,  $\mathbb{B}_h$ ,  $\boldsymbol{\Lambda}_h$  and  $\mathbb{F}_h$  are similar as in (146).

Let the time interval  $\overline{I} = [0, t_p]$  be divided into  $m$  subintervals  $(t_{n-1}, t_n)$ ,  $n = 1, \dots, N_0$ ,  $t_n = n\Delta t$ ,  $\Delta t = t_p/N_0$ . Let us denote by  $\mathbf{u}_n = \mathbf{u}_h(t_n)$ ,  $\mathbf{u}'_n = \mathbf{u}'_h(t_n)$ ,  $\mathbf{u}''_n = \mathbf{u}''_h(t_n)$ . Further, we use the Newmark scheme (see [3, 48]) defined by

$$\begin{aligned} \mathbf{u}^n &= \mathbf{u}^{n-1} + \Delta t (\mathbf{u}')^{n-1} + \frac{1}{2} (\Delta t)^2 ((1 - 2\beta)(\mathbf{u}'')^{n-1} + 2\beta(\mathbf{u}'')^n), \\ (\mathbf{u}')^n &= (\mathbf{u}')^{n-1} + \Delta t ((1 - \gamma)(\mathbf{u}'')^{n-1} + \gamma(\mathbf{u}'')^n), \quad n = 1, \dots, N_0, \end{aligned} \quad (161)$$

where  $\beta, \gamma$  are free parameters,  $0 \leq \beta \leq \frac{1}{2}$ ,  $0 \leq \gamma \leq 1$ . Let  $\mathbf{u}_h(0) \in V_h$ ,  $\mathbf{u}'_h(0) \in V_h$  be a suitable approximations of initial data and let

$$\mathbf{u}_h^0 = \mathbf{u}_h(0) = \mathbf{u}_0, (\mathbf{u}'_h)^0 = \mathbf{u}'_h(0) = \mathbf{u}_1. \quad (162)$$

From (160) assuming that  $\boldsymbol{\Lambda}_h(t) = \mathbf{0}$  it follows

$$(\mathbf{u}''_h)^0 = (\overline{\mathbb{M}}_h)^{-1} (\mathbb{F}_h(0) - \mathbb{C}_h \mathbf{u}'_h(0) - \mathbb{A}_h \mathbf{u}_h(0)). \quad (163)$$

The stability condition of the Newmark scheme yields that  $\gamma \geq \frac{1}{2}$ ,  $\beta \geq \frac{1}{4} (\gamma + \frac{1}{2})^2$  restricting the time step  $\Delta t$  [3, 48, 27].

Denoting  $\boldsymbol{\Lambda}_h^n = \boldsymbol{\Lambda}_h(t_n)$ , then from (160), (161) we find

$$\begin{aligned} (a_1 \overline{\mathbb{M}}_h + a_4 \mathbb{C}_h + \mathbb{A}_h) \mathbf{u}_h^n + \mathbb{B}_h(t_n) \boldsymbol{\Lambda}_h^n &= \overline{\mathbb{F}}_h(t_n), \\ (\mathbf{u}''_h)^n &= a_1 (\mathbf{u}_h^n - \mathbf{u}_h^{n-1}) - a_2 (\mathbf{u}'_h)^{n-1} - a_3 (\mathbf{u}''_h)^{n-1}, \\ (\mathbf{u}'_h)^n &= a_4 (\mathbf{u}_h^n - \mathbf{u}_h^{n-1}) + a_5 (\mathbf{u}'_h)^{n-1} + a_6 (\mathbf{u}''_h)^{n-1}, \quad n = 1, \dots, N_0, \end{aligned} \quad (164)$$

where

$$\begin{aligned} \overline{\mathbb{F}}_h(t_n) &= (a_1 \overline{\mathbb{M}}_h + a_4 \mathbb{C}_h) \mathbf{u}_h^{n-1} + (a_2 \overline{\mathbb{M}}_h - a_5 \mathbb{C}_h) (\mathbf{u}'_h)^{n-1} + \\ &\quad + (a_3 \overline{\mathbb{M}}_h - a_6 \mathbb{C}_h) (\mathbf{u}''_h)^{n-1} + \mathbb{F}_h(t_n), \\ a_1 &= \frac{1}{\beta(\Delta t)^2}, \quad a_2 = \frac{1}{\beta \Delta t}, \quad a_3 = \frac{1 - 2\beta}{2\beta}, \quad a_4 = \frac{\gamma}{\beta \Delta t}, \quad a_5 = 1 - \frac{\gamma}{\beta}, \\ a_6 &= \left(1 - \frac{\gamma}{2\beta}\right) \Delta t. \end{aligned} \quad (165)$$

Since in every time step  $t = t_n$ , due to deformation of the body, the geometry of the contact boundary changed from time to time, we reassemble  $\mathbb{B}_h(t_n)$  with respect to the changes of geometry and the weak distance  $d_h^{sm}(t_n)$  in every  $t = t_n$  as the distance between the colliding bodies may change due to the change of the normal direction and displacements in tangential direction. For  $\beta = 0.25$ ,  $\gamma = 0.5$  the Newmark algorithm is of order 2, for  $\beta \geq 0.25$ ,  $\gamma \geq 0.5$  the Newmark algorithm produces a “numerical damping”.

Then the algorithm using the PDAS method will be the following:

**Algorithm D-PDAS:**

- (i) Initiate  $\mathbf{u}_h^0$ ,  $(\mathbf{u}'_h)^0$ ,  $(\mathbf{u}''_h)^0$  defined by (162), (163) and set  $n = 0$ .
- (ii) Set  $n = n + 1$ , determine  $\overline{\mathbb{F}}_h(t_n)$  from (165), determine the matrix  $\mathbb{B}_h(t_n)$  and the weak distance  $d_h^{sm}(t_n)$ .
- (iii) Compute  $\mathbf{u}_h^n$  from (164a) by using the PDAS algorithm, where by  $\mathcal{A}^n$  we denote the correct active set of  $\mathbf{u}_h^n$  and for the initialization of  $\mathcal{A}_1^n$  in Algorithm PDAS we use the active set of the previous time step  $t = t_{n-1}$ , i.e.  $\mathcal{A}_1^n = \mathcal{A}^{n-1}$ .
- (iv) Compute  $(\mathbf{u}'_h)^n$ ,  $(\mathbf{u}''_h)^n$  by using (164b,c).
- (v) **If**  $n = N_0$  **then** STOP **else** go to (ii).

**3.6. Model Problems in Thermo-visco-elasticity with Long Memory****3.7. Introduction**

Rock slopes are found in mountain areas as well as both in civil and mining applications. Open pit rock slopes are in many ways different from rock slopes in engineering projects as well as rock slopes in mountain areas. The stability of slopes situated on inclined terrain is often influenced by a predestinated slip surface represented by the contact between the upper rock layer and the rest.

The foundations of the engineering constructions transfer and distribute the total loading on the foundation bed soil. As in any stability problem in the soil mechanics, the stability analyses of underground openings in the clayey medium can be carried out in terms of total or effective stresses. In general, the former is usually relevant to the short term behaviour of the soil, although the use of creep constitutive models allows to simulate its time dependency. The effective stress analysis is appropriate for short, intermediate and long term stabilities making allowances for the coupled hydro-mechanical behaviour and the pore water pressure dissipation.

The engineering constructions, like the bridges, represent one of the most difficult problems in the structural engineering. The bridges are often constructed in very complicated geological conditions and, moreover, their supporting structures are heated and/or cooled and consequently deformed in time. Such situations can be simulated by the model problems in the thermo-visco-elastic rheology.

Visco-elastic rocks can be assumed as materials endowed with memory in the sense that the state of stress at the instant time  $t$  depends on all the deformations undergone by the rock material in previous times. Then we speak about the visco-elastic rock materials with long memory. The corresponding constituent law

$$\tau_{ij}^e(t) = c_{ijkl}^{(0)} e_{kl}(\mathbf{u}(t)) + \int_0^t b_{ijkl}(t - \tau) e_{kl}(\mathbf{u}(\tau)) d\tau$$

represents the stress-strain relation for rocks for which the state of stresses at time  $t$  depends on the deformation at the instant  $t$  and on deformations at the times preceeding  $t$ , the so-called history of deformation, where  $c_{ijkl}^{(0)} \equiv c_{ijkl}$  are elastic coefficients of instantaneous

elasticity, which may possibly depend on  $\mathbf{x}$ , but are bounded in  $\mathbf{x}$  and satisfy the conditions of symmetry and ellipticity defined above and repeated below. The coefficients  $b_{ijkl} = b_{ijkl}(\mathbf{x}, t)$ , representing the memory of the rock materials, which depend on  $t$  and possibly on  $\mathbf{x}$ , are bounded in  $\mathbf{x}, t$ , and satisfy the symmetry as well as the regularity conditions introduced above and repeated below. Next, for simplicity the case without damping will be investigated.

### 3.7.1. Formulation of the Model Problem in the Thermo-visco-elastic rheology with Long Memory and Its Weak Solution

#### Formulation of the problem

The model of the system of geological bodies being in mutual contact will be investigated. Let the set  $\Omega \subset \mathbb{R}^N$ ,  $N = 2, 3$ ,  $\Omega = \cup_{\ell=1}^r \Omega^\ell$ , where  $\Omega^\ell$  are domains with Lipschitz boundary  $\partial\Omega^\ell$  and let  $\partial\Omega = \Gamma_u \cup \Gamma_\tau \cup \Gamma_c$  be defined similarly as in previous cases. Let  $t \in I = (0, t_p)$ ,  $t_p > 0$ . Then we will solve the following problem:

**Problem** ( $\mathcal{P}_{lm}$ ): Find a pair of functions  $(T, u) : \Omega \times I \rightarrow (\mathbb{R} \times \mathbb{R}^N) \times I$ ,  $N = 2, 3$ , and a stress tensor  $\tau_{ij} : \Omega \times I \rightarrow \mathbb{R}^{N \times N} \times I$  satisfying

$$\rho \frac{\partial^2 u_i}{\partial t^2} = \frac{\partial}{\partial x_j} \tau_{ij} + f_i \quad \text{in } \Omega \times I; \quad (166)$$

$$\rho c_e \frac{\partial T}{\partial t} + \rho \beta_{ij} T_0 e_{ij}(\mathbf{u}') = \frac{\partial}{\partial x_j} (\kappa_{ij} \frac{\partial T}{\partial x_i}) + W \quad \text{in } \Omega \times I; \quad (167)$$

$$\begin{aligned} \tau_{ij}(t) &= c_{ijkl} e_{kl}(\mathbf{u}(t)) + \int_0^t b_{ijkl}(t - \tau) e_{kl}(\mathbf{u}(\tau)) d\tau - \beta_{ij}(T - T_0) = \\ &= {}^e \tau_{ij} + {}^v \tau_{ij} + {}^T \tau_{ij}; \end{aligned} \quad (168)$$

with the boundary value and contact conditions

$$\begin{aligned} T(\mathbf{x}, t) &= T_1(\mathbf{x}, t) \ (\neq 0 \text{ or } = 0), \ \tau_{ij} n_j = P_i \ (\neq 0 \text{ or } = 0) \\ &\text{on } ({}^1\Gamma_\tau \cup {}^2\Gamma_\tau) \times I, \ \text{meas } {}^i\Gamma_\tau > 0, \ i = 1, 2, \end{aligned} \quad (169)$$

$$\begin{aligned} \kappa_{ij} \frac{\partial T(\mathbf{x}, t)}{\partial x_i} n_j &= 0, \ \mathbf{u}(\mathbf{x}, t) = \mathbf{u}_2(\mathbf{x}, t) \ (\neq 0 \text{ or } = 0) \\ &\text{on } ({}^1\Gamma_u \cup {}^2\Gamma_u) \times I, \ \text{meas } {}^i\Gamma_u \geq 0, \ i = 1, 2, \end{aligned} \quad (170)$$

$$\begin{aligned} T^k(\mathbf{x}, t) &= T^l(\mathbf{x}, t), \ \kappa_{ij} \frac{\partial T(\mathbf{x}, t)}{\partial x_i} n_{j|(k)} = \kappa_{ij} \frac{\partial T(\mathbf{x}, t)}{\partial x_i} n_{j|(l)} \\ &\text{on } \Gamma_c^{kl} \times I, \end{aligned} \quad (171)$$

and the bilateral contact condition with the Tresca model of friction on  $\Gamma_c^{kl} \times I$  of the form

$$\begin{aligned} [u_n]^{kl} &\equiv u_n^k - u_n^l = 0 \quad \text{and} \quad |\boldsymbol{\tau}_t^k| \leq \mathcal{F}_c^{kl} |\boldsymbol{\tau}_n^k| \equiv g_c^{kl}(\mathbf{x}, t), \\ \left\{ \begin{array}{ll} \text{if } |\boldsymbol{\tau}_t^k| < g_c^{kl}(\mathbf{x}, t) & \text{then } [\mathbf{u}_t']^{kl} \equiv \mathbf{u}_t'^k - \mathbf{u}_t'^l = 0, \\ \text{if } |\boldsymbol{\tau}_t^k| = g_c^{kl}(\mathbf{x}, t) & \text{then there exists } \lambda \geq 0 \\ \text{such that } [\mathbf{u}_t']^{kl} \equiv \mathbf{u}_t'^k - \mathbf{u}_t'^l = -\lambda \boldsymbol{\tau}_t^k, \end{array} \right\} &\quad \text{on } \Gamma_c^{kl} \times I, \end{aligned} \quad (172)$$



and the initial conditions

$$T(\mathbf{x}, 0) = T_0(\mathbf{x}), \mathbf{u}(\mathbf{x}, 0) = \mathbf{u}_0(\mathbf{x}), \mathbf{u}'(\mathbf{x}, 0) = \mathbf{u}_1(\mathbf{x}), \quad (173)$$

where  $\rho(\mathbf{x})$  is the density,  $c_e(\mathbf{x})$  the specific heat,  $c(\mathbf{x}) = \rho(\mathbf{x})c_e(\mathbf{x})$  represents the thermal capacity,  $\kappa_{ij}(\mathbf{x})$  the coefficients of thermal conductivity that are symmetric and uniformly positive definite, i.e.

$$\kappa_{ij}(\mathbf{x}) = \kappa_{ji}(\mathbf{x}), \kappa_{ij}(\mathbf{x})\zeta_i\zeta_j \geq \kappa_0|\zeta|^2, \kappa_0 = \text{const.} > 0, \zeta \in \mathbb{R}^N, N = 2, 3, \quad (174)$$

$\beta_{ij}(\mathbf{x})$  is the coefficient of linear thermal expansion,  $W$  the thermal sources,  $\mathbf{f}, \mathbf{P}$  the body and surface forces, the elastic coefficients  $c_{ijkl}(\mathbf{x})$  may possibly depend on  $\mathbf{x}$  but are bounded in  $\mathbf{x}$  and satisfy

$$c_{ijkl} = c_{jikl} = c_{ijlk} = c_{klij}, c_{ijkl}e_{kl}e_{ij} \geq c_0e_{ij}e_{ij}, c_0 > 0, \quad (175)$$

the coefficients  $b_{ijkl} = b_{ijkl}(\mathbf{x}, t)$ , representing the material memory, depend on  $\mathbf{x}$  and  $t$ , are bounded in  $\mathbf{x}, t$  and satisfy the symmetry condition and the regularity assumption, i.e.

$$b_{ijkl} = b_{jikl}, b_{ijkl}, \partial b_{ijkl}/\partial t, \partial^2 b_{ijkl}/\partial t^2 \in L^\infty(\Omega \times I), \quad (176)$$

$T_0(\mathbf{x}), T(\mathbf{x}, t)$  the initial and the actual temperatures,  $\mathbf{u}(\mathbf{x}, t), \boldsymbol{\tau}(\mathbf{x}, t)$  the displacement and the stress vectors,  $\tau_{ij}$  the stress tensor,  $u_n, \mathbf{u}_t, \tau_n, \boldsymbol{\tau}_t$  the normal and tangential components of displacement and stress vectors,  $\mathbf{n}$  the outward normal to the boundary  $\partial\Omega$ ,  $\mathbf{u}_2$  the given function, and where  $\mathcal{F}_c^{kl}$  is a coefficient of friction,  $g_c^{kl}(\mathbf{x}, t)$  are slip limits.

### Variational (weak) solution of the problem

Let us denote by  $(v, w)_0$  the inner product in  $[L^2(\Omega)]^N$ , by  $\|\cdot\|_k, k \in \mathbb{R}^1$ , the norm in  $H^{k,N}(\Omega)$ ,  $H^{k,N}(\Omega) = \cap_{l=1}^r [H^k(\Omega^l)]^N$ , where  $H^k(\Omega)$  denotes the standard Sobolev space,  $H^{0,N}(\Omega) = [L^2(\Omega)]^N$ , and by  $|\cdot|_0$  the norm corresponding to the inner product  $(v, w) = \int_\Omega svwd\mathbf{x}, s \in C(\overline{\Omega}), s \geq s_0, v, w \in H^{1,N}(\Omega), N = 1, 2, 3$ .

Let us assume that  $\rho^\ell, c_e^\ell \in C(\overline{\Omega}^\ell), \rho^\ell \geq \rho_0^\ell > 0, c_e^\ell \geq c_1^\ell > 0, \kappa_{ij}^\ell \in L^\infty(\Omega^\ell), c_{ijkl}^\ell \in L^\infty(\Omega^\ell), \beta_{ij}^\ell \in C^1(\Omega^\ell), W^\ell \in L^2(I; L^2(\Omega^\ell)), \mathbf{f}^\ell \in L^2(I; [L^2(\Omega^\ell)]^N), \mathbf{P} \in L^2(I; [L^2(\Gamma_\tau)]^N), b_{ijkl}^\ell \in L^\infty(\Omega^\ell \times I), g_c^{kl} \in L^\infty(\Gamma_c^{kl}), g_c^{kl} \geq 0 \text{ on } \cup_{k,l} \Gamma_c^{kl}, T_0^\ell \in H^{1,1}(\Omega^\ell), \mathbf{u}_0^\ell, \mathbf{u}_1^\ell \in H^{1,N}(\Omega^\ell)$ .

Let us introduce for  $\mathbf{u}, \mathbf{v} \in H^{1,N}(\Omega), T, z \in H^{1,1}(\Omega)$

$$\begin{aligned} a(\mathbf{u}, \mathbf{v}) &= \sum_{\ell=1}^r a^\ell(\mathbf{u}^\ell, \mathbf{v}^\ell) = \int_\Omega c_{ijkl}e_{kl}(\mathbf{u})e_{ij}(\mathbf{v})d\mathbf{x}, \\ a_1(t; \mathbf{u}, \mathbf{v}) &= \sum_{\ell=1}^r a_1^\ell(t; \mathbf{u}^\ell, \mathbf{v}^\ell) = \int_\Omega b_{ijkl}(t)e_{kl}(\mathbf{u})e_{ij}(\mathbf{v})d\mathbf{x}, \\ (\mathbf{u}'', \mathbf{v}) &= \sum_{\ell=1}^r (\mathbf{u}''^\ell, \mathbf{v}^\ell) = \int_\Omega \rho \mathbf{u}'' \mathbf{v} d\mathbf{x}, \\ (T', z) &= \sum_{\ell=1}^r (T'^\ell, z^\ell) = \int_\Omega \rho c_e T' z d\mathbf{x}, \\ a_T(T, z) &= \sum_{\ell=1}^r a_T^\ell(T^\ell, z^\ell) = \int_\Omega \kappa_{ij} \frac{\partial T}{\partial x_i} \frac{\partial z}{\partial x_j} d\mathbf{x}, \end{aligned}$$

$$\begin{aligned}
(\mathbf{F}, \mathbf{v}) &= \sum_{\iota=1}^r (\mathbf{F}^\iota, \mathbf{v}^\iota) = \int_{\Omega} f_i v_i d\mathbf{x} + \int_{\Gamma_\tau} P_i v_i ds, \\
(W, z) &= \sum_{\iota=1}^r (W^\iota, z^\iota) = \int_{\Omega} W z d\mathbf{x}, \\
j_g(\mathbf{v}) &= \sum_{\iota=1}^r j_g^\iota(\mathbf{v}^\iota) = \int_{\cup_{kl} \Gamma_c^{kl}} g_c^{kl} |\mathbf{v}_t^k - \mathbf{v}_t^l| ds \equiv \langle g_c^{kl}, |\mathbf{v}_t^k - \mathbf{v}_t^l| \rangle_{\cup_{kl} \Gamma_c^{kl}}, \\
b_s(T, \mathbf{v}) &= \sum_{\iota=1}^r b_s^\iota(T^\iota, \mathbf{v}^\iota) = \int_{\Omega} \frac{\partial}{\partial x_j} (\beta_{ij} T) v_i d\mathbf{x}, \\
b_p(\mathbf{v}, z) &= \sum_{\iota=1}^r b_p^\iota(\mathbf{v}^\iota, z^\iota) = \int_{\Omega} \rho T_0 \beta_{ij} \frac{\partial v_i}{\partial x_j} z d\mathbf{x}.
\end{aligned} \tag{177}$$

Since  $\beta_{ij}^\iota \in C^1(\Omega)$ ,  $T^\iota, T_0^\iota \in H^{1,1}(\Omega^\iota)$ , then  $\beta_{ij}^\iota(T^\iota - T_0^\iota) \in H^{1,1}(\Omega^\iota)$  and therefore,  $\frac{\partial}{\partial x_j}(\beta_{ij}^\iota(T^\iota - T_0^\iota)) \in L^2(\Omega^\iota)$ .

Let

$$\begin{aligned}
\mathcal{U}_{ad}(t) &= \{ \mathbf{v} | \mathbf{v} \in H^{1,N}(\Omega), \mathbf{v} = \mathbf{u}'_2(\mathbf{x}, t) \text{ on } \Gamma_u \}, \\
\mathcal{U}_{Tad}(t) &= \{ z | z \in H^{1,1}(\Omega), z = T_1(\mathbf{x}, t) \text{ on } \Gamma_\tau \}.
\end{aligned}$$

Multiplying (166) by  $\mathbf{v} - \mathbf{u}'(t)$  and (167) by  $z - T(t)$ , integrating over  $\Omega$ , using the boundary value conditions and the contact conditions (169)-(172) and the Green theorem, then we have to solve the following problem:

**Problem**  $(\mathcal{P}_{lm})_v$ : find a pair of functions  $(T(t), \mathbf{u}(t))$  such that

$$\begin{aligned}
&(T'(t), z - T(t)) + a_T(T(t), z - T(t)) + b_p(\mathbf{u}(t), z - T(t)) \geq \\
&\geq (W(t), z - T(t)) dt \quad \forall z \in \mathcal{U}_{Tad}(t),
\end{aligned} \tag{178}$$

$$\begin{aligned}
&(\mathbf{u}''(t), \mathbf{v} - \mathbf{u}'(t)) + a(\mathbf{u}, \mathbf{v} - \mathbf{u}'(t)) + \int_0^t a_1(t - \tau; \mathbf{u}(\tau), \mathbf{v} - \mathbf{u}'(t)) d\tau + \\
&+ b_s(T(t) - T_0, \mathbf{v} - \mathbf{u}'(t)) + j_g(\mathbf{v}) - j_g(\mathbf{u}'(t)) \geq \\
&\geq (\mathbf{F}(t), \mathbf{v} - \mathbf{u}'(t)) \quad \forall \mathbf{v} \in \mathcal{U}_{ad}(t),
\end{aligned} \tag{179}$$

with  $\mathbf{u}'(t) \in \mathcal{U}_{ad}(t)$  and the initial conditions (173).

Now let us introduce  $\psi(t)$ ,  $\varphi(t)$  satisfying  $\psi(t) \in H^{1,1}(\Omega)$ ,  $\psi(t) = T_1(t)$  on  $\Gamma_\tau$ ,  $\varphi(t) \in H^{1,N}(\Omega)$ ,  $\varphi(t) = \mathbf{u}_2(t)$  on  $\Gamma_u$  ( $\psi = 0$ , if  $\Gamma_\tau = 0$ ,  $\varphi = 0$ , if  $\Gamma_u = 0$ ), substitute  $T - \psi$  for  $T$  and  $\mathbf{u} - \varphi$  for  $\mathbf{u}$ , keeping the same notation  $T$  and  $\mathbf{u}$  and introduce the spaces

$$\begin{aligned}
{}^1V &= \{ z | z \in H^{1,1}(\Omega), z = 0 \text{ on } \Gamma_\tau \}, \\
V &= \{ \mathbf{v} | \mathbf{v} \in H^{1,N}(\Omega), \mathbf{v} = 0 \text{ on } \Gamma_u \},
\end{aligned}$$

then we have to solve the following problem:

**Problem**  $(\mathcal{P}_{lm})_0$ : find a pair of functions  $(T, \mathbf{u})$  such that

$$\begin{aligned}
 T(t) &\in {}^1V, \mathbf{u}(t) \in V, \\
 (T'(t), z) + a_T(T(t), z) + b_p(\mathbf{u}'(t), z) &= (Q_0(t), z) \quad \forall z \in {}^1V, \\
 (\mathbf{u}''(t), \mathbf{v} - \mathbf{u}'(t)) + a(\mathbf{u}(t), \mathbf{v} - \mathbf{u}'(t)) &+ \int_0^t a_1(t - \tau; \mathbf{u}(\tau), \mathbf{v} - \mathbf{u}'(t)) d\tau + \\
 + b_s(T(t) - T_0, \mathbf{v} - \mathbf{u}'(t)) + j_g(\mathbf{v} + \boldsymbol{\varphi}'(t)) - j_g(\mathbf{u}'(t) + \boldsymbol{\varphi}'(t)) &\geq \\
 \geq (\mathbf{F}_0(t), \mathbf{v} - \mathbf{u}'(t)) \quad \forall \mathbf{v} \in V,
 \end{aligned} \tag{180}$$

where

$$\begin{aligned}
 (Q_0(t), z) &= (W(t), z) - (\psi'(t), z) - a_T(\psi(t), z) - b_p(\boldsymbol{\varphi}'(t), z), \\
 (\mathbf{F}_0(t), \mathbf{v}) &= (\mathbf{F}(t), \mathbf{v}) - (\boldsymbol{\varphi}''(t), \mathbf{v}) - a(\boldsymbol{\varphi}(t), \mathbf{v}) - \\
 &\quad - \int_0^t a_1(t - \tau; \boldsymbol{\varphi}(\tau), \mathbf{v}) d\tau - b_s(\psi(t), \mathbf{v}),
 \end{aligned} \tag{181}$$

with the initial conditions

$$\begin{aligned}
 T(\mathbf{x}, 0) &= T_0(\mathbf{x}) \quad (\text{really } T(\mathbf{x}, 0) = T_0(\mathbf{x}) - \psi(\mathbf{x}, 0)), \\
 \mathbf{u}(\mathbf{x}, 0) &= \mathbf{u}_0(\mathbf{x}) \quad (\text{really } \mathbf{u}(\mathbf{x}) = \mathbf{u}_0(\mathbf{x}) - \boldsymbol{\varphi}(\mathbf{x}, 0)), \\
 \mathbf{u}'(\mathbf{x}, 0) &= \mathbf{u}_1(\mathbf{x}) \quad (\text{really } \mathbf{u}'(\mathbf{x}) = \mathbf{u}_1(\mathbf{x}) - \boldsymbol{\varphi}'(\mathbf{x}, 0)).
 \end{aligned} \tag{182}$$

**Remark 12** *It is evident that from  $\mathbf{u}'(t) \in \mathcal{U}_{ad}$  and from the initial conditions it follows  $\mathbf{u}(\mathbf{x}, t) = \mathbf{u}_2(\mathbf{x}, t) + (\mathbf{u}_0(\mathbf{x}) - \mathbf{u}(\mathbf{x}, 0))$  on  $\Gamma_u$ , from which the boundary condition  $\mathbf{u}(\mathbf{x}, t) = \mathbf{u}_2(\mathbf{x}, t)$  follows if  $\mathbf{u}_0(\mathbf{x}) = \mathbf{u}_2(\mathbf{x}, 0)$  on  $\Gamma_u$  and similarly for the boundary condition on  $\Gamma_\tau$ .*

Then we have the following main result:

**Theorem 7** *Let us assume that*

$$\begin{aligned}
 \mathbf{f}, \mathbf{f}', \mathbf{f}'' &\in L^2(I; [L^2(\Omega)]^N), \quad \mathbf{P}, \mathbf{P}', \mathbf{P}'' \in L^2(I; [L^2(L_\tau)]^N), \\
 W, W', W'' &\in L^2(I; L^2(\Omega)), \\
 \rho, c_e &\in C(\overline{\Omega}), \quad \rho \geq \rho_0 > 0, \quad c_e \geq c_1 > 0, \\
 \beta_{ij}(\mathbf{x}) &\in C^1(\Omega) \quad \forall i, j \in \{1, \dots, N\}, \\
 \kappa_{ij} &\in L^\infty(\Omega) \text{ satisfy the usual symmetry and ellipticity conditions } (174), \\
 c_{ijkl} &\in L^\infty(\Omega) \text{ satisfy the usual conditions of symmetry and ellipticity } (175), \\
 b_{ijkl} &\text{ satisfy the symmetry conditions and the regularity assumption } (176), \\
 g_c^{kl} &\text{ does not depend on } t, \\
 \psi, \psi', \psi'' &\in L^2(I; H^{1,1}(\Omega)), \quad \psi(0) \in H^2(\Omega), \\
 \boldsymbol{\varphi}, \boldsymbol{\varphi}', \boldsymbol{\varphi}'' &\in L^2(I; H^{1,N}(\Omega)), \quad \boldsymbol{\varphi}''', \boldsymbol{\varphi}^{(iv)} \in L^2(I; [L^2(\Omega)]^N), \quad \boldsymbol{\varphi}(0) \in [H^2(\Omega)]^N, \\
 g_c^{kl} &\in L^\infty(\Gamma_c^{kl}), \quad g_c^{kl} \geq 0 \text{ on } \cup_{k,l} \Gamma_c^{kl},
 \end{aligned}$$

$$\begin{aligned}
& \mathbf{u}_2(\mathbf{x}, t) \in L^2(I; H^{1,N}(\Omega)), \quad T_1(\mathbf{x}, t) \in L^2(I; H^{1,1}(\Omega)), \\
& T_0 \in {}^1V, \quad (Q_0(0), z) - a_T(T_0, z) - b_p(\mathbf{u}_1, z) = (T_p, z), \quad T_p \in L^2(\Omega), \\
& \mathbf{u}_0 \in V, \quad (\mathbf{F}_0(0), \mathbf{v}) - a(\mathbf{u}_0, \mathbf{v}) = (\mathbf{u}_p, \mathbf{v}), \quad \mathbf{u}_p \in [L^2(\Omega)]^N, \\
& \mathbf{u}_1 \in V, \quad \mathbf{u}_{1t} + \boldsymbol{\varphi}'_t(0) = 0 \quad \text{on } \cup_{k,l} \Gamma_c^{kl}.
\end{aligned} \tag{183}$$

Then there exists one and only one pair of functions  $(T, \mathbf{u})$  such that

$$\begin{aligned}
& T, T' \in L^\infty(I; {}^1V), \\
& \mathbf{u}, \mathbf{u}' \in L^\infty(I; V), \quad \mathbf{u}'' \in L^2(I; V')
\end{aligned} \tag{184}$$

and satisfying (180)-(182).

**Proof:** The method of the proof is the following:

- (i) The uniqueness of the solution of (180)-(182) will be proved.
- (ii) The problem (180)-(182) will be regularized.
- (iii) The existence of the regularized problem based on the Galerkin approximation will be proved.
- (iv) A priori estimates I and II independent of  $\varepsilon$  will be performed.
- (v) Limitation processes over  $m$  (Galerkin) and  $\varepsilon$  (regularization) will be performed.

### Uniqueness:

Let  $(T^1(t), \mathbf{u}^1(t))$ ,  $(T^2(t), \mathbf{u}^2(t))$  be two solutions of the problem discussed. Let us denote  $(T^*(t), \mathbf{u}^*(t)) = (T^1(t) - T^2(t), \mathbf{u}^1(t) - \mathbf{u}^2(t))$ . Let us put  $(z(t), \mathbf{v}(t)) = (T^2(t), \mathbf{u}^2(t))$  into Eqs (180) for  $(T^1(t), \mathbf{u}^1(t))$  and  $(z(t), \mathbf{v}(t)) = (T^1(t), \mathbf{u}^1(t))$  for  $(T^2(t), \mathbf{u}^2(t))$  and add. Then after some modifications, where we add and subtract desirable terms, we obtain

$$\begin{aligned}
& \frac{1}{2} \frac{d}{dt} \{ |T^*(t)|_0^2 \} + a_T(T^*(t), T^*(t)) + \frac{1}{2} \frac{d}{dt} \{ |\mathbf{u}^{*'}(t)|_0^2 + a(\mathbf{u}^*(t), \mathbf{u}^*(t)) \} \leq \\
& - \int_0^t a_1(t - \tau; \mathbf{u}^*(\tau), \mathbf{u}^{*'}(\tau)) d\tau - [b_s(T^*(t), \mathbf{u}^{*'}(t)) + b_p(\mathbf{u}^{*'}(t), T^*(t))]
\end{aligned}$$

and then

$$\begin{aligned}
& |T^*(t)|_0^2 + \{ |\mathbf{u}^{*'}(t)|_0^2 + a(\mathbf{u}^*(t), \mathbf{u}^*(t)) \} + 2 \int_0^t a_T(T^*(\tau), T^*(\tau)) d\tau \leq \\
& - 2 \int_0^t \int_0^\tau a_1(\tau - \tau_1; \mathbf{u}^*(\tau_1), \mathbf{u}^{*'}(\tau_1)) d\tau_1 d\tau \\
& - 2 \int_0^t [b_s(T^*(\tau), \mathbf{u}^{*'}(\tau)) + b_p(\mathbf{u}^{*'}(\tau), T^*(\tau))] d\tau.
\end{aligned}$$

Since the form  $\mathbf{v} \rightarrow a_1(t; \mathbf{u}, \mathbf{v})$  is continuous on  $V$ , then

$$a_1(t; \mathbf{u}, \mathbf{v}) = (B(t)\mathbf{u}, \mathbf{v}), \quad B(t)\mathbf{u} \in V, \quad B(t) \in \mathcal{L}(V; V') \tag{185}$$

and then

$$\left| \int_0^t \int_0^\tau a_1(\tau - \tau_1; \varphi(\tau_1), \varphi'(\tau)) d\tau_1 d\tau \right| = \quad (186)$$

$$\begin{aligned} &= \left| \int_0^t \left( \int_0^\tau B(\tau - \tau_1) \varphi(\tau_1) d\tau_1, \varphi'(\tau) \right) d\tau \right| = \\ &= \left| \int_0^t \int_\tau^t (B(\tau - \tau_1) \varphi(\tau_1), \varphi'(\tau)) d\tau d\tau_1 \right| = \\ &= \left| \int_0^t (B(t - \tau_1) \varphi(\tau_1), \varphi(t)) d\tau_1 - \int_0^t (B(0) \varphi(\tau_1), \varphi(\tau_1)) d\tau_1 - \right. \\ &\quad \left. - \int_0^t \int_\tau^t (B'(\tau - \tau_1) \varphi(\tau_1), \varphi(\tau)) d\tau d\tau_1 \right| \leq \\ &\leq c \left[ \int_0^t \|\varphi(\tau)\|_1^2 d\tau + \|\varphi(t)\|_1 \int_0^t \|\varphi(\tau)\|_1 d\tau \right] \end{aligned} \quad (187)$$

and since the bilinear forms  $a_T(z, z)$ ,  $a(\mathbf{v}, \mathbf{v})$  are continuous, bounded and coercive, i.e. there exist constants  $c > 0$  such that  $|a_T(w, z)| \leq c\|w\|_1\|z\|_1 \forall w, z \in H^{1,1}(\Omega)$ ,  $a_T(z, z) \geq c\|z\|_1^2 \forall z \in H^{1,1}(\Omega)$ ,  $|a(\mathbf{u}, \mathbf{v})| \leq c\|\mathbf{u}\|_1\|\mathbf{v}\|_1 \forall \mathbf{u}, \mathbf{v} \in H^{1,N}(\Omega)$ ,  $a(\mathbf{v}, \mathbf{v}) \geq c\|\mathbf{v}\|_1^2 \forall \mathbf{v} \in H^{1,N}(\Omega)$  hold, since  $\mathbf{u}^*(t) = \int_0^t \mathbf{u}^{*'}(\tau) d\tau$  and

$$|b_s(T^*(t), \mathbf{u}^{*'}(t)) + b_p(\mathbf{u}^{*'}(t), T^*(t))| \leq c(\|\mathbf{u}^{*'}(t)\|_0 \|T^*(t)\|_1 + \|\mathbf{u}^{*'}(t)\|_1 \|T^*(t)\|_0),$$

thus

$$\begin{aligned} &|T^*(t)|_0^2 + \int_0^t \|T^*(\tau)\|_1^2 d\tau + |\mathbf{u}^{*'}(t)|_0^2 + \|\mathbf{u}^*(t)\|_1^2 \leq \\ &\leq c \int_0^t [|T^*(\tau)|_0^2 + \|T^*(\tau)\|_1^2 + |\mathbf{u}^{*'}(\tau)|_0^2 + \|\mathbf{u}^*(\tau)\|_1^2] d\tau. \end{aligned}$$

Hence  $T^*(t) = 0$ ,  $\mathbf{u}^*(t) = 0$ , follows by applying the Gronwall lemma, and then the uniqueness of the solution is proved.

### Existence:

To prove the existence of the solution of the problem studied, the regularization technique will be used. For this we introduce the convex function  $\psi_\varepsilon : \mathbb{R} \rightarrow \mathbb{R}$  defined by

$$\psi_\varepsilon(x) = \sqrt{x^2 + \varepsilon^2} - \varepsilon, \quad (188)$$

which regularizes the function  $x \rightarrow |x|$ , and which is differentiable and satisfies the following inequality

$$|x| - \psi_\varepsilon(|x|) < \varepsilon, \quad \forall x \in \mathbb{R}, \varepsilon \geq 0. \quad (189)$$

Define a family of regularized friction functionals  $j_{g\varepsilon} : V \rightarrow \mathbb{R}$ , depending on the parameter  $\varepsilon > 0$

$$j_{g\varepsilon}(\mathbf{v}) = \int_{\cup_{k,l} \Gamma_c^{kl}} g_c^{kl}(\mathbf{x}, t) \psi_\varepsilon(|\mathbf{v}_t^k - \mathbf{v}_t^l|) ds \equiv \langle g_c^{kl}, \psi_\varepsilon(|\mathbf{v}_t^k - \mathbf{v}_t^l|) \rangle_{\cup_{k,l} \Gamma_c^{kl}}, \quad (190)$$

which are well-defined, convex and Gâteaux-differentiable with respect to the argument  $\mathbf{v}$ . The partial Gâteaux-derivative of  $j_{g\varepsilon}$  with respect to the argument  $\mathbf{v}$  in the direction  $\mathbf{w} \in V$  is given by

$$(j'_{g\varepsilon}(\mathbf{v}), \mathbf{w}) = \langle g_c^{kl} \chi_\varepsilon(\mathbf{v}_t^k - \mathbf{v}_t^l), \mathbf{w}_t^k - \mathbf{w}_t^l \rangle_{\cup_{k,l} \Gamma_c^{kl}}, \quad \mathbf{v}, \mathbf{w} \in V, \quad (191)$$

where we set  $\chi_\varepsilon(\mathbf{v}_t^k - \mathbf{v}_t^l) = \psi'_\varepsilon(|\mathbf{v}_t^k - \mathbf{v}_t^l|)(\mathbf{v}_t^k - \mathbf{v}_t^l)$ .

Then the regularized problem is the following:

$$(T'_\varepsilon(t), z) + a_T(T_\varepsilon(t), z) + b_p(\mathbf{u}'_\varepsilon(t), z) = (Q_0(t), z) \quad \forall z \in {}^1V, \quad (192)$$

$$\begin{aligned} &(\mathbf{u}''_\varepsilon(t), \mathbf{v}) + a(\mathbf{u}_\varepsilon(t), \mathbf{v}) + \int_0^t a_1(t - \tau; \mathbf{u}_\varepsilon(\tau), \mathbf{v}) d\tau + b_s(T_\varepsilon(t) - T_0, \mathbf{v}) + \\ &+(j'_{g\varepsilon}(\mathbf{u}'_\varepsilon(t) + \boldsymbol{\varphi}'(t), \mathbf{v}) = (\mathbf{F}_0(t), \mathbf{v}) \quad \mathbf{v} \in V, \end{aligned} \quad (193)$$

with the initial conditions

$$T_\varepsilon(\mathbf{x}, 0) = T_0(\mathbf{x}), \mathbf{u}_\varepsilon(\mathbf{x}, 0) = \mathbf{u}_0(\mathbf{x}), \mathbf{u}'_\varepsilon(\mathbf{x}, 0) = \mathbf{u}_1(\mathbf{x}). \quad (194)$$

The existence of  $(T_\varepsilon(t), \mathbf{u}_\varepsilon(t))$  will be proved by means of the finite-dimensional approximation (Galerkin). Let  $\{z_j\}, \{\mathbf{w}_j\}$  be countable basis of the spaces  ${}^1V$  and  $V$ , i.e. each finite subsets of  $\{z_j\}, \{\mathbf{w}_j\}$  are linearly independent and span  $\{z_j | j = 1, 2, \dots\}$ , span  $\{\mathbf{w}_j | j = 1, 2, \dots\}$  are dense in  ${}^1V$  or  $V$ , respectively, as  ${}^1V$  and  $V$  are separable spaces. Let  ${}^1V_m$  and  $V_m$  be spanned by  $\{z_j | 1 \leq j \leq m\}$  or by  $\{\mathbf{w}_j | 1 \leq j \leq m\}$ , respectively, and let us assume that  $z_1 = T_0, \mathbf{w}_1 = \mathbf{u}_0$ . Then the approximate solution  $(T_m(t), \mathbf{u}_m(t))$  of the order  $m$  satisfies the system:

$$\begin{aligned} &T_m(t) \in {}^1V_m, \mathbf{u}_m(t) \in V_m, \\ &(T'_m(t), z_j) + a_T(T_m(t), z_j) + b_p(\mathbf{u}'_m(t), z_j) = (Q_0(t), z_j) \\ &\quad \forall z_j \in {}^1V_m, 1 \leq j \leq m, \end{aligned} \quad (195)$$

$$\begin{aligned} &(\mathbf{u}''_m(t), \mathbf{w}_j) + a(\mathbf{u}_m(t), \mathbf{w}_j) + \\ &+ \int_0^t a_1(t - \tau; \mathbf{u}_m(\tau), \mathbf{w}_j) d\tau + b_s(T_m(t) - T_0, \mathbf{w}_j) + \\ &+(j'_{g\varepsilon}(\mathbf{u}'_m(t) + \boldsymbol{\varphi}'(t), \mathbf{w}_j) = (\mathbf{F}_0(t), \mathbf{w}_j) \quad \mathbf{w}_j \in V_m, 1 \leq j \leq m, \end{aligned} \quad (196)$$

$$\begin{aligned} &T_m(\mathbf{x}, 0) = T_0(\mathbf{x}), \mathbf{u}_m(\mathbf{x}, 0) = \mathbf{u}_0(\mathbf{x}), \mathbf{u}'_m(\mathbf{x}, 0) = \mathbf{u}_{1m}(\mathbf{x}), \\ &\mathbf{u}_{1m} \in [\mathbf{w}_1, \dots, \mathbf{w}_m], z_1 = T_0, \mathbf{w}_1 = \mathbf{u}_0, \mathbf{u}_{1m} \rightarrow \mathbf{u}_1 \text{ in } [L^2(\Omega)]^N \\ &\text{when } m \rightarrow \infty. \end{aligned} \quad (197)$$

Since  $\{z_j\}_{j=1}^m, \{\mathbf{w}_j\}_{j=1}^m$  are linearly independent, the system (195)-(197) is a regular system of ordinary differential equations of the first and the second orders and therefore (195)-(197) uniquely define  $(T_m(t), \mathbf{u}_m(t))$  on the interval  $I_m = [0, t_m]$ .

### A priori estimates I:

To obtain the first estimates we put  $z = T_\varepsilon(t)$  in (192) and  $\mathbf{v} = \mathbf{u}'_\varepsilon(t) + \boldsymbol{\varphi}'(t)$  in (193). Then

$$(T'_\varepsilon(t), T_\varepsilon(t)) + a_T(T_\varepsilon(t), T_\varepsilon(t)) + b_p(\mathbf{u}'_\varepsilon(t), T_\varepsilon(t)) = (Q_0(t), T_\varepsilon(t)), \quad (198)$$

$$\begin{aligned} & (\mathbf{u}''_\varepsilon(t), \mathbf{u}'_\varepsilon(t) + \boldsymbol{\varphi}'(t)) + a(\mathbf{u}_\varepsilon(t), \mathbf{u}'_\varepsilon(t) + \boldsymbol{\varphi}'(t)) + \\ & + \int_0^t a_1(t - \tau; \mathbf{u}_\varepsilon(\tau), \mathbf{u}'_\varepsilon(\tau) + \boldsymbol{\varphi}'(\tau)) d\tau + b_s(T_\varepsilon(t) - T_0, \mathbf{u}'_\varepsilon(t) + \boldsymbol{\varphi}'(t)) + \\ & \boldsymbol{\varphi}'(t), \mathbf{u}'_\varepsilon(t) + \boldsymbol{\varphi}'(t)) = (\mathbf{F}_0(t), \mathbf{u}'_\varepsilon(t) + \boldsymbol{\varphi}'(t)). \end{aligned} \quad (199)$$

Since the form  $a_1(t; \mathbf{u}, \mathbf{v})$  is continuous on  $V$  and since  $(j'_{g_\varepsilon}(\mathbf{w}), \mathbf{w}) \geq 0, \forall \mathbf{w} \in V$ , then

$$\frac{1}{2} \frac{d}{dt} |T_\varepsilon(t)|_0^2 + a_T(T_\varepsilon(t), T_\varepsilon(t)) = (Q_0(t), T_\varepsilon(t)) - b_p(\mathbf{u}'_\varepsilon(t), T_\varepsilon(t)) \quad (200)$$

$$\begin{aligned} & \frac{1}{2} \frac{d}{dt} [\|\mathbf{u}'_\varepsilon(t)\|_0^2 + a(\mathbf{u}_\varepsilon(t), \mathbf{u}_\varepsilon(t))] \leq (\mathbf{F}_0(t), \mathbf{u}'_\varepsilon(t) + \boldsymbol{\varphi}'(t)) - \\ & - b_s(T_\varepsilon(t) - T_0, \mathbf{u}'_\varepsilon(t) + \boldsymbol{\varphi}'(t)) - \int_0^t a_1(t - \tau; \mathbf{u}_\varepsilon(\tau), \mathbf{u}'_\varepsilon(\tau) + \boldsymbol{\varphi}'(\tau)) d\tau - \\ & - (\mathbf{u}''_\varepsilon(t), \boldsymbol{\varphi}'(t)) - a(\mathbf{u}_\varepsilon(t), \boldsymbol{\varphi}'(t)). \end{aligned} \quad (201)$$

Since

$$\begin{aligned} & |b_s(T_\varepsilon(t) - T_0, \mathbf{u}'_\varepsilon(t) + \boldsymbol{\varphi}'(t)) + b_p(\mathbf{u}'_\varepsilon(t), T_\varepsilon(t))| \leq \\ & \leq c(1 + \|T_\varepsilon(t)\|_1 \|\mathbf{u}'_\varepsilon(t)\|_0 + \|T_\varepsilon(t)\|_1 \|\boldsymbol{\varphi}'(t)\|_0 + \|T_\varepsilon(t)\|_0 \|\mathbf{u}'_\varepsilon(t)\|_1) \end{aligned} \quad (202)$$

and since  $|a_1(t - \tau; \mathbf{u}, \mathbf{v})| \leq C(t, \tau) \|\mathbf{u}\|_1 \|\mathbf{v}\|_1 \forall \mathbf{u}, \mathbf{v} \in V$ , with  $C(t, \tau) \in L^\infty(I \times I)$ , and according to (187)

$$\begin{aligned} & \left| \int_0^t \int_0^\tau a_1(\tau - \tau_1; \mathbf{u}_\varepsilon(\tau_1), \mathbf{u}'_\varepsilon(\tau_1)) d\tau_1 d\tau \right| \leq \\ & \leq c \left[ \int_0^t \|\mathbf{u}_\varepsilon(\tau)\|_1^2 d\tau + \|\mathbf{u}_\varepsilon(t)\|_1 \int_0^t \|\mathbf{u}_\varepsilon(\tau)\|_1 d\tau \right], \\ & \left| \int_0^t a_1(t - \tau; \mathbf{u}(\tau), \mathbf{v}) d\tau \right| \leq \int_0^t C(t, \tau) \|\mathbf{u}(\tau)\|_1 \|\mathbf{v}\|_1 d\tau \leq \\ & \leq \|\mathbf{v}\|_1 \int_0^t C(t, \tau) \|\mathbf{u}(\tau)\|_1 d\tau \leq \|C(t, \cdot)\|_{L^1(0, t)} \|\mathbf{v}\|_1 \int_0^t \|\mathbf{u}(\tau)\|_1 d\tau, \end{aligned} \quad (203)$$

then from (200), (201), after integration over  $t$  and by using the coerciveness of the bilinear forms  $a_T(z, z)$  and  $a(\mathbf{v}, \mathbf{v})$  and adding both relations, we obtain

$$\begin{aligned}
& |T_\varepsilon(t)|_0^2 + 2c \int_0^t \|T_\varepsilon(\tau)\|_1^2 d\tau + |\mathbf{u}'_\varepsilon(t)|_0^2 + c\|\mathbf{u}_\varepsilon(t)\|_1^2 \leq \\
& \leq |T_0|_0^2 + |\mathbf{u}_1|_0^2 + c\|\mathbf{u}_0\|_1^2 + 2 \int_0^t (Q_0(\tau), T_\varepsilon(\tau)) d\tau + \\
& + 2 \int_0^t (\mathbf{F}_0(\tau), \mathbf{u}'_\varepsilon(\tau) + \boldsymbol{\varphi}'(\tau)) d\tau - \\
& - 2 \int_0^t [b_p(\mathbf{u}'_\varepsilon(\tau), T_\varepsilon(\tau)) + b_s(T_\varepsilon(\tau) - T_0, \mathbf{u}'_\varepsilon(\tau) + \boldsymbol{\varphi}'(\tau))] d\tau - \\
& - 2 \int_0^t (\mathbf{u}''_\varepsilon(\tau), \boldsymbol{\varphi}'(\tau)) d\tau - 2 \int_0^t a(\mathbf{u}_\varepsilon(\tau), \boldsymbol{\varphi}'(\tau)) d\tau - \\
& - 2 \int_0^t \int_0^\tau a_1(\tau - \tau_1; \mathbf{u}_\varepsilon(\tau_1), \mathbf{u}'_\varepsilon(\tau) + \boldsymbol{\varphi}'(\tau)) d\tau_1 d\tau \leq \\
& \leq |T_0|_0^2 + |\mathbf{u}_1|_0^2 + c\|\mathbf{u}_0\|_1^2 + 2 \int_0^t (Q_0(\tau), T_\varepsilon(\tau)) d\tau + \\
& + 2 \int_0^t (\mathbf{F}_0(\tau), \mathbf{u}'_\varepsilon(\tau) + \boldsymbol{\varphi}'(\tau)) d\tau - \\
& - 2c \int_0^t [1 + \|T_\varepsilon(\tau)\|_1 \|\mathbf{u}'_\varepsilon(\tau)\|_0 + \|T_\varepsilon(\tau)\|_0 \|\mathbf{u}'_\varepsilon(\tau)\|_1] d\tau - \\
& - 2c \left[ \int_0^t \|\mathbf{u}_\varepsilon(\tau)\|_1^2 d\tau + \|\mathbf{u}_\varepsilon(t)\|_1 \int_0^t \|\mathbf{u}_\varepsilon(\tau)\|_1 d\tau \right]. \tag{204}
\end{aligned}$$

According to the assumptions made on  $W, \psi, \mathbf{f}, \mathbf{P}, \boldsymbol{\varphi}$ , then

$$Q_0, Q'_0 \in L^2(I; {}^1V'), \mathbf{F}_0, \mathbf{F}'_0 \in L^2(I; V').$$

Since  $\mathbf{u}_\varepsilon(t) = \mathbf{u}_0 + \int_0^t \mathbf{u}'_\varepsilon(\tau) d\tau$  and  $\|\mathbf{v}\|_0^2 \leq |\mathbf{v}|_0^2$ , then we have

$$\begin{aligned}
& |\mathbf{u}_\varepsilon(t)|_0^2 \leq c \int_0^t |\mathbf{u}'_\varepsilon(\tau)|_0^2 d\tau + 2|\mathbf{u}_0|_0^2, \\
& 2|(Q_0(t), T_\varepsilon(t))| \leq \frac{1}{2}c|T_\varepsilon(t)|_0^2 + c\|Q_0(t)\|_*^2, \\
& 2 \int_0^t (\mathbf{F}_0(\tau), \mathbf{u}'_\varepsilon(\tau) + \boldsymbol{\varphi}'(\tau)) d\tau = \\
& = 2(\mathbf{F}_0(t), \mathbf{u}_\varepsilon(t)) - 2(\mathbf{F}_0(0), \mathbf{u}_\varepsilon(0)) - \\
& - 2 \int_0^t (\mathbf{F}'_0(\tau), \mathbf{u}_\varepsilon(\tau)) d\tau + 2(\mathbf{F}_0(t), \boldsymbol{\varphi}(t)) - \\
& - 2(\mathbf{F}_0(0), \boldsymbol{\varphi}(0)) - 2 \int_0^t (\mathbf{F}'_0(\tau), \boldsymbol{\varphi}(\tau)) d\tau, \\
& 2|(\mathbf{F}_0(t), \mathbf{u}_\varepsilon(t))| \leq \frac{1}{2}c|\mathbf{u}_\varepsilon(t)|_0^2 + c\|\mathbf{F}_0(t)\|_*^2,
\end{aligned}$$



where  $c > 0$  are different constants, then (204) yields

$$\begin{aligned}
 & |T_\varepsilon(t)|_0^2 + \int_0^t \|T_\varepsilon(\tau)\|_1^2 d\tau + |\mathbf{u}'_\varepsilon(t)|_0^2 + \|\mathbf{u}_\varepsilon(t)\|_1^2 \leq \\
 & \leq c + c \int_0^t |T_\varepsilon(\tau)|_0^2 d\tau + c \int_0^t \|Q_0(\tau)\|_*^2 d\tau + \\
 & + c \int_0^t |\mathbf{u}'_\varepsilon(\tau)|_0^2 d\tau + c \int_0^t \|\mathbf{F}_0(\tau)\|_*^2 d\tau - \\
 & - 2c \int_0^t (1 + \|T_\varepsilon(\tau)\|_1 \|\mathbf{u}'_\varepsilon(\tau)\|_0 + \|T_\varepsilon(\tau)\|_0 \|\mathbf{u}'_\varepsilon(\tau)\|_1) d\tau - \\
 & - 2c \left( \int_0^t \|\mathbf{u}_\varepsilon(\tau)\|_1^2 d\tau + \|\mathbf{u}_\varepsilon(t)\|_1 \int_0^t \|\mathbf{u}_\varepsilon(\tau)\|_1 d\tau \right).
 \end{aligned}$$

Hence

$$\begin{aligned}
 & |T_\varepsilon(t)|_0^2 + \int_0^t \|T_\varepsilon(\tau)\|_1^2 d\tau + |\mathbf{u}'_\varepsilon(t)|_0^2 + \|\mathbf{u}_\varepsilon(t)\|_1^2 \leq \\
 & \leq c(1 + \int_0^t (|T_\varepsilon(\tau)|_0^2 + \|T_\varepsilon(\tau)\|_1^2 + |\mathbf{u}'_\varepsilon(\tau)|_0^2 + \|\mathbf{u}_\varepsilon(\tau)\|_1^2) d\tau).
 \end{aligned}$$

Applying the Gronwall lemma, then

$$|T_\varepsilon(t)|_0^2 + \int_0^t \|T_\varepsilon(\tau)\|_1^2 d\tau + |\mathbf{u}'_\varepsilon(t)|_0^2 + \|\mathbf{u}_\varepsilon(t)\|_1^2 \leq c,$$

i.e.

$$|T_\varepsilon(t)|_0 \leq c, \int_0^t \|T_\varepsilon(\tau)\|_1^2 d\tau \leq c, \quad |\mathbf{u}'_\varepsilon(t)|_0 \leq c, \quad \|\mathbf{u}_\varepsilon(t)\|_1 \leq c, \quad t \in I, \quad (205)$$

where  $c = \text{const.} > 0$  denotes various constants independent of  $\varepsilon$ .

Let us set in (192) and (193)  $t = 0$ . Then

$$\begin{aligned}
 & (T'_\varepsilon(0), z) + a_T(T_0, z) + b_p(\mathbf{u}_1, z) = (Q_0(0), z) \quad \forall z \in {}^1V, \\
 & (\mathbf{u}''_\varepsilon(0), \mathbf{v}) + a(\mathbf{u}_0, \mathbf{v}) + (j'_{g\varepsilon}(\mathbf{u}_1 + \boldsymbol{\varphi}'(0)), \mathbf{v}) = (\mathbf{F}_0(0), \mathbf{v}) \quad \mathbf{v} \in V.
 \end{aligned}$$

According to (183), i.e.  $\mathbf{u}_{1t} + \boldsymbol{\varphi}'_t(0) = 0$  on  $\cup_{k,l} \Gamma_c^{kl}$ , we have  $(j'_{g\varepsilon}(\mathbf{u}_1 + \boldsymbol{\varphi}'(0)), \mathbf{v}) = 0$  and since

$$\begin{aligned}
 & (Q_0(0), z) - a_T(T_0, z) - b_p(\mathbf{u}_1, z) = (T_p, z), \quad T_p \in L^2(\Omega), \\
 & (\mathbf{F}_0(0), \mathbf{v}) - a(\mathbf{u}_0, \mathbf{v}) = (\mathbf{u}_p, \mathbf{v}) \quad \mathbf{u}_p \in [L^2(\Omega)]^N,
 \end{aligned}$$

then  $T'_\varepsilon(0) = T_p$ ,  $\mathbf{u}''_\varepsilon(0) = \mathbf{u}_p$ ,  $T'_\varepsilon(0) \in L^2(\Omega)$ ,  $\mathbf{u}''_\varepsilon(0) \in [L^2(\Omega)]^N$ .

### A priori estimates II.

Differentiating (192),(193) with respect to  $t$  we have

$$\begin{aligned} (T_\varepsilon''(t), z) + a_T(T_\varepsilon'(t), z) + b_p(\mathbf{u}_\varepsilon''(t), z) &= (Q_0'(t), z) \quad \forall z \in {}^1V, \\ (\mathbf{u}_\varepsilon'''(t), \mathbf{v}) + a(\mathbf{u}_\varepsilon'(t), \mathbf{v}) + (B(0)\mathbf{u}_\varepsilon(t), \mathbf{v}) &+ \left( \int_0^t B'(t-\tau)\mathbf{u}_\varepsilon(\tau)d\tau, \mathbf{v} \right) + \\ + b_s(T_\varepsilon'(t), \mathbf{v}) + \left( \frac{d}{dt}j'_{g\varepsilon}(\mathbf{u}_\varepsilon'(t) + \boldsymbol{\varphi}'(t)), \mathbf{v} \right) &= (\mathbf{F}_0'(t), \mathbf{v}) \quad \mathbf{v} \in V. \end{aligned} \quad (206)$$

Hence, putting  $z = T_\varepsilon'(t)$ ,  $\mathbf{v} = \mathbf{u}_\varepsilon''(t) + \boldsymbol{\varphi}''(t)$ , we obtain

$$(T_\varepsilon''(t), T_\varepsilon'(t)) + a_T(T_\varepsilon'(t), T_\varepsilon'(t)) + b_p(\mathbf{u}_\varepsilon''(t), T_\varepsilon'(t)) = (Q_0'(t), T_\varepsilon'(t)) \quad \forall z \in {}^1V, \quad (207)$$

$$\begin{aligned} &(\mathbf{u}_\varepsilon'''(t), \mathbf{u}_\varepsilon''(t) + \boldsymbol{\varphi}''(t)) + a(\mathbf{u}_\varepsilon'(t), \mathbf{u}_\varepsilon''(t) + \boldsymbol{\varphi}''(t)) + (B(0)\mathbf{u}_\varepsilon(t), \mathbf{u}_\varepsilon''(t) + \\ &+ \boldsymbol{\varphi}''(t)) + \left( \int_0^t B'(t-\tau)\mathbf{u}_\varepsilon(\tau)d\tau, \mathbf{u}_\varepsilon''(t) + \boldsymbol{\varphi}''(t) \right) + b_s(T_\varepsilon'(t), \mathbf{u}_\varepsilon''(t) + \\ &+ \boldsymbol{\varphi}''(t)) + \left( \frac{d}{dt}j'_{g\varepsilon}(\mathbf{u}_\varepsilon'(t) + \boldsymbol{\varphi}'(t)), \mathbf{u}_\varepsilon''(t) + \boldsymbol{\varphi}''(t) \right) = \\ &= (\mathbf{F}_0'(t), \mathbf{u}_\varepsilon''(t) + \boldsymbol{\varphi}''(t)) \quad \mathbf{v} \in V. \end{aligned} \quad (208)$$

Hence

$$\frac{1}{2} \frac{d}{dt} |T_\varepsilon'(t)|_0^2 + a_T(T_\varepsilon'(t), T_\varepsilon'(t)) + b_p(\mathbf{u}_\varepsilon''(t), T_\varepsilon'(t)) = (Q_0'(t), T_\varepsilon'(t)), \quad (209)$$

$$\begin{aligned} &\frac{1}{2} \frac{d}{dt} [|\mathbf{u}_\varepsilon''(t)|_0^2 + a(\mathbf{u}_\varepsilon'(t), \mathbf{u}_\varepsilon'(t))] + (B(0)\mathbf{u}_\varepsilon(t), \mathbf{u}_\varepsilon''(t) + \boldsymbol{\varphi}''(t)) + \\ &+ \left( \int_0^t B'(t-\tau)\mathbf{u}_\varepsilon(\tau)d\tau, \mathbf{u}_\varepsilon''(t) + \boldsymbol{\varphi}''(t) \right) + b_s(T_\varepsilon'(t), \mathbf{u}_\varepsilon''(t) + \boldsymbol{\varphi}''(t)) + \\ &+ \left( \frac{d}{dt}j'_{g\varepsilon}(\mathbf{u}_\varepsilon'(t) + \boldsymbol{\varphi}'(t)), \mathbf{u}_\varepsilon''(t) + \boldsymbol{\varphi}''(t) \right) = (\mathbf{F}_0'(t), \mathbf{u}_\varepsilon''(t) + \boldsymbol{\varphi}''(t)) - \\ &- (\mathbf{u}_\varepsilon'''(t), \boldsymbol{\varphi}''(t)) - a(\mathbf{u}_\varepsilon'(t), \boldsymbol{\varphi}''(t)), \end{aligned} \quad (210)$$

where

$$\begin{aligned} &\left( \frac{d}{dt}j'_{g\varepsilon}(\mathbf{u}_\varepsilon'(t) + \boldsymbol{\varphi}'(t)), \mathbf{u}_\varepsilon''(t) + \boldsymbol{\varphi}''(t) \right) = \\ &= \left\langle \frac{d}{dt}g_c^{kl}(\mathbf{x}, t)\psi'_\varepsilon(|\mathbf{u}'_{\varepsilon t}(t) + \boldsymbol{\varphi}'_t(t)|)(\mathbf{u}'_{\varepsilon t}(t) + \boldsymbol{\varphi}'_t(t)), \mathbf{u}_\varepsilon''(t) + \boldsymbol{\varphi}''(t) \right\rangle_{\cup_{k,l}\Gamma_c^{kl}}. \end{aligned}$$

Since

$$(j'_{g\varepsilon}(\mathbf{w}), \mathbf{v}) = \int_{\cup_{k,l}\Gamma_c^{kl}} g_c^{kl}(\mathbf{x}, t)\psi'_\varepsilon(|\mathbf{w}_t|)\mathbf{w}_t\mathbf{v}_t ds = \int_{\cup_{k,l}\Gamma_c^{kl}} g_c^{kl}(\mathbf{x}, t)\chi_\varepsilon(\mathbf{w}_t)\mathbf{v}_t ds,$$

then

$$\begin{aligned} \left( \frac{d}{dt} j'_{g\varepsilon}(\mathbf{w}(t), \mathbf{v}) \right) &= \int_{\cup_{k,l} \Gamma_c^{kl}} \frac{\partial g_c^{kl}(\mathbf{x}, t)}{\partial t} \chi_\varepsilon(\mathbf{w}_t(t)) \mathbf{v}_t ds + \\ &+ \int_{\cup_{k,l} \Gamma_c^{kl}} g_c^{kl}(\mathbf{x}, t) \lim_{k \rightarrow 0} \frac{\chi_\varepsilon(\mathbf{w}_t(t+k)) - \chi_\varepsilon(\mathbf{w}_t(t))}{k} \mathbf{v}_t ds. \end{aligned}$$

Thus

$$\begin{aligned} \left( \frac{d}{dt} j'_{g\varepsilon}(\mathbf{w}(t), \mathbf{w}'(t)) \right) &= \int_{\cup_{k,l} \Gamma_c^{kl}} \frac{\partial g_c^{kl}(\mathbf{x}, t)}{\partial t} \chi_\varepsilon(\mathbf{w}_t(t)) \mathbf{w}'_t(t) ds + \\ &+ \int_{\cup_{k,l} \Gamma_c^{kl}} g_c^{kl}(\mathbf{x}, t) \lim_{k \rightarrow 0} \frac{\chi_\varepsilon(\mathbf{w}_t(t+k)) - \chi_\varepsilon(\mathbf{w}_t(t))}{k} \cdot \frac{\mathbf{w}_t(t+k) - \mathbf{w}_t(t)}{k} ds = \\ &= I_1 + I_2 \geq \int_{\cup_{k,l} \Gamma_c^{kl}} \frac{\partial g_c^{kl}(\mathbf{x}, t)}{\partial t} \chi_\varepsilon(\mathbf{w}_t(t)) \mathbf{w}'_t(t) ds = \\ &= \int_{\cup_{k,l} \Gamma_c^{kl}} \frac{\partial g_c^{kl}(\mathbf{x}, t)}{\partial t} \frac{\partial}{\partial t} \chi_\varepsilon(\mathbf{w}_t(t)) ds, \end{aligned}$$

as the integral  $I_2 \geq 0$  due to the property of monotony. Hence and (209), (210)

$$\frac{1}{2} \frac{d}{dt} |T'_\varepsilon(t)|_0^2 + a_T(T'_\varepsilon(t), T'_\varepsilon(t)) + b_p(\mathbf{u}''_\varepsilon(t), T'_\varepsilon(t)) = (Q'_0(t), T'_\varepsilon(t)) \quad (211)$$

$$\begin{aligned} &\frac{1}{2} \frac{d}{dt} [|\mathbf{u}''_\varepsilon(t)|_0^2 + a(\mathbf{u}'_\varepsilon(t), \mathbf{u}'_\varepsilon(t))] + (B(0)\mathbf{u}_\varepsilon(t), \mathbf{u}''_\varepsilon(t) + \varphi''(t)) + \\ &+ \left( \int_0^t B'(t-\tau) \mathbf{u}_\varepsilon(\tau) d\tau, \mathbf{u}''_\varepsilon(t) + \varphi''(t) \right) + b_s(T'_\varepsilon(t), \mathbf{u}''_\varepsilon(t) + \varphi''(t)) + \\ &+ \int_{\cup_{k,l} \Gamma_c^{kl}} \frac{\partial g_c^{kl}(\mathbf{x}, t)}{\partial t} \frac{\partial}{\partial t} \chi_\varepsilon(\mathbf{u}^{kl}_\varepsilon(t) - \mathbf{u}^l_{\varepsilon t}(t) + \varphi^{kl}_t(t) - \varphi^l_t(t)) ds \leq \\ &\leq (\mathbf{F}'_0(t), \mathbf{u}''_\varepsilon(t) + \varphi''(t)) - (\mathbf{u}'''_\varepsilon(t), \varphi''(t)) - a(\mathbf{u}'_\varepsilon(t), \varphi''(t)). \end{aligned} \quad (212)$$

Then we integrate (211), (212) from 0 to  $t$ . Since

$$\begin{aligned} \int_0^t (Q'_0(\tau), T'_\varepsilon(\tau)) d\tau &= (Q'_0(t), T_\varepsilon(t)) - (Q'_0(0), T_0) - \int_0^t (Q''_0(\tau), T_\varepsilon(\tau)) d\tau, \\ \int_0^t (\mathbf{F}'_0(\tau), \mathbf{u}''_\varepsilon(\tau)) d\tau &= (\mathbf{F}'_0(t), \mathbf{u}'_\varepsilon(t)) - (\mathbf{F}'_0(0), \mathbf{u}_1) - \int_0^t (\mathbf{F}''_0(\tau), \mathbf{u}'_\varepsilon(\tau)) d\tau \end{aligned}$$

and according to the assumptions on  $W, \psi, \mathbf{f}, \mathbf{P}, \varphi$  it follows that

$$Q''_0 \in L^2(I; {}^1V'), \mathbf{F}''_0 \in L^2(I; V'),$$

and therefore, since  $y(t) = \int_0^t y'(\tau) d\tau + y_0$ ,  $\|y\|_0^2 \leq |y|_0^2 \leq c\|y\|_1^2$ ,

$$\begin{aligned} \int_0^t (Q'_0(\tau), T'_\varepsilon(\tau)) d\tau &\leq c\|Q'_0(t)\|_* \|T_\varepsilon(t)\|_1 + c + \int_0^t \|Q''_0(\tau)\|_* \|T_\varepsilon(\tau)\|_1 d\tau, \\ \int_0^t (\mathbf{F}'_0(\tau), \mathbf{u}''_\varepsilon(\tau)) d\tau &\leq c\|\mathbf{F}'_0(t)\|_* \|\mathbf{u}'_\varepsilon(t)\|_1 + c + \int_0^t \|\mathbf{F}''_0(\tau)\|_* \|\mathbf{u}'_\varepsilon(\tau)\|_1 d\tau, \end{aligned} \quad (213)$$

$$|b_p(\mathbf{u}_\varepsilon''(t), T'_\varepsilon(t)) + b_s(T'_\varepsilon(t), \mathbf{u}_\varepsilon''(t) + \boldsymbol{\varphi}''(t))| \leq c \|T'_\varepsilon(t)\|_1 (\|\mathbf{u}_\varepsilon''(t)\|_1 + \|\boldsymbol{\varphi}''(t)\|_0), \quad (214)$$

$$\int_0^t (\mathbf{u}_\varepsilon'''(\tau), \boldsymbol{\varphi}''(\tau)) d\tau = (\mathbf{u}_\varepsilon''(t), \boldsymbol{\varphi}''(t)) - (\mathbf{u}_\varepsilon''(0), \boldsymbol{\varphi}''(0)) - \int_0^t (\mathbf{u}_\varepsilon'''(\tau), \boldsymbol{\varphi}'''(\tau)) d\tau, \quad (215)$$

$$\begin{aligned} & \int_0^t \left( \int_0^\tau B'(\tau - \tau_1) \mathbf{u}_\varepsilon(\tau_1) d\tau_1, \mathbf{u}_\varepsilon''(\tau) \right) d\tau = \\ &= \int_0^t \int_{\tau_1}^t (B'(\tau - \tau_1) \mathbf{u}_\varepsilon(\tau_1), \mathbf{u}_\varepsilon''(\tau)) d\tau d\tau_1 = \\ &= \int_0^t [(B'(\tau - \tau_1) \mathbf{u}_\varepsilon(\tau_1), \mathbf{u}_\varepsilon'(t)) - (B'(0) \mathbf{u}_\varepsilon(\tau_1), \mathbf{u}_\varepsilon'(\tau_1))] d\tau_1 - \\ &- \int_0^t \int_{\tau_1}^t (B''(\tau - \tau_1) \mathbf{u}_\varepsilon(\tau_1), \mathbf{u}_\varepsilon'(\tau)) d\tau d\tau_1, \end{aligned}$$

from which, using (176),

$$\left| \int_0^t \left( \int_0^\tau B'(\tau - \tau_1) \mathbf{u}_\varepsilon(\tau_1) d\tau_1, \mathbf{u}_\varepsilon''(\tau) \right) d\tau \right| \leq c \|\mathbf{u}_\varepsilon'(t)\|_1 + c + c \int_0^t \|\mathbf{u}_\varepsilon'(\tau)\|_1 d\tau. \quad (216)$$

Further, we have

$$\begin{aligned} |I| &= \left| \int_0^t \int_{\cup_{k,l} \Gamma_c^{kl}} \frac{\partial g_c^{kl}(\mathbf{x}, \tau)}{\partial \tau} \frac{\partial \chi_\varepsilon(\mathbf{u}_{\varepsilon t}''^k(\tau) - \mathbf{u}_{\varepsilon t}'''(\tau) + \boldsymbol{\varphi}_t''^k(t) - \boldsymbol{\varphi}_t'''(\tau))}{\partial \tau} ds d\tau \right| = \\ &= \left| \int_{\cup_{k,l} \Gamma_c^{kl}} \frac{\partial g_c^{kl}(\mathbf{x}, t)}{\partial t} \chi_\varepsilon(\mathbf{u}_{\varepsilon t}''^k(t) - \mathbf{u}_{\varepsilon t}'''(t) + \boldsymbol{\varphi}_t''^k(t) - \boldsymbol{\varphi}_t'''(t)) ds - \right. \\ &- \int_{\cup_{k,l} \Gamma_c^{kl}} \frac{\partial g_c^{kl}(\mathbf{x}, t)}{\partial t} \chi_\varepsilon(\mathbf{u}_{\varepsilon t}''^k(0) - \mathbf{u}_{\varepsilon t}'''(0) + \boldsymbol{\varphi}_t''^k(0) - \boldsymbol{\varphi}_t'''(0)) ds - \\ &\left. - \int_0^t \int_{\cup_{k,l} \Gamma_c^{kl}} \frac{\partial^2 g_c^{kl}(\mathbf{x}, \tau)}{\partial \tau^2} \chi_\varepsilon(\mathbf{u}_{\varepsilon t}''^k(\tau) - \mathbf{u}_{\varepsilon t}'''(\tau) + \boldsymbol{\varphi}_t''^k(\tau) - \boldsymbol{\varphi}_t'''(\tau)) ds d\tau \right|, \end{aligned}$$

and assuming that  $\frac{\partial g_c^{kl}}{\partial t} = 0$ , i.e. that  $g_c^{kl}$  does not depend on  $t$ , then we have  $|I| = 0$ .

To estimate  $|\mathbf{u}_\varepsilon''(0)|$  from (193), we put  $t = 0$ , and then we have

$$(\mathbf{u}_\varepsilon''(0), \mathbf{v}) + a(\mathbf{u}_\varepsilon(0), \mathbf{v}) + (j'_{g\varepsilon}(\mathbf{u}_\varepsilon'(0) + \boldsymbol{\varphi}_\varepsilon'(0)), \mathbf{v}) = (\mathbf{F}_0(0), \mathbf{v}) \quad \forall \mathbf{v} \in V.$$

Hence and since due to (183)  $\mathbf{u}_{1t} + \boldsymbol{\varphi}'_t(0) = 0$ , then

$$\begin{aligned} (\mathbf{u}_\varepsilon''(0), v) &= (\mathbf{F}_0(0), \mathbf{v}) - a(\mathbf{u}_0, \mathbf{v}) = \\ &= (\mathbf{F}(0), \mathbf{v}) - (\boldsymbol{\varphi}''(0), \mathbf{v}) - a(\boldsymbol{\varphi}(0), \mathbf{v}) - a(\mathbf{u}_0, \mathbf{v}). \end{aligned} \quad (217)$$

Since

$$\begin{aligned} a(\mathbf{u}_0, \mathbf{v}) &= (A\mathbf{u}_0, \mathbf{v}) + \int_{\partial\Omega} \tau_{ij}(\mathbf{u}_0) v_i ds, \quad \forall \mathbf{v} \in V, \\ a(\boldsymbol{\varphi}(0), \mathbf{v}) &= (A\boldsymbol{\varphi}(0), \mathbf{v}) + \int_{\partial\Omega} \tau_{ij}(\boldsymbol{\varphi}(0)) v_i ds, \quad \forall \mathbf{v} \in V, \end{aligned}$$

then from (217) after some modification we obtain

$$\mathbf{u}_\varepsilon''(0) = \mathbf{F}(0) - \boldsymbol{\varphi}''(0) - A(\mathbf{u}_0 + \boldsymbol{\varphi}(0)),$$

from which, using the assumptions of the theorem and since  $|\mathbf{v}|_0^2 \leq c\|\mathbf{v}\|_1^2$ ,

$$\|\mathbf{u}_\varepsilon''(0)\|_1 \leq c.$$

Similarly for  $T'_\varepsilon(0)$  we find  $\|T'_\varepsilon(0)\|_1 \leq c$ .

Summing (211) and (212), which were integrated from 0 to  $t$ , using all estimates and above obtained results, then we obtain

$$\begin{aligned} & |T'_\varepsilon(t)|_0^2 + \int_0^t \|T'_\varepsilon(\tau)\|_1^2 d\tau + |\mathbf{u}_\varepsilon''(t)|_0^2 + \|\mathbf{u}'_\varepsilon(t)\|_1^2 \leq \\ & \leq c[|T'_\varepsilon(0)|_0^2 + |\mathbf{u}_\varepsilon''(0)|_0^2 + \|\mathbf{u}_1\|_1^2 + \int_0^t |T'_\varepsilon(\tau)|_0^2 d\tau + \\ & + \int_0^t \|Q'_0(\tau)\|_*^2 d\tau + \int_0^t |\mathbf{u}'_\varepsilon(\tau)|_0^2 d\tau + \\ & + \int_0^t \|\mathbf{F}'_0(\tau)\|_*^2 d\tau + \int_0^t \|T'_\varepsilon(\tau)\|_1 \|\mathbf{u}_\varepsilon''(\tau)\|_1 d\tau + \\ & + \|\mathbf{u}'_\varepsilon(t)\|_1 + c + \int_0^t \|\mathbf{u}'_\varepsilon(\tau)\|_1^2 d\tau] \leq \\ & \leq c \left( 1 + \int_0^t [|T'_\varepsilon(\tau)|_0^2 + \|T'_\varepsilon(\tau)\|_1^2 + |\mathbf{u}_\varepsilon''(\tau)|_0^2 + \|\mathbf{u}'_\varepsilon(\tau)\|_1^2] d\tau \right) \end{aligned}$$

and applying the Gronwall lemma, we find that

$$|T'_\varepsilon(t)|_0^2 + \int_0^t \|T'_\varepsilon(\tau)\|_1^2 d\tau + |\mathbf{u}_\varepsilon''(t)|_0^2 + \|\mathbf{u}'_\varepsilon(t)\|_1^2 \leq c,$$

from which

$$|T'_\varepsilon(t)|_0^2 \leq c, \int_0^t \|T'_\varepsilon(\tau)\|_1^2 d\tau \leq c, |\mathbf{u}_\varepsilon''(t)|_0^2 \leq c, \|\mathbf{u}'_\varepsilon(t)\|_1^2 \leq c. \quad (218)$$

To prove the limit process over  $\varepsilon$  we select, according to (205), (218), from the sequences  $\{T'_\varepsilon\}$  and  $\{\mathbf{u}_\varepsilon\}$  the subsequences, we denote them again by  $\{T'_\varepsilon\}$  and  $\{\mathbf{u}_\varepsilon\}$ , such that

$$\begin{aligned} T_\varepsilon &\rightarrow T \text{ weakly-star in } L^\infty(I; {}^1V), \\ T'_\varepsilon &\rightarrow T' \text{ weakly in } L^2(I; {}^1V), \\ \mathbf{u}_\varepsilon &\rightarrow \mathbf{u} \text{ weakly-star in } L^\infty(I; V), \\ \mathbf{u}'_\varepsilon &\rightarrow \mathbf{u}' \text{ weakly in } L^\infty(I; V), \\ \mathbf{u}_\varepsilon'' &\rightarrow \mathbf{u}'' \text{ weakly in } L^\infty(I; V'). \end{aligned} \quad (219)$$

From (192), (193) we obtain

$$\begin{aligned}
 & (T'_\varepsilon(t), z - T_\varepsilon(t)) + a_T(T_\varepsilon(t), z - T_\varepsilon(t)) + b_p(\mathbf{u}'_\varepsilon(t), z - T_\varepsilon(t)) \geq \\
 & \geq (Q_0(t), z - T_\varepsilon(t)), \\
 & (\mathbf{u}''_\varepsilon(t), \mathbf{v} - \mathbf{u}'_\varepsilon(t)) + a(\mathbf{u}_\varepsilon(t), \mathbf{v} - \mathbf{u}'_\varepsilon(t)) + \int_0^t a_1(t - \tau; \mathbf{u}_\varepsilon(\tau), \mathbf{v} - \mathbf{u}'_\varepsilon(t)) d\tau + \\
 & + b_s(T_\varepsilon(t) - T_0, \mathbf{v} - \mathbf{u}'_\varepsilon(t)) + j_{g\varepsilon}(\mathbf{v} + \boldsymbol{\varphi}'(t)) - j_{g\varepsilon}(\mathbf{u}'_\varepsilon(t) + \boldsymbol{\varphi}'(t)) - \\
 & - (\mathbf{F}_0(t), \mathbf{v} - \mathbf{u}'_\varepsilon(t)) = j_{g\varepsilon}(\mathbf{v} + \boldsymbol{\varphi}'(t)) - j_{g\varepsilon}(\mathbf{u}'_\varepsilon(t) + \boldsymbol{\varphi}'(t)) - \\
 & - (j'_{g\varepsilon}(\mathbf{u}'_\varepsilon(t) + \boldsymbol{\varphi}'(t)), \mathbf{v} + \boldsymbol{\varphi}'(t)) \geq 0.
 \end{aligned}$$

Hence, putting  $z = z(t)$ ,  $\mathbf{v} = \mathbf{v}(t)$ ,  $z \in L^2(I; {}^1V)$ ,  $\mathbf{v} \in L^2(I; V)$ , and integrating over  $t \in \bar{I}$  we have

$$\begin{aligned}
 & \int_0^{t_p} [(T'_\varepsilon(t), z(t)) + a_T(T_\varepsilon(t), z(t)) + (\mathbf{u}''_\varepsilon(t), \mathbf{v}(t)) + a(\mathbf{u}_\varepsilon(t), \mathbf{v}(t)) + \\
 & + b_p(\mathbf{u}'_\varepsilon(t), z(t)) + \int_0^t a_1(t - \tau; \mathbf{u}_\varepsilon(\tau), \mathbf{v}(t)) d\tau + b_s(T_\varepsilon(t) - T_0, \mathbf{v}(t)) + \\
 & + j_{g\varepsilon}(\mathbf{v}(t) + \boldsymbol{\varphi}'(t)) - (Q_0(t), z(t) - T_\varepsilon(t)) - (\mathbf{F}_0(t), \mathbf{v}(t) - \mathbf{u}'_\varepsilon(t))] dt \geq \\
 & \geq \int_0^{t_p} [(T'_\varepsilon(t), T_\varepsilon(t)) + a_T(T_\varepsilon(t), T_\varepsilon(t)) + (\mathbf{u}''_\varepsilon(t), \mathbf{u}'_\varepsilon(t)) + a(\mathbf{u}_\varepsilon(t), \mathbf{u}'_\varepsilon(t)) + \\
 & + b_p(\mathbf{u}'_\varepsilon(t), T_\varepsilon(t)) + \int_0^t a_1(t - \tau; \mathbf{u}_\varepsilon(\tau), \mathbf{u}'_\varepsilon(t)) d\tau + \\
 & + b_s(T_\varepsilon(t) - T_0, \mathbf{u}'_\varepsilon(t)) + j_{g\varepsilon}(\mathbf{u}'_\varepsilon(t) + \boldsymbol{\varphi}'(t))] dt = \\
 & = \frac{1}{2} [|T_\varepsilon(t_p)|_0^2 + |\mathbf{u}'_\varepsilon(t_p)|_0^2 + a(\mathbf{u}_\varepsilon(t_p), \mathbf{u}_\varepsilon(t_p))] + \int_0^{t_p} a_T(T_\varepsilon(t), T_\varepsilon(t)) dt + \\
 & + \int_0^{t_p} [b_p(\mathbf{u}'_\varepsilon(t), T_\varepsilon(t)) + b_s(T_\varepsilon(t) - T_0, \mathbf{u}'_\varepsilon(t))] dt + \\
 & + \int_0^{t_p} \int_0^t a_1(t - \tau; \mathbf{u}_\varepsilon(\tau), \mathbf{u}'_\varepsilon(t)) d\tau dt + \\
 & + \int_0^{t_p} j_{g\varepsilon}(\mathbf{u}'_\varepsilon(t) + \boldsymbol{\varphi}'(t)) dt - \frac{1}{2} a(\mathbf{u}_0, \mathbf{u}_0) - \frac{1}{2} |T_0|_0^2 - \frac{1}{2} |\mathbf{u}_1|_0^2.
 \end{aligned}$$

Since

$$\begin{aligned}
& \liminf_{\varepsilon \rightarrow 0} \left\{ \frac{1}{2} [|T_\varepsilon(t_p)|_0^2 + |\mathbf{u}'_\varepsilon(t_p)|_0^2 + a(\mathbf{u}_\varepsilon(t_p), \mathbf{u}_\varepsilon(t_p))] + \int_0^{t_p} a_T(T_\varepsilon(t), T_\varepsilon(t)) dt + \right. \\
& + \int_0^{t_p} [b_p(\mathbf{u}'_\varepsilon(t), T_\varepsilon(t)) + b_s(T_\varepsilon(t) - T_0, \mathbf{u}'_\varepsilon(t))] dt + \\
& + \left. \int_0^{t_p} \int_0^t a_1(t - \tau; \mathbf{u}_\varepsilon(\tau), \mathbf{u}'_\varepsilon(t)) d\tau dt + \int_0^{t_p} j_{g\varepsilon}(\mathbf{u}'_\varepsilon(t) + \boldsymbol{\varphi}'(t)) dt \right\} \geq \\
& \geq \frac{1}{2} [|T(t_p)|_0^2 + |\mathbf{u}'(t_p)|_0^2 + a(\mathbf{u}(t_p), \mathbf{u}(t_p))] + \\
& + \int_0^{t_p} a_T(T(t), T(t)) dt + \int_0^{t_p} [b_p(\mathbf{u}'(t), T(t)) + b_s(T(t) - T_0, \mathbf{u}'(t))] dt + \\
& + \int_0^{t_p} \int_0^t a_1(t - \tau; \mathbf{u}(\tau), \mathbf{u}'(t)) d\tau dt + \int_0^{t_p} j_g(\mathbf{u}'(t) + \boldsymbol{\varphi}'(t)) dt \geq \\
& \geq \int_0^{t_p} [(T'(t), T(t)) + (\mathbf{u}''(t), \mathbf{u}'(t)) + a(\mathbf{u}(t), \mathbf{u}'(t))] dt + \int_0^{t_p} a_T(T(t), T(t)) dt + \\
& + \int_0^{t_p} [b_p(\mathbf{u}'(t), T(t)) + b_s(T(t) - T_0, \mathbf{u}'(t))] dt + \\
& + \int_0^{t_p} \int_0^t a_1(t - \tau; \mathbf{u}(\tau), \mathbf{u}'(t)) d\tau dt + \int_0^{t_p} j_g(\mathbf{u}'(t) + \boldsymbol{\varphi}'(t)) dt.
\end{aligned}$$

Therefore,

$$\begin{aligned}
& \int_0^{t_p} \{ (T'(t), z - T(t)) + (\mathbf{u}''(t), \mathbf{v} - \mathbf{u}'(t)) + a(\mathbf{u}'(t), \mathbf{v} - \mathbf{u}'(t)) + \\
& + a_T(T(t), z - T(t)) + b_p(\mathbf{u}'(t), z - T(t)) + b_s(T(t) - T_0, \mathbf{v} - \mathbf{u}'(t)) + \\
& + \int_0^t a_1(t - \tau; \mathbf{u}(\tau), \mathbf{v} - \mathbf{u}'(t)) d\tau + j_g(\mathbf{v} + \boldsymbol{\varphi}'(t)) - j_g(\mathbf{u}'(t) + \\
& + \boldsymbol{\varphi}'(t)) - (Q_0(t), z - T(t)) - (\mathbf{F}_0(t), \mathbf{v} - \mathbf{u}'(t)) \} dt \geq 0 \\
& \quad \forall z \in L^2(I; {}^1V), \mathbf{v} \in L^2(I; V),
\end{aligned}$$

and then (180) follows.

**Remark 13** *It can be shown that the elastic case in the classical linear elasticity is the special case of the problem in the linear visco-elasticity with long memory (see e.g. [8]). If the rocks are loaded very slowly, then the geological bodies are deformed also very slowly and/or if the geological blocks move by an uniform velocity, thus the inertia forces in both cases can be neglected.*

Furthermore, we will also study the case with a zero damping and a zero friction, thus the damping term and the term of friction forces will be omitted. Therefore, we will assume the following variational problem:

find  $\mathbf{u} \in L^\infty(I; V)$  such that

$$a(\mathbf{u}(t), \mathbf{v}) + \int_0^t a_1(t - \tau; \mathbf{u}(\tau), \mathbf{v}) d\tau = (\mathbf{F}(t), \mathbf{v}) \quad \forall \mathbf{v} \in V, \quad \text{a.e. } t \in I, \quad (220)$$

where the bilinear forms  $a(\cdot, \cdot) \equiv a(t, t; \cdot, \cdot)$  and  $a_1(t, \tau; \cdot, \cdot)$  are time dependent bilinear forms, mapping  $V \times V$  into  $\mathbb{R}$ , defined above.

It can be shown that  $a(\cdot, \cdot) \equiv a(t, t; \cdot, \cdot)$  is continuous and  $V$ -coercive, and  $a_1(t, \tau; \cdot, \cdot)$  is continuous and satisfies

$$|a_1(t - \tau; \mathbf{u}, \mathbf{v})| \leq C(t, \tau) \|\mathbf{u}\|_1 \|\mathbf{v}\|_1 \quad \forall \mathbf{u}, \mathbf{v} \in V, \quad \text{with } C(t, \tau) \in L^\infty(I \times I),$$

and due to the assumed regularity of  $\mathbf{f}$  and  $\mathbf{P}$  we have

$$|(\mathbf{F}(t), \mathbf{v})| \leq c(t) \|\mathbf{v}\|_1 \quad \forall \mathbf{v} \in V, \quad \text{with } c(t) = \|\mathbf{f}\|_0 + \|\mathbf{P}\|_0. \quad (221)$$

**Theorem 8** *Under the above assumptions, the solution  $\mathbf{u} \in L^\infty(I; V)$  exists, is unique and depends continuously on  $\mathbf{f}$  and  $\mathbf{P}$ .*

The proof is parallel of that of [38] and is based on the Picard method.

### 3.7.2. Numerical Solution of the Problem

In addition an instantaneous elastic response, rocks under load can display significant creep during sustained loading, which is one of the causes of the landslide. The creep is a viscous effect. Therefore, the viscous rocks with long time memory is one of the possible landslide models because of the significance of the elastic and viscous character. To find analytical solutions of such type of problems are rare and then we must discretize the continuum problem. According to the properties of the visco-elastic rocks the relaxation functions are introduced, thus concerning the nature of the viscoelastic functions we have the following assumptions:

**Assumption** (about relaxation functions): Let  $I = [0, t_p]$ ,  $t_p > 0$ . We will assume that the time dependent part of the generic stress relaxation function  $\varphi(t, \tau)$  defined for  $t, \tau \in I$  satisfies the following:

- (i) regularity:  $\varphi(t, \tau) \in C^\infty(I \times I)$ ,  $0 \leq \tau \leq t \leq t_p$ ,
- (ii) positivity:  $\varphi(t, t) > 0 \quad \forall t \in I$ , and  $\varphi(t, \tau) \geq 0$ ,  $\forall t, \tau \in I$ ,
- (iii) causality:  $\varphi(t, \tau) \equiv 0 \quad \forall \tau > t$ , such that  $\tau, t \in I$ ,
- (iv) fading memory: for every fixed  $t \in I$   $\varphi_{,\tau}(t, \tau) > 0$  when  $\tau \in [0, t]$ ,  $\varphi_{,\tau} = \frac{\partial \varphi}{\partial \tau}$ .

**Remark 14** *These assumptions hold for the time dependent parts of the specific relaxation functions like  $\lambda(t, \tau)$ ,  $\mu(t, \tau)$ ,  $E(t, \tau)$ , etc.*



Firstly, we will discuss the visco-elastic part of the quasi-static problem only. The method of discretization can be based on the semi-discrete and fully-discrete approximation approaches.

### Discrete approximation of the quasi-static problem in visco-elasticity with long memory

The method of discretization proceeds in two steps. Firstly we utilize the Galerkin finite element method for discretization in the space domain. One of the procedures is a semi-discrete approximation of the problem producing a system of Volterra second kind equations. The second procedure is a fully-discrete approximation based on the replacing the Volterra operator with a discrete representation as a quadrature rule like the trapezoidal or the Simpson rules. The numerical scheme based on the trapezoidal rule is numerically stable (see [38, Chap.7]), and does not require starting values as the numerical scheme based on the Simpson rule. Below we construct the semi- and fully-discrete schemes and shortly discuss the possibility conditions of finding semi-exact solutions by treating the semi-discrete solution as an exact elastic solution.

Let us assume that the domain  $\Omega$  has a polygonal boundary and let the domain  $\Omega$  be approximated by such a way that  $\bar{\Omega}_h = \cup_{\ell=1}^r \bar{\Omega}_h^\ell \equiv \bar{\Omega}$  and  $\partial\Omega_h = \partial\Omega$ . Let  $\{\mathcal{T}_h\}$  be a regular family of finite element partitions  $\mathcal{T}_h$  of  $\bar{\Omega}_h$  compatible to the boundary subsets  $\bar{\Gamma}_{\tau h}$ ,  $\bar{\Gamma}_{uh}$  and  $\bar{\Gamma}_{ch}$ . We introduce the standard spaces of linear elements on the regular division  $\mathcal{T}_h = \cup_{\ell=1}^r \mathcal{T}_h^\ell$  of polygonal (for  $N = 2$ ) or polyhedral (for  $N = 3$ ) domains  $\bar{\Omega}_h^\ell$ ,  $\ell = 1, \dots, r$ . We will also assume that each  $\Omega_h^\ell$  has diameter  $h^\ell$ , and set  $h := \max_{\ell} h^\ell$ . Let

$$\begin{aligned} V_h &= V_h^1 \times \dots \times V_h^r = \prod_{\ell=1}^r V_h^\ell, \quad V_h \subset V, \quad \text{where} \\ V_h^\ell &= \{\mathbf{v}_h \in [C(\bar{\Omega}_h^\ell)]^N : \mathbf{v}_h|_{T_{hi}} \in [P_1(T_{hi})]^N \quad \forall T_{hi} \in \mathcal{T}_h^\ell, \quad \mathbf{v}_h = 0 \text{ on } \Gamma_u \cap \partial\Omega^\ell\}, \end{aligned}$$

where by  $T_{hi}$  we denote any triangle (for  $N = 2$ ) and any tetrahedron (for  $N = 3$ ) of the division  $\mathcal{T}_h^\ell$ ,  $\ell = 1, \dots, r$ , and  $a_i$ ,  $i = 1, \dots, q$ , denote the nodes of  $\mathcal{T}_h^\ell$  laying on  $\Gamma_c^{kl}$ .

In the finite element theory with regard to the error estimation the well known approximation property of the space  $V_h$  is the following: let  $s > 1$  and  $m \geq 0$  be positive integers and let  $\mathbf{u} \in V \cap H^{s,N}$ , then we have

$$\inf_{\mathbf{v} \in V_h} \|\mathbf{u} - \mathbf{v}\|_{m,N,\Omega} \leq ch^{s-m} |\mathbf{u}|_{r,N,\Omega} \quad \text{for } s \geq m, \quad (222)$$

where  $c$  is some positive constant depending upon  $\Omega$  the shape of the  $\Omega_h$  but not upon  $\mathbf{u}$ .

**The semi-discrete finite element approximation** to the quasi-static displacement problem is the following:

find  $\mathbf{u}_h \in L(I; V_h)$  such that

$$a(\mathbf{u}_h(t), \mathbf{v}_h) + \int_0^t a_1(t - \tau; \mathbf{u}_h(\tau), \mathbf{v}_h) d\tau = (\mathbf{F}(t), \mathbf{v}_h) \quad \forall \mathbf{v}_h \in V_h, \quad \text{a.e. } t \in I \quad (223)$$

Now we construct the finite dimensional subspaces  $V_h^\ell := \text{span} \{\varphi_j(\mathbf{x})\}_{j=1}^n \subset V^\ell$ ,  $\ell = 1, \dots, r$ , where  $n$  is the number of nodes of the useful division,  $\varphi_j \in P_1$ , where  $P_1$  is a finite dimensional vector space of linear functions and the set  $\{\varphi_j(\mathbf{x})\}$  is linearly

independent. Then from the  $\varphi_j$  we may construct a basis for the space  $V_h$ , so for arbitrary  $\mathbf{u}_h \in V_h$  we select the degrees of freedom for the finite element space to be the values of  $\mathbf{u}_h$  at the nodes of the useful division. Specifying the design of  $\varphi_j$  then  $\mathbf{u}_h$  can be uniquely represented by

$$\mathbf{u}_h(\mathbf{x}) = \sum_{i=1}^n \varphi_i(\mathbf{x})(\mathbf{u}_{1h}(N^i), \dots, \mathbf{u}_{mh}(N^i))^T,$$

where  $N^i$  are the coordinates of the node labeled by the index  $i$ .

About  $\varphi_j$  we will assume that satisfy the properties of relaxation functions.

Then (223) leads to the Volterra system

$$A(t, t)\mathbf{U}(t) + \int_0^t B(t, \tau)\mathbf{U}(\tau)d\tau = F(t), \quad (224)$$

where the time dependent  $A(t, t)$  represents the stiffness matrix,  $B(t, \tau)$  the history matrix of the materials, which can be derived from the bilinear forms  $a(\cdot, \cdot)$  and  $a_1(\cdot, \cdot)$ , the time dependent  $F(t)$  contains the body forces and surface tractions and  $\mathbf{U}(t)$  is a time dependent array of coordinates in the space  $V_h$ .

Due to the Korn inequality, the above assumptions, then  $A(t, t)$  is positive definite and therefore by premultiplying (224) through  $(A(t, t))^{-1}$  we obtain a standard form of the Volterra equation of the second order which admits a unique solution (see e.g. [38]).

**The fully-discrete finite element approximation** to the quasi-static displacement problem is the following:

The fully-discrete problem follows from (224) by replacing the hereditary integral with a suitable numerical quadrature rule.

Let  $n$  be a positive integer and let the interval  $I = [0, t_p]$  be divided into a subintervals  $I_k = \{0 = t_0, \dots, t_n = t_p \in \mathbb{R} : t_{i-1} < t_i, i = 1, \dots, n\} \subset I$  and use the trapezoidal rule. Let us set

$$\begin{aligned} u_i &:= \mathbf{u}(t_i) \quad \text{for } t_i \in I_k, \\ k_i &:= t_i - t_{i-1} \quad \text{for } 1 \leq i \leq n, \quad k := \max_{1 \leq i \leq n} k_i, \end{aligned}$$

then

$$\delta_i(\mathbf{u}) := \int_0^{t_i} \mathbf{u}(\tau)d\tau - \sum_{j=1}^i \frac{k_j}{2}(\mathbf{u}_{j-1} + \mathbf{u}_j), \quad i > 0,$$

and then the trapezoidal rule approximates the integral as  $\delta_i(\mathbf{u}) = 0$  and for the error we have

$$|\delta_i(\mathbf{u})| \leq ck^2 \int_0^{t_i} |\mathbf{u}''(\tau)|d\tau, \quad c = \text{const.} > 0.$$

Then the fully-discrete approximation leads to the following problem:

for each  $t_i \in I_n$  find a function  $\mathbf{u}_{hi}^k \cong \mathbf{u}_h^k(t_i) \in V_h$  such that

$$a(t_i, t_i; \mathbf{u}_{hi}^k, \mathbf{v}_h) + \sum_{j=0}^i w_{ij} a_1(t_i, t_j; \mathbf{u}_{hj}^k, \mathbf{v}_h) = (\mathbf{F}(t_i), \mathbf{v}_h) \quad \forall \mathbf{v}_h \in V_h, \quad (225)$$

where  $w_{ij}$  denote the weights implied by the approximation of the integral by the trapezoidal rule and  $w_{00} = 0$ , and where  $\mathbf{u}_{hi}^k \cong \mathbf{u}_h(t_i) \cong \mathbf{u}(t_i)$ .

Then this problem leads to the following problem:

for each  $t_i \in I_n$  find the vector  $\mathbf{U}_i$  of coordinates of  $V_h$

$$A(t_i, t_i)\mathbf{U}_i + \sum_{j=0}^i w_{ij}B(t_i, t_j)\mathbf{U}_j = \mathbf{F}_i, \quad (226)$$

where  $\mathbf{U}_i = \mathbf{U}(t_i)$ ,  $\mathbf{F}_i = \mathbf{F}(t_i)$ . Hence, for finding  $\{\mathbf{U}_i\}_{i=1}^n$ , it follows

$$\begin{aligned} \left( A(t_i, t_i) + \frac{k_i}{2}B(t_i, t_i) \right) \mathbf{U}_i &= \mathbf{F}_i - \frac{k_i}{2}B(t_i, t_{i-1})\mathbf{U}_{i-1} - \\ &- \sum_{j=1}^{i-1} \frac{k_i}{2}(B(t_i, t_j)\mathbf{U}_j + B(t_i, t_{j-1})\mathbf{U}_{j-1}), \end{aligned} \quad (227)$$

where the starting value  $\mathbf{U}_0$  can be found as the solution of the static linear elastic problem

$$A(t_0, t_0)\mathbf{U}_0 = \mathbf{F}_0. \quad (228)$$

**Remark 15** If we used the higher order quadrature Simpson rule we need as additional starting values  $\mathbf{U}_0$  and  $\mathbf{U}_1$ .

Next, we will present the semi-discrete error estimate and the fully-discrete error estimate. The estimates are based on the abstract theorems [38, 66, 64], mentioned below.

**Theorem 9** Let  $\mathcal{H}$  be a Hilbert space with norm  $\|\cdot\|$  and  $\mathcal{H}_h \subset \mathcal{H}$  be an appropriate finite element space. For almost every  $t \in I = [0, t_p]$ ,  $t_p > 0$ , and with respect to this norm let  $a(t, t; \cdot, \cdot) : \mathcal{H} \times \mathcal{H} \mapsto \mathbb{R}$  be a continuous and coercive bilinear form with constants  $c_0$  and  $c_1$  respectively. Additionally, for almost every  $t - \tau \in I$  let  $a_1(t, \tau; \cdot, \cdot) : \mathcal{H} \times \mathcal{H} \mapsto \mathbb{R}$  and  $L(t; \cdot) : \mathcal{H} \mapsto \mathbb{R}$  be respectively a continuous bilinear form, with constant  $c_2$ , and a continuous linear form with constant  $c_3$ . Then, for the approximation of the abstract Volterra problem: find  $\mathbf{u} \in L^\infty(I; \mathcal{H})$  such that

$$a(t, t; \mathbf{u}(t), \mathbf{v}) + \int_0^t a_1(t - \tau; \mathbf{u}(\tau), \mathbf{v})d\tau = L(t; \mathbf{v}) \quad \forall \mathbf{v} \in \mathcal{H}, \quad \text{a.e. } t \in I \quad (229)$$

by the semi-discrete Galerkin scheme: find  $\mathbf{u}_h \in L^\infty(I; \mathcal{H}_h)$  such that

$$a(t, t; \mathbf{u}_h(t), \mathbf{v}_h) + \int_0^t a_1(t - \tau; \mathbf{u}_h(\tau), \mathbf{v}_h)d\tau = L(t; \mathbf{v}_h) \quad \forall \mathbf{v}_h \in \mathcal{H}_h, \text{ a.e. } t \in I \quad (230)$$

we have,

$$\|\mathbf{u}(t) - \mathbf{u}_h(t)\| \leq c\|\mathbf{u}(t) - \mathbf{v}_h\|_{L^\infty(I; \mathcal{H})} \quad \forall \mathbf{v}_h \in \mathcal{H}_h, \quad \text{a.e. } t \in I, \quad (231)$$

where  $c$  is a positive constant independent of  $\mathbf{u}$ .

For the proof see [66, 64].

Putting  $\mathcal{H} = V$ ,  $\mathcal{H}_h = V_h$ ,  $L(t; \mathbf{v}) = (\mathbf{F}(t), \mathbf{v})$ ,  $L(t; \mathbf{v}_h) = (\mathbf{F}(t), \mathbf{v}_h)$  then we find the following error estimate:

**Theorem 10** *Let the conditions of the previous abstract theorem hold, let the space  $V_h$  satisfy the approximation property (221). Then for the semi-discrete finite element approximation of (220) by (223) under the above conditions the following estimate*

$$\|\mathbf{u}(t) - \mathbf{u}_h(t)\|_{1,N,\Omega} \leq ch^{s-1} \|\mathbf{u}\|_{L^\infty(I; H^{s,N}(\Omega))}, \quad \forall t \in I, \quad (232)$$

where  $c$  is a positive constant independent of  $\mathbf{u}$  and  $h$ , whenever  $\mathbf{u}(t) \in V \cap H^{s,N}(\Omega)$  for some  $s > 1$ .

For the fully-discrete estimate we will use the following abstract theorem:

**Theorem 11** *Let the notation of the previous abstract theorem hold and let  $\mathbf{u}'' \in L^1(I)$  and  $a_1(t, \tau; \cdot, \cdot)$  be twice differentiable with respect to  $\tau$ . Then, the fully discrete trapezoidal approximation to the semi-discrete problem (230) is the following: find  $\mathbf{u}_{hi}^k \in \mathcal{H}_h$  for each  $t_i \in I_k$  such that*

$$a(t_i, t_i; \mathbf{u}_{hi}^k, \mathbf{v}_h) + \sum_{j=0}^i w_{ij} a_1(t_i, t_j; \mathbf{u}_{hj}^k, \mathbf{v}_h) = L(t_i, \mathbf{v}_h) \quad \forall \mathbf{v}_h \in \mathcal{H}_h, \quad (233)$$

where  $I_k = \{0 = t_0, \dots, t_n = t_p \in \mathbb{R}; t_{i-1} < t_i, i = 1, \dots, n\} \subset I$ ,  $n$  integer constant,  $w_{ij}$  are the weights associated with the trapezoidal rule with  $w_{00} = 0$ , then there exists for  $n$  small enough a positive constant  $c = c(\mathbf{u})$  independent of  $n$  such that

$$\max_{t_i \in I_n} \|\mathbf{u}(t_i) - \mathbf{u}_{hi}^k\| \leq c(\|\mathbf{u}(t) - \mathbf{v}_h\|_{L^\infty(I; \mathcal{H})} + k^2) \quad \forall \mathbf{v}_h \in \mathcal{H}_h. \quad (234)$$

For the proof see [38, 63, 64].

Using this theorem onto our investigated problem and taking  $\mathcal{H} = V$ ,  $\mathcal{H}_h = V_h$ , then we have the following result:

**Theorem 12** *Let the assumptions about the data be as above. Then there exists a constant  $c = c(\mathbf{u})$ , independent of  $h$  and  $k$  such that*

$$\max_{t_i \in I_k} \|\mathbf{u}(t_i) - \mathbf{u}_{hi}^k\| \leq c(h^{s-1} + k^2) \quad (235)$$

when  $\mathbf{u}$  satisfies the regularity given in the previous abstract theorem.

### Discrete approximation of the dynamic problem in thermo-visco-elasticity with long memory

Let  $\Omega \subset \mathbb{R}^N$ ,  $N = 2, 3$  be approximated by its polyhedral approximation and let  $\partial\Omega_h = \Gamma_{uh} \cup \Gamma_{\tau h} \cup (\cup_{k,l} \Gamma_{ch}^{kl})$ . Let  $\mathcal{T}_h$  be a partition of  $\bar{\Omega}_h$  by tetrahedra (for  $N = 3$ ) and triangles (for  $N = 2$ )  $T_{hi}$  and let  $h = h(T_{hi})$  be the maximum diameter of tetrahedra

(triangle) element  $T_{hi}$ . We assume that the used family of finite element partitions  $\{\mathcal{T}_h\}$  is regular and, moreover, that it also induces a regular family of finite partitions on  $\cup_{k,l} \Gamma_{ch}^{kl}$ .

Let the spaces  ${}^1V$  and  $V$  be approximated by their finite element spaces  ${}^1V_h$  and  $V_h$ , generated by linear polynomial functions,  ${}^1V_h \subset {}^1V$  and  $V_h \subset V$ .

Then the discrete problem is as follows:

**Problem**  $(\mathcal{P})_d$ : find a pair of functions  $(T_h, \mathbf{u}_h)$ ,  $T_h \in L^2(I; {}^1V_h)$ ,  $\mathbf{u}_h \in L^2(I; V_h)$  such that

$$\begin{aligned} & (T'_h(t), z_h - T_h(t)) + a_T(T_h(t), z_h - T_h(t)) + b_p(\mathbf{u}'_h(t), z_h - T_h(t)) \geq \\ & (Q_0(t), z_h - T_h(t)), \quad \forall z_h \in {}^1V_h, \end{aligned} \quad (236)$$

$$\begin{aligned} & (\mathbf{u}''_h(t), \mathbf{v}_h - \mathbf{u}'_h(t)) + a(\mathbf{u}_h(t), \mathbf{v}_h - \mathbf{u}'_h(t)) + \int_0^t a_1(t - \tau; \mathbf{u}_h(\tau), \\ & \mathbf{v}_h - \mathbf{u}'_h(t)) d\tau + b_s(T_h(t) - T_0, \mathbf{v}_h - \mathbf{u}'_h(t)) + j_g(\mathbf{v}_h + \varphi'_h(t)) - \\ & - j_g(\mathbf{u}'_h(t) + \varphi'_h(t)) \geq (\mathbf{F}_0(t), \mathbf{v}_h - \mathbf{u}'_h(t)) \quad \forall \mathbf{v}_h \in V_h, \end{aligned} \quad (237)$$

with initial conditions

$$T_h(0) = T_{h0}, \mathbf{u}_h(0) = \mathbf{u}_{0h}, \mathbf{u}'_h(0) = \mathbf{u}_{1h}, \quad (238)$$

where  $T_{h0} \in {}^1V_h$ ,  $\mathbf{u}_{0h} \in V_h$ ,  $\mathbf{u}_{1h} \in V_h$  are discrete approximates of  $T_0$  and  $\mathbf{u}_0, \mathbf{u}_1$ .

It can be proved that the discrete problem  $(\mathcal{P})_d$  has a unique solution  $(T_h, \mathbf{u}_h)$ , where  $T_h \in L^2(I; {}^1V_h)$ ,  $\mathbf{u}_h \in L^2(I; V_h)$ .

Since the functional  $j_g(\cdot)$  is not differentiable, then for numerical solution we will introduce the regularization (188)-(189) and the regularized functional  $j_{g\varepsilon}$  by (190), which will be well-defined, convex and Gâteaux-differentiable with respect to the argument  $\mathbf{v}$  and then it can be approximated e.g. by the trapezoidal rule. The functional  $j_{g\varepsilon}$  has a meaning of the frictional forces. Then the problem is equivalent to

$$(T'_h(t), z_h) + a_T(T_h(t), z_h) = (Q_p(t), z_h) \quad \forall z_h \in {}^1V_h, t \in I, \quad (239)$$

$$\begin{aligned} & (\mathbf{u}''_h(t), \mathbf{v}_h) + a(\mathbf{u}_h(t), \mathbf{v}_h) + \int_0^t a_1(t, \tau; \mathbf{u}_h(\tau), \mathbf{v}_h) d\tau = \\ & = (\mathbf{F}_1(t), \mathbf{v}_h) \quad \forall \mathbf{v}_h \in V_h, t \in I, \end{aligned} \quad (240)$$

where we put

$$\mathbf{u}_h(t) \equiv \mathbf{u}_{h\varepsilon}(t), T_h(t) = T_{h\varepsilon}(t)$$

and

$$\begin{aligned} (Q_p(t), z_h) &= (Q_0(t), z_h) - b_p(\mathbf{u}'_h(t), z_h), \\ (\mathbf{F}_1(t), \mathbf{v}_h) &= (\mathbf{F}_0(t), \mathbf{v}_h) - b_s(T_h(t) - T_0, \mathbf{v}_h) - j_{g\varepsilon}(\mathbf{v}_h + \varphi'_h(t)) \end{aligned}$$

Constructing the finite-dimensional subspaces  ${}^1V_h^\iota = \text{span}\{\zeta_j\}_{j=1}^n \in {}^1V^\iota$ ,  $\iota = 1, \dots, r$ , where  $n$  is the number of nodes of the useful division,  $\zeta_j \in P_1$ , where  $P_1$  is a finite-dimensional space of linear functions, the set  $\{\zeta_j\}$  is linearly independent and the space  $V_h^\iota = \text{span}\{\varphi_j\}_{j=1}^n \in V^\iota$ ,  $\iota = 1, \dots, r$ , defined as above. Putting

$$T'_h = k^{-1}(T_h^{i+1} - T_h^i), \mathbf{u}''_h = k^{-2}(\mathbf{u}_h^{i+1} - 2\mathbf{u}_h^i + \mathbf{u}_h^{i-1}),$$

and using the notation  $T_h^{i+1} \equiv T_h$ ,  $\mathbf{u}_h^{i+1} \equiv \mathbf{u}_h$ , then  $T_h$  and  $\mathbf{u}_h$  have the unique representations

$$\begin{aligned} T_h(\mathbf{x}) &= \sum_{i=1}^n \zeta_i(\mathbf{x})(T_{1h}(N^i), \dots, T_{mh}(N^i))^T, \\ \mathbf{u}_h(\mathbf{x}) &= \sum_{i=1}^n \varphi_i(\mathbf{x})(\mathbf{u}_{1h}(N^i), \dots, \mathbf{u}_{mh}(N^i))^T, \end{aligned}$$

where  $N_i \in \mathbb{R}^N$  are the coordinates of the node labelled  $i$ .

Then the semi-implicit scheme in time and the Galerkin finite element approximation in the space variable will be used. The problem for every  $t = t^{i+1} \in I$  then leads to solving the system of linear algebraic equations in the thermal part of the problem and the Volterra system in the visco-elastic part of the problem

$$\begin{aligned} A_T(t)\mathbf{T}(t) &= \mathbf{Q}_p(t), \quad t = t^{i+1} \in I, \\ \mathbb{A}(t, t)\mathbf{U}(t) + \int_0^t \mathbb{B}(t, \tau)\mathbf{U}(\tau)d\tau &= \mathbb{F}(t), \quad t = t^{i+1} \in I, \end{aligned}$$

where  $A_T(t)$ ,  $\mathbb{A}(t, t)$  are the stiffness matrices of the thermal and the visco-elastic parts of the problem, which are positive definite,  $\mathbb{B}(t, \tau)$  is the history matrix of the visco-elastic materials, which can be derived from the bilinear forms  $a_T(\cdot, \cdot)$ ,  $a(t, t; \cdot, \cdot)$ ,  $a_1(t, \tau; \cdot, \cdot)$  and the inner products  $(\cdot, \cdot)$ ,  $\mathbf{Q}_p(t)$  contains the thermal sources and the viscous and deformation heats as well as the inner product  $(T_h^i, z_h)$ ,  $\mathbb{F}(t)$  contains the body and friction forces, the surface tractions and the coupled term evoked by the thermal stresses as well as the inner product  $(-2\mathbf{u}_h^i + \mathbf{u}_h^{i-1}, \mathbf{v}_h)$ . Moreover,  $\mathbf{T}(t)$ ,  $\mathbf{U}(t)$  are time dependent arrays of coordinates in the spaces  ${}^1V_h$  and  $V_h$ . The Eq. (241) is similar to (224) so that the derivation of the error estimate is also similar as above.

**Remark 16** To solve Eq. (241b) the fully-discrete approach can be also used.

## 4. Mathematical Models In Thermo-Hydro-Geomechanical Coupling

### 4.1. Formulation of the Mathematical Model Problem and Its Variational (Weak) Solution

#### 4.1.1. Introduction

A wide variety of geological and geomechanical engineering systems are connected with coupled thermo-hydro-mechanical processes (THM processes). The thermo-hydro-mechanical coupling processes involve processes connected with heat, water and mechanical properties of the loaded and fractured rocks. The nature is non-linear in general. Therefore, for a description of the above aspects of the thermo-hydro-geomechanical processes the coupled thermo-visco-plastic Bingham rheology can be used with a great merit. If the

threshold of plasticity in the Bingham's stress-strain relation is equal to zero, the constitutive relation is identical for the viscous Newtonian liquid and the Bingham rheology is also useful for investigations of the hydro-mechanical processes.

The main objective is to simulate and predict the THM processes in and around the engineered barrier system of the underground geotechnical structures and constructions. Therefore, the THM phenomena are subjects of great interests in projects of High Level Waste Repositories. On the other hand the THM coupling processes, based on the (thermo-)viscoplastic Bingham rheology, also describe hydrological problems and problems of unstable slopes connected with consequences of deluges (Fig. 12).

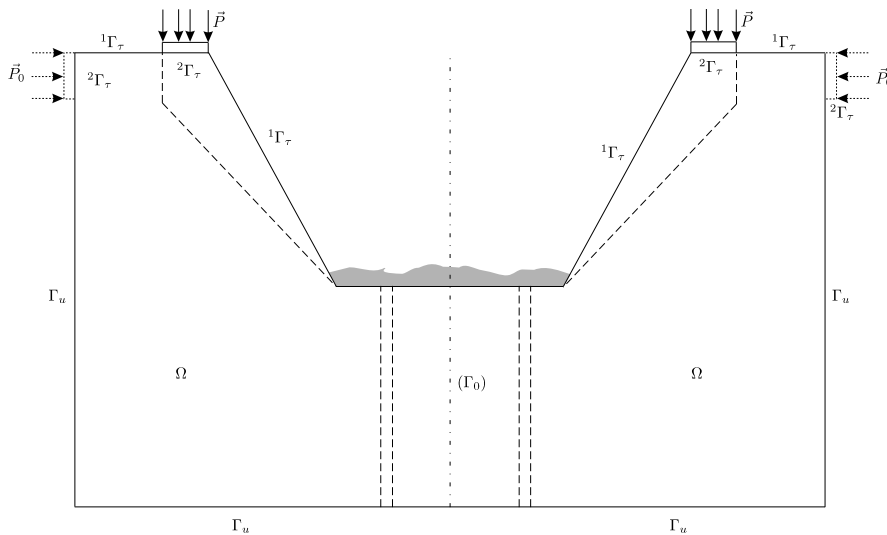


Figure 12. The model of the unstable loaded slopes in the overflowed region.

In this part of the study the development of models to reproduce the geomechanical behaviour of loaded rocks will be a subject of our interest. The idea of the project how to predict the future situation in the endangered regions is based on the mathematical simulation of the coupled thermo-hydro-mechanical and thermo-hydro-dynamical processes together with the climatic processes in the endangered region during the strong climatic load and the consequences of the enormous quantity of water in such regions onto the stability of slopes and onto the security of such regions (see [54, 57]). In the case, if the frosts in the investigated area are assumed then the analogical theory of that of Nedoma (1997) [53] must be used. It is evident that from these above points of view the thermo-visco-plastic rheology of the Bingham type is an optimal approach for modelling of the loaded and unsoaked slopes by the deluges and with the ensuing bigger frosts.

The main goal is to simulate and to predict all effects of the thermo-hydro-mechanical and thermo-hydro-dynamical processes in the unsafe regions, intervened by hurricanes (etc.) in critical situations. The mathematical model discussed will be based on the thermo-visco-plastic rheology of Bingham type coupled with climatic models. The model must be formulated as a 3D model. The Bingham rheology is characterized by two parameters - threshold of plasticity  $\hat{g}$  and threshold of viscosity  $\hat{\mu}$ . From the characteristic properties of the used rheology the following professional demands for the project are requested:

(i) the geometry of the investigated region will be determined from the digitized cartographic maps of the investigated region, (ii) material properties of rocks in the investigated region will be determined from the geological and hydro-dynamical observations and laboratory experiments, (iii) acting loading forces will be determined as resulting data from the climatic, geological and hydrological observations and studies, etc., (iv) temperature and hydro-dynamical data, like flows of water in the rivers, hurricane data and data of its evolution in future, an absorbing capacity of rocks by the water, properties of rocks in connection with the stability of slopes, etc., will be determined from hydro-geological observations and studies.

#### 4.1.2. The Problem Formulation and the Friction Law

Let  $\Omega \subset \mathbb{R}^N$ ,  $N = 2, 3$ ,  $\Omega = \cup_{l=1}^r \Omega^l$ , be a union of bounded domains occupied by visco-plastic bodies with a smooth boundary  $\partial\Omega = \Gamma_u \cup \Gamma_\tau \cup \Gamma_0 \cup \Gamma_c$ , where  $\Gamma_u$  represents one part of the boundary, where the velocity is prescribed;  $\Gamma_\tau$  is the part of the boundary, where the loading is prescribed;  $\Gamma_0$  is the part of the boundary, where the symmetry condition or the bilateral contact condition are given and  $\Gamma_c (= \cup_{k,l} \Gamma_c^{kl}, \Gamma_c^{kl} = \partial\Omega^k \cap \partial\Omega^l, k \neq l, k, l \in \{1, \dots, r\})$  represents the contact boundary. Assume the Eulerian coordinate system as a spatial variable system. Any repeated index implies summation from 1 to  $N$ . Let  $t \in I \equiv (0, t_p)$ ,  $t_p > 0$ , where  $t_p$  is the duration of all processes. Let  $u_n = \mathbf{u} \cdot \mathbf{n}$ ,  $\mathbf{u}_t = \mathbf{u} - u_n \mathbf{n}$ ,  $\boldsymbol{\tau} = (\tau_{ij} n_j)$ ,  $\tau_n = \tau_{ij} n_j n_i$ ,  $\boldsymbol{\tau}_t = \boldsymbol{\tau} - \tau_n \mathbf{n}$  be the normal and tangential components of the velocity and stress vectors. Next, we will solve the following problem:

**Problem ( $\mathcal{P}$ ):** Find a pair of functions  $(T, \mathbf{u}) : \Omega \times I \rightarrow (\mathbb{R} \times \mathbb{R}^N) \times I$ ,  $N = 2, 3$ , and a stress tensor  $\tau_{ij} : \Omega \times I \rightarrow \mathbb{R}^{N \times N} \times I$  satisfying

$$\rho \left( \frac{\partial u_i}{\partial t} + u_k \frac{\partial u_i}{\partial x_k} \right) = \frac{\partial}{\partial x_j} \tau_{ij} + f_i \quad \text{in } \Omega \times I; \quad (241)$$

$$\operatorname{div} \mathbf{u} = 0 \quad \text{in } \Omega \times I; \quad (242)$$

$$\rho c_e \left( \frac{\partial T}{\partial t} + u_k \frac{\partial T}{\partial x_k} \right) - \rho \beta_{ij} T_0 D_{ij}(\mathbf{u}) = \frac{\partial}{\partial x_j} \left( \kappa_{ij} \frac{\partial T}{\partial x_i} \right) + W \quad \text{in } \Omega \times I; \quad (243)$$

$$\tau_{ij} = {}^B \tau_{ij} + {}^T \tau_{ij} = -p \delta_{ij} + \hat{g} D_{ij} D_{II}^{-1/2} + 2\hat{\mu} D_{ij} - \beta_{ij}(T - T_0); \quad (244)$$

provided  $D_{II} \neq 0$ ,  $|\tau^D| \leq 2^{\frac{1}{2}} \hat{g}$  if  $D_{II} = 0$ , with the boundary value and contact conditions

$$T(\mathbf{x}, t) = T_1(\mathbf{x}, t), \quad \tau_{ij} n_j = P_i \quad \text{on } \Gamma_\tau \times I, \quad (245)$$

$$\kappa_{ij} \frac{\partial T(\mathbf{x}, t)}{\partial x_j} n_j = 0, \quad \mathbf{u}(\mathbf{x}, t) = \mathbf{u}_1(\mathbf{x}, t) \quad \text{on } \Gamma_u \times I, \quad (246)$$

$$\kappa_{ij} \frac{\partial T(\mathbf{x}, t)}{\partial x_j} n_j = q(\mathbf{x}, t), \quad u_n(\mathbf{x}, t) = 0, \quad \boldsymbol{\tau}_t(\mathbf{x}, t) = 0 \quad \text{on } \Gamma_0 \times I, \quad (247)$$

$$T^k(\mathbf{x}, t) = T^l(\mathbf{x}, t), \quad \kappa_{ij} \frac{\partial T(\mathbf{x}, t)}{\partial x_j} n_{j|(k)} = \kappa_{ij} \frac{\partial T(\mathbf{x}, t)}{\partial x_j} n_{j|(l)} \quad \text{on } \Gamma_c \times I, \quad (248)$$



and on  $\cup_{k,l} \Gamma_c^{kl} \times I$  the bilateral contact condition with local friction law of the form

$$\begin{aligned} u_n^k - u_n^l &= 0 \quad \text{and} \quad |\tau_t^k| \leq \mathcal{F}_c^{kl} S^{Dk}, \\ \text{if } |\tau_t^k| < \mathcal{F}_c^{kl} S^{Dk} &\text{ then } \mathbf{u}_t^k - \mathbf{u}_t^l = 0, \\ \text{if } |\tau_t^k| = \mathcal{F}_c^{kl} S^{Dk} &\text{ then there exists } \lambda \geq 0 \text{ such that } \mathbf{u}_t^k - \mathbf{u}_t^l = -\lambda \tau_t^k, \end{aligned} \quad (249)$$

where  $\mathcal{F}_c^{kl}$  is a coefficient of friction,  $u_n^k = u_i^k n_i^k$ ,  $u_n^l = -u_i^l n_i^l = u_i^l n_i^k$  and  $\tau_n^k = \tau_n^l \leq 0$ ,  $\tau_t^k = \tau_t^l$ , and the initial conditions

$$T(\mathbf{x}, t_0) = T_0(\mathbf{x}), \quad \mathbf{u}(\mathbf{x}, t_0) = 0. \quad (250)$$

If  $S^D = |\tau_n|$ , then (249) is the classical Coulombian law of friction. Such model problems describe the geomechanical and geodynamical processes in the upper parts of the Earth. If we set  $S^D = |{}^B\tau^D|$  and if we determine  $|{}^B\tau^D|$  from (244) we obtain  $|{}^B\tau^D| = 2^{1/2}\hat{g} + 2\hat{\mu}|D(\mathbf{u})|$ . Then the contact condition (249) depends on the solution of the investigated problem. For simplicity we will assume that  $\mathbf{u}_1(\mathbf{x}, t) = 0$ ,  $T_1(\mathbf{x}, t) = 0$ .

#### 4.1.3. Variational (Weak) Solution of the Problem

We will introduce the Sobolev spaces of vector-functions having generalized derivatives of the (possibly fractional) order  $s$  of the type  $[H^s(\Omega)]^k \equiv H^{s,k}(\Omega)$ , where  $H^s(\Omega) \equiv W_2^s(\Omega)$ . The norm will be denoted by  $\|\cdot\|_{s,k}$  and the scalar product by  $(\cdot, \cdot)_s$  (for each integer  $k$ ). We set  $H^{0,k}(\Omega) \equiv L^{2,k}(\Omega)$ . We introduce the spaces  $C_0^\infty(\Omega)$ ,  $C_0^\infty(\Omega, \mathbb{R}^N) = [C_0^\infty(\Omega)]^N$ ,  $L^p(\Omega)$ ,  $1 \leq p \leq \infty$ , and  $L^\infty(\Omega)$  as usual. Moreover, we define for  $s \geq 1$  the following spaces and sets:

$$\begin{aligned} {}^1H^{s,N}(\Omega) &= \cap_{l=1}^r {}^1H^{s,N}(\Omega^l) = \{\mathbf{v} | \mathbf{v} \in H^{s,N}(\Omega), \operatorname{div} \mathbf{v} = 0 \text{ in } \cup_{l=1}^r \Omega^l, \\ &\quad v_n^k - v_n^l = 0 \text{ on } \cup_{k,l} \Gamma_c^{kl}, v_n|_{\Gamma_0} = 0\}, \\ {}^2H^{s,1}(\Omega) &= \cap_{l=1}^r {}^2H^{s,1}(\Omega^l) = \{z | z \in H^{s,1}(\Omega), z^k = z^l \text{ on } \cup_{k,l} \Gamma_c^{kl}\}, \\ {}^1V_s(\Omega) &= \{\mathbf{v} | \mathbf{v} \in {}^1H^{s,N}(\Omega), \mathbf{v}|_{\Gamma_u} = 0\}, \\ {}^2V_s(\Omega) &= \{z | z \in {}^2H^{s,1}(\Omega), z|_{\Gamma_\tau} = 0\}. \end{aligned}$$

Then  ${}^1H^{s,N}(\Omega)$  is a Hilbert space with the norm  $\|\cdot\|_{s,N}$ ,  ${}^2H^{s,1}(\Omega)$  is a Hilbert space with the norm  $\|\cdot\|_{s,1}$ . For the sake of simplicity we put  ${}^1H^{1,N}(\Omega) = {}^1H(\Omega)$ ,  $\|\cdot\|_{1,N} \equiv \|\cdot\|_1$  and in  $H^{0,N}(\Omega)$ ,  $\|\cdot\|_{0,N} \equiv \|\cdot\|_0$ . Let us put  ${}^1\mathcal{H}(\Omega) = {}^1H^{1,N}(\Omega) \cap C_0^\infty(\Omega, \mathbb{R}^N)$ ,  ${}^2\mathcal{H}(\Omega) = {}^2H^{1,1}(\Omega) \cap C_0^\infty(\Omega)$ . We will denote the dual space of  ${}^1H^{s,N}(\Omega)$  by  $({}^1H^{s,N}(\Omega))'$  and similarly in other cases. Furthermore, we put  $\mathbf{v}' = \frac{\partial \mathbf{v}}{\partial t}$ ,  $z' = \frac{\partial z}{\partial t}$ ,

$$\begin{aligned} {}^1H &= \{\mathbf{v} | \mathbf{v} \in L^2(I; {}^1V_s), \mathbf{v}' \in L^2(I; {}^1H^{0,N}(\Omega)), \mathbf{v}(\mathbf{x}, t_0) = 0\}, \\ {}^2H &= \{z | z \in L^2(I; {}^2V_s), z' \in L^2(I; {}^2H^{0,1}(\Omega)), z(\mathbf{x}, t_0) = T_0(\mathbf{x})\}. \end{aligned}$$

We will denote by  $\mathbf{w}_j$  eigenfunctions of a canonical isomorphism  ${}^1\Lambda_s : {}^1H^{s,N} \rightarrow ({}^1H^{s,N})'$ , i.e.  $(\mathbf{w}, \mathbf{v})_s = \lambda_i(\mathbf{w}_j, \mathbf{v})_0 \forall \mathbf{v} \in {}^1H^{s,N}$ ,  $\|\mathbf{w}_j\|_0 = 1$  and similarly we define  $z_j \in {}^2H^{s,1}$ .

Throughout the paper we will assume that  $\mathbf{f}^\iota(\mathbf{x}, t) \in L^2(I; ({}^1H^{1,N}(\Omega^\iota))')$ ,  $\mathbf{P}(\mathbf{x}, t) \in L^2(I; L^{2,N}(\Gamma_\tau))$ ,  $\partial\beta_{ij}^\iota(\mathbf{x})/\partial x_j \in L^\infty(\Omega^\iota)$ ,  $\forall i, j \in \{1, \dots, N\}$ ,  $q \in L^2(I; L^2(\Gamma_0))$ ,  $T_0^\iota(\mathbf{x}) \in {}^2H^{1,1}(\Omega^\iota)$ ,  $\rho^\iota$ ,  $\hat{g}^\iota$ ,  $\hat{\mu}^\iota$  are piecewise constant and positive,  $W^\iota \in L^2(I; ({}^2H^{1,1}(\Omega^\iota))')$ ,  $\kappa_{ij}^\iota \in L^\infty(\Omega^\iota)$  are Lipschitz on  $\Omega^\iota$ , and satisfy the usual symmetry condition  $\kappa_{ij}^\iota = \kappa_{ji}^\iota$  and  $\kappa_{ij}^\iota \xi_i \xi_j \geq c_T \|\xi\|_1^2$ ,  $\mathbf{x} \in \Omega^\iota$ ,  $\xi \in \mathbb{R}^N$ ,  $c_T = \text{const.} > 0$ ,  $\mathcal{F}_c^{kl} \in L^\infty(\Gamma_c^{kl})$ ,  $\mathcal{F}_c^{kl} \geq 0$  a.e. on  $\cup_{k,l} \Gamma_c^{kl}$ .

For  $\mathbf{u}, \mathbf{v} \in H^{1,N}(\Omega)$ ,  $T, z \in H^{1,1}(\Omega)$  we put

$$\begin{aligned}
 a(\mathbf{u}, \mathbf{v}) &= \sum_{\iota=1}^r a^\iota(\mathbf{u}^\iota, \mathbf{v}^\iota) = 2 \int_{\Omega} \hat{\mu} D_{ij}(\mathbf{u}) D_{ij}(\mathbf{v}) d\mathbf{x}, \\
 (\mathbf{u}', \mathbf{v}) &= \sum_{\iota=1}^r (\mathbf{u}^\iota, \mathbf{v}^\iota) = \int_{\Omega} \rho \mathbf{u}' \mathbf{v} d\mathbf{x}, \quad (T', z) = \sum_{\iota=1}^r (T^\iota, z^\iota) = \int_{\Omega} \rho c_e T' z d\mathbf{x}, \\
 a_T(T, z) &= \sum_{\iota=1}^r a_T^\iota(T^\iota, z^\iota) = \int_{\Omega} \kappa_{ij} \frac{\partial T}{\partial x_i} \frac{\partial z}{\partial x_j} d\mathbf{x}, \\
 S(\mathbf{v}) &= \sum_{\iota=1}^r S^\iota(\mathbf{v}^\iota) = \int_{\Omega} f_i v_i d\mathbf{x} + \int_{\Gamma_\tau} P_i v_i ds \equiv (\mathbf{F}, \mathbf{v}), \\
 s(z) &= \sum_{\iota=1}^r s^\iota(z^\iota) = \int_{\Omega} W z d\mathbf{x} + \int_{\Gamma_0} q z ds \equiv (Q, z), \\
 b_0(\mathbf{v}, g, z) &= \sum_{\iota=1}^r b_0^\iota(\mathbf{v}^\iota, g^\iota, z^\iota) = \int_{\Omega} \rho c_e v_k \frac{\partial g}{\partial x_k} z d\mathbf{x}, \\
 b(\mathbf{u}, \mathbf{v}, \mathbf{w}) &= \sum_{\iota=1}^r b^\iota(\mathbf{u}^\iota, \mathbf{v}^\iota, \mathbf{w}^\iota) = \int_{\Omega} \rho u_i \frac{\partial v_j}{\partial x_i} w_j d\mathbf{x}, \\
 j(\mathbf{v}) &= \sum_{\iota=1}^r j^\iota(\mathbf{v}^\iota) = 2 \int_{\Omega} \hat{g} (D_{II}(\mathbf{v}))^{\frac{1}{2}} d\mathbf{x}, \\
 j_g(\mathbf{v}) &= \sum_{\iota=1}^r j_g^\iota(\mathbf{v}^\iota) = \int_{\cup_{k,l} \Gamma_c^{kl}} \mathcal{F}_c^{kl} |S^D| |\mathbf{v}_t^k - \mathbf{v}_t^l| ds, \\
 b_s(T, \mathbf{v}) &= \sum_{\iota=1}^r b_s^\iota(T^\iota, \mathbf{v}^\iota) = \int_{\Omega} \frac{\partial}{\partial x_j} (\beta_{ij} T) v_i d\mathbf{x}, \\
 b_p(\mathbf{v}, z) &= \sum_{\iota=1}^r b_p^\iota(\mathbf{v}^\iota, z^\iota) = \int_{\Omega} \rho T_0 \beta_{ij} \frac{\partial v_i}{\partial x_j} z d\mathbf{x}.
 \end{aligned}$$

Let us multiply (241) by  $\mathbf{v} - \mathbf{u}(t)$  and (243) by  $z - T(t)$ , respectively, and further add both equations. We integrate the sum over  $\Omega$  and apply the Green theorem satisfying the boundary conditions. Then after some modification, including among other the integration in time over the interval  $I$ , we obtain the following variational (weak) formulation:

**Problem**  $(\mathcal{P})_v$ : Find a pair of functions  $(T, \mathbf{u})$  such that  $T \in {}^2H$ ,  $\mathbf{u} \in {}^1H$  and

$$\begin{aligned} & \int_I [(\mathbf{u}'(t), \mathbf{v} - \mathbf{u}(t)) + (T'(t), z - T(t)) + a(\mathbf{u}(t), \mathbf{v} - \mathbf{u}(t)) + \\ & + a_T(T(t), z - T(t)) + b(\mathbf{u}(t), \mathbf{u}(t), \mathbf{v} - \mathbf{u}(t)) + b_0(\mathbf{u}(t), T(t), z - T(t)) + \\ & + b_s(T(t) - T_0, \mathbf{v} - \mathbf{u}(t)) + b_p(\mathbf{u}(t), z - T(t)) + \\ & + j(\mathbf{v}(t)) - j(\mathbf{u}(t)) + j_g(\mathbf{v}(t)) - j_g(\mathbf{u}(t))] dt \geq \\ & \geq \int_I [S(\mathbf{v} - \mathbf{u}(t)) + s(z - T(t))] dt \quad \forall (\mathbf{v}, z) \in {}^1H \times {}^2H \\ & \text{holds for a.a. } t \in I. \end{aligned} \quad (251)$$

From the above assumptions  $a(\mathbf{u}, \mathbf{v}) = a(\mathbf{v}, \mathbf{u})$ ,  $a_T(T, z) = a_T(z, T)$  and for  $\mathbf{u} \in {}^1H^{1,N}(\Omega)$ ,  $T \in {}^2H^{1,1}(\Omega)$  there exist constants  $c_B > 0$ ,  $c_T > 0$  such that  $a(\mathbf{u}, \mathbf{u}) \geq c_B \|\mathbf{u}\|_{1,N}^2$  for all  $\mathbf{u} \in {}^1H^{1,N}(\Omega)$ ,  $a_T(T, T) \geq c_T \|T\|_{1,1}^2$  for all  $T \in {}^2H^{1,1}(\Omega)$ . Furthermore, we have (see [71])

$$\begin{aligned} |b(\mathbf{u}, \mathbf{v}, \mathbf{w})| & \leq c_4 \|\mathbf{u}\|_{1,N}^{1/2} \|\mathbf{u}\|_{0,N}^{1/2} \|\mathbf{w}\|_{1,N}^{1/2} \|\mathbf{w}\|_{0,N}^{1/2} \|\mathbf{v}\|_{s,N}, \quad s = \frac{1}{2}N, \\ \mathbf{u} & \in {}^1H^{1,N}(\Omega), \mathbf{w} \in H^{s,N}(\Omega), \\ |b_0(\mathbf{u}, y, z)| & \leq c_5 \|\mathbf{u}\|_{1,N}^{1/2} \|\mathbf{u}\|_{0,N}^{1/2} \|z\|_{1,1}^{1/2} \|z\|_{0,1}^{1/2} \|y\|_{s,1}, \quad s = \frac{1}{2}N, \\ \mathbf{u} & \in {}^1H^{1,N}(\Omega), z \in H^{s,1}(\Omega), \\ b(\mathbf{u}, \mathbf{u}, \mathbf{u}) & = 0, b_0(\mathbf{u}, z, z) = 0, \\ \text{since } \mathcal{F}_c^{kl} & \in L^\infty(\Gamma_c^{kl}), \mathcal{F}_c^{kl} \geq 0, \text{ then } j_g(\mathbf{u}(t)) \geq 0, \end{aligned}$$

and moreover, if  $\mathbf{u}, \mathbf{v}, \mathbf{w} \in {}^1\mathcal{H}(\Omega)$  then  $b(\mathbf{u}, \mathbf{v}, \mathbf{w}) + b(\mathbf{u}, \mathbf{w}, \mathbf{v}) = 0$ , which is valid also for  $\mathbf{u} \in L^{2,N}(\Omega)$ ,  $\mathbf{v}, \mathbf{w} \in {}^1H^{1,N}(\Omega)$ ;  $b(\mathbf{u}, \mathbf{u}, \mathbf{v}) = -b(\mathbf{u}, \mathbf{v}, \mathbf{u})$  for  $\mathbf{u}, \mathbf{v} \in {}^1\mathcal{H}(\Omega)$ . Similarly,  $b_0(\mathbf{u}, y, z) + b_0(\mathbf{u}, z, y) = 0$  for  $\mathbf{u} \in {}^1H^{0,N}(\Omega)$ ,  $y, z \in H_0^{1,1}(\Omega)$ .

The main result is represented by the following theorem:

**Theorem 13** Let  $N \geq 2$ ,  $s = \frac{N}{2}$ . Let  $\mathbf{f} \in L^2(I; ({}^1H^{1,N}(\Omega))')$ ,  $\mathbf{P} \in L^2(I; L^{2,N}(\Gamma_\tau))$ ,  $W \in L^2(I; ({}^2H^{1,1}(\Omega))')$ ,  $\frac{\partial \beta_{ij}}{\partial x_j} \in L^\infty(\Omega)$ ,  $\forall i, j \in \{1, \dots, N\}$ ,  $q \in L^2(I; L^2(\Gamma_u))$ ,  $T_1 \in L^2(I; L^2(\Gamma_\tau))$ ,  $T_0(\mathbf{x}) \in H^{1,1}(\Omega)$ ,  $\hat{g}, \hat{\mu}$  are piecewise constant,  $\kappa_{ij} \in L^\infty(\Omega)$ ,  $\mathcal{F}_c^{kl} \in L^\infty(\Gamma_c^{kl})$ ,  $\mathcal{F}_c^{kl} \geq 0$  a.e. on  $\cup_{k,l} \Gamma_c^{kl}$ . Then there exists a pair of functions  $(\mathbf{u}, T)$  such that

$$\begin{aligned} \mathbf{u} & \in L^2(I; {}^1H^{s,N}(\Omega)) \cap L^\infty(I; {}^1H^{0,N}(\Omega)), \mathbf{u}' \in L^2(I; ({}^1H^{1,N}(\Omega))'), \\ T & \in L^2(I; {}^2H^{s,1}(\Omega)) \cap L^\infty(I; {}^2H^{0,1}(\Omega)), \mathbf{u}' \in L^2(I; ({}^2H^{1,1}(\Omega))'), \\ \mathbf{u}(\mathbf{x}, t_0) & = 0, T(\mathbf{x}, t_0) = T_0(\mathbf{x}) \end{aligned}$$

and satisfying the variational inequality (251).

**Proof:** To prove the theorem the triple regularizations will be used [45, 46, 50]. Let us introduce the regularization of  $j(\mathbf{v}(t))$  by

$$j_\varepsilon(\mathbf{v}(t)) = \frac{2}{1+\varepsilon} \int_\Omega \hat{g}(D_{II}(\mathbf{v}(t)))^{(1+\varepsilon)/2} d\mathbf{x}, \quad \varepsilon > 0 \quad \text{and} \quad (j'_\varepsilon(\mathbf{v}), \mathbf{v}) \geq 0. \quad (252)$$

Since the functional  $j_g(\mathbf{v})$  is not differentiable in the Gâteaux sense, therefore it can be regularized by its regularization  $j_{g\varepsilon}(\mathbf{v})$ . We introduce the function  $\psi_\varepsilon : \mathbb{R} \rightarrow \mathbb{R}$  defined as  $\psi_\varepsilon(y) = \sqrt{(y^2 + \varepsilon^2)} - \varepsilon$ , regularizing the function  $y \rightarrow |y|$ . The function  $\psi_\varepsilon$  is differentiable and satisfies the following inequality

$$||y| - \psi_\varepsilon(|y|)| < \varepsilon \quad \forall y \in \mathbb{R}, \varepsilon \geq 0.$$

Then the functional  $j_g(\mathbf{v})$  will be regularized by its regularization  $j_{g\varepsilon}(\mathbf{v})$ , defined by

$$j_{g\varepsilon}(\mathbf{v}(t)) = \int_{\cup_{k,l} \Gamma_c^{kl}} \mathcal{F}_c^{kl} |S_{ij}^D| \psi_\varepsilon(|\mathbf{v}^k - \mathbf{v}^l|) ds \quad \text{and} \quad (j'_{g\varepsilon}(\mathbf{v}), \mathbf{v}) \geq 0. \quad (253)$$

The third regularization will be introduced by adding the viscous terms  $\eta((\mathbf{u}_{\varepsilon\eta}(t), \mathbf{v}))_s$  and  $\eta((T_{\varepsilon\eta}(t), z))_s$ , where  $s = \frac{N}{2}$  and  $\eta$  is a positive number. For  $N = 2$  we obtain  $s = 1$  and  ${}^1H^{s,N}(\Omega) = {}^1H^{1,N}(\Omega)$ ,  ${}^2H^{s,1}(\Omega) = {}^2H^{1,1}(\Omega)$  and the added viscous terms are of the same order as the bilinear form, and therefore, it can be omitted.

Thus we will to solve the regularized problem:

**Problem**  $(\mathcal{P}_r)_v$ : Find a pair of functions  $(\mathbf{u}_{\varepsilon\eta}, T_{\varepsilon\eta}) \in {}^1H \times {}^2H$  such that

$$\begin{aligned} & \int_I [(\mathbf{u}'_{\varepsilon\eta}(t), \mathbf{v} - \mathbf{u}_{\varepsilon\eta}(t)) + (T'_{\varepsilon\eta}(t), z - T_{\varepsilon\eta}(t)) + a(\mathbf{u}_{\varepsilon\eta}(t), \mathbf{v} - \mathbf{u}_{\varepsilon\eta}(t)) + \\ & + a_T(T_{\varepsilon\eta}(t), z - T_{\varepsilon\eta}(t)) + b(\mathbf{u}_{\varepsilon\eta}(t), \mathbf{u}_{\varepsilon\eta}(t), \mathbf{v} - \mathbf{u}_{\varepsilon\eta}(t)) + \\ & + \eta((\mathbf{u}_{\varepsilon\eta}(t), \mathbf{v} - \mathbf{u}_{\varepsilon\eta}(t)))_s \eta((T_{\varepsilon\eta}(t), z - T_{\varepsilon\eta}(t)))_s + \\ & + b_0(\mathbf{u}_{\varepsilon\eta}(t), T_{\varepsilon\eta}(t), z - T_{\varepsilon\eta}(t)) + b_p(\mathbf{u}_{\varepsilon\eta}(t), z - T_{\varepsilon\eta}(t)) \\ & + b_s(T_{\varepsilon\eta}(t) - T_0, \mathbf{v} - \mathbf{u}_{\varepsilon\eta}(t)) + j(\mathbf{v}(t)) - j(\mathbf{u}_{\varepsilon\eta}(t)) + \\ & + j_g(\mathbf{v}(t)) - j_g(\mathbf{u}_{\varepsilon\eta}(t))] dt \geq \int_I [S(\mathbf{v} - \mathbf{u}_{\varepsilon\eta}(t)) + s(z - T_{\varepsilon\eta}(t))] dt \\ & \forall (\mathbf{v}, z) \in {}^1H \times {}^2H. \end{aligned} \quad (254)$$

The method of the proof is similar to that of Theorem 3 in [45] and it is as follows:

- (1) the existence of the solution of (254) will be based on the Galerkin approximation technique;
- (2) a priori estimates I and II independent of  $\varepsilon$  and  $\eta$  will be given;
- (3) limitation processes for the Galerkin approximation (i.e. over  $m$ ) and for  $\varepsilon \rightarrow 0$ ,  $\eta \rightarrow 0$  will be performed;
- (4) the uniqueness of the solution of (251) for  $N = 2$  can be proved only as for  $N = 3$  is still an open problem.

The existence of a pair of functions  $(\mathbf{u}_{\varepsilon\eta}, T_{\varepsilon\eta})$  will be proved by means of the finite-dimensional approximation. The proof is similar of that of [44, 45]. We construct a countable bases of the spaces  ${}^1V_s(\Omega)$  and  ${}^2V_s(\Omega)$ , i.e. each finite subsets are linearly independent and  $\text{span}\{\mathbf{v}_i | i = 1, 2, \dots\}$ ,  $\text{span}\{z_i | i = 1, 2, \dots\}$  are dense in  ${}^1V_s(\Omega)$  and  ${}^2V_s(\Omega)$ , respectively, as  ${}^1V_s(\Omega)$  and  ${}^2V_s(\Omega)$  are separable spaces. Let us construct spaces spanned by

$\{\mathbf{v}_i | 1 \leq j, k \leq m\}$ ,  $\{z_i | 1 \leq j, k \leq m\}$ . Then the approximate solution  $(\mathbf{u}_m, T_m)$  of the order  $m$  satisfies

$$\begin{aligned} & (\mathbf{u}'_m(t), \mathbf{v}_j) + a(\mathbf{u}_m(t), \mathbf{v}_j) + b(\mathbf{u}_m(t), \mathbf{u}_m(t), \mathbf{v}_j) + \eta((\mathbf{u}_m(t), \mathbf{v}_j))_s \\ & + b_s(T_m(t) - T_0, \mathbf{v}_j) + (j'_\varepsilon(\mathbf{u}_m(t), \mathbf{v}_j) + (j'_{g\varepsilon}(\mathbf{u}_m(t), \mathbf{v}_j) = S(\mathbf{v}_j), 1 \leq j \leq m. \\ & (T'_m(t), z_j) + a_T(T_m(t), z_j) + b_0(\mathbf{u}_m(t), T_m(t), z_j) + \eta((T_m(t), z_j))_s \\ & + b_p(\mathbf{u}_m(t), z_j) = s(z_j) \quad 1 \leq j \leq m, \end{aligned} \quad (255)$$

$$\mathbf{u}_m(\mathbf{x}, t_0) = 0, \quad T(\mathbf{x}, t_0) = T_0(\mathbf{x}). \quad (256)$$

Since  $\{\mathbf{v}_j\}_{j=1}^m$ ,  $\{z_j\}_{j=1}^m$  are linearly independent, the system (255), (256) is the regular system of ordinary differential equations of the first order, and therefore (255), (256) uniquely define  $(\mathbf{u}_m, T_m)$  on the interval  $I_m = \langle t_0, t_m \rangle$ .

A priori estimate I:

Using assumptions, relations and estimates mentioned above, we have

$$\begin{aligned} & b(\mathbf{u}_m(t), \mathbf{u}_m(t), \mathbf{u}_m(t)) = 0, \quad b_0(\mathbf{u}_m(t), T_m(t), T_m(t)) = 0, \\ & |b_s((T_m(t) - T_0), \mathbf{u}_m(t)) + b_p(\mathbf{u}_m(t), T_m(t))| \leq \\ & \leq c(1 + \|T_m(t)\|_{1,1} \|\mathbf{u}_m(t)\|_{0,N} + \|T_m(t)\|_{0,1} \|\mathbf{u}_m(t)\|_{1,N}). \end{aligned} \quad (257)$$

Via the integration of (255), with  $\mathbf{v}(t) = \mathbf{u}_m(t)$ ,  $z(t) = T_m(t)$ , in time over  $I_m = (t_0, t_m)$ , and since  $(j'_\varepsilon(\mathbf{v}), \mathbf{v}) \geq 0$ ,  $(j'_{g\varepsilon}(\mathbf{v}), \mathbf{v}) \geq 0$ , using the ellipticity of bilinear forms  $a(\mathbf{u}, \mathbf{u})$ ,  $a_T(T, T)$ , due to (257), then after some modifications as well as applying the Gronwall lemma and after some more algebra, we find the following estimates

$$\|\mathbf{u}_m(t)\|_{0,N} \leq 0, \quad t \in I, \quad \int_I \|\mathbf{u}_m(\tau)\|_{1,N}^2 d\tau \leq c, \quad \eta \int_I \|\mathbf{u}_m(\tau)\|_{s,N}^2 d\tau \leq c \quad (258)$$

$$\|T_m(t)\|_{0,1} \leq 0, \quad t \in I, \quad \int_I \|T_m(\tau)\|_{1,1}^2 d\tau \leq c, \quad \eta \int_I \|T_m(\tau)\|_{s,1}^2 d\tau \leq c. \quad (259)$$

From these estimates we obtain

$\{\mathbf{u}_m(t), m \in \mathbb{N}\}$  is bounded subset in  $L^2(I; {}^1H)$ ,

$\{\eta^{1/2} \mathbf{u}_m(t), m \in \mathbb{N}\}$  is bounded subset in  $L^2(I; {}^1V)$ ,

$\{T_m(t), m \in \mathbb{N}\}$  is bounded subset in  $L^2(I; {}^2H)$ ,

$\{\eta^{1/2} \mathbf{u}_m(t), m \in \mathbb{N}\}$  is bounded subset in  $L^2(I; {}^2V)$ .

To prove a priori estimate II, then similarly as in [8, 44, 45, 48] the system (255), (256) is equivalent to the following system

$$(\mathbf{u}'_m + A_B \mathbf{u}_m + \eta \Lambda_s \mathbf{u}_m + j'_\varepsilon(\mathbf{u}_m) + j'_{g\varepsilon}(\mathbf{u}_m) + h_m - \mathbf{F}, \mathbf{v}_j) = 0, 1 \leq j \leq m, \quad (260)$$

$$(T'_m + A_T T_m + \eta \mathcal{T}_s T_m + g_m - Q, z_j) = 0, 1 \leq j \leq m, \quad (261)$$

with (256), where  $a(\mathbf{u}, \mathbf{v}) = (A_B \mathbf{u}, \mathbf{v})$ ,  $A_B \in \mathcal{L}({}^1V_1, {}^1V'_1)$ ,  $a_T(T, z) = a_T(A_T T, z)$ ,  $A_T \in \mathcal{L}({}^2V_1, {}^2V'_1)$ ,  $((\mathbf{u}, \mathbf{v}))_s = (\Lambda_s \mathbf{u}, \mathbf{v})$ ,  $\Lambda_s \in \mathcal{L}({}^1V_s, {}^1V'_s)$ ,  $((T, z))_s = (\mathcal{T}_s T, z)$ ,  $\mathcal{T}_s \in \mathcal{L}({}^2V_s, {}^2V'_s)$ ,  $b(\mathbf{u}_m, \mathbf{u}_m, \mathbf{v}) + b_s(T_m, \mathbf{v}) = (h_m, \mathbf{v})$ ,  $h_m \in {}^1K_m \subset L^2(I; {}^1V'_s)$ ,  $b_0(\mathbf{u}_m, T_m, z) + b_p(\mathbf{u}_m, z) = (g_m, z)$ ,  $g_m \in {}^2K_m \subset L^2(I; {}^2V'_s)$ . Then applying the technique of orthogonal projection and using the technique of [8] we find that

$$\begin{aligned} \mathbf{u}'_m &\text{ is a bounded subset of } L^2(I; {}^1V'_s), \\ T'_m &\text{ is a bounded subset of } L^2(I; {}^2V'_s). \end{aligned} \quad (262)$$

The limitation over  $m$  (Galerkin), i.e. the convergence of the finite-dimensional approximation for  $\varepsilon, \eta$  being fixed and the limitation over  $\varepsilon, \eta \rightarrow 0$  finish the existence of the solution  $(\mathbf{u}(t), T(t))$  satisfying (251), which completes the proof.

## 4.2. Numerical Approach

The investigated variational problem (251) will be solved numerically in its dynamical and stationary flow (i.e. when the mass movements are uniform or when the system of geological bodies is deformed very slowly) formulations. Next the ideas of numerical solutions will be shortly discussed only.

### 4.2.1. Dynamic Case

Let  $\Omega_h$  be a polyhedral approximation to  $\Omega$  in  $\mathbb{R}^3$  and let its boundary be denoted as  $\partial\Omega_h = \Gamma_{uh} \cup \Gamma_{\tau h} \cup \Gamma_{0h} \cup \Gamma_{ch}$ . Let  $\mathfrak{T}_h$  be a partition of  $\overline{\Omega}_h$  by tetrahedra  $\mathcal{T}_h$ . Let  $h = h(\mathcal{T}_h)$  be the maximum diameter of tetrahedral elements  $\mathcal{T}_h$ . Let  $\mathcal{T}_h \in \mathfrak{T}_h$  be a tetrahedron with vertices  $P_i, i = 1, \dots, 4$  and let  $R_i$  be the barycentres with respect to the points  $P_i, i = 1, \dots, 4$ . Assume that  $\{\mathfrak{T}_h\}$  is a regular family of partitioning  $\mathfrak{T}_h$  of  $\Omega_h$  such that  $\overline{\Omega}_h = \cup_{\mathcal{T}_h \in \mathfrak{T}_h} \mathcal{T}_h$ .

Let  $n$  be an integer and set  $k = t_p/n$ . Let

$$\begin{aligned} \mathbf{f}_k^{i+\Theta} &= \frac{1}{k} \int_{ik}^{(i+\Theta)k} \mathbf{f}(t) dt, \quad i = 0, \dots, n-1, \quad 0 \leq \Theta \leq 1, \quad \mathbf{f}_k^{i+\Theta} \in {}^1V'_s, \\ W_k^{i+\Theta} &= \frac{1}{k} \int_{ik}^{(i+\Theta)k} W(t) dt, \quad i = 0, \dots, n-1, \quad 0 \leq \Theta \leq 1, \quad W_k^{i+\Theta} \in {}^2V'_s. \end{aligned}$$

We start with the initial data  $\mathbf{u}^0 = 0, T^0 = T_0$ . When  $(\mathbf{u}^0, T^0), \dots, (\mathbf{u}^i, T^i)$  are known, we define  $(\mathbf{u}^{i+1}, T^{i+1})$  as an element of  ${}^1V_s \times {}^2V_s$ . The existence of a pair of functions  $(\mathbf{u}^{i+1}, T^{i+1})$  for each fixed  $k$  and each  $i \geq 0$  can be proved. As regards the spatial discretization, there are several classes of possibilities for approximation  ${}^1V_s$  by its finite element space  ${}^1V_h$  [12, 71, 44, 48, 54, 56, 57]. Let the spaces  ${}^1V_s, {}^2V_s$  be approximated by spaces of linear non-conforming functions  ${}^1V_h$  in the visco-plastic part of the problem and by spaces of linear conforming functions  ${}^2V_h$  in the thermal part of the problem. Let  ${}^1\mathcal{V}_h = \{\mathbf{v}_h | v_{hi} \in P_1^*, i = 1, \dots, N, \forall \mathcal{T}_h \in \mathfrak{T}_h, \text{ continuous in barycentres of tetrahedra } B_j, j = 1, \dots, m, \text{ and equal to zero in } B_j \text{ laying on } \Gamma_{uh}, \sum_{i=1, \dots, N} \|v_{hi}\|/x_i = 0, \mathbf{v}_h = 0, \mathbf{x} \in \Omega \setminus \overline{\Omega}_h\}$ , where  $P_1^*$  denotes the space of all non-conforming linear polynomials,  ${}^1V_h =$

$\{\mathbf{v}_h | \mathbf{v}_h \in \mathcal{V}_h, \mathbf{v}_h = \mathbf{u}_1 \text{ on } \Gamma_{uh}\}$  and let  ${}^2\mathcal{V}_h, {}^2V_h$  be the spaces of conforming linear finite elements.

Given a triangulation  $\mathcal{T}_h$  of  $\Omega_h$ , we assume  $(\mathbf{u}_h^0, T_h^0)$  to be given in  ${}^1V_h \times {}^2V_h$ , and, taken so that  $(\mathbf{u}_h^0, T_h^0)$  tends to  $(0, T_0)$  in  ${}^1V_h \times {}^2V_h$  when  $h \rightarrow 0_+$ . Moreover, we will assume that  $\|\mathbf{u}_h^0\|, \|T_h^0\|$  are bounded. We define recursively for each  $k$  and  $h$  a family of elements  $(\mathbf{u}_h^0, T_h^0), \dots, (\mathbf{u}_h^i, T_h^i)$  of  ${}^1V_h \times {}^2V_h$ , which can be based on the semi-implicit scheme. The other schemes like the explicit, implicit, Crank-Nichelson schemes can be also used. The time derivatives will be approximated by the backward differences. Since  $\frac{\mathbf{u}_h^{i+1} - \mathbf{u}_h^i}{k} = \frac{\mathbf{u}_h^{i+\Theta} - \mathbf{u}_h^i}{\Theta k}, \frac{T_h^{i+1} - T_h^i}{k} = \frac{T_h^{i+\Theta} - T_h^i}{\Theta k}, 0 \leq \Theta \leq 1$ , then

$$\begin{aligned} \mathbf{u}_h^{i+\Theta} &= \Theta \mathbf{u}_h^{i+1} + (1 - \Theta) \mathbf{u}_h^i, & T_h^{i+\Theta} &= \Theta T_h^{i+1} + (1 - \Theta) T_h^i, & 0 \leq \Theta \leq 1, \\ \mathbf{u}_h^{i+1} &= \Theta^{-1} \mathbf{u}_h^{i+\Theta} - \frac{(1 - \Theta)}{\Theta} \mathbf{u}_h^i, & T_h^{i+1} &= \Theta_h^{-1} T_h^{i+\Theta} - \frac{(1 - \Theta)}{\Theta} T_h^i, & 0 \leq \Theta \leq 1. \end{aligned}$$

Since the contact conditions depend on the solution of the studied problem, we will assume that  $j_h(\mathbf{v}_h) = j_h(\mathbf{u}_h^i, \mathbf{v}_h)$ . Thus we have the following scheme:

**Scheme ( $\mathcal{P}_{si}$ ):** When  $(\mathbf{u}_h^0, T_h^0), \dots, (\mathbf{u}_h^i, T_h^i)$  are known, then we determine  $(\mathbf{u}_h^{i+1}, T_h^{i+1})$  as a solution in  ${}^1V_h \times {}^2V_h$  of

$$\begin{aligned} &k^{-1}(\mathbf{u}_h^{i+1} - \mathbf{u}_h^i, \mathbf{v}_h - \mathbf{u}_h^{i+\Theta}) + a_h(\mathbf{u}_h^{i+\Theta}, \mathbf{v}_h - \mathbf{u}_h^{i+\Theta}) + \\ &+ b_h(\mathbf{u}_h^i, \mathbf{u}_h^i, \mathbf{v}_h - \mathbf{u}_h^{i+\Theta}) + b_s(T_h^i - T_h^0, \mathbf{v}_h - \mathbf{u}_h^{i+\Theta}) + j_h(\mathbf{v}_h) - j_h(\mathbf{u}_h^{i+\Theta}) + \\ &+ j_{gh}(\mathbf{v}_h) - j_{gh}(\mathbf{u}_h^{i+\Theta}) \geq (\mathbf{F}_h^{i+\Theta}, \mathbf{v}_h - \mathbf{u}_h^{i+\Theta}) \quad \forall \mathbf{v}_h \in {}^1V_h, \end{aligned} \quad (263)$$

$$\begin{aligned} &k^{-1}(T_h^{i+1} - T_h^i, z_h - T_h^{i+\Theta}) + a_{Th}(T_h^{i+\Theta}, z_h - T_h^{i+\Theta}) + \\ &+ b_{0h}(\mathbf{u}_h^i, T_h^i, z_h - T_h^{i+\Theta}) + b_p(k^{-1}(\mathbf{u}_h^i - \mathbf{u}_h^{i-1}), z_h - T_h^{i+\Theta}) \geq \\ &\geq (Q_h^{i+\Theta}, z_h - T_h^{i+\Theta}) \quad z_h \in {}^2V_h. \end{aligned} \quad (264)$$

The scheme is not valid for  $\Theta \geq \frac{1}{2}$ ; for  $\Theta = 1$  we have the semi-implicit scheme and for  $\Theta = \frac{1}{2}$  we have the Crank-Nicholson scheme.

The term  $\hat{g} D_{ij}(\mathbf{u}) D_{II}^{-1/2}(\mathbf{u})$  creates the nondifferential functional  $j(\mathbf{u})$  and since  $\|j_\varepsilon''(\mathbf{u})\|_* \simeq \frac{1}{\varepsilon}$  (see [13]) the problem can be badly conditioned. Therefore, we introduce the multipliers  $m = (m_{ij}), i, j = 1, \dots, N$ , [8, 44, 13] as follows:

$$\begin{aligned} &m_{ij} \in L^\infty(\Omega \times I), \quad m_{ij} = m_{ji} \quad \forall i, j, \quad m_{ii} = 0, \\ &m_{ij} m_{ij} \leq 1 \quad \text{a.e. in } \Omega \times I, \\ &m_{ij} D_{ij}(\mathbf{u}) = (D_{ij}(\mathbf{u}) D_{ij}(\mathbf{u}))^{\frac{1}{2}} = 2^{\frac{1}{2}} D_{II}^{\frac{1}{2}}(\mathbf{u}) \quad \text{a.e. in } \Omega \times I. \end{aligned}$$

Then the stress-strain rate relation can be rewritten in the following form

$$\tau_{ij} = {}^B\tau_{ij} + {}^T\tau_{ij} = -p\delta_{ij} + 2^{\frac{1}{2}}\hat{g}m_{ij} + 2\hat{\mu}D_{ij} - \beta_{ij}(T - T_0).$$

Multipliers  $m \in K = \{m | m_{ij} \in L^\infty(\Omega \times I), \|m\|_\infty \leq 1\}$  can be approximated by tensor's functions piecewise constant on every  $\mathcal{T}_h \in \mathfrak{T}_h$ . Further, we introduce  $K_h =$

$\{m_h | \|m_h\|_\infty \leq 1\}$ ,  $m_{hjl}$  piecewise constant on every  $\mathcal{T}_h$ ,  $m_{hjl} = 0$  on  $\Omega \setminus \Omega_h$ ,  $j, l = 1, \dots, N$ ,  $m_{hjl} = m_{hlj}$ . Then we have the following scheme:

**Scheme**  $(\mathcal{P}_{mi})_{hk}$ : When  $(\mathbf{u}_h^0, T_h^0), \dots, (\mathbf{u}_h^i, T_h^i)$  are known, then we determine  $(\mathbf{u}_h^{i+\Theta}, T_h^{i+1}, m_h^{i+\Theta})$  as

$$\begin{aligned} m_{hjl}^{i+\Theta} m_{hjl}^{i+\Theta} &\leq 1 \quad \text{on every } \mathcal{T}_h \in \mathfrak{T}_h, \\ m_{hjl}^{i+\Theta} &= m_{hlj}^{i+\Theta}, \quad m_{hjl}^{i+\Theta} \in L^\infty(\Omega), \quad 1 \leq j, l \leq N, \\ m_{hjl}^{i+\Theta} D_{jl}(\mathbf{u}_h^{i+\Theta}) &= (D_{jl}(\mathbf{u}_h^{i+\Theta}) D_{jl}(\mathbf{u}_h^{i+\Theta}))^{\frac{1}{2}} \quad \text{on every } \mathcal{T}_h \in \mathfrak{T}_h, \\ (\mathbf{u}_h^{i+\Theta}, \mathbf{v}_h) + k\Theta a_h(\mathbf{u}_h^{i+\Theta}, \mathbf{v}_h) + k\Theta j_{gh}(\mathbf{v}_h) &= \\ = k\Theta(\mathbf{F}_h^{i+\Theta}, \mathbf{v}_h) + (\mathbf{u}_h^i, \mathbf{v}_h) \quad \forall \mathbf{v}_h \in {}^1V_h, \quad i = 0, 1, \dots, n-1, \\ \text{and } \mathbf{u}_h^{i+1} &\text{ will be determined from } \mathbf{u}_h^{i+1} = \Theta^{-1} \mathbf{u}_h^{i+\Theta} + \Theta^{-1}(1 - \Theta) \mathbf{u}_h^i. \end{aligned}$$

$$\begin{aligned} k^{-1}(T_h^{i+1} - T_h^i, z_h - T_h^{i+\Theta}) + a_{Th}(T_h^{i+\Theta}, z_h - T_h^{i+\Theta}) + b_{0h}(\mathbf{u}_h^i, T_h^i, z_h - T_h^{i+\Theta}) \\ + b_p(k^{-1}(\mathbf{u}_h^i - \mathbf{u}_h^{i-1}), z_h - T_h^{i+\Theta}) \geq (Q_h^{i+\Theta}, z_h - T_h^{i+\Theta}) \quad \forall z_h \in {}^2V_h. \end{aligned}$$

Let  $|\cdot|_h$  be the norm in  $L^2(\Omega)$  ( $[L^2(\Omega)]^N$ ),  $\|\cdot\|_h$  in  ${}^1\mathcal{V}_h$ ,  ${}^2V_h$  and  ${}^2\mathcal{V}_h$ ,  ${}^2V_h$ . According to [71]  $|\mathbf{u}_h|_h \leq d_1 \|\mathbf{u}_h\|_h$ ,  $\|\mathbf{u}_h\|_h \leq S(h) |\mathbf{u}_h|_h \quad \forall \mathbf{u}_h \in {}^1\mathcal{V}_h$ ,  $|T_h|_h \leq d_0 \|T_h\|_h$ ,  $\|T_h\|_h \leq S_0(h) |T_h|_h \quad \forall T_h \in {}^2\mathcal{V}_h$ ,  $d_0, d_1$  are independent of  $h$ . Furthermore,  $|b_{0h}(\mathbf{u}_h, T_h, z_h)| \leq c_0 |\mathbf{u}_h|_h |T_h|_h |z_h|_h \quad \forall \mathbf{u}_h \in {}^1\mathcal{V}_h, \forall T_h, z_h \in {}^2\mathcal{V}_h$ ,  $|b_h(\mathbf{u}_h, \mathbf{v}_h, \mathbf{w}_h)| \leq d_1 \|\mathbf{u}_h\|_h \|\mathbf{v}_h\|_h \|\mathbf{w}_h\|_h \quad \forall \mathbf{u}_h, \mathbf{v}_h, \mathbf{w}_h \in {}^1\mathcal{V}_h$ , where  $c_0$  and  $d_1$  do not depend on  $h$ ,  $|b_h(\mathbf{u}_h, \mathbf{u}_h, \mathbf{v}_h)| \leq S_1(h) |\mathbf{u}_h|_h |\mathbf{u}_h|_h |\mathbf{v}_h|_h \quad \forall \mathbf{u}_h, \mathbf{v}_h \in {}^1\mathcal{V}_h$ , where  $S_1(h) \leq d_1 S^2(h)$ ,  $b_h(\mathbf{u}_h, \mathbf{u}_h, \mathbf{u}_h) = 0 \quad \forall \mathbf{u}_h \in {}^1\mathcal{V}_h$ ,  $b_{0h}(\mathbf{u}_h, T_h, z_h) + b_{0h}(\mathbf{u}_h, z_h, T_h) = 0 \quad \forall T_h, z_h \in {}^2\mathcal{V}_h$ ,  $\forall \mathbf{u}_h \in {}^1\mathcal{V}_h$ ,  $|b_{sh}(T_h - T_0, \mathbf{u}_h) + b_{ph}(\mathbf{u}_h, T_h)| \leq c(1 + \|T_h\|_h |\mathbf{u}_h|_h + |T_h|_h \|\mathbf{u}_h\|_h) \quad \forall T_h \in {}^2\mathcal{V}_h, \forall \mathbf{u}_h \in {}^1\mathcal{V}_h$ . Further, we have

$$|(m_h, D\mathbf{v}_h)| \leq |m_h| |D\mathbf{v}_h| = \left( \int_\Omega \sum_{j,l}^N (m_{hjl})^2 d\mathbf{x} \right)^{\frac{1}{2}} \left( \int_\Omega \sum_{j,l}^N (D_{jl}(\mathbf{v}_h))^2 d\mathbf{x} \right)^{\frac{1}{2}}$$

and since

$$\int_\Omega \sum_{j,l}^N (m_{hjl})^2 d\mathbf{x} \leq \text{meas}(\Omega) \quad \forall m_h \in K_h, \quad \int_\Omega \sum_{j,l}^N (D_{jl}(\mathbf{v}_h))^2 d\mathbf{x} \leq \|\mathbf{v}_h\|_{1,N}^2$$

then

$$|k\Theta 2^{\frac{1}{2}} \hat{g}(m_h, D\mathbf{v}_h)| \leq (k\Theta 2^{\frac{1}{2}} \hat{g}(\text{meas}(\Omega)))^{\frac{1}{2}} \|\mathbf{v}_h\|_{1,N}^2 \quad \forall m_h \in K_h.$$

It can be shown that the  $(T_h^i, \mathbf{u}_h^i)$  and  $(T_h^{i+1}, \mathbf{u}_h^{i+1})$  defined by the scheme  $(\mathcal{P}_{si})$  satisfy for  $\Theta \geq \frac{1}{2}$  the following conditions:

**Theorem 14** *Let the family of triangulations  $\{\mathfrak{T}_h\}$  be uniformly regular, and let the angles in the tetrahedra be less or equal to  $\frac{\pi}{2}$ . Let  $k, h$  satisfy  $kS_0(h) \leq d_0$ ,  $kS(h) \leq d_1$ , where*



$d_0, d_1$  are positive constants independent of  $k, h$ . Let  $\Theta \geq \frac{1}{2}$ . Then  $(T_h^i, \mathbf{u}_h^i)$  are defined by the scheme  $(\mathcal{P}_{si})$  and

$$|\mathbf{u}_h^i|^2 \leq c, \quad i = 0, \dots, n, \quad k \sum_{i=0}^{n-1} \|\mathbf{u}_h^{i+\Theta}\|^2 \leq c, \quad k \sum_{i=0}^{n-1} |\mathbf{u}_h^{i+1} - \mathbf{u}_h^i|^2 \leq c, \quad (265)$$

$$|T_h^i|^2 \leq c_0, \quad i = 0, \dots, n, \quad k \sum_{i=0}^{n-1} \|T_h^{i+\Theta}\|^2 \leq c_0, \quad k \sum_{i=0}^{n-1} |T_h^{i+1} - T_h^i|^2 \leq c_0, \quad (266)$$

hold, where  $c, c_0$  are constants independent of  $k, h$ .

The scheme  $(\mathcal{P}_{si})$  is stable and convergent. The proofs are similar of that of [12, 44, 48]. The difficulty in practical computations is connected with the approximation of the constraint  $\operatorname{div} \mathbf{v}_h = 0$ , i.e. the incompressibility condition of the Bingham's fluid. For its approximation see e.g. [71, 44, 48]. The studied problem can be also solved by using the penalty and the regularization techniques similarly as in the stationary flow case.

#### 4.2.2. Stationary Flow Case

Now let us analyze the case when the mass movements are uniform. Then the investigated problem corresponds to the stationary flow of the thermo-Bingham fluid in the region  $\Omega$ . The Eulerian coordinate will be taken as a spatial variable. The analysis of the thermal part of the problem can be solved by the technique as above. The analysis of the visco-plastic part of the problem will be based on the penalization, regularization and finite element techniques. The algorithm then is parallel to that of [30, 56].

Assume that  $\mathbf{u}_1 \neq 0, T_1 = 0$ . Let  ${}^1V_1(\Omega) = \{\mathbf{v} | \mathbf{v} \in {}^1H^{1,N}(\Omega), \mathbf{v}|_{\Gamma_u} = \mathbf{u}_1\}$ ,  ${}^2V_1(\Omega) = \{z | z \in {}^2H^{1,1N}(\Omega), z|_{\Gamma_\tau} = 0\}$ , where  ${}^1H_1^{1,N}(\Omega), {}^2H^{1,1N}(\Omega)$  are defined above.

The problem  $(\mathcal{P})_v$  leads to the following problem:

**Problem  $(\mathcal{P}_{sf})_v$ :** Find a pair of functions  $(T, \mathbf{u})$ ,  $\mathbf{u} \in {}^1V_1, T \in {}^2V_1$  satisfying for every  $t \in I$

$$\begin{aligned} & a(\mathbf{u}(t), \mathbf{v} - \mathbf{u}(t)) + b(\mathbf{u}(t), \mathbf{u}(t), \mathbf{v} - \mathbf{u}(t)) + b_s(T(t) - T_0, \mathbf{v} - \mathbf{u}(t)) + \\ & + j(\mathbf{v}(t)) - j(\mathbf{u}(t)) + j_g(\mathbf{v}(t)) - j_g(\mathbf{u}(t)) \geq S(\mathbf{v} - \mathbf{u}(t)) \quad \forall \mathbf{v} \in {}^1V_1 \\ & (T'(t), z - T(t)) + a_T(T(t), z - T(t)) + b_0(\mathbf{u}(t), T(t), z - T(t)) + \\ & + b_p(\mathbf{u}'(t), z - T(t)) \geq s(z - T(t)) \quad \forall z \in {}^2V_1, \end{aligned} \quad (267)$$

$$T(\mathbf{x}, t_0) = T_0(\mathbf{x}). \quad (268)$$

In connection with the given data, we suppose that  ${}^1V_1 \neq \emptyset, {}^2V_1 \neq \emptyset$  and that the physical data satisfy the same conditions as above. Since the algorithm of the thermal part of the problem  $(\mathcal{P}_{sf})_v$  is parallel of that of the previous case, we will discuss the visco-plastic part of the problem only.

Let us introduce the space  $\mathcal{W}$ , a closed subspace of  $H^{1,N}(\Omega)$ , by

$$\mathcal{W} = \{\mathbf{v} | \mathbf{v} \in H^{1,N}(\Omega), \mathbf{v}|_{\Gamma_u} = \mathbf{0}, v_n|_{\Gamma_0} = 0, v_n^k - v_n^l = 0 \quad \text{on } \cup_{k,l} \Gamma_c^{kl}\}, \quad (269)$$

in which the incompressibility condition  $\operatorname{div} \mathbf{u} = 0$  is not introduced.

Since the linear space  $V = {}^1V_1 - \mathbf{u}_1$ ,  $\mathbf{u}_1 \in {}^1V_1$ , on which the variational problem is formulated, contains the condition of incompressibility representing certain cumbersome for numerical solution, therefore we apply a penalty technique, similarly as in the case of incompressible Newtonian fluid (see [71]). The penalty term will be introduced by

$$P(\mathbf{u}_\varepsilon) = \frac{1}{\varepsilon} c(\mathbf{u}_\varepsilon, \mathbf{u}_\varepsilon), \quad c > 0, \quad \text{where } c(\mathbf{u}, \mathbf{v}) = \int_{\Omega} (\operatorname{div} \mathbf{u})(\operatorname{div} \mathbf{v}) d\mathbf{x}, \quad \forall \mathbf{u}, \mathbf{v} \in H^{1,N}(\Omega).$$

It can be shown that for each  $\varepsilon > 0$  the corresponding penalized variational inequality has a unique solution and that its corresponding solution converges strongly in  $H^{1,N}(\Omega)$  to the solution of the initial problem when  $\varepsilon \rightarrow 0$ .

To solve the penalized problem numerically the finite element technique will be used. Let  $\mathcal{W}_h \subset \mathcal{W}$  be a family of finite element subspaces with the property:

$$\forall \mathbf{v} \in \mathcal{W} \text{ there exists } \mathbf{v}_h \in \mathcal{W}_h \text{ such that } \mathbf{v}_h \rightarrow \mathbf{v} \text{ in } H^{1,N}(\Omega) \text{ for } h \rightarrow 0.$$

Then, setting  $\bar{\mathbf{u}} = \mathbf{u} - \mathbf{u}_1$ , we will solve the following problem:

**Problem**  $(\mathcal{P}_{sf})_h$ : Find  $\bar{\mathbf{u}}_{\varepsilon h} \in \mathcal{W}_h$  satisfying for every  $t \in I$  the variational inequality

$$\begin{aligned} & a_h(\bar{\mathbf{u}}_{\varepsilon h}, \mathbf{v}_h - \bar{\mathbf{u}}_{\varepsilon h}) + b_h(\bar{\mathbf{u}}_{\varepsilon h}, \bar{\mathbf{u}}_{\varepsilon h}, \mathbf{v}_h - \bar{\mathbf{u}}_{\varepsilon h}) + b_{sh}(T_h - T_{0h}, \mathbf{v}_h - \bar{\mathbf{u}}_{\varepsilon h}) + \\ & + j_h(\mathbf{v}_h) - j_h(\bar{\mathbf{u}}_{\varepsilon h}) + j_{gh}(\mathbf{v}_h) - j_{gh}(\bar{\mathbf{u}}_{\varepsilon h}) + \frac{1}{\varepsilon} c_h(\bar{\mathbf{u}}_{\varepsilon h}, \mathbf{v}_h - \bar{\mathbf{u}}_{\varepsilon h}) \geq \\ & \geq S_h(\mathbf{v}_h - \bar{\mathbf{u}}_{\varepsilon h}) \quad \forall \mathbf{v}_h \in \mathcal{W}_h. \end{aligned} \quad (270)$$

**Lemma 6** Let  $\bar{\mathbf{u}}_{\varepsilon h}$  be a solution of (270) for each  $h > 0$  and let  $\bar{\mathbf{u}}_\varepsilon$  be the solution of the penalized problem for a fixed  $\varepsilon > 0$ . Then

$$\bar{\mathbf{u}}_{\varepsilon h} \rightarrow \bar{\mathbf{u}}_\varepsilon \quad \text{strongly in } H^{1,N}(\Omega) \quad \text{when } h \rightarrow 0.$$

The proof is similar of that of Lemma 3.2 of [30].

Since the functionals  $j(\mathbf{v})$  and  $j_g(\mathbf{v})$  are not differentiable in the Gâteaux sense, they can be regularized similarly as above for the case of (253). Then the functionals  $j(\mathbf{v})$  and  $j_g(\mathbf{v})$  will be regularized by their regularizations  $j_\gamma(\mathbf{v})$  and  $j_{g\gamma}(\mathbf{v})$ , defined by

$$\begin{aligned} j_\gamma(\mathbf{v}) &= \int_{\Omega} 2^{1/2} \hat{g} \psi_\gamma(|D(\mathbf{v} + \mathbf{u}_1)|) d\mathbf{x}, \\ j_{g\gamma}(\mathbf{v}) &= \int_{\cup_{kl} \Gamma_c^{kl}} \mathcal{F}_c^{kl} [2^{1/2} \hat{g} + 2\hat{\mu} \psi_\gamma(|\mathbf{v} + \mathbf{u}_1|)] \cdot \psi_\gamma(|\mathbf{v}^k - \mathbf{v}^l + (\mathbf{u}_1^k - \mathbf{u}_1^l)|) ds. \end{aligned}$$

Then we will solve the penalized-regularized problem:

find  $\bar{\mathbf{u}}_{\varepsilon h\gamma} \in \mathcal{W}_h$  satisfying

$$\begin{aligned} & a_h(\bar{\mathbf{u}}_{\varepsilon h\gamma}, \mathbf{v}_h - \bar{\mathbf{u}}_{\varepsilon h\gamma}) + b_h(\bar{\mathbf{u}}_{\varepsilon h\gamma}, \bar{\mathbf{u}}_{\varepsilon h\gamma}, \mathbf{v}_h - \bar{\mathbf{u}}_{\varepsilon h\gamma}) + b_{sh}(T_h - T_{0h}, \mathbf{v}_h - \bar{\mathbf{u}}_{\varepsilon h\gamma}) + \\ & + j_{\gamma h}(\mathbf{v}_h) - j_{\gamma h}(\bar{\mathbf{u}}_{\varepsilon h\gamma}) + j_{g\gamma h}(\mathbf{v}_h) - j_{g\gamma h}(\bar{\mathbf{u}}_{\varepsilon h\gamma}) + \frac{1}{\varepsilon} c_h(\bar{\mathbf{u}}_{\varepsilon h\gamma}, \mathbf{v}_h - \bar{\mathbf{u}}_{\varepsilon h\gamma}) \geq \\ & \geq S_h(\mathbf{v}_h - \bar{\mathbf{u}}_{\varepsilon h\gamma}) \quad \forall \mathbf{v}_h \in \mathcal{W}_h, \end{aligned} \quad (271)$$

where  $\mathcal{W}_h$  is the finite element approximation of the space  $\mathcal{W}$ .

It is easy to show that the functionals  $j_{\gamma h}(\mathbf{v})$  and  $j_{g\gamma h}(\mathbf{v})$  are convex and continuous, and therefore, the problem (271) has a unique solution  $\bar{\mathbf{u}}_{\varepsilon\gamma h} \in \mathcal{W}_h$ . As a result we have the following result:

**Theorem 15** *Let  $\mathbf{u}_\varepsilon = \bar{\mathbf{u}}_\varepsilon + \mathbf{u}_1$ , where  $\bar{\mathbf{u}}_\varepsilon$  is a solution of the penalized problem with homogenous condition on  $\Gamma_u$ ,  $\mathbf{u}_{\varepsilon h} = \bar{\mathbf{u}}_{\varepsilon h} + \mathbf{u}_1$ ,  $\mathbf{u}_{\varepsilon\gamma h} = \bar{\mathbf{u}}_{\varepsilon\gamma h} + \mathbf{u}_1$  for all  $\varepsilon, \gamma, h > 0$ . Let  $(\mathbf{u}, T)$  be the solution of the problem  $(\mathcal{P}_{sf})_v$ . Then*

- (i)  $\mathbf{u}_\varepsilon \rightarrow \mathbf{u}$  strongly in  $H^{1,N}(\Omega)$  when  $\varepsilon \rightarrow 0$ ,
- (ii)  $\mathbf{u}_{\varepsilon h} \rightarrow \mathbf{u}_\varepsilon$  strongly in  $H^{1,N}(\Omega)$  when  $h \rightarrow 0$ ,
- (iii)  $\mathbf{u}_{\varepsilon\gamma h} \rightarrow \mathbf{u}_{\varepsilon h}$  strongly in  $H^{1,N}(\Omega)$  when  $\gamma \rightarrow 0$ ,
- (iv) the semi-implicit scheme for thermal part of the problem is stable and convergent.

(272)

Numerically the thermal part of the problem leads to the approximation by the finite element methods for the parabolic partial differential equations. The visco-plastic part of the problem leads to solving the non-linear algebraic system, which can be solved by e.g. the Newton iterative method.

#### 4.2.3. Algorithm of the Dynamic Visco-plastic Part of the Problem

The thermal part of the problem leads to solving the partial differential equations of parabolic type by using the finite element methods. Since the difficulties are connected with the visco-plastic part of the problem we will discuss the visco-plastic part only. The system (263) is nonlinear as terms  $b_h(\mathbf{u}_h^i, \mathbf{u}_h^i, \mathbf{v}_h)$  and  $j_h(\mathbf{v}_h)$  are nonlinear, and moreover, the functionals  $j_h(\mathbf{v}_h)$  and  $j_{gh}(\mathbf{v}_h)$  are non-differentiable functionals (in the case of  $j_{gh}(\mathbf{v}_h)$  we will use its  $j_{g\in h}(\mathbf{v}_h)$  approximation or we will assume that it depends on velocities in several previous time levels). The difficulty in practical computations is connected with the approximation of the constraint  $\text{div } \mathbf{v}_h = 0$ , i.e. the incompressibility condition of Bingham's fluid, as a certain problem represents finding the basis of the space  ${}^1V_h$  with  $\text{div } \mathbf{v}_h = 0$ . The further numerical difficulty represents the discrete approximation of the pressure. In our study the Uzawa algorithm will be used. The Uzawa algorithm will be used to finding a saddle point of the Lagrangian introduced below. In every step of Uzawa's algorithm the system of linear algebraic equations with sparse positive definite matrix is solved by using the conjugate gradient method.

Let us introduce the bilinear form  $A_h(\mathbf{v}_h, \mathbf{v}_h)$  and the operator  $\bar{A}_h$  on  ${}^1V_h$  by

$$\begin{aligned} A_h(\mathbf{u}_h, \mathbf{v}_h) &= (\mathbf{u}_h, \mathbf{v}_h) + k\Theta a_h(\mathbf{u}_h, \mathbf{v}_h) \quad \forall \mathbf{u}_h, \mathbf{v}_h \in {}^1V_h, \\ (\bar{A}_h \mathbf{u}_h, \mathbf{v}_h) &= (\mathbf{u}_h, \mathbf{v}_h) + k\Theta a_h(\mathbf{u}_h, \mathbf{v}_h) + k\Theta b_h(\mathbf{u}_h, \mathbf{u}_h, \mathbf{v}_h). \end{aligned}$$

Then the problem  $(\mathcal{P}_{mi})_{hk}$  can be rewritten as follows:

**Problem**  $(\mathcal{P}_{mi})_{hkA}$ : Let  $\mathbf{u}_h^0, \mathbf{u}_h^1, \dots, \mathbf{u}_h^i$  be known. Then  $\mathbf{u}_h^{i+\Theta}$  will be determined as

$$\begin{aligned} & A_h(\mathbf{u}_h^{i+\Theta}, \mathbf{v}_h) + k\Theta b_h(\mathbf{u}_h^i, \mathbf{u}_h^{i+\Theta}, \mathbf{v}_h) + k\Theta 2^{\frac{1}{2}} \hat{g}(m_h^{i+\Theta}, D_h \mathbf{v}_h) \\ & + k\Theta j_{g\mathcal{E}h}(\mathbf{v}_h) = (\mathbf{u}_h^i, \mathbf{v}_h) + k\Theta(\mathbf{F}_k^{i+\Theta}, \mathbf{v}_h) \quad \forall \mathbf{v}_h \in {}^1V_h, \\ & (m - m_h^{i+\Theta}, D_h \mathbf{v}_h) \leq 0 \\ & \quad \forall m \in K = \{m | m_{jl} = m_{lj} \in L^\infty(\Omega \times I), \|m\|_\infty \leq 1\}, \\ & \quad j, l = 1, \dots, N, \quad i = 0, 1, \dots, n-1, \quad \frac{1}{2} \leq \Theta \leq 1, \end{aligned} \quad (273)$$

where the last condition is equivalent to that of the problem  $(\mathcal{P}_{mi})_{hk}$  as for  $m_h \in K_h$  we have

$$2^{\frac{1}{2}}(m_h, D_h \mathbf{v}_h) \leq 2^{\frac{1}{2}} \int_{\Omega} (D_{hi}(\mathbf{v}_h) D_{hj}(\mathbf{v}_h))^{\frac{1}{2}} d\mathbf{x} = j_h(\mathbf{v}_h).$$

Let us introduce the Lagrangian  $\mathcal{L}_h(\mathbf{v}_h, m_h)$  by

$$\begin{aligned} \mathcal{L}_h(\mathbf{v}_h, m_h) &= \frac{1}{2}(\bar{A}_h \mathbf{v}_h, \mathbf{v}_h) + k\Theta 2^{\frac{1}{2}} \hat{g}(m_h, D_h \mathbf{v}_h) + k\Theta j_{g\mathcal{E}h}(\mathbf{v}_h) - \langle S_h^i, \mathbf{v}_h \rangle \\ &= \mathcal{J}(\mathbf{v}_h) + (m_h, \Psi_h(\mathbf{v}_h)), \quad \langle S_h^i, \mathbf{v}_h \rangle = (\mathbf{u}_h^i, \mathbf{v}_h) + k\Theta(\mathbf{F}_k^{i+\Theta}, \mathbf{v}_h), \\ \Psi_h(\mathbf{v}_h) &= k\Theta 2^{\frac{1}{2}} \hat{g} D_h \mathbf{v}_h. \end{aligned}$$

Then the problem  $(\mathcal{P}_{mi})_{hkA}$  is equivalent to finding a saddle point of the Lagrangian  $\mathcal{L}_h(\cdot, \cdot): {}^1V_h \times K_h \rightarrow \mathbb{R}$  such that

$$\begin{aligned} \mathcal{L}_h(\mathbf{u}_h^{i+\Theta}, m_h^{i+\Theta}) &\leq \mathcal{L}_h(\mathbf{v}_h, m_h^{i+\Theta}) \quad \forall \mathbf{v}_h \in {}^1V_h, \\ \mathcal{L}_h(\mathbf{u}_h^{i+\Theta}, m_h) &\leq \mathcal{L}_h(\mathbf{u}_h^{i+\Theta}, m_h^{i+\Theta}) \quad \forall m_h \in K_h, \\ i &= 0, 1, \dots, n-1, \quad \frac{1}{2} < \Theta \leq 1. \end{aligned} \quad (274)$$

To find a saddle point the Uzawa algorithm is used. To derive the discrete divergence  $D_h \mathbf{u}_h$  and the discrete approximation of pressure  $p$  the techniques of [71] can be used.

Then both Uzawa's algorithms can be compiled into one Uzawa's algorithm only and the functional  $j_{gh}(\mathbf{v}_h)$  will be approximated e.g. by its regularized form. Then we have

**Algorithm**  $(\mathcal{P}_{mi})_{hkU}$ : Let  $m_h^0$  be arbitrary. Let  $\mathbf{u}_h^k, m_h^k$  be known. Then  $\mathbf{u}_h^{k+1}, m_h^{k+1}$  can be determined as follows:

Let  $p_h^0$  be arbitrary. Let  $\mathbf{w}_h^j, p_h^j$  be known. Then  $\mathbf{w}_h^{j+1}, p_h^{j+1}$  will be determined as follows:

find  $\mathbf{w}_h^{j+1} \in \mathbf{W}_h$  (where  $\mathbf{W}_h$  is the space of the same type of functions as in  ${}^1V_h$ , but no divergence condition is imposed on them) such that

$$\begin{aligned}
& \min \left\{ \frac{1}{2}(\bar{A}_h \mathbf{w}_h, \mathbf{w}_h) + k\Theta 2^{\frac{1}{2}} \hat{g}(m_h^{i+\Theta}, D_h \mathbf{w}_h) - \langle S_h^i, \mathbf{w}_h \rangle - \right. \\
& \quad \left. -(p_h^j, D_h \mathbf{w}_h) + j_{gh}(\mathbf{w}_h) \right\}, \\
& p_h^{j+1}(\mathcal{T}_h) = p_h^j(\mathcal{T}_h) - \rho D_h \mathbf{w}_h^{j+1} \quad \forall \mathcal{T}_h \in \mathfrak{T}_h, \\
& \mathbf{u}_h^{k+1} = \mathbf{w}_h^{j(k)}, \quad \text{where } \mathbf{w}_h^{j(k)} \\
& \text{depends on the requested accuracy of the approximation,} \\
& m_h^{k+1} = P_k(m_h^k + k\Theta 2^{\frac{1}{2}} \hat{g} D_h \mathbf{u}_h^{k+1}), \\
& \mathbf{u}_h^{i+\Theta} = \mathbf{u}_h^k, \quad \mathbf{u}_h^{i+1} = \Theta^{-1}(\mathbf{u}_h^{i+\Theta} - (1 - \Theta)\mathbf{u}_h^i), \\
& i = 0, 1, \dots, n-1, \quad \frac{1}{2} \leq \Theta \leq 1.
\end{aligned} \tag{275}$$

## 5. Numerical Experiments

Geomechanics represents the wide field of problems where mathematical modelling and mathematical simulation can be broadly applied. Many geological and geomechanical systems require the description of mechanical interaction across interfaces if they are to be successfully analyzed. Any geomechanical loads result from an interaction between two or more geological blocks which come into contact with each other. In geoengineering, contact interactions are usually intentional such that a structure, like a bridge, can sustain loads. It is obvious that contact interactions may have a significant influence on the behaviour of the structure or the geomechanical system. Such mechanical interactions are often called contact-impact interactions. The contact between colliding geological bodies is a static phenomenon if the neighbouring geological bodies are in static equilibrium, while a dynamic contact is often much more complicated than in a static case. In spite of its great practical importance in many branches of geosciences and geoengineering, most of the contact processes are dynamic in a restrictive sense. By nature, contact phenomena involve friction phenomena, but the friction effects may be neglected in situations where frictional forces are sufficiently small. This fact will be shortly discussed in the next section of the bridge on the non-stable slope.

In this chapter we will discuss several model problems. Mathematical models will be based on the contact problems which involve systems of (variational) inequalities or non-linear equalities and will be based on the results presented in the previous chapters.

### 5.1. The Bridge on a Non-stable Slope

#### 5.1.1. Introduction

The construction of the bridge represents one of the most difficult problems in the structural engineering. The bridges are often constructed in very difficult geological conditions, e.g. on the undermining areas or on the unstable slopes. Simultaneously, they have to satisfy a great static and/or dynamic loading. The bridge consists of the lower and upper structures and the bridge equipment. The foundations, the foundation bed soil and the rock floor, as

well as the bridge supports (piers, rests, pillars, piles) are included in a lower structure, and the supporting frame (supporting structure) and bridge decking are included in an upper structure. The supporting structure consists from the main supporting frame, bridge decking, bearing and bridge's closer. The main supporting frame can be of slab, beam, vaulted and/or curved types.

The best foundations of the engineering constructions transfer and distribute the total loading on the foundation bed soil and the solid rock floor. The spatial work of the construction results in a composed stressed-strained state, in particular in the zones of active interactions. The design of bridge constructions with sufficient reliability requires determining of parameters of the stressed-strained state. The stressed-strained state is then described by the equilibrium equation and by the boundary value and contact conditions, discussed in Chapter 2 for the statically loaded bridge, and in Chapter 3 for the case when the external forces vary slowly. The emphasis will be on some specific items related to the computer simulation of the foundation elements of the bridge structures situated on the unstable slopes.

### 5.1.2. The Model

Next, we will consider a simple type of the beam bridge with the massive piers and statically loaded by the vehicles. We will investigate two models of the beam bridge with massive piers, one of which is situated on the unstable slope and the second one is situated in the stable rock slope. The foundation of the bridge pier situated on the unstable slope, in the first model case, is situated in the solid rock floor (see Fig. 13) and in the second model case the foundation of the bridge pier is situated in the moving foundation bed soil/rock (Fig. 14). In both model problems the surrounding rocks and soil/rock layers are in contact with the bridge piers. The aim is to analyze the engineering aspects of the performed numerical model of the bridge situated on the unstable slope and to determine the best foundations of the bridge of the beam type because in the real situations the reality is very complicated due to the geological situations in the investigated region and because due to the fact that the contacts between the piers and the surrounding soil layers and rocks are not ideal. The used data correspond to a real upper bridge structure that transfers the external loads to the foundation bed soil and the solid rock floor through the pier foundations.

The supporting structure of the bridge (from the prestressed concrete) consists of the full beams connected by a deck slab. The construction of the bridge is made from the prestressed concrete fixed on one side (right-hand side) and free on the opposite side (left-hand side), which makes certain shifts possible during its deformation. The moving (free) part of the supporting frame of the bridge is modelled by the contact condition with or without Coulombian friction (i.e. between points 5-6). We will assume that the movement of the slope is very slow, so the model can be investigated as a quasistatic in the linear elastic rheology (if the influence of the temperature is considered, then the thermo-elastic rheology will be used). The movement of the unstable part of the slope acting onto the bridge (Figs 13 and 14) is simulated by the boundary condition with prescribed shifts  $\sim 0.01m$  (prescribed displacements between points 1-7) corresponding to the movement of the unstable slope in the different times. On the other parts of the investigated region the rock masiff is assumed to be motionless. On the contact boundaries between the non-stable soil and the rock floor (i.e. between points 7-8 and 9-10 in the first case or between 7-10 in the second case) the

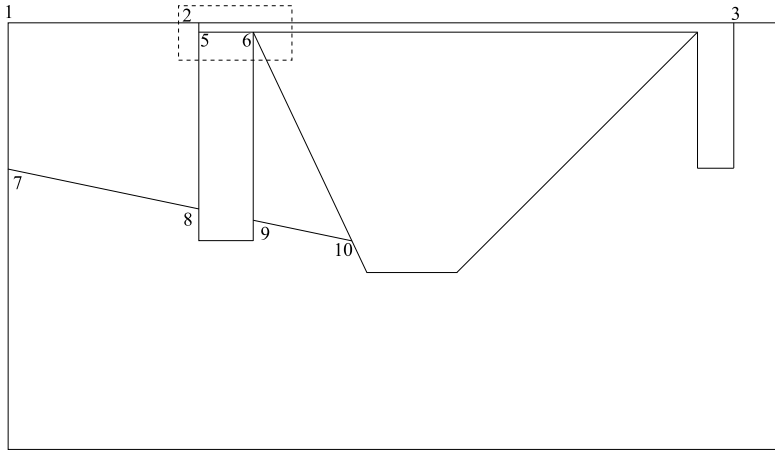


Figure 13. The model of the bridge on the nonstable slope, the pier situated in the stable solid rock floor.

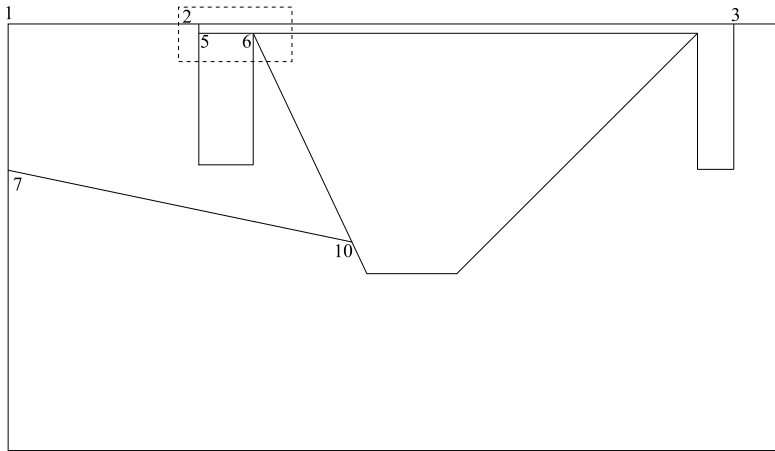


Figure 14. The model of the bridge on the nonstable slope, the pier situated in the moving foundation bed soil/rock.

contact conditions with the Coulombian friction are assumed. The friction limit is assumed to be  $g_c^{kl} \sim 0.1 \times 10^8 [Nm^{-2}]$ . The bridge is loaded by the load  $\mathbf{P} \sim -1.10^6 [Nm^{-2}]$  (between points 2-3), between points 1-2 and 3-4 being assumed  $\mathbf{P} \equiv 0$ . The investigated region is modelled by 5 subregions with different values of the material parameters of the concrete material of the bridge and of the rocks, i.e. the Young modulus  $E [Nm^{-2}]$  and the Poisson's constant  $\mu$  varying from  $E = 0.45 \times 10^{11}$  and  $\mu = 0.17$  to  $E = 0.73 \times 10^{11}$  and  $\mu = 0.31$ .

### 5.1.3. Results and Discussion

We analyze two models of the bridge structure discussed in the previous subsection and compare obtained results, i.e. the first model (Fig. 13) where the foundation of the bridge pier reach the stable rock floor, and the second one (Fig. 14) where the foundation of the

bridge pier is badly founded because the bottom of the pier cannot reach the stable rock floor. We will study the consequences of the movement of the unstable part of the slope onto the bridge pier and onto the stability of the supporting structure of the bridge. In Fig. 15 and Fig. 16 the deformation of the bridge on the unstable slope corresponding to the situations from Fig. 13 and Fig. 14 are presented. The scale factor 100 for the deformations is used. We see that in the first case the bridge pier, according to the pressure of the moving soil materials acting on it, is strained by the bigger pressure powers resulting that the bridge pier is bended and the supporting frame of the bridge is sagged. In the second case corresponding to the model from Fig. 14, the bridge pier moves together with the moving soil/rock materials and therefore the supporting frame of the bridge is deformed. In the Fig. 17 and Fig. 18 we compare the deformations of the bridge in the details of the moving part of the bridge construction (see the detail in Fig. 13) for the case with and without friction. The isolines of vertical stresses  $\tau_{zz}$  for the first model case are given in Fig. 19. The stresses are constant on every finite element and were computed in the centers of the finite elements. The analysis of obtained results suggests the areas which are strained by tension forces, namely in the bridge supporting frame and the areas which are compressed.

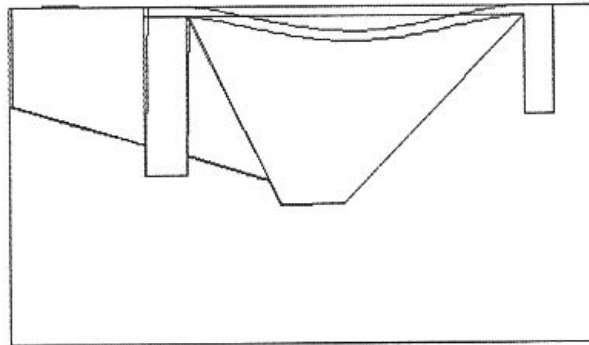


Figure 15. The deformed bridge on the nonstable slope, the pier situated in the stable solid rock floor.

#### 5.1.4. Conclusions and Remarks

As a general conclusion, the quantitative and qualitative analyses of the presented test data show that the obtained results are fully realistic for the finished evaluation. The obtained numerical results suggest that both types of the foundation of the bridge are not correct as in the first case the pier is strained by the bigger forces and, therefore, is bended, while in the second case the bridge pier moves together with the moving part of the nonstable slope. In both cases owing to these facts the supporting frame of the bridge is deformed and sagged. We evaluate these results as a good first step in the simulation of the design of bridge constructions and for the further correct critical determination of the design of bridge construction. Hence, we see that in the new design of the bridge construction the retaining wall situated before or around the bridge pier on the unstable slope and with the foundation in the fixed rocks must be proposed.



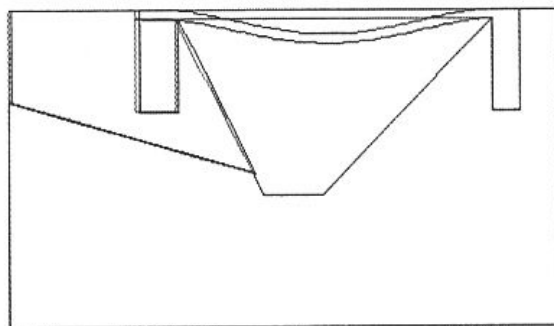


Figure 16. The deformed bridge on the nonstable slope, the pier situated in the moving foundation bed soil/rock.

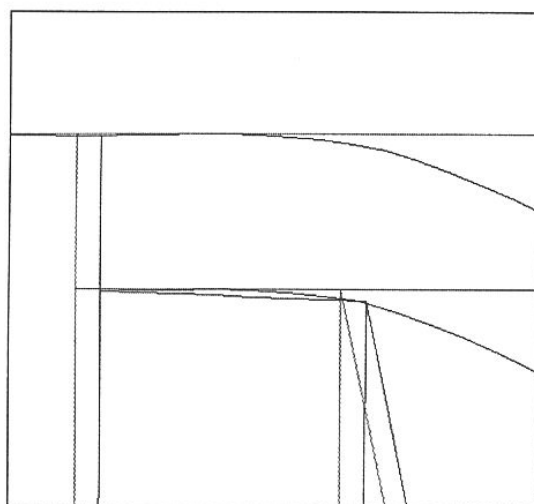


Figure 17. The deformation of the free part of the bridge - the frictionless case.

## 5.2. Modelling of Crustal Movements Having Influence on the Landslide Origin

To analyze geological, tectonic and geodynamic processes on the Earth surface having influence onto the landslide origin and its further evolution, the earth sciences as well as mathematical modelling are usually used. Applied geology distinguishes between fast and slow geological processes, but because the accuracy of our knowledge increased, these terms lost their significance and we introduce the concept of process rates. The rate of

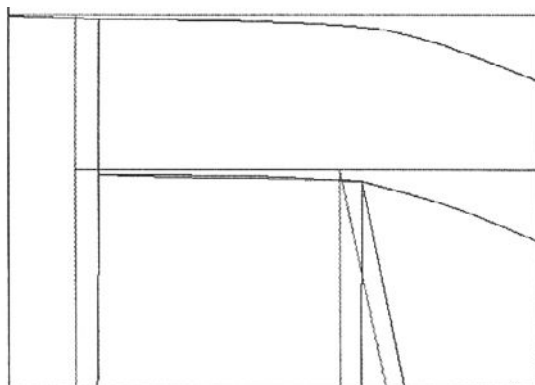


Figure 18. The deformation of the free part of the bridge - the case with friction.

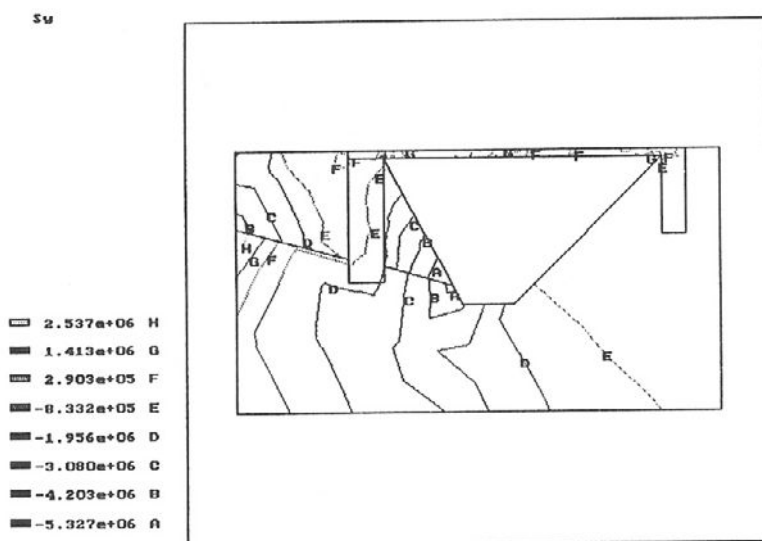


Figure 19. The deformed bridge on the nonstable slope – the distribution of the vertical stress component  $\tau_{22}$ .

processes began to be compared, and which were faster and which slower began to be determined. Then the earth sciences have deduced to a degree that it is necessary to know how many millimeters an area of the mountain range has risen or subsided over the day, the month or the year, respectively. Crustal movements are usually a combination of horizontal and vertical movement components. Tectonic movements do not usually display a constant and regular character but have an episodic character [7]. Rapid movements alternate with longer periods of relative inactivity. From the point of view of longer durations of movements, the average rates of movements are smaller than for the case of smaller movement durations.

The seismicity in the Earth's lithosphere is usually explained by tectonic stresses, ac-

accompanied also by crustal movements. Regions with strong seismicity are areas of continental episodic displacements, upthrusts and downthrusts. Fast movements alternate with quiet periods and depend on geological processes taking place in the deeper parts of the Earth below the lithosphere [7, 48, 58]. The hypothesis which is most probable at this time is that of tectonics of lithospheric plates - plate tectonics.

Boundaries between geological blocks and plates are situated within active seismic zones, where most of the mechanical energy is being consumed, and are of the divergent, transform and convergent types. Convergent boundaries, which will be of our interest in this chapter, occur in sites of oceanic lithospheric consumption – subduction zones, and in those of continental lithospheric collision. Subduction zones are accompanied by intense seismicity in the so-called Wadati-Benioff zones, in which more than 85% of seismic energy is consumed. Continental collisions represent a final stage of the evolution of convergent plate boundaries, characterized by the Alpides.

Sudden and rapid displacements during earthquakes are observed, e.g. Alaska 1899 with large uplift  $\sim 15m$ , Alaska 1965 with an uplift of  $\sim 10m$  on the Montagne Island and  $\sim 8m$  on the continent and Chile 1960 with the vertical deformation along a zone  $\sim 1000km$  long and  $\sim 200km$  wide, with changes in the morphology of the sea floor (subsidence  $\sim 2m$  on the continent and uplifts of  $1 - 3m$  on the shelf and an uplift of  $2.5m$  on the Mocha Island and San Francisco 1906 with deformation  $\sim 7m$  owing to a horizontal slip.

One of the ways of classifying mass movements is by the rate of movement and we distinguish (i) slow movements which take place within days to years, (ii) moderately fast movements which take place within minutes to hours, and (iii) fast movements which take place within seconds or minutes. The slow rate movements are represented by movements of great geological blocks or lithospheric plates. Numerical modelling of interplate deformation in the Central Aleutian arc system (see [48]) shows that the rate of the uplift on the head of the Aleutian arc system is  $\sim 33m/10^4$  year and the rate of the subsidence  $\sim 55m/10^4$  yrs is in the Bearing Sea (the Bearing basin). As it was shown above, owing to the earthquake the sudden and rapid displacements of smaller or greater geological blocks are observed. The mechanism of the global movements, the uplifts and the subsidences, in the broken up rock massif originated owing to the movement of the invasive geological block or owing to the propagated seismic wave (see Fig. 20). Fast movements may be catastrophic, like the most destructive fast mass gravity movement of the landslide (as a combination of rock and snow avalanche) which was happened in the Nevados Huascaran mountain range in Peru (May 31, 1970). The movement had a velocity of about  $\sim 400km\ h^{-1}$ , and  $\sim 21000$  inhabitants died. The landslide then continued as a debris and mud flow down a five-degree slope at a rate of  $\sim 25km\ h^{-1}$ . Landslides from volcanos may be quite fast, e.g. the eruption of the Mt. St. Helens (May 18, 1980), where  $\sim 2800mil.m^3$  of debris were moved at a velocity of  $\sim 350km\ h^{-1}$ . The mechanisms discussed in this section are based on the theory presented in Chapters 2-4. For some applications in the plate tectonic modelling see [48, 58].

For illustration of such application of the method presented above, we constructed two models based on the profile across the Villarica volcano and the profile across the Peru-Chile border (see [58]). In Fig. 21 and 22 we illustrate the rate of interplate principal stresses (in MPa) (where  $\rightarrow\leftarrow$  denotes pressures,  $\leftarrow\rightarrow$  denotes tension stresses). The analyses of the

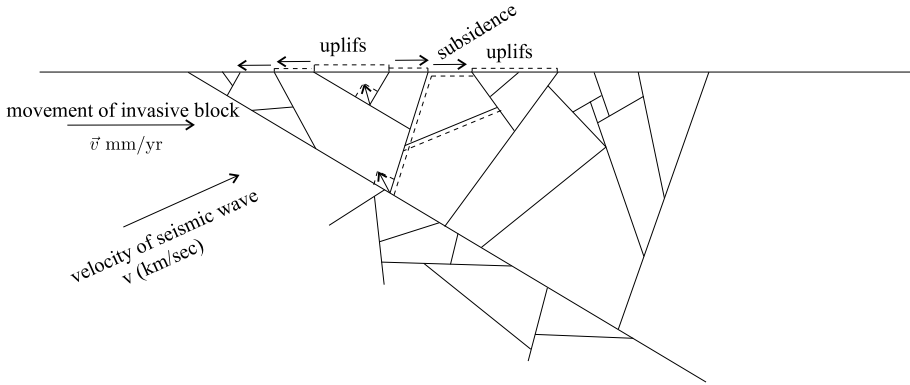


Figure 20. The model of the global movements in the broken up geological blocks – mechanism of uplifts and subsidences.

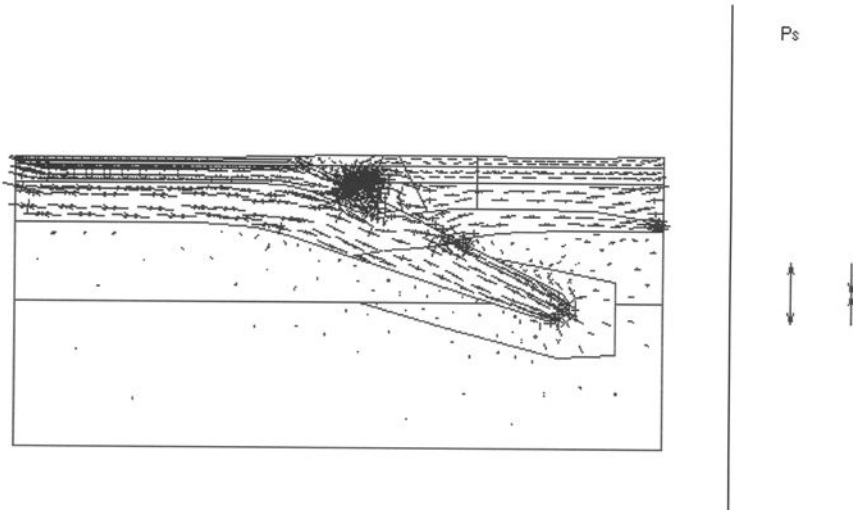


Figure 21. The profile Villarica in the Andes – the rate of intraplate principal stresses (max.  $|0.0652|$  [MPa/yr]).

numerical results indicate e.g. the Wadati-Benioff zone, the aseismic zones and places with great seismic activity as well as the places where volcanic chambers and deep faults originate. The numerical results are in a good agreement with geophysical observations. Similar results were obtained in the analysis of the mathematical model of the Aleution Arc system. Figure 23 illustrates the display of principal stresses at  $t = 10^4$  yrs and  $t = 10^5$  yrs, where the volcano chambers and deep faults are observed. The shape of the volcano chambers in Fig. 23 was deduced from the normal component of the displacement vector  $u_n$  (for better illustration the scale factor was used) because a consequence of the contact conditions on the contact boundary. These areas coincide with the areas where the normal component of the displacement vector is nonzero. Figure 24 illustrates evolution of the normal component of the stress vector  $\tau_n$  (in  $10^9 \text{ Nm}^{-2}$ ) during time (i.e. from  $t = 10^3$  yrs to  $t = 10^5$  yrs), where for  $t = 10^5$  yrs two areas with great pressures and two areas of tension

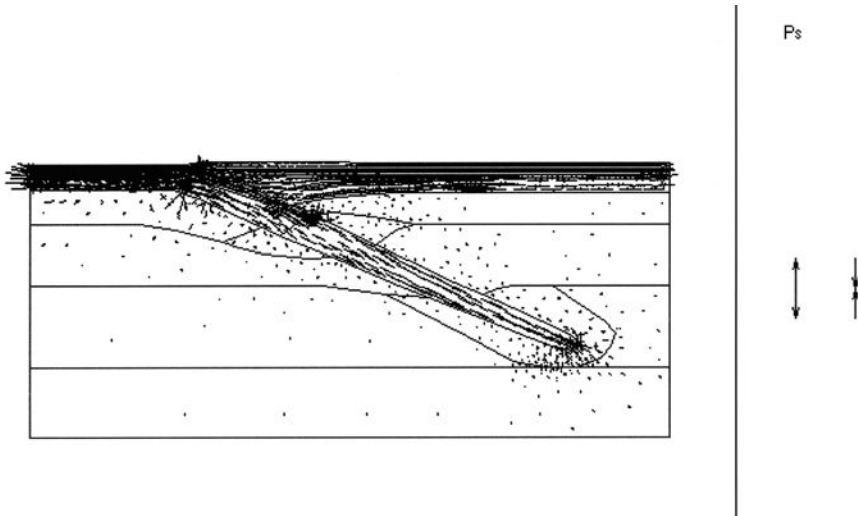


Figure 22. The profile across the Peru/Chile border in the Andes – the rate of intraplate principal stresses (max.  $|0.02977|$  [MPa/yr]).

stresses characterizing zones where the deep faults originate. Furthermore, it is evident that the algorithm of the dynamic contact problem discussed in Chapter 3 also describes the mechanisms of the earthquake origin. One of that is based on the fracture mechanics. The second one follows from the contact theory [51, 52]. Firstly, if the absolute value of the tangential contact stresses acting in the contact zone is less than the frictional forces then the tangential force precludes the mutual motion of both colliding plates and blocks and in this area the deformation energy henceforth cumulates. If the absolute value of tangential contact stresses is equal to the friction force, then there are no forces which can preclude the mutual motion of both plates or blocks. The contact points change their positions in the direction opposite to that in which the tangential contact stresses act and, moreover, one part of the accumulated energy is emanated as an earthquake (see [48]). The discussed mechanism describes also the mineshocks or shocks accompanying the landslides.

### 5.3. The Unstable Loaded Slope in the Overflowed Region

As the numerical experiments the unstable slope without and with the inside situated cylindrical tunnel are investigated (see [54, 60]). The unstable slope is loaded by vertical and horizontal loading in the first model and by vertical loading in the second model with the inside situated tunnel. The studied models are assumed to be three dimensional where the input physical parameters do not depend on the  $x_2$  coordinate.

Since the loading unstable slope does not still slip, the problem leads to the frictionless case, where the threshold of plasticity  $\hat{g}$  and threshold of viscosity  $\hat{\mu}$  do not depend on the  $x_2$  coordinate. For simplicity, these parameters were assumed to be constant ( $\hat{g} = 2.89 \times 10^8 \text{ kg m}^{-2}$ ,  $\hat{\mu} = 2.94 \times 10^6 \text{ kg m}^{-1} \text{ s}^{-1}$ ,  $\rho = 2 \times 10^3 \text{ kg m}^{-3}$ ). The model width is  $18 \text{ m}$ , its height is  $12 \text{ m}$ . The model with vertical and horizontal loading represents the loaded unstable slope during a strong deluge. The slope instability is a consequence of an enormous quantity of water in the region, having also a great influence on the security of the investigated region.

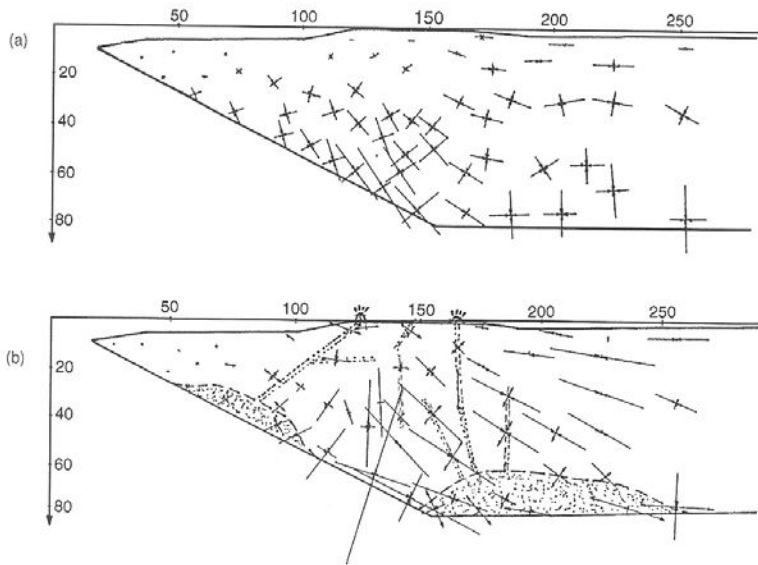


Figure 23. The Aleutian Arc System – the principal stresses in the obducting American plate at time (a)  $t = 10^4$  yrs in  $10^8 \text{Nm}^{-2}$ , (b)  $t = 10^5$  yrs in  $10^9 \text{Nm}^{-2}$ .

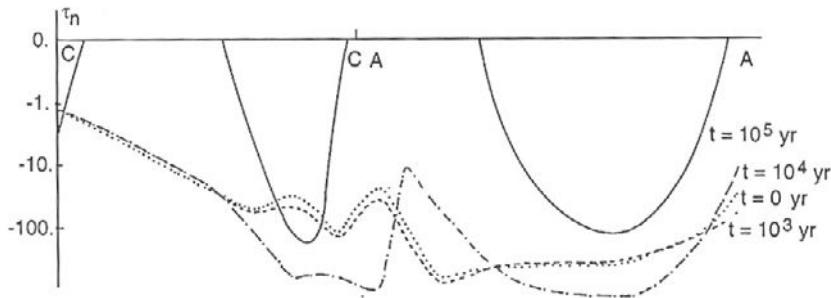


Figure 24. The Aleutian Arc System – the normal stresses  $\tau_n$  in  $10^9 \text{Nm}^{-2}$ .

In Figs 25-35 the models of unstable slopes, loaded by a vertical ( $\mathbf{P} \sim -1000 \text{kg m}^{-2}$ ) and horizontal ( $\mathbf{P}_0$ ) loading, are presented. While in Fig. 25 the distribution of material velocity in a vertically loaded (i.e. by  $\mathbf{P}$ ) unstable slope is presented, in Fig. 26 and Fig. 27 the distributions of a vertical component of velocity and velocity magnitude are presented.

In Fig. 28- Fig. 31 the models of unstable slopes, loaded by vertical  $\mathbf{P}$  and horizontal  $\mathbf{P}_0$  loading, are presented. While in Fig. 28 and Fig. 29 the distributions of vertical component of velocity and velocity magnitude for the same value (approx.  $1000 \text{kg m}^{-2}$ ) of the vertical and horizontal loading (i.e.  $\mathbf{P} \equiv \mathbf{P}_0$ ) are shown; in Fig. 30 and Fig. 31 the distributions of the vertical velocity component and velocity magnitude for the case, where the value of the vertical loading  $\mathbf{P}$  is the same as in the previous case, and the horizontal loading  $\mathbf{P}_0$  is 1.5 times higher than the vertical loading  $\mathbf{P}$ .

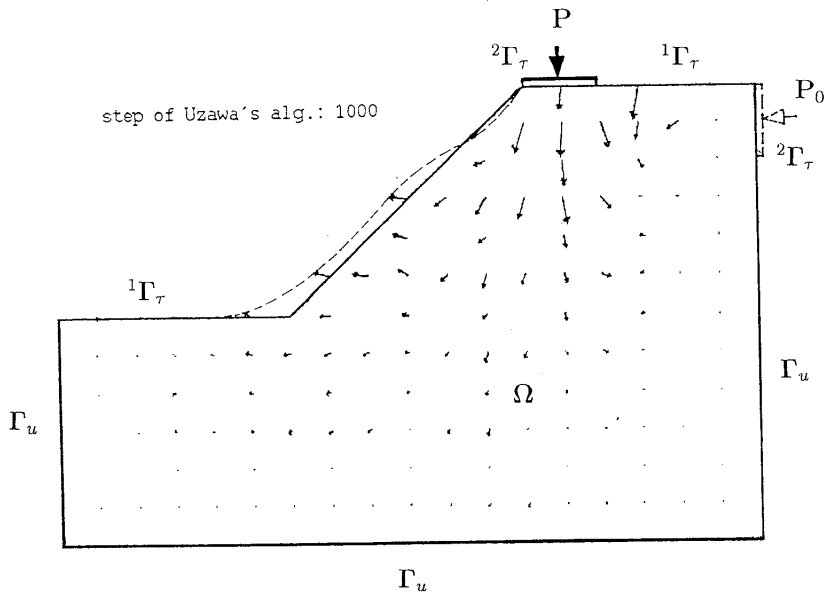


Figure 25. The loaded unstable slope – the velocity distribution in the vertically loading case,  $\mathbf{P} = (0, -1000) [\text{kgm}^{-2}]$ .

Analyses of numerical results suggests zones (of eventually getting free) along which the loosened part of the slope will slide down.

As the further numerical experiment the unstable slope with the inside situated cylindrical tunnel (Fig. 32) is investigated. The slope is loaded on the top by a constant external oblique load  $\mathbf{P}$ . Physical parameters in the model problem (in the SI system) are as follows:  $\mathbf{P} = (100, -1000)$ ,  $\hat{g} = 2.83 \times 10^8 \text{kg m}^{-2}$ ,  $\hat{\mu} = 2.94 \times 10^6 \text{kg m}^{-1} \text{s}^{-1}$ ,  $\rho = 2000 \text{kg m}^{-3}$ . The resulting flow velocity field at the first time step and after 1000 steps of Uzawa's algorithm is presented in Fig. 33. Numerical results in comparison of previous cases indicate relatively great changes of the velocity field, and therefore the ensuing load and deformation of the tunnel.

The algorithm based on the above implicit scheme represents the coupled non-linear problem. A certain difficulty represents finding the basis of  $V_h$  with  $\text{div } \mathbf{v}_h = 0$ . In the present study the Uzawa's algorithm was applied [48, 71]. Since  $j_h(\mathbf{v}_h)$  is a non-differentiable functional, the problem leads to finding a saddle point [11], and therefore the Uzawa's algorithm and the conjugate gradient method were used [20, 11, 48]. The relative errors of the internal and external Uzawa's algorithms are presented (see Figs 34 and 35). The numerical results indicate strong oscillations around a slow exponential average convergence in the case of the internal Uzawa algorithm and an exponential convergence of the outer Uzawa algorithm, similarly as were observed in the previous cases.

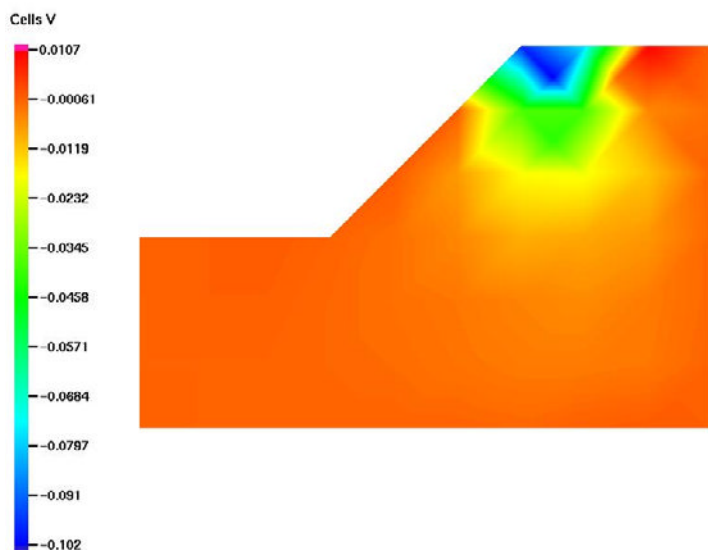


Figure 26. The loaded unstable slope – the distributon of the vertical velocity component in the vertically loading case,  $\mathbf{P} = (0, -1000) [\text{kgm}^{-2}]$ .

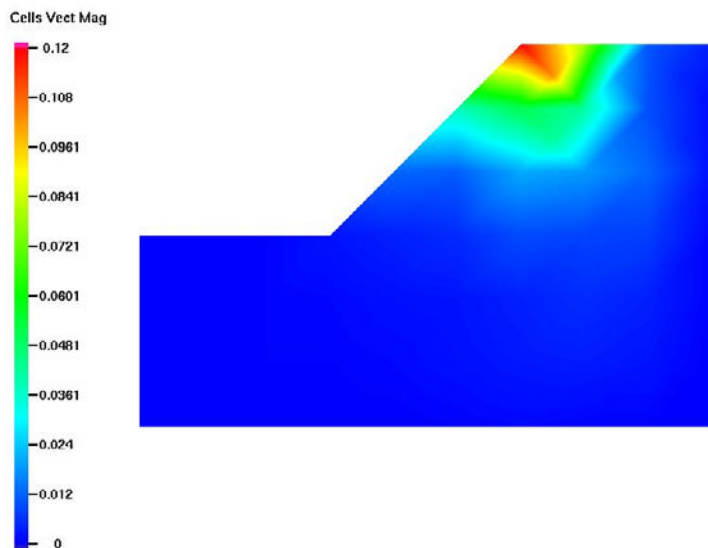


Figure 27. The loaded unstable slope – the distribution of the velocity magnitude in the vertically loading case,  $\mathbf{P} = (0, -1000) [\text{kgm}^{-2}]$ .



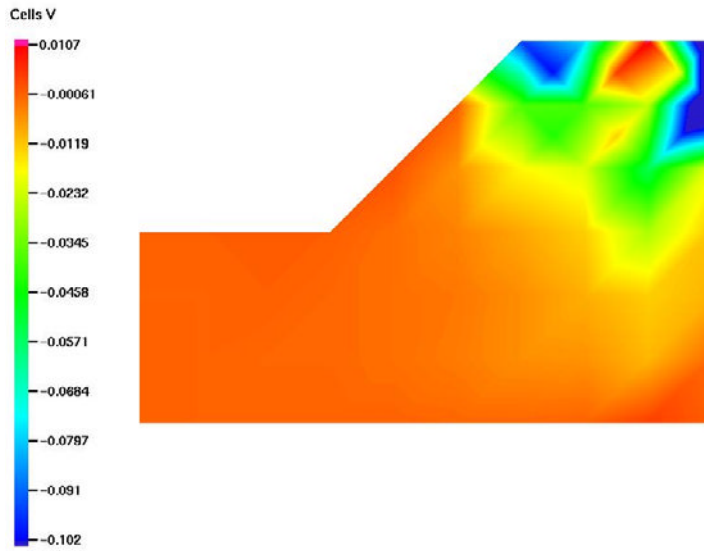


Figure 28. The loaded unstable slope – the distributon of the vertical velocity component in the vertically and horizontally loading case,  $\mathbf{P} = (0, -1000)$ ,  $\mathbf{P}_0 = (-1000, 0)$  [ $\text{kgm}^{-2}$ ].

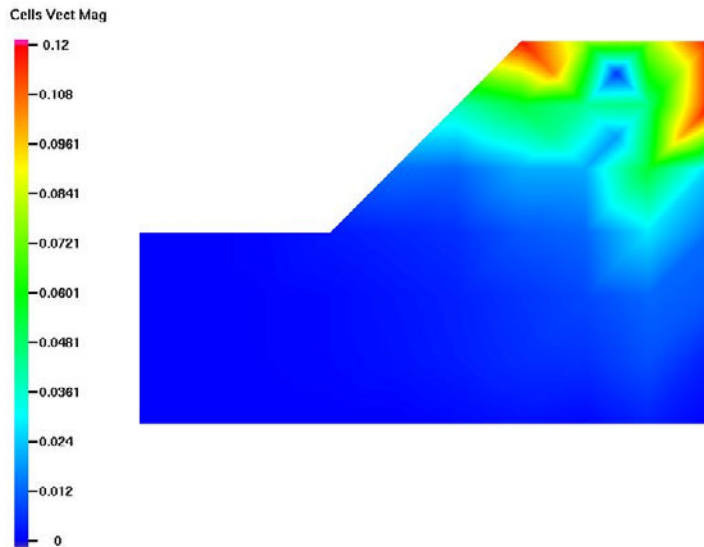


Figure 29. The loaded unstable slope – the distribution of the velocity magnitude in the vertically and horizontally loading case,  $\mathbf{P} = (0, -1000)$ ,  $\mathbf{P}_0 = (-1000, 0)$  [ $\text{kgm}^{-2}$ ].

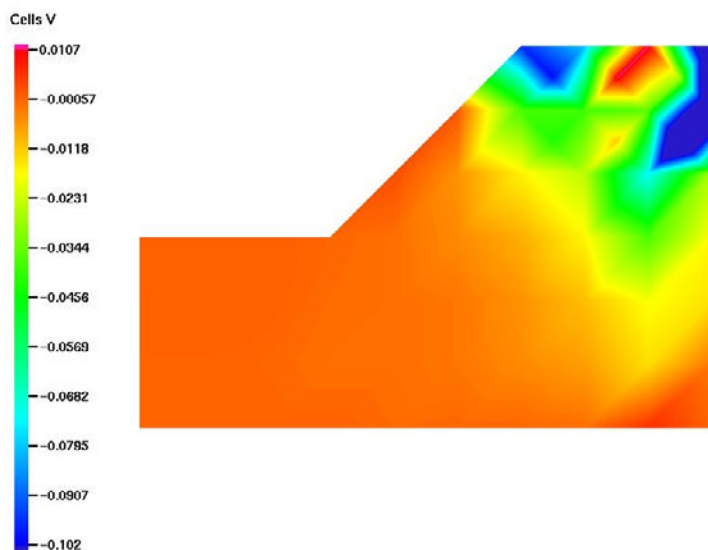


Figure 30. The loaded unstable slope – the distributon of the vertical velocity component in the vertically and horizontally loading case,  $\mathbf{P} = (0, -1000)$ ,  $\mathbf{P}_0 = (-1500, 0)$  [ $\text{kgm}^{-2}$ ].

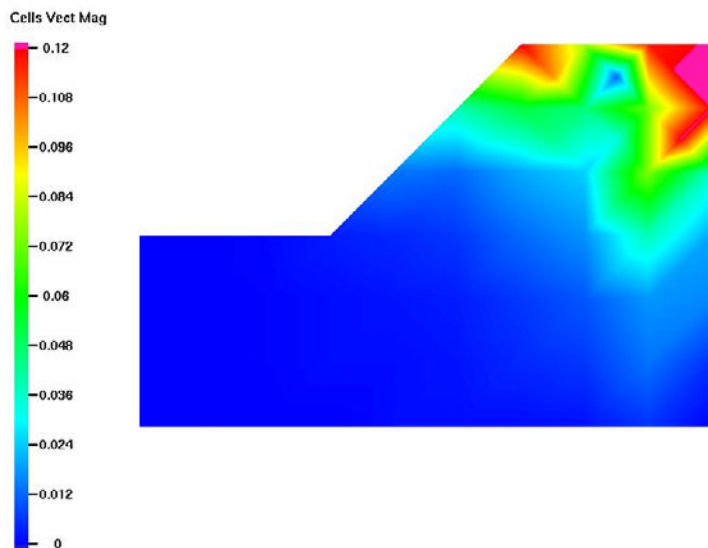


Figure 31. The loaded unstable slope – the distribution of the velocity magnitude in the vertically and horizontally loading case,  $\mathbf{P} = (0, -1000)$ ,  $\mathbf{P}_0 = (-1500, 0)$  [ $\text{kgm}^{-2}$ ].

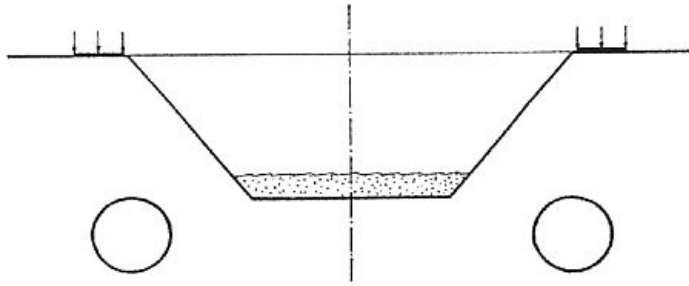


Figure 32. The model of the loaded unstable slope with small tunnels.

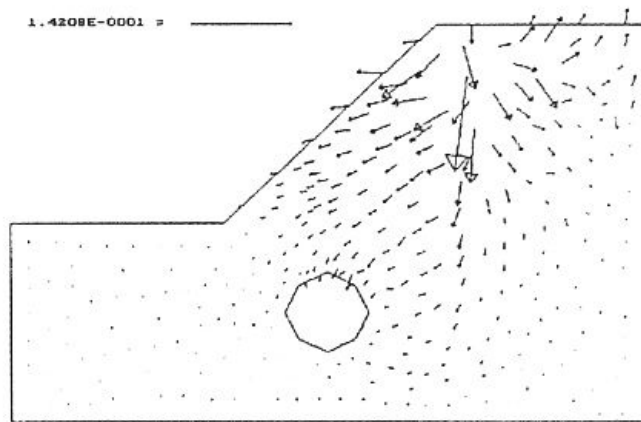


Figure 33. The loaded unstable slope with small tunnels – the distribution of the resulting flow velocity.

## Appendix

### Security of Countries Endangered by Bigger Hurricanes: Proposal of the Research Project

**Global thermo-hydro-mechanical and climatic project** (see [57]):

Last year has been through the **tragedy in New Orleans**. Some idea connected with future security of some parts of country which are endangered by bigger hurricanes with great catastrophic consequences as those in the case of the hurricane Katrina last year, will be presented.

**The idea of the proposal how to predict the future situation in the endangered regions is based on the mathematical simulation of coupled thermo-hydro-mechanical**

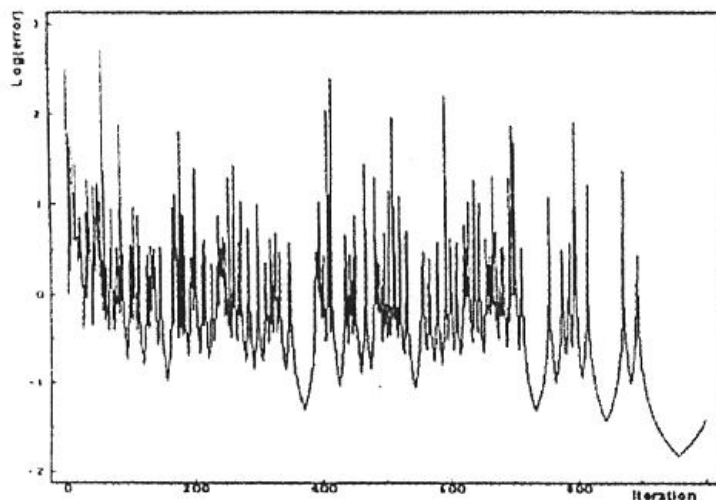


Figure 34. The loaded unstable slope with small tunnels - the relative errors of the internal Uzawa's algorithm.

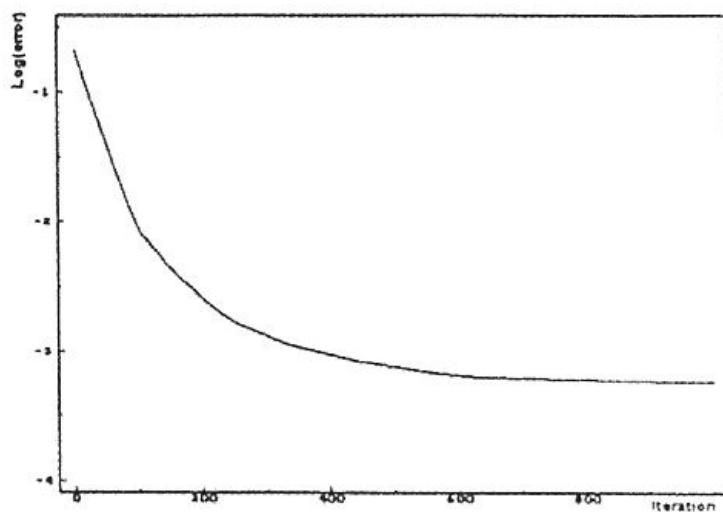


Figure 35. The loaded unstable slope with small tunnels - the relative errors of the external Uzawa's algorithm.

**and thermo-hydro-dynamical processes together with the climatic processes** in the endangered region during the strong hurricane and the consequences of the enormous quantity of water in this region onto the stability of slopes in this region and onto the security of this

region. The region e.g. of Louisiana with New Orleans' non-stable seashores, seaside, wharves, lakes and dams represents the characteristic reason for application of such model situations in practice.

**The rheology** used in our model can describe situations in endangered regions with respect to all effects of great hurricanes, to bigger storms with great fallout of water, resulting deluges and the ensuing relevant landslides.

**The main goal of the presented idea is to connect the climatic observations and the corresponding climatic models with the thermo-hydro-dynamic and the thermo-hydro-mechanic models, with the possibility to estimate future destruction of these endangered regions with landslides of the non-stable slopes.**

**The integral part of this idea is to determine the causes of risks** in endangered regions and the determination of characteristic parameters for their evaluations and analyses.

**The goal is to help with specification and categorization of all these causes with aims at removal relevant risks and symptoms of a crisis in such critical situations.** Such complex evaluations of the future situation then start to be an important foundation for elaboration of the "Analyses of risks" for critical situations in such endangered regions.

#### **Requirement for the input information and data:**

**The main goal** is to simulate and to predict all effects of the thermo-hydro-mechanical and thermo-hydro-dynamical processes in the unsafe regions, intervened by hurricanes (etc.) in critical situations.

#### **Mathematical model:**

**The mathematical model discussed will be based on the thermo-visco-plastic rheology of Bingham type coupled with climatic and hydrological models.**

**The model** must be formulated as the 3D model. The Bingham rheology is characterized by two parameters - threshold of plasticity  $g$  and threshold of viscosity  $\mu$ . The threshold of viscosity  $\mu$  has the same meaning as in the case of Newtonian liquid, the threshold of plasticity  $g$  is from interval 0 to  $\infty$ . For  $g = 0$  the environment is described by liquid, for very small  $g$  the environment is characterized by the liquid saturated more or less by minerals and rocks and for  $g \rightarrow \infty$  we have absolutely rigid materials. Therefore, between  $g = 0$  and  $g \rightarrow \infty$  we can model all types of rocks, which are loaded by external forces as loading forces induced by the hurricane, weights of rainfalls, weights of materials in the rockcovers, weights of industrial buildings, etc. The values of  $g$  must be determined from mechanical properties of rocks from the investigated regions. From the characteristic properties of the used rheology the following professional demands are requested:

- **the geometry of the investigated region** will be determined from the digitized cartographic maps of the investigated region,
- **material properties of rock massive in the investigated region**, i.e. the input physical data as  $g$ ,  $\mu$ , temperatures, etc. will be determined from the geological and hydro-dynamical observations and laboratory experiments,
- **acting loading forces** will be determined as resulting data from the climatic, geological and hydrological observations and studies as well as loading forces developed by the weight of the industrial objects, etc.,

- **temperature and hydro-dynamical data**, like flows of water in the rivers in the investigated region, hurricane data and data of its evolution in future, an absorbing capacity of rocks by the water, properties of rocks in connection with stability of slopes, etc., will be determined from hydro-geological observations and studies,
- **influences of the sea surges of the rushing up hurricane's waves** in the presented model will be modelled by the boundary value conditions and they will be determined from climatic observations and studies.

**The result of the presented model** will be in distributions of velocity and displacement fields in the investigated region, their horizontal and vertical components, thermal field, estimations of the passage of flood waves, estimates of quantity of the running water in the investigated region, estimates of the quantity of water, which can be intercepted by dams and swamps, estimates of possible waterlogging and therefore, unstable slopes and prediction of their incidental landslides during the critical situations, etc.

**It is evident that cooperation of specialists from climatology, geology, hydrology and mathematics as well as of specialists from the workplace of the National Hurricane's Center in Miami, are fundamental for successfully close of the project.**

## Acknowledgements

The author thanks to my Mgr. and PhD. students or co-workers Anna Dusová-Hejlová, Jaroslav Česenek, Ivo Hladík, Zdeněk Kestřánek, M. Novický and Luboš Tomášek who computed some numerical models presented in the last part of my contribution and for their help with preparations of the numerical codes. My sincere thanks go to Mrs Hana Bílková for her assistance in preparing the illustrations and for typing much of this part of the book and making me aware of deadlines. I would like to thank to all people who help with preparation of my part of the book.

## References

- [1] R. A. Adams, *Sobolev Spaces*, Academic Press, New York, 1975.
- [2] Andersson, Existence Results for Quasi-Static Contact Problem with Coulomb Friction, *Appl. Math. Optim.*, **42**, 2000, 169-202.
- [3] K. Bathe, *Finite Element Method*, Springer Vlg., Berlin, 1986.
- [4] S. Brunsen, F. Schmid, M. Schäfer, B. Wohlmuth, A Fast and Robust Iterative Solver for Nonlinear Contact Problems Using a Primal-Dual Active Set Strategy and Algebraic Multigrid, *Int. J. Numer. Math. Engng.* **69**, 2007, 524-543.
- [5] J. Céa, *Optimisation, théorie et algorithms*, Dunod, Paris, 1971.
- [6] M. Cocou, G. Scarella, G., Analysis of a Class of Dynamic Unilateral Contact Problems with Friction for Viscoelastic Bodies, In: Wriggers, P., Nackenhorst, V. (Eds), Analysis and Simulation of Contact Problems. *Lecture Notes in Applied and Computational Mechanics*, vol. 27, Springer Vlg, Berlin, Heidelberg, 2006, 137-144.

- 
- [7] C. Doglioni et al., Orogeus and slabs vs. direction of subduction, *Earth-Science Reviews* **45**, 1999, 167-208.
  - [8] G. Duvaut, J. L. Lions, *Inequalities in Mechanics and Physics*, Springer Vlg., Berlin, Heidelberg, New York, 1975.
  - [9] Ch. Eck, *Existenz und Regularität der Lösungen für Kontaktprobleme mit Reibung*, PhD Thesis, University of Stuttgart, 1996.
  - [10] Ch. Eck, J. Jarušek, J. Krbeč, *Unilateral Contact Problems. Variational Methods and Existence Theorems*. Chapman & Hall/CRC, Taylor & Francis Group, Boca Raton, London, New York, Singapore, 2005.
  - [11] I. Ekeland, R. Temam, R., *Convex Analysis and Variational Problems*. North-Holland, Amsterdam, 1976.
  - [12] R. Glowinski, J. L. Lions, R. Trémolières, R., *Numerical Analysis of Variational Inequalities*, North-Holland, Amsterdam, 1976.
  - [13] R. Glowinski, Finite Element Methods in Incompressible Viscous Flow. In P.G. Ciarlet, J.L. Lions (Eds), *Handbook of Numerical Analysis, Numerical Methods for Fluids* (Part 3), vol. IX, Elsevier, Amsterdam, 2003.
  - [14] W. Han, M. Sofonea, *Quasistatic Contact in Viscoelasticity and Viscoplasticity*, AMS, Intern. Press, Providence, NJ, 2002.
  - [15] J. Haslinger, M. Tvrdý, Approximation and Numerical Realization of Contact Problems with Friction, *Apl. Mat.*, **28**, 1983, 55-71.
  - [16] J. Haslinger, I. Hlaváček, Approximation of the Signorini Problem with Friction by a Mixed Finite Element Method. *J. Math. Anal. Appl.* **86**, 1982, 99-122.
  - [17] J. Haslinger, I. Hlaváček, J. Nečas, Numerical Methods for Unilateral Problems in Solid Mechanics, In: *Handbook of Numerical Analysis*, vol. IV, Elsevier, Amsterdam, 1996, 313-486.
  - [18] M. Hintermüller, K. Ito, K. Kunish, The Primal-Dual Active Set Strategy as Semi-Smooth Newton Method. *SIAM J. Optim.*, **13**, 2003, 867-888.
  - [19] M. Hintermüller, V. Kovtunencko, K. Kunish, The Primal-Dual Active Set Method for a Crack Problem with Non-Penetration, *IMA J. Appl. Math.* **69**, 2004, 1-26.
  - [20] I. Hladík, J. Nedoma, On the Numerical Solution of an Initial Boundary Value Problem for the Visco-Plastic Bingham Fluid, In: Dolezalova, M. (Ed.). *Numerical Methods in Geomechanics*, Prague, 1992, 141-144.
  - [21] I. Hlaváček, Mixed Finite Element Analysis of Semi-Coercive Unilateral Contact Problem with Given Friction. *Tech. Report* no **921**, ICS AS CR, Prague, 2004.
  - [22] I. Hlaváček, J. Lovíšek, A Finite Element Analysis for the Signorini Problem in Plane Elastostatics, *Apl. Mat.* **22**, 1977, 215-228.

- 
- [23] I. Hlaváček, J. Haslinger, J. Nečas, J. Lovíšek, *Solution of Variational Inequalities in Mechanics*, Springer Vlg., New York, 1988.
- [24] I. Hlaváček, J. Nedoma, On a Solution of a Generalized Semi-Coercive Contact Problem in Thermo-Elasticity, *Math. Comput. Simulat.*, **60**, 2002, 1-17.
- [25] I. Hlaváček, J. Nedoma, Reliable Solution of an Unilateral Contact Problem with Friction and Uncertain Data in Thermo-Elasticity, *Mathematics and Computers in Simulation* **67**, 2005, 559-580.
- [26] E. Hoek, J.W. Bray, *Underground Excavations in Rock*, Institution of Mining and Metallurgy, London, 1981, 358pp.
- [27] S. Hüeber, B.I. Wolkmuth, A Primal-Dual Active Set Strategy for Non-Linear Multi-body Contact Problems, *Comput. Meth. Appl. Mech. Engrg.*, **194**, (2005a), 3147-3166.
- [28] S. Hüeber, B.I. Wolkmuth, An Optimal a Priori Estimate for Non-Linear Multibody Contact Problems, *SIAM J. Numer. Anal.*, **43**, 2005b, 156-173.
- [29] S. Hüeber, M. Mair, B.I. Wolkmuth, A Priori Estimates and an Inexact Primal-Dual Active Set Strategy for Linear and Quadratic Finite Elements Applied to Multibody Contact Problems, *Applied Numerical Mathematics*, **54**, 2005, 555-576.
- [30] I.R. Ionescu, M. Sofonea, M., *Functional and Numerical Methods in Viscoplasticity*, Oxford Univ. Press, Oxford, 1993.
- [31] J. Jarušek, Contact Problems with Bounded Friction. Coercive Case, *Czechoslovak Math. J.* **33**(108), 1983, 237-261.
- [32] J. Jarušek, Dynamic Contact Problems with Given Friction for Viscoelastic Bodies, *Czechoslovak Math. J.* **46**(121), 1996, 475-487.
- [33] J. Jarušek, C. Eck, Dynamic Contact Problems with Small Coulomb Friction for Viscoelastic Bodies. Existence of Solutions, *Mathematical Models and Methods in Applied Sciences* **9**, 1999, 11-34.
- [34] Z. Kestřánek, *Numerical Analysis of 3D Contact Problem of Signorini Type with Friction in Thermo-Elasticity, h-Version of Finite Element Approximation*, PhD Thesis, FJFI CVUT, Prague (in Czech), 1999.
- [35] Z. Kestřánek, J. Nedoma, The Conjugate Projected Gradient Method-Numerical Tests and Results, *Tech. Report No 677*, ICS AS CR, Prague, 1996.
- [36] Z. Kestřánek, J. Nedoma, Numerical Simulation of a Bridge on a Non-Stable Slope: Comparison of Results Based on Contact Problem without and with Friction, In: Z. Rakowski (Ed.), *Geomechanics* **96**, Balkema, Rotterdam, 1997, 169-174.
- [37] G. Kuhn, Boundary Element Technique in Elastostatics and Linear Fracture Mechanics. Theory and Engineering Applications, In: *CISM Courses Lectures*, vol. 301, Springer, Vienna, 1988, 109-169.



- 
- [38] P. Linz, *Analytical and Numerical Methods for Volterra Equations*, SIAM, Philadelphia, 1985.
- [39] J.L. Lions, E. Magenes, *Non-Homogenous Boundary Value Problems and Applications*, Springer Vlg., Berlin, Heidelberg, New York (Vol. I-II (1972), Vol. III (1973)).
- [40] J. Nečas, *Les méthodes directes en équations elliptiques*, Academia, Prague, 1967.
- [41] J. Nečas, I. Hlaváček, *Mathematical Theory of Elastic and Elasto-Plastic Bodies. An Introduction*, Elsevier, Amsterdam, Oxford, New York, 1981.
- [42] J. Nedoma, On one Type of Signorini Problem without Friction in Linear Thermo-Elasticity, *Appl. Math.*, **28**, 6, 1983, 393-407.
- [43] J. Nedoma, On the Signorini Problem with Friction in Linear Thermo-Elasticity: the Quasi-Coupled 2D-Case, *Appl. Math.*, **32**, 3, 1987, 186-199.
- [44] J. Nedoma, Finite Element Analysis in Nuclear Safety, Tech. Report V-550, ICS AS CR, Prague, In: J.R. Whiteman (Ed). *The Mathematics of Finite Elements and Applications*, John Wiley&Sons, Chichester, 1993.
- [45] J. Nedoma, Equations of Magnetodynamics in Incompressible Thermo-Bingham's Fluid under the Gravity Effect, *J.Comput. Appl. Math.* **59**, 1995, 109-128.
- [46] J. Nedoma, Nonlinear Analysis of the Generalized Thermo-Magneto-Dynamic Problem, *J.Comput. Appl. Math.* **63**, 1-3, 1995 393-402.
- [47] J. Nedoma, On a Coupled Stefan-Like Problem in Thermo-Visco-Plastic Rheology, *J.Comput. Appl. Math.* **84**, 1997, 45-80.
- [48] J. Nedoma, *Numerical Modelling in Applied Geodynamics*, John Wiley&Sons, New York, 1998.
- [49] J. Nedoma, Contact Problem in Biomechanics and Iterative Solution Methods for Constrained Optimization. Theory, *Technical Report No. V-756*, Institute of Computer Sciences AS CR, Prague, 1998.
- [50] J. Nedoma, Analysis of a Coupled System of Equations of a Global Dynamic Model of the Earth, *Mathematics and Computers in Simulation*, **50**, 1999, 265-283.
- [51] J. Nedoma, *Finite Element Analysis of Elastic (Seismic) Wave Propagation in Region with Unilateral Contacts*, In: Arabnia, H.R. (Ed.), Proc. Conference PDPTA'2000, Las Vegas, USA, 2000.
- [52] J. Nedoma, Dynamic Contact Problems with Friction in Elasticity and Thermo-Elasticity, In: Feistauer. M., Rannacher, R., Kozel, K. (Eds), *Proc. of the 4th Conference on Numerical Modelling in Continuum Mechanics*, MATFYZPRESS, Prague, 2001.
- [53] J. Nedoma, Numerical Solution of a Stefan-like Problem in Bingham Rheology, *Mathematics and Computers in Simulation*, **61**, 2003, 271-281.

- 
- [54] J. Nedoma, On a Coupled Thermo-Hydro-Mechanical Problem Based on the Thermo-Visco-Plastic Rheology, In: Proceedings of ICCSA-2003, *Lecture Notes in Computer Science*, vol. 2667, Springer, Berlin, 2003, 977-986.
  - [55] J. Nedoma, *Mathematical Models of the Artificial Total Replacement of Joints. I. Dynamical Loading of TEP and TKR, Mathematical 2D and 3D Models*, TR 950, ICS AS CR, November 2005 (in Czech).
  - [56] J. Nedoma, On a Solvability of Contact Problems with Visco-Plastic Friction in the Thermo-Visco-Plastic Bingham Rheology, *Future Generation Computer Systems*, **22**, 2006, 484-499.
  - [57] J. Nedoma, *Security of Countries Endangered by Bigger Hurricanes: Proposal of the Research Project*, Presented at the conference FEMTEC2006, El Paso, TX, USA and as an open letter to the Government of USA, 2005.
  - [58] J. Nedoma, Tectonics along the Himalayan and Andean Mountain Ranges, Numerical Analyses of Collision and Subduction Zones, *Technical Report* No 1011, 2007.
  - [59] J. Nedoma, M. Bartoš, Z. Kestřánek sen., Z. Kestřánek jr., J. Stehlík, Numerical Methods for Constrained Optimization in 2D and 3D Biomechanics, *Numer. Linear Algebra Appl.*, **6**, 1999, 557-586.
  - [60] J. Nedoma, L. Tomášek On a Solvability of Hydro-Mechanical Problem Based on Contact Problem with Visco-Plastic Friction in Bingham Rheology, *J. Comput. Appl. Math.* **218**, 2008, 116-124.
  - [61] P. D. Panagiotopoulos, *Inequality Problems in Mechanics and Applications*, Birkhäuser, Boston, Basel, Stuttgart, 1985.
  - [62] B. N. Pschenichny, Yu. M. Danilin, *Numerical Methods in Extremal Problems*, Mir, Moscow.
  - [63] S. Shaw, *Finite Element and Discrete Time Methods for Continuum Problems with Memory and Applications to Viscoelasticity*, Ph.D. Thesis, BICOM, Brunel University, 1993.
  - [64] S. Shaw, J.R. Whiteman, J.R., *Towards Robust Adaptive FEMs for Partial Differential Volterra Equation Problem Arising in Viscoelasticity Theory*, In Whiteman, J.R. (Ed.). *The Mathematics of Finite Elements and Applications*. MAFELAP 1996, Wiley, Chichester, 1997, 55-80.
  - [65] S. Shaw, J.R. Whiteman, *Robust Adaptive FE Schemes for Viscoelastic Solid Deformation. An Investigative Study*, BICOM, Final report for the US Army's European Research Office Seed Project, Brunel University, February 10, 1999 (preprint).
  - [66] S. Shaw, M.K. Warby, J.R. Whiteman, An Error Bound via the Ritz-Volterra Projection for a Fully Discrete Approximation to a Hyperbolic Integrodifferential Equation, *Technical Report 94/3*, Brunel University, Uxbridge, U.K., 1994.

- 
- [67] S. Shaw, M.K. Warby, J.R. Whiteman, *An Introduction to the Theory and Numerical Analysis of Visco-Elasticity Problems*, Proc. Summer School “Industrial Mathematics and Mathematical Modelling”, University of West Bohemia, 1997.
- [68] P. Shi, M. Shillor, Existence of a Solution to the n-Dimensional Problem of Thermo-Elastic Contact, *Comm. PDE*, **17**, 1992, 1597-1618.
- [69] M. Shillor, Recent Advances in Contact Mechanics, *Special Issue of Math. Comput. Modelling* **28**, 1998, 4-8.
- [70] J. Sjöberg, *Large Scale Slope Stability in Open Pit Mining - A Review*, TR-1996:10T, Luleå University of Technology, Sweden, 1996.
- [71] R. Temam, Navier-Stokes Equations, *Theory and Numerical Methods*, North-Holland, Amsterdam, 1979.
- [72] P. Wriggers, *Computational Contact Mechanics*, John Wiley&Sons, Chichester, 2002.
- [73] P. Wriggers, P.D. Panagiotopoulos, *New Developments in Contact Problems*, Springer Vlg., Wien, New York, 1999.
- [74] B. I. Wolhuth, R. Krause, Monotone Multigrid Methods on Nonmatching Grids for Non-Linear Multibody Contact Problems, *SIAM J. Sci. Comput.*, **25**, 1, 2003, 324-347.
- [75] O. Záruba, M. Mencl, Landslides and Their Control, *Developments in Geotechnical Engineering*, **31**, Elsevier Scientific Publishing Company, Amsterdam, 1982.



# INDEX

## A

ABC, 219  
 Abundance, 204  
 accessibility, 162, 166  
 accuracy, 136, 138, 143, 146, 149, 150, 154, 155,  
     157, 158, 163, 164, 165, 167, 203, 214, 216, 233,  
     234, 235, 237, 238, 241, 367, 371  
 acquisitions, 3, 146, 157, 158, 159, 161  
 activation, 2, 7, 15, 20, 37, 40, 41, 47, 48, 51, 54, 55,  
     58, 60, 63, 254  
 ad hoc, 152  
 Adams, 384  
 adaptation, 100  
 adjustment, 153  
 administration, 87  
 Africa, 172, 174  
 age, 18, 46, 50, 55, 60, 144, 193, 194  
 agent, 81  
 agents, 2, 26, 62, 145, 178  
 agricultural, 15, 51, 55, 60, 62, 63, 108, 109, 114,  
     130  
 air, 80, 140, 141, 146, 147, 150, 162, 163, 164, 169  
 Alabama, 234  
 Alaska, 98, 198, 234, 373  
 algorithm, 156, 291, 292, 293, 294, 312, 316, 317,  
     325, 326, 327, 328, 329, 363, 365, 366, 375, 377,  
     382  
 alimentation, 161  
 alluvial, viii, 10, 11, 14, 22, 25, 27, 35, 36, 37, 38,  
     39, 50, 51, 55, 68, 73, 78, 103, 107, 108, 109, 256,  
     258  
 Alps, 26, 106, 107, 109, 112, 114, 175  
 alternative, 141, 165  
 amplitude, 156, 157, 159, 160, 211, 215, 220, 221,  
     275  
 AMS, 323, 324, 385  
 Amsterdam, 385, 387, 389  
 Andes, 248, 264, 374, 375  
 animals, 106  
 ANN, 323, 324  
 annual rate, 76

anomalous, viii, 19, 26, 35, 73, 256  
 ANS, 323, 324  
 antenna, 143, 147, 156, 157, 159  
 anthropic, 37, 47, 55, 57, 60, 62  
 anthropic factors, 47  
 anthropogenic, viii, 74, 88  
 application, 111, 143, 152, 158, 159, 161, 168, 169,  
     173, 175, 205, 208, 228, 249, 373, 383  
 applied mathematics, 295  
 aquifers, 13, 40, 46, 48, 70, 108  
 argument, 279, 336, 351  
 arid, 9, 11, 178, 193, 194, 197  
 Army, 209, 388  
 ash, xi, 201, 202  
 Asia, 197  
 Asian, 196, 197, 198, 268  
 assessment, x, 101, 128, 133, 134, 138, 153, 158,  
     160, 161, 167, 173, 179, 180, 190, 248, 267  
 assumptions, 233, 296, 299, 305, 338, 341, 343, 346,  
     348, 350, 357, 359  
 asymmetry, 10, 36, 256  
 Athens, 225, 248  
 Atlantic, 74, 84, 85, 86, 87, 100, 101, 102, 103  
 Atlantic Multidecadal Oscillation (AMO), 87  
 Atlas, 197  
 atmosphere, 151  
 atmospheric pressure, 232  
 attitudes, 29  
*Aurora*, 78, 88  
 Austria, ix, 105, 106, 107, 117, 130, 131, 169  
 availability, 116, 150, 151, 154, 159, 162  
 averaging, 213, 216  
 awareness, 142

## B

backscattered, 156, 157  
 banks, 6, 13, 29, 30, 42, 75  
 barrier, 268, 353  
 Bayesian, 94  
 beaches, 53, 55  
 beams, 368  
 beer, 76

behavior, 94, 96, 103, 134, 136, 249  
 Belgium, 167, 170  
 bell, 51  
 benchmark, 140, 147, 165  
 benchmarks, 138, 139, 147, 159, 161, 164  
 bending, 124, 127  
 benefits, 166  
 biaxial, 145  
 biodiversity, 106  
 biological processes, 102  
 birth, 179  
 Black Sea, 107, 110  
 blocks, xi, 5, 7, 18, 22, 24, 29, 42, 48, 57, 88, 89, 90,  
 138, 152, 184, 185, 225, 226, 227, 228, 230, 243,  
 247, 295, 345, 367, 373, 374, 375  
 bonds, 50  
 Boston, 173, 388  
 boundary conditions, 138, 213, 214, 215, 285, 287,  
 308, 310, 356  
 boundary value problem, 306  
 bounds, 186, 187  
 buildings, 82, 86, 87, 97, 98, 110, 114, 139, 157,  
 158, 163, 175, 383  
 buses, 87

## C

cables, 135, 150  
 calibration, 146, 150, 158, 163, 166, 207  
 Canada, 70, 171, 209  
 canals, 18, 55  
 capacity, 37, 40, 47, 109, 271, 331, 354, 384  
 carbonates, 6  
 Caribbean, 80, 86, 87  
 Caribbean Sea, 86  
 carrier, 143, 145  
 case study, 70, 142, 173, 243  
 catchments, xii, 50, 111, 166, 251  
 categorization, 269, 383  
 Caucasus, 197  
 causality, 346  
 cement, 76, 90, 185  
 Central America, 104, 187, 195  
 Central Asia, 196, 197  
 Central Europe, 106  
 channels, 10, 14, 22, 57, 107, 128, 256, 267  
 Chile, 373, 375  
 China, 178  
 CIPA, 168, 170  
 circulation, 14, 37, 47, 58, 80, 101  
 CISM, 168, 386  
 classes, 12, 79, 360  
 classical, x, 134, 139, 142, 148, 159, 280, 282, 285,  
 287, 291, 298, 305, 306, 307, 345, 355  
 classification, 12, 16, 70, 79, 80, 88, 151, 160, 180,  
 203, 204, 230  
 clay, 51, 88, 93, 121, 185, 204, 234, 235, 240, 266  
 climate change, 71, 87, 103, 174  
 climatology, 100, 269, 384  
 clouds, x, 134, 137, 142, 149, 150, 163, 174  
 CO<sub>2</sub>, 169  
 coastal areas, 63  
 coastal zone, 57  
 codes, 96, 226, 229, 384  
 coherence, 135, 158, 159, 160, 163  
 collisions, 373  
 colonisation, 55  
 colonization, 56  
 Colorado, 102, 170  
 colors, 153  
 communities, 87, 127, 267  
 community, 16  
 compensation, 142  
 complement, 164  
 compliance, 300  
 components, 136, 228, 270, 271, 273, 274, 276, 277,  
 278, 286, 294, 296, 297, 306, 307, 311, 314, 317,  
 331, 354, 372, 384  
 composition, 36, 185, 267  
 comprehension, 50  
 compressive strength, 205, 207  
 computation, xi, 138, 150, 211, 212, 214, 215, 216,  
 285  
 concentration, 13, 36, 47, 216  
 concrete, 120, 123, 124, 125, 126, 127, 147, 148,  
 167, 214, 368, 369  
 conditioning, 28, 47  
 conduction, 272  
 conductive, 101  
 conductivity, 13, 272, 278, 286, 331  
 confidence, 192  
 configuration, 7, 37, 145, 161, 211, 214, 226, 241,  
 242, 243, 246, 247, 270  
 conformity, 9, 13  
 Congress, 129, 130, 167, 174  
 congruence, 42  
 conjugate gradient method, 216, 293, 316, 365, 377  
 conservation, 55, 57, 272  
 consolidation, 135, 202, 208, 231, 232, 234, 237, 268  
 constant rate, 305  
 constraints, 63, 140, 203, 254, 292, 293, 294, 316,  
 321, 325  
 construction, 15, 47, 78, 93, 94, 96, 100, 114, 116,  
 119, 120, 125, 127, 128, 147, 167, 178, 202, 211,  
 213, 255, 259, 367, 368, 370  
 construction sites, 127  
 consultants, 243  
 consumption, 47, 161, 373  
 continuity, 13, 15, 31, 286  
 control, viii, 2, 3, 13, 20, 24, 25, 26, 27, 36, 40, 45,  
 47, 50, 51, 53, 62, 71, 101, 103, 124, 138, 139,  
 142, 145, 146, 149, 159, 164, 170, 171, 257, 284  
 convection, 107  
 convective, 80  
 convergence, 36, 290, 292, 294, 303, 304, 316, 360,  
 377  
 conversion, 207

convex, 17, 18, 20, 31, 58, 79, 286, 287, 290, 311, 316, 322, 335, 336, 351, 365  
 coordination, 111  
 correlation, 48, 96, 158, 165, 171, 180, 186, 187, 191, 235  
 correlations, 17, 47, 60, 180, 193  
 cost-effective, 165  
 costs, ix, 106, 118, 119, 124, 128, 129, 135, 155  
 Coulomb, 227, 270, 295, 296, 306, 384, 386  
 couples, 157, 296, 305  
 coupling, 267, 268, 269, 275, 285, 321, 323, 352, 353  
 coverage, 142, 155  
 covering, 24, 60, 61, 62, 76, 100, 127, 128, 148, 185, 256  
 crack, 264, 265, 306, 307  
 CRC, 385  
 creep, 69, 174, 264, 265, 267, 269, 295, 329, 346  
 critical analysis, 3  
 critical state, 231, 232  
 critical value, 243, 244, 246  
 Croatia, 106  
 crops, 56, 63  
 cross-validation, 165  
 crust, 179, 199, 264  
 crystalline, 69, 171  
 cultivation, 55, 60  
 cultural heritage, 175  
 culture, 194  
 cycles, 55, 158, 159  
 Czech Republic, 263, 268

## D

damping, 215, 217, 270, 271, 296, 305, 306, 308, 309, 321, 322, 328, 330, 345  
 data analysis, 261  
 data availability, 165, 166  
 data processing, 164  
 data set, x, 133, 134, 166  
 database, 94, 101, 111, 190  
 dating, 159, 194  
 death, 86, 92  
 deaths, 87  
 decay, 39, 47, 54, 62  
 decision making, 75  
 decomposition, 309, 311, 312, 323  
 decompression, 26  
 definition, xii, 2, 50, 55, 100, 134, 155, 251, 253, 292, 302, 320, 324, 326  
 deforestation, 51, 55, 57  
 deformation, viii, 2, 9, 12, 19, 20, 26, 27, 28, 31, 40, 44, 45, 47, 51, 53, 63, 66, 68, 69, 70, 71, 73, 98, 137, 154, 163, 165, 166, 168, 174, 175, 216, 221, 228, 242, 246, 254, 255, 258, 259, 260, 267, 270, 272, 273, 274, 277, 328, 329, 352, 368, 370, 371, 372, 373, 375, 377

degradation, xi, 131, 188, 189, 193, 225, 226, 229, 247  
 degrees of freedom, 322, 348  
 delivery, 119  
 density, ix, 26, 93, 105, 107, 108, 110, 149, 154, 163, 243, 271, 272, 278, 286, 296, 306, 328, 331  
 deposition, 38, 94, 185, 186, 188  
 deposits, viii, 3, 9, 10, 11, 12, 14, 18, 22, 23, 24, 26, 27, 28, 29, 31, 36, 37, 38, 39, 40, 42, 45, 50, 51, 53, 55, 57, 62, 66, 73, 78, 108, 113, 114, 116, 119, 179, 185, 186, 198, 214, 256, 257  
 depression, 19, 22, 23, 34, 74, 85, 125, 183, 186, 189, 256  
 derivatives, 271, 282, 355, 361  
 destruction, 7, 87, 252, 267, 269, 383  
 detachment, 79, 88, 103, 184, 185, 188, 189, 258  
 detection, 148, 152, 153, 157, 172, 173  
 detritus, viii, 73, 185  
 deviation, 31, 35, 155, 191, 206  
 diaphragm, 24, 40  
 differential equations, 327  
 differentiation, 55, 163, 235  
 diffusion, 3  
 dilation, 232, 233  
 Dirichlet boundary conditions, 320  
 Dirichlet condition, 283  
 disaster, 86, 111, 129, 179  
 disaster relief, 111  
 discharges, viii, 13, 73, 107  
 discontinuity, 48, 62, 88, 145, 205, 264  
 discordance, 24, 31  
 discretization, 212, 284, 323, 347, 360  
 dislocation, 2, 3, 20, 25, 26, 36, 253  
 dislocations, x, 7, 22, 31, 37, 46, 54, 164, 177, 194, 197  
 disorder, 2, 63  
 dispersion, 47  
 displacement, x, xi, 7, 13, 19, 20, 25, 30, 34, 42, 69, 94, 97, 114, 124, 125, 133, 134, 135, 136, 137, 145, 146, 148, 157, 158, 160, 162, 163, 164, 165, 166, 170, 171, 174, 175, 180, 194, 198, 213, 214, 215, 216, 219, 220, 221, 225, 226, 227, 228, 229, 230, 231, 232, 233, 235, 238, 241, 242, 243, 245, 246, 247, 248, 249, 257, 270, 271, 272, 273, 274, 276, 277, 284, 286, 292, 294, 295, 296, 305, 306, 307, 308, 310, 311, 317, 319, 331, 347, 348, 374, 384  
 disposition, 13, 14, 18, 34  
 distortions, 152  
 distribution, 13, 14, 16, 79, 100, 101, 104, 136, 137, 151, 154, 187, 190, 193, 215, 253, 255, 267, 284, 372, 376, 377, 378, 379, 380, 381  
 distribution function, 193  
 divergence, 366  
 diversity, 178, 192  
 division, 13, 122, 314, 315, 347, 348, 351  
 drainage, viii, xii, 22, 24, 47, 56, 60, 66, 73, 108, 117, 120, 121, 122, 123, 124, 125, 127, 128, 251, 255, 256, 257, 260

droughts, 107, 108, 109, 127  
*duality*, 318  
 dumping, 124, 213  
 duration, 48, 94, 95, 96, 102, 135, 164, 178, 191,  
 246, 278, 279, 280, 296, 305, 354

## E

early warning, 163, 166  
 earth, ix, 3, 64, 105, 111, 117, 124, 160, 173, 264,  
 265, 267, 371, 372  
 Earth Science, 130, 174, 197, 201, 260  
 earthquake, x, xi, xii, 7, 8, 19, 98, 99, 102, 106, 111,  
 130, 131, 169, 177, 178, 179, 180, 181, 182, 183,  
 184, 185, 186, 187, 188, 189, 190, 191, 192, 193,  
 194, 195, 196, 197, 198, 211, 212, 214, 222, 225,  
 241, 242, 246, 249, 251, 252, 253, 254, 257, 259,  
 260, 261, 267, 269, 373, 375  
 ecologism, 127  
 economic crisis, 76  
 economic damages, 114, 127  
 economic losses, viii, 74, 98  
 Education, 68, 111  
 elaboration, 100, 150, 158, 165, 166, 269, 383  
 elasticity, 214, 276, 277, 284, 286, 298, 305, 308,  
 320, 321, 322, 330, 345  
 electromagnetic, 156, 158  
 energy, 3, 47, 145, 156, 161, 187, 195, 198, 272,  
 373, 375  
 energy consumption, 161  
 England, 249  
 enlargement, 61, 117  
 entropy, 272  
 environment, 15, 100, 107, 111, 179, 180, 214, 216,  
 259, 383  
 environmental conditions, x, 134, 151, 160  
 environmental context, x, 133  
 environmental impact, 198  
 epidemic, 82  
 equality, 187, 316  
 equilibrium, 228, 241, 242, 272, 276, 289, 308, 367,  
 368  
 equipment, 367  
 erosion, x, 9, 11, 20, 22, 24, 26, 27, 29, 38, 39, 40,  
 51, 55, 57, 58, 62, 69, 78, 88, 94, 107, 108, 109,  
 116, 130, 171, 177, 178, 188, 190, 191, 192, 193,  
 194, 195, 196, 197, 257, 267  
 error estimation, 347  
 estates, 55  
 estimating, x, xi, 94, 156, 177, 178, 180, 181, 182,  
 183, 188, 190, 192, 193, 194, 195, 236  
 estuaries, 55  
 Euclidean space, 282  
 Eulerian, 278, 354, 363  
 Eurasia, 198  
 Euro, 106  
 Europe, 66, 106, 107, 109, 111, 113, 115, 117, 119,  
 121, 123, 125, 127, 128, 129, 131, 173, 174

European Commission, 248, 249  
 European Community, 67  
 European Space Agency, 166  
 European Union, 127, 142, 166  
 evacuation, 97, 119, 128  
 evolution, vii, 1, 2, 3, 9, 11, 15, 23, 25, 28, 29, 34,  
 45, 47, 48, 50, 52, 53, 58, 64, 66, 69, 70, 102, 104,  
 134, 135, 136, 137, 154, 157, 159, 162, 163, 169,  
 173, 175, 179, 189, 197, 254, 255, 260, 267, 268,  
 297, 306, 307, 354, 371, 373, 374, 384  
 excitation, 178  
 execution, 121, 123, 124, 127, 128  
 exercise, 204  
 expert, 135, 162  
 expertise, 153, 165, 166  
 exploitation, 137, 145, 151, 160, 161, 162, 165  
 exposure, 45, 48  
 extraction, 169, 174, 202

## F

facies, 5, 14, 65  
 factor analysis, 75  
 failure, vii, viii, xi, 2, 48, 73, 134, 137, 163, 174,  
 180, 183, 188, 201, 205, 206, 208, 209, 227, 228,  
 229, 241, 264, 265, 266, 267, 295, 297  
 family, 289, 311, 335, 347, 351, 360, 361, 362, 364  
 famine, 69  
 farming, viii, 2, 57, 60  
 fascia, 67, 68  
 fatalities, xi, 98, 242, 251  
 faults, xii, 7, 9, 12, 13, 20, 21, 27, 29, 31, 34, 36, 45,  
 53, 62, 65, 66, 99, 179, 180, 183, 184, 189, 251,  
 252, 254, 255, 256, 257, 258, 259, 264, 374, 375  
 fax, 133  
 February, 388  
 FEMA, 101  
 Fermi, 261  
 film, 153  
 filtration, 58  
 financial resources, 127, 128, 129  
 financial support, ix, 106, 120  
 financing, 127  
 fines, 235  
 finite element method, 212, 215, 222, 310, 312, 347,  
 365  
 fire, 111  
 fire hazard, 111  
 fires, 107, 127  
 fishing, 106  
 flank, 7, 19, 22, 23, 25, 26, 27, 29, 34, 41, 45, 50, 74,  
 172, 185, 208  
 flexibility, 161  
 flood, 11, 65, 74, 81, 87, 107, 108, 109, 111, 278,  
 384  
 flooding, ix, 74, 81, 87, 106, 111, 114, 117  
 flow, ix, 14, 16, 18, 24, 47, 48, 56, 58, 65, 71, 86, 87,  
 93, 94, 95, 97, 101, 102, 105, 110, 112, 113, 114,



116, 117, 124, 125, 129, 160, 255, 268, 273, 275, 278, 280, 284, 286, 360, 363, 373, 377, 381  
 flow rate, 86, 87  
 fluctuations, 11, 51, 135, 147  
 fluid, 65, 278, 280, 363, 364, 365  
 fluvial, xii, 22, 24, 26, 27, 29, 38, 39, 41, 42, 45, 50, 55, 78, 107, 110, 119, 186, 251, 255, 257, 259  
 fluvial-lacustrine, 14, 27, 31, 186  
 focusing, x, 134, 187, 195  
 folding, 29  
 forecasting, 65, 100, 134, 180  
 forests, ix, 105  
 fossil, ix, 105, 112, 117  
 Fourier, 215, 216, 220, 221  
 fracture, 31, 204, 306, 375  
 fractures, 10, 12, 13, 14, 20, 21, 29, 31, 33, 34, 41, 42, 45, 48, 51, 52, 53, 90, 92, 93, 203, 267  
 fragility, 12  
 fragmentation, 60  
 framing, 143, 189  
 France, 70, 168, 170, 173, 175  
 freedom, 322, 348  
 freezing, 80, 118  
 friction, 12, 22, 231, 232, 234, 240, 241, 243, 245, 246, 270, 273, 274, 275, 276, 277, 278, 281, 282, 284, 285, 288, 291, 292, 295, 296, 297, 298, 299, 305, 306, 307, 308, 309, 311, 312, 316, 318, 320, 330, 331, 335, 345, 352, 355, 367, 368, 369, 370, 372, 375  
 fusion, 6

## G

Galileo, 142  
 GDP, 106  
 generalization, 273  
 generation, 22, 74, 94, 151, 164, 170, 172, 178, 229, 231, 233, 235  
 genetic factors, 36  
 geochemical, xi, 201  
 geography, 103  
 geology, 65, 69, 77, 79, 100, 119, 128, 167, 180, 187, 253, 254, 256, 269, 371, 384  
 geophysical, ix, 31, 33, 119, 128, 130, 133, 135, 142, 163, 168, 259, 374  
 Germany, 102, 130, 168, 172  
 GIS, 111  
 glacial deposits, 186  
 glaciation, 25, 27, 295  
 glaciations, 27, 64, 193, 195  
 glaciers, 26, 69, 165, 178, 184  
 glass, xi, 76, 201, 202  
 Global Positioning System, 31, 70, 136, 136, 137, 138, 142, 143, 147, 149, 150, 164, 167, 168, 169, 171, 172, 173, 174, 175, 176, 187  
 goals, 270  
 government, 78, 86, 97  
 grading, 267

grain, 6, 18, 22, 78, 231  
 graph, 306  
 gravitation, 69  
 gravitational collapse, 19  
 gravitational field, 139  
 gravitational stress, 14, 62, 70, 295  
 gravity, vii, 2, 9, 17, 18, 19, 21, 26, 36, 40, 50, 53, 62, 180, 225, 248, 295, 373  
 grazing, 55  
 Greece, 168, 225  
 grids, 153  
 ground-based, 148, 151, 166, 169, 172, 173, 174, 175  
 groundwater, 14, 37, 47, 58, 70, 100, 107, 120, 124, 125, 135, 137, 147, 205, 264, 267  
 grouping, 122  
 growth, viii, 74, 76, 77, 78, 96  
 growth rate, 76  
 GSA, 102  
 GSM, 161  
 guidance, 208  
 Guinea, 193, 198  
 Gulf Coast, viii, 73, 74  
 Gulf of Mexico, 85, 87

## H

handling, 151  
 hanging, 27, 256, 258  
 Harvard, 191  
 Hawaii, xi, 201, 202  
 hazards, xi, xii, 96, 101, 102, 106, 119, 127, 130, 134, 172, 180, 197, 201, 263  
 heat, 107, 268, 272, 273, 275, 276, 281, 284, 286, 352  
 heat conductivity, 286  
 height, 3, 9, 10, 22, 25, 36, 37, 40, 50, 54, 120, 139, 140, 151, 155, 164, 189, 214, 289, 375  
 hemisphere, 179, 198  
 heterogeneity, 135, 136  
 heterogeneous, 121, 212  
 high resolution, x, 133, 151, 153, 156, 159, 165, 187  
 high risk, 90, 137, 145, 175  
 high-frequency, 154  
 Hilbert, 282, 283, 349, 355  
 Hilbert space, 282, 283, 349, 355  
 Holland, 261, 389  
 Holocene, x, 11, 22, 24, 27, 28, 38, 41, 50, 65, 68, 69, 70, 104, 177, 178, 181, 184, 185, 187, 189, 190, 192, 193, 195, 198, 251, 254  
 homogenous, 365  
 hospitals, 78  
 host, 147  
 House, 173  
 households, viii, 74  
 human, viii, xii, 3, 7, 11, 15, 58, 68, 74, 88, 89, 90, 94, 107, 109, 118, 259, 263  
 human activity, 107

humidity, 146  
Hungary, 106  
hurricane, viii, 74, 84, 85, 86, 87, 93, 96, 97, 100,  
102, 103, 268, 354, 381, 382, 383, 384  
hurricanes, xii, 74, 85, 87, 96, 103, 263, 268, 269,  
353, 381, 383  
hydro, 58  
hydrologic, xi, 47, 107, 114, 116, 201  
hydrological, 108, 109, 110, 116, 131, 187, 195, 268,  
353, 354, 383  
hydrology, 172, 269, 384  
hydropower, 110  
hydrostatic pressure, 62  
hyperbolic, 299  
hypothesis, viii, 2, 21, 24, 36, 37, 40, 42, 140, 373

# I

ice, 85, 171, 188  
identification, 100, 151, 154, 166, 249, 253  
identity, 26, 189, 192, 279, 323  
illumination, 156  
IMA, 385  
imagery, x, 133, 151, 152, 161, 162, 168, 180  
images, 60, 148, 150, 151, 152, 153, 154, 155, 156,  
157, 158, 159, 160, 164, 165, 166, 168, 171, 187  
imaging, 150, 165, 170  
immersion, 6, 7, 45  
immigration, 77  
implementation, 137  
in situ, 163, 166, 185, 367  
inactive, 53, 135, 325, 326  
income, 86  
incompressible, 278, 280, 364  
indication, 16, 35  
indicators, 172  
indices, 251, 254, 270, 293, 323  
indirect measure, 205  
individuality, 48  
industrial, 90, 98, 383  
industry, 76, 90, 148  
inequality, 270, 284, 291, 299, 301, 302, 310, 325,  
335, 348, 357, 358, 364  
inertia, 241, 273, 305, 308, 345  
influenza, 69  
infrared, 145, 147  
infrastructure, viii, xi, 74, 100, 110, 111, 127, 142,  
211, 212, 213, 219  
inhomogeneities, 195  
initial state, 296  
initiation, 94, 264  
injuries, 90, 92, 97, 98  
inspection, 96, 204  
instabilities, 109, 148, 202  
instability, viii, 60, 64, 74, 94, 98, 101, 109, 134,  
135, 137, 145, 159, 160, 161, 167, 170, 264, 265,  
295

instruments, 135, 138, 139, 143, 145, 147, 149, 150,  
154, 156, 159, 164  
integration, x, 133, 142, 146, 150, 163, 166, 215,  
337, 356, 359  
intensity, 6, 7, 8, 13, 19, 40, 42, 45, 51, 75, 94, 95,  
96, 99, 100, 102, 106, 107, 135, 149, 178, 180,  
183, 187, 189, 191  
interaction, viii, 2, 74, 196, 212, 216, 318, 367  
interaction effect, 216  
interactions, 367, 368  
intercalation, 48, 62  
interdisciplinary, ix, 106, 119, 128  
interface, 214, 226, 227, 228, 229, 232, 243, 246,  
247, 273, 306  
internet, 111  
interpretation, 19, 24, 26, 29, 31, 37, 40, 41, 42, 44,  
49, 58, 96, 137, 145, 164, 165, 166, 174, 187, 255,  
261  
interval, 10, 154, 165, 178, 179, 190, 191, 194, 216,  
270, 282, 283, 296, 299, 306, 328, 336, 348, 356,  
359, 383  
intervention, 119, 128  
intrinsic, viii, 2, 134, 157, 222  
invasive, 373  
inventories, 137, 166, 187, 193, 197  
inversion, xii, 251, 260  
Investigations, 179  
ions, 69, 96, 109, 152, 323  
iron, 76  
irrigation, 94, 100  
island, xi, 201, 208  
isolation, 9  
isomorphism, 355  
isotropic, 222, 271, 275  
ITA, 168  
Italy, vii, 1, 2, 3, 4, 5, 7, 9, 10, 11, 13, 15, 16, 17, 19,  
21, 23, 25, 27, 29, 31, 33, 35, 37, 39, 41, 43, 45,  
47, 49, 50, 51, 53, 55, 56, 57, 59, 61, 63, 64, 65,  
66, 67, 68, 69, 70, 71, 102, 106, 107, 113, 129,  
133, 167, 169, 170, 173, 175, 251, 256, 257, 259,  
260, 261  
iteration, 293, 294, 317

# J

January, 11, 80, 129, 249  
Japan, 129, 222, 249  
Japanese, 249  
joints, 34, 36, 48, 263, 264  
judgment, 135  
Jun, 84, 85  
Jurassic, viii, 73, 103  
justification, 60

**K**

kinematics, 2, 3, 7, 18, 19, 20, 26, 27, 28, 31, 34, 36, 37, 40, 42, 47, 49, 50, 63, 103, 136, 137, 163, 165, 170, 270  
 knots, 84, 85  
 Kobe, 248

**L**

labor-intensive, 127  
 Lagrange multipliers, 291, 314, 322, 323  
 Lagrangian, 291, 317, 318, 320, 365, 366  
 Lagrangian formulation, 318, 320  
 lakes, 108, 139, 140, 383  
 land, 47, 55, 58, 60, 80, 96, 100, 106, 107, 108, 109, 110, 114, 119, 130, 152, 161, 165, 267  
 land use, 47, 60, 96, 100, 161  
 landscapes, 131  
 laptop, 203  
 large-scale, xi, 63, 67, 201, 208, 212, 214, 294  
 laser, 116, 131, 143, 145, 149, 150, 151, 163, 167, 168, 172, 173, 174, 175  
 lasers, 149, 171  
 Last Glacial Maximum, 64  
 Late Quaternary, 67  
 law, ix, 106, 118, 119, 128, 155, 191, 272, 274, 276, 280, 281, 282, 285, 297, 298, 306, 307, 308, 309, 329, 355  
 laws, 100, 195, 267, 271, 278  
 lead, ix, 20, 34, 50, 106, 110, 128, 145, 160, 179, 189, 270, 306  
 Least squares, 172  
 legislation, 100, 128  
 lens, 153  
 lenses, 153  
 limestones, 5, 6, 12, 13, 18, 19, 20, 22, 25, 26, 31, 34, 36, 37, 53  
 limitation, 140, 158, 270, 358, 360  
 limitations, 165, 193, 194, 207  
 linear, xi, 20, 24, 25, 50, 78, 158, 189, 214, 225, 226, 227, 241, 242, 243, 247, 267, 270, 271, 276, 282, 284, 289, 290, 292, 293, 296, 298, 299, 305, 306, 308, 310, 311, 314, 317, 320, 331, 345, 347, 349, 351, 352, 360, 361, 364, 365, 368  
 linear function, 311, 347, 351  
 links, 195, 268  
 liquefaction, 248  
 lithologic, viii, 74, 204  
 lithosphere, 197, 269, 372, 373  
 Little Ice Age, 11, 51, 55  
 living conditions, 106  
 location, xi, 10, 17, 33, 59, 99, 136, 156, 163, 165, 180, 186, 192, 201, 204, 205, 216, 228, 234, 243, 253, 258  
 logging, xi, 201, 202, 205, 208  
 logistics, 161, 163

London, 63, 64, 66, 69, 101, 130, 175, 249, 260, 385, 386  
 long distance, 143, 149  
 long period, 2, 45, 159  
 long-term, 102, 107, 137, 145, 170, 179, 197  
 Los Angeles, 222  
 losses, xii, 74, 263  
 Louisiana, 383  
 lying, 50, 109, 251, 253, 259

**M**

machinery, 114  
 machines, 127  
 magnetic, xi, 201  
 maintenance, 55, 127, 134, 135, 161, 163  
 malaria, 82  
 Malta, 173  
 management, 3, 127, 134, 161, 162, 166, 169  
 management practices, 166  
 man-made, 94, 134, 257  
 mantle, 66, 195, 196, 280  
 mapping, x, 16, 66, 74, 119, 134, 136, 137, 148, 151, 152, 165, 170, 173, 175, 183, 195, 197, 199, 255, 282, 318, 346  
 Mathematical Methods, 263  
 mathematics, 269, 384  
 matrix, 22, 36, 55, 89, 138, 143, 213, 215, 292, 293, 294, 315, 316, 317, 320, 323, 324, 325, 326, 327, 328, 329, 348, 352, 365  
 MCS, 7, 8, 45  
 measurement, 104, 131, 137, 139, 140, 141, 144, 145, 146, 148, 149, 152, 155, 159, 162, 173, 174, 278  
 measures, 55, 100, 110, 112, 119, 120, 122, 124, 127, 128, 129, 134, 149, 156, 158, 306, 318  
 mechanical energy, 373  
 mechanical properties, 268, 352, 383  
 media, 212, 278  
 median, 206  
 Mediterranean, xi, 51, 55, 66, 102, 107, 110, 129, 251  
 melting, 135, 280  
 memory, 139, 161, 271, 276, 277, 295, 296, 305, 306, 320, 321, 329, 330, 331, 345, 346, 347, 350  
 mercury, 106, 147  
 Mesozoic, 102  
 metals, 179  
 meteor, 85  
 meteorological, 2, 85, 95, 96, 108, 137, 163  
 metric, 13, 18, 24, 25, 153, 154  
 metropolitan area, 76, 102  
 Mexican, 80, 87, 98  
 Mexico, 73, 74, 75, 76, 77, 78, 79, 80, 81, 83, 84, 85, 86, 87, 89, 91, 93, 95, 97, 98, 99, 100, 101, 102, 103, 104, 174  
 Miami, 269, 384  
 microprocessors, 145

- microwave, 173  
 migration, 35, 106, 257  
 military, 256  
 minerals, 93, 383  
 mining, 89, 92, 202, 294, 329  
 Miocene, 65  
 Mississippi, 234  
 Missouri, 249  
 MMA, viii, 73, 74, 75, 76, 77, 78, 79, 80, 81, 83, 85, 86, 87, 88, 89, 90, 93, 94, 95, 96, 97, 98, 99, 100  
 mobile phone, 143  
 modeling, x, 114, 116, 117, 119, 127, 128, 130, 133, 137, 146, 154, 167, 171, 213, 261  
 models, 3, 19, 40, 53, 114, 116, 150, 153, 154, 159, 163, 175, 219, 229, 232, 253, 259, 267, 268, 269, 295, 296, 329, 346, 353, 367, 368, 369, 373, 375, 376, 383, 384  
 modulation, 101  
 modulus, 369  
 moisture, 94, 151, 158, 186  
 moisture content, 94  
 momentum, 272  
 Mongolia, 183  
 monograph, 179  
 monotone, 309  
 Montana, 97  
 morphogenesis, 3, 9, 68, 70  
 morphogenetic processes, 27  
 morphological, viii, x, 2, 6, 9, 21, 22, 40, 53, 55, 58, 69, 78, 94, 109, 131, 134, 135, 137, 179, 255  
 morphology, 10, 57, 100, 110, 149, 150, 171, 173, 189, 252, 258, 373  
 morphometric, 18, 68  
 Moscow, 196, 197, 198, 388  
 motion, x, xi, 98, 102, 104, 151, 168, 171, 176, 177, 180, 191, 194, 211, 212, 213, 214, 215, 216, 222, 225, 226, 227, 228, 232, 241, 242, 246, 247, 248, 249, 270, 272, 274, 305, 375  
 mountains, 27, 28, 70, 78, 87, 96, 130, 179, 182, 188, 264  
 mouth, 87  
 movement, vii, ix, x, xi, 3, 19, 21, 23, 29, 30, 31, 34, 37, 39, 41, 48, 49, 50, 51, 53, 63, 67, 71, 74, 88, 89, 92, 94, 96, 97, 105, 114, 120, 134, 137, 154, 157, 158, 163, 169, 174, 225, 226, 228, 247, 254, 267, 296, 368, 370, 372, 373  
 multidisciplinary, 259  
 multiplier, 317, 319, 323, 327  
 multivariate, 110, 130  
 multivariate statistics, 130  
 150, 154, 159, 166, 179, 180, 201, 216, 263, 264, 294  
 natural disasters, ix, xii, 106, 107, 127, 133, 263  
 natural environment, 100, 107, 179, 180  
 natural hazards, 96, 106, 127, 134, 263  
 natural resources, 127  
 Navier-Stokes, 389  
 navigation system, 142  
 neglect, 188  
 neof ormation, 20, 62  
 Netherlands, 66, 70  
 network, vii, xii, 1, 9, 10, 11, 14, 18, 22, 23, 24, 29, 31, 35, 45, 46, 47, 48, 50, 51, 53, 54, 56, 60, 62, 106, 107, 110, 119, 127, 138, 143, 145, 147, 164, 165, 166, 183, 191, 251, 252, 254, 255, 256, 257, 259  
 Nevada, 198, 201  
 New Jersey, 248, 261  
 New Orleans, 268, 381, 383  
 New York, 69, 71, 170, 197, 209, 384, 385, 386, 387, 389  
 New Zealand, 167, 209  
 Newton, 365, 385  
 Newtonian, 268, 280, 353, 364, 383  
 Nicaragua, 172  
 nodes, xi, 225, 226, 227, 241, 246, 247, 294, 311, 314, 315, 317, 323, 347, 348, 351  
 noise, 151  
 non-linear, 158, 216, 268, 273, 300, 352, 365, 367, 377  
 non-uniform, 241, 243  
 normal, 7, 53, 66, 102, 125, 157, 229, 231, 232, 241, 253, 261, 270, 271, 273, 274, 276, 277, 278, 286, 296, 300, 306, 307, 311, 314, 318, 328, 331, 354, 374, 376  
 norms, 282  
 North America, 76, 104  
 North American Free Trade Agreement, 76  
 North Atlantic, 87  
 North Carolina, 176  
 Northeast, 78, 79, 84, 98, 102  
 Norway, 234  
 nucleus, 7  
 Nuevo León, 101, 102, 103, 104  
 numerical analysis, 214, 284  
 numerical computations, 212

## O

- observations, x, 31, 103, 119, 128, 133, 137, 138, 143, 149, 158, 164, 166, 178, 185, 196, 206, 253, 254, 269, 354, 374, 383, 384  
 occlusion, 150  
 OCR, 233  
 offshore, vii, 254, 255  
 oil, 53  
 online, 203  
 operator, 145, 151, 293, 347, 365

## N

- nares, 103  
 NASA, 173  
*national*, 16, 40, 76, 102, 106, 128, 256  
 natural, viii, ix, xi, xii, 47, 54, 55, 56, 57, 73, 74, 87, 94, 96, 100, 106, 107, 108, 127, 133, 134, 143,

optical, 151, 155, 156, 166  
 optimization, 114, 130, 292, 325  
 optimization method, 292  
 oral, 15, 59, 60  
 orbit, 156, 157  
 ordinary differential equations, 302, 336, 359  
 organic, 194  
 organic matter, 194  
 organization, 202  
 orientation, 13, 20, 34, 35, 45, 47, 48, 152, 154, 158, 205, 253, 259  
 oscillation, 53, 62  
 oscillations, viii, 2, 53, 178, 377  
 outliers, 150

## P

Pacific, 74  
 pairing, 282, 318  
 Pap, 101  
 paper, 102, 119, 120, 127, 129, 134, 178, 251, 259, 356  
 Papua New Guinea, 193, 198  
 parabolic, 115, 116, 117, 365  
 parallel simulation, 222  
 parameter, 13, 80, 158, 160, 188, 191, 192, 231, 232, 235, 289, 302, 303, 304, 311, 316, 335  
 Paris, 248, 384  
 partial differential equations, 365  
 particles, 229  
 partition, 311, 319, 321, 350, 360  
 passive, 13, 24, 37, 142, 254  
 pastoral, 55  
 pastures, 114  
 penalty, 299, 300, 304, 312, 363, 364  
 per capita, 106  
 performance, 139, 149, 150, 214  
 periodic, 137  
 permafrost, 185, 188, 189  
 permeability, viii, 2, 13, 14, 47, 57, 107  
 permit, 25, 148, 149, 163, 164  
 perturbation, 212  
 Peru, 178, 179, 373, 375  
 PGA, 98, 99  
 Philadelphia, 387  
 phone, 143  
 photographs, 58, 136, 153, 164, 169, 175, 187, 203  
 physics, 269  
 pitch, 149  
 planar, 18, 49  
 planetary, 168  
 planning, 3, 111, 119, 127, 128, 129, 172, 248, 250  
 plants, 106, 110  
 plastic, 45, 48, 232, 279  
 plasticity, 250, 268, 279, 353, 375, 383  
 platforms, 71, 152, 160  
 play, x, 133, 135, 195, 269

Pleistocene, vii, 1, 5, 6, 7, 9, 10, 11, 12, 13, 19, 22, 24, 25, 27, 28, 34, 37, 38, 39, 40, 45, 47, 50, 53, 62, 64, 65, 66, 178, 183, 185, 186, 193, 195, 254, 256  
 Pliocene, vii, 1, 6, 7, 12, 13, 41, 50, 52, 65, 71  
 Poisson, 369  
 polarization, 157  
 pollution, 108  
 polygenic, 10, 22, 45  
 polygons, 139  
 polynomial, 159, 319, 351  
 polynomial functions, 351  
 polynomials, 360  
 poor, 47, 48, 94, 190, 203  
 population, 50, 76, 77, 78, 90, 98, 100, 101, 106, 109, 159, 259  
 population density, 106  
 pore, ix, 47, 54, 58, 62, 75, 94, 100, 104, 105, 117, 135, 137, 226, 228, 229, 230, 231, 232, 233, 234, 235, 237, 241, 245, 246, 248, 268, 329  
 porous, 14  
 Portugal, 68  
 power, 87, 179  
 power lines, 87  
 power stations, 179  
 powers, 370  
 PPP, 143, 144  
 precipitation, 11, 13, 80, 83, 85, 86, 87, 93, 94, 101, 106, 107, 108, 111, 112, 116, 267  
 preconditioning, 294, 316  
 prediction, xi, 98, 102, 137, 152, 166, 174, 196, 212, 225, 227, 232, 242, 248, 267, 384  
 predisposing factors, 2, 39, 48, 51  
 preference, 179  
 preparedness, 134  
 pressure, 40, 47, 62, 75, 87, 94, 100, 135, 146, 205, 228, 230, 231, 232, 233, 234, 235, 239, 241, 245, 246, 279, 329, 365, 366, 370  
 prevention, viii, 74, 88, 100, 111, 127, 134  
 private, 86  
 probability, x, 133, 187  
 probability density function, 187  
 probability distribution, 187  
 production, 60, 100, 109, 119, 151  
 productivity, 55, 161  
 program, 129, 241  
 promote, 202  
 propagation, 7, 155, 160, 211, 212  
 property, 86, 127, 214, 277, 278, 280, 298, 299, 308, 341, 347, 350, 364  
 proportionality, 274  
 proposition, 68, 232  
 protection, 75, 111, 119, 127, 169, 170  
 public, 82, 86, 119  
 pulse, 149, 150  
 pulses, 149

**Q**

Quebec, 174

**R**

radar, 108, 151, 156, 157, 158, 159, 160, 165, 166, 167, 170, 172, 173, 175, 176  
 radiation, 148, 158  
 radio, 143, 161  
 radius, 7, 98, 140, 146, 205, 214, 289  
 rail, 159, 160  
 rain, 11, 81, 120, 175  
 rainfall, viii, ix, 11, 73, 74, 75, 78, 80, 81, 82, 83, 84, 85, 86, 87, 88, 90, 92, 93, 94, 95, 96, 97, 98, 100, 101, 103, 105, 107, 110, 111, 112, 114, 116, 119, 125, 128, 130, 135, 136, 137, 171, 186  
 range, vii, viii, x, 73, 74, 78, 87, 89, 90, 92, 93, 96, 99, 100, 133, 143, 145, 148, 149, 150, 152, 153, 155, 156, 157, 159, 160, 163, 183, 184, 187, 189, 191, 192, 193, 202, 205, 206, 207, 235, 253, 372, 373  
 rationality, 212  
 Rayleigh, 215  
 reading, 101, 138  
 real time, 137, 143, 150, 152, 162, 166  
 reality, 264, 368  
 reasoning, 125  
 reception, 158  
 recognition, xi, 2, 70, 172, 201  
 reconstruction, 150, 165, 168, 252, 260  
 recovery, 134  
 recreation, 172  
 recrystallization, 280  
 rectification, 139, 153, 154, 168  
 recurrence, 53, 107, 178, 179, 180, 183, 188, 189, 190, 191, 194, 198  
 reduction, 9, 20, 24, 26, 54, 76, 129, 151, 156, 164, 199, 253  
 redundancy, 135, 146  
 reference frame, 145, 146  
 reference system, 143, 145, 149, 154, 160  
 refining, 179  
 reflectivity, 150, 157, 159  
 refraction index, 140  
 refractive index, 147  
 regional, 3, 6, 9, 12, 13, 16, 65, 78, 95, 111, 113, 137, 151, 155, 166, 171, 178, 183, 187, 190, 191, 192, 193, 195, 196, 254, 260, 261  
 regression, 60, 78  
 regular, 7, 11, 28, 120, 137, 181, 206, 289, 293, 311, 314, 336, 347, 351, 359, 360, 362, 372  
 regulations, 100  
 relationship, 15, 18, 94, 188, 189, 190, 193, 198, 230, 232  
 relationships, 70, 131, 134, 155, 180, 188, 198, 230, 233, 235, 252

relaxation, 346, 348  
 reliability, 42, 205, 284, 368  
 remediation, ix, 106, 119, 120, 122, 124, 128  
 remodelling, 2, 48  
 remote sensing, 119, 128, 135, 142, 151, 152, 163, 166, 168, 180  
 repair, 117  
*repeatability*, 145, 146, 261  
 representative samples, 18  
 research, x, 3, 15, 26, 38, 40, 50, 100, 101, 102, 129, 177, 180, 194, 211, 248, 265  
 Research and Development, 68, 248  
 resection, x, 133, 137, 152, 153, 154, 164  
 reservoir, 31, 33, 36  
 reservoirs, 108, 110  
 residential, 78, 86, 96, 97, 100, 114, 118, 242  
 residential buildings, 100, 242  
 resistance, 226, 228, 229, 240, 241, 243, 244, 248  
 resolution, x, xi, 133, 136, 143, 149, 151, 152, 153, 155, 156, 159, 160, 162, 163, 164, 165, 166, 167, 171, 187, 191, 211, 212  
 resources, 107, 127, 128, 129  
 restitution, 152, 153  
 retention, 117, 130  
 returns, 150  
 rheology, 267, 268, 269, 270, 271, 276, 277, 278, 279, 280, 295, 305, 307, 321, 329, 330, 352, 353, 368, 383  
 rings, 138  
 risk, viii, x, 3, 15, 16, 36, 40, 42, 67, 73, 74, 90, 92, 98, 100, 119, 127, 128, 131, 133, 134, 135, 137, 145, 161, 162, 166, 171, 178, 179, 180, 183, 195, 196, 199, 259, 294  
 risk assessment, 166  
 risk management, 134, 161, 162, 166  
 risks, 100, 102, 269, 383  
 rivers, 10, 26, 78, 81, 107, 108, 109, 110, 139, 140, 183, 255, 267, 354, 384  
 roadmap, 174  
 robbery, 145  
 robotic, 137, 145, 146, 164  
 robustness, 146  
 rocky, 6, 15, 29, 41, 47, 147  
 rods, 164  
 rotations, 24, 25, 288  
 roughness, 150, 187, 195, 204, 273  
 runoff, ix, 105, 107, 112  
 rural, 47, 54, 55, 56, 58, 59, 60  
 Russia, x, 177, 178, 180, 181, 183, 192, 194, 195, 198  
 Russian, x, 142, 177, 178, 179, 181, 182, 183, 188, 189, 193, 195, 196, 197, 198, 199  
 Russian Academy of Sciences, 177, 179, 198

**S**

safety, 74, 117, 124, 127, 241  
 sample, 20, 40, 58, 59, 206, 231, 233, 236, 237

- sampling, 136, 162, 164, 165  
sand, 78, 108, 109, 235, 243, 249  
sandstones, 6, 18, 41, 78  
SAR, 70, 156, 157, 158, 159, 163, 165, 167, 168,  
169, 170, 171, 173, 174, 175  
satellite, 142, 143, 144, 146, 151, 152, 155, 156, 157,  
158, 159, 163, 164, 165, 168, 169, 171, 172, 174,  
187  
satellite imagery, 151, 152  
saturation, 243, 267  
scalar, 279, 282, 284, 286, 287, 289, 290, 322, 355  
scaling, 153  
Schmid, 384  
school, 78, 106  
scientific community, 16  
scientific knowledge, 18  
scientists, 179  
sea floor, 373  
sea level, 11, 53, 54, 62, 69, 87, 184, 202, 206  
seasonal variations, 135  
security, 75, 268, 353, 375, 381, 382  
sediment, 7, 79, 109, 110, 117, 119, 128  
sedimentation, 9, 65, 68, 110, 267  
sediments, 6, 7, 11, 14, 38, 40, 45, 53, 71, 78, 104,  
109, 110, 182, 183, 185, 186, 194, 196  
segmentation, 260  
seismic, viii, x, xi, xii, 2, 3, 7, 13, 19, 34, 36, 46, 53,  
70, 79, 98, 99, 102, 104, 177, 178, 179, 180, 183,  
185, 187, 189, 191, 194, 195, 196, 211, 212, 213,  
214, 216, 222, 225, 226, 227, 229, 241, 242, 246,  
247, 248, 249, 253, 261, 263, 264, 295, 373, 374  
semiarid, 193, 197  
sensing, 119, 128, 135, 142, 151, 152, 163, 166, 168,  
173, 180  
sensors, 135, 136, 137, 142, 143, 145, 151, 155, 156,  
159, 161, 165, 166  
separation, 157, 158, 206, 229, 230, 246  
series, 135, 136, 140, 143, 145, 146, 151, 154, 158,  
159, 163, 165, 242, 254, 257  
services, 143  
settlements, viii, 7, 55, 57, 60, 74, 81, 90, 106, 109  
sewage, 47  
shape, 10, 13, 17, 23, 24, 26, 27, 29, 31, 64, 117,  
127, 142, 149, 152, 205, 232, 294, 323, 347, 374  
shear, ix, 2, 19, 20, 24, 25, 26, 31, 34, 37, 41, 45, 46,  
47, 58, 87, 105, 112, 124, 229, 230, 231, 232, 233,  
234, 235, 236, 237, 238, 239, 241, 243, 246, 250,  
263, 264, 265, 266, 279, 295  
shear strength, 230, 235, 237  
shock, 180, 191, 192  
shocks, 2, 7, 8, 178, 179, 180, 189, 191, 194, 264,  
267, 268, 269, 294, 295, 375  
short period, 82, 85  
shortage, 179, 194  
short-term, 137  
signals, 143, 147, 156  
signs, 23  
SII, 279  
similarity, 93  
simulation, xi, 211, 212, 214, 215, 216, 222, 268,  
269, 283, 295, 305, 353, 367, 368, 370, 381  
simulations, 212, 242  
Singapore, 385  
singular, 212, 306  
singularities, 306  
sites, 18, 60, 61, 79, 96, 100, 162, 242, 373  
skills, 151  
slaves, 157  
Slovenia, viii, ix, 105, 106, 107, 108, 109, 110, 111,  
112, 113, 114, 115, 117, 118, 119, 120, 121, 123,  
125, 127, 128, 129, 130, 131  
smoothness, 283, 296, 305  
Sobolev space, 282, 283, 286, 303, 355  
software, 111, 127, 165, 188  
soil, x, xi, 12, 47, 55, 57, 75, 79, 94, 102, 107, 108,  
109, 114, 120, 147, 151, 158, 177, 178, 201, 202,  
212, 214, 215, 216, 217, 218, 219, 225, 226, 229,  
230, 231, 232, 233, 235, 236, 241, 242, 243, 249,  
250, 267, 329, 367, 368, 369, 370, 371  
soil erosion, 107  
soils, 57, 109, 120, 127, 136, 194, 229, 230, 232,  
234, 248, 264, 265, 266, 267  
solidification, 280  
solutions, 68, 119, 128, 144, 278, 289, 290, 291, 295,  
301, 303, 305, 306, 334, 346, 347, 360  
South Africa, 172, 174  
Spain, 67, 167  
spatial, 14, 16, 18, 94, 109, 127, 134, 135, 136, 137,  
143, 151, 152, 154, 156, 157, 163, 164, 165, 166,  
175, 211, 212, 213, 270, 278, 294, 295, 354, 360,  
363, 368  
spatial heterogeneity, 135, 136  
species, 106  
specific heat, 271, 331  
spectrum, 215, 220, 221, 268  
speed, 135, 149, 231, 232, 233  
speed of light, 149  
sporadic, 26, 58  
springs, 13, 22, 37, 40, 42, 47, 50, 57, 107, 124  
SSS, 84, 85  
St. Louis, 249  
stability, vii, viii, xi, 29, 48, 51, 57, 62, 67, 74, 75,  
94, 119, 124, 128, 142, 145, 146, 147, 165, 202,  
205, 225, 226, 227, 229, 241, 243, 247, 249, 264,  
267, 268, 280, 295, 328, 329, 353, 354, 370, 382,  
384  
stabilization, 51, 120, 124  
stabilize, 119, 120, 128  
stages, 18, 136, 166, 231, 234, 235  
stakeholders, 135  
standard deviation, 187, 190  
statistical analysis, 107, 116, 159  
statistics, 130  
steel, 76, 148  
stiffness, 213, 232, 267, 292, 294, 315, 316, 317,  
324, 328, 348, 352  
stochastic, 213, 223  
storage, 135, 145, 161, 203

storms, 11, 96, 129, 269, 383  
 strain, 174, 212, 229, 232, 236, 267, 271, 278, 279, 286, 297, 307  
 strains, 249  
 strategic, 106, 166  
 strategies, viii, 74, 88, 149, 153  
 stratification, 5, 12, 13, 20, 31, 37, 48  
 streams, 62, 83, 94, 108, 252, 267  
 strength, xi, 86, 201, 202, 205, 206, 207, 208, 209, 225, 226, 228, 229, 230, 231, 232, 234, 235, 236, 237, 241, 242, 243, 247, 264, 267, 295  
 stress, ix, 14, 19, 34, 62, 69, 105, 112, 135, 199, 204, 229, 230, 231, 232, 233, 234, 235, 237, 238, 239, 241, 242, 253, 260, 264, 267, 269, 270, 273, 274, 275, 276, 277, 278, 279, 280, 281, 284, 286, 291, 295, 296, 306, 307, 314, 322, 329, 330, 331, 346, 354, 372, 374  
 striae, 31  
 structural changes, 175  
 structural characteristics, 9  
 STRUCTURE, 211  
 structuring, 6, 11, 12  
 students, 384  
 subjective, 153  
 substitution, 5  
 suburbs, 86  
 suffering, 76  
 summer, 11, 80, 111, 122, 125  
 superposition, 258  
 supply, 24, 119, 150  
 surface area, 183, 188, 193  
 surface layer, 109, 212  
 surface roughness, 150  
 surface water, 94, 100, 107, 108, 120, 125  
 surface wave, 187  
 susceptibility, 109, 110, 130, 137  
 swamps, 384  
 swarms, 71  
 Sweden, 389  
 Switzerland, 130  
 symmetry, 139, 271, 273, 278, 281, 285, 286, 330, 331, 333, 354  
 symptoms, 269, 383  
 synthesis, xii, 3, 176, 251  
 systems, vii, 1, 3, 13, 14, 15, 27, 31, 34, 40, 45, 69, 76, 94, 95, 119, 128, 135, 142, 146, 150, 153, 154, 156, 157, 161, 163, 166, 173, 174, 252, 253, 255, 268, 302, 327, 352, 367

## T

Taiwan, 106, 107, 129, 130  
 targets, 158, 159, 161  
 technology, 125, 164, 165, 169, 170  
 telephone, 87  
 temperature, 80, 81, 135, 146, 148, 151, 159, 272, 273, 276, 277, 278, 281, 284, 286, 354, 368, 384  
 temporal, x, 94, 134, 135, 136, 137, 152, 157, 158, 159, 162, 163, 164, 165, 168, 175  
 tensile, 205, 264  
 tensile strength, 205  
 tension, 39, 264, 265, 370, 373, 374  
 terraces, 11, 27, 38, 55, 57, 69, 78, 257  
 territorial, 3, 58  
 territory, vii, 1, 3, 9, 16, 19, 50, 60, 106, 107, 108, 109, 256  
 testimony, 7  
 Texas, 87, 98, 99, 101, 102, 103, 104  
 Thai, 209  
 theory, 104, 153, 179, 212, 216, 229, 232, 261, 267, 269, 270, 273, 284, 302, 309, 347, 353, 373, 375  
 thermal expansion, 271, 280, 286, 331  
 thermodynamic, 272  
 thermodynamics, 273  
 Thessaloniki, 168  
 third order, 10, 39  
 threat, 109, 110, 131, 202  
 three-dimensional, xi, 137, 145, 147, 150, 152, 153, 211, 264  
 threshold, 57, 94, 99, 116, 163, 187, 268, 279, 353, 375, 383  
 thresholds, 94, 95, 96, 100, 102, 137  
 time, x, 2, 11, 12, 17, 29, 45, 55, 58, 76, 85, 88, 92, 97, 106, 120, 125, 128, 134, 137, 139, 143, 144, 146, 149, 150, 151, 152, 154, 156, 157, 158, 159, 160, 161, 163, 164, 165, 166, 174, 177, 178, 180, 187, 188, 189, 190, 191, 193, 194, 195, 203, 204, 205, 206, 214, 215, 219, 225, 228, 241, 242, 243, 245, 246, 252, 257, 259, 267, 270, 271, 272, 273, 276, 282, 283, 295, 296, 298, 299, 305, 306, 307, 308, 309, 310, 311, 312, 314, 318, 319, 320, 321, 323, 325, 326, 328, 329, 346, 348, 352, 356, 359, 361, 365, 373, 374, 376, 377  
 time constraints, 203  
 time increment, 215, 242  
 time resolution, 165  
 time series, 143, 154  
 timing, x, 134, 135, 142, 145, 161, 177, 180, 194  
 tin, 270  
 Tokyo, 171, 211  
 topographic, viii, x, xii, 9, 18, 22, 29, 36, 42, 47, 73, 80, 90, 133, 136, 137, 142, 145, 149, 150, 152, 157, 158, 163, 164, 165, 171, 172, 188, 242, 246, 251, 252, 253, 256, 257, 258  
 topological, 282  
 total costs, 128  
 total energy, 183  
 tracking, 146, 151, 163  
 traction, 48, 309  
 trade, 80  
 traffic, 106, 109  
 training, 111  
 trajectory, 243  
 transcription, 139  
 transfer, 161, 329, 368



transformation, 15, 54, 55, 62, 153, 188, 228, 241, 287, 293, 311, 321, 323, 324  
transformations, 61, 154  
transgression, 6  
transition, 5, 78, 182, 183, 184, 185, 276, 295  
translation, 48  
translational, 20, 27, 29, 34, 40, 41, 47, 48, 51, 90, 92, 96, 98, 100, 114, 125, 138, 174  
transmission, 145, 156, 158, 161  
transparent, 215  
transport, 2, 24, 37  
transport phenomena, 2  
trees, 150  
trend, 17, 18, 31, 34, 42, 58, 79, 135, 253, 256  
trial, 204  
triangulation, x, 133, 137, 149, 164, 289, 292, 361  
Triassic, 69  
triggers, vii, 178, 180, 189  
tropical storms, 80, 84, 85, 103  
tsunami, 202, 267  
Turkey, 167, 172, 249  
two-dimensional, 114, 116, 128, 152, 212, 222  
typhoon, 129  
typology, 255

## U

Umbria, 7, 66  
uncertainty, 2, 159  
UNESCO, 65  
uniform, 14, 241, 345, 360, 363  
United Kingdom, 101, 104, 168, 201  
United Nations, 166, 323  
United States, 70, 142, 201  
universal law, 195  
urban areas, 102, 109, 158, 179  
urban centers, 76, 100  
urban settlement, 55  
urbanization, 15, 62, 88, 93, 98, 100  
USSR, 179, 196, 197, 198  
Utah, 234

## V

validation, x, 133, 170, 205  
validity, 96, 214, 270  
values, 11, 12, 13, 14, 17, 18, 22, 24, 36, 46, 47, 48, 58, 59, 62, 85, 94, 98, 99, 107, 114, 122, 127, 157, 192, 196, 202, 203, 204, 205, 206, 207, 208, 215, 231, 233, 234, 235, 237, 238, 241, 242, 243, 244, 246, 254, 267, 278, 282, 289, 296, 347, 348, 349, 369, 383  
vandalism, 145  
variability, 11, 80, 94, 109, 134, 204  
variable, viii, 18, 22, 45, 48, 73, 204, 208, 226, 248, 260, 277, 278, 283, 293, 298, 308, 312, 352, 354, 363

variables, 94, 135, 283, 312  
variance, 155  
variance-covariance matrix, 138, 143  
variation, 213, 243  
vector, 213, 216, 257, 270, 271, 272, 281, 284, 286, 287, 288, 289, 290, 292, 293, 294, 296, 298, 299, 306, 307, 314, 315, 316, 317, 320, 324, 327, 347, 349, 374  
vegetation, ix, 34, 48, 55, 75, 94, 100, 105, 108, 110, 150, 151, 161, 163, 165, 267  
vehicles, 368  
velocity, 12, 48, 86, 114, 115, 135, 142, 146, 151, 157, 158, 160, 161, 162, 163, 164, 168, 174, 215, 226, 227, 241, 245, 246, 270, 271, 273, 278, 281, 296, 306, 345, 354, 373, 376, 377, 378, 379, 380, 381, 384  
vibration, 88, 100  
victims, 16  
Victoria, 98  
village, ix, 29, 34, 42, 50, 51, 63, 67, 105, 111, 112, 114, 116, 117, 118, 119, 124, 129, 252, 257  
vineyard, 60, 61  
violent, 100  
viscoelastic functions, 346  
viscosity, 279, 353, 375, 383  
visible, 2, 9, 25, 29, 34, 37, 40, 42, 163  
volcanic activity, 165

## W

warning systems, 94, 95, 119, 128, 166  
water, ix, 10, 14, 20, 29, 35, 36, 40, 45, 46, 47, 50, 51, 57, 60, 92, 94, 105, 106, 107, 108, 112, 117, 122, 124, 125, 127, 128, 193, 241, 242, 243, 255, 267, 268, 269, 329, 352, 353, 354, 375, 382, 383, 384  
water resources, 107  
water table, 14, 46, 241, 242, 243  
watershed, 25, 130, 185  
watersheds, 27, 40, 53, 107, 131, 185  
wave propagation, xi, 211, 212, 214, 222  
wavelengths, 158, 159  
wavelet, 172  
weakness, 207, 264  
weathering, 12, 14, 20, 62, 89, 109  
web, 85  
welding, 36  
wells, 120, 122, 123, 124, 125, 126, 127, 128  
wetting, 264, 295  
wind, 80, 85, 87, 135  
wine, 60  
winter, 80, 120  
wintertime, 80, 107  
withdrawal, 26, 28, 42, 45, 51, 62  
woods, 55, 56  
workplace, 269, 384

**X**

X-axis, 160

**Z**

zoning, 179, 180, 194, 195, 196

**Y**

Y-axis, 160  
yield, 136, 150, 159, 163, 171, 278, 279